Integral modelling of jets of variable composition in generalised crossflows

Wilson, Michael

Award date:
1986

Awarding institution:
University of Bath

INTEGRAL MODELLING OF JETS OF VARIABLE COMPOSITION IN GENERALISED CROSSFLOWS

submitted by Michael Wilson

for the degree of Ph.D

of the University of Bath

1986

ProQuest LLC
789 East Eisenhower Parkway
P.O. Box 1346
Ann Arbor, MI 48106-1346

ACKNOWLEDGEMENTS

I would like to thank the following:

Professor Frank Wallace for his patient guidance and support for the modelling programme, and for his invaluable advice on many matters.

Professor Dan Adler for his inspiring assistance in identifying the potential of the analysis and its principal requirements.

Dr. Julian Packer for his enlightening and stimulating supervision in the initial stages of the work, and for his continuing co-operation and interest in its progress.

Mrs. Hazel Ford for her dilligent typing of Part I.

SUMMARY

The development and performance of a comprehensive computer model for the prediction of round, axisymmetric or deflected turbulent jets and sprays is described.

From a review of experimental and theoretical studies, the basis for a detailed integral analysis of jet mixing is established. The subsequent formulation includes momentum, heat and mass transfer, and computer predictions are enhanced with the use, in modified form, of an existing sub-model for jet cross-section shape and property profile distortion due to crossflow. The length of the potential core is determined in the course of the numerical solution, and the transitional region of developing flow beyond the end of the core is represented. The faster rate of diffusion of mass relative to momentum is modeled semi-empirically.

Numerical results are assessed against a wide range of data concerning jets of uniform and variable composition, particular attention being paid to the method of determination of empirical coefficients. Diesel spray predictions illustrate the intended application within a multi-zone combustion model, developed concurrently.

CONTENTS

CONTENTS cont'd

CONTENTS cont'd

CONTENTS cont'd

CONTENTS cont'd

CONTENTS cont'd

PART I

BASIC ANALYSIS

CHAPTER 1

MODELLING OF DIESEL SPRAYS IN SWIRL

CHAPTER 1 - MODELLING OF DIESEL SPRAYS IN SWIRL

1.1 Introduction to the Thesis Structure and Material

Detailed fuel-air mixing investigations at Bath University are being carried out both in terms of experiment and analysis. Experimental work began with hydraulic models permitting a ready interpretation of the effects of swirl on mixing; the subsequent construction of a novel, high swirl combustion bomb has allowed very detailed studies of spray formation and combustion, under conditions similar to those in direct injection Diesel engines.

The experimental work has been accompanied by the implementation of theoretical models simulating the injection and mixing process with air swirl. The present work has been concerned with the re-examination of the fundamental mathematical analysis underlying the modelling work, leading to the construction of a model capable of quantitative predictions for assessment against a variety of experimental data; earlier models have been shown to give reasonable qualitative predictions of the mixing process. The opportunity has also been taken to investigate how far a simplified analysis of the governing flow equations may be developed in order to compete in terms of detail with more direct and time-consuming numerical solution schemes, developed elsewhere. It is envisaged that the mixing model will be used in conjunction with mutli-zone chemical kinetic models (under development at Bath) for the simulation of fuel combustion processes.

1.2 Fuel-Air Mixing Requirements for Combustion in the High Swirl D.I. Diesel Engine

The Direct Injection (D.I.) Diesel engine is now under intense development, directed towards its use as a power source for passenger cars, in view of its substantially improved fuel economy compared with, for example, equivalent spark ignition engines. The development procedure must recognise current and future legislation, and address the problems of relatively high exhaust pollutant emission and combustion noise, associated with this type of engine.

These problems may be overcome, in great measure, by the proper control of fuel-air mixing in the combustion chamber. The introduction of bulk motion, such as swirl, to the cylinder charge, enhances the mixing process and the effectiveness of the subsequent combustion. Combustion chamber geometry, the intake system and piston movement all influence the generation of air motion in a particular engine, and a careful matching of fuel injection to air flow is essential, in order to bring the largest possible proportion of air into contact with fuel during combustion.

Combustion in a Diesel engine comprises compression ignition of a heterogeneous distribution of fuel and air, with subsequent continuous mixing throughout the period of burning (1). The history of the combustion process may be traced by examination of the burning rate (energy release rate) versus crank angle (time) diagram, as illustrated in Fig. 1.1. Four distinct stages are identified.

The first stage is the ignition delay period, determined by the time which is necessary for the preparation of a stoichometric, combustible mixture of fuel and air after the start of injection, and hence by the injection characteristics (fuel quantity and rate of injection, the spray pattern according to the number of nozzles, the injection pressure and droplet sizes) and the conditions in the chamber (air temperature and pressure, air motion and turbulence levels, engine speed) (2,3). A negative net heat release during this period (Fig. 1.1) is due to heat absorption by the evaporating fuel (Section 1.3). The length of the ignition delay influences the rapidity of the subsequent combustion event.

The second stage of combustion is instigated by self-ignition of suitably prepared regions of fuel vapour and air within the spray (Fig.1.1): the onset of combustion is associated with a rapid rise in pressure and the high 'pre-mixed burning' rate continues until all the prepared fuel has been consumed. The rate of burning is controlled by reaction kinetics : longer ignition delays result in relatively larger proportions of prepared fuel, and hence higher burning rates and more violent combustion.

The third stage in the process (Fig. 1.1) represents the establishment of diffusion-controlled burning : the fuel jet burns with a luminous, highly turbulent diffusion flame. Grigg and Syed (4) suggested that the mixing rate in the fuel jet controls the rate of heat release during this stage.

In the final stage, the combustion tail (Fig. 1.1), the remaining fuel burns at a very low rate, which may be temperature controlled (5). For a typical engine at 2,000 rev/min., the entire event occupies less than 3 ms.

The combustion chamber geometry, fuel injection pattern and spray development all affect the shape of the burning rate diagram, while the general character of the diagram is preserved. Henein (6) considered the understanding of the dynamics of the fuel jet an important base for Diesel engine combustion models, and a qualitative description of fuel injection and mixing, to the point of combustion, is now undertaken.

1.3 Physical Description of the Fuel Spray

Fuel is introduced into the high pressure (about 60 bar), high temperature (about 650K) air of the combustion chamber, the volume contained by the cylinder walls and the piston surface near top dead centre, in the form of high pressure jets (injection pressure 200-600 bar) from a multi-hole injector. The diameter of each nozzle is of the order of 0.3 mm.

The character of the spray is established by the break-up of the inherently unstable liquid jet. The distance to which the liquid jet persists, and the size of the droplets formed upon disintegration, reduces with increasing injection velocity, air turbulence and chamber air density. Under the supercritical conditions of temperature and pressure extant in the D.I. Diesel engine, with air swirl and high injection pressure, the liquid jet is atomised very near the nozzle upon injection into a mist of very fine droplets (of the order of 10 - 30 μm (6,7)). Vaporisation of fuel prior to this disintegration is considered to be negligible (8). The spray begins to entrain air and the relative velocity of the small droplets rapidly decays (7).

In contact with the air under high pressure, and at a temperature beyond the ignition point of the fuel, a thin film of vapour immediately develops on each droplet surface, enclosing a liquid core : heat energy from the air near the droplet is transferred to the liquid surface to accomplish the evaporation. In the regions of combustible fuel-air mixtures, ignition occurs when the temperature of the fuel vapour and local air layers rises (by heat transfer from the neighbouring air bulk) to the ignition temperature. Part of the heat from combustion serves to evaporate the droplet's liquid core, and the burning rate then depends upon the supply of fresh air from without the burning region (9,10).

Following Way (11), the physical preparation processes described above may be summarised as :-

a) atomisation of fuel into droplets
b) heat transfer for droplet evaporation
c) entrainment of air by the fuel spray
d) micro-mixing of fuel and air into a combustible mixture

1.4 Modelling Methods

1.4.1 Introduction

Realistic modelling of fluid motion and fuel burning has obvious advantages in terms of hastening and simplifying engine design, development and performance studies. According to the preceding discussions, three processes may be identified for modelling consideration :-

1. The detail of the air motion in a chamber of particular geometry.
2. The formation of the evaporating fuel spray (the physical processes a) - d) above)
3. The combustion reactions and subsequent mixing.

The three processes, of course, are intimately related (12).

Measurements of the air motion in engine combustion chambers have been reported by many workers (13,14,15), and against the resource of data, detailed predictive schemes may be assessed (Section 1.4.2). In contrast, observations of spray formation and burning are more usually made using specially designed rigs and bombs, in order to simplify air motion and its control (with a fixed volume, rotating cylindrical chamber, for example), and to permit relatively easy access for instrumentation. Such work has been described by Vara Prasad and Subir Kar (16,17), Elkotb and Rafat (18), Rife and Heywood (7) (structure of sprays for quiescent and swirling cases at constant temperature), Adler and Lyn (19), Lakshminarayan and Dent (20) (evaporation and interaction with swirl) and others. The measurements obtained provide the necessary 'bench mark' data for the assessment of theoretical models (Section 1.4.3), and many of these studies are referred to again later in this thesis.

1.4.2 Air Motion

The most significant modelling work in this area concerns the application of finite-difference numerical solution schemes, for the prediction of the flow of fluids, to the engine situation. The most sophisticated 'in-cylinder' computer software is probably that from the continuing investigations at Imperial College, under Gosman (21,22,23); many other studies are cited by Gosman and Harvey (23). Matsuoka (15) et al have

reported a combined experimental/theoretical study.

Finite-difference schemes seek to solve the partial differential equations for conservation of mass, momentum and energy, in three space dimensions and in time, and are often referred to as multi-dimensional models. An introductory description of the general procedure is given later (Appendix A). The solution of the discretized equations is carried out on a finite difference grid, which, in the case of engine computations, may have the appearance of that in Fig. 1.2a reproduced from Gosman and Harvey (23) (axial symmetry assumed), or Fig. 1.2b from Brandstätter (24) et al. For the accurate representation of irregular boundaries, the equations are solved in a system of general, curvilinear, orthogonal co-ordinates (23). In order to account for valve and piston movement, a flexible (time-dependent) grid is constructed : for Fig.1.2a, that part of the grid lying within the piston bowl translates with it, while between the top of the bowl and the cylinder head, the mesh expands and contracts with the piston motion. The generation of the grid is thus itself a considerable computational task, and a particularly fine resolution is necessary in order to reduce numerical errors and properly represent the finer detail of the flow (near the inlet valve, for example) : Brandstätter (24) et al used a total of more than 16,000 grid cells.

Fields of values for all dependent variables must be specified as initial conditions for the solution procedure (velocity and temperature of the chamber air at every finite-difference grid-cell location, and the turbulence intensity there; also the velocity profile within the valve gap in some work), and these are often inferred from experiment or from the results of previous calculations (23,24). The numerical solution yields equally detailed descriptions of the spatial and temporal distributions of the flow properties (15,23,25) and reveals very complex, three-dimensional flowfields; indeed Brandstätter (24) et al report the difficulties in interpreting the development of the flow and the need for improved post-processing facilities (high-resolution colour graphics, use of video etc.)

The finite difference studies offer the possibility of resolving the

complicated, three-dimensional, recirculating flow structures occurring in engine chambers to sufficient accuracy for most engineering problems, with a detail unobtainable by other means. However, the schemes are not yet fully established, even though well advanced: computer times are substantial, some doubts persist concerning the modelling of turbulence, and finite-difference grids must apparently be very fine in order to suppress numerical errors. Full reliance cannot yet be placed on quantitative results.

1.4.3 Formation of the Fuel Spray

The incorporation of fuel injection and spray formation into in-cylinder finite-difference schemes is not as far advanced as the gas motion predictions (see below), and rival approaches to spray modelling are reported in the literature. A review of such work is presented.

In the Gosman code mentioned above (23), known as RPM, the spray is represented by a statistical sample of discrete, different sized droplets, introduced at the injector and tracked by solving the equations of motion for their position and velocity vectors, being coupled to the predicted air motion through the local gas velocity vector. Further conservation equations must be solved for changes in droplet mass and temperature : droplet drag, evaporation rate and heat transfer coefficients must be supplied (23). The mass, momentum and energy exchanges with the gas influence the air motion computations. A different representation of injection has recently been described by Bassoli (25) et al.

The combustion simulation reported by Bassoli (25) et al required about 20 cpu hours computer run time on a VAX 780 (this was for a 2-d, axial symmetry calculation), with about one third of the time being required for mixing prior to combustion. In view of the very great computational demands implied by these schemes, and the continuing development of the method, it is reasonable (at the time of writing) to consider a less fundamental approach to the modelling of components in the combustion process.

The formulation of simplified, quasi-steady equations for spray

formation, air entrainment, combustion and heat transfer phenomena is known as phenomenological modelling. Controlling parameters in the simplified equations are derived from engine design and operating variables. A synthesis of the equations describing the different processes, together with mass and energy conservation conditions, yields predictions of global characteristics such as instantaneous air entrainment and mixing rates, cylinder pressure, heat release rate etc. without the detailed spatial property variations afforded by the finite-difference schemes. The most successful phenomenological models consider the prediction of entrainment and mixing in the fuel spray to be the proper base for a combustion model (7) (Whitehouse and Abughres (26) (1975), Chiu, Shahed and Lyn (27) (1976), Meguerdichian and Watson (5) (1978), Dent and Mehta (28) (1981)).

Several approaches to the modelling of the fuel spray have been considered in the literature. The calculation of the histories of single drops vaporising in a gas stream was discussed by El Wakil (8) et al, Borman and Johnson (9) and others. The superposition of such calculations for drops of different diameters, determined from assumed droplet size distributions at the nozzle (6), gives an account of the spray mixing region. Interaction between droplets could be partially accounted for by using the Sauter mean diameter (6) in the heat and mass transfer calculations (29). These models generally suffer from too great a dependence upon empirical laws and experimental correlations (10), especially in their prospective extension to combustion.

Greater success has resulted from the application of continuum mechanics to the problem of spray development. Melton (30), Newman and Brzustowski (31) and Rife and Heywood (7) all worked in terms of the liquid spray, atomised near the nozzle, as a fog of very small droplets carried along with the velocity of the entrained air : under these conditions, it is possible to resort either to the classical, single-phase jet theory of Abramovich (32) (see later) or its two-phase spray extension.

Newman and Brzustowski (31) found that a liquid jet near the thermodynamic critical region could be adequately treated as a dense, single phase jet. The analysis can be further simplified if the dense jet is

then replaced by an air-air jet, with momentum equivalent to the fuel momentum leaving the injector nozzle. This approach has been adopted in previous work at Bath University, in connection with experiments on the effect of swirl on jet mixing using a water rig (33,34,35): the most recent work in this area is that of Maniatacos (36).

A more direct and flexible approach than this is to adapt the classical turbulent jet theory to two-phase sprays : Abramovich (32) presented such an analysis in the case of an axisymmetric air jet contaminated with small, dense particles moving at the speed of the air flow. Rife and Heywood (7) used this model to obtain good agreement with their own data for a quiescent, isothermal Diesel spray. Adler and Lyn (19) (1971), also on this basis, described a highly ambitious continuum mechanics treatment for a spray evaporating in a gaseous swirl. The model comprised :-

1. An evaporation function, describing the instantaneous, mean state of vaporisation in the spray, using the droplet history theory of El Wakil (8) et al with the Sauter mean diameter included from Bose and Pei (29) (see above).

2. A spray analysis, in which the usual boundary layer assumptions were imposed (see later) in order to make use of the powerful integral method (32). Conservation equations for momentum, heat content and injected material were written for the mixing region. Entrainment into the spray was accounted for by a width-growth law for the mixing region, modified from Abramovich (32).

3. A differential equation for the jet centreline, obtained by balancing the gas force exerted by the deflecting flow (swirl) and the centrifugal force due to jet curvature.

Although this model demonstrated the considerable potential of the integral method in its application to fuel sprays, still its implementation and use by Packer (35) identified the limitations and fundamental inaccuracy in the spray analysis, for lower rates of air entrainment were predicted as the level of swirl was increased. This deficiency may be traced directly to the derived width-growth law (19), which includes no facility for the representation of enhanced mixing (so entrainment) due to a crossflow.

The study of crossflow-enhanced mixing in single-phase (air-air) jets, and its formulation for integral modelling, has been the subject of much discussion in the literature in the period since the appearance of the Adler and Lyn work (1971). This later work provides the foundation for the analysis in Chapter 4. The modelling of deflected air jets has stemmed largely from the observations of Platten and Keffer (37,38), and later Kamotami and Greber (39), that the component crossflow velocities in the direction of, and normal to, the local jet trajectory independently control the entrainment rate (the 'enhanced mixing coefficient', an empirical parameter in integral models which governs the latter contribution to entrainment, is the principal topic for discussion later in this thesis).

Extensions to two-phase Diesel sprays have been attempted by Rife and Heywood (7), Sinnamon (40) et al and Mehta and Gupta (41), for isothermal mixing in swirl, with considerable success; this work, for example, offers the prospect of an improved spray analysis for use in the model of Adler and Lyn (19). The spray is subjected to a relatively simple crossflow type deduced from measurements of air motion in engines, usually a variant of solid-body rotation (41).

1.4.4 Combustion Modelling

Since combustion is not a consideration in the modelling work to be described later, only a brief review of more recent work is given here. A basis is established for the detailed spray mixing analysis subsequently undertaken.

The in-cylinder calculations of Gosman and Harvey (23) demonstrate the ability of the finite-difference schemes to produce qualitatively correct behaviour in terms of, for example, ignition delay, rapid premixed combustion and the transition to diffusion burning. The combustion model incorporates :-

a) an Arrhenius-type expression for fuel consumption rate in the chemically controlled premixed stage.

b) a burning rate equation for the diffusion-burning stage, relating fuel consumption to the predicted turbulence levels,

and both require tuning of empirical coefficients. Quantitative

assessment of the work is precluded by the absence of the necessary in-cylinder experimental data.

The phenomenological combustion models of Chiu, Shahed and Lyn (27) and Dent and Mehta (28) merit attention here. Both models are based upon integral formulations for the mixing of the spray, after Abramovich (32).

Chiu, Shahed and Lyn (27) employed an expression, correlated from available data, for the penetration with time of the spray tip in swirl (the motion of the tail, after the end of injection, was similarly accounted for), and a largely empirical formulation for jet spread dependent upon injection conditions (including swirl rate). The flow structure (velocity, temperature and concentration distributions) within this envelope was obtained by an analysis of the spray as a turbulent vapour jet, with equivalent momentum leaving the nozzle. At the instant of ignition, several zones of equal mass were imposed upon the computed spray as shown in Fig. 1.3.(the four zones shown may be further sub-divided), and burning, considered to occur in zones with equivalence ratios lying between rich and lean limits, continued at a rate determined by the predicted rate of entrainment of air. Combustion effects upon the spray model were not included directly. This model has been implemented, modified and extended at Bath University by White (42).

The combustion model of Dent and Mehta (28) followed from a spray analysis including the effects of droplet vaporisation. The model was restricted to quiescent chamber conditions, and tip penetration again evaluated using an empirical correlation. Fuel droplet size across the spray was distributed empirically around an instantaneous Sauter mean diameter; vaporisation rates were evaluated from mass-transfer considerations, and enhancement of vaporisation during combustion was accounted for. These considerations represent an extension to the droplet evaporation model of Adler and Lyn (19). The spray inner structure was determined from the two-phase spray theory of Abramovich (32) for undeflected jets. Ignition delay was computed by correlation from available data, and again combustion was considered to occur in zones of equal mass satisfying fuel

vapour/air ratio limits of flammability. Predictions of cylinder pressure generally compared well with experimental data (28).

The transient nature of the injection event in these models is partly accounted for by the use of correlations for spray tip penetration. However, such an empirical base precludes generality with respect to air motion etc. The objective of the present study is the construction of an integral spray-mixing model for the prediction of the trajectory and inner structure of the spray in a prescribed cross-flow. As mentioned in Section 1.4.3, models for isothermal sprays have already been presented (7,40,41): important entrainment and deflection coefficients appearing in the models (Chapter 4), however, are set according to very limited Diesel spray data, and their values vary between the different studies. In view of the primary assumption that the spray can be treated essentially as a dense, single phase jet (Section 1.4.3), the following approach is adopted here :-

1. The classical treatment of the steady, axisymmetric, constant density jet (32) is reproduced in order to establish the model - Chapter 3.

2. The model is extended to the deflected jet at constant density, according to the entrainment observations of Platten and Keffer (37) (Section 1.4.3) - Chapter 4.

3. The effects of temperature and composition variation are considered - Chapter 5.

4. The empirical coefficients in the model are set and assessed by recourse to the considerable available data concerning single phase jets - Chapter 7.

5. The model is applied to Diesel-type sprays. The validity of the single-phase, steady, dense jet analogy (Section 1.4.3) is considered - Chapter 8.

The prospects for the inclusion of a droplet evaporation model (19,28)

and use in connection with a multi-zone combustion model (42) are also discussed in Chapter 8.

For simplicity, the analysis is restricted to the spray prior to impingement on the chamber wall. The development of wall boundary layers was accounted for by Dent and Mehta (28), based upon the review of experimental and theoretical work given by Rajaratnam (43). The same modelling approach has been investigated at Bath University by Idoum (44) and Fraudeau (45).

1.5 Simplifications for the Modelling of Diesel Sprays

In order to apply the classical integral methods to the Diesel spray envisaged as a dense, turbulent jet (Section 1.4.3), the following preliminary assumptions are made :-

1. The transient injection event may be represented, with sufficient accuracy, by a steady-state spray.

2. The relative velocity of droplets in the spray to the entrained air is very small. Profiles of velocity, temperature and concentration prior to combustion are those observed in single phase jets.

These conditions are the essential prerequisites for a comprehensive analysis of the single phase, steady, turbulent jet, which represents the bulk of the present work to be described in subsequent chapters.

The photographic records of Adler and Lyn (19), Newman and Brustowski (31), Rife and Heywood (7), Way (34), Packer (35) and others, confirm that it is a reasonable approximation to enclose the transient isothermal or vaporising spray within a steady envelope for both quiescent injection and injection into swirl. Packer (46) applied the methods of Kuo and Bracco (47), for examination of the approach to steadiness in the flow behind the tip in sprays, to a typical diesel spray and concluded that at any instant over 80% of the flow could be said to be steady. Lakshminarayan and Dent (20) concluded, from detailed experimental work, that the central regions of a transient, axisymmetric, vaporising spray were comparable to a steady-state jet. Consideration has been given in the literature to experimental and analytical descriptions of the spray tip and tail (detachment after the end of injection), and the effects upon penetration and local mixing (20,27,40).

Newman and Brzustowski (31) and Rife and Heywood (7) concluded that the relative velocity of droplets in the spray would be small, the droplets themselves being very small for Diesel at supercritical engine conditions (Section 1.3). The droplet history obtained by Packer (35) from the Adler/Lyn (19) model, at typical engine conditions, showed that the relative velocity of the mean droplet decayed very rapidly with distance from the nozzle.

With regard to property profiles, Vara Prasad and Subir Kar (16,17) and Lakshminarayan and Dent (20) found from their experiments that distributions of velocity and concentration in axisymmetric non-vaporising and vaporising sprays were not unlike those observed in single-phase jets (Section 2.5.3). Newman and Brzustowski (31) concluded, from heat transfer estimates, that thermal equilibrium could be assumed to exist in the spray between the liquid droplets and the gas surrounding them. The form of the temperature and concentration profiles is discussed in Chapter 5.

With these similarities identified, an integral analysis of single phase jets may now proceed.

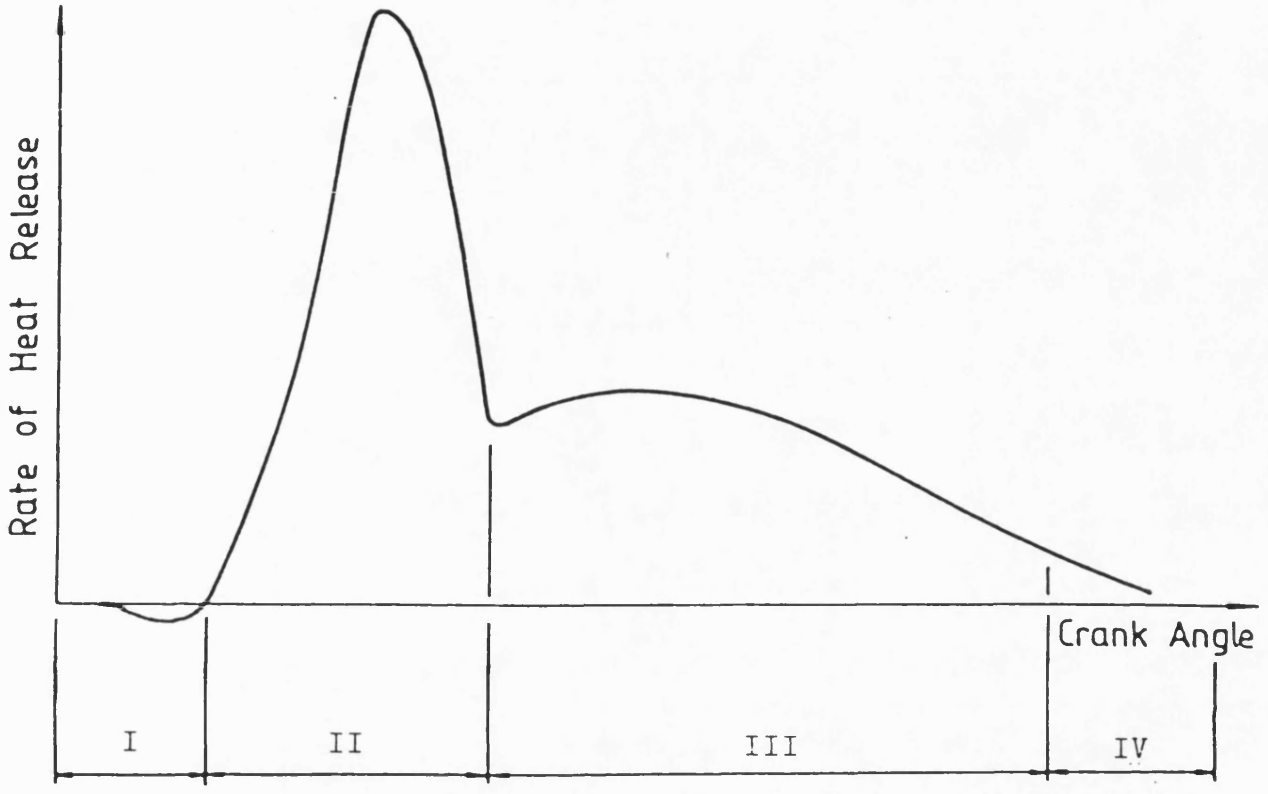

I - IGNITION DELAY
II - PRE-MIXED BURNING
III - MIXING AND DIFFUSION CONTROLLED BURNING
IV - COMBUSTION TAIL

FIG 1.1 FOUR STAGES OF HEAT RELEASE

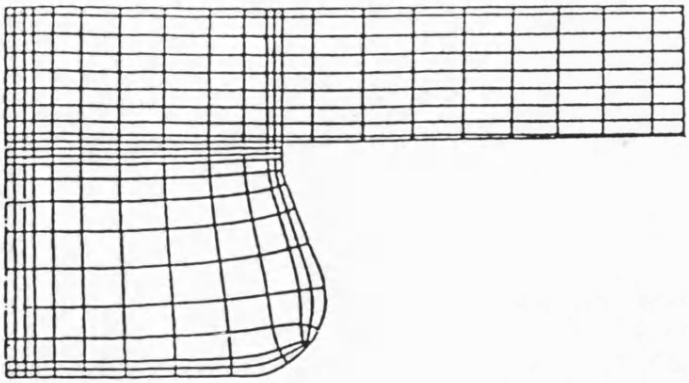

(a) GOSMAN AND HARVEY (23)

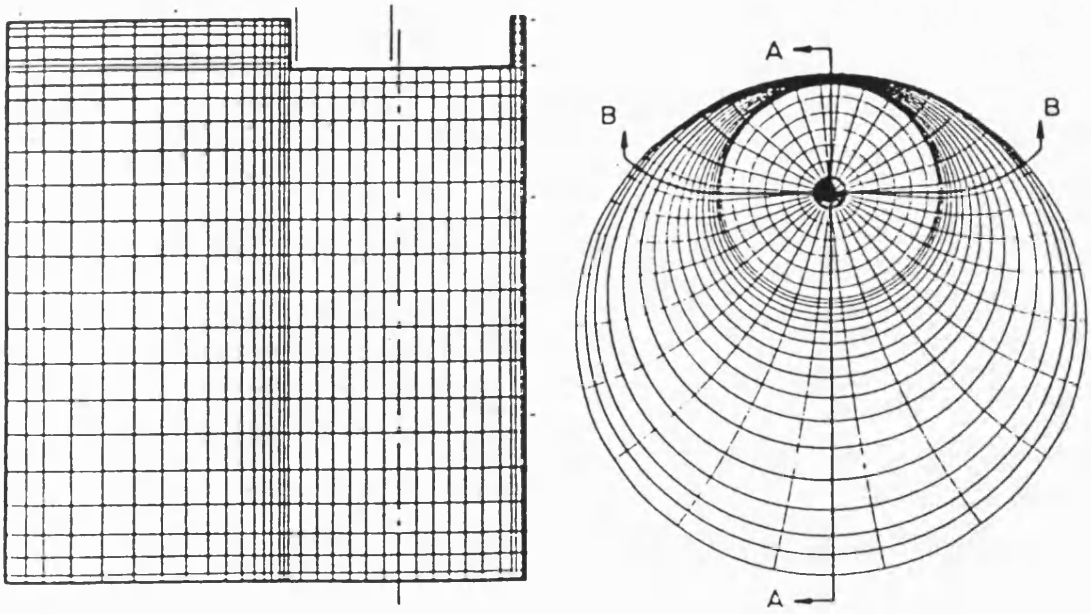

(b) BRANDSTÄTTER ET. AL. (24)

FIG. 1.2 COMPUTATIONAL MESH FOR FINITE-DIFFERENCE SCHEMES

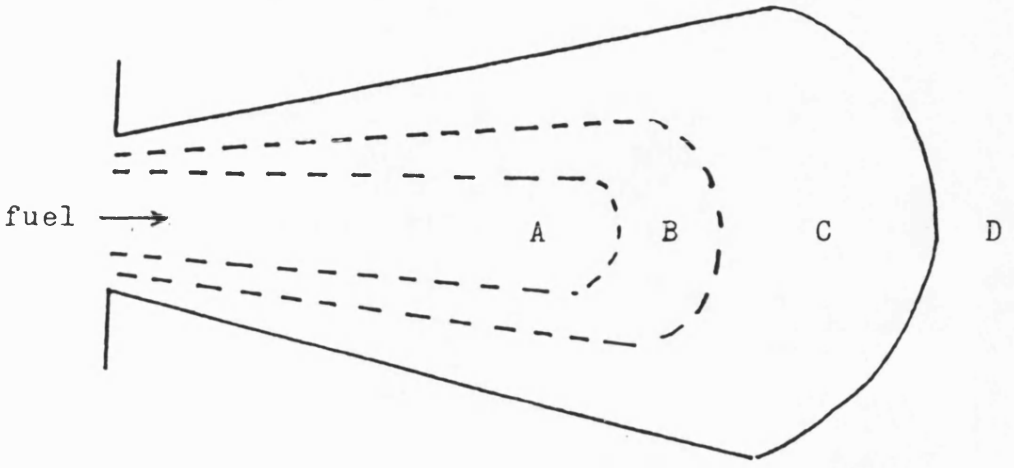

KEY:-

A vaporised fuel and products
B burning volume
C oxidant and products
D oxidant only

FIG. 1.3 FOUR ZONE COMBUSTION MODEL

CHAPTER 2

INTEGRATED CONSERVATION EQUATIONS FOR AN AXISYMMETRIC JET

CHAPTER 2 - NOTATION

A - Jet Area (m^2)

b - width of turbulent mixing zone (m)

E_m - mass entrainment rate

G - width growth coefficient for an axisymmetric jet

m - velocity ratio ($= w/u_o$)

n - density ratio ($= \rho_\infty/\rho_o$)

r - radial ordinate (m)

r_c - radial location of jet inner mixing boundary (m)

r_2 - " " " " outer " " "

t - time (s)

T - temperature (K)

u - velocity (ms^{-1})

w - free stream velocity ($= u_\infty$)

x - dimensionless radial ordinate for the mixing zone

x_i - co-ordinate in i-direction

z - axial distance (m)

z_c - length of initial region (m)

z_D - length to the transition section (m)

U_{v_I} - dimensionless velocity profile in the initial region

U_{v_M} - " " " " " main "

$\Gamma_\psi^\sim$ - diffusion coefficient for property ψ

θ - temperature ratio ($= T_o/T_\infty$)

Θ - cylindrical polar co-ordinate

ρ - density (kg/m^3)

ϕ - general scalar flow property

ψ - general flow property

Superscripts

$\sim$ - instantaneous

$'$ - fluctuating

Subscripts

0 - at the nozzle ($z=0$)

1 - on the jet axis

∞ - in the free stream

m - maximum

r - in the r direction

Θ - in the Θ "

z - in the z "

CHAPTER 2 - INTEGRATED CONSERVATION EQUATIONS FOR AN AXISYMMETRIC JET

2.1 Introduction

In this Chapter, the conservation equation for a general flow property $\tilde{\psi}$ is rewritten under the regime of a set of simplifying assumptions pertinent to a long, thin shear flow such as an axisymmetric jet. Such simplifications reduce both the scope and generality of the subsequent mathematical statement, but also make easier the solution of the more specialised problem, by :-

1) Transforming partial to ordinary differential equations, for which numerical solutions are significantly more straightforward, and

2) Eliminating troublesome terms which require turbulence model closures.

The unknown term in the simplified equation system is the local rate of entrainment of air into the jet flow (Section 2.2). Using similarity of velocity profiles in axisymmetric jets (Section 2.3), an equation is derived for the jet spread (Section 2.4), from which the entrainment rate may be deduced (Section 2.5).

2.2 Integration of General Equation

It is understood that a turbulent flow is properly represented by the three-dimensional, time-dependent Navier-Stokes equations, describing the principles of conservation of mass (continuity), momentum (Newton's Second Law of Motion), and so called 'scalar' quantities - for example energy (First Law of Thermodynamics) or chemical species - upon application of appropriate boundary conditions (48):-

Continuity

$$\frac{\partial}{\partial t}\tilde{\rho} + \frac{\partial}{\partial x_j}\left\{\tilde{\rho}\tilde{u}_j\right\} = 0 \qquad (2.1)$$

Conservation of Momentum (i-component)

$$\frac{\partial}{\partial t}\left\{\tilde{\rho}\tilde{u}_i\right\} + \frac{\partial}{\partial x_j}\left\{\tilde{\rho}\tilde{u}_j\tilde{u}_i\right\} = -\frac{\partial \tilde{P}}{\partial x_i} + \frac{\partial}{\partial x_j}\left\{\mu\left[\frac{\partial \tilde{u}_i}{\partial x_j} + \frac{\partial \tilde{u}_j}{\partial x_i}\right]\right\} + S_{\tilde{u}_i} \qquad (2.2)$$

Conservation of Scalar Quantity $\tilde{\phi}$

$$\frac{\partial}{\partial t}\left\{\tilde{\rho}\tilde{\phi}\right\} + \frac{\partial}{\partial x_j}\left\{\tilde{\rho}\tilde{u}_j\tilde{\phi}\right\} = S_{\tilde{\phi}} + \frac{\partial}{\partial x_j}\left\{\Gamma_\phi \frac{\partial \tilde{\phi}}{\partial x_j}\right\} \qquad (2.3)$$

where $\tilde{P}$ is the instantaneous pressure, μ is the laminar dynamic viscosity and Γ_ϕ is a diffusion coefficient for the property $\tilde{\phi}$.

The evident similarity of form between these equations motivates their expression in the following general form, where $\tilde{\psi}$ replaces $\tilde{u}_i$ in 2.2 or $\tilde{\phi}$ in 2.3.

$$\frac{\partial}{\partial t}\left\{\tilde{\rho}\tilde{\psi}\right\} + \frac{\partial}{\partial x_j}\left\{\tilde{\rho}\tilde{u}_j\tilde{\psi}\right\} = \frac{\partial}{\partial x_j}\left\{\Gamma_{\tilde{\psi}}\frac{\partial \tilde{\psi}}{\partial x_j}\right\} + S_{\tilde{\psi}} \qquad (2.4)$$

unsteady convection diffusion general source

Setting $\tilde{\psi} = 1$ recovers the continuity equation 2.1 and $\tilde{\psi} \equiv u_i$ gives

2.2 with some terms such as pressure regrouped into the generalised source in 2.4 above. In Appendix A, it is shown that 2.4 must be simplified for practical solutions, and that this is achieved by time averaging to give the Reynolds equations for the mean flow. For the axisymmetric geometry (r, θ, z), also written as (x_1,x_2,x_3) for compactness, these equations may be written as :-

$$\frac{\partial}{\partial t}\{\rho r\psi\} + \frac{\partial}{\partial x_j}\{\rho r u_j \psi\} = \frac{\partial}{\partial x_j}\left\{\Gamma_\psi r \frac{\partial \psi}{\partial x_j} - \overline{r\rho u_j'\psi'}\right\} + S_\psi \quad (2.5)$$

Instantaneous properties $\tilde{\rho}$, $\tilde{u}_j$,$\tilde{\psi}$ in 2.4 are replaced in 2.5 by their mean flow (time-averaged) counterparts : procedures for dealing with the turbulent fluctuation correlations $\overline{\rho u_j'\psi'}$ are described in Appendix A.

For the present work concerning axisymmetric jets, the following boundary layer simplifying assumptions are now invoked (32,43):-

a) for an axisymmetric jet, $u_\theta \equiv u_2 \equiv 0$ by symmetry :
   all terms involving u_2 and its derivatives vanish from 2.5

b) the axially directed velocity predominates (32) ($u_z >> u_r$)

c) radial gradients ($\frac{\partial}{\partial r} \equiv \frac{\partial}{\partial x_1}$) are more important than axial gradients, due to the long, thin nature of the flow.

d) the flow is steady with respect to time ($\frac{\partial}{\partial t} \equiv 0$).

e) for high Reynolds number free turbulent jets, viscous stresses are negligible compared to the turbulent shear stresses: the Γ_ψ terms in 2.5 will be dropped.

f) pressure $\tilde{P}$ is constant. This is a reasonable assumption for free jets (32).

For simplicity the discussion is restricted to sourceless flows.

Possible source terms are considered in the later analysis (Chapters 4 and 5). With these stipulations, a) - f), the general conservation equation 2.5 becomes (32) :-

$$\frac{\partial}{\partial x_j}\left\{\rho r u_j \psi\right\} = -\frac{\partial}{\partial r}\left\{\overline{r\rho u_r' \psi'}\right\} \qquad (2.6)$$

this is the familiar boundary layer form of the equations of motion, in the absence of sources. In particular, the conservation of mass (continuity) equation is recovered through the setting of $\psi \equiv 1$ in 2.6

$$\frac{\partial}{\partial x_j}\left\{\rho r u_j\right\} = \frac{\partial}{\partial z}\left\{\rho r u_z\right\} + \frac{\partial}{\partial r}\left\{\rho r u_r\right\} \qquad (2.7)$$

recalling that $\frac{\partial}{\partial \theta} \equiv 0$ through axial symmetry.

Equation 2.6 may be further simplified by integration over a cross-section of the shear flow in the plane z = constant. The integration, by symmetry, need only be taken across the width of the flow from $r = 0$ to $r = r_2(z)$. The former location describes a point z on the jet axis, while the latter describes a point on the outer boundary in the same plane of the jet. The position $r = r_2(z)$ is here chosen so that :-

$$\left.\frac{\partial \psi}{\partial r}\right|_{r_2(z)} < \varepsilon \text{ , where } \varepsilon \text{ is a prescribed, small value} \qquad (2.8)$$

Upon performing this integration. 2.6 becomes, in full :-

$$\int_0^{r_2(z)} \frac{\partial}{\partial z}\left(\rho r u_z \psi\right) dr + \int_0^{r_2(z)} \frac{\partial}{\partial r}\left(\rho r u_r \psi\right) dr = -\int_0^{r_2(z)} \frac{\partial}{\partial r}\left(r\overline{\rho u_r' \psi'}\right) dr \qquad (2.9)$$

Each term appearing in 2.9 is now considered in turn, bearing in mind the continuity equation 2.7 and the following general statement of a

rule due to Leibnitz :-

$$\int_{a(x)}^{b(x)} \frac{\partial}{\partial x} f(x,y)dy = \frac{d}{dx}\int_{a(x)}^{b(x)} f(x,y)dy + f(x,a)\frac{da}{dx} + f(x,b)\frac{db}{dx} \qquad (2.10)$$

(see H.W. Reddick and F.H. Miller : Advanced Mathematics for Engineers, Wiley, New York 1962).

The first term in 2.9 becomes, by 2.10 :-

$$\int_0^{r_2(z)} \frac{\partial}{\partial z}\left(\rho r u_z \psi\right) dr = \frac{d}{dz}\int_0^{r_2(z)} \rho r u_z \psi dr + 0 - (\rho r u_z \psi)\left|_{r=r_2(z)} \frac{dr_2}{dz}(z)\right. \qquad (2.11)$$

since $a(z) \equiv 0 \Rightarrow da/dz = 0$. For the second term in 2.9 :-

$$\int_0^{r_2(z)} \frac{\partial}{\partial r}\left(\rho r u_r \psi\right)dr = [\rho r u_r \psi]_0^{r_2(z)} = (\rho r u_r \psi)\Big|_{r=r_2(z)}$$

$$= \psi_\infty (\rho r u_r)\Big|_{r=r_2(z)} = \psi_\infty \int_0^{r_2(z)} \frac{\partial}{\partial z}\left(\rho r u_r\right)dr$$

$$= -\psi_\infty \int_0^{r_2(z)} \frac{\partial}{\partial z}\left(\rho r u_z\right)dr$$

The last transformation is obtained from the continuity equation 2.7. Hence :-

$$\int_0^{r_2(z)} \frac{\partial}{\partial r}\left(\rho r u_r \psi\right) dr = -\psi_\infty \int_0^{r_2(z)} \frac{\partial}{\partial z}\left(\rho r u_z\right) dr$$

$$= -\psi_\infty \left\{ \frac{d}{dz}\int_0^{r_2(z)} \rho r u_z dr + 0 - (\rho r u_z)\left|\frac{dr_2}{dz}(z)\right|_{r=r_2(z)} \right\}$$

$$= -\psi_\infty \frac{d}{dz}\int_0^{r_2(z)} \rho r u_z dr + (\rho r u_z \psi)\left|\frac{dr_2}{dz}(z)\right|_{r=r_2(z)} \qquad (2.12)$$

The term on the right hand side of 2.9 becomes:-

$$\int_0^{r_2(z)} \frac{\partial}{\partial r}\left(r\,\overline{\rho u_r' \psi'}\right) dr = [\rho r \overline{u_r' \psi'}] + (\rho r \overline{u_r' \psi'})\Big|_{r=r_2(z)} \qquad (2.13)$$

It is recorded in Appendix A that the correlation $\rho \overline{u_r' \psi'}$ could be related, through the gradient transport hypothesis (after Prandtl), to the mean property gradient:-

$$\overline{u_r' \psi'} \propto \frac{\partial \psi}{\partial r}$$

Now from 2.8, the jet outer boundary $r_2(z)$ is defined so that $\partial\psi/\partial r$ is negligibly small there: therefore, this definition ensures that the fluctuating component correlation term 2.13 disappears (for a free jet) as a result of integration. For a wall boundary layer, the right hand side term in 2.9 contributes a wall shear stress expression to the conservation equation (43).

Combining 2.11 and 2.12, and discarding 2.13 as zero gives the following re-expression of the integral conservation equation 2.9:-

$$\frac{d}{dz}\int_0^{r_2(z)} \rho r u_z \psi dr - F(r_2) - \psi_\infty \frac{d}{dz}\int_0^{r_2(z)} \rho r u_z dr + F(r_2) = 0$$

where $F(r_2) = (\rho r u_z \psi)\left|\frac{dr_2}{dz}(z)\right|_{r=r_2(z)}$, so that:-

so that:-

$$\frac{d}{dz}\int_0^{r_2(z)} \rho r u_z \psi \, dr = \psi_\infty \frac{d}{dz}\int_0^{r_2(z)} \rho r u_z \, dr \qquad (2.14a)$$

and the reduction in complexity of the mathematical system is achieved. For an axisymmetric jet, area $A(z)$, $A(z)=\pi r_2^2(z)$, so that the general (sourceless) integrated conservation equation could also be written as:-

$$\frac{d}{dz}\int_A \rho r u_z \psi \, dA = \psi_\infty \frac{d}{dz}\int_A \rho r u_z \, dA \qquad (2.14b)$$

The continuity (conservation of mass) condition is no longer recoverable from 2.14, since that condition itself was used in the derivation: setting $\psi \equiv 1$ in 2.14 only results in a truism. Continuity may be expressed in an integral balance upon consideration of the control volume in Fig. 2.1. The mass flux across the face at z_2 is increased from that across the face at z_1 by the amount of fluid entrained into the jet envelope, from the free stream through the surface A_3, over the distance δz. In the limit as $\delta z \to 0$:-

$$\frac{d}{dz}\int_A \rho u_z dA = E_m \qquad (2.15)$$

This statement defines the rate of entrainment E_m of free stream fluid: the velocities within the jet envelope are assumed to be everywhere parallel to the jet axis z (a consequence of assumption b) above), and velocity may simply be written as $u \equiv u_z$. In the free stream $u \equiv u_\infty$:-

$$\frac{d}{dz}\int_A \rho u \, dA = E_m \qquad (2.16)$$

The entrainment rate is not known a priori, but can be accounted for in the light of the following experimental observations.

2.3 Velocity Profile Similarity

A diagram of an axisymmetric jet is given in Fig. 2.2a, after Abramovich (32). For uniform injection velocity u_o, there will exist a significant initial region (Chapter 3) before turbulent mixing reaches the jet axis, at some point $z=z_c$, and the axial velocity u_m begins to decay. Some distance further downstream, a main region of fully developed flow is established (see later). Experimental and theoretical studies of axisymmetric jets have been reviewed by Abramovich (32), Rajaratnam (43) and Schetz (49).

Measurements made in the initial region have been reported by Kuethe (50) (1935), Corrsin (51) (1946), Forstall and Shapiro (52) (1950), Abramovich (32,53) (1963 and 1967) and Rajaratnam and Pani (54) (1972). The experiments covered a range of variation for the velocity ratio m (Fig. 2.1a), initial degree of heating θ and injection density ratio n :-

$$m = \frac{w}{u_o} \quad ; \quad \theta = \frac{T_o}{T_\infty} \quad ; \quad n = \frac{\rho_\infty}{\rho_o} \tag{2.17}$$

(for air-air jets etc., $n = \theta$).

A definition sketch of the initial region is given in Fig. 2.2b. The plane of the turbulent annular shear layer, of local width b(z), separates two streams of uniform velocity fluid : one ($r>r_2(z)$) that of the coflowing stream, the other ($r<r_c(z)$) that of the undisturbed injectant core. It is interesting to compare radial distributions of velocity, across the width of the shear layer, at different axial stations in the initial region of jets subject to various values of the parameters m,n and θ. In order to draw useful conclusions, measured velocity profiles are usually expressed in terms of the non-dimensional excess velocity function U_{v_I} (Fig. 2.2b), defined by :-

$$U_{v_I}(r,z) = \frac{u(r,z) - w}{u_o - w} \equiv \frac{\Delta u}{\Delta u_o} \qquad r \in [r_c, r_2] \tag{2.18}$$

This distribution is then plotted against a radial ordinate made dimensionless by the local width b(z) of the mixing zone. Such an ordinate is :-

$$x = \frac{r - r_c}{b} = \frac{r - r_c}{r_2 - r_c} \qquad r \in [r_c, r_2] \qquad (2.19)$$

so $x \in [0,1]$ traces the velocity profile across the mixing zone, measured from the inner mixing boundary $r_c(z)$. A selection from the available data is plotted in this way in Fig. 2.3, and the plot is representative of the data as a whole (Abramovich (32)). The conclusion drawn from Fig. 2.3 is the similarity, at different axial stations, of the profile U_{v_I} and its universality with respect to m,n and θ over the range shown. This universality is expressed as :-

$$U_{v_I}(r,z) = U_{v_I}(x) \qquad z \in [0,z_c] \qquad (2.20)$$

Several attempts have been made to determine the nature of U_{v_I} from theoretical considerations. Using the theories of free turbulence due to Prandtl, Tollmien and Göertler (and others) solved the partial differential equations for a jet in a stationary medium (m=0) to obtain U_{v_I} within an unknown constant, which could be determined from experiment. Abramovich (32) and Rajaratnam (43) both give full accounts of these investigations. The Tollmien solution for U_{v_I} is transcendental and defined numerically; the Göertler solution is exponential and very similar to the latter. Although there is good correlation of the data in Fig. 2.3, still there is possibly sufficient scatter to qualify the general statement of universality. It is apparent, however, that this scatter is due to the collection of data from different sources rather than any inherent influence upon the distribution of m or θ. The measurements of Rajaratnam and Pani (54) describe a distribution which is rather less full than that followed by the Abramovich (32) data : discrepancies may be due in part to the difficulty in locating the mixing zone boundaries $r_c(z)$ and $r_2(z)$ (53).

The data in Fig. 2.3 is in sufficiently good agreement with the empirical relation due to Schlichting (55):-

$$U_{v_I}(x) = 1 - (1 - [1-x]^{3/2})^2 \qquad (2.21)$$

Abramovich (53) made measurements in variable density axisymmetric jets with n=0.27 (heated Freon-12 in air), n=1.7 (heated air in air) and

n=7 (helium in air) and concluded that U_{v_I} was not independent of n. However, the presentation of the experimental data makes any further investigation very difficult, and the usual assumption of universality of U_{v_I} (32) is retained here.

Measurements of velocity in the main region of axisymmetric turbulent jets for various values of m,n and θ have been reported by Hinze and Zijnen (56), Corrsin and Uberoi (57) (1950), Landis and Shapiro (58) (1951), Abramovich (32,53) (1963 and 1967), Rajaratnam and Pani (54) (1972), Chriss (59) (1968) and many others. The dimensionless excess velocity profile U_{v_M} at any station in the main region (Fig. 2.2a) is defined in a similar way to U_{v_I}:-

$$U_{v_M}(r,z) = \frac{u(r,z) - w}{u_m(z) - w} = \frac{\Delta u}{\Delta u_m} \qquad r \in [o, r_2] \qquad (2.22)$$

Here $u_m(z)$ is the maximum jet velocity, at the axial station z, which occurs at the jet axis (Chapter 3). It is usual (32) to plot U_{v_M}, deduced from experimental data, against the non-dimensional radial ordinate η:-

$$\eta = \frac{r}{r_{\frac{1}{2}}(z)} \qquad (2.23a)$$

where $r_{\frac{1}{2}}$ is the local jet 'half-radius', defined from :-

$$U_{v_M}(r_{\frac{1}{2}}) = \frac{1}{2} \qquad (2.23b)$$

as that distance at which the excess jet velocity is one half of the arithmetic mean of the axial and free stream velocities. This quantity is more readily determined, experimentally, than the location of the outer mixing boundary, $r_2(z)$, where the jet flow merges asymptotically with the free stream (by (2.8)).

A selection from the available data is presented in this way in Fig. 2.4: the measurements correspond to observations made at different axial stations in the main region of the jets in the various cases. The distributions again appear to be similar with z and uninfluenced by variation in m or θ over the range shown. The similarity of

U_{V_M} is first observed some distance downstream from the end of the initial region (49) (Chapter 3).

As with U_{V_I}, the velocity profile in the main region has been determined theoretically, Tollmien applied the Prandtl mixing length hypothesis, and Göertler the Prandtl eddy viscosity model (Appendix A), in order to solve the equations of motion to yield U_{V_M} within an empirical constant (see Rajaratnam (43) or Abramovich (32)). More empirically, the Schlichting (55) formula :-

$$U_{V_M}(\eta) = (1 - [0.44\ \eta]^{3/2})^2 \qquad (2.24)$$

is in close agreement with the Tollmien and Göertler solutions, and appears to describe adequately well the experimental variation (Fig. 2.4). According to Landis and Shapiro (58), and Abramovich (53), the distribution of velocity can be represented by a cosine rule:-

$$U_{V_M}(\eta) = \frac{1}{2}\left(1 + \cos\left\{\frac{\pi r}{2r_{\frac{1}{2}}}\right\}\right) \qquad (2.25)$$

these experiments pertaining to jets of variable composition. The correspondence between 2.24 and 2.25 is reasonably good (53). The variation of the density parameter n in these experimental observations appears to indicate universality of U_{V_M} with n : Newman and Brzustowski (31) report that their analysis of the work of Corrsin and Uberoi (57) leads to the conclusion that similarity may indeed be assumed when $n < 1$ (dense jets). Similarity of U_{V_M} was also concluded by Chriss (59) in the investigation of jets when $n >> 1$ (light jets).

For the later theoretical work it is convenient to work not with the ordinate η but again with x. In the main region, the inner mixing boundary coincides with the jet axis z ($r_c = 0$). Therefore, from (19)

$$x = \frac{r}{b} \qquad r \in [0,\ b(z)] \qquad (2.26)$$

The definition of U_{V_M} from (2.24), for example, becomes :-

$$U_{V_M}(x) = (1 - x^{3/2})^2 \qquad (2.27)$$

since U_{v_M} ($r = 0.44b$) = $\frac{1}{2}$. The prescription (2.25) could be similarly amended. When U_{v_M} is written as a function of x, it is interesting to compare it with the initial region velocity profile U_{v_I}, as the definition of the dimensionless radial ordinate is consistent : such a comparison is given in Fig. 2.5, using the Schlichting (55) formulae (2.21) and (2.27) for the two distributions. The velocity profiles are significantly different in the two regions of similarity, with U_{v_M} being less full than U_{v_I}. The difference is due to the different character of the flow in the two regions : in the initial region, as has been mentioned, the mixing zone is bounded by two streams of uniform velocity, while in the main region the shear layers, having merged at the jet axis from $z = z_c$, form a single turbulent mixing zone or free shear flow. It is this observation which prompts the decomposition of the jet flow into three regions :-

1. An initial region originating at the nozzle, within which, for uniform injection velocity, there is a core of fluid centred about the jet axis undisturbed by turbulent mixing, and a similarity distribution $U_{v_I}(x)$ for velocity across the turbulent mixing zone.

2. A main region, extending downstream from some axial station, z_D, beyond the end z_c of the initial region, in which a similarity distribution $U_{v_M}(x)$ describes the variation in velocity across the jet at any cross-section.

3. A region of transition, extending from z_c to z_D, within which the velocity profile develops continuously from U_{v_I} to U_{v_M} (a region of developing flow).

A theoretical analysis of each of these regions is undertaken in Chapter 3.

2.4 Spread of Axisymmetric Jets

Following Abramovich (32), this velocity profile similarity is now used to derive a propagation equation for the thickening rate db/dz of an axisymmetric jet. The transverse velocity fluctuations $u_2' \equiv u_r'$ are considered to decide the thickening rate of the mixing zone, width b(z):-

$$\frac{db}{dt} \sim u_2' \sim - \ell \frac{\partial u_z}{\partial r}$$

where the Prandtl mixing length hypothesis (Appendix A) has been invoked to express u_2' in terms of a mixing length ℓ. As a consequence of similarity (32), the transverse, z-directed (longitudinal) velocity gradient is proportional to the difference in the velocities at the boundaries of the mixing zone (at $r = r_c$, $u = u_m$; at $r = r_2$, $u = u_\infty = w$):-

$$\frac{\partial u_z}{\partial r} \sim \frac{(u_m - w)}{b}$$

Hence :-

$$\frac{db}{dt} \sim \frac{\ell}{b} (u_m - w) \sim (u_m - w)$$

since ℓ/b = constant (equality of dimensionless mixing lengths at different cross-sections is a consequence of similarity (32)). Also

$$\frac{db}{dt} = \frac{db}{dz} \cdot \frac{dz}{dt} = \frac{db}{dz} \cdot u^*$$

where $u^* = dz/dt$ is a characteristic velocity for the mixing zone (see below). Combining these results :-

$$\frac{db}{dz} \sim \frac{(u_m - w)}{u^*} \qquad (2.28)$$

This expression is the basis for the propagation equation, and is completed upon specification of the characteristic velocity u^*. This is 'properly' determined as the mean mass velocity in a variable density jet :-

$$u^* = \int_{r_c}^{r_2} \rho u \, dr \Big/ \int_{r_c}^{r_2} \rho \, dr \qquad (2.28a)$$

as confirmed experimentally by Abramovich (53). More useful for analytical work is the following approximate relation (32) :-

$$u^* = \frac{\rho_1 u_m + \rho_\infty w}{\rho_1 + \rho_\infty} \qquad (2.28b)$$

where $\rho_1(z)$ and $u_m(z)$ are, respectively, the density and velocity at the jet axis. The validity of this simplification is discussed below. Substitution of (2.28b) in (2.28a) gives :-

$$\frac{db}{dz} \sim \frac{(1 + \bar{\rho})}{2} \cdot \frac{u_m - w}{u_m + \bar{\rho} w}$$

or :-

$$\frac{db}{dz} = G \frac{(1 + \bar{\rho})}{2} \cdot \frac{u_m - w}{u_m + \bar{\rho} w} \qquad (2.29)$$

where :-

$$\bar{\rho} = \frac{\rho_\infty}{\rho_1} \qquad (2.29a)$$

and G is a width growth constant which must be determined from experiments.* (Chapter 3). The range of applicability of (2.29) is limited in certain ways :-

1. When $m = w/u_o$ is greater than about 0.4, jet spread is under-predicted by (2.24) according to experimental data (32). The derivation given above supposes that turbulence in the mixing zone is due solely to the difference in the velocities u_o and w,

---

* The similarity condition was established separately for the initial and main regions in Section 2.3; hence G may take different values in the different regions.

and that the turbulence levels in the uniform velocity streams are negligible in comparison. When the difference in velocities becomes sufficiently small ($m > 0.4$), it is the finite turbulence intensity in the undisturbed streams which controls the thickening rate of the mixing zone, ahead of the turbulence in the zone itself.

2. For a jet in a counterflowing stream ($w/u_o < 0$), the thickening rate of the mixing zone is not a function of w but is the same as that for a jet spreading through a stationary medium (32) ($w = 0$). This has repercussions for the prediction of jets discharged at an angle to a crossflow (Chapter 7).

3. The approximation for u^* in (2.28b) may be poor in some cases. Abramovich (32) gives a full account, but it may be stated that the propagation equation will be more accurate for dense ($n < 1$) than for light ($n > 1$) jets (see Fig. 2.6). Abramovich (32) found (2.29) to be valid in the range $0.32 < n < 1.43$, and the performance of the equation is discussed in Chapter 7.

2.5 Closure

The propagation equation (29) provides the necessary information for evaluation of the entrainment rate E_m appearing in (2.16). Consider for simplicity a constant density jet when $w = 0$:-

$$\frac{d}{dZ}\int_A \rho u \, dA = \frac{d}{dZ}\left\{ u_m \rho \int_A U_{V_M}(x) \, dA \right\}$$

for the main region, using (2.22) with $w = 0$. Because $U_{V_M}(x)$ is a similarity profile, the average value K_1 of U_{V_M} over A is constant.

Hence:-

$$\frac{d}{dZ}\int_A \rho u \, dA = E_m = 2\pi b \, K_1 \, u_m \, \frac{db}{dZ}$$

so that E_m may be evaluated (Chapter 3). Other workers, starting with Morton et al (60) (1956), prescribed E_m directly from the concept of turbulent entrainment :-

$$E_m = \alpha\rho(u_o - w)$$

for a constant density jet in a coflowing stream. The empirical constant α must be determined by experiment (61). Both propagation equation and entrainment model methods have been extended to jets in crossflows (Chapter 4).

The propagation equation or entrainment model plays the same role, in rendering mathematically closed the integrated conservation equation system (2.16), as the turbulence model closures for the partial differential Reynolds equation set (2.5) (Appendix A). The inter-relationship between some of these different models is discussed by Sill and Schetz (62).

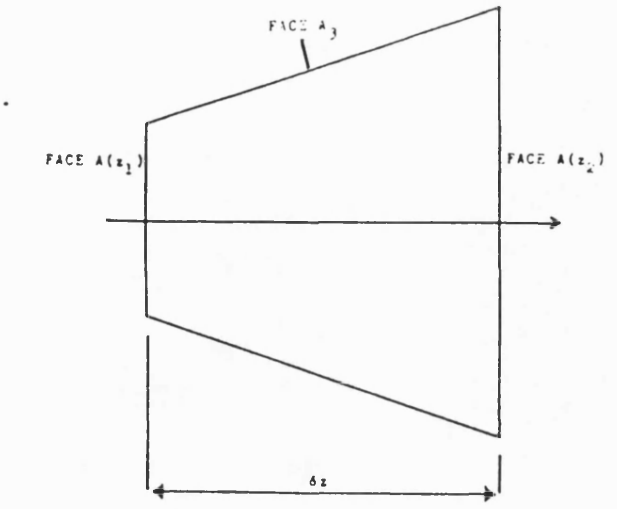

FIG. 2.1 CONTROL VOLUME FOR CONTINUITY

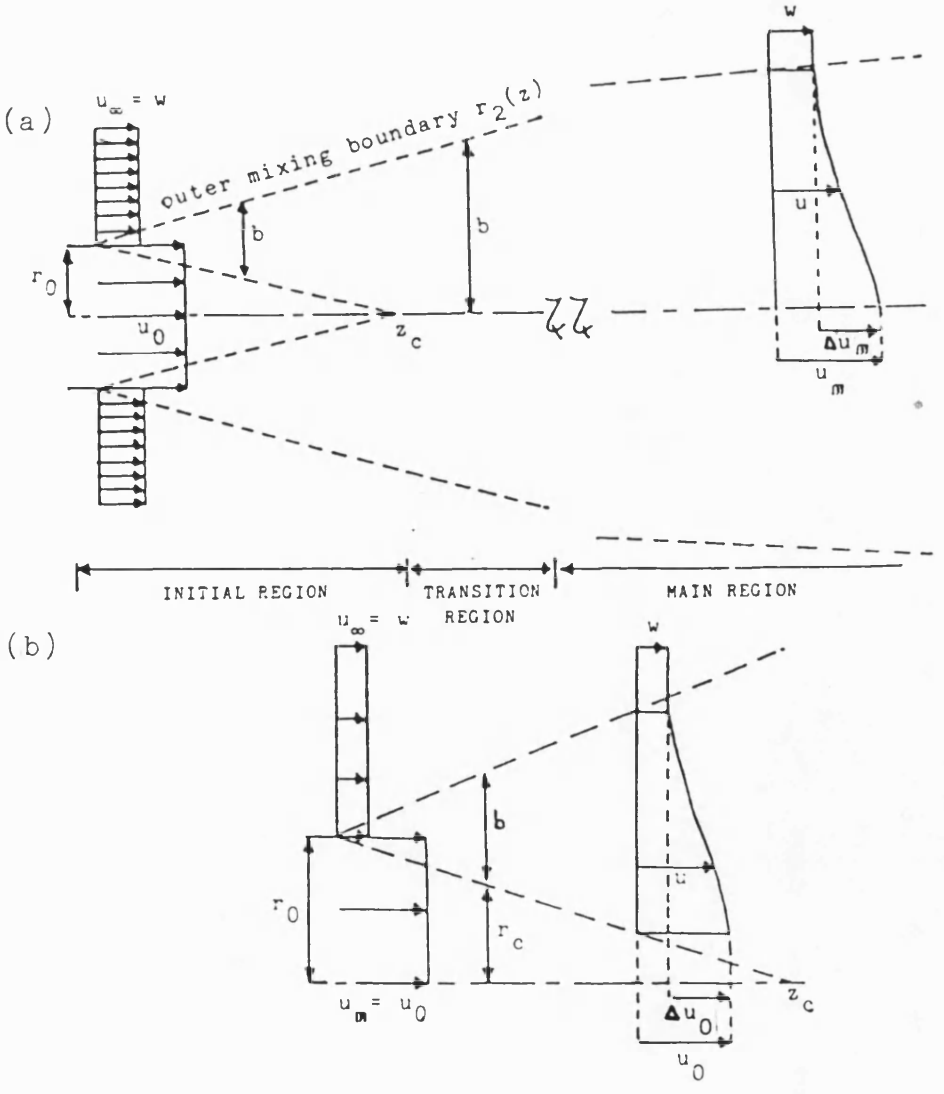

FIG. 2.2 DEFINITION SKETCHES FOR AN AXISYMMETRIC JET

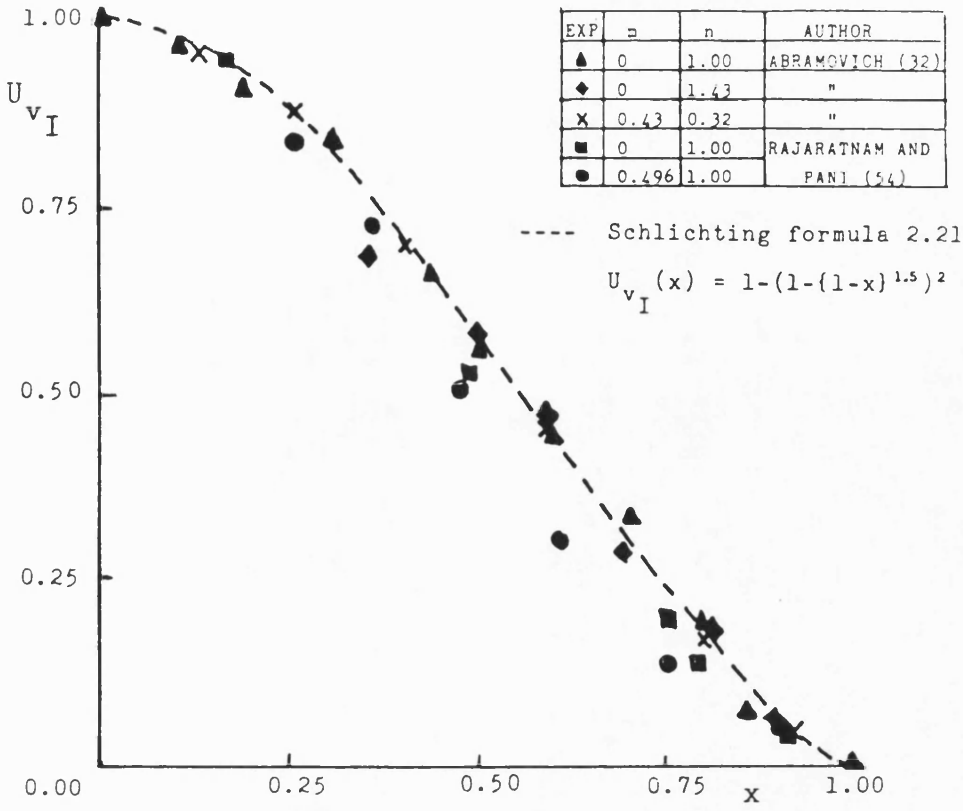

FIG 2.3 DIMENSIONLESS VELOCITY PROFILE FOR THE INITIAL REGION

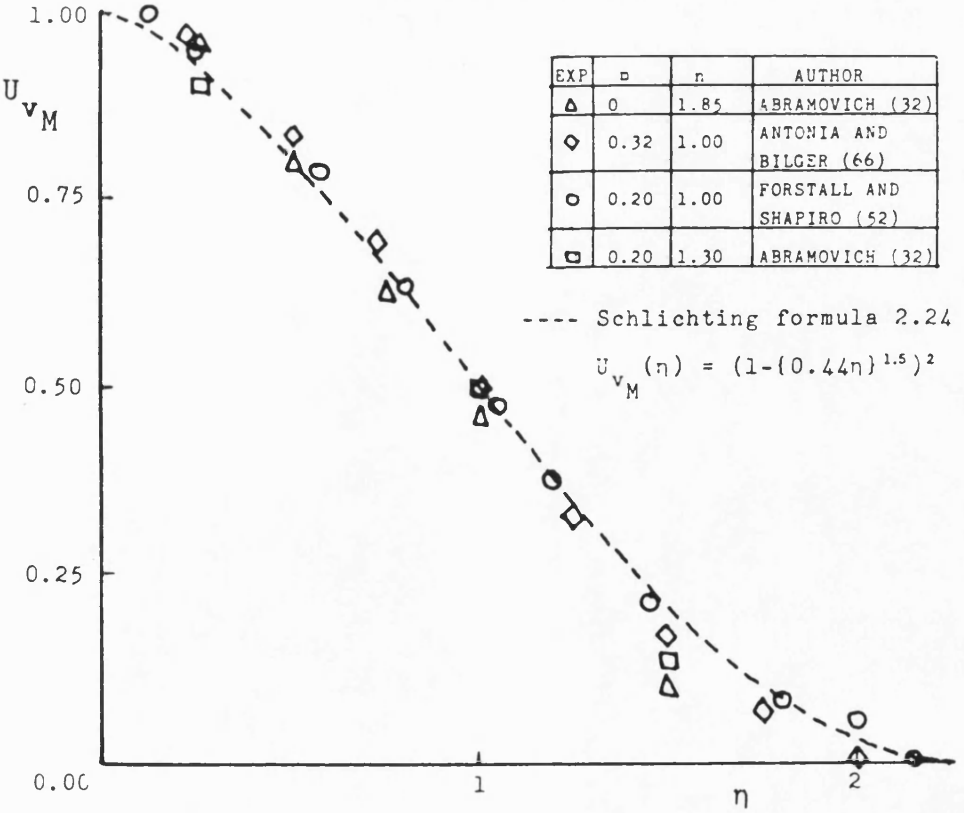

FIG 2.4 DIMENSIONLESS MAIN REGION VELOCITY PROFILE

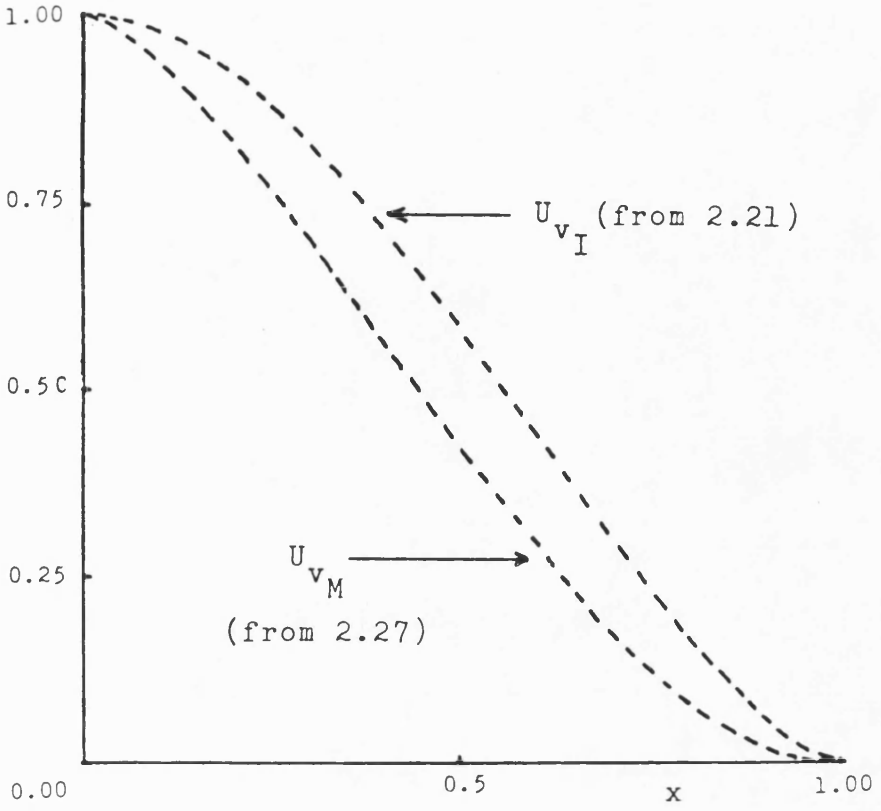

FIG 2.5 COMPARISON OF SIMILARITY PROFILES FOR VELOCITY (INITIAL AND MAIN REGIONS)

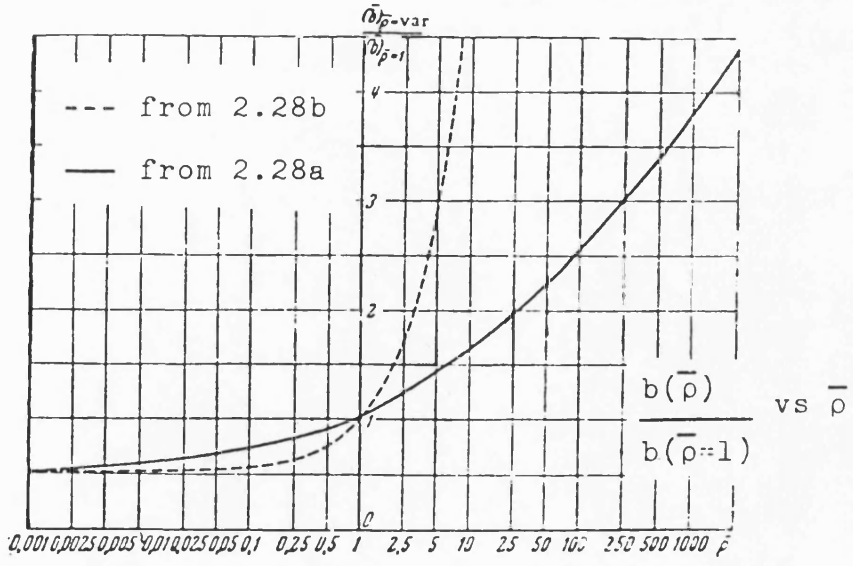

$\bar{\rho} = \rho_\infty/\rho_1$ ρ_1: density on the jet axis

FIG 2.6 DENSITY DEPENDENCE IN THE PROPAGATION EQUATION FROM (32)

CHAPTER 3

INTEGRAL ANALYSIS OF THE ISOTHERMAL, ISODENSE, AXISYMMETRIC JET

Chapter 3 - Notation

A - jet area (m^2)
A_c - area of constant velcoity core (m^2)
A_D - area of turbulent mixing zone (m^2)
A_0 - nozzle area (m^2)

b - width of turbulent mixing zone (m)
b_c - jet radius at z_c

C_E, C_{E_m} - entrainment coefficients

E_m - mass entrainment rate (kgs^{-1})

F_i^N - integral averages defined in 3.12a

G - width growth coefficient for mixing zone
G_I - constant value for G in the initial region
G_M - " " " " " " main region

h_v - jet excess axial velocity (ms^{-1})

I_N = $\int_A U_v^N dA \quad N=1,2$

K_N - average value of U_v^N over A N=1,2

m - velocity ratio (=w/u_0)
$\dot{m}$ - jet mass flux

r_0 - nozzle radius (m)
r_2 - jet outer mixing boundary (m)

u - jet velocity (ms^{-1})
u_m - jet axial velocity (ms^{-1})
U_v - dimensionless excess jet velocity profile
U_{v_I} - dimensionless velocity profile in the initial region
U_{v_M} - dimensionless velocity profile in the main region

w - velocity in the external stream (ms^{-1})

x - dimensionless radial ordinate for the mixing zone ($=(r-r_c/b)$) $x \in [0,1]$

z - jet centreline co-ordinate (m)

z_c - length of the initial region (m)

z_D - end of the transition region - start of the main region (m)

ρ - density (kg/m^3)

Superscripts

$\bar{}$ - normalised by r_0

Subscripts

0 - at the nozzle

D - at the transition section z_D

CHAPTER 3 - INTEGRAL ANALYSIS OF THE ISOTHERMAL, ISODENSE, AXISYMMETRIC JET

3.1 Introduction

The simple case of a steady-state, isothermal, isodense straight jet is the natural reference base for any more general jet mixing theory and merits a detailed investigation on two counts :-

1. A relative abundance of experimental data is available concerning this type of jet, which is drawn upon in Section 3.6.

2. An analysis of the governing equations may be carried through, and a formal solution completed in the limiting case of a jet exhausting into a stationary medium, commonly termed a submerged jet. Such an analysis illustrates significant features of the theory which remain important in the prediction of, for example, the heated and deflected jets to be discussed in the later chapters, and for which the theoretical development of this chapter will provide the foundation.

An integral theory will be established for an isothermal, isodense axisymmetric free jet, following the classical analysis of Abramovich (32). In Section 3.6, the empirical input for the theory will be chosen, so that predictions are in good agreement with the experimental data. In this way, the fundamental empirical input is determined before the extension of the theory, to those cases where analytical solutions are precluded.

3.2 Qualitative Description of the Flow

A schematic diagram of the free jet flow is given in Fig. 3.1. For simplicity, three assumptions are made concerning the flow:-

1. The injection velocity across the nozzle is uniform and equal to u_o.

2. The velocity w of the coflowing stream is constant.

3. Pressure gradients in the axial direction may be neglected.

Assumption 3. is reasonable if 2. is observed (32). With regard to w, following the observations of Abramovich (32) detailed in Chaper 2, it is assumed that $w/u_o < 0.4$. Assumption 1. can be relaxed in the context of a numerical solution by admitting the presence of a boundary layer on the inside of the nozzle (Chapter 7).

Following Abramovich (32), the flow in Fig. 3.1 has been divided into three regions. The analysis of the initial and main regions, which is well established, is united by a realistic description of the flow development in the transition region. Previous treatments of the transition region are considered in Sections 3.5 and 3.6.

3.3 Theory of the Initial Region

With regard to Fig. 3.1, the discontinuity in velocities between the jet and the external stream causes shear stresses to be set up and turbulent shear layers established around the nozzle lip. The developing shear layers constitute an annular mixing zone, the inner boundary of which (Fig. 3.2) invades the stream of nozzle fluid and encloses an approximately conical region, termed the potential core, which is not influenced by turbulent mixing and within which the jet exit velocity u_o is preserved. The core persists to that axial station z_c where the developing shear layers merge at the jet axis (Fig. 3.2): the region $z \in [o, z_c]$, sometimes called the development or potential core region, or zone of establishment, is here termed the initial region.

The starting-point for the analysis of the flow in the initial region

is the condition of axial momentum conservation. For a steady-state, axisymmetric jet satisfying the assumptions 2) and 3), the axial momentum conservation equation may be written in the form derived in Chapter 2:

$$\frac{d}{dZ}\int_A \rho u^2 \, dA = w \frac{d}{dZ}\int_A \rho u \, dA \qquad (3.1)$$

Recall that the outer mixing boundary, $r_2(z)$, is chosen so that the velocity gradient in the radial direction is negligible at r_2, so that there is no shear term in 3.1 (Chapter 2). The assumed velocity distribution (see below) is the actual result of shearing effects. In view of the constant density assumption of this chapter, ρ may be eliminated from (3.1). When (3.1) is then integrated from the jet nozzle ($z = o$, $A = A_o \equiv \pi r_o^2$, $u \equiv u_o$), along the jet centreline to that axial station $z < z_c$, where the cross section area is $A = \pi r_2^2$, the result is :-

$$u_o^2 \pi r_o^2 - w u_o \pi r_o^2 = \int_A u^2 \, dA - w \int_A u \, dA \qquad (3.2)$$

In order to proceed, it is necessary to characterise both the geometry of the mixing zone and the distribution of the jet velocity u within it. So, the width b of the mixing zone at z is determined from the width growth law (2.29) of Abramovich (32) (derived in Chapter 2) at constant density:-

$$\frac{db}{dz} = G_I \frac{(1-m)}{(1+m)} \qquad z < z_c \qquad (3.3)$$

where m is the principal velocity ratio :-

$$m = \frac{w}{u_o} \qquad (3.3a)$$

and G_I is a constant, determined from experimental observations near the nozzle of submerged jets (Abramovich (32)). The value of G_I is considered in Section 3.6. The mixing region width b at the station $z < z_c$ is found upon integration of (3.3) from the jet nozzle ($z = o$, $b(o) = o$ using 1. above):-

$$b = G_I \frac{(1-m)}{(1+m)} z \qquad z < z_c \qquad (3.4)$$

With regard to velocity, the normalised excess velocity distribution U_{v_I} in the mixing zone of the initial region, defined by :-

$$U_{v_I}(r,z) = \frac{u(r,z) - w}{u_o - w} \qquad r \in [r_c, r_2] \qquad (3.5)$$

was concluded in Chapter 2 to exhibit similarity at different axial stations within the initial region, and to be a function of the single non-dimensional parameter x (Fig. 3.2):-

$$U_{v_I} \equiv U_{v_I}(x) \qquad \left\{ \begin{array}{l} x = \dfrac{r-r_c}{b} \qquad (3.6) \\ \\ r \in [r_c, b] \Rightarrow x \in [o,1] \end{array} \right.$$

The non-dimensional ordinate x traces the normalised excess velocity profile from the inner boundary of the mixing zone (at a particular z-station), where the velocity is that of the undisturbed core, u_o ($x=o$, $U_{v_I}= 1$), to the outer edge of the jet where the velocity is that of the external stream, w ($x = 1$, $U_{v_I}= o$), (Fig. 3.2). It is not necessary (nor indeed desirable) to prescribe at this stage an explicit dependence for U_{v_I} upon the parameter x; instead, it is sufficient to work with a general velocity profile U_{v_I} and demand only that the boundary and similarity conditions described above are observed.

Thus :-

$$\left. \begin{array}{l} U_{v_I} \equiv U_{v_I}(x) \qquad x \in [o,1] \\ \\ U_{v_I}(o) = 1, \; U_{v_I}(1) = 0 \end{array} \right\} \qquad (3.7)$$

Following Adler and Baron (63), and Packer (35), the jet velocity u(r,z) is decomposed into the external stream velocity and an excess velocity component. In the mixing zone (Fig. 3.2):-

$$u(r,z) = h_{v_o} U_{v_I}(x) + w \qquad r \in [r_c, r_2], \; z \in [o, z_c] \qquad (3.8)$$

where the excess velocity at injection is :-

$$h_{v_o} = u_o - w \tag{3.8a}$$

Within the potential core the jet velocity is constant :-

$$u(r,z) \equiv u_o = h_{v_o} + w \qquad \begin{matrix} r \in [o, r_c] \\ z \in [o, z_c] \end{matrix} \tag{3.9}$$

Fig. 3.2 also illustrates the geometry of the jet cross-section A at any station, and its decomposition into the area A_c of the potential core, and the area A_D of the annular mixing zone :-

$$\left.\begin{matrix} A_c = \pi r_c^2, \; A_D = A - A_c = \pi(r_2^2 - r_c^2) \\ A = A_c + A_D \end{matrix}\right\} \tag{3.10}$$

It remains to substitute from (3.8), (3.9) and (3.10) into the axial momentum conservation equation (3.2) :-

$$(hv_o+w)\pi r_o^2 - w(hv_o+w)\pi r_o^2 = \int_{A_c}(hv_o+w)^2 \, dA_c + \int_{A_D}(h_{v_o}U_{v_I}+w)^2 \, dA_D$$

$$- w\int_{A_c}(h_{v_o}+w)dA_c - w\int_{A_D}(h_{v_o} U_{v_I}+w) \, dA_D$$

i.e.

$$(hv_o+w)\pi r_o^2 - w(h_{v_o}+w)\pi r_o^2 = \int_{A_D}(h_{v_o} U_{v_I}+w)^2 \, dA_D - w\int_{A_D}(h_{v_o} U_{v_I}+w) \, dA_D$$

$$+ (h_{v_o}+w)^2\pi r_c^2 - w(h_{v_o}+w)\pi r_c^2$$

Upon rearrangement,

$$(hv_o+w)h_{v_o}\,\pi(r_o^2-r_c^2) = \int_{A_D}[h_{v}^2{}_o\, U_{v_I}^2 + 2w\, h_{v_o}\, U_{v_I} + w^2 - w\, h_{v_o}\, U_{v_I} - w^2]dA_D$$

i.e.

$$(h_{v_o}+w)h_{v_o}\pi(r_o^2-r_c^2) = h_{v_o}\int_{A_D}U_{v_I}^2 \, dA_D + w\int_{A_D}U_{v_I} \, dA_D \tag{3.11}$$

The integrals of (3.11) are written as follows, using (3.5) and (3.7):-

$$\int_{A_D} U_{v_I}^N \, dA_D = 2\pi \int_{r_c}^{r_c+b} U_{v_I}^N (r) r \, dr \qquad dA_D = 2\pi r dr$$

$$= 2\pi \int_0^1 U_{v_I}^N (x) \, (r_c + xb) b dx \qquad r = r_c + xb, \quad dr = b dx$$

$$= 2\pi \left\{ r_c b \int_0^1 U_{v_I}^N (x) dx + b^2 \int_0^1 U_{v_I}^N (x) x \, dx \right\}$$

or, in compact notation :-

$$\int_{A_D} U_{v_I}^N \, dA_D = 2\pi (r_c b \, F_o^N + b^2 \, F_1^N) \qquad N = 1,2 \qquad (3.12)$$

where

$$F_i^N = \int_0^1 U_{v_I}^N (x) x^i \, dx \qquad N = 1,2 \qquad (3.12a)$$

(defining $x^\circ \equiv 1$) The F_i^N are constants as a consequence of the assumed similarity of U_{v_I}, expressed by (3.6). Using (3.12) in (3.11) gives :-

$$(h_{v_o}+w)(r_o^2 - r_c^2) = 2h_{v_o} [r_c b \, F_o^2 + b^2 \, F_1^2] + 2w[r_c b F_o^1 + b^2 F_1^1] \qquad (3.13)$$

Recalling the definition of the velocity ratio parameter m from (3.3a):

$$m = \frac{w}{u_o} \equiv \frac{w}{h_{v_o}+w} \qquad (3.14)$$

from (3.8a). Using this in (3.13) gives:-

$$r_o^2 - r_c^2 = 2(1-m)[r_c b F_o^2 + b^2 F_1^2] + 2m[r_c b F_o 1 + b^2 F_1^1] \qquad (3.15)$$

This is a quadratic equation for r_c, the radial extent of the potential core through the initial region. Grouping terms in the usual way :-

$$r_c^2 + 2b[F_o^2 + m(F_o^1 - F_o^2)]r_c + \{2b^2[F_1^2 + m(F_1^1 - F_1^2)] - r_o^2\} = 0 \qquad (3.16)$$

The solution when m = 0 will be used in Section 3.6. The location of the inner mixing boundary is a function of the assumed velocity profile (through the F_i^n) and the constant G_I (through b). At the end of the potential core ($z=z_c$, $b=b_c$, $r_c=0$), (3.16) reduces to :-

$$\left(\frac{b_c}{r_o}\right)^2 = \frac{1}{2F_1^2 + 2m(F_1^1 - F_1^2)} \qquad (3.17)$$

Then, from (3.4), the length z_c of the potential core is given by :-

$$\frac{z_c}{r_o} = \frac{(1+m)}{G_I(1-m)\sqrt{2F_1^2 + 2m(F_1^1-F_1^2)}} \qquad (3.18)$$

This is a general statement of the equation given by Abramovich (32):-

$$\frac{z_c}{r_o} = \frac{(1+m)}{0.27(1-m)\sqrt{0.214 + 0.144m}}$$

and the latter is recovered when G_I and U_{v_I} are chosen to be those used by Abramovich (Section 3.6).

The other quantity of importance, in view of the available experimental data, is the change with axial distance, in the initial region, of the mass flux across the jet cross-section. This has been measured by Ricou and Spalding (61), Hill (64) and others. The mass flux within the jet is normalised by the origin mass flux :-

$$\frac{\dot{m}}{\dot{m}_o} = \frac{\int_A u\, dA}{\int_{A_o} u_o\, dA_o} = \frac{\rho(h_{v_o} + w)\pi r_c^2 + \rho h_{v_o}\int_{A_D} U_{v_I}\, dA + \rho w A_D}{\rho(h_{v_o} + w)\,\pi r_o^2} \qquad (3.19)$$

Simplifying, and using (3.12a) :-

$$\frac{\dot{m}}{\dot{m}_o} = \frac{r_c^2 + 2(1-m)(r_c b F_o^1 + b^2 F_1^1) + m(r_2^2 - r_c^2)}{r_o^2} \qquad (3.20)$$

(3.20) is very much simplified in the case of a submerged jet (m=0):-

$$\left.\frac{\dot{m}}{\dot{m}_o}\right|_{m=0} = \frac{r_c^2 + 2b(r_c F_o^1 + b F_1^1)}{r_o^2} \qquad (3.21)$$

The mass flux at the end of the potential core is given, in general, by (3.20) with $r_c = 0$ (so that $r_2(z_c) = b_c$):-

$$\left.\frac{\dot{m}}{\dot{m}_o}\right|_{z=z_c} = [2F_1^1 + m(1-2F_1^1)]\left[\frac{b_c}{r_o}\right]^2 \qquad (3.22)$$

For a submerged jet, using (3.17):-

$$\left.\frac{\dot{m}}{\dot{m}_o}\right|_{m=0,z=z_c} = 2F_1^1\left[\frac{b_c}{r_o}\right]^2\Bigg/_{m=0} = \frac{F_1^1}{F_1^2} \qquad (3.23)$$

This most clearly demonstrates that the predicted mass flux at the end of the initial region is determined solely by the choice of the velocity profile U_{v_I}, and this result is used in assessing core length predictions in Section 3.6.

3.4 Theory of the Main Region

Measurements in axisymmetric jets at axial locations far downstream of the nozzle have been reported by Abramovich (32), Corrsin (51), Hinze and Zijnen (56), Albertson (65), Antonia and Bilger (66) and others, and the data has been reviewed by Rajaratnam (43). The downstream, or main region, appears as one of fully developed flow and will here be analysed as such. Abramovich (32) proposed the following law for the rate of spread of an isothermal, isodense axisymmetric jet in a coflowing stream (Chapter 2):-

$$\frac{db}{dz} = G_M \cdot \frac{u_m(z) - w}{u_m(z) + w} \qquad (3.24)$$

The maximum jet velocity $u_m(z)$ in a cross-section (occurring on the jet axis) is shown in Fig. 3.3. In the main region u_m decays with increasing penetration through turbulent mixing at the jet axis. The velocity on the jet axis is again written in terms of the velocity of the external stream and an excess component:-

$$u_m(z) = h_v(z) + w \qquad (3.25)$$

h_v is a decreasing function of z with a limiting value of zero, as far downstream the jet eventually becomes indistinguishable from the free stream with velocity w. When (3.25) is used in (3.24), the width growth law becomes :-

$$\frac{db}{dz} = G_M \left(\frac{h_v}{h_v + 2w} \right) \qquad (3.26)$$

(3.24) is very closely related to (3.3); in the initial region, the condition $u_m \equiv u_o$ simplifies the expression. In the main region, (3.26) implies that the jet boundary is curved when $w \neq 0$ (as h_v decreases). Abramovich (32) gives $G_M = 0.22$ and this value has been almost universally accepted in the literature (62).

The flow in the main region is again determined from the principle of axial momentum conservation, together with the assumed width growth law. The normalised excess velocity distribution, U_{v_M}, of the main region (Fig. 3.3) is defined in a similar way to U_{v_I} of the previous section (see (3.5):-

$$U_{V_M}(r,z) = \frac{u(r,z) - w}{u_m(z) - w} \qquad r \in [o, b(z)] \quad (3.27)$$

in comparing (3.27) with (3.5), recall that $u_m \equiv u_o$ in the initial region and that, in the main region, the mixing zone inner boundary is the jet axis itself, as the undistrubed core has been eroded ($r_c \equiv 0$). In Chapter 2, similarity of U_{V_M} at successive axial stations in the main region was established from the experimental data; the same general constraints may therefore be applied to U_{V_M} as were imposed upon U_{V_I} in (3.7):-

$$U_{V_M} \equiv U_{V_M}(x) \qquad \text{where } x = r/b \text{ (as } r_c \equiv 0)$$
$$U_{V_M} = 1, \; U_{V_M}(1) = 0 \qquad (3.28)$$

and the distribution, over a cross-section, of the jet velocity $u(r,z)$, in the main region, written as :-

$$u(r,z) = h_v(z)\, U_{V_M}(x) + w \qquad (3.29)$$

with $h_v(z)$ defined by (3.25).

The axial momentum conservation equation is again given by (3.1). Upon eliminating the constant ρ, and substituting for u from (3.29), (3.1) becomes :-

$$\frac{d}{dz}\int_A (h_v\, U_{V_M} + w)^2 \, dA = w \frac{d}{dz}\int_A (h_v\, U_{V_M} + w)\, dA$$

Upon rearrangement and the introduction of a compact notation, this is written as :-

$$\frac{d}{dz}\{h_v^2\, I_2 + 2h_v w\, I_1 + w^2\, A\} = w \frac{d}{dz}\{h_v\, I_1 + wA\} \qquad (3.30)$$

where

$$I_N = \int_A U_{V_M}^N \, dA \qquad N = 1,2 \qquad (3.30a)$$

(3.30) can be expanded, simplified, and written as an equation for the rate of change with axial distance of the excess mean velocity function h_v in the main region :-

$$\frac{dh_v}{dZ} = \frac{-h_v\left\{w\frac{dI_1}{dz} + h_v\frac{dI_2}{dz}\right\}}{wI_1 + h_vI_2} \qquad (3.31)$$

The integrals in (3.31) are written as follows, using (3.30A) and (3.28)

$$I_N = \int_A U_{V_M}^N \, dA = 2\pi \int_{r=o}^{r=b} U_{V_M}^N (r)\, r\, dr$$

$$= 2\pi \int_o^1 U_{V_M}^N (x)\, xb^2\, dx \qquad \begin{matrix} r=xb \\ dr=bdx \end{matrix}$$

$$= 2\pi b^2 \int_o^1 U_{V_M}^N (x)\, x\, dx \qquad N=1,2$$

This result is, as expected, equivalent to the initial region form (3.12) with $r_c \triangleq 0$. Since $A = \pi b^2$, the result may be written as :-

$$I_N = K_N A \qquad (3.32)$$

where

$$K_N = \frac{1}{A}\int_A U_{V_M}^N \, dA = 2\int_o^1 U_{V_M}^N (x)x\, dx \qquad N=1,2 \qquad (3.32a)$$

The K_N are constants as a consequence of similarity. Using this result :-

$$\frac{dI_N}{dz} = K_N \frac{dA}{dz} \tag{3.33}$$

and substituting (3.32) and (3.33) into (3.31) gives :-

$$\frac{dh_v}{dz} = - \frac{h_v(wK_1 + h_v K_2)}{A\,(wK_1 + 2h_v K_2)} \cdot \frac{dA}{dz} \tag{3.34}$$

This equation may be integrated by the method of separation of variables. Upon rearrangement :-

$$\frac{(wK_1 + 2h_v K_2)}{(wK_1 + h_v K_2)} \left\{ \frac{1}{h_v} \cdot \frac{dh_v}{dz} \right\} = - \frac{1}{A} \frac{dA}{dz}$$

which could be written as :-

$$\frac{d}{dz} \ell n \{h_v(wK_1 + h_v K_2)\} = - \frac{d}{dz} \ell n \{A\} \tag{3.35}$$

In order to effect a solution for the decay of h_v with increasing penetration, (3.35) should be integrated from the origin of the main region to the general station z. The origin of the main region in this analysis is taken to mean the first axial station, z_D (Fig. 3.1), at which fully developed flow may reasonably be assumed (and therefore to which the discussion of this section applies): this is called the transition section. The location of this station by analysis is considered in the next section; it is only necessary here to define, at z_D, the jet cross-section area $A(z_D) = \pi b^2{}_D$ and the value h_{v_D} for the axial velocity excess (note that if $z_D > z_c$, $h_{v_D} < h_{v_o}$ due to mixing at the jet axis). Upon integration of (3.35), from z_D to some downstream station z where the excess axial velocity is h_v, and the jet cross-section area A:-

$$\frac{(wK_1 + h_v K_2)}{(wK_2 + h_{v_D} K_2)} \left(\frac{h_v}{h_{v_D}} \right) = \frac{A(z_D)}{A} = \left(\frac{b_D}{b} \right)^2 \tag{3.36}$$

where the jet radius b at z is determined from (3.26). The solution of the coupled set, (3.26) and (3.36), is more involved than instructive (see Abramovich (32)) and demonstrates the observation of Schetz (49) that the classical analytical techniques extend only with difficulty

to problems where $w \neq 0$. In this chapter, it is the intention to illustrate significant features of the theory prior to its general statement (Chapters 4 and 5), and in this respect it is useful to consider only the case when $w = 0$. The solution here is quite trivial, since (3.26) becomes :-

$$\left.\frac{db}{dz}\right/_{m=o} = G_M \qquad z > z_D \quad (3.37)$$

integrating to :-

$$b/_{m=o} = G_M(z - z_D) + b_D \qquad z > z_D \quad (3.38)$$

Furthermore, (3.36) is, simply :-

$$\left(\frac{h_v}{h_{v_D}}\right)/_{m=o} = \frac{b_D}{b} \qquad z > z_D \quad (3.39)$$

Substituting for b from (3.38) gives :-

$$\left(\frac{h_v}{h_{v_D}}\right)/_{m=o} = \frac{b_D}{G_M(z-z_D) + b_D} = \frac{1}{\left[1 - \frac{G_M z_D}{b_D}\right] + G_M \cdot \frac{z}{b_D}} \quad (3.40)$$

Clearly this could also be written as :-

$$\left(\frac{h_v}{h_{v_o}}\right)/_{m=o} = \frac{(h_{v_D}/h_{v_o})}{\left[1 - \frac{G_M z_D}{b_D}\right] + \frac{G_M r_o}{b_D} \cdot \frac{z}{r_o}} \quad (3.41)$$

(3.41) is now in the form

$$\left(\frac{h_v}{h_{v_o}}\right)/_{m=o} = \frac{1}{C_1 + C_2 \cdot \frac{z}{r_o}} \qquad C_1, C_2 \text{ constant}$$

As (z/r_o) becomes large, the following limiting form is observed :-

$$\left(\frac{h_v}{h_{v_o}}\right)\Big/_{m=o} \rightarrow \frac{1}{C_2}\left(\frac{z}{r_o}\right)^{-1}, \qquad C_2 = \frac{h_{v_o}}{h_{v_D}} \cdot \frac{G_M r_o}{b_D} \tag{3.42}$$

which is the much reported power law decay for axial velocity (49), appropriate to the flow some distance downstream from the nozzle: the nature of the approximation is considered in Section 3.6.

In practice, the most interesting feature of the main region is the change in the jet mass flux through entrainment at successive axial stations. From the definition (3.19), using the notation of this section :-

$$\frac{\dot{m}}{\dot{m}_o} = \frac{\int_A u \, dA}{\int_{A_o} u_o dA_o} = \frac{h_v \int_A U_{v_M} dA + wA}{(h_{v_o}+w)A_o}$$

or

$$\frac{\dot{m}}{\dot{m}_o} = \frac{(h_v K_1 + w)}{(h_{v_o} + w)} \cdot \left(\frac{A}{A_o}\right)$$

$$= \left[K_1 \left(\frac{h_v}{h_{v_o}}\right)\left(\frac{h_{v_o}}{h_{v_o} + w}\right) + \frac{w}{h_{v_o} + w}\right] \left\{\frac{b}{r_o}\right\}^2$$

$$= \left[K_1 (1-m)\left(\frac{h_v}{h_{v_o}}\right) + m\right] \left\{\frac{b}{r_o}\right\}^2 \tag{3.43}$$

using (3.14) for m. When m=o :-

$$\frac{\dot{m}}{\dot{m}_o}\Big/_{m=o} = K_1 \left(\frac{h_v}{h_{v_o}}\right)\left\{\frac{b}{r_o}\right\}^2 \tag{3.44}$$

It is interesting to consider the entrainment of external fluid into the jet envelope in the main region of a submerged jet, as this has been the subject of previous investigation (61). The entrainment rate E_m is defined as the rate of change of the jet mass flux :-

$$E_m = \frac{d}{dz} \int_A \rho u \, dA \qquad (3.45)$$

(this equation, a general statement of the continuity equation, is the basis for the entrainment models described in Chapters 2 and 4). Ricou and Spalding (61) found that the rate of entrainment into a submerged (m=o) jet, in the main region, was constant at any axial station, and obtained the following correlation :-

$$E_m \Big/_{m=o} = C_E \sqrt{\pi} \, \rho u_o r_o \qquad (3.46)$$

where

$$C_E = 0.28 \qquad (3.46a)$$

is the most reliable value for the entrainment constant (61). An equation in the form of (3.46) may be obtained by the expansion of (3.45) :-

$$E_m \Big/_{m=o} = \rho \frac{d}{dz} \{h_v I_1\} = \rho \{ h_v \frac{dI_1}{dz} + I_1 \frac{dh_v}{dz} \} \qquad (3.47)$$

using the notation of this section. Using (3.33) and (3.34) with w=o, (3.47) becomes :-

$$E_m \Big/_{m=o} = \rho \left\{ h_v K_1 \frac{dA}{dz} - \frac{h_v K_1}{2} \frac{dA}{dz} \right\} = \rho \frac{K_1 h_v}{2} \frac{dA}{dz}$$

For the axisymmetric submerged jet in the main region, using (3.37) :-

$$\frac{dA}{dz} = 2\pi b \frac{db}{dz} = 2\pi b \, G_M$$

Hence, in the above :-

$$E_m \Big/_{m=o} = \rho K_1 G_M \pi h_v b \qquad (3.48)$$

When m=o, the axial momentum equation (3.1) integrates simply to :-

$$\int_{A_o} u_o^2 \, dA_o = \int_A u^2 \, dA$$

In the main region, therefore, this gives :-

$$u_o^2 \, \pi r_o^2 = h_v^2 \, K_2 \, A = h_v^2 \, K_2 \, \pi b^2$$

Hence, in (3.48)

$$u_o^2 \, r_o^2 = K_2 \, h_v^2 \, b^2 \quad => \quad E_m \Big/_{m=o} = \frac{\pi K_1 \, G_M \, \rho u_o r_o}{\sqrt{K_2}}$$

This result can be written in a form equivalent to the correlation (3.46)

$$E_m \Big/_{m=o} = C_{E_m} \sqrt{\pi} \, \rho \, u_o r_o \qquad (3.49)$$

where

$$C_{E_m} = \frac{\sqrt{\pi} \, G_M \, K_1}{\sqrt{K_2}} \qquad (3.49a)$$

In Section 3.6 the settings for the width growth constant G_M and velocity profile U_{VM} are assessed by comparing resulting values for (3.49a) with (3.46a).

Before attempting predictions, the conditions at, and location of, the transition section at z_D must be determined. This is the subject of the remaining part of the analysis.

3.5 Theory of the Transition Region

The width growth law (3.3), for the mixing zone of the initial region, was derived by Abramovich (32) assuming the shear layer to be created between parallel infinite and semi-infinite streams of uniform velocity (Chapter 2). Further, the width growth law (3.26) is applicable to a fully developed turbulent jet, which could also be termed a free shear flow. From the end of the potential core, however, the shear layers of the initial region merge at the jet axis and there will be a region of the flow, the transition region, within which the flow conditions approach those of the fully developed or main region, as discussed in the previous section.

In order to characterise the transition region as one of developing flow, consider the velocity profile U_{v_I} of Section 3.3 and U_{v_M} of Section 3.4 (Fig. 3.3). The experimental data relating to these profiles was discussed in Chapter 2: it was observed that when plotted against the radial ordinate x, U_{v_I} was more full than U_{v_M}; that is to say, over the length $z \in [z_c, z_D]$, the velocity profile U_v across the jet width b must continuously develop from U_{v_I} at z_c to U_{v_M} at z_D (see Fig. 3.3). Profile development is a feature of straight jet predictions using a turbulence model approach (Appendix A), and if an integral model is to offer competitive detail, it should be devised to represent it. In the past, many workers have neglected this region, although Schetz (67) has brought attention to its importance. Others, such as Newman and Brzustowski (31), have used a simplified form of perhaps the most complete integral model-type analysis, due to Abramovich (32). The method and merits of this latter will be described later. The lack of analytical work is unsurprising since very little experimental work seems to have been done; indeed, the only such seems to be that of Albertson (65), who undertook the very difficult task of locating the transition section z_D of jets for various values of m (see Abramovich (32)). An integral model analysis will seek to represent the effects of the flow structure rather than its causes, and there will be three such effects to be prescribed in the transition region :-

1. A width growth law for b on $[z_c, z_D]$. The growth laws for the initial and main regions were derived by Abramovich assuming similarity of the velocity profile. In the transition region a more empirical prescription will be sought.

2. The representation of the developing velocity profile.

3. The length z_D to the transition section.

In this section a general theory is presented which addresses the points 1, 2 and 3. Some preliminary predictions are then attempted in Section 3.6.

In describing the transition region of a submerged jet, Abramovich (32) notes that the outer mixing boundary of the jet is observed to be approximately a projection of the outer mixing boundary of the initial region. In Fig. 3.4, this profers a geometric motivation for the growth rate of the jet at the end of the potential core :-

$$\left.\frac{db}{dz}\right|_{m=o,\ z=z_c} = G(z_c) \tag{3.50}$$

where :-

$$G(z_c) = \tan\theta = \left.\left(\frac{b_c - r_o}{z_c}\right)\right|_{m=o} \tag{3.50a}$$

The assumption of a straight outer boundary is a simplification and would lead to a growth rate which is not smooth across the transition section (Fig. 3.4), since at z_D, where the main region relations of the last section apply, the width growth law is given by (3.37):-

$$\left.\frac{db}{dz}\right|_{m=o,z=z_D} = G_M$$

and in Section 3.6 it will be seen that $G(z_c)$ and G_M are significantly different. Thus, the assumption of a straight outer boundary in the transition region of a submerged jet must be abandoned; instead, a smooth solution is ensured using (3.37) as a boundary condition on the growth rate in the transition region :-

$$\left.\frac{db}{dz}\right|_{m=o,z=z_D} = G(z_D) \tag{3.51}$$

where

$$G(z_D) = G_M \tag{3.51a}$$

The jet growth rate on $[z_c, z_D]$ might then be expressed, for a submerged jet, as :-

$$\frac{db}{dz}\Big/_{m=o} = G(z) \qquad z\in[z_c, z_D] \tag{3.52}$$

where G(z) is some smooth function satisfying the boundary conditions (3.50a) and (3.51a). In the case of the jet in a coflowing stream (3.52) might be modified by analogy with (3.26):-

$$\frac{db}{dz} = G(z)\left(\frac{h_v}{h_v + 2w}\right) \qquad z\in[z_c, z_D] \tag{3.53}$$

A function such as G(z) is best investigated by variation as a parameter within a computer program (Chapter 6): in Section 3.6 a simple linear form is used, and appears satisfactory in later work (Chapter 7).

In order to represent a developing velocity profile in the analysis it is only necessary to allow the normalised excess velocity profile U_v in the transition region to vary with the axial station z :-

$$U_v \equiv U_v(x,z) = \frac{u(x,z) - w}{u_m(z) - w} \qquad \begin{matrix} x=r/b(z)\in[0,1] \\ z\in[z_c, z_D] \end{matrix} \tag{3.54}$$

The profile U_v must satisfy the following constraints :-

$$\left.\begin{aligned} U_v(0,z) &= 1 \qquad U_v(1,z) = 0 \\ U_v(x,z_c) &= U_{v_I}(x) \\ U_v(x,z_D) &= U_{v_{M_1}}(x) \end{aligned}\right\} \tag{3.55}$$

The axial momentum equation (3.1) can now be used to obtain an equation for the excess velocity decay along the jet axis in the transition region, using :-

$$u_m(z) = h_v(z) + w \qquad z\epsilon[z_c, z_D]$$

$$u(r,z) = h_v(z)\, U_v(x) + w \qquad z\epsilon[z_c, z_D] \qquad (3.56)$$

The method is identical to that used for the main region and the same equation (3.31) ensues :-

$$\frac{dh_v}{dz} = \frac{-h_v\left\{ w\frac{dI_1}{dz} + h_v\frac{dI_2}{dz}\right\}}{wI_1 + h_v I_2} \qquad z\epsilon[z_c, z_D] \qquad (3.57)$$

The difference between (3.57) and (3.31) lies in the definition of the integrals I_N :-

$$I_N = \int_A U_v^N\,(r,z)\,dA \qquad N = 1,2 \qquad z\epsilon[z_c, z_D] \qquad (3.57a)$$

By analogy with (3.32), the I_N could be written as :-

$$I_N = K_N(z)\,A \qquad z\epsilon[z_c, z_D] \quad N = 1,2 \qquad (3.57b)$$

In the transition region the $K_N(z)$ are not constant (cf. (3.32)) because U_v is not a similarity profile. By (3.55) and (3.32a) :-

$$K_N(z_D) = K_N \qquad N = 1,2$$

ensures continuity. Differentiating (3.57b) gives

$$\frac{dI_N}{dz} = K_N(z)\frac{dA}{dz} + A\frac{dK_N}{dz}(z) \qquad z\epsilon[z_c, z_D] \quad N = 1,2 \qquad (3.58)$$

and upon substitution (3.57) becomes :-

$$\frac{dh_v}{dz} = \frac{-h_v\,(wK_1(z) + h_v K_2(z))}{A\,(wK_1(z) + 2h_v K_2(z))}\cdot\frac{dA}{dz} - \frac{h_v\left\{ w\frac{dK_1(z)}{dz} + h_v\frac{dK_2(z)}{dz}\right\}}{(wK_1(z) + 2h_v K_2(z))} \qquad (3.59)$$

It was noted above that the mixing region profile U_{v_I} is apparently more full than U_{v_M} (Fig. 3.3); as a consequence :-

$$\frac{dK_N(z)}{dz} < 0 \qquad N=1,2 \quad z\epsilon[z_c, z_D)$$

the extra term on the right hand side of (3.59) (compared with (3.34)) is therefore positive and will act to inhibit the velocity decay rate on the jet axis in the transition region (see Section 3.6). Again it is not instructive to solve (3.59) directly, but for the case w=o the solution is once more straightforward. In this case, (3.59) becomes :-

$$\left.\frac{dh_v}{dz}\right|_{m=o} = -\frac{hv}{2A}\frac{dA}{dZ} - \frac{hv}{2K_2(z)}\frac{dK_2(z)}{dz} \qquad z\epsilon(z_c, z_D) \qquad (3.60)$$

For a solution in the transition region, (3.50) must be integrated from the end of the potential core (Fig. 3.3). The result is, by separation of variables :-

$$\left.\frac{hv(z)}{hv_o}\right|_{m=o} = \sqrt{\frac{K_2(z_c)}{K_2(z)}}\cdot\sqrt{\frac{A(z_c)}{A(z)}} = \sqrt{\frac{K_2(z_c)}{K_2(z)}}\left\{\frac{b_c}{b(z)}\right\} \qquad (3.61)$$

The inhibiting effect of profile development upon velocity decay is evident ($K_2(z_c)/K_2(z) > 1$). For $K_2(z_c)$, using (3.55), (3.57b) and (3.12) at $r_c = 0$:-

$$K_2(z_c) = 2F_1^2 \qquad (3.61a)$$

(3.61) must be solved with (3.52) for b, and this is done in the next section. The derivation of the mass flux in the transition region does not differ from that by which (3.43) was obtained; the result is :-

$$\frac{\dot{m}}{\dot{m}_o} = \left[K_1(z).(1-m)\left\{\frac{h_v}{hv_o}\right\} + m\right]\left[\frac{b}{r_o}\right]^2 \qquad z\epsilon[z_c, z_D] \qquad (3.62)$$

The last undetermined quantity is z_D itself. From the available data, Abramovich (32) observed that :-

$$\frac{z_D}{z_c} \simeq 1.5 \tag{3.63}$$

was not a serious oversimplification when $m < 0.4$ (or indeed for variable density jets). This approximation is employed in the next section, in which the preceding results are used in the prediction of an axisymmetric submerged jet.

3.6 A Comparison of Prediction with Experiment for the Submerged Jet

3.6.1 The Initial Region

The most important quantity to be predicted is the length z_c of the potential core. Although this section is predominantly concerned with the case m = 0, use is also made of the well-documented case m = 0.25 for validation of the initial region theory. The general core length formula is (3.18), and it is necessary to specify a precise form for U_{v_I} and value for the width growth coefficient G_I. The Abramovich (32) formula for U_{v_I} is in sufficiently good agreement with the experimental data (Chaper 2):-

$$U_{v_I}(x) = 1 - (1- [1-x]^{3/2})^2 \qquad x\in[0,1] \tag{3.64}$$

The ordinate x is defined in (3.6). When (3.64) is used to carry out the integrations in (3.12a) :-

$$F_1^1 = 0.177; \quad F_1^2 = 0.105 \tag{3.65}$$

Substituting these values into (3.18) gives the core length formula of Abramovich (32) :-

$$\frac{z_c}{r_o} = \frac{(1 + m)}{G_I(1-m).\sqrt{0.21 + 0.144m}} \tag{3.66}$$

Based upon the available data, Abramovich (32) gave :-

$$G_I = 0.27 \tag{3.67}$$

The predictions of (3.66) with (3.67) are displayed in Figure 3.5 and are there compared with the measurements of Rajaratnam and Pani (54) and the empirical equation of Forstall and Shapiro (52) :-

$$\frac{z_c}{r_o} = 8 + 24m$$

this being based upon their own series of measurements.

The data available to Abramovich (32) appears to be principally that of Albertson (65) and Forstall and Shapiro (52), which suggest $z_c \approx 8\ r_o$ for submerged jets, and in which case (3.66) and (3.67) gives an accurate prediction (Fig. 3.5). This, however, is by no means conclusive : Rajaratnam and Pani (54) measured $z_c \approx 10\ r_o$, and such a value is also mentioned by Keffer and Baines (69) in a general discussion of the initial region of a submerged jet. As further corroboration, the method of location of the transition section (to be described later) appears to lead to the following conclusions :-

1. $\left.\frac{z_c}{r_o}\right/_{m=o} \approx 10\ r_o$

2. In Albertson's experiments (65), the jet may suffer from the presence of a significant boundary layer on the inside of the nozzle, leading to a reduction in the length of the core, compared with a jet of uniform injection velocity.

Finally, Patrick (70) and Platten and Keffer (37) both appear to measure $z_c > 8\ r_o$ in isodense, isothermal jets directed normal to significant crossflows. Keffer and Baines (69) observe that the action of a crossflow is to promote turbulent mixing and thus reduce the length of the undisturbed core of fluid (see Chapter 4); as the crossflow velocity diminishes toward zero and the flow approaches that of a submerged jet, in Patrick's experiments (70), z_c approaches a value which is not less than $10\ r_o$ (Chapter 7). Therefore, on the basis of these observations, and especially if realistic predictions of the core length in deflected jets are to be made in the later chapters, the $m = 0$ core length prediction $z_c = 8\ r_o$, from Abramovich, must be considered to be too low.

Having reached this conclusion, it is necessary to re-assess the choice of constants for the general core length formula (3.18). The Abramovich definition for U_{v_I} in (3.64) appears to be adequate and will not be departed from in this chapter of preliminary analysis. It is necessary, then, to advert to the constant G_I : it transpires that there is considerable justification in questioning the value in (3.67).

Abramovich (32) explains that G_I is determined in proportion to another coefficient a, which is evaluated from submerged jet experiments :-

$$G_I \sim a$$

The coefficient a appears to increase as a function of the non-uniformity of the injection velocity profile at the plane of the nozzle (32). Albertson measured a = 0.096 in the experiment from which Abramovich inferred $G_I = 0.27$, while Rajaratnam (43) records that, in the experiments of Trupel, the injection velocity was virtually uniform and that, in this case, a = 0.066 was determined. If the proportionality relation is used, this gives $G_I = 0.198$, so that a wide variation in G_I seems to be possible according to the fine detail of the injection conditions in the different experiments. Baron (71), in a deflected jet computer model, used the Abramovich core length formula (3.66) with G_I reset at 0.167 in order to obtain a submerged jet core length (reported by Platten and Keffer (37)) which exceeds any other value given in the literature. Presumably the 'Trupel' value $G_I = 0.198$ should be taken as a lower limit. Because of this indeterminacy, it is really only possible to proceed intuitively. Interestingly, if G_I is chosen arbitrarily using the main region width-growth constant (which is seemingly well-established - Section 3.4):-

$$G_I = G_M = 0.22 \qquad (3.68)$$

the following prediction is afforded by (3.66) :-

$$\left.\frac{z_c}{r_o}\right/_{m=o} = 9.92 \qquad (3.69)$$

which is a reasonable prediction according to the remarks made above. Consider also the prediction when m = 0.25, using (3.66) with (3.68):-

$$\left.\frac{z_c}{r_o}\right/_{m=0.25} = 15.15$$

This is in poor agreement with the data of Rajaratnam and Pani (54) (Fig. 3.5), but sufficiently close to the value $z_c \simeq 14\ r_o$ determined by Landis and Shapiro (58) (for an almost constant density jet) and to the empirical relation in Fig. 3.5 to support the use of this revised value for G_I in the subsequent work. It is this apparent overprediction at $m \simeq 0.25$ which motivates against the use of $G_I = 0.198$ (from Trupel), as this would result in yet higher values for z_c.

The length of the initial region, when $m = o$, with the choice of constants as discussed is given by (3.69). The predicted mass flux at the end of the core is given by (3.23) and (3.65) as :-

$$\left.\frac{\dot{m}}{\dot{m}_o}\right/_{m=o,z=z_c} = \frac{F_1^1}{F_1^2} = \frac{0.177}{0.105} = 1.69 \text{ approx.} \qquad (3.70)$$

From the measurements of Sforza(72) and those collected by Hill (64) it might be concluded that :-

$$\left.\frac{\dot{m}}{\dot{m}_o}\right/_{m=o,\ z=9.92\ r_o} \simeq 1.8 - 1.9 \qquad (3.71)$$

The location of the inner boundary r_c of the mixing zone is, according to the theory, given by (3.16).

The solution of (3.16) may be written as :-

$$\left[\frac{r_c}{r_o}\right] = -B_D\left[\frac{b}{r_o}\right] \pm \sqrt{B_0^2\left[\frac{b}{r_o}\right]^2 - 2B_1\left[\frac{b}{r_o}\right]^2 + 1} \qquad (3.72)$$

where

$$B_0 = F_o^{\,2} + m(F_o^{\,1} - F_o^{\,2})$$
$$B_1 = F_1^{\,2} + m(F_1^{\,1} - F_1^{\,2}) \qquad (3.72a)$$

Here $F_1^{\,1}$ and $F_1^{\,2}$ are known from (3.65) and $F_o^{\,1}$, $F_o^{\,2}$ are evaluated from (3.12a) using U_{vI} defined by (3.64):-

$$F_1^{\,1} = 0.177, \quad F_1^{\,2} = 0.105, \quad F_o^{\,1} = 0.55, \quad F_o^{\,2} = 0.273 \qquad (3.72b)$$

In particular, when m=o, (3.72) becomes :-

$$\bar{r}_{c\,/\,m=o} = -F_o^{\,2}\bar{b} + \sqrt{\bar{b}^2\{(F_o^{\,2})^2 - 2F_1^{\,2}\} + 1} \qquad (3.73)$$

where

$$\bar{r}_c = \frac{r_c}{r_o}, \quad \bar{b} = \frac{b}{r_o} \qquad (3.73a)$$

Such an equation has been written by Rajaratnam (43). The possibility of the negative square root is excluded as $\bar{r}_c$ is certainly non-negative. When b is determined from (3.4), both r_c and $r_2 = r_c + b$ may be determined throughout the initial region. Such predictions for a submerged jet are recorded in Table 3.1 and are compared with the experimental results of Rajaratnam and Pani (54) in Fig. 3.6; agreement appears to be satisfactory if the non-uniformity of the velocities at the plane of the nozzle (z=o) in the experiment is taken into account. A further comparison with experiment (from the same source) is given for the case m=0.257 (Table 3.2 and Fig. 3.6), and here the agreement is less satisfactory. The elongation of the initial region exaggerates the influence of the initial non-uniformity in velocity (see Chapter 7).

Having determined r_c and r_2 as functions of z, the mass flux in a

submerged jet at any station in the initial region may be computed from (3.21). The results of such calculations are recorded later, after the following discussion of the downstream regions.

3.6.2 The Transition and Main Regions

The following analysis, after Abramovich (32), was used by Newman and Brzustowzki (31) in locating the transition section z_D of a submerged jet. The axial momentum conservation equation is integrated to z_D (for uniform injection velocity u_o), the station at which a fully developed mean flow is assumed to be finally established. From (3.2):-

$$\int_{A(z_D)} \rho u^2 dA = \rho (u_m^2 K_2 \pi b^2) / _{z=z_D} = \rho h_{v_D}^2 K_2 \pi b_D^2 = \rho U_o^2 K_2 \pi r_o^2 \qquad (3.74)$$

or :-

$$\rho h_{v_D}^2 K_2 \pi b_D^2 = \mathcal{M}_o, \text{ where } \mathcal{M}_o = \rho u_o^2 K_2 \pi r_o^2 \qquad (3.75)$$

Now (3.75) motivates the replacement of the jet, as described in Fig. 3.1 with an equivalent, fully developed jet, issuing from a point source with momentum $\mathcal{M}_o$. The jets become coincident at z_D, as illustrated in Fig. 3.7. This idea has been discussed by Abramovich. According to Albertson, the location along the z-axis of the 'point source', called the virtual origin of the jet, varies as a function of the parameter m (in a complicated manner - see also Rajaratnam (43)), and that when m=o, the virtual origin rests approximately at the plane of the nozzle (z=o).

Newman and Brzustowzki (31) assumed that $h_{v_D} = h_{vo} \equiv u_o$ in order to find b_D from (3.74) :-

$$\frac{b_D}{r_o} / _{m=o} \frac{1}{\sqrt{K_2}} \qquad (3.76)$$

In particular, using the Abramovich definition for the main region velocity profile (given in Chapter 2):-

$$U_{V_M}(x) = (1-x^{3/2})^2 \quad ; \quad x = r/b(z) \quad [o,1] \tag{3.77}$$

K_2 may be evaluated from (3.32a) as :-

$$K_2 = 0.138 \text{ approx.} \tag{3.78}$$

Then :-

$$\left.\frac{b_D}{r_o}\right/_{m=o} = \frac{1}{\sqrt{K_2}} \approx 2.692 \tag{3.79}$$

Use is now made of the approximation mentioned in Section 3.5, that the boundary $r_2(z)$ on $[z_c, z_D]$ is a projection of the approximately linear outer mixing boundary in the initial region (see Fig. 3.6). A relation is obtained for the axial station z_D at which the jet width is b_D:-

$$\bar{z}_D = (\bar{b}_D - 1) \quad [\bar{z}_c / (\bar{b}_c - 1)] \tag{3.80}$$

where an overbar denotes a quantity normalised by r_o. Using the results from the previous section, for a constant density jet :-

$$\bar{z}_c = 9.912, \quad \bar{b}_c = G_I \bar{z}_c = 2.18 \tag{3.80a}$$

Hence, from (3.80)

$$\bar{z}_D = 14.2 \Rightarrow \frac{z_D}{z_c} = 1.43 \tag{3.81}$$

This result compares favourably with the Abramovich observation (3.63) that $z_D/z_c \approx 1.5$ The analytical method is not exact, since $h_{v_D} \neq h_{v_o}$ and $r_2(z)$ is not exactly linear on $[o,z_D]$, and is often used in conjunction with a power law approximation for the velocity decay in the main region :-

$$\left.\frac{h_v}{h_{v_o}}\right/_{m=o} = \bar{z}_D \, \bar{z}^{-1} \tag{3.82}$$

(cf(3.42)). Semi-empirical models of this type, with z_D based upon velocity decay measurements, are discussed by Rajaratnam (43). In Trupel's (uniform injection velocity) experiments, for example :-

$$\bar{z}_D \Big/_{m=o} = 14.64 \tag{3.83}$$

in (3.82), while for the data of Albertson :-

$$\bar{z}_D \Big/_{m=o} = 12.4 \tag{3.84}$$

Comparing these results with (3.81) suggests that Albertson's data suffers from the presence of a significant boundary layer at the nozzle, as discussed in the previous section. For the Albertson data Abramovich gave $\bar{z}_c \approx 8$, so that, using (3.84):-

$$\frac{\bar{z}_D}{\bar{z}_c} \Big/_{\substack{m=o \\ \text{Albertson} \\ \text{data}}} = \frac{12.4}{8} = 1.55$$

The approximation $z_D/z_c = 1.5$ appears to be reasonable for a range of injection profile examples.

The virtual origin method of locating z_D is avoided in the present work : the variation in the virtual origin location with m, n, nozzle velocity profile and the introduction of a crossflow is not well documented, and the empirical relation (3.63) for z_D is likely to be just as accurate, as well as allowing for a more natural description of developing flow beyond z_c.

The equations of Section 3.5 are now used to predict the submerged jet in the transition region. For simplicity a linear variation for G(z) and $K_2(z)$ will be assumed over $[z_c, z_D]$:-

$$G(z) = G(z_c) + \frac{[G_m - G(z_c)]}{(z_D - z_c)} (z - z_c) \quad z \in [z_c, z_D] \tag{3.85}$$

$$K_2(z_c) = K_2(z_c) + \frac{[K_2 - K_2(z_c)]}{(z_D - z_c)} (z - z_c) \quad z \in [z_c, z_D] \tag{3.86}$$

These choices ensure a continuous (but not smooth) variation at Z_c, z_D for G and K_2, this being the penalty for a straightforward analytic solution. Thus, $G(z_c)$ is computed from (3.50a) using the results, (3.80a), from the initial region analysis :-

$$G(z_c) = \frac{2.18 - 1}{9.912} = 0.119 \tag{3.87}$$

Using (3.77) for U_{v_M}, K_2 is given by (3.78). Also, from (3.51a) and (3.72b) :-

$$K_2(z_c) = 2F_1^2 = 0.21 \tag{3.88}$$

For m=o, (3.85) is used with (3.87) in (3.52) integrated from z_c:-

$$b_{m=o}/ = \int_{\eta=z_c}^{\eta=z} G(\eta)\, d\eta + b_c \qquad z\epsilon[z_c, z_D]$$

$$= G(z_c)(z-z_c) + \frac{[G_m - G(z_c)]}{(z_D-z_c)} \left\{ \frac{(z^2-z_c^2)}{2} - z_c(z-z_c) \right\} + b_c$$

Simplifying, and substituting for G_M, $G(z_c)$, z_c, b_c, and z_D as determined above gives :-

$$b_{m=o}/ = 0.119\,(z-9.912r_o) + \frac{0.101}{9.912r_o}(z-9.912r_o)^2 + 2.18$$

or

$$\bar{b}_{m=o}/ = 0.119(\bar{z}-9.912) + 0.01\,(\bar{z}-0.912)^2 + 2.18 \quad z\epsilon[z_c, z_D] \tag{3.89}$$

The variation for K_2 is found by (3.86) with the appropriate substitutions:-

$$K_2(z) = 0.21 - 0.0145\,(\bar{z}-9.912) \qquad z\epsilon[z_c, z_D] \tag{3.90}$$

The velocity decay along the jet axis is determined from (3.61) :-

$$\left.\frac{h_v}{h_{v_o}}\right/_{m=o} = \sqrt{\frac{0.21}{K_2(z)}}\quad\frac{2.18}{\bar{b}} \qquad z\in[z_c,z_D] \quad (3.91)$$

The mass flux is then determined from (3.62); for a full solution, it would be necessary to specify the variation of K_1 with z, itself consistent with the variation of $K_2(z)$. This is not particularly instructive, however, and the theory will be validated by comparing with experiment the predicted mass flux at the end of the transition region. The solutions of (3.89), (3.90) and (3.91) are detailed in Table 3.3, the final results being at $z_D = 1.5z_c$. Using these results in (3.62), and noting that for U_{v_M} defined by (3.77),

$$K_1 \equiv K_1(z_D) = 0.257 \qquad \text{(from definition (3.32a))} \qquad (3.92)$$

it follows that :-

$$\left.\frac{\dot{m}}{\dot{m}_o}\right/_{m=o,z=z_D} = K_1\left[\frac{h_{v_D}}{h_{v_o}}\right]\left[\frac{b_D}{r_o}\right]^2 = 2.09 \text{ approx.}$$

According to the data of Sforza (72):-

$$\left.\frac{\dot{m}}{\dot{m}_o}\right/_{m=o,\bar{z}=5} \simeq 2.1 \rightarrow 2.3$$

The agreement is reasonable given the crudity of the treatment in this section. The predictions are now completed using the main region equations from Section 3.4.

The width growth constant and velocity profile U_{v_M} for the main region are taken directly from Abramovich :-

$$G_M = 0.22, \quad U_{v_M} = (1-x^{3/2})^2 \quad x\in[o,1] \qquad (3.93)$$

The jet width b is given by (3.38). Substituting for G_M and z_D, b_D as determined above :-

$$\bar{b}\ /_{m=o} = 0.22\ (\bar{z} - 14.868) + 3.02 \qquad z>z_D \qquad (3.94)$$

The axial velocity is given by (3.41) with appropriate substitutions :-

$$\frac{h_v}{h_{v_o}}\ /_{m=o} = \frac{0.89}{-0.083 + 0.07285\ \bar{z}} \qquad z>z_D \qquad (3.95)$$

The mass flux can then be found from (3.44), with K_1 taking its value from (3.92). The results of these computations are given in Table 3.4. In Fig. 3.8, the results of this section for each of the jet regions are compared with the axial velocity decay data of Albertson (reported by Abramovich (32)). This data is apparently confirmed, in the main region, by data from other sources reported by Abramovich (32) and Schatzmann (73). The predictions of this section are in close agreement with the data : in the transition region, the rate of decay of velocity is smaller than in the main region, as predicted by the present theory. The 'point source' or 'virtual origin' treatment of the transition region does not represent this detail (the Abramovich solution of this type is also given in Fig. 3.8). The predictions lie above Albertson's data for the transition region as a result of nozzle boundary layer effects in the experiment. Further downstream (z/D_o greater than about 10) the influence of the fine detail of the injection is lost. For the main region, it is interesting to revert to the power law approximation for velocity decay from (43) :-

$$\frac{h_v}{h_{v_o}}\ /_{m=o} \rightarrow \frac{1}{C_2}\left[\frac{z}{r_o}\right]^{-1} \qquad (3.96)$$

where, from the results of this section :-

$$\frac{1}{C_2} = \frac{h_{v_o}}{h_{v_D}} \cdot \frac{G_M r_o}{b_D} = 12.17 \qquad (3.96a)$$

If equality is assumed in (3.96), the resulting velocity predictions fall below the results of the more complete analysis (the solutions of course converge as z increases) as a result of the simplification of form from (3.41). This simplification is somewhat offset in the 'virtual origin' theory by the further assumptions $h_{v_D} \equiv h_{v_o}$ and those concerning b_D, so that in this case the power-law decay is identical to the

Abramovich solution in Fig. 3.8. The present solution is thus more sophisticated in terms of both transition and main region analyses, and this is important for the detailed representation of more complicated cases (Chapter 7).

Finally, the predicted mass flux when m=o is compared with the available data in Fig. 3.9. As discussed in Section 3.4, the entrainment rate is constant throughout the main region, which, according to the data, begins at about z/D_o = 7-8. The simple prediction of z_D, the transition section, as $z_D/D_o = 1.5z_c/D_o \approx 7.44$, appears to be adequate, and the mass flux predictions themselves agree with the data for both the initial and main regions. The entrainment constant, defined in (3.49a), C_{E_m} for the main regions, with the empirical input prescribed in (3.93), is evaluated as :-

$$C_{E_m} = \frac{\sqrt{\pi}\, G_M\, K_1}{\sqrt{K_2}} = \frac{\sqrt{\pi} \times 0.22 \times 0.257}{0.138} = 0.27$$

which compares favourably with the value C_E = 0.28 reported by Ricou and Spalding (61). It is noted that the cosine profile definition for U_{v_m}, recalled here from Chapter 2 :-

$$U_{v_M}(x) = \frac{1}{2}\,[1 + \cos\pi x]$$

gives an even better value for C_{E_m} in comparison with C_E :-

$$\{K_1 = 0.2974,\ K_2 = 0.1724\}\ /\ \underset{\text{cosine profile}}{\Rightarrow}\ C_{E_m} = 0.279$$

However, the model is sufficiently insensitive to the choice for U_{v_M} (cf.(3.36)) to permit the continued use of the Schlichting formula in (3.93), as will be demonstrated in Chapter 7.

z/r_0	b/r_0	r_c/r_0	r_2/r_0
1	0.22	0.9367	1.1567
2	0.44	0.8667	1.3067
3	0.66	0.7899	1.4499
4	0.88	0.7059	1.5859
5	1.10	0.6141	1.7141
6	1.32	0.5137	1.8357
7	1.54	0.4053	1.9463
8	1.76	0.2813	2.0413
9	1.98	0.1442	2.1242
9.912	2.18	0	2.1800

TABLE 3.1 PREDICTION OF THE MIXING ZONE BOUNDARIES WHEN m=0 (INITIAL REGION)

z/r_0	b/r_0	r_c/r_0	r_2/r_0
2	0.26	0.906	1.167
4	0.52	0.803	1.323
6	0.78	0.692	1.472
8	1.04	0.570	1.610
10	1.30	0.437	1.737
12	1.56	0.292	1.852
14	1.82	0.131	1.952
15.473	2.01	0	2.012

TABLE 3.2 PREDICTION OF THE MIXING ZONE BOUNDARIES WHEN m=0.257 (INITIAL REGION)

z/r_0	b/r_0	$K_2(z)$	h_v/h_{v0}
9.912	2.18	0.210	1
11	2.32	0.194	0.977
13	2.64	0.165	0.931
14.868	3.02	0.138	0.890

TABLE 3.3 PREDICTION OF A SUBMERGED JET IN THE TRANSITION REGION

z/r_0	b/r_0	h_v/h_{v0}	$\dot{m}/\dot{m}_0$
14.868	3.02	0.890	2.09
20	4.15	0.648	2.87
30	6.35	0.423	4.38
40	8.65	0.314	5.90
50	10.75	0.250	7.43
60	12.95	0.208	8.96

TABLE 3.4 PREDICTION OF A SUBMERGED JET IN THE MAIN REGION

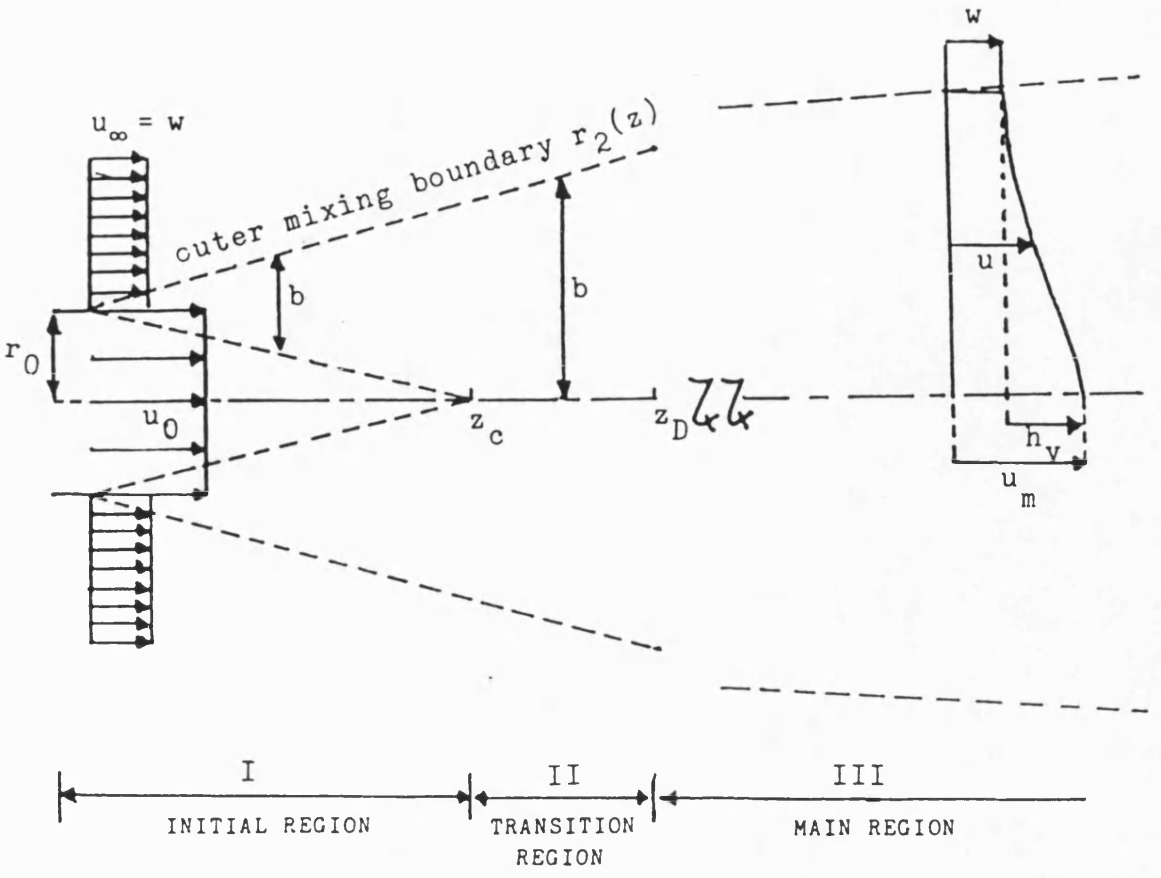

FIG 3.1 SCHEMATIC OF A JET

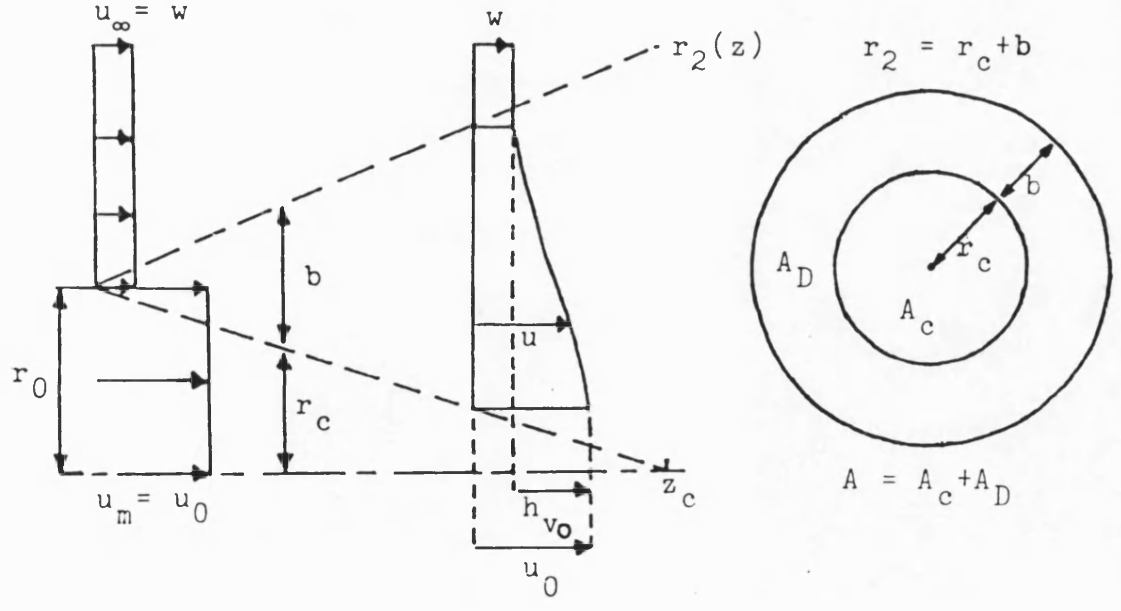

FIG. 3.2 THE INITIAL REGION

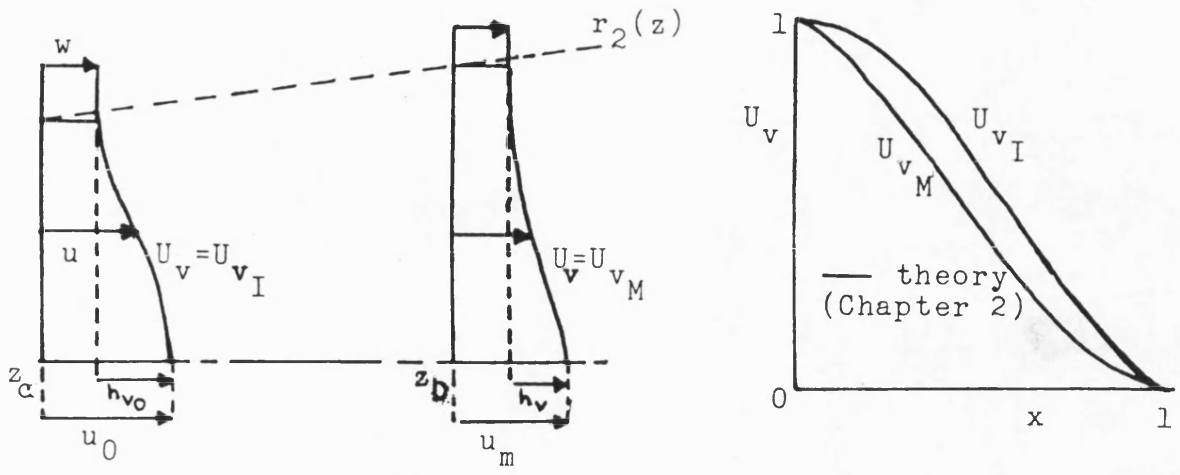

FIG. 3.3 DEVELOPING FLOW IN THE TRANSITION REGION

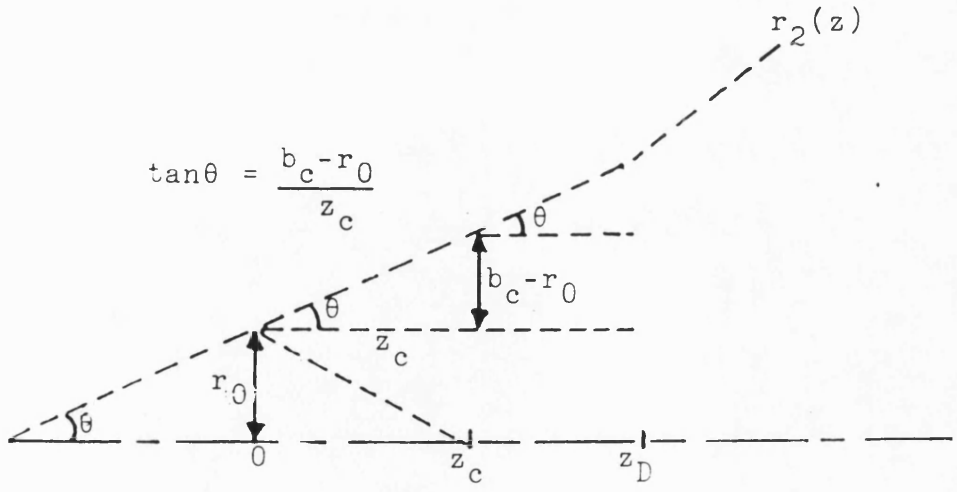

FIG. 3.4 JET SPREAD IN THE TRANSITION REGION

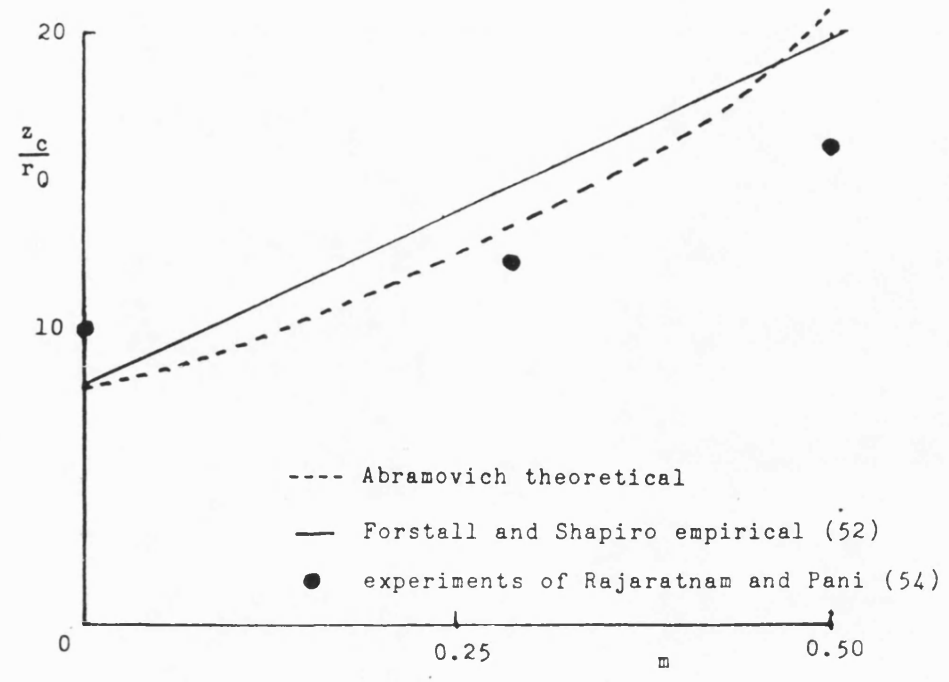

FIG. 3.5 VARIATION OF THE LENGTH OF THE INITIAL REGION WITH VELOCITY RATIO m

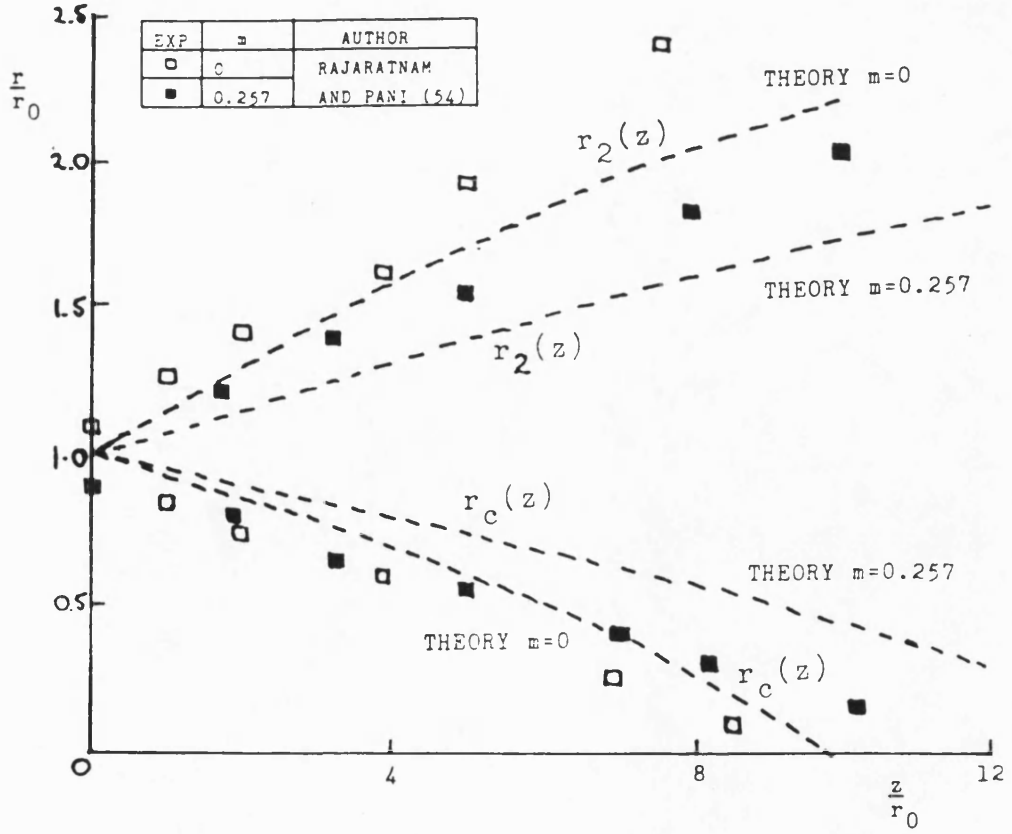

FIG. 3.6 ANALYTICAL SOLUTION FOR THE INNER AND OUTER MIXING BOUNDARIES

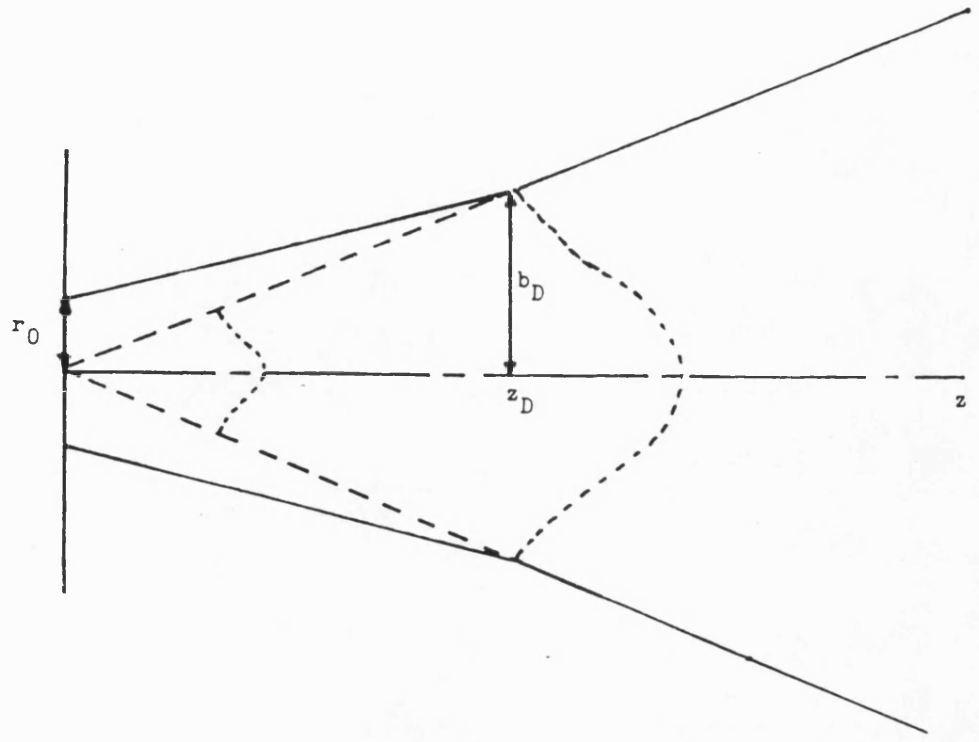

FIG. 3.7 TURBULENT JET AS A POINT SOURCE OF MOMENTUM MATCHED AT THE TRANSITION SECTION

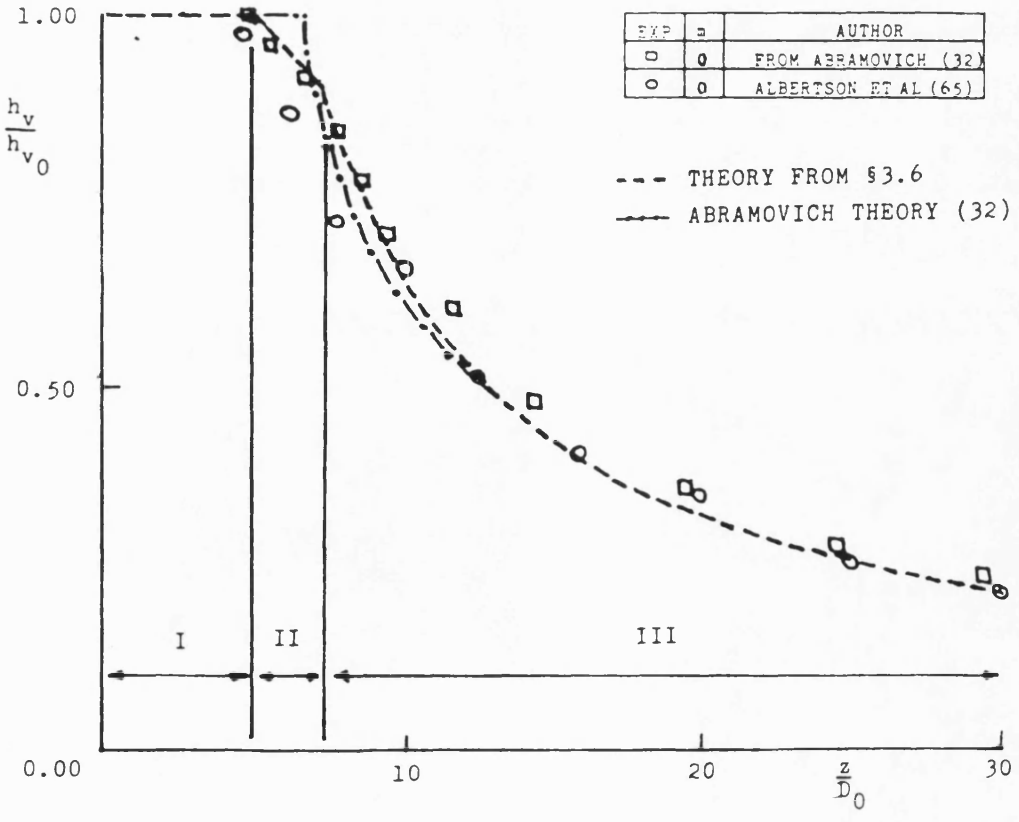

FIG. 3.8 AXIAL VELOCITY DECAY IN A SUBMERGED JET

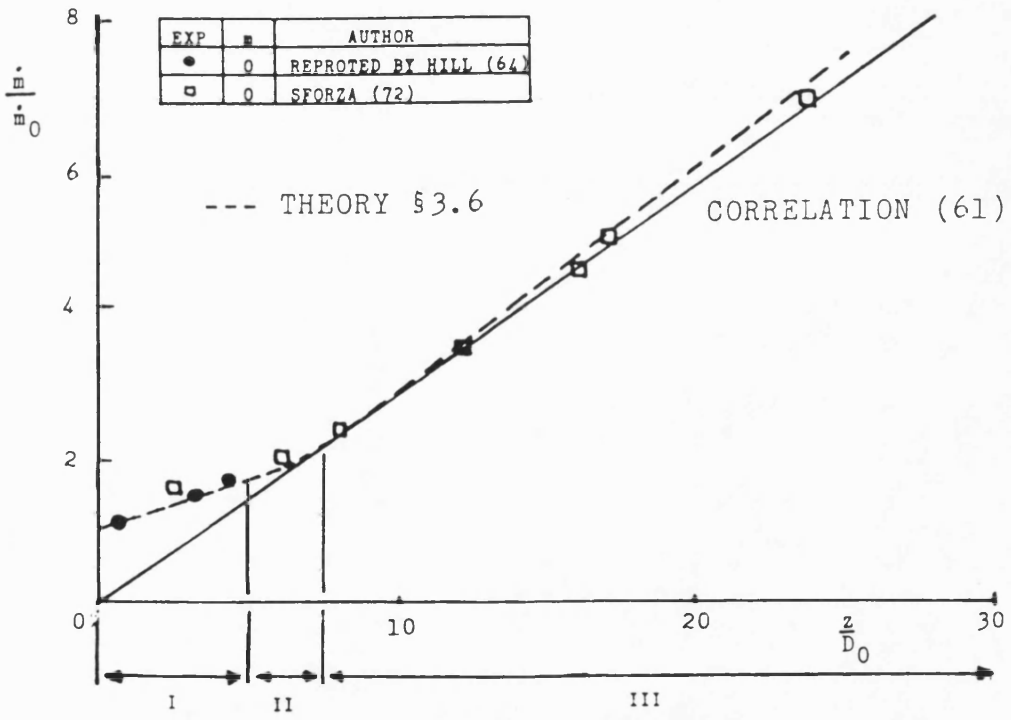

FIG. 3.9 INCREASE IN MASS FLUX WITH AXIAL DISTANCE IN A SUBMERGED JET

PART II

THE COMPUTER JET MIXING MODEL

CHAPTER 4

AN INTEGRAL THEORY FOR A CONSTANT DENSITY, ROUND TURBULENT JET IN A CROSSFLOW

Chapter 4 - Notation

A - jet cross-section area (m^2)
A_c - area of constant velocity core (m^2)
A_D - area of turbulent mixing zone (m^2)
A_R - ellipse major to minor axis ratio
A_0 - nozzle area (m^2)
A_1 - coefficient in propagation equation 4.18a
A_3 - surface shown in Fig. 4.8 (m^2)

b - effective mixing zone width (Fig. 4.6a) (m)
b_c - jet width at the end of the initial region (m)
b_X, b_Y - jet width in X,Y direction (Fig. 4.1) (m)

c - length of perimeter of jet cross-section (m)
C_D - drag coefficient

D_0 - nozzle diameter (m)

E_m - mass entrainment rate (kgs^{-1})
E_0 - axisymmetric jet entrainment coefficient
E_1 - enhanced entrainment coefficient

F_b - body force
F_D - drag force
F_i^n - integral averages defined in 3.12a

G - Abramovich width growth coefficient
G_I - constant value for G in the initial region
G_1 - enhanced spreading rate coefficient in 4.18

h_v - maximum excess velocity function (ms^{-1})

$I_n = \int_A \rho U_v^n dA \qquad n=0,1,2$

K_n - average value of I_n over A (4.30c)

P - static pressure

P_c - term defined in 4.30a

q - dynamic pressure

r_c - effective core radius (Fig. 4.6a) (m)
r_0 - nozzle radius (m)
r_z - jet centreline polar co-ordinate (Fig. 4.7a)
R - extra spreading due to crossflow in 4.9 (m)
R_c - centreline radius of curvature (m)

t - time (s)

u - jet velocity (ms^{-1})
$\bar{u}_j$ - average jet velocity over A (ms^{-1})
U_v - excess velocity distribution function $U_v \in [0,1]$
U_{v_I} - velocity distribution across the width of the mixing zone in the initial region

v_E - entrainment velocity (ms^{-1})

w - crossflow velocity (ms^{-1})
x_z, y_z - co-ordinates in trajectory plane (Fig. 4.7a)
X_z, Y_z - " " cross-section plane (Fig. 4.5)

z - jet centreline co-ordinate (m)
z_c - constant velocity core (initial region) length (m)

C - jet perimeter
$\mathcal{F}$ - spreading rate function
$\mathcal{F}_0$ - axisymmetric jet spreading rate
$\mathcal{F}_1$ - enhanced jet spreading rate due to crossflow
$\mathcal{M}$ - momentum flux
$\mathcal{R}$ - velocity ratio $=w/u_0$
S - surface of V
V - control volume in Fig. 4.8

α - angle defined in Fig. 4.10 (rad)
β - angle defined in Fig. 4.7a (rad)

γ	-	angle defined in Fig. 4.10 (rad)
δr_z		
$\delta\theta_z$	-	elemental lengths defined in Fig. 4.10 (m)
δ_z		
η	=	$\beta+\alpha-(\pi/2)$ (rad)
θ_z	-	angle defined in Fig. 4.7a (rad)
ξ	-	distance along jet axis (m)
ρ	-	density (kgm^{-3})
τ	-	shear stress

Subscripts

A_c	-	pertaining to the core
A_D	-	pertaining to the mixing zone
$\mathfrak{L}$	-	in the centreline direction
m	-	maximum or value on the jet axis
N	-	normal to the jet centreline direction
0	-	at the nozzle
∞	-	in the free stream

Superscripts

$\bar{}$	-	normalised by r_0
$\rightarrow$	-	vector quantity

Chapter 4
An Integral Theory For A Constant Density, Round Turbulent Jet In A Crossflow

4.1 Introduction

The particular configuration of a round jet exhausting into a crossflow has been studied experimentally by Ruggeri et al (74)(1951), Jordinson (75)(1956), Gordier (68)(1959), Abramovich (32)(1963), Keffer and Baines (69)(1963), Patrick (70)(1967), Pratte and Baines (76)(1967), Platten and Keffer (37)(1968), Margason (77)(1968), Ramsey (78)(1969), Kamotami and Greber (39)(1971), Campbell and Schetz (79)(1973), Crabb (80)(1979) and others. In order to place some bounds upon a preliminary discussion, attention is for the moment restricted to some observations upon isothermal, isodense injections normal to a uniform crossflow; a review of the data of this type has been given by Rajaratnam (43). Under these conditions, it is appropriate to characterise the injection event in terms of the ratio R of the crossflow velocity to the (assumed uniform) injection velocity u_0:-

$$R = \frac{w}{u_0} \tag{4.1}$$

Keffer and Baines (69), and others, prefer the reciprocal definiton for R, and this is avoided here only because, according to 4.1, the free jet limit (w=0) is described by R=0, rather than the untidy $R \to \infty$. In some cases (Chapter 7) it is more suggestive to work with R^{-1}.

Experimental observations show that, due to the stagnation pressure exerted by the external stream, and momentum exchanges prompted by turbulent mixing, the jet is deflected by the crossflow (69). A definition sketch of such a jet is given in Fig. 4.1, where it has been divided, for descriptive purposes, into three regions (following Keffer (81)):-

1/ An initial region, originating at the nozzle, in which there persists (for a uniform injection velocity profile) an undisturbed core of constant velocity and total pressure (in analogy with the

potential core in the initial region of an axisymmetric jet).

2/ A curvilinear region, or region of maximum deflection, in which the jet cross-section distorts into a characteristic kidney shape, and in which two distinct entrainment mechanisms can be identified.

3/ A far region, in which the jet approaches asymptotically, and becomes indistinguishable from, the main stream.

Some remarks concerning each of these regions will now be made.

4.2 Qualitative Description Of The Flow

4.2.1 The Initial Region

At the nozzle, the injectant is assumed to posess a low level of turbulence intensity relative to that which subsequently develops (this is also assumed to be true for the external stream). Due to steep velocity gradients at the jet edge, an annular, turbulent mixing zone is quickly established from the nozzle lip and thickens with increasing penetration. Concerning the injection velocity profile itself, both Kamotami and Greber (39) and Crabb (80) report that this is not affected by the presence of the crossflow provided R less than about 1/4, but that some distortion of the inlet profile may occur at higher velocity ratios.

As in the straight jet, the annular mixing zone again encloses an undisturbed, constant velocity core; the rate of mixing in the turbulent zone, however, is here significantly enhanced due to the tangential shear stresses induced by the crossflow. Correspondingly, the length of the constant velocity core is shorter than that observed in a submerged (R=0) jet (as described in Chapter 3), as is clear from the experimental data collected by Snel (82). The measurements of Pratte and Baines (76) in this context

support Keffer's note (81) that the flow in the initial region may depend upon Reynolds number, although the data is insufficiently complete to be conclusive.

For moderate crossflow velocities (R less than about 1/4) the core is not greatly deflected by the crossflow and its tip, at the end of the initial region, rests at the axis of the jet approximately above the centre of the nozzle. Keffer and Baines (69), Kamotami and Greber (39) and Crabb (80) observe that at higher velocity ratios the core is deflected by the pressure field and the maximum velocity point may depart from the momentum centreline within the initial region: for this reason, and others mentioned above, the constraint $R<4$ will be imposed upon the succeeding theoretical discussion (see also Chapter 7).

4.2.2 The Region Of Maximum Deflection

As has been indicated, this region is dominated by the continuous distortion of the initially circular jet cross section; indeed, the distortion process itself must be in progress in the initial region due to the action of the crossflow, but it is in this second region that the distortion becomes manifest. The manner and repercussions of this process will now be described.

In a submerged jet ($R=0$), entrainment of external fluid into the turbulent mixing zone occurs uniformly around the outer mixing boundary. In the case of a jet in a crossflow, this situation is altered considerably. Upon injection, the jet presents a blockage to the external flow, which is decelerated at the jet upstream surface, creating a high pressure region. The sides of the jet are subjected to a strong lateral shearing stress: peripheral layers of jet fluid lose momentum through turbulent mixing and are deflected downstream, drawn into a low pressure region at the jet downstream surface (created by separation of the crossflow from the edges of the jet) and re-presented for entrainment (Jordinson (75) compares this with the flow around a porous cylinder, with suction to allow for entrainment). A helical circulation pattern is established (Fig. 4.2a) and the

implied entrainment into the jet envelope augments the turbulent entrainment due to the discontinuity in velocities, which continues as for the submerged jet, although itself considerably enhanced by the large scale mixing within the jet caused by the shearing action of the crossflow (69,80). These then, are the twin entrainment mechanisms which would need to be represented in an analytical model.

The helical circulation will continue while the jet has a component of velocity normal to the crossflow, and this helicity is usually interpreted as a pair of counter-rotating vorticies, located at the extremes of the characteristic kidney shape which the deflected jet cross-section is observed to acquire (Fig. 4.2b), and connected by circulation free fluid (75,39,80). The size, separation and angular velocity of the vortices increase as the jet is progressively deflected in this region (43), and the continuous distortion precludes physical similarity in different cross-sections (39). According to Keffer and Baines (69), the external stream is only slightly affected by the presence of the jet and the mean crossflow velocity can be considered to be unaltered (this is also discussed by Braun and McAllister (83).

The strong mixing processes serve to disperse axial momentum over a steadily increasing jet area, the decay with penetration of maximum jet velocity, and the increase in jet mass flux, being more rapid than in the submerged jet (Keffer and Baines (69)). The jet velocity over a particular cross-section is essentially parallel to the jet centreline direction at that section (69). The definition of the jet centreline is given later.

4.2.3 The Far Region

At some distance downstream, the jet will have been so deflected so as to have become almost parallel to the external stream, leaving the pair of counter-rotating vorticies moving at (approximately) the speed of the crossflow. (Kamotami and Greber (39)). Pratte and Baines (76) found these vorticies to exist even one thousand nozzle diameters

downstream from the injection point. As the velocity difference at the jet boundary decreases, so the angular velocity of these vorticies decreases: entrainment in the far region must be due almost entirely to the vortex action (again since the velocity discontinuity is very small), so that the entrainment rate, and hence the jet spreading rate, decreases (Pratte and Baines (76)).

4.3 Review Of Analytical Methods For Deflected Jets

Quite clearly from the preceding discussion appear three characteristic features of a turbulent jet in a crossflow:-

1/ The continuous rolling up of the jet cross-secton area into a kidney shape, dominated by a pair of counter-rotating vortices.

2/ The associated enhanced rate of entrainment of external stream fluid into the jet envelope (relative to the turbulent entrainment into an axisymmetric jet), due to the lateral shearing effects of the crossflow.

3/ The streamline curvature within the jet structure through deflection by the external stream.

All these effects have been amply reproduced in the solution, by finite difference/turbulence model methods, of the governing equations in their partial differential statement (Appendix). In particular, Chien and Schetz (84) obtain the velocity field near the nozzle for a transverse jet using only a crude eddy viscosity turbulence model: the computed jet centreline compares well with appropriate experimental data and the effect of the injection on the velocity in the external stream is well exhibited (Fig. 4.3), the most significant change in the (nominally constant) crossflow being observed downstream from the jet, where a sizeable recirculation zone has resulted from blockage effects. Also, Jones and McGuirk (85) have used a two-equation turbulence model scheme to reveal the trajectory, and velocity and

temperature contours, in a confined, deflected jet (Appendix). The distortion of the jet cross-section is a feature of the computed results, as was the case in the work by Crabb (80).

Although the finite-difference schemes can represent the full, three-dimensional structure of deflected jets, computer storage and solution time requirements become rapidly prohibitive (84). The use of higher level turbulence closures, fundamentally more correct than two-equation models in flows with strong streamline curvature, only increases these requirements (Appendix).

The full-field methods could be said to solve the equations of motion within an Eulerian framework; that is to say, the solution is obtained for the flow at a discrete set of control cells with positions fixed in space. In view of the complexity of such schemes, it is worthwhile to consider the alternative approach in which a control volume is followed from injection, in a Lagrangian framework, and a solution for the flow obtained upon accounting for the forces acting upon it. The numerical task is further reduced by considering, as in Chapter 3, greatly simplified, integrated forms of the equations of motion. Since the unconfined deflected jet still has a predominant flow direction (because, as noted in Section 4.2.2, velocities within the jet are approximately parallel to the centreline direction), it is not unreasonable to attempt such an integral analysis.

Early attempts at the prediction of deflected jets concentrated upon the determination of an expression for the jet axis, defined as the locus of maximum velocity points in successive cross-sections, being the most directly measurable property of the flow. The analysis of Abramovich (32) is typical in this respect. Thus, Abramovich considered the jet to be deflected by the pressure differences induced in the free stream, and obtained an equation for the jet axis by balancing centrifugal and blockage forces acting perpendicularly to the jet trajectory. One serious drawback is the simplifying assumption that the component of jet momentum perpendicular

to the free stream remains constant. Blockage of the external flow by the jet structure was determined by assuming the jet to present a 'solid body' obstruction; the deflection mechanism that this implies was approximated by a drag force F_D acting upon the jet envelope (32):-

$$F_D = C_D b_X \frac{\rho w_N^2}{2}$$

where C_D is a drag coefficient and b_X is the width of the surface which the jet presents to the crossflow component w_N normal to the direction of the jet axis (Fig. 4.1). The use of a drag force deflecting mechanism is common to almost all later treatments, and the manner of the representation is considered again in Section 4.6.4. Abramovich (32) acknowledged the distortion of the jet cross-section shape by assuming that shape to be an ellipse (with a constant ratio A_R=5:1 for the major to minor axis), and prescribing empirically a variation for b_X:-

$$b_X = 2.25D_0 + 0.22\xi$$

where ξ repreesnts distance along the jet axis. Thus, all three of the phenomena enumerated above are accounted for: that the model is incomplete is exemplified by the fact that unrealistically large values must be assigned to the drag coefficient in the deflecting mechanism in order to obtain agreement with measured and predicted trajectories ($C_D \simeq 3$: see later and Braun and McAllister (83)). Other analytical methods of this type are described by Rajaratnam (43).

Platten and Keffer (37) constructed an integral model again assuming jet momentum perpendicular to the free stream to be preserved. The momentum of the jet in the direction of the free stream was assumed to be increased by the momentum of the entrained fluid (43). The most interesting feature of the analysis is the definition of an 'entrainment velocity' v_E normal to the deflected jet axis, being the sum of an 'axisymmetric' component and a second term accounting for

jet curvature. The (enhanced) entrainment rate is then introduced into the model through the integrated continuity equation (Chapter 2), written as:-

$$\frac{d}{d\xi}(\rho A\bar{u}_j) = \rho c v_E = E_m$$

where $\bar{u}_j$ is the average jet velocity over A, and c defines the perimeter or outer mixing boundary of the jet (Platten and Keffer (37) found, from their own experiments, that $c=\sigma\sqrt{A}$ with $\sigma\simeq 4.6$. Constancy of the empirical shape factor σ implies that the distorting cross-section shapes are replaced throughout by a 'typical' distorted section). Empirical entrainment coefficients, for the terms comprising v_E, were deduced by matching predicted and observed trajectories: it was found that the entrainment into a jet in crossflow is about an order of magnitude larger than that into a submerged jet.

Kamotami and Greber (39) also argued that, because the component w_N, of the crossflow velocity w, normal to the local jet centreline direction controls independently the rotational velocity field (Fig. 4.2a), it is reasonable to follow Platten and Keffer (37) and introduce entrainment coefficients E_0 and E_1 such that:-

$$v_E = E_0(u_m - w_\ell) + E_1 w_N \qquad (4.2)$$

where w_ℓ is the external velocity component in the centreline direction. The ability to determine values for E_0 and E_1, so as to describe analytically their own mass flux data, caused them to suggest that the normal and parallel components of the crossflow velocity independently control the entrainment rate. This is the basis for the extension of the entrainment models of Chapter 2 to the problem of deflected jets, an extra emprical coefficient (such as E_1 above) being introduced.

A force not accounted for by Abramovich (32) or Platten and Keffer (37) is that due to the entrainment of fluid into

the jet from the external flow (only the consequent spread of the jet is represented). In this respect the model of Wooler (86) is an improvement to the integral method. Wooler (86) prescribed the following form for the entrainment rate E_m:-

$$E_m = \rho E_1 w_N + \frac{\rho E_0 (\bar{u}_j - w_\ell) c}{1 + E_2 w_N / \bar{u}_j}$$

E_0 is the submerged jet entrainment coefficient (61) (see Chapter 3): E_1 and E_2 were set by Wooler to give agreement between prediction and experiment for jet axes (86). The model is simplified, by assuming deflection of the axis to be slight, so that an analytical solution may be obtained, for trajectory only, from integrated continuity and normal and tangential momentum equations (similar to those derived later for the present model). A drag force, with C_D=1.8 (a representative value for an ellipse) was used, with b_X deduced by assuming an elliptical cross-section shape to develop (in a predetermined distance) with A_R=4:1. Methods such as this have been investigated, and extended, at Bath University by Idoum (44) and Fraudeau (45).

Campbell and Schetz (79) proposed the following entrainment function:-

$$E_m = \frac{A}{c} \rho E^* (\bar{u}_j - w)$$

E^* is an entrainment coefficient which was correlated by trajectory matching (79). In their setting $E^* \to 0$ as $z \to 0$, while entrainment rates near the nozzle are certainly non-zero (64): submerged jet values were thus imposed until larger values were predicted by the function. A similar problem was mentioned by Snel (82). Upon computer solution of integrated continuity, momentum and energy equations (similar to those to be derived later), spreading rate, trajectory and average jet velocity and temperature were predicted. The assumed jet shape was an ellipse with A_R=5:1, and C_D=1.6 was assumed in keeping with the solid body

argument. Underprediction of jet spread and increase in mass flux was attributed to the empirical entrainment function (79) (see Chapter 7).

Finally in this review of entrainment models, the semi-empirical deflected jet analysis due to Snel (82) merits attention. By assuming a series solution of the integrated equations beyond the initial region, Snel obtained an entrainment function which is again of the straight jet/ crossflow enhancement superposition type:-

$$E_m = E_{\substack{\text{straight} \\ \text{jet}}} + E'(R,z)_{\substack{\text{deflected} \\ \text{jet}}}$$

Here E' represents the enhanced mixing due to the crossflow. In finding analytical curve fits to published velocity decay data (part of the empirical input to the model), Snel observed that good fits to the data downstream lay above the measurements made in the vicinity of the end of the initial region: this, it is recalled, is precisely the behaviour observed in Chapter 3 for a simple 'power law' decay fit to axisymmetric jet velocity, and suggests that also in deflected jets there will be a transitional region of developing flow in the early portion of the maximum deflection region. This is an unsuprising conclusion, if it can be assumed that the local cross-section distortion just downstream from the initial region is comparatively slight, as would appear to be the case (Chapter 7).

The most significant comments made by Snel (82) concern the definition of the jet axis: of all the integral models for deflected jets reported in the literature, it is apparently only Snel who accounts for the fact that such models cannot predict directly the locus of maximum velocity points (the jet axis), but only the 'momentum centreline' based upon the integrated velocity profiles over cross-sections (see later). Due to asymmetry in the distorted jet shapes (Fig. 4.1), the momentum centre and maximum velocity point do not in general coincide (43). Snel's analysis of the axis definition

problem is adopted later for the present theory, and shown to be significant in obtaining good predictions (Chapter 7).

All the integral model methods described here have been applied successfully to predict the deflection of a jet in a given, uniform crossflow. The Abramovich (32) and Wooler (86) models are straightforward and adopt limited, analytical solutions for trajectories, although extensions to more flexible numerical solutions allow for added sophistication in terms of crossflow type, etc. (45). The method of Snel (82) depends too heavily upon empirical input and would not generalise easily to variable density or non-uniform crossflow cases: the model of Campbell and Schetz (79), which is a generalisation of the Wooler-type analysis, is the most complete of the methods described (buoyancy effects in variable density jets, general crossflow types and three-dimensional trajectories are permitted). Perhaps its only weakness is that the predicted average jet velocity and temperature cannot be compared very meaningfully with measured values of maximum velocity and temperature appearing in the literature (79), so that the detailed performance of the model is difficult to assess.

For the present research, it was the intention to construct a jet mixing model of the integral type which would:-

a) offer predictions which compete, in terms of generality and resolved flow detail, with the more direct and problematic turbulence model solutions for unconfined jets, and

b) describe realistically the fields of velocity, temperature and injectant concentration within the jet envelope under swirl (35).

The realistic representation of property profiles in the distorted jet cross-sections (39) was not undertaken in any of the models described above, so that none would be

suitable for the present work, in view of b). In fact, the model of Adler and Baron (63) alone appears to satisfy this requirement, and is described in the next section.

4.4 The Integral Model Of Adler And Baron

Many of the methods and details of this model (63,71) persist in the present analysis, and the development of the momentum theory is undertaken in the succeeding sections. The constant density model was implemented as a computer program at Bath University by Packer (35), with uniform crossflow replaced by swirl.

Adler and Baron (63) devised, as a part of the model, a method for the computer prediction of the rolling up of the jet cross-section into a kidney shape, under the influence of a crossflow (Section 4.2). The equations for the shape change were those given by Lu (63,71,35), and are developed by seeding vortices on the jet periphery at injection and calculating their displacement due to the velocities induced by the crossflow (Fig. 4.4). Viscous damping effects allow the predicted rolling-up rate to be matched with experimental observations (63). Such a procedure had earlier been proposed by Braun and McAllister (83), Hacket and Miller (87) and Margason (88): Adler and Baron (63) coupled the distortion model to an integral jet mixing theory by obtaining realistic distributions for jet velocity within the shapes. First, an auxiliary equation (the Poisson equation) was solved, by a finite-difference method, within the domain bounded by each newly predicted jet perimeter: the solution, defined numerically, was then subjected to an empirical transformation (63,71) in order to represent velocity fields measured by Kamotami and Greber (39) in cross-sections of similar shape (Fig. 4.5). The resulting sequence of velocity profiles exhibited non-similarity because of the progressive jet shape distortion. These distributions could then be used in the integrated momentum equations: the computer implementation of shape and velocity profile distortion algorithms was described by Packer (35), and that work has been adapted for use in the present model, as described in Chapter 6. The

relative importance of these effects in the momentum theory is then assessed in Chapter 7.

Closure in the momentum theory of Adler and Baron (63) is achieved through a propagation equation (Chapters 2 and 3), rather than an entrainment model, and the form of such an equation is now discussed.

4.5 A Propagation Equation For Deflected Jets

4.5.1 Superposition Of Growth Effects

Integral models for deflected jets employing a propagation equation have been described by Abramovich (32)(1963) (see Section 4.3), Adler and Lyn (39)(1971), Sucec and Bowley (89)(1976), Shirakashi and Tomita (90)(1978) and Adler and Baron (63)(1978). The details of the momentum theory do not vary very greatly from that to be described below (except for the early Abramovich study). Both Sucec and Bowley (89) and Shirakashi and Tomita (90) conclude that the spread of a constant density jet in a crossflow may be characterised by that of the submerged axisymmetric jet (Chapter 3). This is at odds with the observations of Keffer and Baines (69) upon the increase in mixing (spreading) rate for deflected jets (Section 4.2.3). In fact, these two models (89,90) were concerned only with the prediction of deflection: any deficiency in entrainment could be compensated by the assumptions concerning the drag force deflecting mechanism (see Chapter 7). Adler and Lyn (19) used (essentially) the straight jet propagation equation 3.24 in their model, with $w \rightarrow w_{\ell}$, the local component of crossflow in the instantaneous centreline direction. This component acts, in 3.24, in the same way as a 'coflowing stream' velocity (Chapter 3), progressively reducing the spreading rate as w_{ℓ} increases. The model thus predicted lower entrainment rates as the crossflow velocity was increased (Packer (35)): again, these results do not comply with observations on enhanced mixing (39,69).

The entrainment models described in Section 4.3 sought to represent entrainment as a combination of 'submerged jet' and 'enhanced mixing due to a crossflow' components,

following the observations of Keffer (81) upon entrainment patterns for jets in crossflows (Section 4.2.2). A propagation equation may be derived upon similar principles (Baron (71)):-

$$\frac{dA}{dz} \propto \sqrt{A}\{\alpha_0(u_m - w_t) + \alpha_1 w_N\} \qquad (4.3)$$

(this may be compared with 4.2 for the entrainment velocity v_E). Components of the crossflow velocity w normal and parallel to the local jet centreline direction independently control the spreading rate. The constant α_0 will be determined from axisymmetric jet data (Chapter 3): Adler and Baron (63) assumed that the enhanced growth rate could be characterised as the growth rate of a vortex pair, as investigated by Tulin and Schwartz (92,93). The results obtained with this model were found to be very satisfactory, and the present work is an extension both of the model and its implementation at Bath University by Packer (35).

The form of the propagation equation in this study appears as a conclusion to the following general derivation.

4.5.2 A General Superposition Propagation Equation

A general statement of such an equation is complicated by the geometry of the (possibly distorted) jet cross-section: a typical shape for the maximum deflection region (Section 4.2.2) is shown in Fig. 4.6, the possibility of the existence of a constant velocity core being included. As in Chapter 3, $A_c(z)$ denotes the area of the core, and $A_D(z)$ is the area of the turbulent mixing zone. If the jet cross section area is $A_D(z)$, then:-

$$A(z) = A_c(z) + A_D(z) \qquad (4.4)$$

Beyond the end of the intitial region (Section 4.2.1) $A_c \equiv 0$ (no core), so that $A(z) \equiv A_D(z)$ (Fig. 4.6b).

The 'width' b(z) of the mixing zone, area $A_D(z)$ is not as

easily defined as in the axisymmetric jet, nor is the 'centre of mixing' (Fig. 4.6). For the integral analysis, the effective widths $r_c(z)$ and $b(z)$ are defined as:-

$$r_c(z) = \left(\frac{A_c(z)}{\pi}\right)^{\frac{1}{2}} ; \quad b(z) = \left(\frac{A(z)}{\pi}\right)^{\frac{1}{2}} - r_c(z) \qquad (4.5)$$

These definitions are obviously compatible with those of Chapter 3, for the core radius r_c and mixing zone width b in straight jets.

In analogy with the theoretical development in Chapter 3, a propagation equation should be sought in the general form:-

$$\frac{db}{dz} = \mathcal{F}(u_m, w, z)$$

or, for notational simplicity:-

$$\frac{db}{dz} = \mathcal{F}(z) \qquad (4.6)$$

In an axisymmetric jet, entrainment across the outer mixing boundary is uniform around the jet edge: in a deflected jet, such symmetry cannot be expected (Section 4.2.2). It may be observed that 4.6 takes no account of this lack of symmetry, but expresses a (possibly crossflow enhanced) rate of entrainment which is averaged around the jet boundary, since the definition of b(z) in 4.5 is essentially a process of integration. Thus, there is no coupling between the propagation equation and any treatment of the distortion of cross-section shapes (Chapters 6 and 7).

The linear superposition of growth mechanisms (Section 4.2.2 and Section 4.5.1) is expressed in 4.6 as follows:-

$$\frac{db}{dz} = \mathcal{F}(z) = \mathcal{F}_0(z) + \mathcal{F}_1(z) \qquad (4.7)$$

Here $\mathcal{F}_0(z)$ represents the growth of an axisymmetric jet (constant density in this chapter): if the jet is deflected,

there will be a non-zero component w_ℓ of the crossflow velocity in the centreline direction. The function $\mathcal{F}_0(z)$ is therefore taken, from Chapter 3, as:-

$$\mathcal{F}_0(z) = \left.\frac{db}{dz}\right|_{\substack{\text{axisymmetric}\\ \text{jet}}} = G(z)\left(\frac{u_m(z) - w_\ell(z)}{u_m(z) + w_\ell(z)}\right) \qquad (4.8)$$

which is a $\left.\begin{matrix}\text{axisymmetric}\\ \text{jet}\end{matrix}\right|$ ement of the equations for the initial, transition and main regions 3.3, 3.53 and 3.24.

The term $\mathcal{F}_1(z)$ in 4.7 seeks to express the average rate of extra spreading of the jet due to the crossflow:-

$$\mathcal{F}_1(z) = \frac{dR}{dz} \qquad (4.9)$$

where:-

$$R(z) = \left.b(z)\right|_{\substack{\text{defined}\\ \text{by 4.5}}} - \left.b(z)\right|_{\substack{\text{straight}\\ \text{jet}}} \qquad (4.9a)$$

The form for $\mathcal{F}_1(z)$ used by Adler and Baron (63) is used in the present work, and the details are given later.

For the generality of the model, and the incorporation of the numerical representation of realistic cross-section shapes and velocity profiles in the predictive scheme, it is necessary to work in terms of the jet cross-section area A rather than the effective widths r_c and b. Using the definitions from 4.4 and 4.5, the variation in the area A_D of the turbulent mixing zone (Fig. 4.6) is given by:-

$$\frac{dA}{dz}_D = \frac{d}{dz}\{A - A_c\} = \pi\frac{d}{dz}\{(r_c + b)^2 - r_c^2\}$$

That is:-

$$\frac{dA}{dz}_D = \pi\frac{d}{dz}\{b(b + 2r_c)\}$$

(beyond the end of the initial region, $A_c=0 \Rightarrow r_c=0$). This expression is expanded keeping 4.5 in mind:-

$$\frac{dA}{dz}_D = \pi\left\{(b + 2r_c)\frac{db}{dz} + b\frac{db}{dz} + 2b\frac{dr}{dz}_c\right\}$$
$$= 2\pi\left\{(b + r_c)\frac{db}{dz} + b\frac{dr}{dz}_c\right\}$$
$$= 2\sqrt{\pi A}\left\{\frac{db}{dz} + b\sqrt{\frac{\pi}{A}}\frac{dr}{dz}_c\right\}$$

Since, from 4.5, $dA_c/dz = 2\pi r_c dr_c/dz$, this equation becomes, with 4.7:-

$$\frac{dA}{dz}_D = 2\sqrt{\pi A}\left\{\mathcal{F}_0(z) + \mathcal{F}_1(z) + \frac{b}{2\sqrt{AA_c}}\frac{dA}{dz}_c\right\} \qquad (4.10)$$

$\mathcal{F}_0(z)$ will be given by 4.8 and $\mathcal{F}_1(z)$ by 4.9. As in Chapter 3, this equation must be solved, in the intial region, with an equation for the variation in the extent of the undisturbed core, area A_c, and this is considered later.

4.5.3 The Effect Of Enhanced Mixing Upon The Length Of The Initial Region

Adler and Baron (63) did not use a propagation equation in the initial region in their (constant density) model, but determined its length z_c (in a uniform crossflow) from the correlation of Kamotami and Greber (39):-

$$\bar{z}_c = \frac{1}{\frac{1}{\bar{z}_c}\Big|_{\mathcal{R}=0} + c\mathcal{R}} \quad ; \quad \bar{z}_c = z_c/r_0 \ , \ c=0.36 \qquad (4.11)$$

which was obtained by an entrainment and geometrical analysis. Enhanced entrainment was considered to be proportional to $\mathcal{R}$, the constant of proportionality being c.

Consider now the use of 4.10 in predicting z_c. From the discussion in Section 4.2, it is not unreasonable to consider, at constant density, the transverse injection of a jet into a uniform crossflow in which there is no significant

deflection or distortion over the length of the initial region ($\mathcal{R}<1/4$). In this case, the initial region mixing zone velocity distribution U_{v_I} may be assumed to be that observed in axisymmetric jets[1] (Chapter 3). If there is no deflection, $w_{\ell}=0$ and the axial momentum equation is the same (neglecting pressure effects) as for the submerged jet of Chapter 3:-

$$\frac{d}{dz}\int_A u^2 dA = w_{\ell}\frac{d}{dz}\int_A u dA = 0 \qquad (4.12)$$

This equation may be manipulated to give:-

$$\frac{b_c}{r_0} = \frac{1}{\sqrt{2F_1^2}} \qquad (4.13)$$

using the methods and notation of Chapter 3. For a submerged jet, it was seen that z_c was given by:-

$$\bar{z}_c\Big|_{\mathcal{R}=0} = \frac{1}{G_I\sqrt{2F_1^2}} \quad \text{since } \bar{b}_c = G_I\bar{z}_c \qquad (4.14)$$

For the intiial region of a jet in a crossflow, the width growth law is given by 4.7 with 4.8 and 4.9. Putting $w_{\ell}=0$:-

$$\frac{db}{dz} = G_I + \frac{dR}{dz}$$

Upon integration from ($z=0$, $b=0$, $R(0)=0$) to the end of the initial region ($z=z_c$, $b=b_c$, $R(z)=R(z_c)$):-

$$b_c = G_I z_c + R(z_c)$$

Thus, in 4.13:-

$$\bar{b}_c = G_I\bar{z}_c + \bar{R}(z_c) = \frac{1}{\sqrt{2F_1^2}}$$

Hence:-

$$\bar{z}_c = \frac{1}{G_I\sqrt{2F_1^2}} - \frac{\bar{R}(z_c)}{G_I}$$

or, in view of 4.14:-

$$\bar{z}_c = \bar{z}_c\Big|_{\mathcal{R}=0} - \frac{\bar{R}(z_c)}{G_I} \qquad (4.15)$$

Now z_c is certainly non-zero and positive, therefore:-

$$\bar{z}_c\Big|_{\mathcal{R}=0} > \frac{\bar{R}(z_c)}{G_I} \Rightarrow \bar{X} = \frac{\bar{R}(z_c)}{G_I\bar{z}_c\Big|_{\mathcal{R}=0}} < 1 \qquad (4.16)$$

4.15 can be written as:-

$$\bar{z}_c = \bar{z}_c\Big|_{\mathcal{R}=0}\{1 - \bar{X}\}$$

The bracketed term, in view of 4.16, could be considered here as the first two terms in the binomial expansion of $\{1 + \bar{X}\}^{-1}$:-

$$\{1 + \bar{X}\}^{-1} = \{1 - \bar{X}\} + \Sigma$$

where Σ is the summation of the remaining terms. Hence:-

$$\bar{z}_c = \bar{z}_c\Big|_{\mathcal{R}=0}\{1 - \bar{X}\} = \bar{z}_c\Big|_{\mathcal{R}=0}\left[\{1 + \bar{X}\}^{-1} - \Sigma\right]$$

or:-

$$\bar{z}_c = \frac{\bar{z}_c\Big|_{\mathcal{R}=0}}{1 + \bar{X}} - \Sigma' \quad ; \quad \Sigma' = \bar{z}_c\Big|_{\mathcal{R}=0}\Sigma$$

or:-

$$\frac{\overline{z}}{z_c} = \frac{1}{\left.\frac{\overline{1}}{\overline{z}_c}\right|_{\mathcal{R}=0} + \overline{F}\mathcal{R}} - \Sigma' \qquad (4.17)$$

where:-

$$\overline{F} = \left.\frac{\overline{X}}{\overline{z}_c}\right|_{\mathcal{R}=0} + \frac{\overline{R}(z_c)}{G_I \mathcal{R}(\left.\overline{z}_c\right|_{\mathcal{R}=0})^2} \qquad (4.17a)$$

The first term is of similar form to 4.11 from Kamotami and Greber (39): if the extra spreading rate R(z) is roughly proportional to the velocity ratio $\mathcal{R}$ in the initial region ($z<z_c$) then $\overline{F}$ in 4.17a is roughly constant with variation in $\mathcal{R}$. The broad similarity between 4.11 and 4.17 suggests that, in extending the use of the propagation equation into the initial region, the core length z_c (in relation to the Adler and Baron work (63)) is equivalently but implicitly determined. The present method is an advance in terms of reduction in empirical input (z_c determined within the solution scheme), generality with respect to crossflow type and ready adaptability to variable density jets (4.11 applies only to constant density jets in uniform crossflows).

4.5.4 An Expression For The Increase In Spreading Rate

The form for the extra, crossflow-related spreading rate $\mathcal{F}_1(z)$ in 4.7 and 4.9, was taken by Adler and Baron (63) from the work of Tulin and Schwartz (92,93) on the growth of a vortex pair. The same functional variation is used here, in the absence of any more justified representation:-

$$\mathcal{F}_1(z) = \frac{dR}{dz} = \frac{G_1(z)}{\left(\frac{A}{A_0}\right)^{(1-A_1)/2} + 0.5}\left(\frac{w_N(z)}{u_m(z) + w_\ell(z)}\right) \qquad (4.18)$$

Baron (71) gave the velocity-related denominator in 4.18 (and in 4.8 for $\mathcal{F}_0(z)$) as $u_m(z)$ rather than $u_m(z) + w_\ell(z)$, but this is not compatible with the reduced propagation equation for axisymmetric jets (Chapter 3). The term A_1 in 4.18 was given by Packer (35), for use with swirling flow,

as:-

$$A_1(z) = \exp\left\{\frac{-2zw_N(0)}{\pi D_0 u_0}\right\}\left(\frac{u_0}{6.2w}\right) \qquad (4.18a)$$

Such a form appears to give good results for constant density jets (63,35), although validity is not confirmed. Adler and Baron set $G_I \equiv 0.38$ directly from Tulin and Schwartz (92,93). In the present work it was found to be neceessary to prescribe different values for G_1 in the initial and subsequent regions (Chapter 7).

When 4.8 and 4.18 are used in 4.10, the propagation equation is:-

$$\frac{dA}{dz}_D = 2\sqrt{\pi A}\left\{G(z)\left(\frac{u_m - w_\ell}{u_m + w_\ell}\right) + \frac{G_1(z)}{\left(\frac{A}{A_0}\right)^{(1-A_1)/2} + 0.5}\left(\frac{w_N}{u_m + w_\ell}\right) + \frac{b}{2\sqrt{AA_c}}\frac{dA_c}{dz}\right\} \qquad (4.18b)$$

Having established a basis for system closure with a propagation equation, the momentum theory will now be derived following Baron (71).

4.6 Integrated Momentum Conservation Equations For The Deflected Jet

4.6.1 Introduction

Following the review of analytical methods presented in Section 4.3, the deflected jet will be analysed by writing momentum conservation equations in the direction of the jet centreline z (defined below), and in the direction N normal to it. The derivation is based upon that of Baron (71) and Adler and Baron (63). To facilitate the discussion, reference is made to the definition sketches of the jet geometry and inner structure in Fig. 4.7. A non-uniform distribution for the velocity w in the external stream is permitted: the position of the jet centreline is defined below in terms of

the polar co-ordinates (r_z, θ_z) as shown.

In addition to the constant density assumption of this chapter, the following simplifying assumptions are introduced (after Adler and Baron (63)):-

1/ The jet centreline is defined as the locus of momentum centres of successive cross-sections. It is the independent variable in the solution.

2/ The external flowfield is irrotational.

3/ The flow is turbulent.

4/ The flow is steady with respect to time.

5/ Velocities within the jet are parallel to the centreline (69).

6/ The jet cross-section boundary is the surface at which the excess velocity in the centreline direction is less than a prescribed small value (Chapter 2).

7/ Pressure on cross-sections is uniform and proportional to $w_{\ell}=w\cos\beta$ (used by Adler and Baron (63) in the modelling of pressure gradients - Section 4.6.4).

These assumptions encompass those of Chapters 2 and 3 and extend them for the following derivation. Assumption 5/ is sufficient to ensure that the deflected jet flow is similar to that of an axisymmetric jet (with the complication of streamline curvature): the resulting integrated conservation equations have the same general form as those formally derived for straight jets in Chapter 2.

At any location within the jet the velocity in the centreline direction is given by (Fig. 4.7b):-

$$u = h_v(z)U_v(z) + w\cos\beta \qquad (4.19)$$

in analogy with its definition in Chapter 3. Here, $U_v(z)$ is the (assumed known) two-dimensional, non-similar velocity distribution in deflected jets, defined over the entire cross-section and so including any constant velocity core ($U_v \equiv 1$), and $h_v(z)$ is the maximum excess jet velocity in the cross-section at z:-

$$h_v(z) = u_m(z) - w\cos\beta \qquad (4.19a)$$

These definitions are entirely compatible with those of Chapter 3 for straight jets.

The integrated continuity equation is no different from that of Chapter 2:-

$$\frac{d}{dz}\int_A \rho u dA = E_m \qquad (4.20)$$

The entrainment rate E_m can be known from 4.20 and the propagation equation 4.18b.

4.6.2 Conservation Of Momentum In The Centreline Direction

This equation is constructed by balancing z-components of the forces acting upon the control volume shown in Fig. 4.8. This has volume V and surface $S_V = A(z_1) + A(z_2) + A_3$: if δz is assumed sufficiently small, the faces $A(z_1)$ and $A(z_2)$ can be assumed to be parallel. Baron (71) and Campbell and Schetz (79) write the integral balance in the following way:-

$$\underbrace{\iiint_V \vec{F_b} dV}_{\text{body forces}} + \underbrace{\frac{d}{dt}\iiint_V \rho\vec{u} dV}_{\text{unsteady}} + \underbrace{\iint_{S_V} \rho\vec{u}(\vec{u}.d\vec{S_V})}_{\text{momentum flux}} + \underbrace{\iint_{S_V} p d\vec{S_V}}_{\text{surface forces}} = 0 \qquad (4.21)$$

The only body force in $\vec{F_b}$ in this chapter is a centrifugal force due to jet deflection (Section 4.6.4): buoyancy effects

are discussed in Chapter 5. The surface force $\mathcal{P}$ will be a result of pressure gradients. For an assumed steady flow, the temporal derivative vanishes from 4.21.

In the z-direction, the momentum flux surface integral expands as:-

$$\mathcal{M}_z = \int_{A(z_2)} \rho u^2 dA - \int_{A(z_1)} \rho u^2 dA - \int_{A_3} \rho v_3 u dA$$

v_3 is a characteristic velocity for the entrained fluid. As $\delta z \to 0$, $A_3 \to (A(z_2)-A(z_1))$ and $v_3 \to w_\zeta = w\cos\beta$. The limiting form of $\mathcal{M}_z$ is:-

$$\mathcal{M}_z \to \left\{ \frac{d}{dz} \int_A \rho u^2 dA - w\cos\beta \frac{d}{dz} \int_A \rho u dA \right\} dz \qquad (4.22)$$

The surface force $\mathcal{P}$ is free from any shear stress contribution in view of the definition of the jet boundary in assumption 6/ above: the velocity profile U_V is required to satisfy the physical boundary condition $\partial U_V/\partial N \to 0$ near the boundary. The assumed velocity distribution is the actual result of viscous effects. In contrast, Campbell and Schetz (94) used a uniformly distributed, averaged velocity $\bar{u}_j$ over a particular cross-section and were obliged to include a model for the shear stress τ, due to the boundary discontinuity in velocities. An eddy viscosity form was chosen:-

$$\tau \propto \frac{\partial u}{\partial N} \quad ; \quad \frac{\partial u}{\partial N} = \frac{\bar{u}_j - w_\zeta}{b}$$

In the present model $\mathcal{P}$ is made up only from the static pressure distribution P ($\mathcal{P} \equiv P$). Baron (71) and Campbell and Schetz (79) expand the z-component of the pressure surface integral in 4.21 using truncated Taylor series expansions for P (constant over a cross-section by assumption 7/) and A, based at $A(z_1)$ (Fig. 4.8), in order to evaluate $A(z_2)$ and $P(z_2)$. It is assumed that $A_3 = A(z_2) - A(z_1)$ so that,

as $\delta z \to 0$ (writing $P(z_1)=P$, $A(z_1)=A$):-

$$\iint_{S_V} P\,dS_{V_z} \simeq -PA + \left(P + \frac{dP}{dz}dz\right)\left(A + \frac{dA}{dz}dz\right) - \left[\frac{P + \left(P + \frac{dP}{dz}dz\right)}{2}\right]\left(\left[A + \frac{dA}{dz}dz\right] - A\right)$$

The right hand side expands to:-

$$-PA + PA + P\frac{dA}{dz}dz + A\frac{dP}{dz}dz + \frac{dP}{dz}\frac{dA}{dz}dzdz - P\frac{dA}{dz}dz - \frac{dP}{dz}\frac{dA}{dz}\frac{dzdz}{2}$$

Hence:-

$$\iint_{S_V} P\,dS_{V_z} \simeq A\frac{dP}{dz}dz + \frac{dP}{dz}\frac{dA}{dz}\frac{dzdz}{2} \simeq A\frac{dP}{dz}dz \qquad (4.23)$$

to first order in dz. The pressure force per unit length is therefore AdP/dz.

Of the analytical models described earlier, only Baron (71) and Campbell and Schetz (79) include pressure effects in the centreline momentum equation. Baron (71) finds dP/dz by writing Euler's equation for the z-direction velocity component $w_\xi = w\cos\beta$ (Fig. 4.7b) of the irrotational external flow:-

$$\frac{dP}{dz} = -\rho_\infty w\cos\beta \frac{d}{dz}(w\cos\beta)$$

Campbell and Schetz (94) assumed that the free stream static pressure field around the jet perimeter imposes itself on the jet flow. There are large variations in free stream pressure due to the blockage effect: an estimate of this variation was obtained by assuming that pressures on the upstream part of the jet boundary (Fig. 4.1) are given by potential flow theory for a circular cylinder, and pressures on the downstream part are equal to the free stream pressure.

This crude approximation for the local surface pressure P_1 was used in the expression:-

$$P = \int_C P_1 dC \Big/ \int_C dC$$

to obtain the average static pressure P acting on the jet perimeter C. This integration gave (94):-

$$P = P_\infty - \frac{1}{2}(q_\infty)_N = P_\infty - \frac{1}{2}\rho_\infty(\frac{w\sin\beta}{2})^2$$

where P_∞ is the free stream static pressure and $(q_\infty)_N$ is the free stream dynamic pressure normal to the trajectory. Differentiating this expression for P:-

$$\frac{dP}{dz} = -\rho_\infty \frac{w^2}{2} \sin\beta\cos\beta \frac{d\beta}{dz} \qquad (4.24)$$

The same result was obtained by Baron (71). According to Kamotami and Greber (39) the pressure force serves to decrease only slightly the jet maximum velocity (see Chapter 7).

The centreline momentum equation is obtained, from 4.21, by summing and equating to zero 4.22 and 4.23:-

$$\frac{d}{dz}\int_A \rho u^2 dA = w\cos\beta \frac{d}{dz}\int_A \rho u dA - A\frac{dP}{dz} \qquad (4.25)$$

dP/dz may be evaluated from 4.24: for simplicity, the substitution is not made explicitly in the following derivations. The similarity of form between 4.25 and the axisymmetric jet form of Chapter 3 is evident.

For the momentum theory, 4.25 is manipulated in the following way: the velocity u is substituted from 4.19 and the integral expressions are expanded to give:-

$$\frac{d}{dz}\{w^2\cos^2\beta I_0 + 2h_v w\cos\beta I_1 + h_v^2 I_2\} = w\cos\beta\frac{d}{dz}\{w\cos\beta I_0 + h_v I_1\} - A\frac{dP}{dz} \qquad (4.26)$$

where:-

$$I_n = \int_A \rho U_V{}^n dA \qquad n = 0,1,2 \qquad (4.26a)$$

4.26 may be further expanded, and then rearranged, to yield (as in Chapter 3) an equation for the variation of the excess jet velocity function h_v:-

$$\frac{dh}{dz}_v = \frac{(w\cos\beta I_0 + 2h_v I_1)\left(w\sin\beta\frac{d\beta}{dz} - \cos\beta\frac{dw}{dz}\right)}{(w\cos\beta I_1 + 2h_v I_2)} - \frac{w\cos\beta h_v\frac{dI_1}{dz} - h_v^2\frac{dI}{dz}_2 - A\frac{dP}{dz}}{(w\cos\beta I_1 + 2h_v I_2)} \qquad (4.27)$$

The terms in the first grouping are associated directly with crossflow effects: when the jet is not deflected (β, $d\beta/dz$ and dw/dz equal to zero) and pressure is constant, 4.27 reduces to the excess velocity decay statement downstream of the end of the initial region in an axisymmetric jet, 3.31.

The jet density ρ, although constant in this chapter, has not been eliminated from the equations (and is included in the integral definitions 4.26a) in order to ensure their compatibility with the equations of Chapter 5 for variable density jets.

The equation 4.27 is used to predict velocity decay beyond the end of the initial region (as in Chapter 3). Because the definition of U_v has been extended here (from that of U_{v_I} in 3.7 of Chapter 3) to include the constant velocity core in the initial region, 4.27 remains valid in the initial region, and its use there is now explained.

4.6.3 An Equation For The Extent Of The Undisturbed Core In The Initial Region

In Chapter 3, the analysis of the initial region was as follows: the propagation equation was applied to determine the width b of the mixing zone at a station z, and the radial extent of the core could then be deduced from the principle of axial momentum conservation (Section 3.3). Exactly the same approach is adopted here for deflected jets. The general statement of the propagation equation is given in 4.10.

The characteristic property of the initial region is that the maximum jet velocity u_m at any cross-section (ocurring in the undisturbed core) remains at the injection velocity u_0. From 4.19a, for the initial (core) region:-

$$h_v(z) = u_m(z) - w\cos\beta = u_o - w\cos\beta \qquad z<z_c \quad (4.28)$$

Hence:-

$$\frac{dh}{dz}_v = -\frac{d}{dz}\{w\cos\beta\} = w\sin\beta\frac{d\beta}{dz} - \cos\beta\frac{dw}{dz} \qquad z<z_c \quad (4.29)$$

Adler and Baron (63) did not use a propagation equation in this region: z_c was prescribed from 4.11, and 4.29 was used for the variation of h_v. The analysis of the initial region (71) may be shown to be at fault (Chapter 6).

For the present work, 4.29 may be used to substitute for dh_v/dz in the centreline momentum equation expressed as 4.27. Upon rearrangement, this gives:-

$$-(w\cos\beta I_1 + 2h_v I_2)\frac{d}{dz}\{w\cos\beta\} = -(w\cos\beta I_0 + 2h_v I_1)\frac{d}{dz}\{w\cos\beta\}$$
$$-w\cos\beta h_v\frac{dI_1}{dz} - h_v^2\frac{dI_2}{dz} - A\frac{dP}{dz}$$

or, in compact notation:-

$$P_c - h_v\left\{w\cos\beta\frac{dI_1}{dz} + h_v\frac{dI_2}{dz}\right\} - A\frac{dP}{dz} = 0 \qquad (4.30)$$

where:-

$$P_c = \{w\cos\beta(I_1 - I_0) - 2h_v(I_2-I_1)\}\frac{d}{dz}\{w\cos\beta\} \qquad (4.30a)$$

The jet cross-section area A is written in terms of the constant velocity core area A_c and the turbulent mixing zone area A_D (Fig. 4.6a), as in Section 4.5.2:-

$$A = A_c + A_D \qquad (4.4)$$

The integrals I_n in 4.30, defined in 4.26a, may be written in terms of undisturbed core and mixing zone contributions:-

$$I_n = K_n A = I_{nA_c} + I_{nA_D} = K_{nA_c}A_c + K_{nA_D}A_D \qquad (4.30b)$$

where:-

$$K_n = \frac{1}{A}\int_A \rho U_v^n dA \qquad n=0,1,2 \qquad (4.30c)$$

$$K_{nA_i} = \frac{1}{A_i}\int_{A_i} \rho U_v^n dA_i \qquad n=0,1,2 \quad i= c \text{ or } D \qquad (4.30d)$$

For constant density jets, since $U_v \equiv 1$ over A_c, $K_{nA_c} = \rho_\infty$, but again the general term is retained for complete compatibility with the equations of Chapter 5. The unknown quantity in 4.30 is not h_v, in view of 4.28 and 4.29, but the core area A_c. Using 4.30b,c, and d in 4.30 gives:-

$$P_c - h_v\left\{w\cos\beta\frac{dK_1}{dz} + h_v\frac{dK_2}{dz}\right\}A - h_v\left\{w\cos\beta K_{1A_D} + h_v K_{2A_D}\right\}\frac{dA}{dz}D$$

$$- h_v\{w\cos\beta K_{1A_c} + h_v K_{2A_c}\}\frac{dA}{dz}c - A\frac{dP}{dz} = 0$$

from which a differential equation for the rate of change of the core area A_c may be deduced:-

$$\frac{dA}{dz}_c = \left[P_c - h_v \left\{ w\cos\beta \frac{dK_1}{dz} + h_v \frac{dK_2}{dz} \right\} A - h_v \{ w\cos\beta K_{1A_D} + h_v K_{2A_D} \} \frac{dA}{dz}_D - A \frac{dP}{dz} \right] \Bigg/ h_v \{ w\cos\beta K_{1A_c} + h_v K_{2A_c} \} \qquad (4.31)$$

The term P_c from 4.30a is zero for an axisymmetric jet. The core area equation 4.31 must be coupled for solution with a propagation equation of the general form 4.10. The full form of this equation for the present work was given in 4.18b: using 4.19a for u_m, and putting $w_t = w\cos\beta$, $w_N = w\sin\beta$ (Fig. 4.7b), 4.18b becomes:-

$$\frac{dA}{dz}_D = 2\sqrt{\pi A} \left\{ \frac{G(z) h_v}{(h_v + 2w\cos\beta)} + \frac{G_1(z)}{\left(\frac{A_0}{A}\right)^{(1-A_1)/2} + 0.5} \left(\frac{w\sin\beta}{h_v + 2w\cos\beta} \right) + \frac{b}{2\sqrt{AA_c}} \frac{dA}{dz}_c \right\} \qquad (4.32)$$

In the intial region $G(z) = G_I = 0.22$ (Chapter 3).

The equations 4.31 and 4.32 also apply (with appropriate simplifications) to axisymmetric jets, and it is possible to recover from them the relevant equations of Chapter 3. The predicted condition $A_c = 0$ determines z_c, the end of the initial region, beyond which the form 4.27 of the momentum equation is used to predict the decay of the excess jet velocity h_v.

More remarks concerning 4.31 are made in Chapter 6 (computer implementation). The predictions afforded by the model are discussed in Chapter 7.

4.6.4 Momentum Equation Normal To The Centreline Direction

This equation will represent the balance of forces acting perpendicularly to the local jet centreline direction. The derivation and form of this equation is common to Wooler (86), Campbell and Schetz (79) and Baron (71).

The equation is obtained by taking N components of each term in the vector equation 4.21. The result is (63,79):-

$$-\int_A \frac{\rho u^2 dA}{R_c} = \rho \frac{C_D}{2}(w\sin\beta)^2 b_X + w\sin\beta \frac{d}{dz}\int_A \rho u dA \qquad (4.33)$$

centrifugal body force | surface forces | momentum flux M_N

The centrifugal force is a consequence of the jet mass following a curved path; the radius of curvature R_c of the jet streamlines is discussed below. The integrated surface shear and pressure forces, which cannot be calculated directly, are represented as a total drag force on the jet, due to blockage of the external flow by the jet envelope. The jet is usually considered as a solid body for the evaluation of the drag coefficient C_D (Section 4.3) - a suitable value for the present work is discussed in Chapter 7. The local jet width b_X is shown in Fig. 4.1; more generally, b_X could be replaced by a characteristic width such as $2\sqrt{A/\pi}$. According to Shirakashi and Tomita (90), the expression $C_D b_X$ should be treated as a single empirical coefficient, in view of the approximate nature of the drag force itself (Chapter 7).

The momentum flux in the N-direction is represented by the rate of entry of mass into the control volume through the surface A_3 (the entrainment rate E_m) multiplied by the N-direction component of the velocity w in the free stream.

For the centrifugal force term, Wooler (86) and Baron (71) assumed the width of the jet to be small compared with R_c, so that R_c can be taken as constant over A. From Fig. 4.9, the radius of curvature R_c is given by:-

$$R_c = \frac{(1 + y_z'^2)^{1.5}}{y_z''} \quad ; \quad y_z' = \frac{dy}{dx}_z = \tan\{\beta + \alpha - \frac{\pi}{2}\} \qquad (4.34)$$

The angle α gives the local direction of the crossflow velocity relative to the y_z axis (see also Fig. 4.10). Setting $\eta=\beta+\alpha-(\pi/2)$ and following the derivation of Baron (71), 4.34 gives:-

$$R_c = \frac{(1 + \tan^2(\eta))^{1.5}}{\frac{d}{dx_z}(\tan(\eta))} = \frac{(1 + \tan^2(\eta))^{1.5}}{\frac{d}{d\eta}(\tan(\eta))\frac{d\eta}{dz}\frac{dz}{dx_z}}$$

since $dx_z/dz = \cos(\eta)$ (Fig. 4.9), this gives:-

$$R_c = \frac{\left(\frac{\cos^2(\eta) + \sin^2(\eta)}{\cos^2(\eta)}\right)^{1.5}}{\frac{1}{\cos^2(\eta)}\frac{d}{dz}\frac{1}{\cos(\eta)}} = \frac{1}{d\eta/dz} \qquad (4.35)$$

recalling $\eta=\beta+\alpha-(\pi/2)$. The centrifugal body force term in 4.33 becomes:-

$$-\int_A \frac{\rho u^2 dA}{R_c} = -\frac{d\eta}{dz}\int_A \rho u^2 dA = -\left(\frac{d\beta}{dz} + \frac{d\alpha}{dz}\right)\int_A \rho u^2 dA \qquad (4.36)$$

Adler and Baron (63) worked only in the case of a uniform crossflow parallel to the x_z axis, defined in the present work by $\alpha\equiv\pi/2$ (Fig. 4.9). This gives $d\alpha/dz\equiv 0$ in 4.36 and the body force term is the same as that used by Adler and Baron (63) and Packer (35). For central injection into swirl, $d\alpha/dz$ may be evaluated by backward differencing with the values of α at successive solution steps (Section 4.7). In the present work, the effect of the $d\alpha/dz$ term was found to be slight and, in the absence of detailed experimental results for further assessment, is neglected below. As a consequence of this simplification, the model is not applicable to the case of side injection into swirl: reconsideration of the force balance in 4.33 will also be necessary for this case (19).

Using 4.36 in 4.33 (and neglecting the $d\alpha/dz$ term), substituting for u from 4.19, expanding and rearranging, an equation is obtained for the rate of change of the angle β:-

$$\frac{d\beta}{dz} = \frac{\left[\frac{\rho C_D}{2}(w\sin\beta)^2 b_X + w\sin\beta\left\{\cos\beta\left[w\frac{dI_0}{dz} + I_0\frac{dw}{dz}\right] + h_v\frac{dI_1}{dz} + I_1\frac{dh}{dz}_v\right\}\right]}{(w^2 I_0\{\sin^2\beta - \cos^2\beta\} - 2h_v I_1 w\cos\beta - h_v^2 I_2)} \qquad (4.37)$$

(the integrals I_n are defined in 4.26a). The equation is applied both within and downstream of the initial region.

4.7 Co-ordinate Relationships

Consider Fig 4.10, where the angles β, α, and γ are all defined for a general crossflow case.

In Fig. 4.10b, use of the sine rule on the elemental triangle gives:-

$$\frac{\delta r_z}{\sin(\beta+\gamma)} = \frac{r_z \delta\theta_z}{\sin(\frac{\pi}{2} - (\beta+\gamma))} = \delta z$$

Hence, in the limit as $\delta_z \to 0$:-

$$dr_z = dz\,\sin(\beta+\gamma)$$
$$d\theta_z = \frac{dz\,\cos(\beta+\gamma)}{r_z} \qquad (4.38)$$

The prescription of α in three cases of primary importance is here identified:-

1/ The straight jet: $w \perp (\theta_z \equiv 0) \Rightarrow \alpha \equiv \pi/2$ (Fig. 4.10a)
Hence $\beta \equiv 0$, $\gamma = \theta_z \equiv \pi/2$ (Fig. 4.10a)
In 4.38:-

$$dr_z = dz\,\sin(0+\tfrac{\pi}{2}) \equiv dz$$
$$d\theta_z = dz\,\cos(\tfrac{\pi}{2})/r_z \equiv 0$$

2/ The uniform direction crossflow (the Adler and Baron model (63))

$w \perp (\theta_z \equiv 0) \Rightarrow \alpha = \pi/2 \Rightarrow \gamma = \theta_z$ (where θ_z will vary)

In 4.38:-

$$dr_z = dz \sin(\beta + \theta_z)$$

$$d\theta_z = dz \cos(\beta + \theta_z)/r_z$$

3/ Force-vortex swirl (central injection)

$w \perp r_z \Rightarrow \alpha = (\pi/2) - \theta_z \Rightarrow \gamma \equiv 0$ (Fig, 4.10b)

In 4.38:-

$$dr_z = dz \sin\beta$$

$$d\theta_z = dz \cos\beta/r_z$$

This latter was the single co-ordinate system used by Packer (35): predicted uniform direction crossflow trajectories were in error.

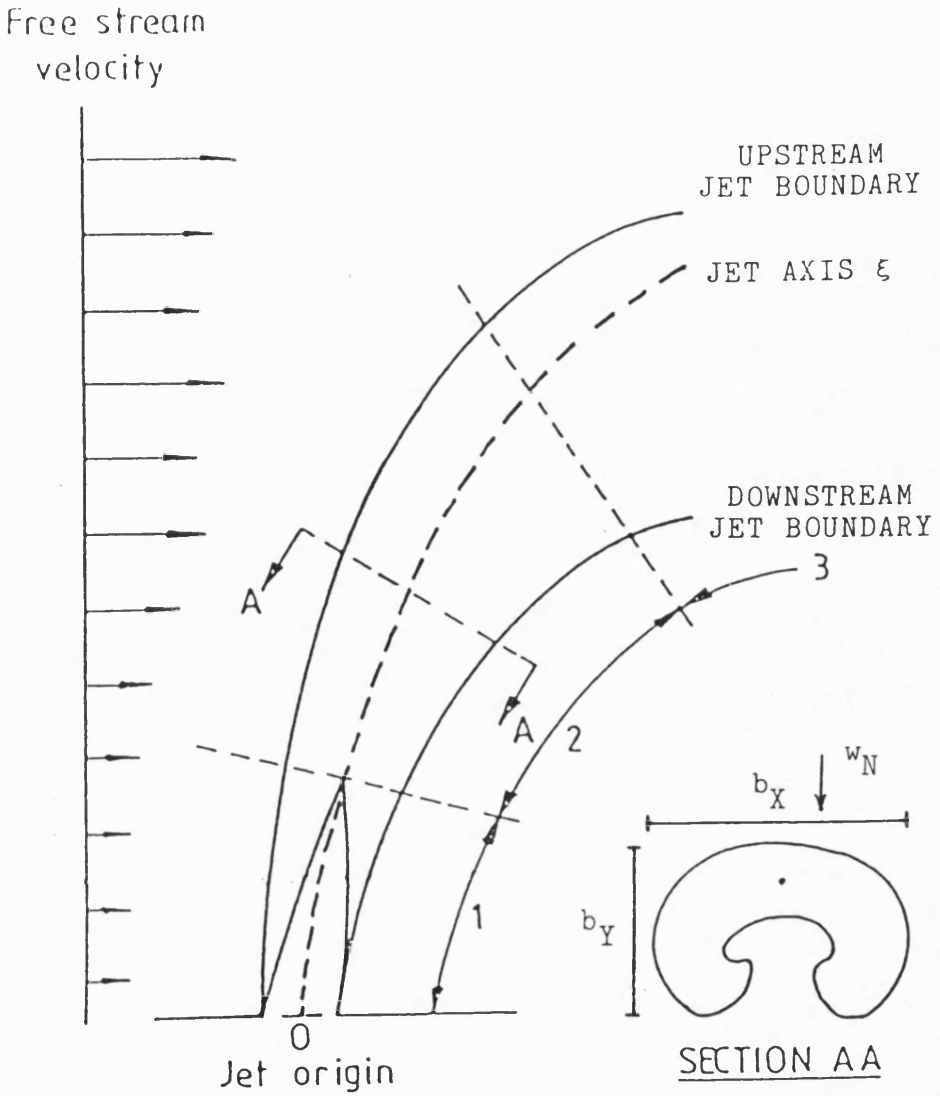

KEY:-

1 - INITIAL REGION
2 - CURVILINEAR REGION
3 - FAR REGION

FIG 4.1 DIAGRAM OF A JET IN A CROSSFLOW

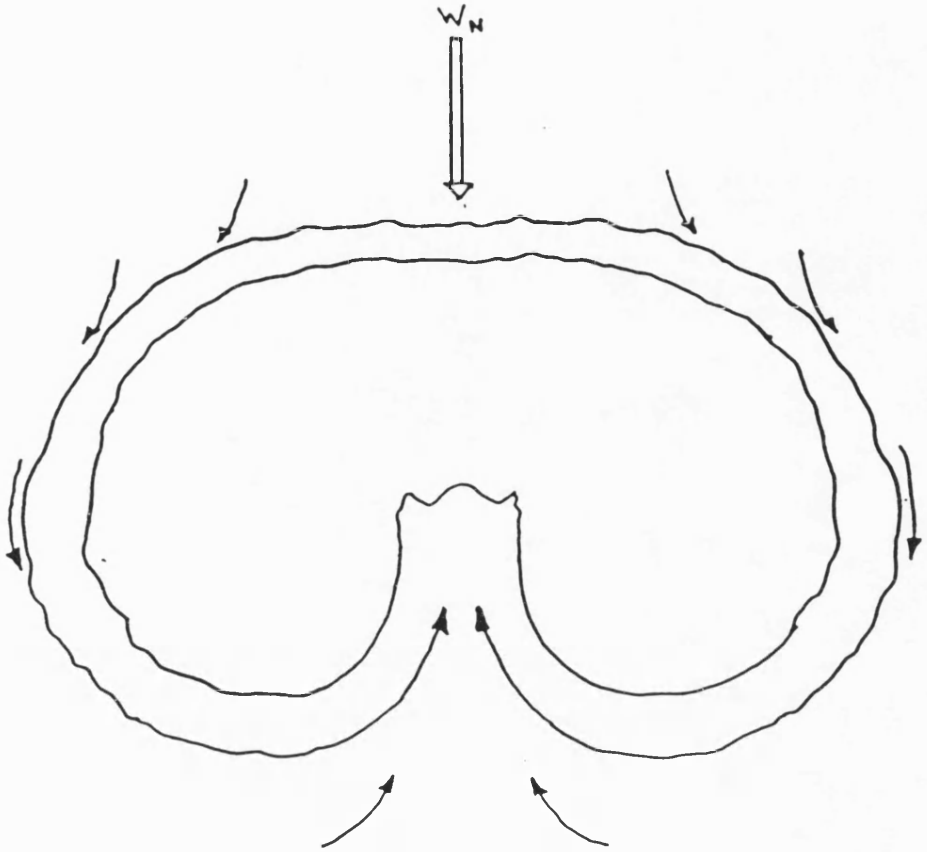

FIG 4.2a HELICAL CIRCULATION PATTERNS

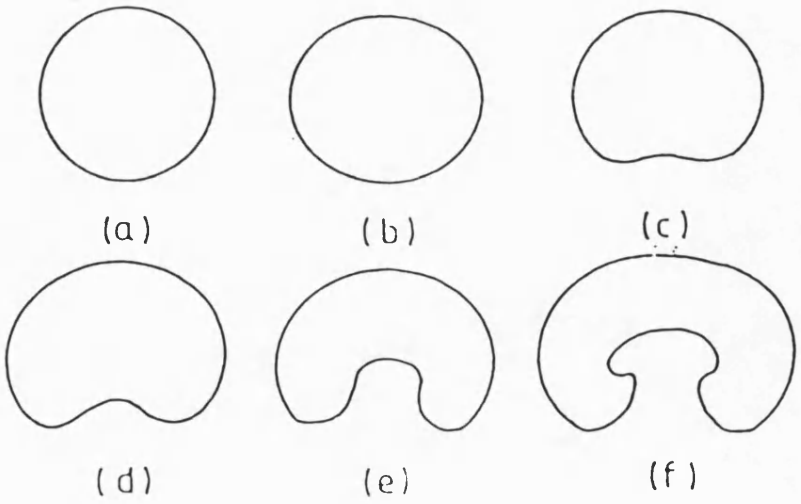

FIG 4.2b CROSS-SECTION DISTORTION SEQUENCE

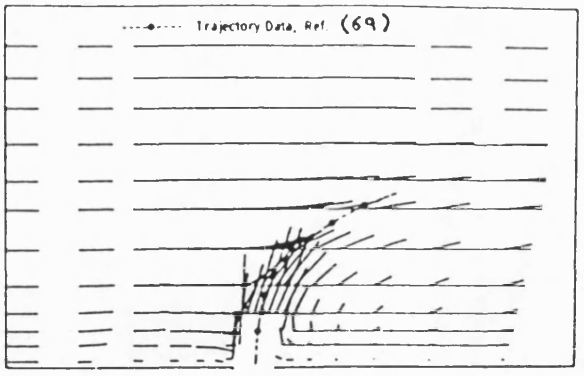

FIG 4.3 VELOCITY VECTORS AT $R^{-1}=4$ FROM THE FINITE-DIFFERENCE SOLUTION OF CHIEN AND SCHETZ (84)

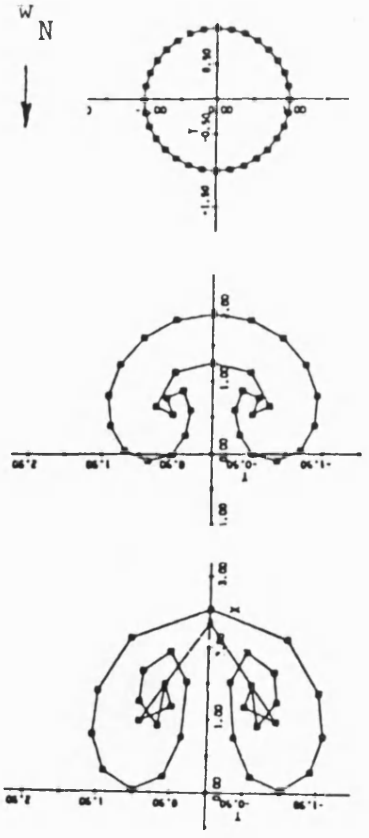

FIG 4.4 JET CROSS-SECTION DISTORTION PREDICTIONS BY HACKET AND MILLER (87) USING THE VORTEX SHEET MODEL

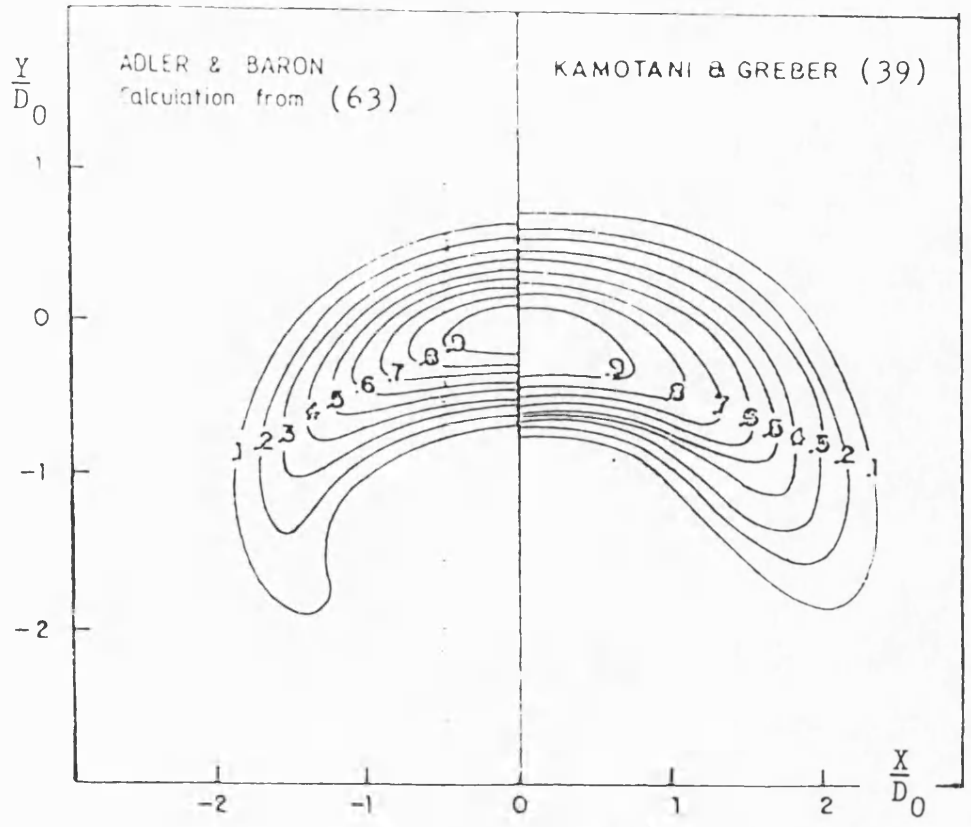

FIG 4.5a JET SHAPE AND U_v AT R^{-1} = 3.91 AND ξ/D_0 = 7

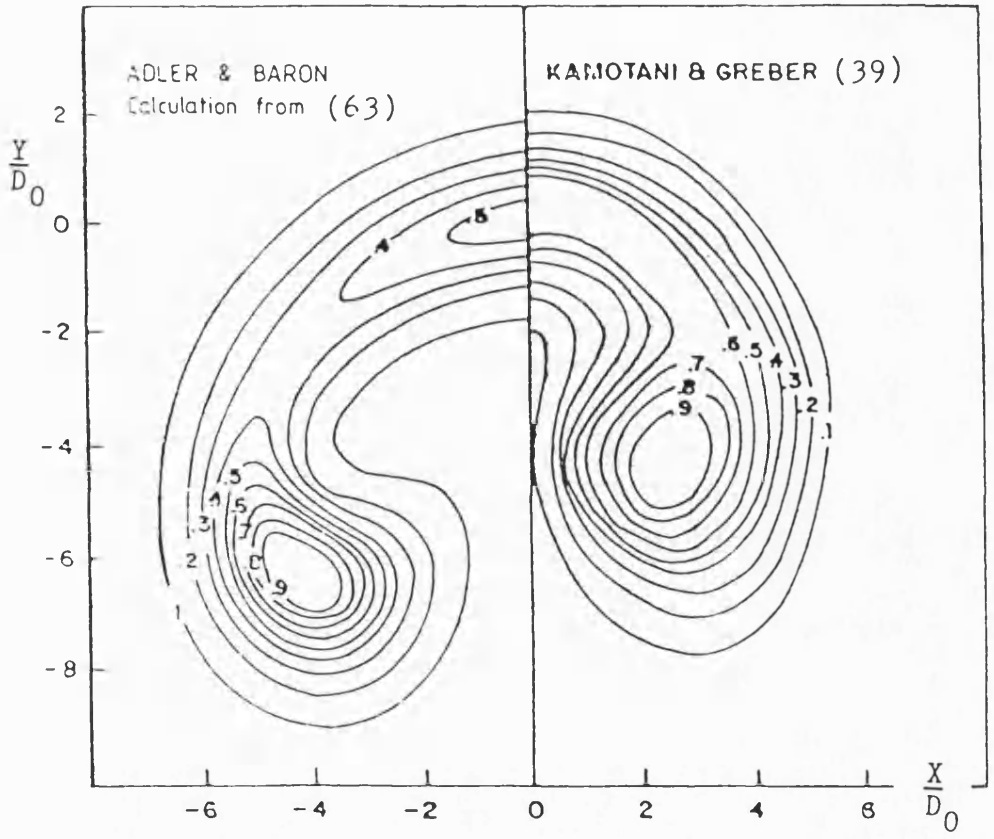

FIG 4.5b JET SHAPE AND U_v AT R^{-1} = 7.73 AND ξ/D_0=23

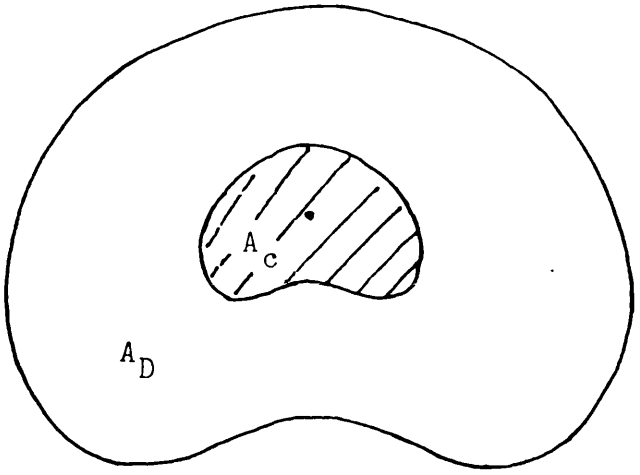

A_c: area of constant velocity core
A_D: area of turbulent mixing zone

$A = A_c + A_D$ $\qquad r_c = \sqrt{A_c/\pi}$

$b = \sqrt{A/\pi} - r_c$

(a) INITIAL REGION INCLUDING UNDISTURBED CORE

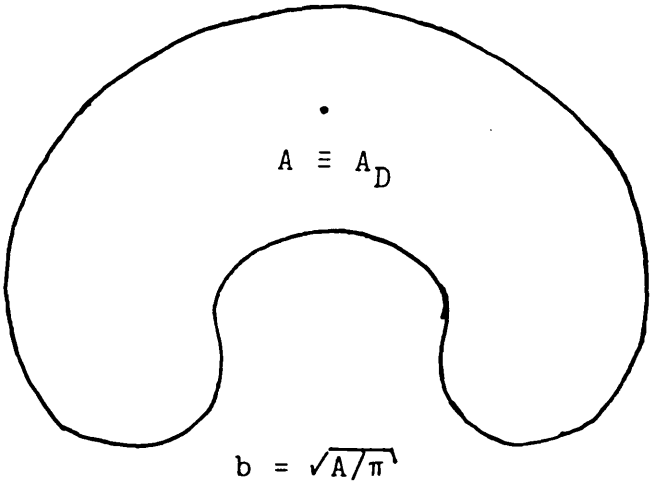

(b) BEYOND THE INITIAL REGION

FIG 4.6 DEFINITIONS FOR JET AREAS AND EFFECTIVE WIDTHS

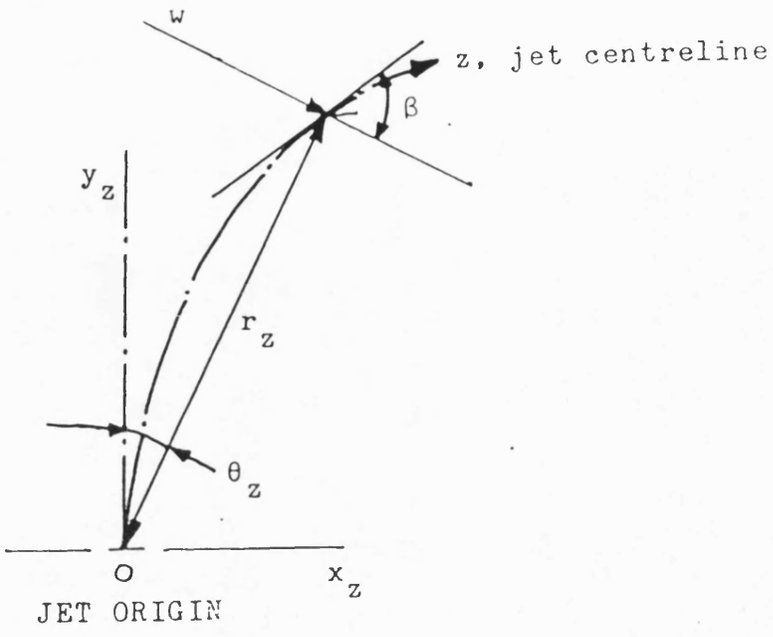

FIG 4.7a DEFINITION SKETCH OF THE JET GEOMETRY

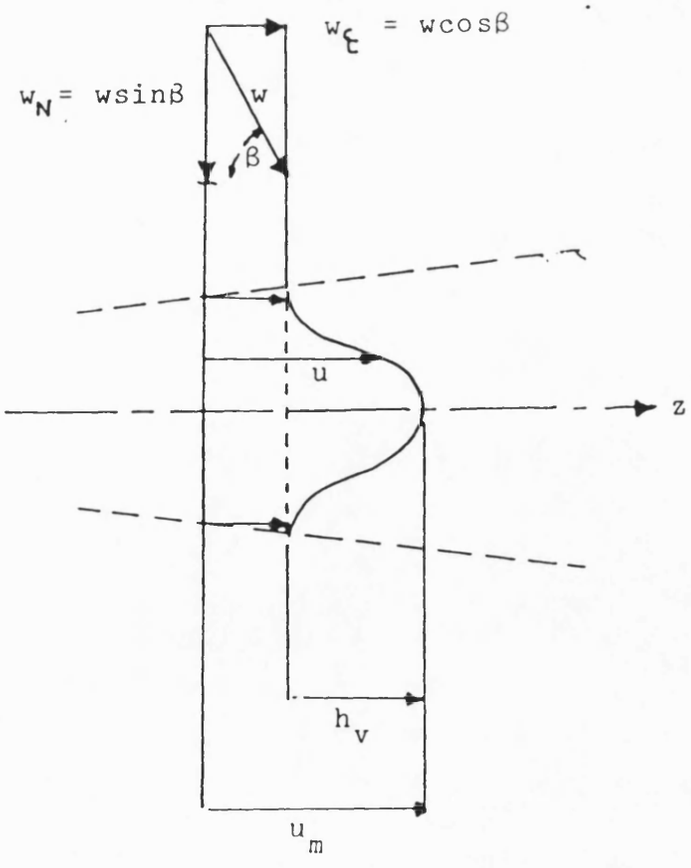

FIG 4.7b DEFINITION SKETCH OF THE JET INNER STRUCTURE

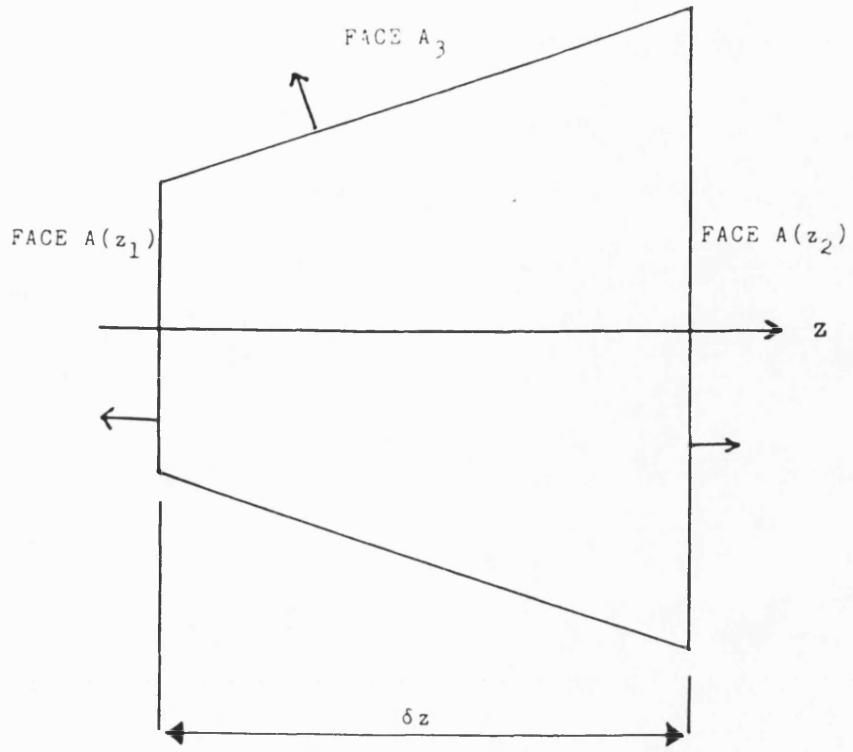

POSITIVE NORMAL TO EACH SURFACE DIRECTED OUTWARDS

FIG 4.8 CONTROL VOLUME IN THE JET

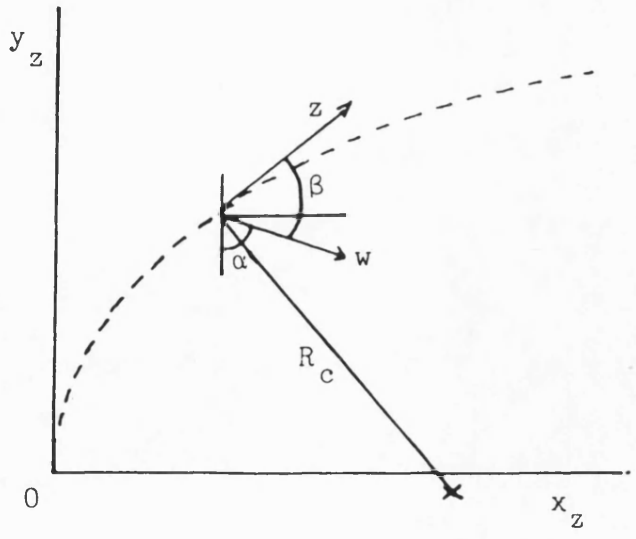

FIG. 4.9 JET RADIUS OF CURVATURE

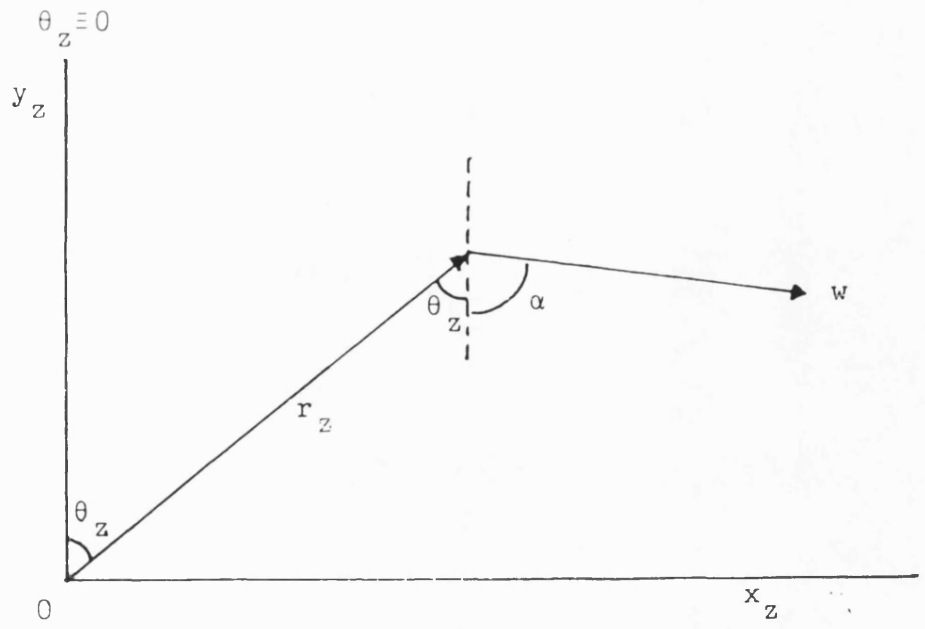

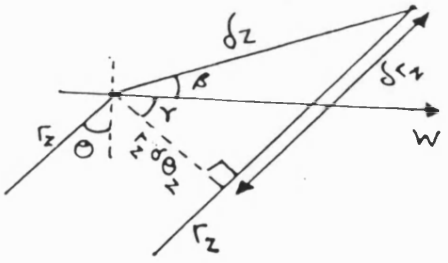

$$\theta + \alpha - \gamma = \frac{\pi}{2}$$

DEFINITIONS:-

- β: ANGLE BETWEEN $\mathfrak{L}$ AND CROSSFLOW
- α: ANGLE BETWEEN $\theta_z \equiv 0$ AND CROSSFLOW
- γ: ANGLE BETWEEN $\perp$ TO r_z AND CROSSFLOW

FIG. 4.10 GENERAL CO-ORDINATE RELATIONSHIPS

CHAPTER 5

AN ANALYSIS OF THE EFFECTS OF COMPOSITION VARIATION

Chapter 5 - Notation

A - jet area (m^2)
A_u - $=A_v$ (m^2)
A_c - area of injectant property core (m^2)
A_D - area of turbulent mixing zone (m^2)
A_0 - nozzle area (m^2)
A_ψ - jet area pertaining to property ψ (m^2)
A_1 - term in 5.25

b - width of turbulent mixing zone (m)
b_{i1}, b_{i2} - widths defined in 5.31 and Fig. 5.9c (i=v or s)

c - mass concentration of injectant
c' - concentration fluctuation
C_p - specific heat (J/kgK)
C_{pi} - injectant specific heat (J/kgK)
$\overline{C}_p$ - ratio of specific heats ($C_{pi}/C_{p\infty}$)

D_0 - nozzle diameter (m)
D_T - turbulent mass diffusion coefficient

E_m - mass entrainment rate (kgs^{-1})
F_r - Froude number
F_w, F_β
F_v, F_n - defined in 5.19

G - width growth rate coefficient for an axisymmetric jet
G_1 - enhanced growth rate coefficient

h_c - maximum concentration function
h_T - maximum temperature difference function (K)
h_v - maximum excess velocity function (ms^{-1})

I_n - property distribution integrals defined in 5.19a, 5.19b and 5.23a (n=0,...,9)

K_n, K_{nA_c}
K_{nA_D} - integral average values defined in 5.26d

Le_T - turbulent Lewis number

m - axisymmetric jet velocity ratio ($=w/u_0$)
M - fluid molecular weight (kg/Kmol)
n - density ratio at injection ($=\rho_\infty/\rho_0$)

P - pressure
P_c - term defined in 5.26c
Pr_T - turbulent Prandtl number

r - jet radial ordinate (m)
r_c - jet inner mixing (core) boundary (m)
r_2 - jet outer mixing boundary (m)
$r_{\frac{1}{2}}$ - jet half width defined in 5.6
r_0 - nozzle radius (m)
R_0 - universal gas constant

Sc_T - turbulent Schmidt number

T - temperature (K)
T' - temperature fluctuation (K)

u - jet velocity (ms^{-1})
u_r' - radial velocity fluctuation (ms^{-1})

U_c - concentration distribution function $U_c \in [0,1]$
U_T - temperature distribution function $U_T \in [0,1]$
U_s - $=U_c \equiv U_T$
U_v - velocity distribution function $U_v \in [0,1]$
U_{i_I} - mixing zone property profile in the initial region (i=v,c or T)
U_{i_M} - property profile in the main region of an axisymmetric jet (i=v,c or T)
U_{s_I} - $=U_{c_I}=U_{T_I}$
U_{s_M} - $=U_{c_M}=U_{T_M}$

w	-	external stream velocity (ms^{-1})
x	-	dimensionless radial ordinate for the mixing zone defined in 5.39c
x_z, y_z	-	co-ordinates in trajectory plane (Fig. 5.11)
z	-	jet centreline co-ordinate (m)
z_c	-	end of constant property core (m)
z_D	-	end of transition region (m)
$\mathcal{F}_0, \mathcal{F}_1$	-	axisymmetric and crossflow components of jet spreading rate in 4.7
R	-	velocity ratio for jet in a uniform crossflow ($=w/u_0$)
β	-	angle between centreline direction and crossflow (Fig. 4.7a) (rad)
δ	-	diffusion ratio defined in 5.35
δ_c, δ_2	-	diffusion rate coefficents defined in 5.31c and Fig. 5.9c
$\delta_{\frac{1}{2}}$	-	ratio of jet half widths in 5.7
η	-	radial ordinate normalised by jet half width in 5.8
θ	-	temperature ratio at injection ($=T_0/T_\infty$)
κ_T	-	turbulent thermal conductivity
ν_T	-	eddy viscosity
ρ	-	density (kg/m^3)
$\bar{\rho}$	-	$=\rho_\infty/\rho_1$
ρ_1	-	density on the jet axis (kg/m^3)
$\rho_{i,1}$	-	injectant density on the jet axis (kg/m^3)
ψ	-	general flow property (=u, c or T)

Subscripts

0	-	at the jet origin (z=0)
s	-	pertaining to scalars (c or T)
v	-	pertaining to velocity
∞	-	in the external stream
m	-	maximum

Chapter 5
An Analysis Of The Effects Of Composition Variation

5.1 Introduction

In this chapter, the variation of fluid density within axisymmetric and deflected turbulent jets is permitted. For gas-gas jets, differences in temperature and chemical composition between the injectant and free streams are characterised by the temperature and density ratios θ and n, recalled from Chapter 2:-

$$\theta = \frac{T_0}{T_\infty} \quad ; \quad n = \frac{\rho_\infty}{\rho_0} = \frac{T_0 M_\infty}{T_\infty M_i} \qquad (2.17)$$

Experimental data available in the literature, concerning axisymmetric jets of variable composition and density, is discussed in Section 5.2, and some of the observations guide the later analysis.

Conservation equations for energy and injected material are written and manipulated in Section 5.4. The necessary modifications to the momentum theory of Chapter 4 are made (Section 5.6) in order to represent variable density effects.

The 'scalar' (concentration and temperature) mixing field is assumed to be 'driven' by the momentum theory, and experimental observations (on the faster rate of diffusion of mass than momentum in axisymmetric jets) are used to ensure conservation of scalar properties, through the initial region, as a part of the analysis (Section 5.8).

The approximate treatment of the scalar mixing field is extended empirically, and with analytical convenience in mind, to include also deflected jets, for which experimental data is scarce (Section 5.9).

5.2 Temperature And Concentration Distributions In Axisymmetric Jets

Measurements of the 'scalar' mixing field in axisymmetric jets of uniform and variable composition have been reported by Landis and Shapiro (58)(1950), Abramovich (32,53)(1963 and 1967), Chriss (59)(1968), Sforza (72)(1978), Shirakashi and Tomita (90)(1978) and others. Measurements made in the main region (Chapter 3) are discussed first, and consideration is then given to the limited amount of data available for the initial region.

Dimensionless distributions of temperature and injectant concentration by mass over a jet cross-section are defined as follows, in analogy with the main region excess velocity profile U_{v_M} (Chapter 3):-

$$U_{T_M}(r,z) = \frac{\Delta T}{\Delta T_m} = \frac{T(r,z) - T_\infty}{T_m(z) - T_\infty} \tag{5.1}$$

$$U_{c_M}(r,z) = \frac{\Delta c}{\Delta c_m} = \frac{c(r,z)}{c_m(z)} \tag{5.2}$$

Equation 5.2 is simplified as the concentration in the free stream is zero ($c_\infty \equiv 0$): c is defined in 5.20 (Section 5.5). Abramovich (32), Thring and Newby (95) and others consider U_{T_M} and U_{c_M} to be identical: following Abramovich (32), measured distributions are plotted in Fig. 5.1 against the radial ordinate η_v, recalled from Chapter 2:-

$$\eta_v = r/r_{\frac{1}{2}v} \; ; \quad U_{v_M}(r_{\frac{1}{2}v}) = \tfrac{1}{2} \tag{5.3}$$

The distributions, obtained from measurements at different axial stations, appear to display similarity with z, and universality with respect to velocity ratio m, n and θ over this range. Data obtained over a wider range is considered below.

With the use of the 'vorticity' theory of turbulence, Taylor (32) obtained the following relation for $U_{c_M} = U_{T_M}$ by, assuming (as a boundary condition) that the jet boundary

surfaces for velocity, concentration and temperature coincide:-

$$U_{T_M} \equiv U_{c_M} = \sqrt{U_{v_M}} = (1-\{0.44\eta_v\}^{1.5})^2 \qquad (5.4)$$

by 2.24. This analytical profile is not an entirely convincing representation of the data, as shown in Fig. 5.1.

Landis and Shapiro (58) compared pointwise determinations of U_{T_M}, in a heated air-air experiment, with their own measurements of the velocity profile, while Chriss (59) plotted measured concentration and velocity distributions for an H_2 jet in air. Both sets of measurements, made at specific axial stations in the main region, were plotted against radial distance normalised by the nozzle radius r_0: the plots are reproduced in Fig. 5.2. It is observed that the 'scalar' profiles are fuller and wider than that of velocity. Landis and Shapiro (58) concluded from their experiments that the transport mechanisms for mass and momentum are the same, but that the diffusion of mass is more rapid than that of momentum. A turbulent mass diffusion coefficient D_T may be introduced through:-

$$\rho D_T \frac{\partial c}{\partial r} = -\rho \overline{u_r' c'}$$

(see Appendix) and related to turbulent momentum diffusion, through a turbulent Schmidt number Sc_T, or to heat transfer through a turbulent Lewis number Le_T:-

$$-\kappa_T \frac{\partial T}{\partial r} = \rho C_p \overline{u_r' T'}$$

$$Pr_T = \frac{\nu_T}{\kappa_T/\rho C_p}$$

$$Sc_T = \nu_T/D_T \quad ; \quad Le_T = Pr_T/Sc_T$$

where ν_T is the eddy kinematic viscosity and Pr_T is a turbulent Prandtl number (Appendix). Most workers (49) agree

that, for axisymmetric jets:-

$$Pr_T \simeq Sc_T \simeq 0.7 \Rightarrow Le_T \simeq 1.0$$

displaying the equal rates of diffusion for concentration and temperature, and the slower rate of diffusion for momentum, as indicated in Fig. 5.2. The assumption of coincident mixing boundaries, by which 5.4 was obtained, is seen to be in error, and the definition of separate boundary surfaces (Fig. 5.2) might be made, in analogy with the thermal and momentum thicknesses in flat-plate boundary layer theory. This is the form which the later analysis takes (Section 5.8).

It is clear from Fig. 5.1 that the 'velocity' half width $r_{\frac{1}{2}v}$ from 5.3 does not correspond to the half width of the measured temperature or concentration distribution. Assuming these latter to be identical (Fig. 5.1), it is convenient to refer to the single 'scalar' profile U_{s_M}:-

$$U_{s_M} = U_{T_M} \equiv U_{c_M} \qquad (5.5)$$

The scalar half width $r_{\frac{1}{2}s}$ is defined similarly to $r_{\frac{1}{2}v}$ in 5.3. In general:-

$$U_{i_M}(r_{\frac{1}{2}i}) = \tfrac{1}{2} \quad ; \quad i = s \text{ or } v \qquad (5.6)$$

The location $r_{\frac{1}{2}i}$ is more readily determined experimentally than the boundary of A_i ($i = v$ or s), where $U_{i_M} \to 0$. Measurements of the ratio $\delta_{\frac{1}{2}}$, where:-

$$\delta_{\frac{1}{2}} = \frac{r_{\frac{1}{2}s}}{r_{\frac{1}{2}v}} \qquad (5.7)$$

have been reported by Abramovich (32), Sforza (72), Shirakashi and Tomita (90) and Chen and Rodi (96), and generally are found to lie in the range:-

$$\delta_{\frac{1}{2}} \in [1.0, 1.178] \text{ approx.} \qquad (5.7a)$$

the value being roughly constant in the individual studies: the data of Abramovich (53), however, suggests a complicated variation of $\delta_{\frac{1}{2}}$ with m and n. When measured distributions of velocity, temperature and concentration are plotted, not against η_v, but against the 'proper' radial ordinate η_i:-

$$\eta = \frac{r}{r_{\frac{1}{2}i}} \quad ; \quad i = v,c \text{ or } T \tag{5.8}$$

all three distributions appear to coincide (Landis and Shapiro (58), Abramovich (53)). This procedure has been carried out empirically for the data in Fig. 5.1, assuming 5.5 for equivalence of the scalar profiles, and $\delta_{\frac{1}{2}} \simeq 1.2$ (from Fig. 5.1). It is noted from Fig. 5.1 that, if the analytical relation 5.4 is used to determine the scalar half-width, a value $\delta_{\frac{1}{2}} \simeq 1.45$ is obtained, which is not in accordance with 5.7a: thus, the relation 5.4 is rejected.

The replot of data upon proper co-ordinates is shown in Fig. 5.3: considerable correlation is achieved and the distributions are adequately well described by the Schlichting formula extended from Chapter 2:-

$$U_{i_M}(\eta_i) = (1-\{0.44\eta_i\}^{1.5})^2 \qquad z>z_{Ds}, \quad i= v \text{ or } s \tag{5.9}$$

This is the functional form used in this analysis for the main region profiles in axisymmetric jets (Chapter 6). The correlation of velocity, temperature and concentration data from Abramovich (53), for jets in the range $m \in [0,1]$, $n \in [0.27,7]$ and various values of $\theta>1$, is also given in Fig. 5.3. The axial station z_{Ds} is the first at which U_{s_M}, represented by 5.9, is observed (ie the start of the scalar main region), and is termed the scalar transition section. The transition section z_{Dv} was similarly defined in Chapter 3: generally, $z_{Ds}<z_{Dv}$ (53,31) (Section 5.7).

In the initial region (Chapter 3), dimensionless profiles of temperature and concentration across the width $b_v(z)$ of the turbulent mixing zone (Fig. 5.4) are defined as:-

$$U_{T_I}(r,z) = \frac{T(r,z) - T_\infty}{T_0 - T_\infty} \qquad (5.10)$$

$$U_{c_I}(r,z) = \frac{c(r,z)}{c_0} \qquad (5.11)$$

similarly to 5.1 and 5.2, since $T_m \equiv T_0$, $c_m \equiv c_0 (=1)$ in the initial region (Fig. 5.4).

Abramovich (32) plotted measured distributions U_{T_I} and U_{c_I} against the dimensionless radial ordinate x_v, recalled from Chapter 2:-

$$x_v = \frac{r - r_{cv}}{r_{2v} \; r_{cv}} \quad ; \qquad r \in [r_{cv}, r_{2v}] \qquad (5.12)$$

The inner and outer dynamic mixing boundaries $r_{cv}(z)$ and $r_{2v}(z)$ are shown in Fig. 5.4. It is noted that the use of 5.12 as the radial ordinate assumes implicitly that the inner and outer mixing boundaries for the 'scalar' profiles, 5.10 and 5.11, coincide with the dynamic boundaries. Taylor (32) also made this assumption, in order to complete a theoretical solution for 5.10 and 5.11: temperature and concentration distributions were deduced to be identical (in comparison with 5.5) and given by:-

$$U_{s_I} = U_{T_I} \equiv U_{c_I} = 1 - x_v \qquad (5.13)$$

This distribution is compared with experimental temperature observations in Fig. 5.5. The measurements were made at different axial stations in the initial region, and Abramovich (32) concluded universality of U_{v_I} with respect to z,m n and θ . Newman and Brzustowski (31) considered that 5.13 might not always suffice, and, for injectants with specific heats greatly different from that of the ambient fluid, made the following 'intuitive' modification to the temperature distribution, based upon experimental data (97):-

$$U_{T_I}(x_v) = (1-x_v)/\{(1-x_v) + (x_v/\bar{C_p})\} \; ; \; \bar{C_p} = \frac{C_{pi}}{C_{p\infty}} \qquad (5.14)$$

The modification was not made to the main region profile (31) U_{T_M} assumed to be given by 5.4.

In accordance with the observations made above concerning the main region, it should be possible to define separate mixing boundaries for mass and momentum in the initial region. This was demonstrated experimentally by Abramovich (53), and some of the results are reproduced in Fig. 5.6a. For each experiment, it was found that the profiles of velocity, temperature and concentration were independent of z and m (a similarity condition), but that the form of the profiles depended upon density ratio n, hence not universal. However, the method of presentation of the results makes any further investigation very difficult (53). In Section 5.8, universal distributions of flow properties are sought using an intuitive argument, the analytical result 5.13 being an oversimplification.

The more rapid rate of diffusion of mass in the initial region (compared to momentum) would lead to a more rapid erosion of the 'core' of constant scalar properties (Fig. 5.6b). Direct evidence for this may be identified in the axial property decay data of Landis and Shapiro (58) (Fig. 5.6c) and others, the decay of 'scalar' quantities on the axis preceding slightly that of velocity.

5.3 Separate Diffusion Rates For Mass And Momentum

In Chapter 2, a general integrated conservation equation for a mean flow property ψ was derived for an axisymmetric jet. The equation, 2.16, might be written as:-

$$\frac{d}{dz}\int_{A_\psi} \rho u \psi \, dA_\psi = \psi_\infty E_m \qquad (5.15)$$

The boundary of A_ψ is defined (Chapter 2) as that radial

location where the transverse property gradient becomes negligibly small:-

$$\left.\frac{\partial \psi}{\partial r}\right|_{\substack{\text{boundary} \\ \text{of } A_\psi}} < \varepsilon \; ; \qquad \varepsilon \text{ small} \tag{5.15a}$$

In Section 5.2 it was shown from experiments that mass and momentum boundaries defined in this way do not coincide (see Fig. 5.2). It is possible to define separate areas A_u (for axial momentum conservation by $\psi \equiv u$ in 5.15, as in Chapters 3 and 4) and A_s (for injectant mass conservation by $\psi \equiv c$ - see later), as shown in Fig. 5.7. It has been assumed for simplicity that temperature and concentration boundaries coincide at the edge of the 'scalar' jet area A_s (58), and that:-

$$\delta^2 = \frac{A_s}{A_u} > 1 \tag{5.15b}$$

based upon the remarks in Section 5.2. The 'momentum' area A_u is hereafter written A_v, since the velocity profile U_v is to be taken over it. The concept of separate mixing boundaries extends to deflected jets of distorted cross section as shown in Fig. 5.7. A quantitative definition of A_s in relation to A_v is given in Section 5.9.

5.4 Conservation Of Energy

With respect to the elemental control volume shown in Fig. 5.8, conservation of energy is expressed by the following balance, after Packer (35):-

> static enthalpy and kinetic energy (H) leaving surface 2 = H entering through surface 1 + entrained H from the external flow + radiative heat transfer to the volume + heat generation in the volume + boundary friction - phase change

neglecting changes in potential energy. In the absence of

chemical reaction, radiation, heat generation and phase change terms are ignored (see Chapter 8). Campbell and Schetz (79) assumed a uniform, average temperature over a cross-section in a non-isothermal jet, and a heat transfer term was required in view of the implied temperature difference across the jet boundary. In the present work, the temperature profile U_T is prescribed so as to satisfy the physical boundary condition $U_T \to 0$ at the boundary of A_s (Section 5.2), and no such term is required. Similarly, there is no boundary friction contribution. The assumed profile U_T is the actual result of shearing effects.

The absolute temperature T at any point in a jet cross section is defined in a similar way to velocity (Chapter 4):-

$$T = h_T(z)U_T + T_\infty \tag{5.16}$$

where:-

$$h_T(z) = T_m(z) - T_\infty \tag{5.16a}$$

The dimensionless temperature difference profile U_T is taken over the entire area A_s, so in the initial region it includes ${}^{U}T_I$ (Section 5.2) and the constant temperature core where $U_T \equiv 1$. In the main region of an axisymmetric jet, $U_T \equiv {}^{U}T_M$ (Section 5.2). The setting of U_T for deflected jets of distorted cross-section is described in Section 5.9.

In Chapter 4 it was assumed that the usual 'boundary layer' assumptions for thin shear flows could be applied also to deflected jets. Under these conditions, the conservation of energy equation, in the absence of sources (written by Packer (35) in view of the balance described above), is given directly from 5.15:-

$$\frac{d}{dz}\int_{A_s} \rho u H dA_s = H_\infty \frac{d}{dz}\int_{A_v} \rho u dA_v \tag{5.17}$$

where:-

$$H = C_p T + \tfrac{1}{2}u^2 \quad ; \quad H_\infty = C_{p\infty} T_\infty + \tfrac{1}{2}w^2 \qquad (5.17a)$$

and the definition of the mass entrainment rate E_m is recalled from Chapter 4:-

$$E_m = \frac{d}{dz}\int_{A_v} \rho u dA_v \qquad (5.18)$$

Other workers (19,31,79) write an equation for conservation of excess heat content:-

$$\frac{d}{dz}\int_{A_s} \rho u C_p T dA_s = C_{p\infty} T_\infty E_m$$

The jet velocity u is given by 4.19 (Chapter 4):-

$$u = h_v(z) U_v + w\cos\beta \qquad (4.19)$$

Substitution of 5.16, 5.18 and 4.19 in 5.17 gives, upon expansion and rearrangement (35), an equation for the rate of change of the temperature difference function $h_T(z)$:-

$$\frac{dh_T}{dz} = -\frac{\left[F_w\frac{dw}{dz} + F_\beta\frac{d\beta}{dz} + F_v\frac{dh_v}{dz} + \sum_0^2 F_n\frac{dI_n}{dz}\right]}{h_v I_4 + w\cos\beta I_6} \qquad (5.19)$$

where, from Chapter 4:-

$$I_n = \int_{A_v} \rho U_v^n dA_v \qquad n = 0,1,2 \qquad (5.19a)$$

and:-

$$I_3 = \int_{A_s} \rho C_p U_v dA_s \quad ; \quad I_4 = \int_{A_s} \rho C_p U_v U_T dA_s$$

$$I_5 = \int_{A_s} \rho C_p dA_s \quad ; \quad I_6 = \int_{A_s} \rho C_p U_T dA_s \quad ; \quad I_7 = \int_{A_v} \rho U_v^3 dA_v \qquad (5.19b)$$

and:-

$$F_w = \cos\beta\{T_\infty I_5 + h_T I_6 + \frac{3}{2}w^2\cos\beta I_0 + 3w\cos\beta h_v I_1 + \frac{3}{2}h_v^2 I_2 - C_{p\infty}T_\infty I_0 - \frac{3}{2}w^2 I_0\} - wh_v I_1 \quad (5.19c)$$

$$F_\beta = -w\sin\beta\{\frac{3}{2}w^2\cos^2\beta I_0 + 3w\cos\beta h_v I_1 + \frac{3}{2}h_v I_2 + T_\infty I_5 + h_T I_6 - C_{p\infty}T_\infty I_0 - \frac{w^2}{2}I_0\} \quad (5.19d)$$

$$F_v = \frac{3}{2}(w\cos\beta)^2 I_1 + 3h_v w\cos\beta I_2 + \frac{3}{2}h_v I_7 + T_\infty I_3 + h_T I_4 - (C_{p\infty}T_\infty + \frac{w^2}{2})I_1 \quad (5.19e)$$

$$F_0 = w\cos\beta\{\frac{w^2}{2}\cos^2\beta - C_{p\infty}T_\infty - \frac{w^2}{2}\} \quad (5.19f)$$

$$F_1 = h_v\{\frac{3}{2}w^2\cos^2\beta - C_{p\infty}T_\infty - \frac{w^2}{2}\} \quad (5.19g)$$

$$F_2 = \frac{3}{2}w\cos\beta h_v^2 \quad (5.19h)$$

$$F_3 = h_v T_\infty \quad (5.19i)$$

$$F_4 = h_v h_T \quad (5.19j)$$

$$F_5 = w\cos\beta T_\infty \quad (5.19k)$$

$$F_6 = h_T w\cos\beta \quad (5.19l)$$

$$F_7 = \frac{h_v^3}{2} \quad (5.19m)$$

Equation 5.19 is applied beyond the end of the constant velocity core, prior to which $T_m \equiv T_0 \Rightarrow h_T \equiv h_{T0}$ (Section 5.8).

5.5 Conservation Of Injected Material

The mass concentration c of the injectant at any point is defined as:-

$$c = \frac{\text{mass of injectant}}{\text{mass of injectant + mass of free stream fluid}} \qquad (5.20)$$

and at any jet cross-section A_s is distributed as:-

$$c = h_c(z)U_c + c_\infty \equiv h_c(z)U_c \qquad (5.21)$$

where:-

$$h_c(z) = c_m(z) \qquad (5.21a)$$

Conservation of injected material requires that the injectant flux across A_s is constant. From 5.15, with $\psi \equiv c$ and $c_\infty \equiv 0$:-

$$\frac{d}{dz}\int_{A_s} \rho u c dA_s = 0 \qquad (5.22)$$

Substitution for u from 4.19 and c from 5.21 gives, upon rearrangement (35), an equation for the rate of change of the concentration function $h_c(z)$:-

$$\frac{dh_c}{dz} = \frac{h_c\left(w\sin\beta I_9\frac{d\beta}{dz} - I_8\frac{dh_v}{dz} - h_v\frac{dI_8}{dz} - \cos\beta I_9\frac{dw}{dz} - w\cos\beta\frac{dI_9}{dz}\right)}{h_v I_8 + w\cos\beta I_9} \qquad (5.23)$$

where:-

$$I_8 = \int_{A_s} \rho U_c U_v dA_s \quad ; \qquad I_9 = \int_{A_s} \rho U_c dA_s \qquad (5.23a)$$

within the scalar core, $h_c \equiv h_{c0} \Rightarrow dh_c/dz \equiv 0$ (Section 5.8).

5.6 Variable Density Effects In The Momentum Theory

5.6.1 Buoyancy

A general vector expression of momentum conservation in constant density jets was given in 4.21 (Chapter 4). The only possible alteration to 4.21 in the case of variable density jets would be the inclusion of buoyancy effects in the body force term. Buoyant jets have been studied experimentally and analytically by Schatzmann (73), Steward and Guruz (98), Campbell and Schetz (79) and many others; reviews have been given by Schetz (49) and Chen and Rodi (96).

The ratio of inertia to buoyant forces may be expressed as a Froude number (49):-

$$F_r = \frac{u_0^2}{g\{(\rho_\infty - \rho_0)/\rho_0\}D_0}$$

where g is the acceleration due to gravity and D_0 is the nozzle diameter. For variable density jets, the theory without the inclusion of buoyancy effects is compared with experiment in Chapter 7: for the prospective application to Diesel sprays (Chapter 8), it is assumed that the injection velocity is sufficiently large to swamp the effects of gravity, and the modelling of buoyancy has not been undertaken.

5.6.2 A Density Dependent Propagation Equation

A propagation equation, for the growth of the dynamic mixing zone width $b_v(z)$ (Fig. 5.4), for the two regions of similarity in an axisymmetric jet, was derived in Chapter 2:-

$$\frac{db_v}{dz} = G(z)\frac{(1+\bar{\rho})}{2}\left(\frac{u_m - w}{u_m + \bar{\rho}w}\right) \quad ; \quad \bar{\rho} = \frac{\rho_\infty}{\rho_1} \qquad (2.29)$$

ρ_1 being the density on the jet axis ($U_c=U_T=1$). In view of the developments in Chapters 3 and 4, this equation is written in the following way (see below):-

$$\frac{db}{dz}_v = G(z)\frac{(1+\bar{\rho})}{2}\left\{\frac{u_m - w\cos\beta}{u_m + \bar{\rho}|w\cos\beta}\right\} = G(z)\frac{(1+\bar{\rho})}{2}\left\{\frac{h_v}{h_v+(1+\bar{\rho})w\cos\beta}\right\} \quad (5.24)$$

The variation of G(z) in the intitial, transition and main regions was described in Chapter 3.

In the absence of conclusive data, the dependence for the enhanced jet growth rate term $\mathcal{F}_1(z)$ in a crossflow, 4.18, is postulated by analogy with 5.24 above. In Chapter 4, the growth rate of the mixing zone was written as:-

$$\frac{db}{dz}_v = \mathcal{F}_0(z) + \mathcal{F}_1(z) \quad (4.7)$$

The axisymmetric jet part $\mathcal{F}_0(z)$ is given by 5.24 for variable density jets, and the enhanced spreading rate term $\mathcal{F}_1(z)$ is modified from 4.18 to give:-

$$\mathcal{F}_1(z) = \frac{G_1(z)}{\left(\frac{A_0}{A_v}\right)^{(1-A_1)/2} + 0.5} \cdot \frac{(1+\bar{\rho})}{2}\left(\frac{w\sin\beta}{h_v+(1+\bar{\rho})w\cos\beta}\right) \quad (5.25)$$

The term A_1 was defined in Chapter 4. The propagation equation 4.32 for the growth rate of the dynamic mixing zone $A_{Dv}(z)$ (see Fig. 5.9b), derived in Chapter 4 and amended for variable density jets is then:-

$$\frac{dA}{dz}_{Dv} = 2\sqrt{\pi A_v}\left(\mathcal{F}_0(z) + \mathcal{F}_1(z) + \frac{b_v}{2\sqrt{A_v A_{cv}}}\frac{dA}{dz}_{cv}\right) \quad (5.26a)$$

with $\mathcal{F}_0(z)$ given by 5.24 and $\mathcal{F}_1(z)$ given by 5.25. The equation for dA_{cv}/dz, the rate of change of the constant velocity core area, requires no alteration from 4.31:-

$$\frac{dA}{dz}_{cv} = \left[P_c - h_v\left\{w\cos\beta\frac{dK_1}{dz} + h_v\frac{dK_2}{dz}\right\}A - h_v\{w\cos\beta K_1 A_{Dv} + h_v K_2 A_{Dv}\}\frac{dA}{dz}_{Dv} - A\frac{dP}{dz}\right] \Big/ h_v\{w\cos\beta K_1 A_{cv} + h_v K_2 A_{cv}\} \quad (5.26b)$$

where, as in Chapter 4:-

$$P_c = \{w\cos\beta(I_1-I_0) + 2h_v(I_2-I_1)\}\frac{d}{dz}\{w\cos\beta\} \qquad (5.26c)$$

and:-

$$K_n = \frac{1}{A_v}\int_{A_v}\rho U_v^n dA_v \quad ; \quad K_{nA_{Dv_i}} = \frac{1}{A_{Dv}}\int_{A_{Dv}}\rho U_v^n dA_{Dv}$$

$$K_{nA_c} = \frac{1}{A_{cv}}\int_{A_{cv}}\rho U_v^n dA_{cv} \qquad (5.26d)$$

The jet momentum area A_v is given by $A_v = A_{cv} + A_{Dv}$ (beyond the end of the velocity core $A_{cv} \equiv 0$). The predictions afforded by the semi-empirical equation 5.26a are discussed in Chapters 7 and 8.

5.7 Distributions Of Density And Specific Heat

In the initial period of testing of the computer program based upon the model (Chapter 6), a very simple density characterisation was employed in order to study parametrically the effects of composition variation (46). For isothermal jets, the ρ distribution at a cross-section A_s was taken from the theory of incompressible mixtures:-

$$\rho = (\rho_0-\rho_\infty)c + \rho_\infty \quad ; \quad c = h_c U_c \qquad (5.27)$$

and this motivated the use of a simple distribution in the study of heated jets:-

$$\rho = (\rho_{i,1}-\rho_\infty)h_c U_c + \rho_\infty \qquad (5.27a)$$

where $\rho_{i,1}$ is the injectant density on the jet axis (where $U_c = U_T = 1$), computed from the ideal gas law:-

$$\rho_{i,1} = PM_i/(R_0 T_m) \quad ; \quad M_i = \text{injectant molecular weight} \qquad (5.27b)$$

Although these distributions are not themselves suitable for predictive purposes, the linearity of 5.27 and 5.27a in the function $h_c(z)$ allows great economies to be made in computer times, compared with more correct distributions (Chapter 7).

Newman and Brzustowski (31), Sinnamon et al (40), Mehta and Gupta (41) and Lakshminarayan and Dent (20) used the following formulation for density in single phase, isothermal jets:-

$$\rho = \frac{\rho_0}{c + (\rho_0/\rho_\infty)(1-c)} = \frac{\rho_0}{h_c U_c + (\rho_0/\rho_\infty)(1-h_c U_c)} \quad (5.28)$$

Adler and Lyn (19) derived an expression extending 5.28 to pointwise density in a two-phase, nonisothermal jet, which for the single phase case simplifies to:-

$$\rho = \frac{P}{R_0 T}\left[\frac{(1-c)}{M_\infty} + \frac{c}{M_i}\right]^{-1} \quad (5.29)$$

(temperature T is given by 5.16), making use of the ideal gas law. The different density distributions are assessed in Chapter 7.

Following Adler and Lyn (19), variation of C_p across the jet may be taken from the theory of mixtures:-

$$C_p = (C_{pi} - C_{p\infty})h_c U_c + C_{p\infty} \quad (5.30)$$

provided the C_p values are not too greatly dependent upon temperature. More correctly, C_p could be set in special cases directly from gas property considerations (42), or from 5.30 amended to include temperature dependence of the fluid specific heats (Chapter 7). Abramovich (32) and Campbell and Schetz (79) assumed a constant value for C_p throughout.

5.8 Location Of The Scalar Mixing Boundaries

In view of Section 5.2, a dual jet development is envisaged for the analysis in which separate mixing boundaries are defined for velocity and the 'scalar' quantities (being temperature and concentration). For simplicity, the rates of diffusion of heat and mass are assumed equal (Section 5.2). A definition sketch for this configuration is given in Fig. 5.9 for an axisymmetric jet. The direct extension of the results to a deflected jet, of possibly distorted cross-section, is indicated in Section 5.9.

For the initial region, a nominal axis of mixing is defined as the continuation of the line of the nozzle edge at $r \equiv r_0$ (Fig. 5.9c). The width of the momentum mixing zone is denoted b_v, and the width of the scalar mixing zone b_s. From Section 5.2, $b_s > b_v$. In quantitative terms, the following assumptions are made (Fig. 5.9c), based upon a mixing surface at $r \equiv r_0$:-

$$b_v(z) = r_{2v}(z) - r_{cv}(z) \; ; \quad b_s(z) = r_{2s}(z) - r_{cs}(z) \qquad (5.31a)$$

$$b_{i1} = r_0 - r_{ci} \; ; \quad b_{i2} = r_{2i} - r_0 \qquad i = v \text{ or } s \qquad (5.31b)$$

$$\frac{b_{s1}}{b_{v1}} = 1 + \delta_c \; ; \quad \frac{b_{s2}}{b_{v2}} = 1 + \delta_2 \qquad (5.31c)$$

$$b_v = b_{v1} + b_{v2} \; ; \quad b_s = b_{s1} + b_{s2} \qquad (5.31d)$$

The coefficients δ_c and δ_2 (assumed, for simplicity, to be constants - see later) express the relative displacement of the inner and outer scalar mixing boundaries (r_{cs} and r_{2s}) from the dynamic boundaries (r_{cv} and r_{2v}, known from the propagation equation and the momentum theory- Chapters 3 and 4), due to the faster rate of diffusion (Fig. 5.9b and c). At the nozzle, $b_{s2} = b_{v2} = 0$ is used instead of the relation in 5.31c: a 'uniform' injection velocity is defined by setting $b_{v1}(z=0)$ at a very small, positive value (implying a negligibly slight nozzle boundary layer), so that the inner mixing boundaries can be located with 5.31c.

The most significant consequence of the setting $\delta_c>0$ in the initial region is the relatively more rapid erosion of the constant scalar property core (Fig. 5.9c). The end of the scalar core ($r_{cs}=0$) occurs at the axial station $z=z_{cs}$, where, using 5.31b and 5.31c:-

$$r_{cs}=0 \Rightarrow (1+\delta_c)b_{vl} = r_0 \qquad (5.32)$$

Substituting for b_{vl} (the distance to which the dynamic mixing zone encroaches into the free stream - Fig. 5.9c) from 5.31b, the station z_{cs} is thus determined by:-

$$(1+\delta_c)b_{vl}(z_{cs}) = (1+\delta_c)(r_0-r_{cv}(z_{cs})) = r_0$$

or, since $A_{cv} = \pi r_{cv}^2$ (Fig. 5.9b):-

$$(1+\delta_c)(1-\sqrt{A_{cv}(z_{cs})/A_0}) = 1 \Rightarrow \left(\frac{A_{cv}(z_{cs})}{A_0}\right)^{\frac{1}{2}} = \frac{\delta_c}{1+\delta_c} \qquad (5.33)$$

Beyond z_{cs}, temperature and concentration begin to decay on the jet axis, predicted by 5.19 and 5.23, prior to the decay of axial velocity (confirmed experimentally, as in Fig. 5.6c). Since $A_{cv}(z)$ is always known, from the solution of the differential equation 5.26b, the station z_{cs} is determined, analytically in 5.33, from the momentum theory and the prescribed value δ_c.

Over the distance $z_{cs}\leqslant z\leqslant z_{cv}$ (Fig. 5.9c), δ_c must vary with z in order to satisfy 5.32 ($A_{cs}\equiv 0$):-

$$\delta_c(z) = \frac{\bar{r}_{cv}(z)}{1 - \bar{r}_{cv}(z)} \quad \text{where } \bar{r}_{cv}(z) = \left(\frac{A_{cv}(z)}{A_0}\right)^{\frac{1}{2}} \qquad (5.34)$$

so $\delta_c\to 0$ as $z\to z_{cv}$ ($A_{cv}\to 0$).

At $z=z_{cv}$, the end of the constant velocity core (Fig. 5.9c), the 'centre of mixing' is moved from the projection of the nozzle lip (used for 5.31) to the jet axis itself ($b_v\equiv r_{2v}$ in Fig. 5.9d). The mass/momentum diffusion ratio δ (see 5.15b) is written as:-

$$\delta(z) = \frac{b_s(z)}{b_v(z)} \equiv \left(\frac{A_s(z)}{A_v(z)}\right)^{\frac{1}{2}} \qquad z \geq z_{cv} \qquad (5.35)$$

To ensure continuity at z_{cv}, $\delta(z_{cv})$ is defined as (see Fig. 5.9c):-

$$\delta(z_{cv}) = \frac{b_s(z_{cv})}{b_v(z_{cv})} = \frac{r_0 + (1+\delta_2)b_{2v}(z_{cv})}{b_v(z_{cv})} \qquad (5.35a)$$

The coefficients δ_c, δ_2 and δ must be evaluated empirically, and recourse is made to the observations in Section 5.2. For the main region, from 5.7a:-

$$\delta_{\frac{1}{2}} = \frac{r_{\frac{1}{2}s}}{r_{\frac{1}{2}}} \in [1.0\ ,\ 1.178] \qquad (5.7a)$$

while the data in Fig. 5.2 (and Chriss (59)) may be used, very crudely, to suggest, for 5.35:-

$$\delta_{\frac{1}{2}} \in [1.07\ ,\ 1.16] \qquad (5.36)$$

Nothing other than a constant setting for δ in the main region is justified in the present work, although this is certainly an oversimplification (53).

Constant values for δ_c and δ_2 in the initial region may be found by consideration of the injectant mass conservation condition 5.22. It is noted that, as yet, no guarantee has been made of satisfaction of 5.22 through the initial region. Only momentum conservation is ensured, via the 'velocity' propagation and core area equations (5.26a and 5.26b). In this analysis, it must always be possible to satisfy 5.22 and 5.17 (injected material and energy conservation) <u>implicitly</u>, from the momentum theory (which gives b_v), and δ_c and δ_2 (which then give b_s).

As a limiting case, consider a submerged (w=0), isothermal, axisymmetric jet in the initial region $z \leq z_{cs}$ (so that $u_m=u_0$, $c_m=1$, $u=u_0U_v$, $c=U_c$). Integration of the momentum conservation equation (Chapter 3) and the injectant mass

conservation equation 5.22 gives:-

$$K_2(z)A_v(z) = A_o \quad ; \quad K_2(z) = \frac{1}{A_v}\int_{A_v}\rho U_v^2 dA_v \qquad (5.37a)$$

$$K_8(z)A_s(z) = A_o \quad ; \quad K_8(z) = \frac{1}{A_s}\int_{A_s}\rho U_v U_c dA_s \qquad (5.37b)$$

With the assumption of coincident mixing boundaries ($\delta_c \equiv \delta_2 \equiv 0 \Rightarrow A_s \equiv A_v \Rightarrow z_{cs} \equiv z_{cv}$), and the resulting theoretical property profiles U_{v_I} and U_{c_I} (2.21 and 5.13 respectively (32)), it may be shown that $K_8/K_2 \simeq 0.9$ for a constant density jet at the end of the initial region, in violation of the conservation requirement $K_8 \equiv K_2$ from 5.37a and 5.37b.

The arbitrary setting $U_{c_I} \equiv U_{v_I}$ (from 2.21) automatically satisfies $K_8 \equiv K_2$, but this equivalence of profiles is not confirmed experimentally (Section 5.2). However, setting $\delta_c, \delta_2 > 0$ (Fig. 10a) and defining:-

$$U_{c_I}(x_s) = 1-(1-\{1-x_s\}^{1.5})^2 \quad ; \quad x_s = \frac{r - r_{cs}}{r_{2s} - r_{cs}} \qquad (5.38)$$

in analogy with 2.21 for $U_{v_I}(x_v)$, brings the scalar profile into close agreement with the data, while it has been confirmed numerically that 5.37b is still satisfied (approximately) through the (scalar) initial region ($z<z_{cs}$). The choice of values for δ_c and δ_2 (assumed for simplicity to be equal) was guided by 5.36, and $\delta_c = \delta_2 \simeq 0.16$ gave the best results over a range axisymmetric and deflected jets (Chapter 7). From Fig. 5.10b, a larger value for δ_c would improve the agreement between $U_{c_I}(x_s)$ and the experimental data, but such a value would lie outside the range indicated by 5.36 (taken as a reference base for the present work).

The conservation of energy condition 5.17 can also be satisfied, approximately, through the initial region (with $U_{T_I} \equiv U_{c_I}$ in 5.38), although modification may be necessary

when C_{p0} and $C_{p\infty}$ are very different (31) (Section 5.2), or when source terms such as phase change occur in the conservation condition (Chapter 8).

It is consistent with these findings to set δ in 5.35 at about 1.16 (constant main region value). The effect on predictions of ignoring variation of the diffusion coefficients with m, n or θ (53) is likely to be slight (Chapter 7).

Hence, universal property profiles for axisymmetric jets in this analysis are written in the following forms, from 2.21, 5.38 and 5.9:-

$$U_{i_I}(x_i) = 1-(1-\{1-x_i\}^{1.5})^2 \quad ; \quad i = v \text{ or } s \quad z<z_{ci} \quad (5.39a)$$

$$U_{i_M}(x_i) = (1-x_i^{1.5})^2 \quad ; \quad i = v \text{ or } s \quad z>z_{Di} \quad (5.39b)$$

where:-

$$x_i = \frac{r - r_{ci}}{r_{2i} - r_{ci}} \in [0,1] \quad ; \quad i = v \text{ or } s \quad \text{all } z \quad (5.39c)$$

The scalar and velocity transition sections z_{Di} (Fig. 5.9a and Fig. 5.9d) are assumed (empirically) to be given by the relation from Chapter 3 (32):-

$$\frac{z_{Di}}{z_{ci}} = 1.5 \quad ; \quad i = v \text{ or } s \quad (5.39d)$$

the z_{ci} being predicted from the analysis (Chapter 7). A linear variation for δ between $\delta(z_{cv})$ in 5.35a and the constant main region value (established at z_{Dv} - Fig. 5.9d) is assumed, in analogy with the variation of G(z) in the 'velocity' transition region $z\in[z_{cv}, z_{Dv}]$ (Chapter 3). The representation of developing property profiles in the transition region (Chapters 2 and 3) is described in Chapter 6.

5.9 Further Assumptions For Deflected Jets

Deflected jets of variable density have been studied mainly in the form of heated air jets in air (74,78,39). Patrick (70) measured the axes of constant density jets in a uniform crossflow, defined as the locus of points of maximum velocity and nozzle fluid concentration: the concentration axis was found always to follow a lower path than the velocity axis for the same jet. The axes were found to be expressible by (70):-

$$\frac{y_z}{D_0} = \mathcal{R}^{0.85}\left(\frac{x_z}{D_0}\right)^n \quad ; \qquad \begin{matrix} n=0.34 \text{ (concentration)} \\ n=0.38 \text{ (velocity)} \end{matrix} \qquad (5.40)$$

as illustrated in Fig. 5.11a for transverse injection into a uniform crossflow w at $\mathcal{R}=w/u_0=1/8$. Similarly, Kamotami and Greber (39) found the maximum temperature axis in deflected jets to fall below the velocity axis (Fig. 5.11b). The data concerning this effect is scarce, and no attempt has been made in the present work to account for it directly (see Chapter 7): it is assumed for simplicity that the points of maximum velocity, concentration and temperature difference in cross-sections coincide (so that $U_v=U_c=U_T=1$ at the same point).

With this assumption, it is quite straightforward to infer empirically the scalar distribution U_s ($\equiv U_T=U_c$) from the velocity distribution U_v, which may be assumed known over any distorted cross-section from the profile distortion sub-model of Adler and Baron (63) (Chapter 4 and Chapter 6). Although these scalar profiles may not be in as good agreement with measured profiles as the predicted velocity profiles, still a facility for recognising the influence of the vortex structure in cross-sections will be provided.

The scalar jet area A_s, over which U_s will be defined, is always known by extension of the results of Section 5.8, putting $A_s=\pi r_{2s}^2$, $A_{cs}=\pi r_{cs}^2$ (Fig. 5.9b). Using 5.31c:-

$$r_{2s} = r_0 + b_{s2} = r_0 + b_{v2} + \delta_2 b_{v2} = r_{2v} + \delta_2 b_{v2}$$

in the initial region. By 5.31b:-

$$r_{2s} = r_{2v} + \delta_2 b_{v2} = r_{2v} + \delta_2(r_{2v} - r_0)$$

Hence:-

$$A_s = \{(1+\delta_2)\sqrt{A_v} - \delta_2\sqrt{A_0}\}^2 \qquad z\in[0, z_{cv}] \qquad (5.41a)$$

Beyond z_{cv}, A_s is determined directly from 5.35:-

$$A_s = \delta^2 A_v \qquad z\geqslant z_{cv} \qquad (5.41b)$$

(The difference in determination of A_s is due to the shift in the assumed axis of mixing - Section 5.8). Similarly, by manipulation of 5.31:-

$$A_{cs} = \{(1+\delta_c)\sqrt{A_{cv}} - \delta_c\sqrt{A_0}\}^2 \qquad z\leqslant z_{cs} \qquad (5.42)$$

with the end of the scalar core z_{cs} ($A_{cs}(z_{cs})=0$) given by 5.33.

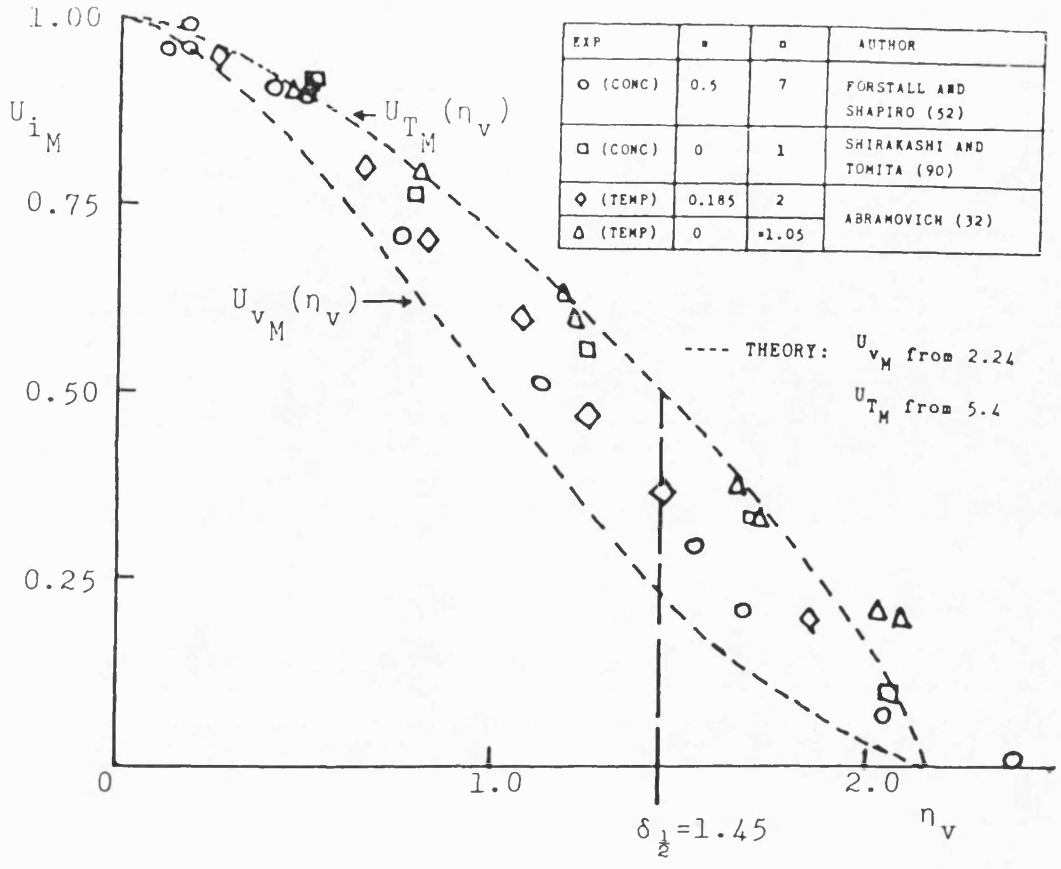

FIG. 5.1 VELOCITY AND TEMPERATURE PROFILES IN THE MAIN REGION PLOTTED AGAINST THE VELOCITY HALF-WIDTH

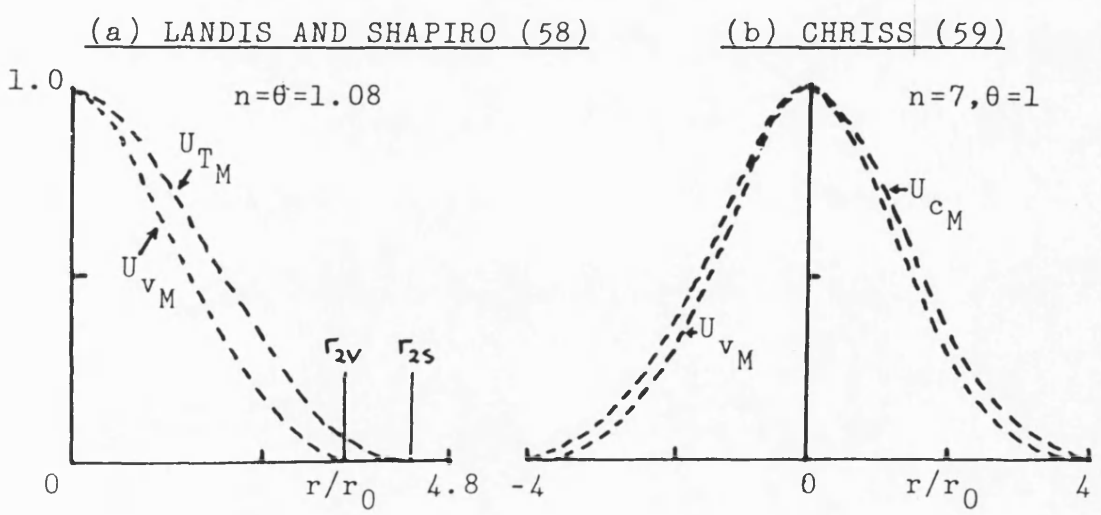

FIG. 5.2 PROPERTY PROFILES FOR THE MAIN REGION

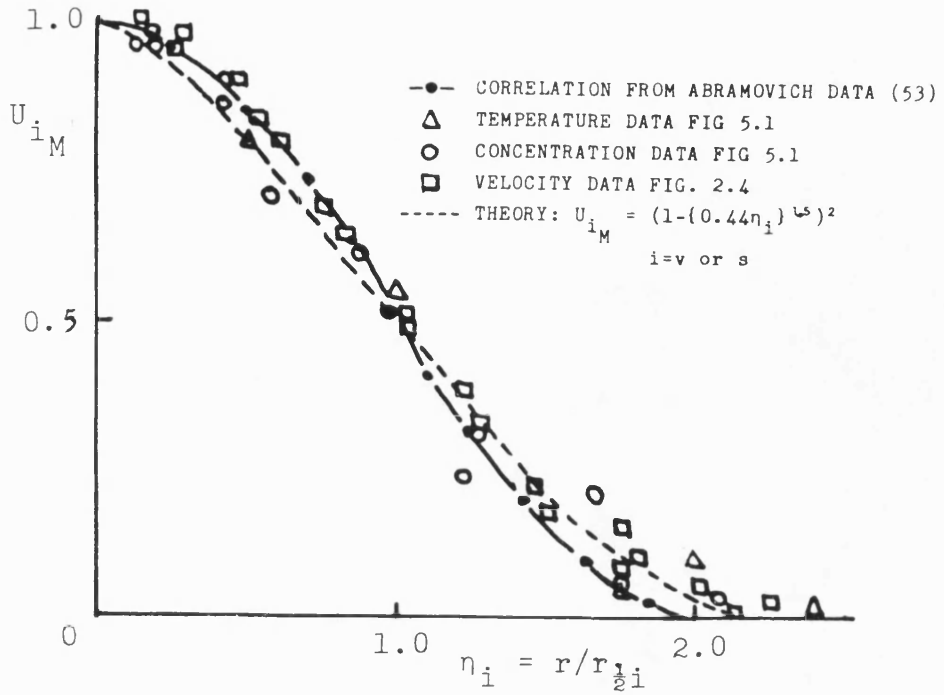

FIG. 5.3 PROPERTY PROFILES IN THE MAIN REGION PLOTTED UPON NATURAL CO-ORDINATES

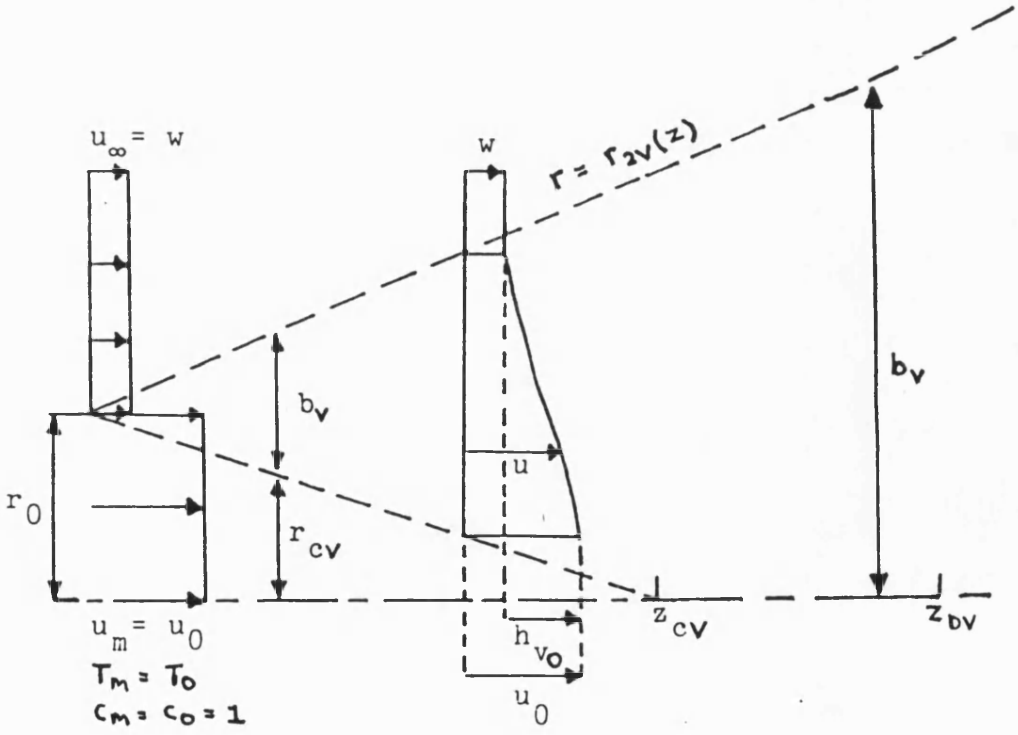

FIG. 5.4 VELOCITY BOUNDARIES IN THE INITIAL REGION

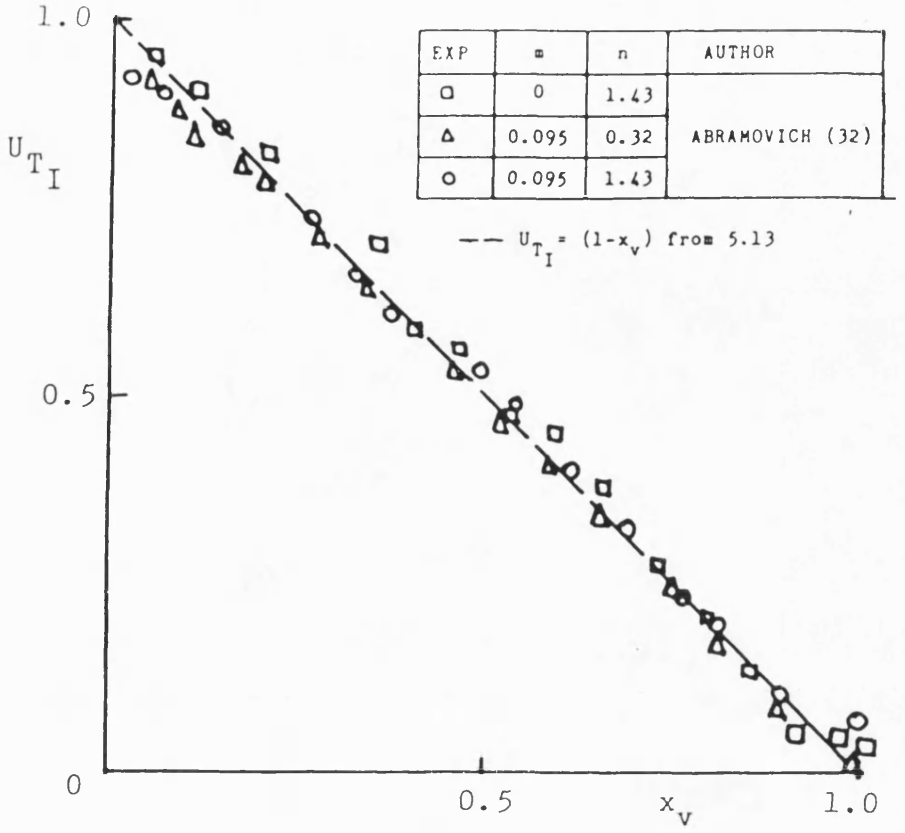

FIG. 5.5 DIMENSIONLESS TEMPERATURE PROFILE IN THE INITIAL REGION

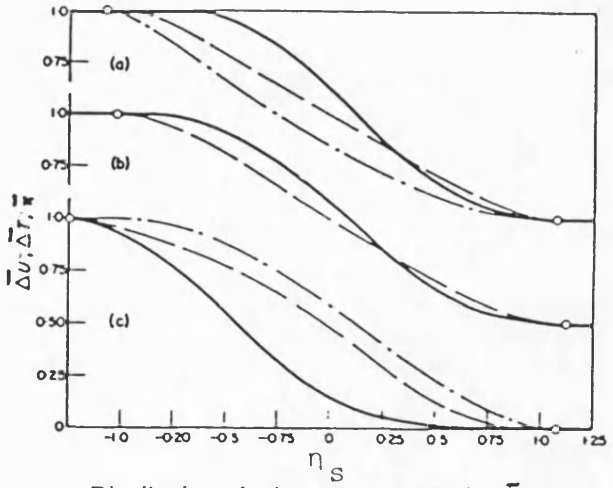

$$\eta_s = \frac{r - r_{\frac{1}{2}s}}{r_{2s} - r_{cs}}$$

$$\overline{\Delta F} = \frac{\Delta F}{\Delta F} = \frac{F - F_\infty}{F_0 - F_\infty}$$

F = u, T or ϰ

Distribution of relative excess velocity $\overline{\Delta u}$ (solid line), temperature $\overline{\Delta T}$ (dotted line) and volume concentration $\overline{\varkappa}$ (hatch-dot line) on the coordinate η_s for mixing zone of jets of different gases (n = var): (a) $n = 0.27$ (b) $n = 1.3$; (c) $n \approx 7$.

Light circles designate the boundaries of mixing zone.

FIG. 5.6a MEASURED PROPERTY PROFILES IN THE INITIAL REGION (53)

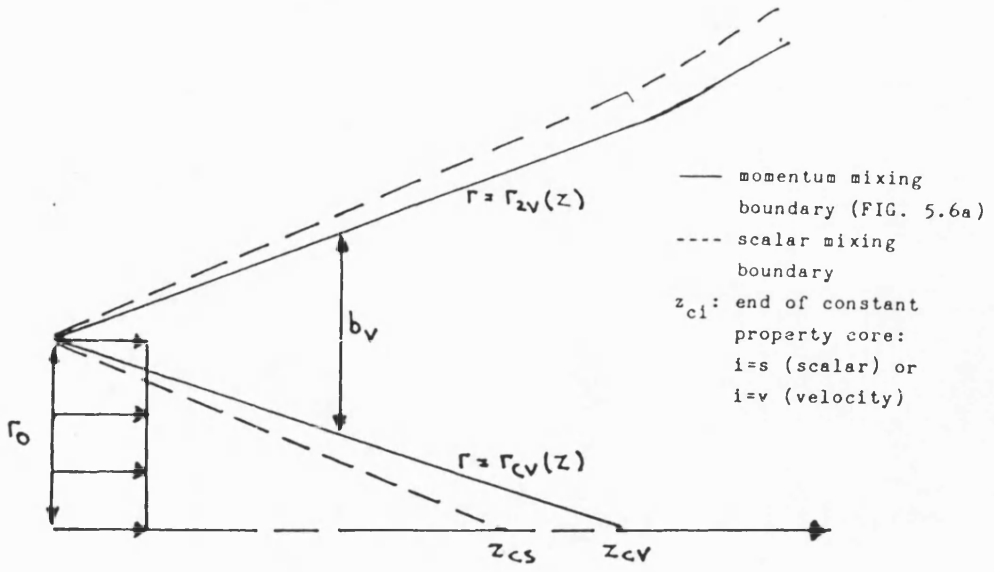

FIG. 5.6b EFFECT OF FASTER MIXING RATE ON SCALAR CORE LENGTH

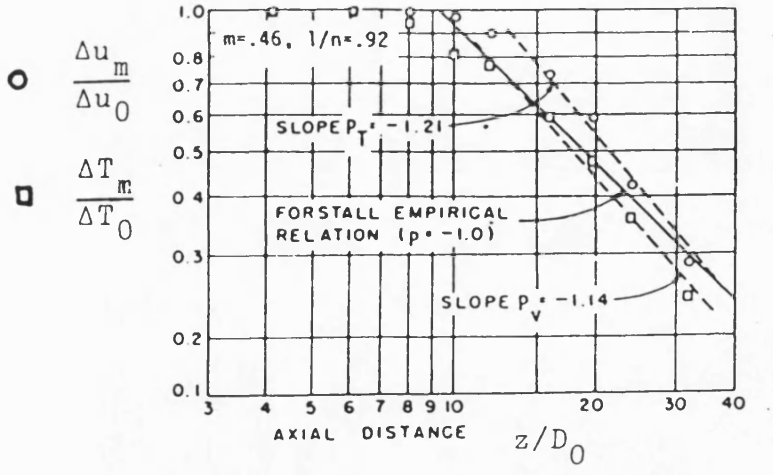

P, P_v, P_T empirical coefficients for axial 'power law' decays (Chapter 3)

axial temperature decay precedes slightly that of velocity

FIG. 5.6c MEASURED VELOCITY AND TEMPERATURE DECAY (58)

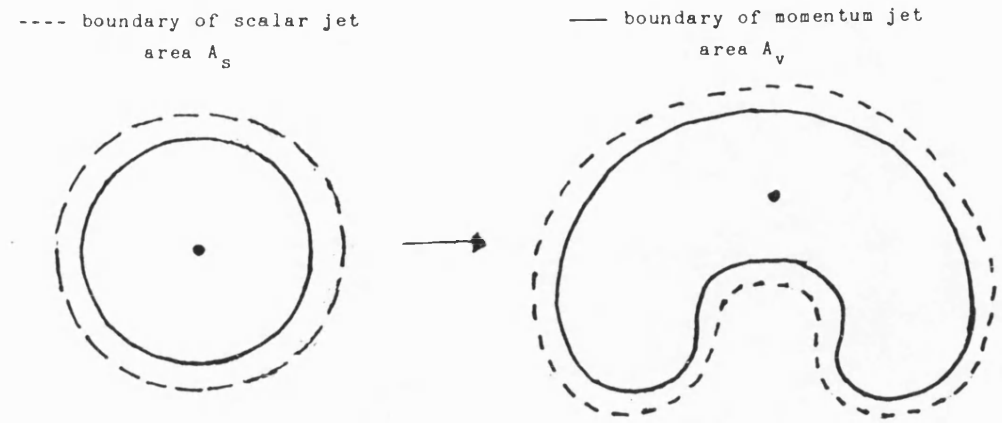

(a) CIRCULAR SECTION (b) DISTORTED SECTION

FIG. 5.7 MOMENTUM AND SCALAR JET AREAS

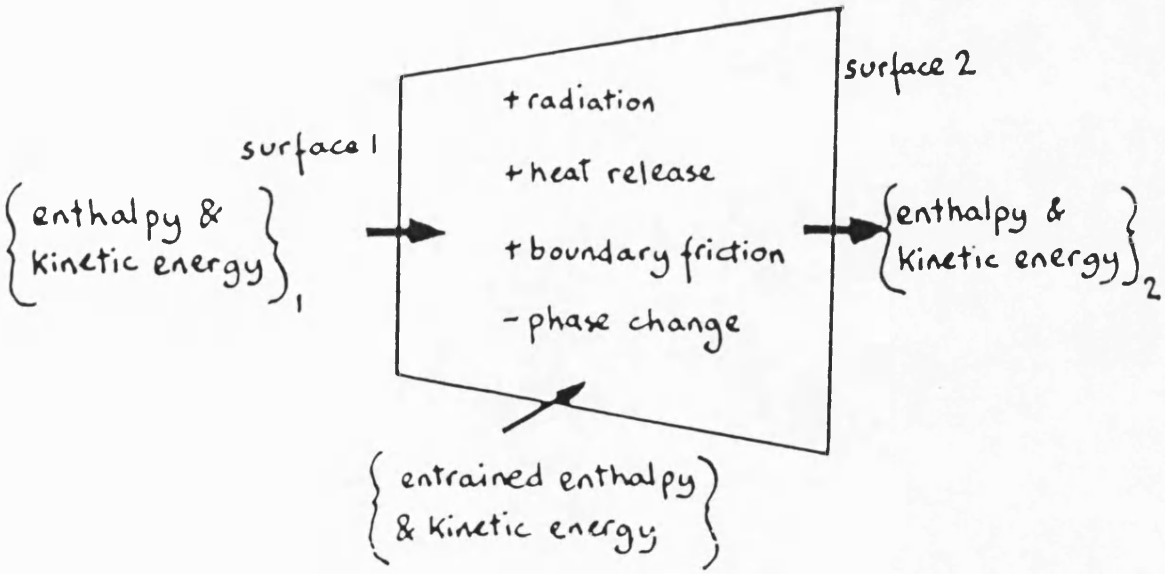

FIG. 5.8 CONTROL VOLUME FOR ENERGY BALANCE

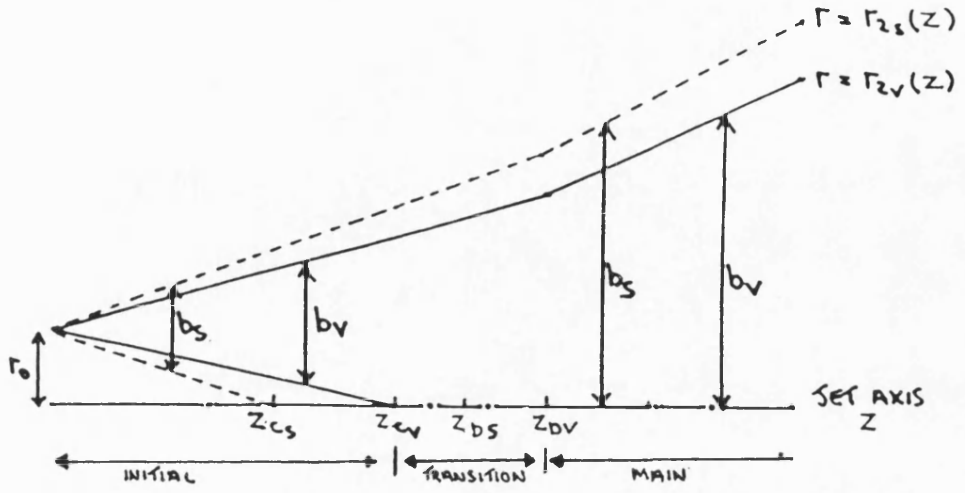

FIG. 5.9a DEFINITION SKETCH FOR DUAL JET DEVELOPMENT

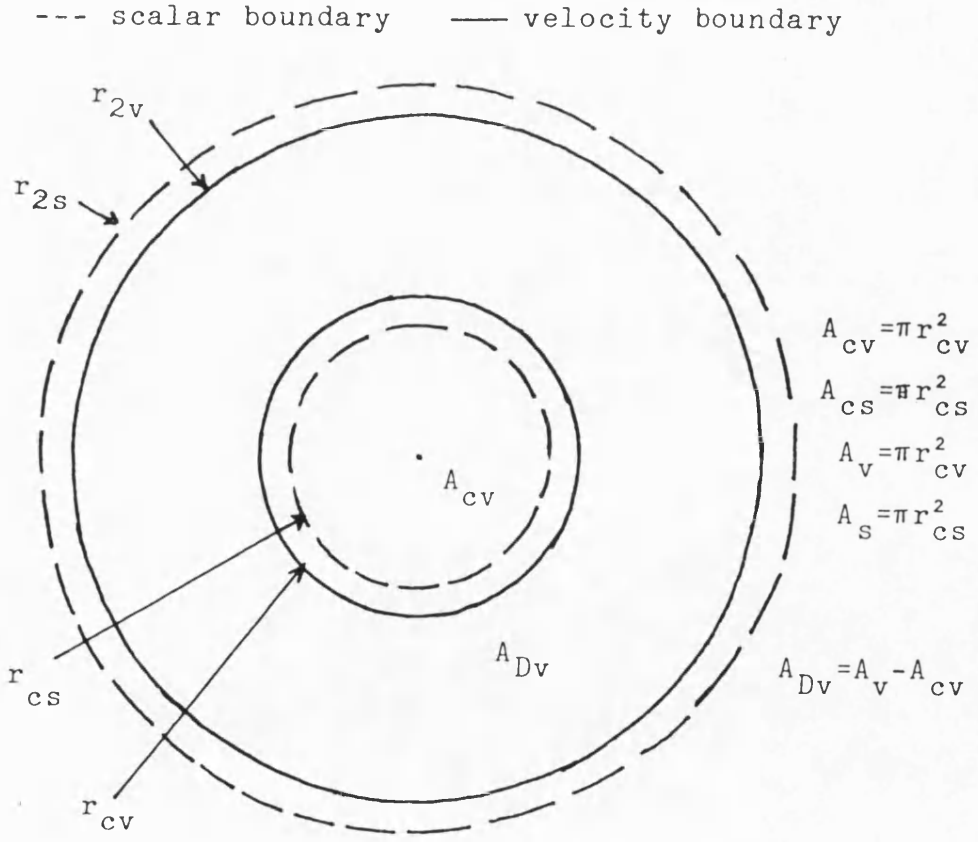

FIG. 5.9b MIXING BOUNDARIES FOR MASS AND MOMENTUM IN AN AXISYMMETRIC JET INCLUDING A POSSIBLE CORE OF CONSTANT VELOCITY OR SCALAR PROPERTY

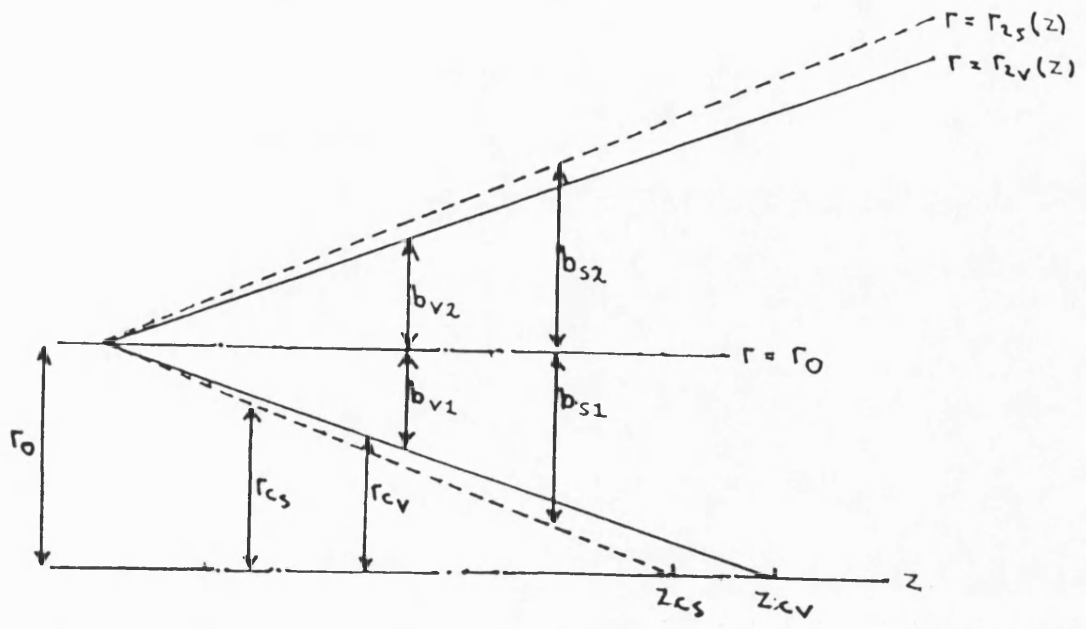

FIG. 5.9c DEFINITION SKETCH FOR THE INITIAL REGION

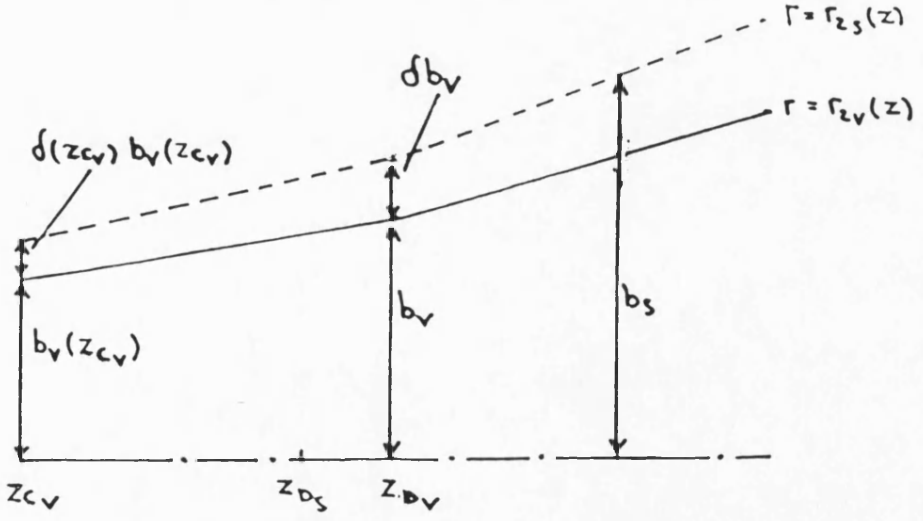

FIG. 5.9d THE TRANSITION AND MAIN REGIONS

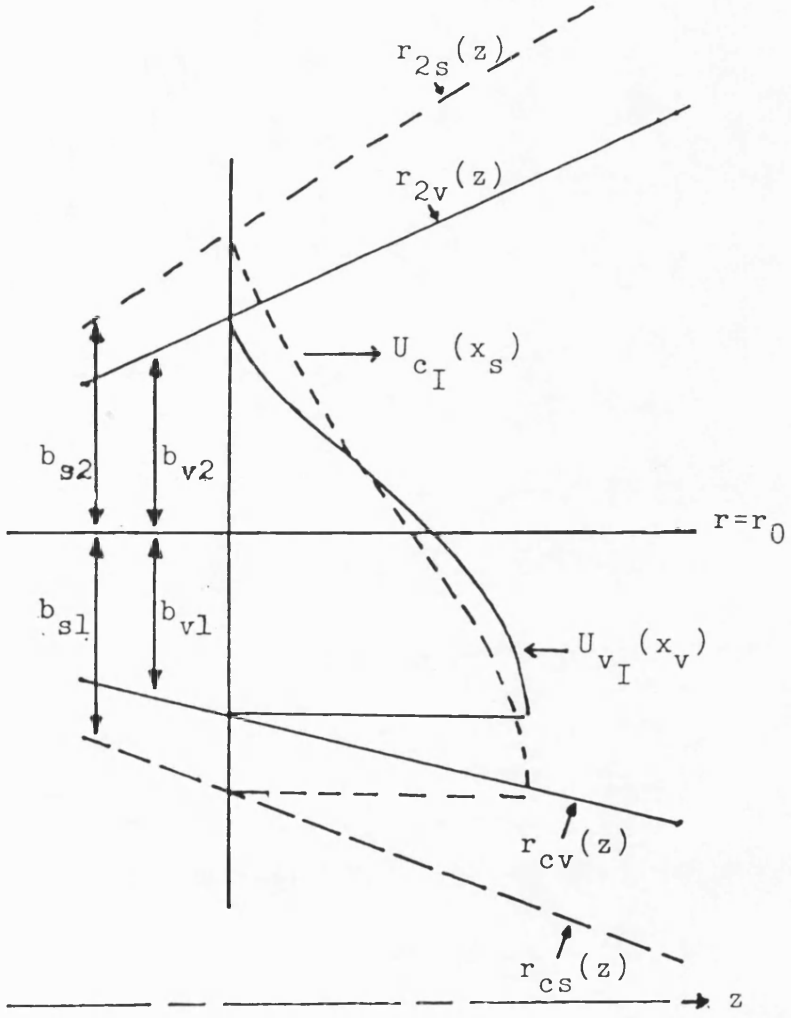

FIG. 5.10a PROPERTY PROFILES IN THE INITIAL REGION

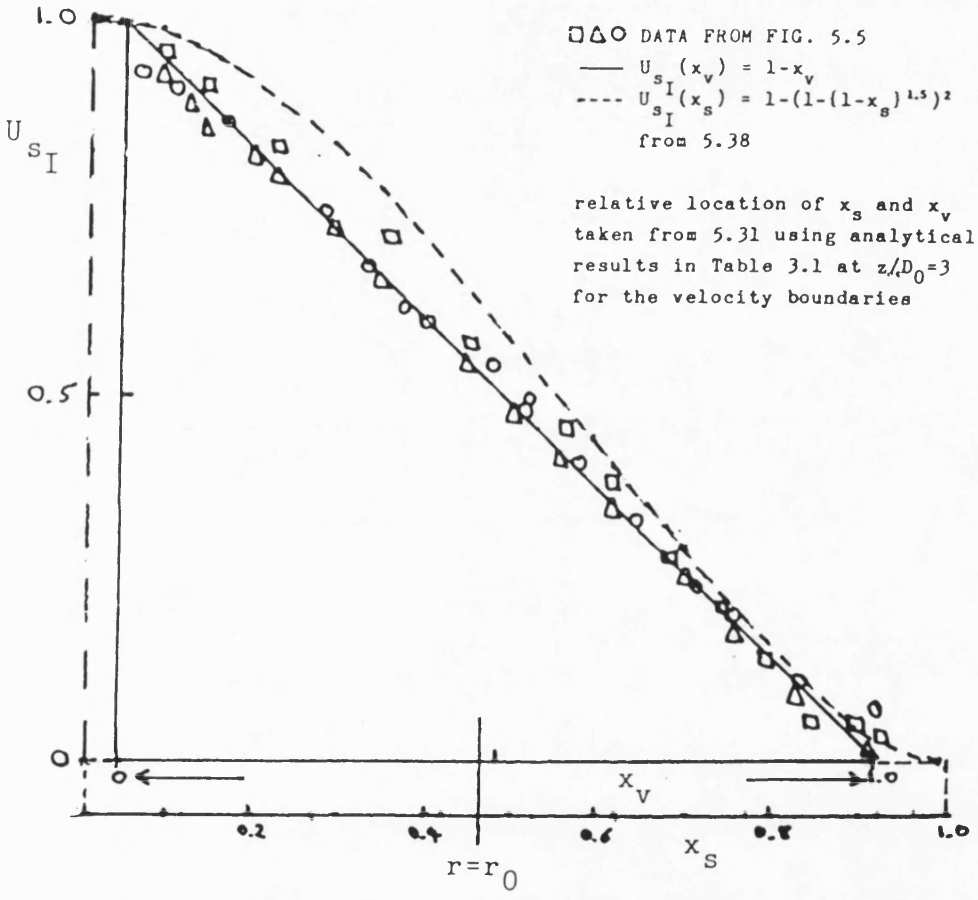

FIG. 5.10b MIXING BOUNDARIES FOR MASS AND MOMENTUM

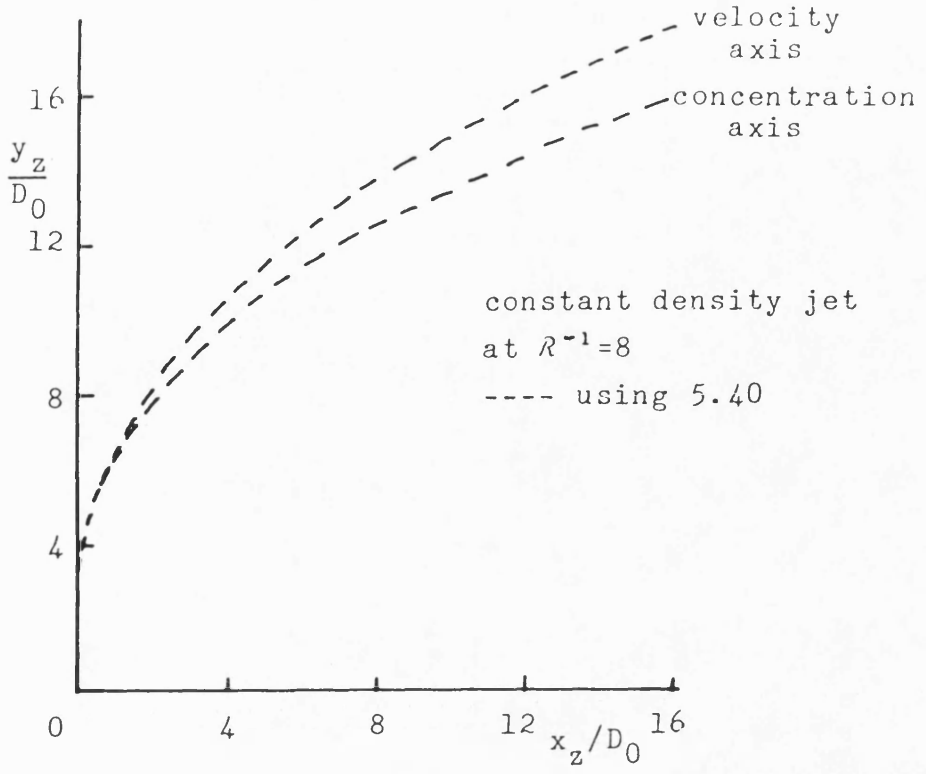

FIG. 5.11a VELOCITY AND CONCENTRATION AXES USING THE CORRELATION FROM PATRICK (70)

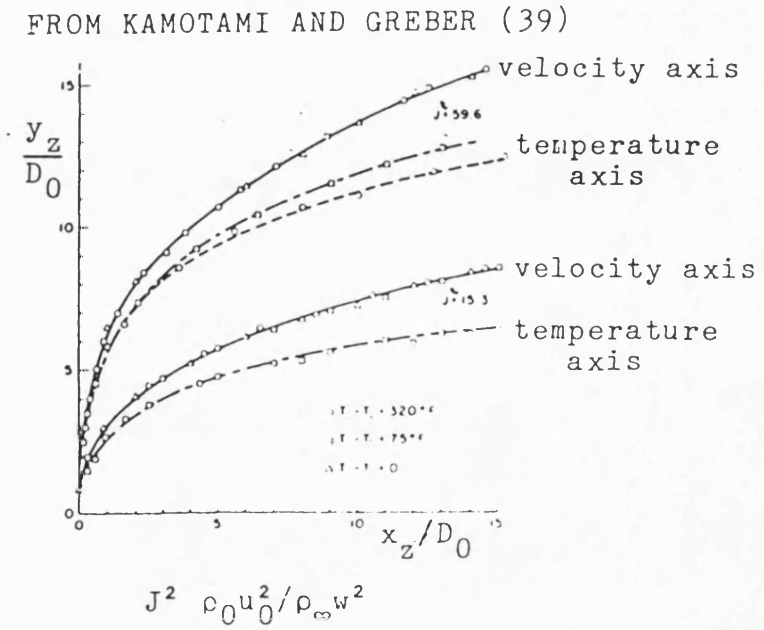

FIG. 5.11b MEASURED VELOCITY AND TEMPERATURE AXES

CHAPTER 6

COMPUTER IMPLEMENTATION

Chapter 6 - Notation

A	-	jet area (m^2)
A_c	-	area of constant property core (m^2)
A_D	-	area of turbulent mixing zone (m^2)
A_0	-	nozzle area (m^2)
A_{shape}	-	area of shape from distortion sub-model (m^2)
b	-	width of turbulent mixing zone (m)
b_X, b_Y	-	dimensions of cross-section shape shown in Fig. 6.5 (m)
c	-	mass concentration of injectant
C_p	-	specific heat (J/kgK)
C_r	-	ratio z_D/z_c (empirical relation)
dr_z	-	incremental length for polar co-ordinate r_z (m)
dt	-	incremental time step (s)
dz	-	incremental length along jet centreline (m)
$d\theta_z$	-	incremental change in polar co-ordinate θ_z (rad)
D_0	-	nozzle diameter (m)
E_m	-	mass entrainment rate (kgs^{-1})
F_i^n	-	integral averages defined in 3.12a
G	-	Abramovich width-growth coefficient for an axisymmetric jet
G_1	-	enhanced spreading rate coefficient
h_c	-	maximum concentration function
h_T	-	maximum temperature difference function (K)
h_v	-	maximum excess velocity function (ms^{-1})
I_n	-	property profiles integrals (n=0,...,9) defined in Chapter 5
K_n	-	integral averages defined in 6.1b

K_{nA_D} - integral average over the dynamic mixing zone defined in 4.30d

$\dot{m}$ - mass flux across jet area A

p,q - distortion parameters

r - radial ordinate in a cross-section of an axisymmetric jet (m)

r_c - radius of constant property core (m)

r_0 - nozzle radius (m)

r_2 - outer mixing boundary (m)

r_z - jet polar co-ordinate (Fig. 4.7a)

$\overline{S}$ - normalised solution of $\nabla^2 S=1$ $(=S/S_{max})$

$\overline{S}_1$ - auxiliary function for profile generation including property core

t - time (s)

T - temperature (K)

u - jet velocity (ms^{-1})

u_{mean} - average jet velocity in a cross-section (ms^{-1})

U_c - concentration distribution function

U_T - temperature distribution function

U_v - velocity distribution function

U_{v_I}, U_{v_M} - similarity profiles for velocity in the initial and main regions of an axisymmetric jet

w - velocity of fluid in the external stream (ms^{-1})

w_N - component of crossflow velocity normal to the centreline direction (ms^{-1})

x - dimensionless radial ordinate defined in 5.39c

x_z, y_z - co-ordinates in trajectory plane

z - jet centreline co-ordinate (m)

z_c	-	end of constant property core (m)
z_D	-	end of transition region (m)
g	-	geometric parameter in 6.13
$\mathcal{R}$	-	velocity ratio for a jet in a uniform crossflow ($=w/u_0$)
α	-	angle defined in Fig. 4.10
β	-	angle defined in Fig. 4.7a
γ	-	angle defined in Fig. 4.10
θ_z	-	polar co-ordinate of jet centreline (Fig. 4.7a) (rad)
ν_T	-	turbulent dynamic viscosity
δ	-	diffusion ratio defined in 6.39
δ_c, δ_2	-	diffusion rate coefficients defined in Chapter 5
ω	-	swirl rate (rad/sec)

Subscripts

0	-	at the jet origin (z=0)
s	-	pertaining to scalars
v	-	pertaining to velocity
∞	-	in the external stream

Chapter 6
Computer Implementation

6.1 Introduction

In order to make use of the theory in Chapters 4 and 5, it was necessary, of course, to fashion a computer program for the (numerical) solution of the rather involved system of coupled, ordinary differential equations which describe the principles of conservation of momentum, energy and injected species, together with the propagation equation for the spread of the turbulent mixing zone. In this chapter, the construction and content of the resulting fortran code will be described.

The present analytical study has been based upon the constant density theory of a round jet in a uniform crossflow presented by Adler and Baron (63)(1978), the significant feature of that work being a facility for the accurate representation of the velocity distribution U_v over any cross-section A in the jet, U_v being highly nonsimilar due to distortion of the jet shape by the crossflow (Chapter 4). Packer (35) considered this to be an advance in the integral method, in terms of the prediction of the inner structure of the deflected jet, and implemented the Adler and Baron model as a computer program at Bath University (35)(1983). The model was extended by him to account for force vortex flow in the external stream, as a first step towards the prediction of the mixing phenomena then being observed in the water rig and high swirl combustion chamber, which have been designed and built at Bath (33,34,35,36,42). The theoretical model included preliminary formulations of scalar conservation equations, with the computer program restricted to the constant density case (35).

The present work (Chapters 3-5) extends the method of Adler and Baron (63) to the case of nonisothermal round jets of variable composition, injected into a prescribed crossflow. Furthermore, a great deal of attention has been given to the description of axisymmetric jets, leading to an analytical

description of the initial and transition regions which supercedes the simplified, empirical treatment of Baron (71) (Chapter 4 and later). The work of Adler and Baron (63), and later Packer (35), can be considered to have established the following procedures as improvements to the original integral method:-

1/ An analytical expression for the cross-section area growth rate of a jet deflected by a crossflow.

2/ The representation of cross-section distortion, and use of realistic property distributions in the momentum theory.

In the present work, the predictive facility of the method has been enhanced by reassessment of the major empirical input: for example, Baron (71) set the width growth constant G_I for the mixing zone in the initial region of the submerged axisymmetric jet at an unrealistically low value, in order to obtain a length for the initial region in this particular problem which is not supported in the literature (see Chapter 3). Also, Adler and Baron (63) presented comparisons between predicted momentum trajectories and measured maximum velocity axes at comparable injection conditions; although the predicted curves fit the measured points sufficiently well, the two trajectories should not in fact be expected to coincide, in view of the distortion of cross-section shape (Chapter 7). It is significant, in this respect, that Adler and Baron (63) gave no comparison between predicted axial velocity decay and experimental data: twin velocity and trajectory comparisons are a more stringent test of the empirical input, as will be shown in Chapter 7.

The computer program developed by Packer (35) was primarily concerned with the construction of subroutines to perform the following functions:-

1/ The prediction of the jet cross-section distortion.

2/ The calculation of the velocity profile U_v over the distorted shape.

3/ The evaluation of the integrals of the velocity distribution over the cross-section.

4/ The solution of the set of ordinary differential equations.

Hence, it was natural that the starting point for the programming of the present, enlarged model should be the program due to Packer (35), and in particular those subroutines mentioned above. In view of the greater scope of the present work, it was considered appropriate to construct an entirely new code, within which would be included the cross-section distortion sub-model, altered as little as possible from Packer (35). Attention could then be given to the entirely new features of the model, principally the prediction of the scalar mixing field (Chapter 5) and the analytical treatment of the initial region (Chapter 4).

In the next section, a working flowchart for the computer program is introduced, which defines the major operations to be carried out during the numerical solution scheme. Each of these blocks is then considered in detail in the succeeding sections.

6.2 Outline Solution Procedure

A sketch of the sequence of the numerical solution appears in Fig. 6.1. In the integral method, the jet centreline z is defined as the locus of momentum centres in successive cross-sections: this is the single independent variable in the problem after the introduction of some simplifying assumptions (Chapters 2-4). Assuming that each of the dependent variables (A, h_v, β, h_c, h_T - Chapters 4-5) is known

at a particular station z, the system of ordinary differential equations describing the variation, with z, of these variables, can be treated as an initial value problem, and the solution advanced by forward marching integration to the station z+dz. The origin of the solution scheme lies at the plane of the nozzle (z=0) (in some turbulence model solutions, the numerical solution is begun near the end of the initial region (49)). Adler and Baron (63) also solved their equations as an initial value problem, using a four point Runge-Kutta procedure, while Packer used a variable order, variable step Gear method, primarily intended for stiff systems (see Section 6.6.2). In view of the very complicated nature of the equations, the Gear method has been retained for the present work.

In the initial value problem specification, the unknowns at a particular solution step z_k (such as the derivatives of the distribution integrals I_n) can be approximated by backward differences:-

$$\left.\frac{dI_n}{dz}\right|_{z_k} = \frac{I_n(z=z_k) - I_n(z=z_{k-1})}{\left.dz\right|_{z_{k-1}}} \qquad (6.1a)$$

and so forth. The formulation of the problem in this way has the benefit of simplicity with regard to coding and of stability with regard to the numerical solution: the penalty, naturally, is in terms of accuracy in the numerical results. With an implicit method (and iterative solution procedure), for example upwind differencing in 6.1a, numerically accurate results could be obtained with step lengths much larger than those required for the initial value problem; the expedients of simplicity and stability have been considered more important at present, and step lengths can be maintained reasonably short without incurring very great computer run times (Chapter 7).

For greater accuracy in the initial value problem, the computer implementation emphasises the importance of the

average values K_n of the integrals I_n (Chapter 4): it is through these averages that the effects of profile development and distortion are most easily monitored (see Chapter 7). Thus, the numerical integrations which determine the I_n are used to give:-

$$K_n = \frac{1}{A}\frac{dI}{dz}n \qquad (6.1b)$$

The derivatives of the integrals are not found, in the program, directly from 6.1a, but from:-

$$\left.\frac{dI}{dz}n\right|_{z_k} = K_n(z_k)\left.\frac{dA}{dz}\right|_{z_k} + \frac{A(z_k)\{K_n(z_k) - K_n(z_{k-1})\}}{\left.dz\right|_{z_k-1}} \qquad (6.1c)$$

This procedure has the benefit of making available the $K_n(z)$ for profile monitoring; furthermore, the effects of profile development are treated separately in the second term of 6.1c (Chapter 3 and Chapter 7), making the derivative evaluation more accurate than 6.1a, since dA/dz is known explicitly at z_k from the propagation equation (together, in the initial region, with the core area equation - Chapters 4 and 5). In the limiting case of the submerged, axisymmetric jet at constant density, for example, $K_n(z)$ is constant in the main region (by similarity) and dI_n/dz is determined correctly at z_k using the computed value of dA/dz at z_k. The emphasis on the evaluation of K_n is indicated in Section 6.5.

At the beginning of the program, data defining the injection conditions and chamber geometry are taken from an input file; markers and constants for the program are initialised, and the class of the problem (crossflow type, inclusion of the cross-section distortion sub-model, etc) is identified. This information is then restated as preliminary output at the head of the numerical results. Details of the initialisation and problem definition sequence are given in Section 6.3

The remainder of the solution loop (shown in Fig. 6.1) is concerned with the construction of the system of differential equations and its numerical solution over a prescribed step, length dz. After the first solution step, the distortion of the cross-section from its initially circular shape is considered in the presence of a crossflow (Section 6.4). The profiles of excess jet velocity, concentration and temperature difference (U_v,U_c,U_T) are then determined, in order that the integrals I_n may be evaluated at the current axial station, and their derivatives dI_n/dz determined (Section 6.5). The extant conditions are then output to results files (Section 6.7); the solution step length dz is defined, and the differential equation system is solved over dz (Section 6.6); upon completion of this task, the jet trajectory is incremented from the co-ordinate relationships discussed in Chapter 4 (Section 6.3.3). If the solution scheme has not reached a predefined limit (Section 6.7), the cycle is repeated and the solution advances downstream.

Throughout the coding of each of these procedures, the author has attempted to preserve the generality of the program with respect to empirical input, in order to explore parametrically the effects of various physical influences. These effects are described and discussed in Chapter 7.

6.3 Problem Definition

6.3.1 Outline Of Sequence

A diagram of the problem definition sequence is given in Fig. 6.2. The sequence involves marker and constant initialisation and a first call to two major subroutines:-

1/ subroutine polar - the crossflow definition and step length subroutine.

2/ subroutine sect - the cross-section distortion sub-model.

In this section, the subroutine polar is fully described. Details of the subroutine sect are given in Section 6.4.

6.3.2 Data Input And Initialisation

The input data to the computer model is summarised in Table 6.1. Details of the chamber and of the ambient fluid are prescribed; it is assumed that injections are of the gas into gas type, so that the injectant and ambient fluid densities can later be determined from the gas law (Section 6.5) - in Chapter 8, the extra input and programing required for the prescription of a liquid injectant is described. The radius at injection, r_i, allows the injection point to be displaced from the centre of a cylindrical chamber (for example).

The degree of development, rc0, defines the assumed width of the boundary layer originating from the inner edge of the nozzle lip at injection:-

$$rc0 = \frac{r_c(z=0)}{r_0} \qquad (6.2)$$

Since $D_0=2r_0$ is known, $r_c(z=0)$ is known from 6.2 and the initial width b_0 of the momentum mixing zone can be determined:-

$$b_0 = r_0 - r_c(z=0) \; ; \quad A_D(0) = A_0 - A_c(0) \qquad (6.3)$$

These are initial conditions upon the propagation equation (dA_D/dz) and core area equation (dA_c/dz). The boundary layer is thus treated as an annular shear layer, across the width b_0 of which the initial region velocity profile $U_{v_I}(x)$ will be defined (Section 6.5). For a uniform injection profile, b_0 is not set to zero, but to an arbitrarily small value (see Chapter 5: the author has used rc0=0.9995 for the uniform injection predictions in Chapter 7): this allows the initial width b_{0s} of the scalar mixing zone to be conveniently defined (Chapter 5 and Section 6.5). At the opposite extreme, the input condition rc0=0 defines a fully developed velocity profile at injection: this no core

(z_c=0) condition causes the main region profile $U_{v_M}(x)$ to be defined across the width r_0 (no transition region).

It is noted that boundary layers on the outside of the nozzle lip, such as those described by Rajaratnam and Pani (43), are not included in the modelling or computer program (see Chapter 7).

Consequent to the input of the data given in Table 6.1, via a call to the subroutine in-out (Section 6.7), some solution controls and markers are initialised.

A marker nt0 is defaulted to a value of 1. For isothermal flow ($T_0=T_\infty$ => $h_T\equiv 0$), nt0 is reset to 0 and those sections of the program dealing only with the construction and solution of the dh_T/dz equation are not accessed.

The system of differential equations is different in the initial region to the system downstream of it (Chapters 4 and 5). The equations which are to be solved at any solution step are identified by markers:-

isolvad for $\frac{dA}{dz}_D$; isolvhv for $\frac{dh}{dz}_v$

isolvac for $\frac{dA}{dz}_c$; isolvct for $\frac{dh}{dz}_c$ and $\frac{dh}{dz}_T$

The propagation equation (dA_D/dz) is always solved, but may be 'turned off' temporarily when A_c=0 is predicted (see Scetion 6.6.1). The equations for the excess properties (h_v,h_c,h_T) are only solved beyond the end of their respective initial regions (z_c or z_{cs}: see Section 6.5.4). The particular equations are not solved when the relevant marker is set to zero: as a default, the initial region equations are identified for solution at z=0, and subsequently overwritten in the case rc0=0 (no core).

The empirical width growth coefficients G(z) and $G_1(z)$ are defined for the initial region and beyond the transition

region (G(z) varies linearly in the transition region - Chapter 3: $G_1(z)$ is constant beyond z_c - Chapter 7). The value $C_r=z_D/z_c$ is defined ($C_r=1.5$) for determination of the length of the transition region. At the origin, the setting $z_c=-1$ is made, so that a fully developed injection ($z_c=0$) may be properly distinguished from those initial region solutions where the end of the core has not yet been predicted. Values for the empirical coefficients are then assigned (as initial or downstream settings) according to the sign of z_c.

Problem definition is completed by the specification of the type of the flow into which the jet is injected, and this is the duty of the subroutine polar.

6.3.3 Subroutine 'polar'

This subroutine is divided into four sections (Fig. 6.3), accessed separately by the setting of the marker ncall, which perform the following operations:-

1/ The setting of the injection orientation with respect to the crossflow; that is, initialisation of the angles β and θ_z.
Not subsequently accessed.

2/ The incrementing of the jet trajectory, after each solution step, using the relations derived in Chapter 4.

3/ The setting of the angles α and γ for the next solution step, and the evaluation of dr_z and $d\theta_z$ - dependent upon crossflow type (Chapter 4): the evaluation of the crossflow w at the new station, and the local value of dw/dz. At the first call (z=0), the details of the crossflow type are output (Section 6.7).

4/ The determination of the step length dz over which the equations shall be solved. This

section is accessed immediately before the solution of the differential equations, so that backward differences, etc have been evaluated with the correct value for dz. In the initial region, relatively short steps are required because of rapid changes with z of the integrals I_1 and I_2 (due to the changing geometry of the annular mixing zone - Chapter 4 and later). Furthermore, short steps are required near the nozzle (dI_n/dz not known at the first step) and near the end of the end of the initial region (Section 6.6.1). Thus, a parabolic variation for dz is permitted in the initial region:-

$$dz = dz|_{z=0} + 4(dz_{max}-dz|_{z=0})(1-\hat{r}_c)\hat{r}_c \quad (6.4)$$

where $dz|_{z=0}$ is the first step length prescribed and dz_{max} is the maximum step size permitted for the initial region. The step size varies with the local extent of the constant velocity core:-

$$\hat{r}_c = \left(\frac{A_c}{A_c(0)}\right)^{\frac{1}{2}} \quad (6.4a)$$

The formula 6.4 ensures that the maximum step size occurs when $\hat{r}_c=\frac{1}{2}$.
In the transition region, short steps are required to resolve the development of property profiles (Section 6.5), while further downstream longer step lengths can be used, giving acceptable accuracy (see Chapter 7). Thus, a linear increase in dz is permitted beyond the initial region:-

$$dz = \min\{ dz_{z=0} + C_{grid}(z-z_c), dz^*\}$$

where C_{grid} is an expansion factor. An upper bound for dz as $dz^*=D_0/2$ was used in this work.

6.4 Cross-Section Distortion Sub-Model

The coding concerned with the distortion of the jet cross section has been collected into the subroutine sect, which is itself divided into initialisation and solution cycle sections. The structure of sect is shown in Fig. 6.4.

In the initialisation sequence, a fixed number (nvort) of vortices are located around the circular jet periphery using the subroutine co-ord, taken directly from Packer (35). The dimensions of this circle are stored so that later results can be scaled.

In the cause of generality, the assumed jet velocity profile is prescribed numerically, regardless of the nature of the problem. Thus, for an axisymmetric jet, the known functional relations for similarity profiles (Chapters 2,3 and 5) are not used directly, but are defined at the notes of a finite-difference grid (stored as a two-dimensional array). This representation has the following advantages:-

a) The treatment of the development of profiles in the transition region is easily accomplished, and,

b) The solution procedure with similarity profiles is completely compatible with that for nonsimilar, distorting profiles, which are only defined numerically.

Thus, in the initialisation sequence, the nozzle velocity profile must be prescribed. Adler and Baron (63) determined velocity profiles from the auxiliary function S, being the solution of Poisson's equation:-

$$\nabla^2 S = Q \quad ; \quad \begin{matrix} S=0 \text{ on jet} \\ \text{shape boundary} \end{matrix} \quad ; \quad Q \text{ constant} \qquad (6.5)$$

(the value of Q is arbitrary in view of later normalisation. A value Q=1 has been used here). The solution of 6.5 over (distorted) cross-section shapes is by a finite difference

method written into the subroutine epdel, described by Packer (35). In the present work, the most recently computed base distribution $\overline{S}$ is always held in storage for the computation of property profiles (Section 6.5). At the origin, the shape is a circle and $\overline{S}=S/S_{max}$ is given, by analytical solution of 6.5, as:-

$$\overline{S} = 1 - \left(\frac{r}{r_2}\right)^2 \qquad (6.6)$$

where r_2 is the radius of the circle (at $z=0, r_2=r_0$). This function is evaluated, at the nodal points of a finite difference grid, by an original subroutine called generate, and is subsequently manipulated for the construction of the profiles U_v, U_c, U_T (Section 6.5). In an axisymmetric jet, because the cross-section shape is always circular, the base distribution $\overline{S}$ is never recomputed.

In section II of the subroutine sect, cross-section distortion over a solution step is considered. The local displacement of the vortices, seeded around the jet periphery, and the storage of the new co-ordinates of each vortex, is accomplished by a call to the subroutine vortex: the calculation of the vortex displacement and its computer implementation in this subroutine is completely described by Packer (35). The displacement is with respect to time, and the time step at the current station z_k is dt_{k-1}, where:-

$$dt_{k-1} = \frac{dz}{u_{mean}}\Bigg|_{z_k-1} = \frac{z_k - z_{k-1}}{u_{mean}|_{z_{k-1}}}$$

where the average jet velocity u_{mean} is defined in Section 6.7. This procedure ensures that the cross-section shape is predicted at the current station z_k (prior to any integral evaluations) by updating the shape at the previous step.

The vortex displacement theory is for inviscid, incompressible flow. In order to permit matching with the distortion rate for cross-sections observed in real jets (39), a damping term is included in the theory which contains a 'turbulent dynamic viscosity' ν_T (63,35). Increasing the value of ν_T from zero (the inviscid case) reduces the predicted rate of shape distortion - the setting of ν_T is described in Chapter 7.

Whenever a new cross-section shape is generated, a new base distribution is described over it by a call to the subroutine epdel (35). The subroutine imposes a finite difference grid over the new shape which is of the same resolution as that used by the subroutine generate (for the original base distribution) (Fig. 6.5). The Poisson equation is solved over the new shape (subject to S=0 on and outside the boundary - (35)): the numerically defined solution S is normalised to give the new base distribution $\overline{S}$. The setting of property profiles from $\overline{S}$ is described in Section 6.5.

For the purpose of scaling the distortion sub-model shape to fit the predicted jet area A, the area A_{shape} of the distorted shape is required. Following Packer (35), a copy is made of the array holding the 'node-defined' $\overline{S}$. A binary distribution B is then generated as follows:-

$\overline{B}$ = 1 if $\overline{S}>0$ (nodal point within jet shape)
$\overline{B}$ = 0 if $\overline{S}=0$ (nodal point on or outside jet shape)

The area A_{shape} can then be known, in principle, by numerical integration of B over the rectangular grid. The binary distribution, however, is not continuous across the boundary of the jet shape; hence it is poorly integrated by numerical methods. For example, there is an error of about 8% in integrating B numerically over a circle of known radius, even when a sophisticated Monte-Carlo technique is used (such as that used by Packer (35)). At present, it has been assumed that the same percentage error is incurred in

the integration regardless of the current jet shape: this is a questionable assumption, since it is likely that the error will increase with the relative increase in length of the shape boundary as it deforms, across which the functional discontinuity exists. This uncertainty in A_{shape} was not mentioned by Packer (35) and may affect evaluation of the integrals I_n using distorted property profiles (see Chapter 7).

With A_{shape} assumed known, the predicted widths b_X and b_Y of distorted shapes can be found by scaling of the sub-model results (b_X and b_Y are defined in Fig. 4.1). The predicted spread of deflected jets can then be interpreted (Chapter 7).

Adler and Baron (63) assumed that when $\beta<30$ degrees, the jet enters the far region (Chapter 4) and is sufficiently alligned with the crossflow to arrest the distortion of the cross-section shape: the last computed jet shape and distribution $\overline{S}$ can be used at every subsequent station (a similarity condition).

6.5 Integrals Of Property Distributions

6.5.1 Introduction

A sketch of the procedure for the evaluation of the distribution integrals (Chapters 4 and 5) is shown in Fig. 6.6. The principal features to be described are:-

a) The setting of the velocity, temperature and concentration distributions using the base distribution $\overline{S}$, and

b) The evaluation of the integrals in the initial region.

6.5.2 Property Distributions

Adler and Baron (63) described a method for the prediction of the velocity profile in successive sections of a jet deflected by a crossflow. Two distortion parameters, p and q, were introduced, and the distorted velocity profile was found from the base distribution $\overline{S}$ (Section 6.4), using:-

$$U_v = \bar{S}^{\bar{S}(p-q)+q+1} \qquad (6.7)$$

$\bar{S}$ is known at the nodes of a finite-difference grid (see Section 6.4): $\bar{S} \in [0,1]$. The parameters p and q were adjusted, by Adler and Baron (63), so that the profiles corresponded to measured velocity profiles from Kamotami and Greber (39) (the matching ability was illustrated in Fig. 4.5). Good agreement was obtained using the following variation for p and q (63):-

$$p = 0.15 + 0.126(z-z_c)/(15D_0-z_c) \qquad (6.8a)$$

$$q = 0.945 \qquad (6.8b)$$

recalling that z_c was an empirical input to the Adler and Baron model (63). Packer did not use p and q in his implementation, but set $U_v=\bar{S}$ for his parametric studies (35).

In describing the original model, Baron (71) makes no reference to the prediction of axisymmetric jets, and in particular to the setting, through p and q, of the mixing zone similarity profiles in this limiting case. Since the prediction of axisymmetric jets is an important consideration in the present work, the use of the parameters p and q has been reassessed under these conditions, then extended to deflected jets.

It is assumed that the profile U_v in the main region of an axysimmetric jet is adequately described by the Schlichting formula (Chapter 2):-

$$U_{v_M}(x) = (1-x^{1.5})^2 \qquad (6.9)$$

In Fig. 6.7a, an attempt has been made to approximate 6.9 using 6.7 (in which $\bar{S}$ is given by 6.6 for the circular jet section). The parameter p is influential within the domain of $\bar{S}$, while q affects the profile near the boundary. A good representation of 6.9 is obtained with the following values:-

$$p_M = 2.5 \quad ; \quad q_M = 0.945 \qquad (6.10a)$$

For comparison, the settings in 6.8 from Adler and Baron (63) have been used in Fig. 6.7b to produce profiles U_v at different axial stations z ($z_c \simeq 5D_0$ for a simple jet - see Chapter 3); it can be seen that 6.9 is not particularly well described, and the main region velocity profile is not similar. Therefore the settings in 6.10a are preferred here.

The initial region velocity profile ${}^{U}v_I(x)$ (Chapter 3) can also be represented by suitable choices for p and q. Assuming here that $A_c=0$, ${}^{U}v_I$ is taken over the entire jet width in the same way as ${}^{U}v_M$ above. As illustrated in Fig. 6.8a, the optimum choices for p and q are:-

$$p_I = 1 \quad ; \quad q_I = 0.5 \qquad (6.10b)$$

(the analytical profile 2.21 for ${}^{U}v_I(x)$ has been used here).

The procedure of Adler and Baron (63) for the setting of initial region velocity profiles evinces some inconsistency. Across the jet width r_2 at some station z, $U_v=1$ within the constant velocity core ($r<r_c$). With r_c and r_2 known at z, Adler and Baron (63) used 6.7 to find U_v, then 'cut' U_v so defined at $r=r_c$. Renormalisation of U_v to give again $U_v=1$ in the core then gave U_v with its core and mixing zone (${}^{U}v_I$) components. For Fig. 6.8b, ${}^{U}v_I(x)$ has been calculated in this way at three axial stations in the initial region of a simple jet: use has been made of the theoretical results for $r_c(z)$, b(z) and $r_2(z)$ from Table 3.1. The resulting computed profiles are not smooth across the inner edge of the mixing zone (x=0), due to the 'cutting' of the profile at the core edge, and the profiles are not similar through the initial region. Agreement with the functional relation 2.21 is only obtained near the end of the initial region (Fig. 6.8b - $z_c=5D_0$). For the present work, the prediction of the mixing zone boundaries $r_c(z)$ and $r_2(z)$ (by the methods of Chapter 4) depends significantly upon the

accurate representation of the profile U_{v_I} (through the integral averages K_{nA_D} in 4.31), and an improved procedure for the prescription of the initial region velocity profile in the present work is described in the next section.

Having established these values (6.10a and 6.10b) for p and q, the representation of the developing velocity profile in the transition region (Chapter 3) reduces to the variation, in some way, of p and q between their initial and main region values. This variation should be the subject of computer optimisation, although for simplicity a linear variation with z between z_c and z_D has been used in the present work, with satisafactory results (Chapter 7).

It was demonstrated in Chapter 5 that, in view of the separate diffusion rates for mass and momentum, the scalar profiles U_c and U_T (assumed to be identical) could be considered to exhibit the same functional variation as U_v, when a proper ordinate x_s is used to trace the profiles across the 'scalar' mixing width b_s. The consequence here is that the same values for p and q (from 6.10a and 6.10b) will suffice for both velocity and scalar profiles, although the domain of the scalar profiles will be larger (see Section 6.5.3).

With p and q known for axisymmetric jets, it is necessary to consider whether these values must alter in order to represent accurately the profiles observed in deflected jets of distorted cross-section shape (39). It is demonstrated in Chapter 7 that realistic profiles can be generated without alteration of p and q: profile distortion is mainly a consequence of the change in the base distribution $\bar{S}$, following shape distortion (Section 6.4).

In the light of these discussions it is assumed that U_v, U_c and U_T are known at any axial station in the solution scheme, so that it remains to evaluate the integrals I_n at a particular cross-section A. It is necessary to distinguish between the solution procedures within and then beyond the initial region.

6.5.3 Profile Integrals In The Initial Region

It is clear from Chapters 4 and 5 that the set of governing equations appears in considerably reduced form in the initial region: the scalar conservation equations are not solved explicitly, and the centreline momentum equation is reworked (see Section 6.6). Here, it is observed that the core area equation 4.31 (for dA_c/dz) requires the evaluation of the integrals involving the velocity profile over the momentum mixing zone area A_D. In Chapter 4 (and 4.31) these were used in the following way:-

$$K_{nA_D} = \frac{I_{nA_D}}{A_D} \quad \text{where} \quad I_{nA_D} = \int_{A_D} \rho U_v^n dA_D \quad n=0,1,2 \quad (4.30d)$$

the average values of the complete integrals I_n are also required (see 4.31). In discussing the evaluation of the I_{nA_D}, the simple case of a constant density, axisymmetric jet is considered, and the results then extended to the variable density jet: this allows a comparison between the present work and that of Baron (71).

In the Baron model (71), there is no core area equation; the length of the initial region is computed empirically (Chapter 4). The core is assumed to be conical and the integrals I_n (n=0,1,2) - required for the $d\beta/dz$ equation 4.37 - evaluated as:-

$$I_n = \rho A_c + K_{nA_D}(z) A_D \quad (6.11)$$

where:-

$$K_{nA_D}(z) = \frac{1}{A_D(z)} \int_{A_D} \rho U_{v_I}^n dA_D \qquad n = 0,1,2 \qquad (6.11a)$$

is the average value of U_{v_I} over the mixing zone multiplied by the constant fluid density. Baron (71) made the further assumption that, assuming U_{v_I} is a similarity profile:-

K_{nA_D} = constant for each n

which implies that the average value of the velocity profile over the mixing zone is constant (this was a consequence of profile and geometric similarity for the main region, as shown in Chapter 3). This would considerably simplify the core area equation 4.31, but the conclusion may be shown to be at fault. The reason is that, although similarity of the profile across the width b of the mixing zone (Fig. 3.1b) is a reasonable assumption if there is no shape distortion, the mixing zone itself cannot exhibit geometric similarity. Consider an axisymmetric jet in the initial region:-

$$I_{nA_D} = \rho\int_{A_D} U_v^n dA_D = 2\pi\rho\{r_c b F_0^n + b^2 F_1^n\} \; ; \; F_i^n = \int_0^1 U_{v_I}^n (x) x^i dx$$

using the methods and notation of Chapter 3. This result could also be written as:-

$$\begin{aligned} I_{nA_D} &= \rho\pi\{b^2 F_0^n + 2br_c F_0^n + 2b^2 F_1^n - b^2 F_0^n\} \\ &= \rho F_0^n \pi b(b+2r_c) + \rho\pi b^2\{2F_1^n - F_0^n\} \\ &= \rho F_0^n A_D + \rho\pi b^2\{2F_1^n - F_0^n\} \end{aligned}$$

Thus:-

$$K_{nA_D} = \frac{I_{nA_D}}{A_D} = \rho F_0^n + \frac{\rho\pi b^2}{A_D}\{2F_1^n - F_0^n\} \qquad (6.12)$$

The average value of I_{nA_D} over A_D thus depends upon the geometric parameter $g(z)$:-

$$g(z) = \frac{\pi b^2}{A_D} = \frac{b}{b+2r_c} \qquad (6.13)$$

for an axisymmetric jet (an equivalent result for distorted cross-sections follows from the effective width definitions for b and r_c in 4.5). Baron's assumption K_{nA_D} = constant

cannot be true, since, for uniform injection velocity:-

$$\text{at } z=0,\ b=0 \Rightarrow\ g(0) = 0$$
$$\text{at } z=z_c,\ r_c=0 \Rightarrow\ g(z_c) = 1$$

and $\{2F_1^n - F_0^n\} \neq 0$ (Chapter 3). It is the change in the geometry of the annular mixing zone, through the initial region, which precludes the assumption of constant average values for the integrals over the mixing zone. The result 6.12, however, may be used as follows:-

$$K_{nA_D}(z=0) = \rho \bar{F}_0^n$$

$$K_{nA_D}(z=z_c) = 2\rho F_1^n$$

Hence, 6.12 may be written as:-

$$K_{nA_D} = K_{nA_D}(0) + g(z)\{K_{nA_D}(z_c) - K_{nA_D}(0)\} \qquad (6.14)$$

and this describes the variation of K_{nA_D} through the initial region. It is suggested that this is a significant reason why Baron (71) gave no details of the predicted flow in the initial region in his presentation of results (63). In the present work, integral averages are evaluated at every step as described below.

The numerically defined profile U_v in the initial region must include the constant velocity core (where $U_v=1$), and an improvement to the method of Baron (described above) has been devised. At a particular station z in the initial region, where the widths r_c, b and r_2 are all known (see Fig. 6.9), U_v is given by:-

$$U_v(r) = \begin{cases} 1 & r<r_c \\ U_{v_I}(x) & x = \dfrac{r - r_c}{b} \in [0,1] \end{cases} \qquad (6.15)$$

where $U_{v_I}(x)$ is the mixing zone similarity profile from Fig. 6.8a. From the above discussion, the profile 6.15 may

be generated using the following base distribution:-

$$\bar{S}_1(r) = \begin{cases} 1 & r<r_c \\ 1 - x^2 & x = \dfrac{r - r_c}{b} \in [0,1] \end{cases} \qquad (6.16)$$

(see Fig. 6.10a and b) in the formula 6.7:-

$$U_v = \bar{S}_1^{\bar{S}_1(p-q)+q+1} \qquad (6.17)$$

Since the base distribution $\bar{S}$ is known at any station (Section 6.4), it is convenient to define $\bar{S}_1$ in terms of $\bar{S}$. Note that:-

$$(1 - x^2) = 1 - \left\{\frac{r - r_c}{r_2 - r_c}\right\}^2 = 1 - \frac{1}{c_v^2}\left\{\frac{r}{r_2} - \frac{r_c}{r_2}\right\}^2 \qquad (6.18)$$

where:-

$$c_v = 1 - \left(\frac{r_c}{r_2}\right) = 1 - \left(\frac{A_c}{A}\right)^{\frac{1}{2}} \qquad (6.18a)$$

Since, from 6.6 and 6.18a:-

$$\frac{r}{r_2} = (1 - \bar{S})^{\frac{1}{2}} \quad ; \quad \frac{r_c}{r_2} = 1 - c_v \qquad (6.18b)$$

it follows that:-

$$(1 - x^2) = 1 - \frac{1}{c_v^2}\{(1-\bar{S})^{\frac{1}{2}} + c_v - 1\}^2 \qquad (6.18c)$$

for use in 6.16. The parameters p and q in 6.17 take the values prescribed in 6.10b for the initial region. Computer plots of the profile U_v so generated are reproduced in Fig. 6.10c-e.

The same scheme applies to the initial region of deflected jets, provided shape distortion is not very great. This is a very reasonable assumption for jets in moderate crossflows, for example uniform crossflows with $R = w/u_0$

less than about 1/4 (Chapter 4). Generality in the prescribed mixing zone profile is preserved since its form depends only upon the values assigned to p and q, while any nozzle velocity profile, from uniform (b(0)=0) to fully developed (r_c=0) may be set.

The numerical technique used to integrate U_v over the cross section (for the determination of the I_n) is discussed in Section 6.5.5. Here, it must be said that all numerical integration techniques assume some condition concerning smoothness in the integrand: the trapezoidal rule, for example (Section 6.5.5), assumes the integrand to be twice differentiable in its domain, in order to place some bound upon the expected error. In Section 6.4, it was observed that significant errors were incurred upon integration of a distribution discontinuous across the jet boundary, and a similar problem may arise in the integration of U_v in the initial region. Near the nozzle, in a uniform injection problem, the width b of the mixing zone will be very small compared with the local jet radius r_2 (see Fig. 6.9), and in such a case the finite-difference grid (Fig. 6.5) may be too coarse to properly resolve the mixing zone and its velocity profile. This situation is depicted in Fig. 6.11. As b becomes small, U_v approaches the binary distribution $\overline{B}$ from Section 6.4 and errors will again occur in the integrations: in particular, I_{nA_D} cannot be found with any accuracy.

For a constant density jet, it was shown earlier that:-

$$K_{nA_D}(z) = K_{nA_D}(0) + g(z)\{K_{nA_D}(z_c) - K_{nA_D}(0)\} \qquad (6.14)$$

The value $K_{nA_D}(z_c)$ is easily determined by numerical integration as there is no problem of resolution (r_c=0 in Fig. 6.11b). The integration could be taken over any circle of known radius, setting A_c=0 in the construction of $\overline{S}_1$ in 6.16. Also, U_v may be integrated with sufficient accuracy over any area A* so long as the associated width b* is set to give sufficiently good resolution of the mixing zone.

With b* and A* known, A_c^* and A_D^* may be deduced, and from 6.11:-

$$I_n^* = \rho A_c^* + K_{nA_D}^* A_D^*$$

may be evaluated directly. So, $K_{nA_D}^*$ is deduced from:-

$$K_{nA_D}^* = \frac{I_n^* - \rho A_c^*}{A_D^*} \qquad (6.19)$$

The two equations 614 and 6.19 may be used to write:-

$$K_{nA_D}^* = K_{nA_D}(0) + g^*\{K_{nA_D}(z_c) - K_{nA_D}(0)\} \qquad (6.20)$$

where, from 6.13:-

$$g^* = \frac{b^*}{b^*+2r_c^*} \quad ; \quad r_c^* \neq 0,\ b^* \neq 0 \qquad (6.20a)$$

Hence, $K_{nA_D}(0)$ is deduced:-

$$K_{nA_D}(0) = \frac{K_{nA_D}^* - g^* K_{nA_D}(z_c)}{1 - g^*} \qquad (6.20b)$$

A computation of this type is carried out prior to the first integral evaluations (at z=0) in the computer program (see Fig. 6.6), to determine K_{nA_D} at z=0 and $z=z_c$ assuming circular cross-sections. The annular mixing zone A_D is deemed to be poorly resolved at a solution station z if $g(z)<g_{min}$ (see 6.13), in which case $K_{nA_D}(z)$ is evaluated from 6.14: the author has identified $g_{min}=0.7$ as a suitable condition. When $g(z)>g_{min}$, $K_{nA_D}(z)$ is evaluated directly from numerical integration over A(z):-

$$K_{nA_D}(z) = \frac{1}{A_D(z)}\{I_n(z) - \rho A_c(z)\} \qquad (6.21)$$

(at constant density). This permits profile distortion in the initial region, except near the nozzle itself.

All the results obtained above can be extended to the case of variable density jets. For the axisymmetric geometry, the mixing boundaries for the velocity and 'scalar' fields (Chapter 5) are shown in Fig. 6.12: relations for locating the scalar boundaries (denoted by the suffix s) from the dynamic boundaries (denoted by the suffix v in Fig. 6.12 but dropped from earlier discussions in this chapter for simplicity), in order to represent the faster rate of diffusion of mass than momentum, were devised in Chapter 5.

The base distribution $\overline{S}$ (Section 6.4) has been defined over the jet momentum area $A_v \equiv A$. The scalar area A_s is greater than A_v, while the scalar core A_{cs} is smaller than $A_{cv} \equiv A_c$ at the same station z (Fig. 6.12). From Chapter 5:-

$$A_s = \{(1+\delta_2)\sqrt{A_v} - \delta_2\sqrt{A_0}\}^2 \qquad z \leqslant z_{cv} \qquad (5.41a)$$

$$A_{cs} = \{(1+\delta_c)\sqrt{A_{cv}} - \delta_c\sqrt{A_0}\}^2 \qquad z \leqslant z_{cs} \qquad (5.42)$$

where $\delta_c = \delta_2 = 0{,}165$ in the initial region (Chapter 5). In order to enclose A_s, the finite difference grid over which $\overline{S}$ is defined is expanded in the X and Y directions (Fig.6.5) by a factor $(A_s/A_v)^{\frac{1}{2}}$. For axisymmetric jets, $\overline{S}$ becomes, under this expansion, by inspection of 6.6:-

$$\overline{S} = 1 - \left(\frac{r}{r_{2s}}\right)^2 \quad ; \quad A_s = \pi r_{2s}^2 \qquad (6.22)$$

In view of this expansion, and the functional equivalence of the scalar and velocity mixing zone profiles when taken over the scalar and velocity mixing zones (Fig. 6.12 and Chapter 5), the scalar profile $U_s (= U_c = U_T$ by assumption) is given, by analogy with 6.16 to 6.18 above, by 6.17 with:-

$$\overline{S}_1 = 1 - \frac{1}{c_s^2}\{(1-\overline{S})^{\frac{1}{2}} + c_s - 1\}^2 \quad ; \quad c_s = 1 - \left(\frac{A_{cs}}{A_s}\right)^{\frac{1}{2}} \qquad (6.23)$$

subject to $\overline{S}_1 \in [0,1]$. The velocity profile U_v is given from 6.16 and 6.17, where in this case:-

$$\bar{S}_1(r) = \begin{cases} 1 & r<r_{cv} \\ 1 - x_v^2 & x_v = \dfrac{r - r_{cv}}{b_v} \in [0,1] \end{cases} \qquad (6.16)$$

and, since the grid has been expanded and $\bar{S}$ is given now by 6.22:-

$$(1 - x_v^2) = 1 - \left(\frac{r - r_{cv}}{r_{2v} - r_{cv}}\right)^2 = 1 - \frac{1}{c_v^2}\left\{\left[\frac{r_{2s}}{r_{2v}}\right]\frac{r}{r_{2s}} - \frac{r_{cv}}{r_{2v}}\right\}^2$$

Manipulations similar to those in 6.18 give:-

$$(1 - x_v^2) = 1 - \frac{1}{c_v^2}\left\{\left(\frac{A_s}{A_v}\right)^{\frac{1}{2}}(1-\bar{S})^{\frac{1}{2}} + c_v - 1\right\}^2 \qquad (6.24)$$

where again:-

$$c_v = 1 - \left(\frac{A_{cv}}{A_v}\right)^{\frac{1}{2}} \qquad (6.18a)$$

In the computer program (Fig. 6.6), following the expansion of the finite difference grid from A_v to A_s, the profiles U_i (i=s or v) are constructed from the above relations expressed in the following algorithm:-

$$\phi_i = 1 - \frac{1}{c_i^2}\left\{\left(\frac{A_s}{A_i}\right)^{\frac{1}{2}}(1-\bar{S})^{\frac{1}{2}} + c_i + 1\right\}^2 \qquad (6.25)$$

where:-

$$c_i = 1 - \left(\frac{A_{ci}}{A_i}\right)^{\frac{1}{2}} ; \quad \phi_{imin}=0, \ \phi_{imax}=1 \quad (i=s \text{ or } v) \qquad (6.25a)$$

and:-

$$U_i = \phi_i^{\phi_i(p-q)+q+1} \qquad (6.25b)$$

In the initial region p and q take the values in 6.10b. Because 6.25 is phrased in terms of jet areas, the algorithm

may be extended empirically to the case of distorted jet cross sections, where $\bar{S}$ will no longer be given by 6.22.

The mixing zone integral averages K_{nA_D} in variable density jets can still be evaluated from 6.14, or 6.21 with $\rho \to \rho_0$, the injectant density (assuming approximately constant density in the velocity core - see Fig. 6.12):-

$$K_{nA_D}(z) = \frac{1}{A_D(z)}\{I_n(z) - \rho_0 A_c(z)\} \qquad (6.26)$$

6.5.4 Profile Integrals Beyond The Initial Region

From Chapter 5 (in particular 5.33), the coefficient δ_c determines the end z_{cs} of the scalar core ($A_{cs}(z_{cs})=0$) from the predicted erosion of the velocity core:-

$$A_{cs} = 0 \text{ when } \left(\frac{A_{cv}(z)}{A_0}\right)^{\frac{1}{2}} = \frac{\delta_c}{1+\delta_c} \qquad (6.27)$$

Thereafter ($z>z_{cs}$), from Chapter 5:-

$$\delta_c = \frac{(A_{cv}/A_0)^{\frac{1}{2}}}{1 - (A_{cv}/A_0)^{\frac{1}{2}}} \qquad (6.28)$$

so $\delta_c \to 0$ as $z \to z_{cv}$ ($A_{cv}(z_{cv})=0$). The prescription of δ beyond the end of the constant velocity core, where:-

$$\delta^2 = \frac{A_s}{A_v} \qquad (6.29)$$

was described in Chapter 5, and gives the expansion factor for the finite-difference grid. The length of the scalar and velocity transition regions is given by 5.39d: the profile development in the transition region is accomplished by linear variation of p and q between the values in 6.10a and 6.10b (the profiles are still generated by 6.25a-c with the core area equal to zero). Profiles of jets of distorted cross-section generated in this way are illustrated in Chapter 7.

This section is concluded with a description of the numerical integration technique.

6.5.5 Romberg Integration

For the evaluation of the integrals I_n, each integrand (n=0,...,9) is constructed in turn by combining as necessary the properties ρ, and C_p and the profiles U_i (Fig. 6.6b), all of which are computed and stored at the nodes of separate finite-difference grids. The U_i are generated, by the relations given in Sections 6.5.3 and 6.5.4, from within a manipulative subroutine called intgrnd: other sections of the same subroutine are accessed to compute density and specific heat at the nodal points of the grid, so that it is a simple matter to alter profiles or vary formulations for the jet properties (Chapter 5 and Chapter 7).

The requirements of the numerical integration technique have been closely studied. Packer (35) used a Monte-Carlo, random-sampling, iterative method (99), primarily for the integration of complicated velocity profiles in distorted cross-sections. Such methods, in fact, find their application in integrations where the dimensionality is high (typically six or greater): Packer (35) needed only to evaluate A_{shape} (Section 6.4), I_0, I_1 and I_2 for the momentum theory. The Monte-Carlo integration subroutine (NAG d01faf - see (100) or (35)) required 30 cpu seconds on the Honeywell Multics machine to complete each integration: at every iteration, the integrand is evaluated at a number of randomly-chosen points, so that an interpolation routine must be available for use with the node-defined integrand (35). Interpolation was the principal time-consuming operation in the integrations. In the present model, there are in general eleven integrations to be carried out (A_{shape}, I_0,...,I_9) rather than four (35), due to the inclusion of the scalar conservation equations, and use of the Monte-Carlo method would be prohibitively time-consuming.

The alternative is a method of the rule-evaluation type: Gauss quadrature was not considered, since again the points at which which the integrand is evalauated cannot be chosen in advance, so that interpolations would once more be necessary. A method such as the trapezoidal rule is more

appropriate when the integrand is known at a discrete set of points. The accuracy of the integration then depends upon the spacing between the known values, so upon the degree of resolution of the finite difference grid over which the distributions are defined. The finest grid which can be employed, with acceptable storage and computer-time requirements, for the computation of the base distribution in the subroutine epdel (Section 6.4) is of the order 33x33: this, then, excluding any interpolation procedures, places a bound upon the number of points available for the integrations. In order to achieve the highest possible accuracy with this set of known values, the trapezoidal rule is applied iteratively, in a sequence known as Romberg integration.

Consider first the numerical integration of a general function f, by the trapezoidal rule, where f is known at n points $\{x_i : i=1,n\}$ at uniform intervals h upon x a,b , with $x_1=a$ and $x_n=b$:-

$$I = \int_a^b f(x)dx = \frac{h}{2}\{f(x_1) + 2f(x_2) + \ldots + 2f(x_{n-1}) + f(x_n)\} + \mathcal{E} \quad (6.30)$$

The final term represents the error in the numerical integration, provided f is sufficiently smooth. Suppose:-

$$\mathcal{E} = O(h^2) \simeq Ch^2 \quad ; \quad C \text{ constant}$$

In obvious notation, 6.30 can then be written as:-

$$I \simeq I_h + Ch^2 \quad (6.31)$$

The fact that the trapezoidal rule approximates f by a straight line over each interval h implies that the method will be inaccurate unless h is small. If interpolations or spacing refinement are ruled out (see above), it is still of course possible to make the interval between points larger, say Kh (where K is an integer), so that only some of the available function points are used. The integral I

is estimated as:-

$$I \simeq I_{Kh} + C(Kh)^2 \qquad (6.32)$$

Now I_{Kh} will surely be less accurate than I_h, but 6.31 and 6.32 can be combined so as to eliminate C:-

$$(K^2-1)I \simeq K^2 I_h - I_{Kh} = (K^2-1)I_h + I_h - I_{Kh} \qquad (6.33)$$

or:-

$$I \simeq I_h + \frac{1}{(K^2-1)}(I_h - I_{Kh}) \qquad (6.34)$$

By this method, the $O(h^2)$ error term is eliminated. It may be shown (101) that the error in 6.34 is $O(h^4)$, so that the accuracy of the new estimate is better than that of either I_{Kh} or I_h. In principle, the method could then be applied again to I_{Kh} and I_{K^2h} (say) to give another estimate of $O(h^4)$: it would then be possible to combine these two estimates to give a yet more accurate ($O(h^6)$) estimate, and so on until successive estimates converge.

The method may also be applied to double integrals, by application first of the trapezoidal rule in both x and y directions over an equispaced grid (spacing h) of n known function values in each direction:-

$$\iint_A f(x,y)\,dA = \int_c^d \int_a^b f(x,y)\,dx\;dy \qquad \begin{matrix} x & a,b \\ y & c,d \end{matrix}$$

Again by the trapezoidal rule:-

$$\int_a^b f(x,y_i)\,dx \simeq \frac{h}{2}\{f(x_1,y_i)+2f(x_2,y_i)+\ldots+2f(x_{n-1},y_i)+f(x_n,y_i)\}$$

$$\equiv F(y_i)$$

Then:-

$$\int_c^d \int_a^b f(x,y)dx\ dy = \int_a^d F(y)dy = \frac{h}{2}\{F(y_1)+2F(y_2)+\ldots+F(y_{n-1})+F(y_n)\}$$

The error may again be shown to be $O(h^2)$ (102), and the Romberg integration procedure is identical to that described above.

In the present work, the integrand is defined at the nodal points of an equispaced grid with (n+1) rows and (n+1) columns. The value of n is chosen so that a sequence of intervals h, Kh, $K^2h,\ldots,K^rh$ may be taken with the points at which the integrand is to be evaluated always occuring at nodes of the grid (obviating interpolation). In this way a sequence of approximations to an integral is constructed, using first all, then successively fewer of the known points. Each pair of estimates of the same order accuracy are used in 6.34 to obtain an estimate of improved accuracy: when two such have been computed, a more accurate estimate is derived. The process continues until the estimates converge, or until the process reaches its limit (depending on the interval sequence). For a 33x33 grid (as used in the present program), the intervals Δh used are:-

$$\Delta h = h, 2h, 4h, 8h, 16h, 32h$$

where h is the spacing of the grid in the X or Y direction (Fig. 6.5). The method applies to grids with different interval widths in the two directions, the analysis taking $\Delta h_X = \alpha \Delta h_Y$, α constant (102).

The computer implementation uses successively finer subgrids (finally using all the available integrand values) to estimate the integral and performs extrapolations (by 6.34) whenever possible. The subroutine, called romberg, is modified from that given by Gerald (102) in order to permit a two-dimensional, node-defined integrand, and for the purposes of the jet program returns the average value of the integral (see 6.1c).

6.6 The Solution Of The Differential Equations

6.6.1 Ordering Of The Equations

Provision is made for the numerical solution of the following equations, derived in Chapters 4 and 5:-

i) The propagation equation (dA_D/dz) - equation 5.26a
ii) The core area equation (dA_c/dz) - equation 5.26b
iii) The excess velocity decay equation (dh_v/dz) - equation 4.27
iv) The rate of change of angle β ($d\beta/dz$) - equation 4.37
v) The axial injectant concentration decay equation (dh_c/dz) - equation 5.23
vi) The axial temperature difference decay equation (dh_T/dz) - equation 5.19

The integral terms appearing in these equations are evaluated by the methods described in Section 6.5 (see also Fig. 6.6), and a differential equation solution subroutine called 'soleqn' (Section 6.6.2) is called to solve the system over over a step dz (Section 6.3.3 and Fig. 6.3): the equations themselves are supplied from a subroutine called odes, accessed by soleqn at intermediate steps in the solution from z to z+dz. The structure of the subroutine odes is shown in Fig. 6.13.

It is natural, because the propagation equation 'drives' the theoretical solution, that this should be placed first in the ordering of the system: the core area equation is placed second in view of the close coupling between the two (5.26a and 5.26b). Even so, serious instability was observed in the solution of this pair of equations as originally written: a smooth solution for the outer and inner mixing boundaries (Fig. 6.14) could not be obtained. The problem was overcome by partial uncoupling of the equations: 5.26b was used to substitute for dA_c/dz in the propagation equation 5.26a, rearrangement giving:-

$$\frac{dA_D}{dz} = \frac{2\sqrt{\pi A}\left[\mathcal{F}_0(z) + \mathcal{F}_1(z) - \frac{bA}{2\sqrt{AA_c}} \cdot \frac{w\cos\beta\frac{dK_1}{dz} + h_v\frac{dK_2}{dz} + A\frac{dP}{dz}}{\{w\cos\beta K_{1A_c} + h_v K_{2A_c}\}}\right]}{\left[1 + \frac{\{w\cos\beta K_{1A_D} + h_v K_{2A_D}\}}{\{w\cos\beta K_{1A_c} + h_v K_{2A_c}\}} \cdot \frac{b}{2\sqrt{AA_c}}\right]} \quad (6.35)$$

(in the notation of Chapters 4 and 5 - the suffix v is dropped for simplicity), where:-

$$b = \sqrt{\frac{A}{\pi}} - \sqrt{\frac{A}{\pi}_c} \quad (6.35a)$$

The numerical solution of 6.35 and 5.26b is entirely stable and appears to give good predictions (Chapter 7).

The condition $A_c \to 0$ does not raise a singularity in 5.26a, since:-

$$\frac{1}{\sqrt{A_c}}\frac{dA}{dz}_c = \frac{2}{\sqrt{\pi}}\frac{dr}{dz}_c \to 0 \quad \text{as} \quad r_c \to 0 \quad \text{(see Fig. 6.14)}$$

In 6.35 however, the dA_c/dz term is split and a possible singularity as $A_c \to 0$ must be considered. In the computer program, the numerical solution of the pair of equations is terminated when $(A_c(z_m)/A_0) < \overline{A}_{cmin}$ is predicted at some station z_m, where A_{cmin} must be prescribed (a value 0.0005 was used for the predictions in Chapter 7). The end of the constant velocity core is then determined by extrapolation (using a truncated Taylor series) from the point $(z_m, A_c(z_m))$ at which the solution has been stopped to the point $(z_c, A_c=0)$ (Fig. 6.14). Since dA_c/dz at z_m is known in the numerical solution, from its latest evaluation within odes:-

$$A_c(z_c) = 0 \simeq A_c(z_m) + (z_c - z_m)\frac{dA}{dz}_c\Big|_{z=z_m}$$

Hence:-

$$z_c \simeq \left(z_m \frac{dA}{dz}c \Big|_{z=z_m} - A_c(z_m) \right) \Big/ \frac{dA}{dz}c \Big|_{z=z_m} \qquad (6.36)$$

Similar extrapolations are used to determine the values of the other dependent variables at z_c.

If the condition $(A_c(z_m)/A_0)<\bar{A}_{cmin}$ is raised within a solution step, as is likely, so that $z_k<z_m<z_{k+1}$ for some integer k, the solution of all the equations is temporarily halted at z_m (from within odes) by setting to zero all the markers isolvad, isolvac etc described in Section 6.3.2. The solver subroutine soleqn then proceeds to the end of the current solution step without altering any of the conditions predicted at z_m: on exit at z_{k+1}, z is reset as z_m and z_c is computed from 6.36.

At $z=z_c$, A_c and dA_c/dz are set identically to zero and all the markers except isolvac are reset to 1. The point $z=z_c$ must be treated as one of dicontinuity in the solution; the values of the dI_n/dz cannot be found by backward differences at z_c, due to the change in the nature of the inner mixing boundary downstream of the end of the core (Fig. 6.14). Hence, the unknown derivatives are set to zero for the first step away from z_c: the implied errors are not serious if the step is short.

The ordering of the equations (in odes) to be used beyond z_c is quite clear. The equations from the momentum theory are written in advance of the scalar equations (Fig. 6.13), as the former represent the foundation of the model. The coupling between the momentum and scalar equations has not been found to cause any instability: some comments, however, must be made concerning the dh_v/dz and $d\beta/dz$ equations.

In the initial region $(z<z_c)$, the jet excess velocity function is determined from the condition of constant velocity within the core:-

$$\frac{dh_v}{dz} = - \frac{d}{dz}\{w\cos\beta\} \qquad (4.29)$$

Hence the $d\beta/dz$ equation must be solved in the initial region. The equation for the change in h_v (4.29 in the initial region or 4.27 beyond it) is wriiten in advance of the $d\beta/dz$ equation 4.37 (Fig. 6.13). This follows from the assumption that deflection under a crossflow is a complicating action upon an axisymmetric jet (Chapter 4), so that the $d\beta/dz$ equation is of secondary importance to that for dh_v/dz.

For typical swirl input conditions (h_{v0}=100ms^{-1}, β_0=90°, swirl rate ω=500 rad/sec) at constant density, it was observed that, in the maximum deflection region (Chapter 4):-

$$\left|\frac{dh_v}{dz}\right| \simeq 10^5 \quad ; \quad \left|\frac{d\beta}{dz}\right| \simeq 10^2$$

The wide difference in magnitude between these two terms, and their interrelationship in 4.27 and 4.37, causes difficulty in the numerical solution of the equations, manifest in exceptionally long computer run times (see below). In the initial region, where the rate of decay of h_v is much slower, or in the case of injection into stronger crossflows, where $|d\beta/dz|$ is larger, no instability was observed. The wide variation in magnitudes stated above so conditions the coupled pair of equations that solution steps must be very greatly subdivided, within soleqn, in order to obtain an accurate solution. This subdividing of the interval may be monitored through the number of calls made to the subroutine odes, for derivative re-evaluations, over each step dz: for an axisymmetric jet, it was found that about 80 such calls were made over each step in the main region, while this rose to more than 2000 in the problem case identified above. Computer times under these circumstances become prohibitively long, and in some jet into weak crossflow cases, no solution could be obtained to the required accuracy (Section 6.6.2).

Once again, this problem has been overcome by partially uncoupling the dh_v/dz and $d\beta/dz$ equations. This is done by holding $d\beta/dz$ constant in the dh_v/dz equation over the step from z_k to z_{k+1} (any k):-

$$\frac{d\beta}{dz} = \left.\frac{d\beta}{dz}\right|_{z=z_k}$$

while the $d\beta/dz$ equation itself is not altered. The error involved in this simplification is slight, provided steps are kept reasonably short (Chapter 7): the procedure radically improves the conditioning problem, the number of calls to odes reducing from 2000, for the case mentioned above, to about 100-200. Thus, any relative magnitude of crossflow, from very strong to very weak, is permitted (Chapter 7).

6.6.2 The Subroutine 'soleqn'

The name soleqn is used here as a general name for the subroutine called in order to solve the differential equation over a step dz, as two such routines have been considered (see below). The call statement is:-

```
call soleqn(z,zend,n,y,tol,odes,work,iwork,ifail)
```

and the parameters have the following significance:-

z(real) - on entry, z contains the initial value of the independent variable. On exit it contains zend, or the value of z at which any error occurs.

zend(real) - the final value z+dz of the independent variable.

n(integer) - the number of differential equations in the system. In this work n=6 (Section 6.6.1) although all the equations are not always used (Fig. 6.13).

y(real array)	-	on entry, y(1),...,y(n) hold the values of the dependent variables at z (the ordering is given in Section 6.6.1). On succesful exit, these labels contain the values of the dependent variables at zend.
tol(real)	-	on entry tol is set to a positive tolerance as a demand upon the absolute accuracy of the computed solution (see below).
odes(external subroutine)	-	for derivative evaluations (Section 6.6.1)
w(real array)	-	working space.
iw(integer)	-	size of the w array.
ifail(integer)	-	failure flag: returned as zero upon succesful exit at zend, otherwise as a positive number depending on the error.

The accuracy parameter tol has been given a value 10^{-8} in the presnt work. This appears to be the least stringent value which may be used in obtaining stable numerical solutions. When a value tol=10^{-7} was used, the following behaviour was observed in the numerical results:-

a) The prediction $A_c \to 0$ could not be guaranteed as A_c became small. This is due to the inherent singularity in the revised equation 6.35 and the less precise solution for A_c when tol is increased. The value of $\overline{A}_{cmin}$ was required to be much larger than that given in Section 6.6.1, in order to halt the numerical solution before the onset of instability.

b) The stability of the predictions downstream could not be guaranteed, with jet axial velocity

not monotonic decreasing (with z) in some deflected jet predictions.

In order to solve the equation system in his program, Packer (35) made a call to the NAG library subroutine d02eaf (35,100): the call statement is exactly that given above for soleqn, and this NAG subroutine has also been used in the present program. In the cause of system independence, an almost identical subroutine has been made available, by the author, by implementation and minor modification of the subroutine stint, listed in the collected algorithms from ACM (103). Preliminary investigation of stint showed the results to agree with those of the NAG routine at the same value for tol, while requiring less computer time to produce a solution.

A description of the Gear method, which both these routines employ, and its computer implementation is given by Hall and Watt (104).

6.7 Output From The Computer Model

A specimen of the output of numerical results is shown in Fig. 6.15. Output other than the specialised cross-section shape and property distribution data, used for computer plotting, is directed from a subroutine called in_out. This subroutine is divided into two sections: the first is concerned with data input and program declaration (Section 6.3.2), and the second with the determination of some details of the flow at the current solution station z. It is mentioned that such output is produced immediately before the evaluation of dz for the next solution step (and a fresh call to 'soleqn' - Section 6.6), so that the flow properties are properly computed from the extant conditions at z, already used in the initial value formulation for the next incremental solution step.

Numerical results are directed either to a structured file (Fig. 6.15) or to data files to be used by plotting programs. In the structured file, problem specifications

and the initial conditions are followed by the predicted values of the following quantities at selected axial stations:-

$$\frac{z}{D_0} \ , \ h_v \ , \ \beta \ , \ T_m \ , \ h_c \ , \ v_{ratio} \ , \ u_m, \ u_{mean}, \ \left(\frac{A}{A_0}\right)^{\frac{1}{2}} \ , \ E_m \ , \ TIME$$

The quantities not defined elsewhere are:-

$$v_{ratio} = \frac{w_N}{u_m} = \frac{w\sin\beta}{h_v + w\sin\beta}$$

$$TIME\Big|_{z_k} = TIME\Big|_{z_{k-1}} + \frac{(z_k - z_{k-1})}{u_m(z_{k-1})}$$

and:-

$$u_{mean} = \frac{\int_A \rho u^2 dA}{\int_A \rho u dA} = \frac{h_v^2 I_2 + 2h_v w\cos\beta I_1 + w^2\cos^2\beta I_0}{h_v I_1 + w\cos\beta I_0}$$

$$E_m = \frac{d}{dz}\int_A \rho u dA = \frac{d}{dz}\{h_v I_1 + w\cos\beta I_0\}$$

The variable TIME allows comparison between program predictions and experiment for the position of the jet tip with time (Chapter 8). The character 'C' is printed in the first column when the end of the constant velocity core ($z=z_c$) is predicted (Fig. 6.15). Other data related to the numerical solution itself (such as the value A_{shape}, profile integral averages, the number of evaluation calls to the subroutine odes, etc - all described earlier in this chapter) is output to a separate file.

The prescription of stopping criteria for the program is also made from within in_out. The following settings have been made:-

a) A limit on the number (nstep) of solution steps, given in the input data (Section 6.3.2)

b) The excess velocity h_v becoming zero.
c) The same condition ocurring upon β, h_T or h_c.
d) The radial penetration r_z exceeding the maximum value given in the input data (Section 6.3.2).

The output of numerical results is terminated with the statement 'LIMIT' appearing beneath that column upon whose principal variable the stopping condition has operated (Fig. 6.15).

INPUT	var	UNITS
CHAMBER DATA		
NOZZLE DIAMETER	d0	m
RADIUS AT INJECTION	ri	m
CHAMBER DIAMETER	rm	m
AMBIENT FLUID DATA		
CHAMBER PRESSURE	p	bar
CHAMBER TEMPERATURE	ta	K
MOLECULAR WEIGHT OF AMBIENT	amw	Kg/Kmol
INJECTION DATA		
MOLECULAR WEIGHT OF INJECTANT	fmw	Kg/Kmol
INJECTION VELOCITY	um	ms^{-1}
INJECTION TEMPERATURE	tcl	K
DEGREE OF DEVELOPMENT OF NOZZLE VELOCITY PROFILE	rc0	nondim.
MONITORS		
NUMBER OF SOLUTION STEPS	nstep	nondim.
OUTPUT INTERVAL	wstep	nondim.

TABLE 6.1 PROGRAM INPUT DATA

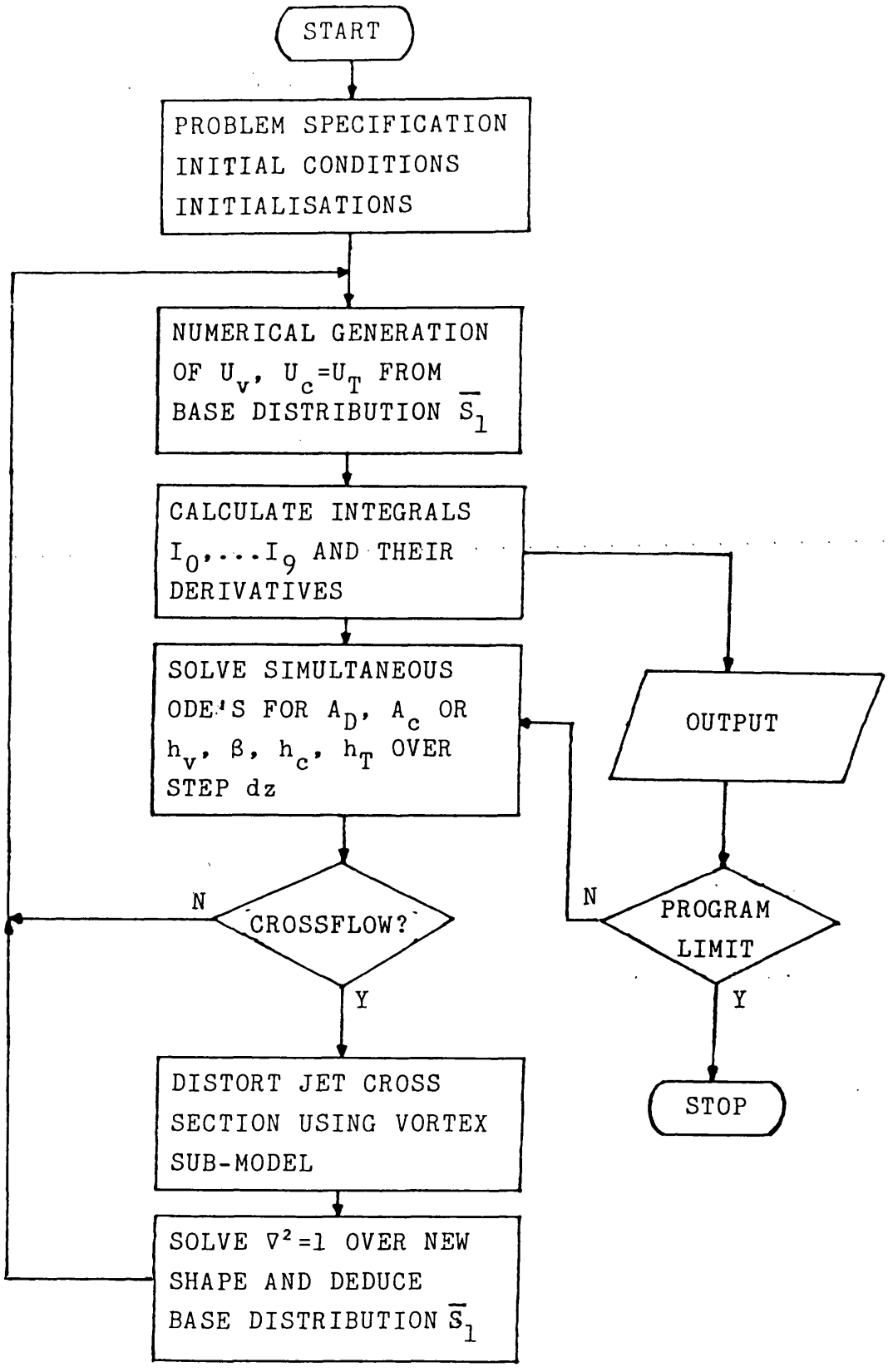

FIG 6.1 OUTLINE SOLUTION PROCEDURE

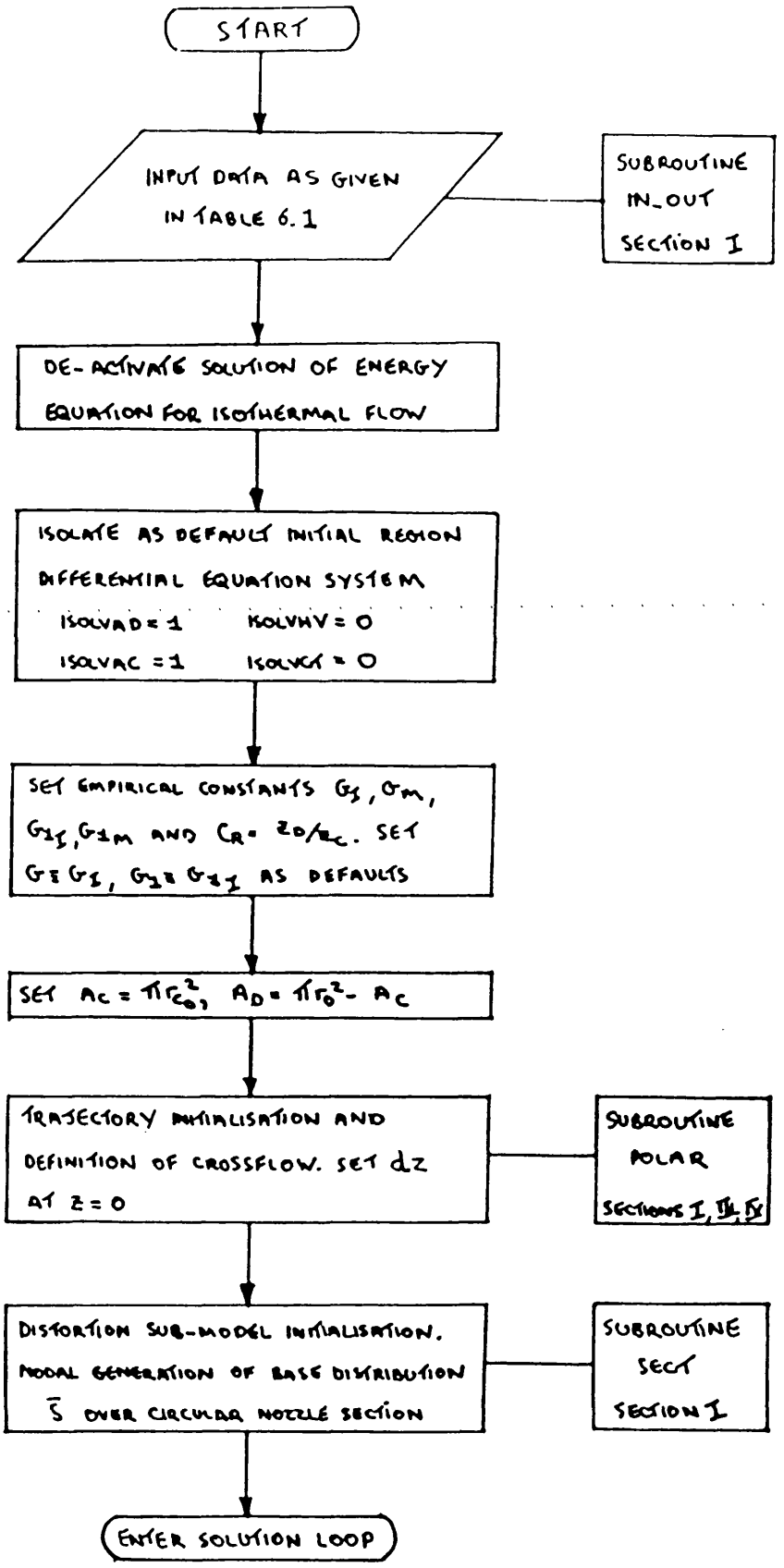

FIG. 6.2 PROBLEM DEFINITION SEQUENCE

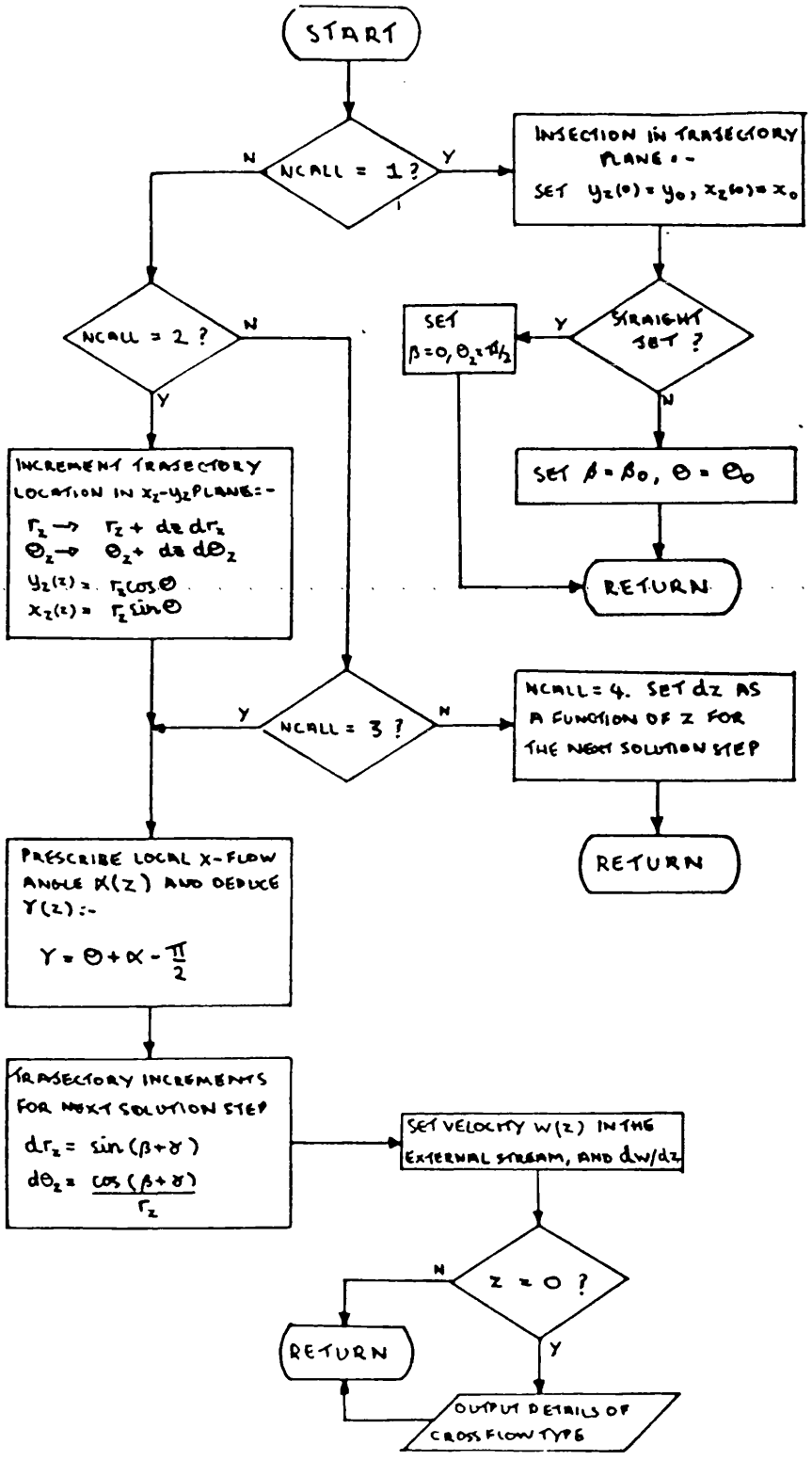

FIG. 6.3 THE SUBROUTINE POLAR

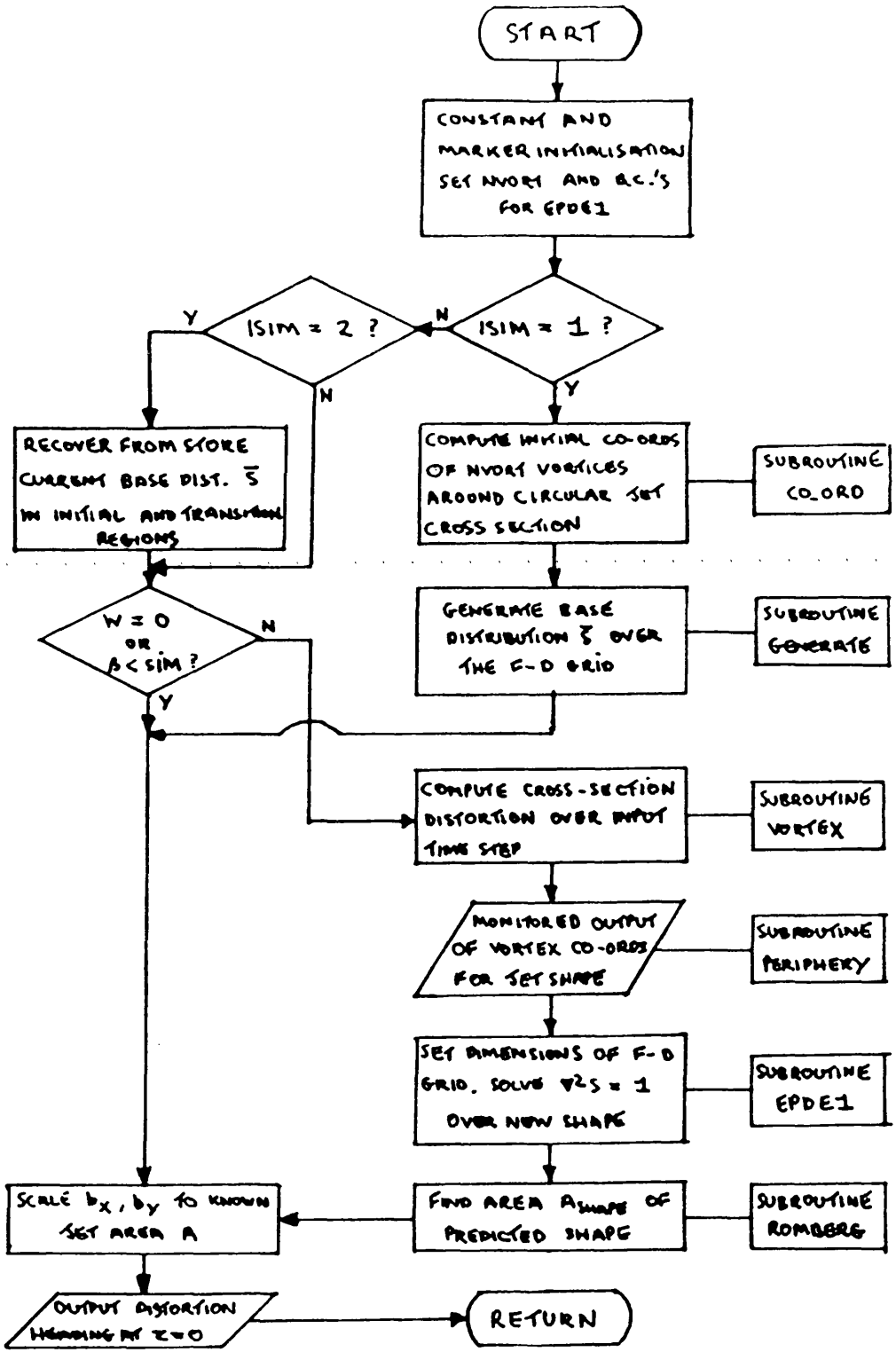

FIG. 6.4 THE SUBROUTINE SECT

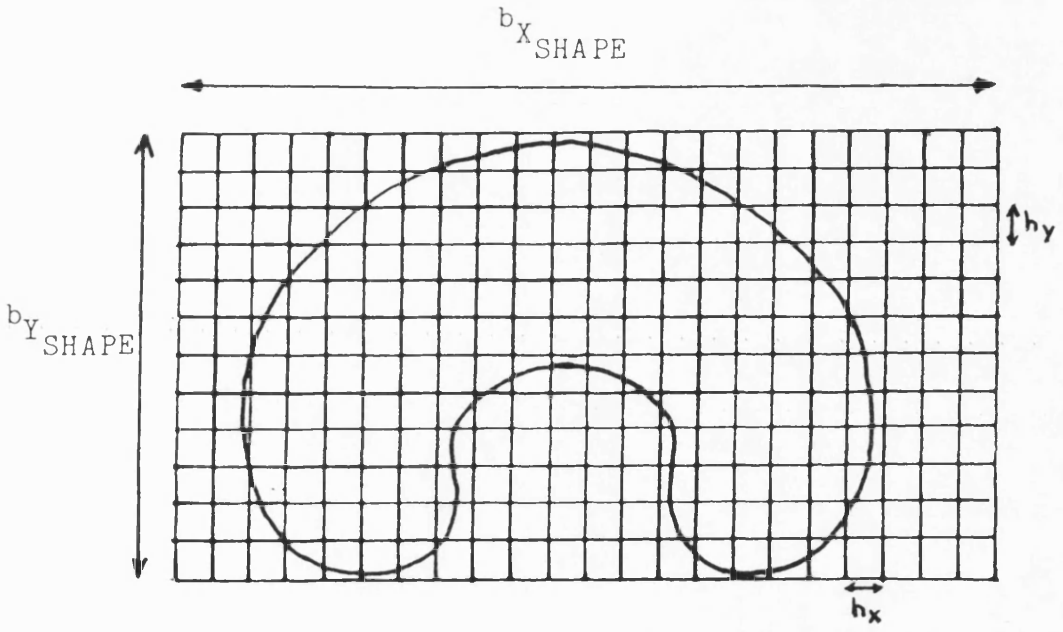

A_{SHAPE}: AREA OF PREDICTED SHAPE

SCALING FOR JET MIXING MODEL:-

$$b_X = b_{X_{SHAPE}} (A/A_{SHAPE})^{\frac{1}{2}}$$

$$b_Y = b_{Y_{SHAPE}} (A/A_{SHAPE})^{\frac{1}{2}}$$

FIG. 6.5 FINITE DIFFERENCE GRID

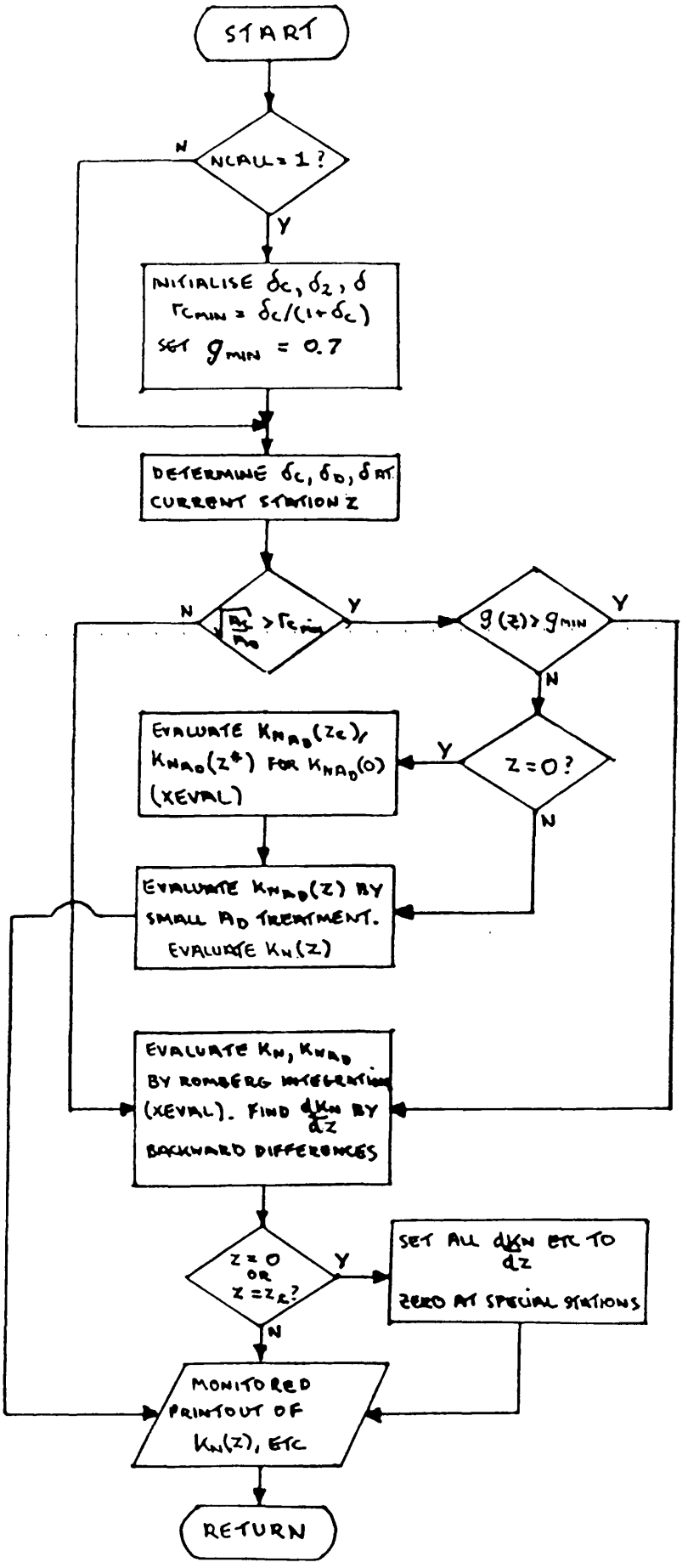

FIG. 6.6a THE SUBROUTINE KN FOR INTEGRAL EVALUATIONS

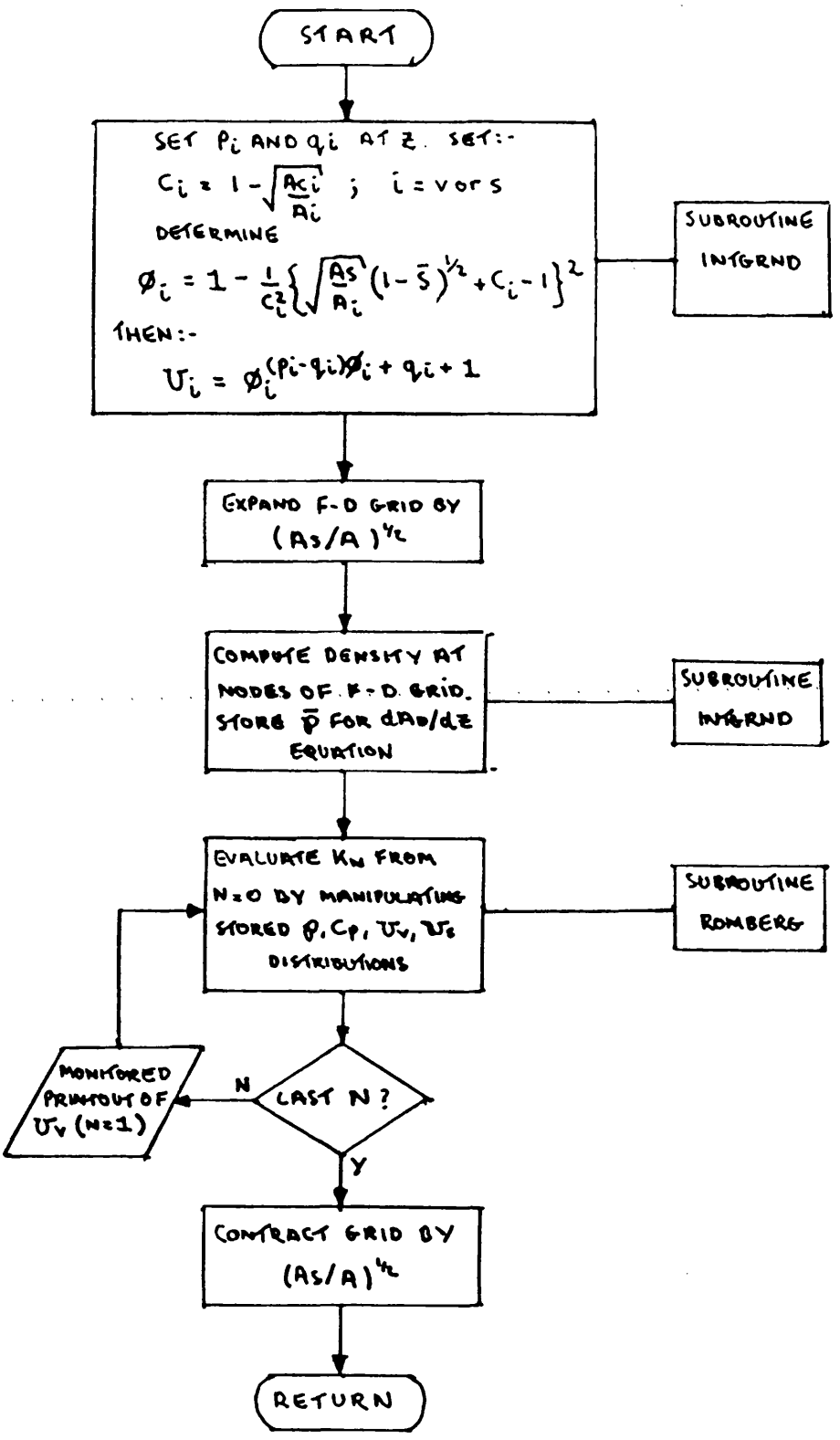

FIG. 6.6b INTEGRAL EVALUATIONS BY XEVAL

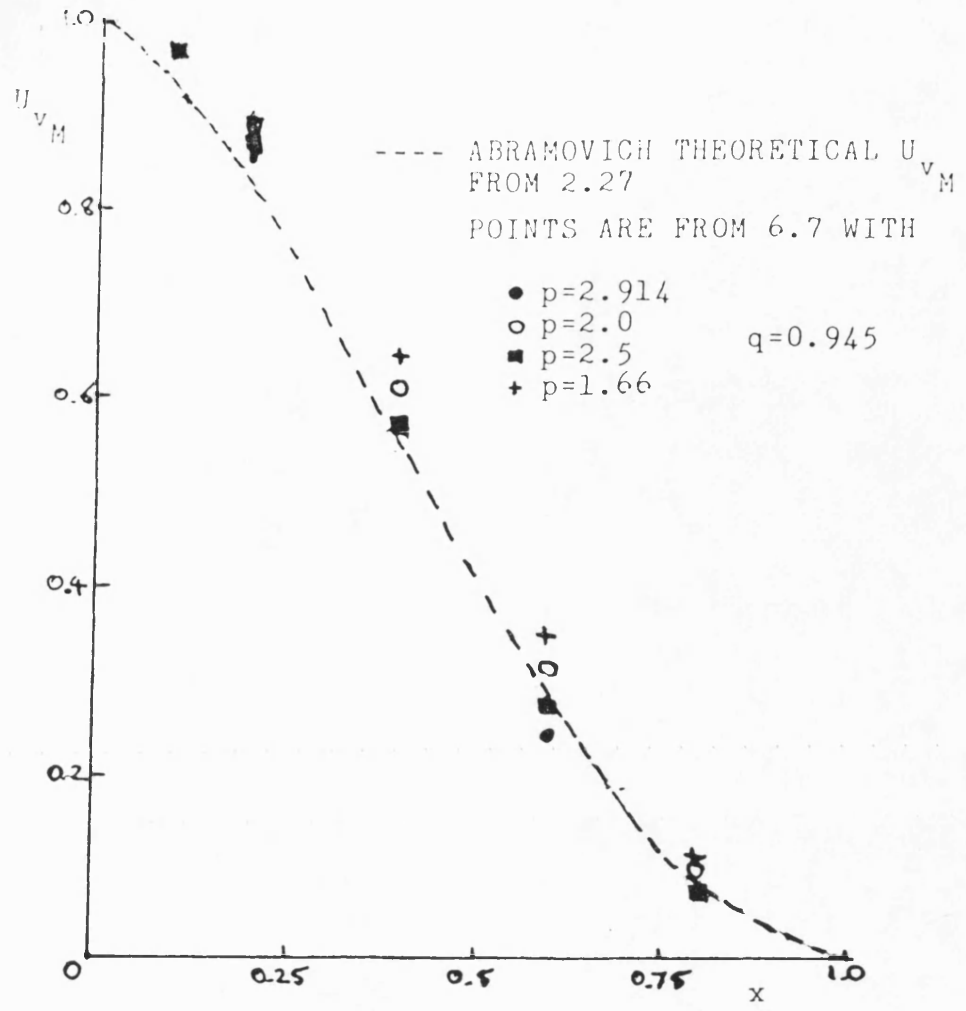

FIG. 6.7a CONSTRUCTION OF THE MAIN REGION VELOCITY PROFILE

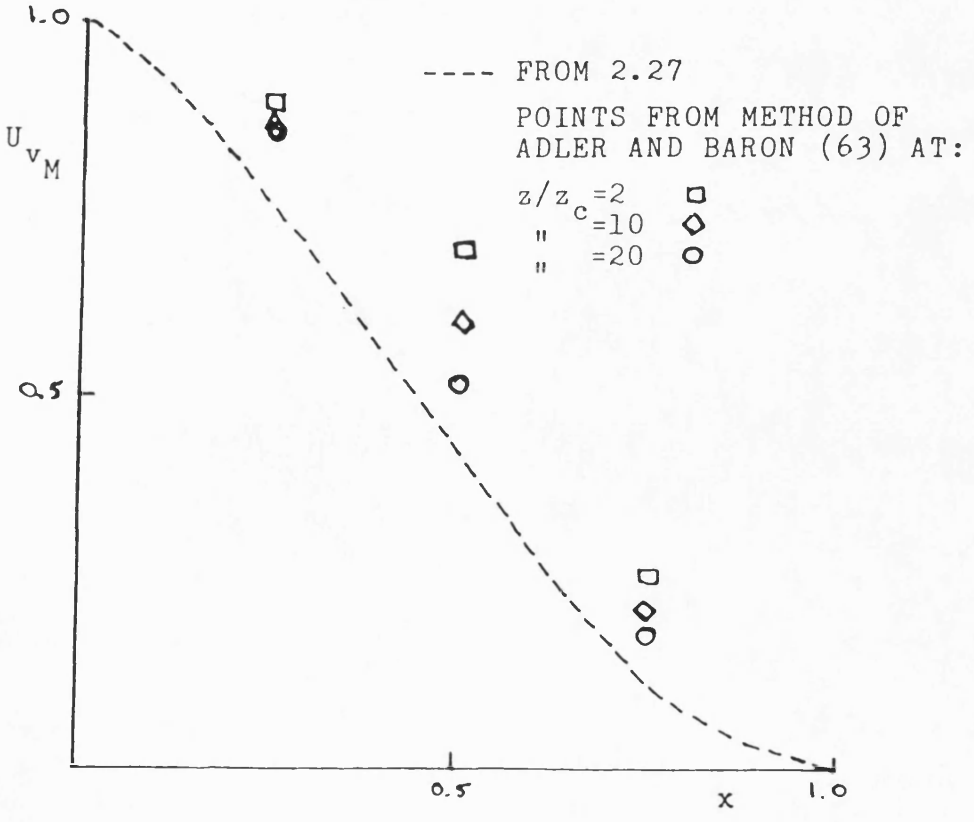

FIG. 6.7b PROFILE CONSTRUCTION BY ADLER AND BARON (63)

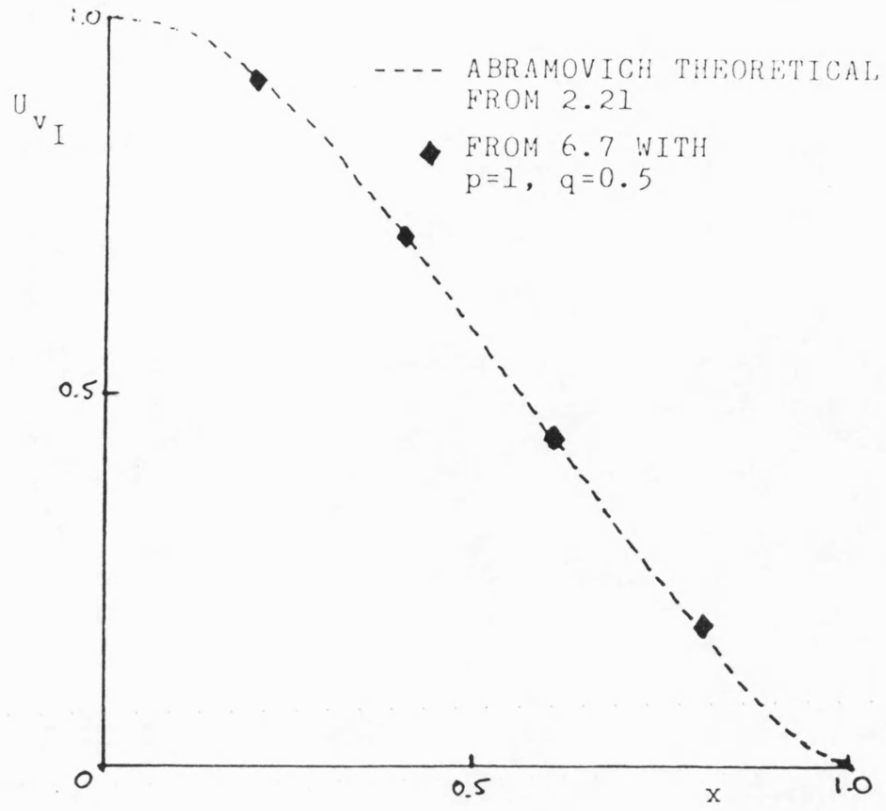

FIG. 6.8a CONSTRUCTION OF THE INITIAL REGION VELOCITY PROFILE

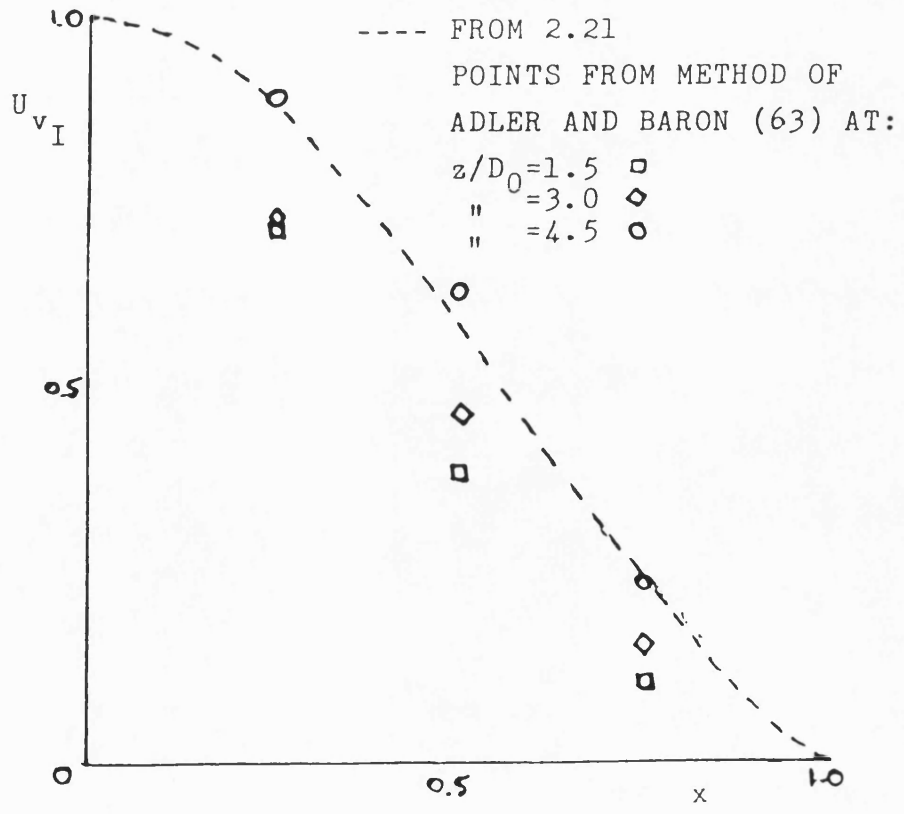

FIG. 6.8b CONSTRUCTION BY ADLER AND BARON (63)

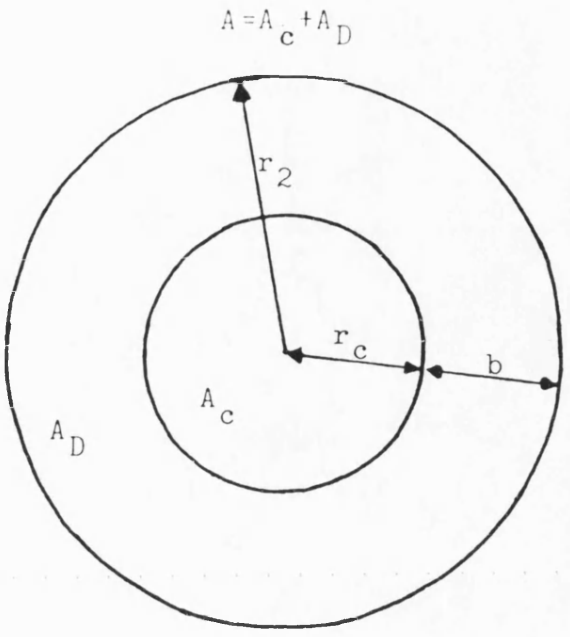

FIG. 6.9 GEOMETRY OF THE JET CROSS-SECTION

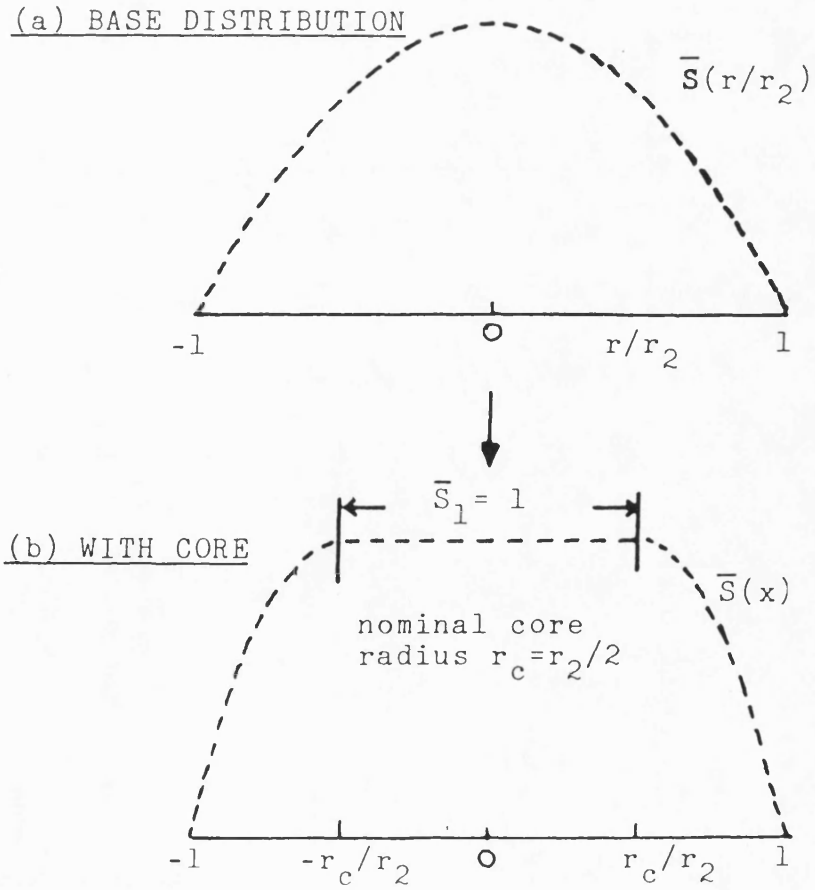

FIG. 6.10 TRANSFORMATION OF BASE DISTRIBUTION $\bar{S}$ IN THE INITIAL REGION

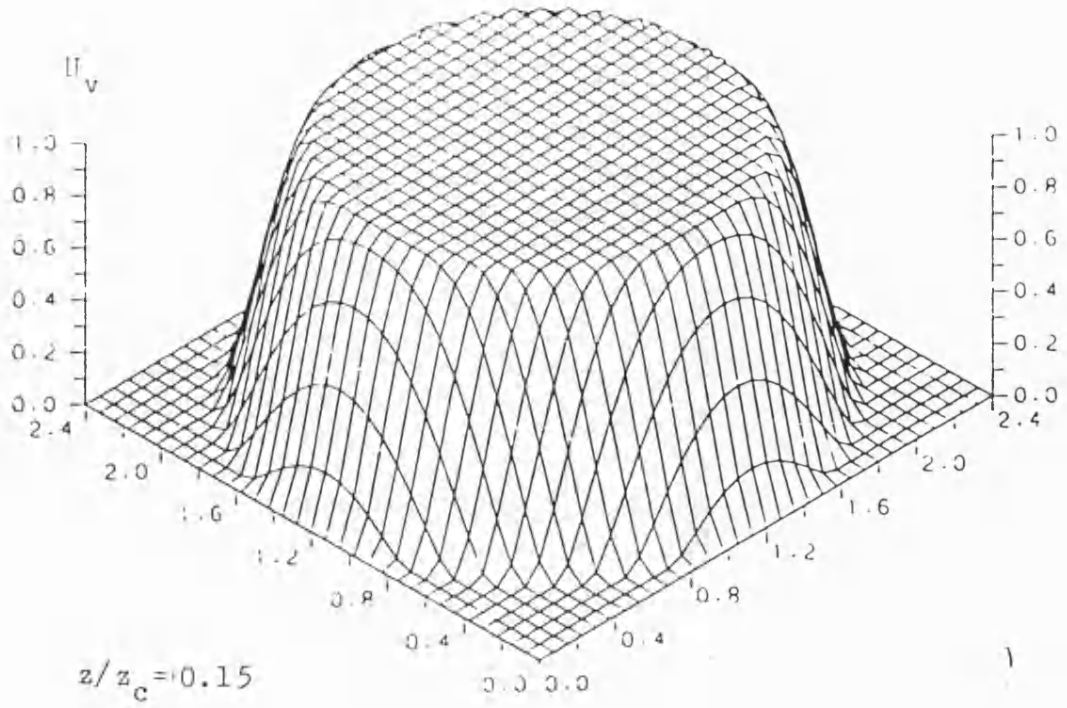

FIG. 6.10c INITIAL REGION VELOCITY PROFILE

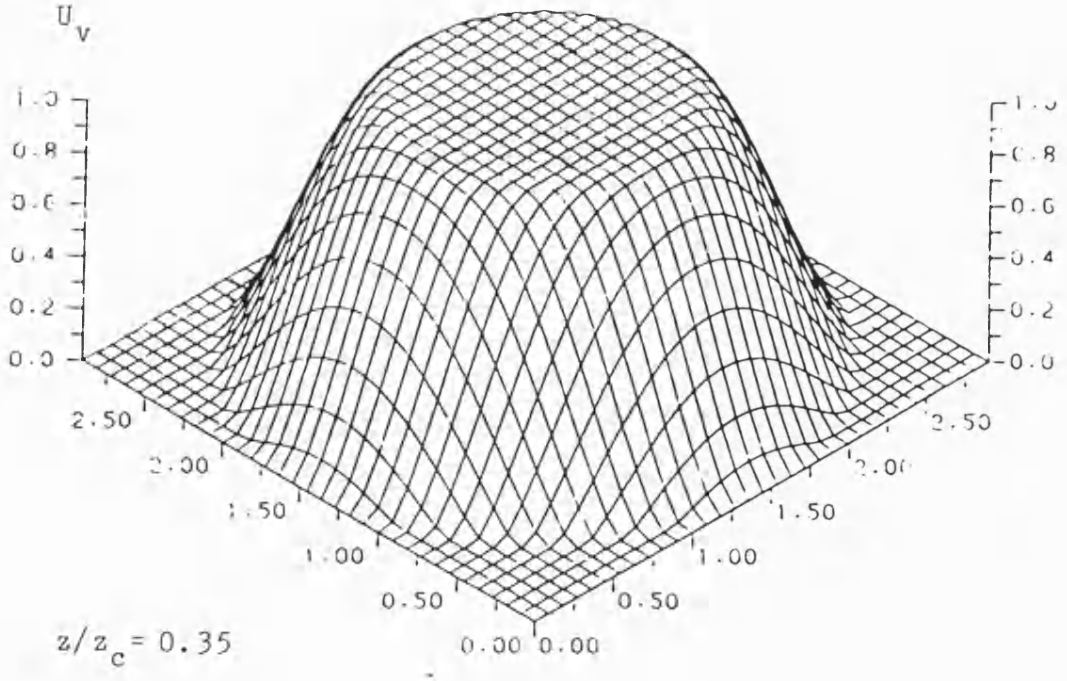

FIG. 6.10d INITIAL REGION VELOCITY PROFILE

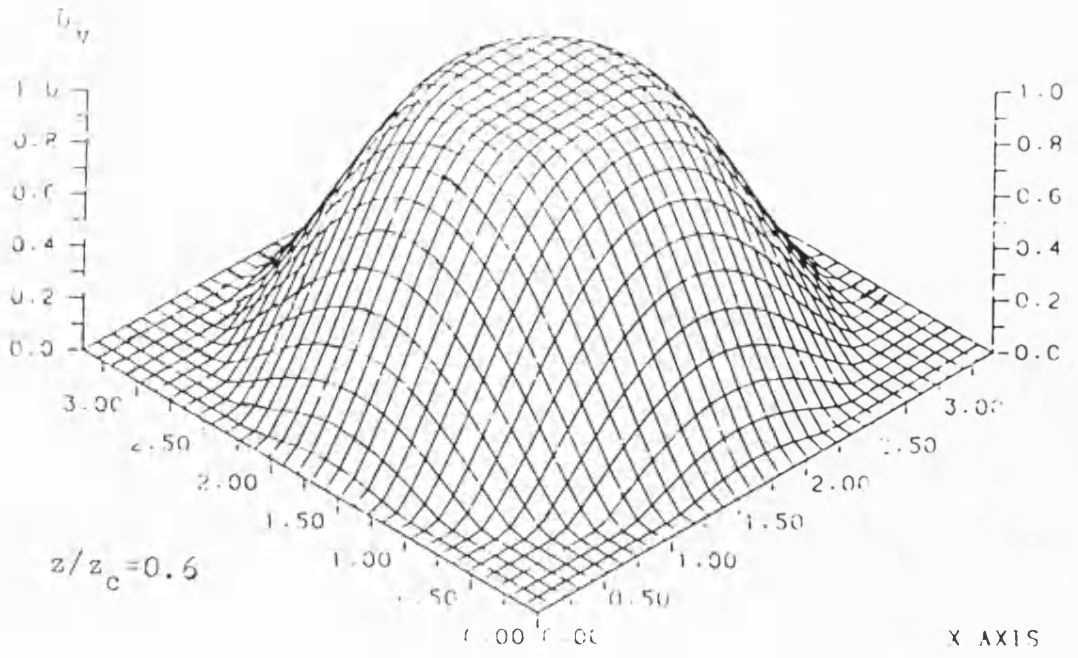

FIG. 6.10e INITIAL REGION VELOCITY PROFILE

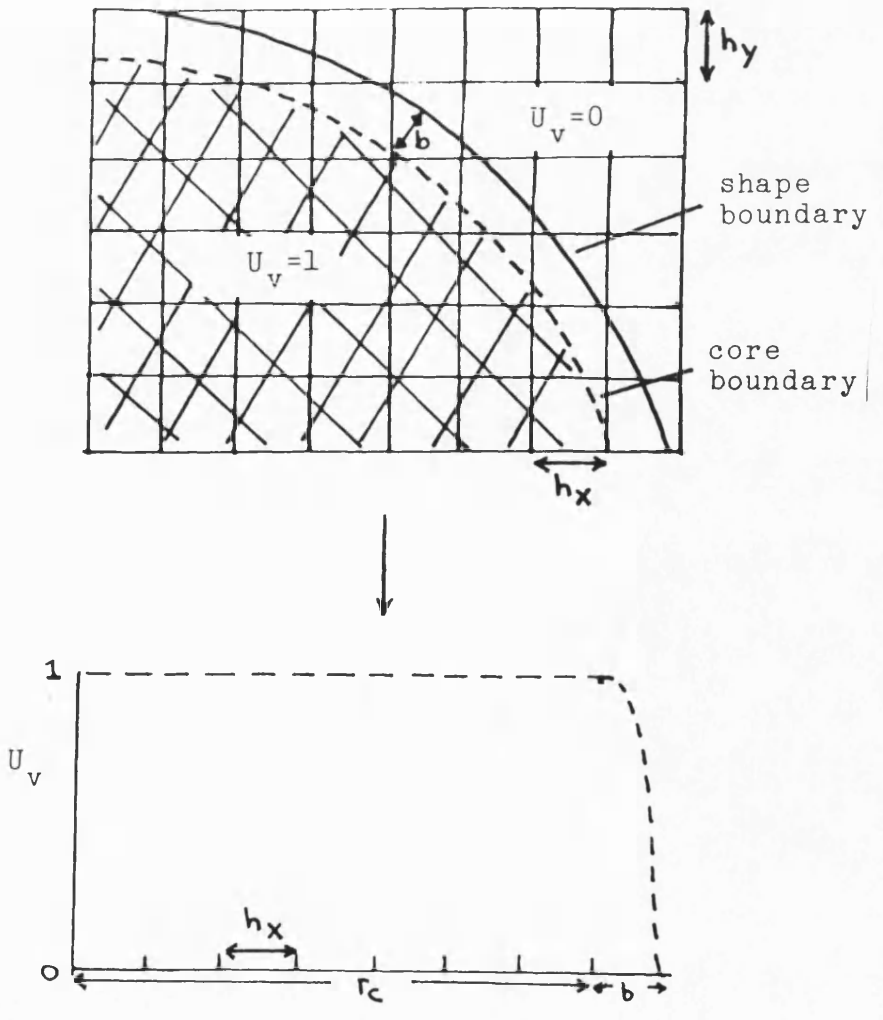

FIG. 6.11 POORLY RESOLVED MIXING ZONE WIDTH b

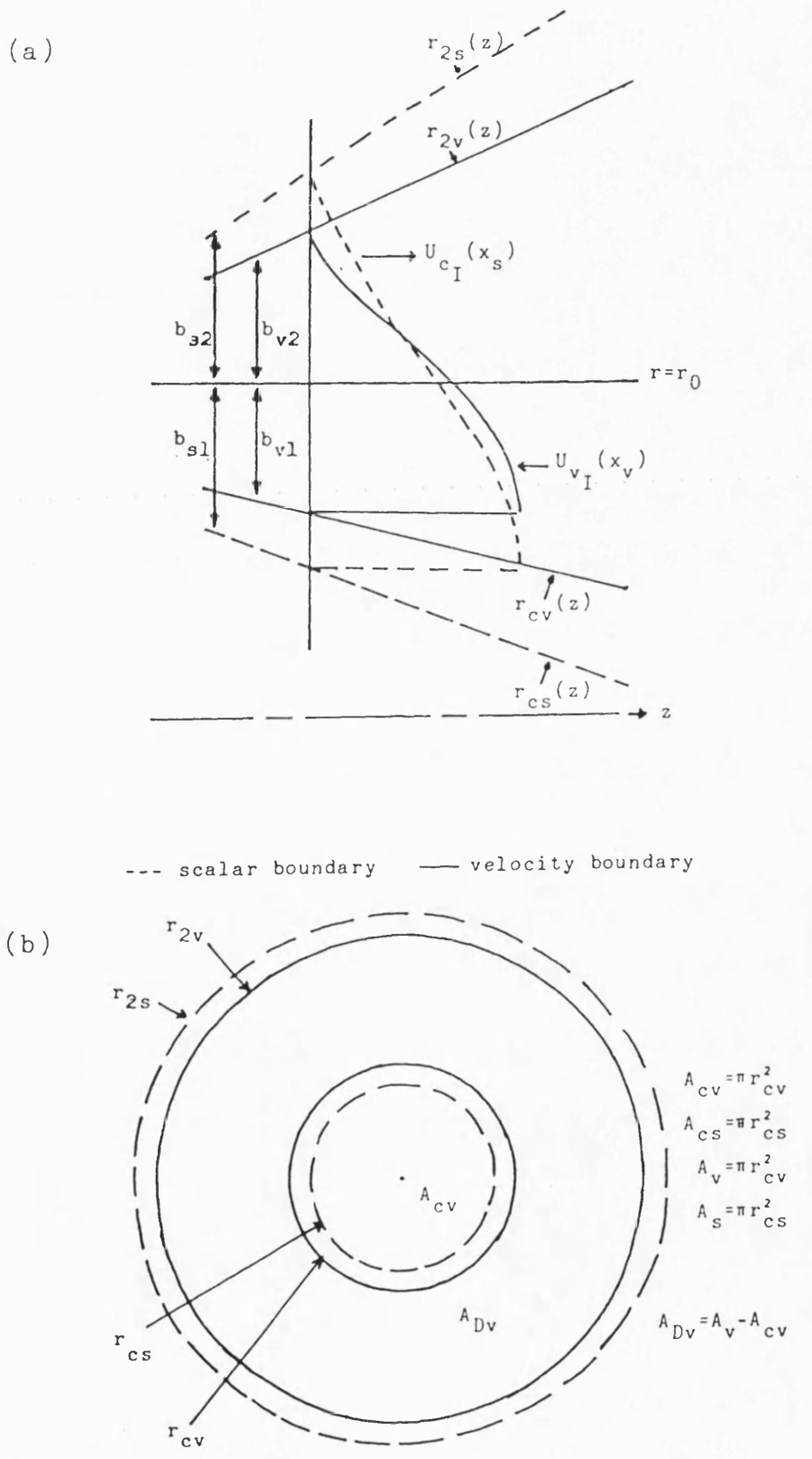

FIG. 6.12 MIXING ZONE WIDTHS FOR VELOCITY AND SCALARS (FROM CHAPTER 5)

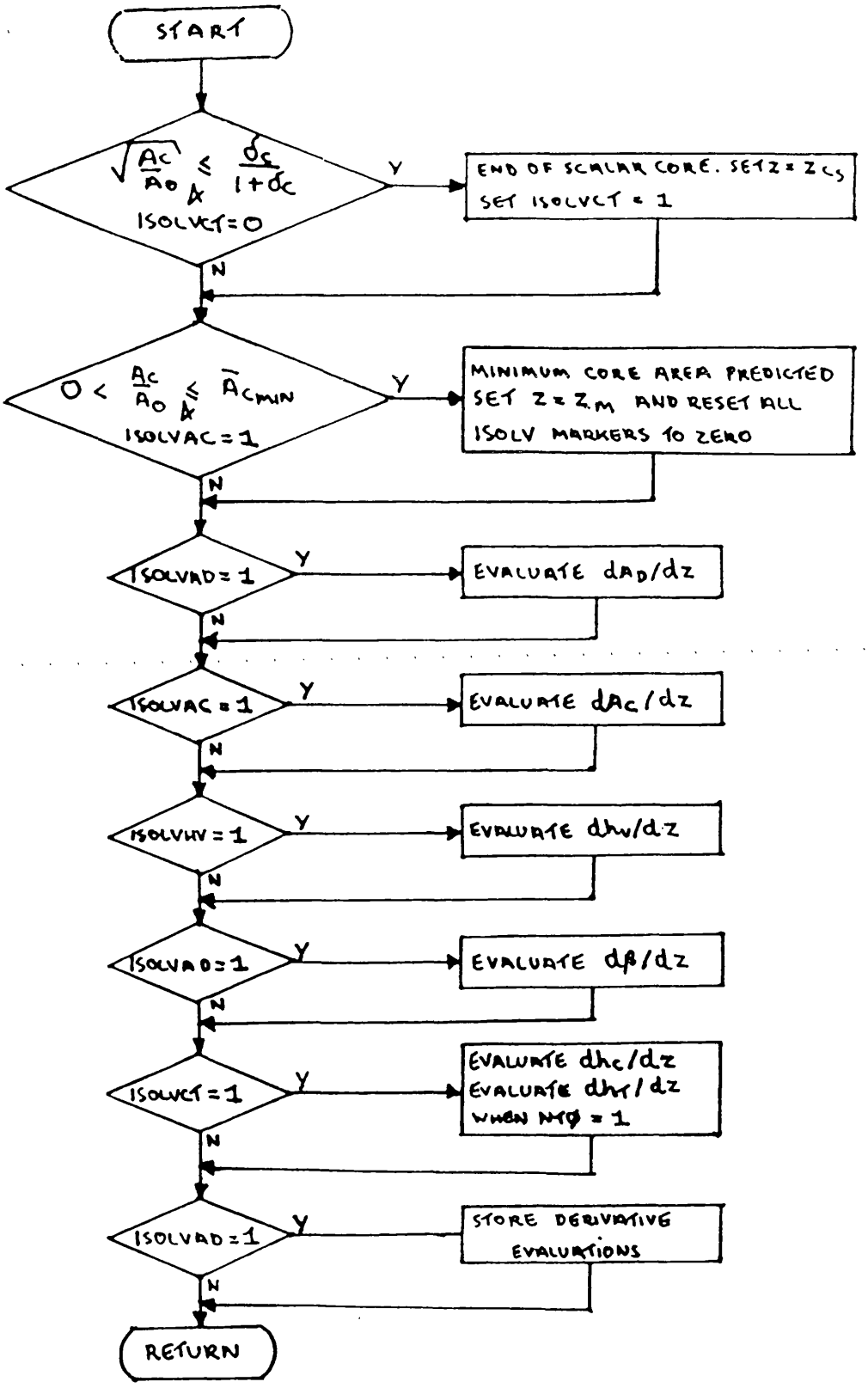

FIG. 6.13 THE SUBROUTINE ODES

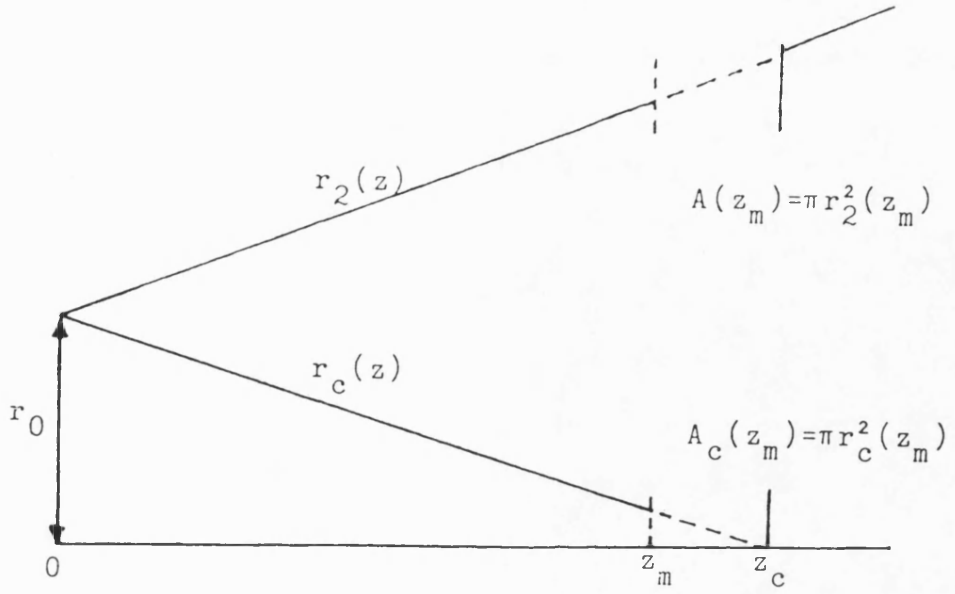

FIG. 6.14 EXTRAPOLATION TO THE END OF THE CORE

- PROGRAM SPRAY -

- FLOW TYPE - FORCE-VORTEX : SW = 500.00

- CROSS-SECTION DISTORTION

- INTEGRAL FORMULATION: DIRECT

injection data :- c-l da/df n = 0.145 tcl/ta = 0.923 cpf/cpa = 2.641

djet =.200-02 rco/ho = 0.9995

0.000	100.000	90.00	600.00	1.000	0.00	100.00	100.00	1.00	14.154	.000+00
1.014	100.000	89.99	600.00	1.000	0.01	100.00	97.60	1.19	1.417	.200-04
2.708	99.998	89.96	600.00	1.000	0.03	100.00	93.37	1.50	0.836	.560-04
5.237	99.991	89.79	600.00	1.000	0.05	100.00	86.46	1.99	1.078	.110-03
8.157	99.982	89.27	600.00	1.000	0.08	100.01	77.40	2.62	1.594	.180-03
9.719	99.795	88.71	600.52	0.989	0.10	100.01	72.10	3.01	2.007	.220-03
C 9.958	99.772	88.63	600.55	0.984	0.10	100.01	70.67	3.06	6.346	.230-03
10.708	99.695	88.39	604.99	0.973	0.11	99.59	69.13	3.24	2.017	.250-03
11.458	98.125	88.01	605.46	0.958	0.12	98.52	67.18	3.47	2.146	.270-03
12.429	95.695	87.34	605.89	0.929	0.13	96.26	64.02	3.83	2.995	.300-03
14.433	87.372	84.93	606.12	0.836	0.16	88.65	55.46	4.92	5.229	.370-03
17.335	63.927	76.05	610.63	0.622	0.25	68.10	39.05	7.52	15.772	.490-03
21.559	18.549	42.22	621.80	0.350	0.41	34.07	22.12	13.87	48.988	.790-03

LIMIT

FIG. 6.15 EXAMPLE COMPUTER OUTPUT

CHAPTER 7

PRESENTATION OF THEORETICAL RESULTS AND COMPARISON WITH EXPERIMENT

Chapter 7 - Notation

A	-	jet area (m^2)
A_c	-	area of constant property core (m^2)
A_D	-	area of turbulent mixing zone (m^2)
A_0	-	nozzle area (m^2)
b	-	mixing zone width (m)
b_X, b_Y	-	jet dimensions defined in Fig. 7.25
c	-	injectant mass concentration
C_p	-	specific heat capacity (J/kgK)
$\overline{C}_p$	-	ratio of specific heats ($C_{pi}/C_{p\infty}$)
dx_z, dy_z	-	incremental lengths in Fig. 7.27 (m)
dz	-	solution step length (m)
E_m	-	mass entrainment rate (kgs^{-1})
G	-	width growth coefficient for an axisymmetric jet
G_I, G_M	-	constant values for G in the initial and main regions
G_l	-	enhanced jet spreading rate coefficient
G_{lI}, G_{lM}	-	constant values for G_l in the initial and downstream regions
h_c	-	maximum concentration function ($=c_m$)
h_T	-	maximum temperature difference function ($=\Delta T_m$)
h_v	-	maximum excess velocity function ($=u_m - w\cos\beta$)
I_n	-	property distribution integrals (Chapter 5)
J	-	momentum ratio ($=1/n\mathcal{R}^2$)$^{\frac{1}{2}}$
K_n	-	average value of I_n in 7.24
m	-	velocity ratio for axisymmetric jets ($=w/u_0$)
$\dot{m}$	-	jet mass flux

M	-	fluid molecular weight (kg/Kmol)
n	-	injection density ratio ($=\rho_\infty/\rho_0$)
N	-	direction normal to centreline direction in Fig. 7.27
p,q	-	distortion parameters
P	-	pressure
r_c	-	boundary of constant property core (m)
r_2	-	outer mixing boundary (m)
$r_{\frac{1}{2}}$	-	jet half width defined in 7.1 (m)
r_0	-	nozzle radius (m)
r_z	-	polar co-ordinate for jet centreline (m)
R_0	-	universal gas constant
T	-	temperature (K)
u	-	jet velocity (ms^{-1})
U_c	-	concentration distribution function
U_{c_I}, U_{c_M}	-	" " " for the mixing zone in the initial and main regions of an axisymmetric jet
U_T	-	temperature distribution function
U_{T_I}, U_{T_M}	-	" " " for the initial and main regions of an axisymmetric jet
U_v	-	as above for jet velocity
U_{v_I}, U_{v_M}		
$\overline{U}_v$	-	average value of U_v over A
w	-	external stream velocity (ms^{-1})
w_N, w	-	components of velocity w normal and parallel to jet centreline direction (ms^{-1})
x_z, y_z	-	co-ordinates of trajectory plane
Y_c	-	distance defined in Fig. 7.25

z	-	jet centreline co-ordinate
z_c	-	end of constant property core
z_D	-	end of transition region
$\mathcal{R}$	-	velocity ratio for uniform crossflow ($=w/u_0$)
β	-	angle between jet centreline direction and crossflow
δ	-	diffusion coefficient (Chapter 5)
δ_c, δ_2	-	diffusion coefficients (Chapter 5)
Δu	-	$=u-w$
ΔT	-	$=T-T_\infty$
θ	-	injection temperature ratio ($=T_0/T_\infty$)
θ_z	-	jet centreline polar co-ordinate (rad)
ν_T	-	turbulent dynamic viscosity
ξ	-	jet maximum velocity axis
ρ	-	density (kg/m^3)
$\overline{\rho}$	-	$=\rho_\infty/\rho_1$
ω	-	swirl rate

Subscripts

0	-	at the nozzle
m	-	maximum value in a cross-section
i	-	injectant
s	-	pertaining to scalars
v	-	pertaining to velocity
1	-	on the jet axis
∞	-	in the free stream

Superscripts

$\rightarrow$	-	vector
$\hat{}$	-	unit vector

Chapter 7
Presentation Of Theoretical Results And Comparison With Experiment

7.1 General Introduction

In this chapter, the performance of the computer model described in Chapter 6 will be discussed. In general, three distinct topics require attention:-

1/ The determination of the necessary empirical input to the model, by comparison between prediction and experiment in a number of test cases.

2/ Comparisons between predictions afforded by the model (optimised from point 1/) and the available resource of experimental data.

3/ The examination of the range of applicability of the model, with respect to the various injection characteristics (crossflow types, injection velocity, temperature and composition, etc), determined both from 2/ and from the parametric variation of input to the computer program.

In the first part of this chapter, each of these topics is considered, in turn, in the case of an axisymmetric jet. In the second part, the prediction of deflected jets is undertaken, with particular attention being paid to the method of determination of the empirical input (point 1/ above). The relationship between the present work and those integral models described in Chapter 4 is discussed.

7.2 Prediction Of Axisymmetric Jets

7.2.1 The Submerged Jet At Constant Density

This limiting case ($m=w/u_0=0$) was considered in detail during the theoretical development in Chapter 3, an analytical solution being completed for the steady mean flow. The problem constitutes the test case for straight jets. The assumed mixing zone, radial velocity profiles and the associated width growth coefficents for the three regions were prescribed earlier (see Chapters 3 and 6)). The principal geometric relations describing the jet structure are summarised in Fig. 7.1a.

In the computer model, velocity profiles are generated numerically by the auxiliary function method of Adler and Baron; development of the velocity profile in the transition region is accounted for by linear variation of the distortion parameters p and q (Chapter 6 and Fig. 7.1a).

The computer prediction of the submerged (m=0) jet enabled by these settings is illustrated in Fig. 7.1b, in terms of the decay of the normalised axial velocity u_m with axial distance z. A uniform injection velocity $u_0=100ms^{-1}$ was prescribed arbitrarily, and used in all other predictions except where given otherwise. The prediction in Fig. 7.1b is almost identical (in the main region) to the analytical solution in Fig. 3.7, and this is taken as an indication that a sufficiently accurate numerical solution can be obtained with the step sizes used for the prediction: the initial step size was $dz=D_0/10$, increasing to $D_0/2$ by $z/D_0=20$, and remaining thereafter at that value (the setting of dz was described in Chapter 6).

The prediction of velocity decay in the transition region (Fig. 7.1b) is more natural than in the Abramovich-type analysis, where no decay from $u_m=u_0$ is permitted until the start of the main region: axial velocity then follows a power law decay (Chapter 3). According to the present work, the velocity u_m reduces to about 90% of the injection velocity u_0 at the transition section z_D ($z_D\simeq 7.5D_o$ in

Fig. 7.1b). The data of Albertson et al (65) is affected by the presence of a nozzle boundary layer (see later), as are the measurements of Kamotami and Greber (39): the details of the flow near the nozzle do not influence the behaviour in the downstream limit, as illustrated in Fig. 7.1c using data at large axial distances collected by Chen and Rodi (96).

The predicted increase in jet mass flux with axial distance is again very similar to the analytical solution from Chapter 3, comparing well with the experimental data (Fig. 7.2). The entrainment rate into the jet in the initial region is approximately one third of the constant rate in the main region (Hill (43,64) and Chapter 3). The mass flux measurements of Sforza (72) (Fig. 7.2) are discussed again later in the context of variable density jets.

Rajaratnam and Pani (54) reported measurements of the outer mixing boundary $r_2(z)$ for a submerged, constant density jet. In view of the difficulty in determining r_2, as that radius where the transverse velocity gradient becomes negligibly small (Chapter 2), it is more usual to determine experimentally the jet half-width according to velocity, denoted $r_{\frac{1}{2}}(z)$:-

$$U_v(r_{\frac{1}{2}}) = \tfrac{1}{2} \qquad (7.1)$$

For the main region, assuming the similarity profile U_{v_M} for velocity from Chapter 2:-

$$U_{v_M} = U_v = \{1-0.44(r/r_{\frac{1}{2}})^{1.5}\}^2 \qquad (2.24)$$

The outer boundary r_2 may be found from 7.1 and measured values of $r_{\frac{1}{2}}(z)$:-

$$U_{v_M}(r_2) = 0 \Rightarrow r_2(z) = \frac{r_{\frac{1}{2}}(z)}{0.44} \qquad (7.1a)$$

Data for the main region was manipulated in this way by

Abramovich (32): the results, together with the data from Rajaratnam and Pani (54) are shown in Fig. 7.3 for the assessment of predicted jet spread. The computed boundary falls slightly below the experimental points. In general, these measurements are more sensitive to the detail of the injection conditions than the 'integrated' mass flux data in Fig. 7.2: Rajaratnam and Pani (54) identified a boundary layer on the outside of the nozzle (r_2/r_0=1,1 at z=0 in Fig. 7.3), which is not accounted for in this work. Part of the discrepancy between prediction and experiment in the main region may be attributed to the effect of a nozzle boundary, reducing the length of the core (see later), while any further error will be due to the empirical spreading rate assumptions for the transition region (although this is likely to be slight).

The nozzle fluid concentration field for this jet can be predicted using the semi-empirical, mass/momentum diffusion assumptions described in Chapter 5. For verification of the computer model, the value of the integral I_c, where:-

$$I_c = \int_{A_s} \rho u c dA_s$$

and the 'scalar' mixing area A_s was defined in Chapter 5, was monitored at each solution step within the initial region, and was found to remain approximately constant, in accordance with the principle of conservation of injected material (Chapter 5):-

$$\frac{dI_c}{dz} = 0$$

By 'approximately constant' is meant that I_c did not vary between any two solution stations by a percentage greater than did the integral $I_u = \int_A \rho u^2 dA$, the condition I_u=constant being maintained, within the accuracy of the numerical solution, in satisfaction of the condition of axial momentum conservation, upon which the theory of the initial region depends (Chapter 3).

In order to satisfy the injectant conservation condition, it was necessary to define separate mixing boundaries for velocity and 'scalars' (concentration and temperature): the scalar boundaries are displaced from those predicted for velocity using the empirical coefficients δ_c (for the core boundary), δ_2 (for the outer mixing boundary in the initial region) and δ (for that boundary beyond the end of the core). The details were given in Chapter 5. Computer optimisation (based on the monitoring of I_c) suggested the following:-

$$\delta_c=\delta_2=0.165 \text{ giving, by inference } \delta = \left(\frac{A_s}{A}\right)^{\frac{1}{2}}=1.165\left(\begin{matrix}\text{main}\\ \text{region}\end{matrix}\right)$$

The setting $\delta_c>0$ causes a more rapid erosion of the core of constant concentration than of velocity (Chapter 5), as shown in Fig. 7.4a (the end of the scalar core is denoted z_{cs}). Decay of injectant concentration on the axis therefore precedes velocity decay, as indicated in Fig. 7.4b, where predicted concentration decay with distance along the axis is compared with the measurements of Chigier and Beer (105) and Shirakashi and Tomita (90). Agreement in the transition region is improved upon allowing for a nozzle boundary layer at the nozzle (90) (see below), while the downstream limit is well represented (Fig. 7.4c) according to the data of Becker et al and Birch et al (given in (96)). Also shown in Fig. 7.4a is the difference between the analytical solution for the (velocity) core boundary from Chapter 3, which shows slight curvature, and the computer solution, for which the boundary is straight. The length z_c of the core is the same in both cases, and the loss of detail in the numerical solution is not significant.

The setting $\delta=1.165$ for the main region may be compared with the data from many sources collected by Chen and Rodi (96), which suggests a (mean) value $\delta=1.178$. A comparison between computer predictions showed that there was no significant effect, on concentration decay, of variation of δ between these values.

Finally in this section, predictions are recorded for the case of a submerged jet with a boundary layer inside the nozzle lip. Recourse is made to the measurements of the inner mixing boundary reported by Rajaratnam and Pani (54). The boundary layer is accounted for in the computer model by the initial condition (at z=0) on the velocity core area A_c (Chapter 6). For the results of Rajaratnam and Pani (54) (Fig. 7.5a) this condition was taken as:-

$$\left(\frac{A_c}{A_0}\right)^{\frac{1}{2}} = \frac{r_c}{r_0} = 0.9 \quad \text{at } z = 0 \qquad (7.2)$$

and the resulting computed mixing boundary compares favourably with the data. The reduction in core length z_c, as a result of this nonuniformity at the nozzle (Fig. 7.5a), brings predicted axial velocity and concentration decays into closer agreement with the experimental data in the transition region, as shown in Fig. 7.5b and Fig. 7.5c (the nozzle profile measurements of Kamotami and Greber (39) suggested $r_c/r_0 \simeq 0.94$ in their experiments).

7.2.2 The Constant Density Jet In A Coflowing Stream

Although not directly related to the study of deflected jets, toward which the present work is ultimately directed, this particular configuration remains of importance in the assessment of the predictive capabilities of the computer program. First, the resource of experimental data provides the necessary axial property decay, and spreading rate, information for the investigation of velocity field predictions and, in the extension to variable density jets, of temperature and composition computations (Section 7.2.3). Also, in the case of a deflected jet, the velocity component w of crossflow in the centreline direction plays a similar role in the propagation equation (Chapter 4), in inhibiting mixing, as the coflowing stream velocity w considered below.

The prediction of the inner edge of the mixing zone in the initial region, $r_c(z)$, for a constant density jet in a coflowing stream is shown in Fig. 7.6. The ratio of the

coflowing stream to the injection velocity is $m=w/u_0=0.257$, and measurements in this case have been reported by Rajaratnam and Pani (54). The nozzle boundary layer apparent in the experiment (Fig. 7.6) has been accounted for in the computations: the analytical solution for uniform injection velocity (Chapter 3) is included for comparison.

The effect of a non-zero velocity in the external stream is to inhibit turbulent mixing, compared with the submerged (m=0) jet. This is demonstrated in Fig. 7.7 by the prediction of the case m=0.25 and the data for that case from Forstall and Shapiro (52) (supplemented by data for an almost constant density case (58)). The length of the initial region is greater, and the excess axial velocity decay less rapid, than for the case m=0. The latter, Δu_m, is defined by:-

$$\Delta u_m = u_m - w = h_v \qquad (7.3)$$

and is a dependent variable in the numerical solution (Chapter 4). The prediction of the initial region length and velocity decay is reasonably good (Fig. 7.7), and the effect of a boundary layer at the nozzle (set from 7.2) on velocity decay is illustrated (Landis and Shapiro (52) reported, for their experiments, only that the nozzle velocity profile was 'nearly uniform').

The predicted spread of the jet when m=0.25 is shown in Fig. 7.8a, and is found to be in reasonable agreement with the available data. The curved jet boundary in the main region is a consequence of the dependence of the width growth law on the decreasing function h_v when w>0 (see Chapter 3):-

$$\frac{dr_2}{dz} = \frac{db}{dz} = 0.22\left(\frac{h_v}{h_v + 2w}\right) \qquad z>z_D \qquad (7.4)$$

For the flow far downstream, predictions in Fig. 7.8b are compared with the observations of Antonia and Bilger (66) under the conditions m=0.222 and m=0.333: the jet half width $r_{\frac{1}{2}}$ was determined from the computed boundary r_2, in

the main region, using 7.1a.

Further predictions concerning this type of jet are given in connection with variable density flows.

7.2.3 The Effects Of Temperature And Composition Variation

7.2.3a Isothermal Jets

Newman and Brzustowski (31) reported measurements of an isothermal, liquid spray of carbon dioxide in nitrogen: the flow was treated analytically as a dense, single-phase, submerged jet (m=0) after the theory of Abramovich (32), upon the assumption that the liquid atomised into a fine mist of droplets very near the nozzle (Chapter 1). The relevant initial conditions for the experiment were given as:-

injection velocity:	$u_0=2.2ms^{-1}$
chamber temperature:	$T_\infty=22^\circ C$
chamber pressure:	P=900psig
density ratio $n=\rho_\infty/\rho_0$:	n=0.27
nozzle diameter:	$D_0=0.66mm$

The prediction of velocity decay on the jet axis, by the present computer program, under these conditions is given in Fig. 7.9 in comparison with the experimental data. The density distribution used in the computations was that given by Newman and Brzustowski (31) (see Chapter 5):-

$$\rho = \frac{\rho_0}{c + (\rho_0/\rho_\infty)(1-c)} \quad ; \quad c = h_c U_c \qquad (7.5)$$

where c is the injectant concentration by mass at any point. The principal feature of the results is the reduced rate of mixing in the dense jet (n<1) compared to the constant density case (n=1). The length of the initial region is predicted as $z_c/D_0 \simeq 9.84$, about double that in the isodense case (Fig. 7.9). The velocity decay further downstream is in agreement with the experimental data, and with the solution of Newman and Brzustowski (31) in the main region. The length of the transition region, in the latter work,

was determined by the 'point source of momentum' method described in Chapter 3, so that there was no decay of velocity prior to the start of the main region. The theory was restricted solely to the case m=0. The other velocity decay prediction shown in Fig. 7.9 is discussed later.

In Fig. 7.10, the predicted outer mixing boundary $r_2(z)$ for the (m=0,n=0.27) jet is shown in comparison with the approximate, observed jet envelope traced from a photograph (31). The jet flow appears to be properly enclosed by the computed boundary.

A more rigorous assessment of the jet spread is a comparison between the predicted and measured increase in mass flux along the jet. No such data was given (31), but Ricou and Spalding (61) and Sforza (72) observed that, when m=0, the normalised jet mass flux, $\dot{m}/\dot{m}_0$, where:-

$$\dot{m}(z) = \int_{A(z)} \rho u dA \qquad (7.6)$$

is a simple function of the quantity $\sqrt{n}(z/D_0)$. The data from Fig. 7.2 (in fact obtained from a number of variable density jet experiments (72)) is replotted in this way in Fig. 7.11a. Although the general trend is correctly reproduced in the numerical solution for the n=0.27 case, some underprediction of the increase in mass flux (hence entrainment rate) is indicated for the dense jet (Fig. 7.11a). The error is due to the simplified density-dependence in the propagation equation (32) (Chapter 2). The implications of this error are considered later.

If it is assumed that the length z_D to the end of the transition region is sufficiently accurately given by $z_D/z_c=1.5$ (Chapter 3), the correlation of mass flux data in Fig. 7.11a has the following implication for the length z_c of the initial region:-

$$z_c|_{n=var} = (1/\sqrt{n})(z_c|_{n=1}) \simeq 5D_0/\sqrt{n} \qquad (7.7)$$

(by Fig. 7.1b). Thus, when n=0.27:-

$$z_c|_{n=0.27} \simeq 9.62D_0 \qquad (7.8)$$

The present prediction gave $z_c|_{n=0.27} \simeq 9.84$.

Any distribution for density ρ over the jet cross-section may be prescribed, in the program, from within the manipulative subroutine called intgrnd (Chapter 6): the (m=0,n=0.27) case was also run with pointwise density calculated from the theory of mixtures (for incompressible fluids):-

$$\rho = (\rho_0-\rho_\infty)c + \rho_\infty \quad ; \quad c = h_c U_c \qquad (7.9)$$

and the results in terms of velocity decay are shown in Fig. 7.9. The predicted core length is shorter (see below) than with the Newman and Brzustowski distribution 7.5 (31), and the prediction is apparently less accurate when 7.9 is used.

The reason for this discussion of possible settings for the density ρ is to indicate the influence of the density formulation on computer run-times. Consider, for example, the evaluation of the integral I_1 (Chapter 4):-

$$I_1 = \int_A \rho U_v dA \qquad (7.10a)$$

Denoting by ρ_{NB} the density distribution 7.5 (from (31)), the integral is evaluated as:-

$$I_{1NB} = \int_A \rho_{NB} U_v dA = \rho_0 \int_A \frac{U_v}{h_c U_c + (\rho_0/\rho_\infty)(1-h_c U_c)} dA \qquad (7.10b)$$

(for an isothermal jet). If the theory of mixtures distribution ρ_{MX} from 7.9 is used, the integral 7.10a is evaluated as I_{1MX}:-

$$I_{1MX} = \int_A \rho_{MX} U_v dA = (\rho_0 - \rho_\infty) h_c \int_A U_c U_v dA + \rho_\infty \int_A U_v dA \qquad (7.10c)$$

In the main region of an axisymmetric jet, the profiles U_c and U_v are described by the similarity profiles given in Chapter 5. The average values of the profile integrals in 7.10c are therefore constants in the main region (see Chapter 3):-

$$Q_{cv} = \frac{1}{A}\int_A U_c U_v dA = \text{constant} \qquad z>z_D$$

$$Q_v = \frac{1}{A}\int_A U_v dA = \text{constant} \qquad z>z_D$$

and it is only necessary to evaluate the integrals once (at the start of the main region). The integral in 7.10b must be evaluated explicitly at every station in the main region, as the integrand contains the decreasing function $h_c(z)$. The same general remarks apply to all the integrals I_n appearing in the set of differential equations (Chapters 4 and 5): because the main region is the longest in any full prediction (Fig. 7.9), computer run-times may be significantly reduced by avoiding numerical integrations for each I_n at every solution step. For the results in Fig. 7.9 (to $z=45D_0$), the run-time using the ρ_{MX} distribution 7.9 was about half that required for the solution using ρ_{NB} from 7.5.

The two density distributions are compared in Fig. 7.11b, under the conditions $n=0.27$, $h_c=0.9$ (chosen arbitrarily), and with U_c chosen as the main region similarity profile U_{c_M} (Chapter 5). The ρ_{MX} distribution is considerably more full than that of ρ_{NB}, and this explains the reduction in the length z_c of the core in Fig. 7.9 with the use of the theory of mixtures distribution. In the initial region, the mixing zone width is determined from the propagation equation, with $w=0$ (Chapter 5):-

$$\frac{db}{dz} = G_I\frac{(1+n)}{2} \qquad ; \qquad n = \frac{\rho_\infty}{\rho_0}$$

which is not influenced by the chosen distribution for density (a consequence of the simplification made during its derivation - Chapter 2). There will be greater momentum associated with the annular mixing zone (width b), at any station, if the distribution ρ_{MX} is employed, relative to that if ρ_{NB} is used (in view of Fig. 7.11b), so that the constant velocity core must be correspondingly less wide as a consequence of axial momentum conservation. Hence, the core is eroded more rapidly when the distribution ρ_{MX} is prescribed.

It is quite clear from Fig. 7.9 that the distribution ρ_{MX} gives a less accurate prediction of velocity decay than the more correct distribution ρ_{NB}. However, an accurate curve fit to the ρ_{NB} distribution (Fig. 7.11b), by a function linear in h_c would recover the saving in computing time afforded by 7.9 and give sufficiently accurate results. No such calculations, however, have been performed by the author.

In order to assess the prediction of axial mass concentration c, the prediction of an isothermal, submerged (m=0), single phase CO_2→air jet (n=0.66) is shown in Fig. 7.12 in terms of axial velocity and concentration decay, and the results are compared with data for this case collected by Chen and Rodi (96). The agreement is sufficiently good, and part of the discrepancy may again be due to nonuniform nozzle property profiles. Fig. 7.12 also shows parametrically the effect of density ratio n<1 on axial property decay when m=0, using predictions from appropriate cases discussed earlier.

It had been intended to investigate the prediction by the program of isothermal 'light' jets (n>>1, eg Helium→air), by comparison with data from Chriss (59) and Abramovich (53). However, it is indicated below that the propagation

equation becomes inaccurate at large values of n, and attention is turned immediately to the prediction of nonisothermal, axisymmetric jets.

7.2.3b Nonisothermal Jets

Data pertaining to nonisothermal air→air jets has been given by Abramovich (53) and others, and predictions by the computer program for this class of problem are described first. Computed velocity decays are given in Fig. 7.13 for three heated ($n=\theta=T_0/T_\infty>1$), submerged ($m=0$) jets which have been studied experimentally (63,53). Uniform injection property profiles were prescribed; the free stream temperature was T_∞=300K and pressure P set at 1bar. Jet density was computed from the ideal gas law:-

$$\rho = \frac{\rho_\infty T_\infty}{T} = \frac{\rho_\infty T_\infty}{T_\infty + h_T U_T}$$

where h_T is the temperature difference on the jet axis at any cross-section (Chapter 5).

Although the variation with θ of the length of the initial region (where $\Delta u_m/\Delta_0=1$) appears to be quite well represented in Fig. 7.13, the rate of decay of velocity downstream is clearly overpredicted in the cases θ=1.7 and 1.85. This unsatisfactory performance is again due to the oversimplified density dependence in the propagation equation (Chapter 2): the analytical solutions of Abramovich (32) when θ=1.85 and 3.25 are almost identical with those in Fig. 7.13. The inaccuracy of the propagation equation increases with increasing n (32), so that the apparently satisfactory prediction for $n=\theta=3.25$ is probably fortuitous (the data, for example, may be affected by a nozzle boundary layer). According to mass flux calculations, given later, the spread of the jet at θ=3.25 is severely overpredicted. The discrepancy between the predicted length of the initial region, for these heated jets, and the length according to the correlation 7.7 is illustrated in Table 7.1. The errors are more significant than in the case n=0.27 considered above. The predicted growth of submerged jets, at different

values of the injection density ratio n, is shown in Fig. 7.14.

The predicted decay of jet temperature difference (where $\Delta T_m = T_m - T_\infty = h_T$) along the axis, associated with the velocity decay in Fig. 7.13 when m=0 and θ=1.7, is shown in Fig. 7.15, and compared with the limited experimental data from Abramovich (53). Agreement appears to be satisfactory. The data for the case θ=1.85 (32) suggests that this hotter jet loses its excess temperature more slowly than the cooler (θ=1.7) jet, contrary to simple reasoning. According to Abramovich (32), the main region temperature profile in this experiment was less full than the assumed distribution U_{T_M} (Chapter 5). The predicted temperature decay for the case (m=0,θ=3.25) is also given in Fig. 7.15 to show the effect of variation in temperature ratio θ: no experimental information was available for comparison. The predictions were obtained using the settings for δ_c, δ_2 and δ described in Section 7.2.1, and a formulation for specific heat C_p, at any point, taken from the theory of mixtures (19):-

$$C_p = (C_{pl} - C_{p\infty})h_c U_c + C_{p\infty} \qquad (7.11)$$

where C_{pl} is the C_p value of air on the jet axis ($T=T_m$). The evaluation of C_p in more complicated cases is described later (Section 7.2.3b).

Further experimental information is available for heated air jets in air when m>0 (non-zero coflowing stream velocity w). Comparisons between predictions by the computer program, assuming uniform injection properties, and experimental data appear in Fig. 7.16-18. Axial temperature decay precedes and is more rapid than that of velocity: Fig. 7.16 also illustrates the effect of an initial nozzle boundary layer (specified from 7.2) on the computed decays.

According to these results, the model appears to predict adequately well the heated air jet in a coflowing stream. In particular, in view of Fig. 7.17a and Fig. 7.18a, the

predictions of velocity decay for the cases (m=0.16,θ=1.7) and (m=0.211,θ=1.85) correspond more closely with the appropriate data than those for related submerged jet cases (m=0,θ=1.7) and (m=0,θ=1.85), shown in Fig. 7.13. The more complicated form of the propagation equation (Chapter 5) for a jet in a coflowing stream (w>0):-

$$\frac{db}{dz} = G(z)\frac{(1+\bar{\rho})}{2}\left(\frac{h_v}{h_v+(1+\bar{\rho})w}\right) \quad ; \quad \bar{\rho}=\frac{\rho_\infty}{\rho_1}$$

where ρ_1 is the density on the jet axis, compared with the submerged jet form (w=0) may serve to reduce the relative importance of the simplified density dependence, so improving the predictions.

The initial conditions for the remaining predictions in this section were chosen for comparison of results with the data of Abramovich (53), for heated jets of the refrigerant Freon-12 exhausting into air:-

$$M_i = 121,\ T_\infty=300K,\ P=1bar,\theta=1.128 \Rightarrow n=0.27 \qquad (7.12)$$

for various values of the parameter m. These studies permit an investigation of the effect of the prescribed C_p distribution upon the numerical solution.

Consideration is given first to the submerged jet case (m=0). For a preliminary prediction, the specific heat C_p was calculated from 7.11, assuming the C_p values of the injectant (Freon-12) and air to be the same at all temperatures. This is a serious oversimplification, to be relaxed shortly. Uniform property profiles were assumed across the nozzle, and the prediction of velocity decay with axial distance afforded by these settings is given in Fig. 7.19. Pointwise density in this nonisothermal jet of variable composition was computed using the relation from Adler and Lyn (19) (Chapter 5):-

$$\rho = \frac{P}{R_0 T}\left[\frac{(1-c)}{M_\infty} + \frac{c}{M_i}\right]^{-1} \quad ; \quad \begin{matrix} c=h_c U_c \\ T=h_T U_T + T_\infty \end{matrix} \qquad (7.13)$$

which is an extension of 7.5 to the nonisothermal case. Jet axial velocities are overpredicted according to the experimental data; the initial degree of heating θ is relatively low (see 7.12), and the velocity prediction in Fig. 7.19 is almost identical to that for the isothermal (θ=1) jet at n=0.27 in Fig. 7.9. The measured velocities in Fig. 7.19 are lower than those in the isothermal experiment (Fig. 7.9), and there are two possible causes:-

1/ The difference in C_p values of Freon-12 and air, which will affect jet temperature and density.

2/ The presence of a boundary layer at the nozzle in the experiment.

The influence of C_p upon the solution was assessed by recourse to the tabulated properties of Freon-12 (106). The variation of its specific heat (C_{pi}) with temperature (at a pressure of 1bar), over the necessary temperature range for the computations, is shown in Fig. 7.20. The ratio of injectant to free stream (air) C_p values at injection (θ=1.128) is:-

$$\overline{C}_{p0} = \left.\frac{C_{pi}}{C_{p\infty}}\right|_{z=0} = 0.634 \qquad (7.14)$$

(C_p values for air used within the program ($C_{p\infty}$ here) are calculated by a gas property subroutine modified from White (42)). The preliminary assumption of air C_p values for the injectant is therefore inadequate. In a second computation, pointwise C_p within the jet was evaluated from:-

$$C_p = (C_{pi,1} - C_{p\infty})h_c U_c + C_{p\infty} \qquad (7.15)$$

which is similar to 7.11, but with $C_{pi,l}$ defined as the local injectant specific heat at the jet axis ($T=T_m$), inferred from Fig. 7.20. The variation of C_{pi} and air specific heat across the jet is again neglected (see Section 7.3.8).

The computed velocity decay, associated with the prediction incorporating 7.15, was found to be almost almost identical with that in Fig. 7.19 (for which 7.11 was used to find C_p): apparently, there is no great effect of C_p variation upon jet axial velocity u_m (see below). The comparison of computed axial temperature decays in Fig. 7.21 shows, as expected, that the decay is more rapid when C_p is determined from the more realistic equation 7.15, as average jet C_p values are everywhere lower than when 7.11 is used (in view of 7.14). No temperature data for this case was available for comparison (see later).

It must be recalled that the conservation conditions for energy and injected material are not ensured explicitly in the initial region, but are assumed to be satisfied <u>implicitly</u> from the momentum theory, upon appropriate settings for the mixing zone, radial profiles $^{U}T_I$ (for temperature) and $^{U}c_I$ (for concentration), and for the mass/momentum diffusion ratio coefficients (Chapter 5 and Section 7.2.1). In the present case, of a submerged jet (m=0), the injected material conservation condition is (Chapter 5):-

$$I_c = \int_{A_s} \rho u c dA_s = I_c(z=0) = \rho_0 u_0 \pi r_0^2 \qquad (7.16a)$$

and the energy conservation condition is (Chapter 5):-

$$I_H = \int_{A} \rho u H dA = I_H' = I_H(z=0) + C_{p\infty} T_\infty \{\dot{m} - \dot{m}_0\} \qquad (7.16b)$$

where:-

$$H = C_p T + \tfrac{1}{2}u^2 \quad ; \quad \dot{m} = \int_A \rho u dA \qquad (7.16c)$$

The integrals I_c and I_H were monitored through the initial region during the solution of the submerged Freon jet problem. When 7.11 is used, jet C_p values are roughly constant and 7.16b is approximately satisfied. When 7.15 is used to compute C_p, I_H and I_H' in 7.16b differ by about 7% (in $I_H(z=0)$) at the end of the initial region. This error is due to the influence of the difference in specific heats (see 7.14) on the initial region temperature profile ${}^{U}T_I$, which has not been accounted for in this work, due to limitations in time and available data. According to Abramovich (97), and Newman and Brzustowski (31), an increase in fullness of the profile ${}^{U}T_I$ accompanies a decrease in specific heat ratio $\overline{C}_{p0}$.

Abramovich (53) reported the existence of a slight nozzle boundary layer, of displacement thickness $0.03r_0$, in the Freon→air experiments. The effect, on the predicted velocity decay, of an assumed nozzle boundary layer of width $b(z=0)$ equal to $0.03r_0$ is also shown in Fig. 7.19. The computed jet spread is not very greatly affected by this setting, and is shown in Fig. 7.22, for uniform injection velocity, in terms of jet half width $r_{\frac{1}{2}}$ compared with experiment (53). Part of the discrepancy will again be due to the simplified density dependence in the propagation equation (Section 7.2.3a).

Abramovich (53) also gave details of measurements taken in a Freon-12→air jet with a coflowing stream velocity w such that $m=w/u_0=0.2$. The other injection conditions were again those in 7.12: computer predictions for this case, assuming uniform injection profiles, are shown in Fig. 7.23a-d. Broad agreement with the experimental data is observed. In Fig. 7.23b, the slight underprediction of axial temperatures in the transition region may again be due to the simple setting for ${}^{U}T_I$ (see above), for the development of U_T in the transition region governs in part the rate of axial

temperature decay there. Also shown is a prediction assuming air C_p values for the injectant (equation 7.11); this is in poor agreement with the data, although predictions for the other quantities were not significantly affected.

In Fig. 7.23d, the predicted increase in jet mass flux with distance is in agreement with the data; apparently, there is no great influence of velocity ratio m in this case (53).

7.2.4 Range Of Applicability

The predictions discussed in the preceding sections show that the computer program may be used to predict with sufficient accuracy a wide variety of free, axisymmetric jets of variable composition. The present work differs from earlier analyses (32) by including an empirical treatment of the developing flow in the transition region (Chapter 3 and Chapter 6). For this study, the development of the velocity profile is prescribed in the simplest and most convenient manner (Chapter 6): the accuracy of the predictions for, say, velocity decay in the transition region is acceptable (see for example Fig. 7.1b and Fig. 7.9). A more realistic representation of the developing profiles, and jet spread, in the transition region may be prescribed from a closer analysis of the entrainment measurements of Hill (64), for the early part of a constant density jet, and the half-width measurements of Landis and Shapiro (58).

The principal constraints on the application of the program to axisymmetric jets concern the values for the velocity ratio m and density ratio n. An assumption underlying the propagation equation (Chapter 2) is that turbulence levels in the undisturbed injectant and free streams are very small, compared with those in the turbulent mixing zone, and this is reasonable provided $m<0.4$ (approx.) (32): modifications to the propagation equation to account for higher velocity ratio cases are proposed by Abramovich (32).

Errors in the prediction of variable density jets (in

Section 7.2.3) are due to the simplified density dependence in the propagation equation (Chapter 2). The deficiency is most manifest in a comparison between predicted and measured increase in mass flux with distance in submerged jets (m=0), as shown in Fig. 7.24 for three cases considered earlier. The prediction of light jets (n>1) is less accurate than that of dense jets (n<1): the prediction when (m=0,n=3.25) is very poor (Fig. 7.24). For this reason, and that given above, it was not possible to make use of the data of Chriss (59), Zakkay et al (107) or Alpinieri (108) (all for m>0, n>>1) in this assessment. Again, Abramovich (32) has proposed an empirical correction to the propagation equation for the treatment of light jets. Density-related errors are not as severe when the added complication of a non-zero coflowing stream velocity is introduced (see Section 7.2.3b). The application of the program to the prediction of very dense (n<<1), two-phase sprays is discussed in Chapter 8.

Finally, when the specific heats of the injectant and free stream fluids are very different, the variation of the initial region temperature profile ${}^{U}T_{I}$ with specific heat ratio $\overline{C}_{p0}$ (Chapter 5) should be included in the modelling, in order to properly satisfy the energy conservation condition in the initial region (Section 7.2.3b).

7.3 Prediction Of Deflected Jets

7.3.1 Introduction

The prediction of the round turbulent jet in a crossflow has been the subject of many previous investigations: some of the treatments were discussed in Chapter 4, as an introduction to the development of the present model. Central to all the integral methods is the determination of empirical coefficients (by comparison with the available data) in order to obtain proper predictions for some or all of the following features of the flow:-

1/ The deflection of the jet axis upon penetration into a given crossflow.

2/ The spread of the jet with distance along its axis owing to entrainment of fluid from the free stream, manifest in the increase in jet mass flux and cross-sectional area.

3/ The decay along the axis of the principal properties of the injectant (velocity, concentration and temperature).

Point 1/ may be cited as the characteristic feature of the jet in a crossflow. The definition of the jet axis is discussed shortly. Points 2/ and 3/ have been considered above in the context of axisymmetric jets (Section 7.2), and the introduction of a crossflow may be considered (purely in terms of integral modelling) as a complicating feature which enhances turbulent mixing (Chapter 4).

7.3.2 Method Of Determination Of Empirical Input

The extra empirical input required for these predictions was indicated in Chapter 4. Putting aside (at this stage) the assumptions concerning property profiles (U_V,U_T,U_C), the extra empirical coefficients appearing in the present model, and requiring evaluation, may be summarised as follows, with reference to the three points made above:-

1a/ The unknown quantities in the idealised drag force F_D (per unit length - see Chapter 4):-

$$F_D = \frac{C_D \rho b_X w_N^2}{2}$$

being the coefficient C_D and the local jet width b_X (Fig. 7.25). The drag force is considered here as a general deflecting mechanism allowing matching of predicted trajectories with test data (see later).

2a/ The enhanced mixing coefficient $G_1(z)$ in the propagation equation (see Chapter 4 and Section 7.3.5a). This plays the role of the entrainment coefficient of, say, Wooler (86) or Campbell and Schetz (94) (Chapter 4) in controlling entrainment, through the continuity equation.

As for the axisymmetric jet, the prescription of a realistic spreading (entrainment) rate should provide, in consequence, for a good account of the property decay mentioned in point 3/. It is this observation which has prompted the manner of the determination of values for $G_1(z)$, C_D and b_X. It is interesting, first, to consider the evaluation procedure for empirical input adopted by other workers: the discussion is limited to those models which include a 'proper' consideration of entrainment as a deflecting mechanism (models of the Wooler (86) type - Chapter 4).

The following observations appear to apply to the models of Wooler (86), Sucec and Bowley (89), Shirakashi and Tomita (90), Campbell and Schetz (79,94) and Adler and Baron (63). Empirical input is determined solely upon the basis of comparison between computed and measured trajectories. Where there is no free parameter controlling entrainment (in the models of Sucec and Bowley (89) and Shirakashi and Tomita (90), jet spread in a crossflow is

assumed to be no different from that in a submerged jet - Section 4.5.1), coefficients C_D and b_X for the drag force need only be chosen so that trajectory predictions agree reasonably well with experiments. In this class of model, no resolution of the inner structure of the jet (such as velocity) is attempted. In the Wooler analysis (86) there are both drag and entrainment coefficients to be determined (see Section 4.3). The drag force unknowns were stipulated first, from the solid body argument:-

$C_D = 1.8$ (a representative value for an ellipse)

$b_X^2 = \frac{A}{K_b}$ (K_b shape coefficient)

The new coefficient K_b was determined by assuming the jet cross-section shape to change, linearly, from a circle to a 4:1 ellipse in a distance predetermined from the injection conditions (86). With the magnitude of the drag force fixed in this way, (constant) values of the entrainment coefficients were found so that predicted trajectories agreed with selected data. No assessment of the validity of the resulting entrainment predictions was made.

The Wooler-type analysis may be extended to include the prediction of the detail of the flow, such as jet velocity (45). Campbell and Schetz (79) carried this out, and determined empirical input in the same way as Wooler (although chosen values were different (79)). Predicted, cross-section averaged velocities could not be compared usefully with the available data for maximum jet velocity (79). However, the predicted increase in mass flux and cross-section area was shown to be underpredicted, by comparison with experiment, and the entrainment settings brought into question. Possible explanations for these deficiencies are given later.

Adler and Baron (63) prescribed an empirical variation for C_D to account for changing jet shape: the width b_X was known directly from the numerically predicted cross-section

shape (Chapter 6): coefficients in the propagation equation were prescribed directly (so that there was, in effect, no free entrainment parameter (63)). Jet trajectories appeared to be well predicted and mass flux results were in accordance with the measurements of Kamotami and Greber (39). Predicted jet maximum velocity decays, although available, were not assessed (see later).

There are two objections to the method of determination of empirical input described above. In the first instance, it would be more natural to extend those methods from axisymmetric jet predictions (Chapter 3 and Section 7.2), where the spreading rate coefficient is prescribed in order to predict axial property decays sufficiently accurately, and in consequence the 'integrated' quantities (mass flux and area growth). In deflected jets, the drag force deflecting mechanism should have only secondary influence on jet velocity, so that a better procedure for the setting of empirical input than that described above would be:-

a) The setting of the extra spreading rate coefficient $G_1(z)$ in order to properly predict velocity decay test data, employing 'nominal' initial values for drag-related coefficients, and

b) the prescription of optimum variations for C_D and b_X in order to obtain matches with observed trajectories.

In this approach, empirical coefficients are determined according to those processes which they are deemed to govern (velocity decay for the spreading rate coefficient $G_1(z)$ - see below, deflection for the coefficients in the deflecting mechanism). In the Wooler (86) and Campbell and Schetz (79,94) models, the highly empirical drag force (an idealisation for the surface force term in the normal momentum equation - see Chapter 4) is evaluated first, from

the unconfirmed solid body argument. The entrainment rate, which is the dominant factor in determining the jet behaviour (69) (see later), is then prescribed merely to augment the drag force as necessary for trajectory matching.

It is mentioned here that, for the present work, velocity decay is preferred, as test data, to jet spread or entrainment measurements, in view of greater availability in the literature (Keffer and Baines (69), Patrick (70) and others) and the considerable scatter in the experimental data on entrainment and area growth (discussed later), this being due to the integrated nature of these measurements and the difficulty in locating accurately the mixing boundary of the jet.

The second objection to the determination of empirical coefficients solely from trajectory data stems from the definition of the jet trajectory itself; this is discussed in the next section.

7.3.3 The Definition Of The Jet Trajectory

The trajectory data most often quoted in connection with integral model predictions is that due to Jordinson (75), Keffer and Baines (69) and Kamotami and Greber (39). All these measurements represent the locus of maximum velocity (or total pressure) points in successive jet cross-sections (in the plane of the trajectory) - this is termed the jet maximum velocity axis, and is denoted by ξ. Other workers, such as Platten and Keffer (37), Patrick (70) and Campbell and Schetz (109) obtained from photographs the jet 'visualisation centreline', located midway between the upstream and downstream jet boundaries (Fig. 7.25). In the maximum deflection region (Chapter 4), this centreline lies below the maximum velocity axis (Fig. 7.26), as a result of elongation of the jet cross-section in the trajectory plane, due to the sweeping action of the crossflow. Patrick (70) emphasised the importance of recognising the difference in these characterisations of deflection in theoretical work.

Snel (82) discussed in detail the prediction of jet trajectories by the integral method. The jet centreline z in the integral theory, the independent variable in the equation system, was defined in Chapter 4 as the locus of momentum centres in successive jet cross-sections. As discussed by Snel (82), the momentum centre z in a typical, crossflow-distorted cross-section will be displaced somewhat downstream (in the direction of the normal component of crossflow w_N) from the maximum velocity point ξ in that section, as shown in Fig. 7.25. The distance Y_c between the momentum centre z and ξ will become appreciable as the cross-section area grows large.

Snel (82) presented an approximate analysis intended to estimate Y_c in a typical 'horseshoe' cross-section such as that shown in Fig. 7.25. With some further simplifying assumptions, and the use of a velocity distribution related to that observed in axisymmetric jets (Chapter 3), Snel (82) derived an approximate expression for Y_c which, in the context of the present work, may be written as:-

$$\frac{Y_c}{D_0} = \frac{\sqrt{\pi}}{2}\left[\frac{h_v^2 + 8.3h_v w + 52w^2}{25h_v^2 + 110h_v w + 310w^2}\right]\left(\frac{A}{A_0}\right)^{\frac{1}{2}} \qquad (7.17)$$

The constants arise from integration of the assumed velocity profile U_v. From Chapter 4, pointwise jet velocity u is given by:-

$$u = h_v U_v + w \quad ; \quad h_v = u_m - w \qquad U_v \in [0,1] \qquad (7.17a)$$

and u_m is the maximum jet velocity in a cross-section, occurring on the axis ξ. The estimate 7.17 is not restricted to a particular crossflow type. In the far region (see Section 4.2.3), as $h_v \to 0$, the relation has the following limiting form:-

$$\frac{Y_c}{D_0} = \frac{52}{620}\left\{\frac{\pi A}{A_0}\right\}^{\frac{1}{2}} \simeq 0.149\left\{\frac{A}{A_0}\right\}^{\frac{1}{2}} \quad \text{as } h_v \to 0 \qquad (7.17b)$$

There is a small error in 7.17 owing to the assumption of a typical distorted shape, for at the nozzle the relation gives:-

$$\left.\frac{Y_c}{D_0}\right|_{\substack{z=0\\w=0}} = \frac{\sqrt{\pi}}{50} \simeq 0.0355 \qquad (7.17c)$$

Unless the crossflow velocity is large, there is little jet shape distortion in the initial region (69,80), and the relation 7.17 more properly applies to the flow beyond the end of the transition region (see later).

The estimate 7.17 has been used in the present work to find the maximum velocity axis ξ from the momentum centreline z (located by the co-ordinate relationships derived in Chapter 4). At any cross-section, the problem is to displace the maximum velocity point $(x_z(\xi), y_z(\xi))$ (x_z and y_z define the trajectory plane in Fig. 7.26) a distance Y_c (from 7.17) from the momentum centre at $(x_z(z), y_z(z))$ (see Fig. 7.25), in the plane of the jet cross-section. Within the numerical solution scheme, this is done by defining the local orientation of the momentum centreline z, with the increments dx_z and dy_z shown in Fig. 7.27. These increments are known over each solution step dz in the numerical solution (Chapter 6).

The local tangent $\vec{z}$ to the momentum centreline is given by (Fig. 7.27):-

$$\vec{z} = dx_z\hat{x}_z + dy_z\hat{y}_z \equiv (dx_z, dy_z)$$

where $\hat{x}_z$ and $\hat{y}_z$ are unit vectors. The inner product of $\vec{z}$ with its normal $\vec{N}$ is zero. Hence:-

$$\vec{z}.\vec{N} = (dx_z, dy_z)(Nx_z, Ny_z) = 0$$

Thus $\vec{N} = \pm(-dy_z, dx_z)$. The positive sense for $\vec{N}$ is chosen so that the maximum velocity axis is displaced in the direction shown in Fig. 7.27. The unit normal $\hat{N}$ is given by:-

$$\hat{N} = \frac{\vec{N}}{|\vec{N}|} = \frac{1}{\sqrt{dx_z^2+dy_z^2}}(-dy_z, dx_z)$$

The maximum velocity point $\xi=(x_z(\xi),y_z(\xi))$ is distant Y_c from $z=(x_z(z),y_z(z))$. Hence:-

$$(x_z(\xi),y_z(\xi)) = (x_z(z),y_z(z)) + Y_c\hat{N} \qquad (7.18a)$$

and:-

$$x_z(\xi) = x_z(z) - \frac{Y_c dy_z}{\sqrt{dx_z^2+dy_z^2}}$$

$$y_z(\xi) = y_z(z) + \frac{Y_c dx_z}{\sqrt{dx_z^2+dy_z^2}} \qquad (7.18b)$$

It is recalled that all the integral models considered in Section 7.3.2 were assessed by matching predicted momentum centrelines with measured axes ξ. From Fig. 7.27, this implies that the momentum centrelines are underdeflected according to these models: since the magnitude of the drag force is always fixed (Section 7.3.2), the predictions from these models would be improved by an increase in jet entrainment rates to increase centreline deflection (Campbell and Schetz (79) identified underprediction of entrainment in their model).

7.3.4 Structure Of The Predictive Sequence

In the succeeding sections, the computer prediction of round jets in different types of crossflows is discussed. Values and expressions for empirical coefficients (see Section 7.3.2) are obtained in Section 7.3.5 with reference to a test case well documented in the literature. The magnitude in the difference in trajectory definitions (Section 7.3.3) is displayed. In order to separate the different components of the model, the predictions in Section 7.3.5 do not include the effects of cross-section and property profile distortion (the velocity profile U_v is that used for the axisymmetric jet predictions in

Section 7.2). Also, the pressure gradient term in the centreline direction momentum equation (Section 4.6.2) is neglected (39). All these 'pressure effects' are introduced in Section 7.3.6 in order to assess their relative importance.

The prediction of constant density jets in swirl and other crossflows is dicussed in Section 7.3.7, and in Section 7.3.8 the effects of composition variation are considered.

7.3.5 The Jet In A Uniform Crossflow At Constant Density

7.3.5a Test Case For Empirical Coefficients

The first task is the computer optimisation of empirical coefficients. The treatment of the transition region is exactly analogous with that for the axisymmetric jet (Chapter 3), and the empirical relation $z_D/z_c=1.5$ (see Fig. 7.1a) is again assumed throughout. Realistic values for the enhanced growth rate coefficient $G_1(z)$ in the propagation equation:(see Section 4.5.4):-

$$\mathcal{F}_1(z) = \frac{G_1(z)}{\left(\frac{A_0}{A}\right)^{(1-A_1)/2} + 0.5\left(\frac{w_N(z)}{u_m(z) + w_t(z)}\right)} \qquad (4.18)$$

(for the constant density case), where, from Section 4.5.2:-

$$\left.\frac{db}{dz}\right|_{\substack{\text{deflected}\\ \text{jet}}} = \left.\frac{db}{dz}\right|_{\substack{\text{axisymmetric}\\ \text{jet}}} + \mathcal{F}_1(z) \qquad (4.7)$$

are determined by comparison between predictions and test data for a single case reported in the literature. The transverse injection ($\beta(z=0)=\pi/2, \theta_z(z=0)=0$) case $R=w/u_0=1/6$ is sufficiently severe, and is well documented by Keffer and Baines (69).

The coefficient $G_1(z)$ is adjusted solely on the basis of predicted maximum velocity decay: it will not do, however, to ignore the contribution of the drag force entirely from these studies (as there will be some secondary effect on the

decay of velocity, through the coupling of the momentum equations - Chapter 4). Preliminary variations for the coefficients C_D and b_X are thus prescribed as follows:-

$$\begin{aligned} C_D &= 1.0 \text{ (value appropriate to a circular cylinder)} \\ b_X &= 2\left(\frac{A}{\pi}\right)^{\frac{1}{2}} \text{ (effective jet diameter - from 4.5)} \end{aligned} \qquad (7.19)$$

According to the majority of the discussions in the literature (86,89), these are the smallest values which may be assigned to the coefficients, in keeping with the solid body argument (Chapter 4).

In analogy with the way in which the width growth coefficient G_I determines the length z_c of the initial region in an axisymmetric jet (Chapter 3), it is the enhanced growth coefficient $G_1(z)$ which controls the prediction of the initial region length in a deflected jet; or, more correctly, the reduction in that length from the submerged jet value owing to more rapid turbulent mixing. It is first assumed that $G_1=G_{1I}$ (a constant) throughout the initial region, again in analogy with G_I. There is no precedent for the setting of a value for G_{1I} to be found in the work of Adler and Baron (63), as the initial region length z_c was determined from a correlation (chapter 4). In the present computer model, the value $G_{1I}=2.3$ resulted in a length $z_c \simeq 2.2D_0$ for the initial region, when $R=1/6$ (recall that, for a submerged constant density jet, $z_c \simeq 5D_0$ - Fig. 7.1b). Such a value is in agreement with the measurements of Keffer and Baines (69) (see below). It may also be assumed that the nozzle velocity profile in the experiment was essentially uniform (83), so that $G_{1I}=2.3$ may be taken as a 'proper' evaluation, not influenced by nozzle boundary layer effects (Section 3.6 and Section 7.2.1). There is very little deflection of the momentum centreline z in the initial region (69), so that the omission of the centreline pressure term has no bearing upon the determination of G_{1I}. The boundaries of the mixing zone in the initial region were again found to be approximately straight.

To complete a numerical solution, $G_1(z)$ must be assigned a value beyond the end of the initial region (there is no justification for anything other than a constant setting). A suitable value was determined by computer optimisation as $G_{1M}=1.6$, the resulting solution for velocity decay being shown in Fig. 7.28 in comparison with the experimental data of Keffer and Baines (69). The jet velocity Δu_m on the axis ξ (Section 7.3.3) is defined by:-

$$u_m(\xi) = u_m(\xi) - w \qquad (7.20)$$

(distance ξ along the axis can be deduced, from distance z along the momentum centreline, by integrating along the curve defined by the set of co-ordinate pairs, generated by 7.18b). The measurements of Gordier (reported by Patrick (70)) for a water-water jet at R=1/6 are also included in Fig. 7.20, in order to verify the prediction in the downstream limit ($\xi/D_0>20$). According to the measurements of Kamotami and Greber (39), the jet has suffered severe cross-section distortion by this stage (see Section 7.3.6), so that the simple 'circle-similarity' assumption made here (neglecting pressure distortion) gives a suprisingly good account of velocity decay. Patrick (70) found that the decay of the dimensionless excess velocity $\Delta u_m/\Delta u_0$ could be represented by simple and familiar approximations:-

$$\frac{\Delta u_m}{\Delta u_0} \quad \frac{1}{C_1 + C_2(\xi/D_0)} \qquad \begin{array}{l}\text{for transverse injection} \\ C_1,\ C_2 \text{ constants depending} \\ \text{upon } R\end{array} \qquad (7.21)$$

It is recalled from Section 3.4 that such an expression was obtained from an analysis of the main region equations for a submerged jet.

7.3.5b Trajectory Predictions

Having established in this way the growth rate of the jet, the magnitude of the predicted deflection at R=1/6 may be considered. The momentum centreline z, obtained with the C_D and b_X settings in 7.19, is shown in Fig. 7.29 together with the maximum velocity axis estimated by the methods of

Section 7.3.3. The error in this estimate will be less than the implied error if the centreline z is made to pass through the measured maximum velocity points (63,79) (see Fig. 7.29).

Although the predicted axis ξ appears to be in good agreement with the data in Fig. 7.29 for R≈1/6, the significant scatter in the data makes difficult any conclusive statement. Instead, the performance of trajectory prediction over a range of values for R is investigated, using data available in the literature. The computer prediction of maximum velocity axes in six transverse injection cases is shown in Fig. 7.30, in comparison with experimental results from several sources. A consistent overprediction of the deflection of the axis, observable at larger penetration distances, is apparent in the results for R^{-1}=6,8,10 and 18. The predicted axis at R^{-1}=4 appears to be good, while the R^{-1}=30 prediction lies close to the measurements of Patrick (70), for R^{-1}=27.3 and 28.6, again indicating overdeflection in the (weaker crossflow) prediction.

The inference drawn from Fig. 7.30 is that predicted axes ξ are overdeflected with the drag settings C_D=1.0 and $b_X=2\sqrt{A/\pi}$ in 7.19, while the velocity decay prediction in Fig. 7.28 is taken as an indication that this overdeflection will not be due primarily to overentrainment.

In order to improve trajectory predictions, the coefficient C_D may be reset to a value less than unity. A suitable value was determined, by computer optimisation, as C_D=0.6, b_X remaining unaltered. There is some secondary effect of deflection upon velocity decay, and it was necessary to adjust the value of G_{1M} from 1.6 to 1.7 in order to recover the velocity decay prediction in Fig. 7.28 with the new value for C_D. The resulting predictions for the jet axis ξ at different values for R are shown in Fig. 7.31. The predictions appear to be improved (from those in Fig. 7.30), yet for jets in very weak crossflows (Fig. 7.32) deflection

appears to be underpredicted according to the data of Patrick (70). No data was available for corroboration of the measurements of Patrick (70) in the weaker crossflow cases.

The value C_D=0.6 used here is considerably less than that in most other models, for which $C_D \simeq 1.5$ (63,86,79). The relative importance of entrainment as a deflecting mechanism is emphasised in the present work: for example, the setting of the spreading rate through G_{1M}=0.38 by Adler and Baron (63) would completely fail to predict the rapid rate of velocity decay in Fig. 7.28 (G_{1M}=1.7 in this work). None of the models described in Section 7.3.2 were properly assessed in terms of entrainment (see later). The drag force is introduced, as a modelling convenience, as a replacement for the integrated normal surface forces (Chapter 4), and in this respect it is difficult to assign any physical significance to the coefficients C_D and b_X. Shirakashi and Tomita (90) assumed that only the 'high velocity' part of the jet cross-section (defined by $U_v > 0.5$) would act as a solid body, affecting the setting of b_X: this is a possible explanation for a reduction in the 'combined coefficient' $C_D b_X$, from the magnitude implied by the solid body argument. In view of this uncertainty, and the difference between ξ and z (Section 7.3.3), the jet trajectory is the most difficult property of the flow to predict analytically. With the model of Campbell and Schetz (94), for example, predicted trajectories agree with measured maximum velocity axes ξ when $R^{-1}<10$; at R^{-1}=18 and 30, however, the predicted trajectories are close to the authors' own 'visualisation centrelines' (Section 7.3.3), which are quite different from the corresponding maximum velocity axes (Fig. 7.30).

7.3.5c Axial Velocity And Concentration Decay

Patrick (70) gave measurements of the decay of maximum velocity and concentration (of nozzle fluid) in constant density, deflected jets in the range $R^{-1} \in [12,54]$ (transverse injection). Predicted velocity decay along the jet axis is

compared with this and other data in Fig. 7.33 (the decay at $R^{-1}=6$ is the same as that shown in Fig, 7.28). The predictions are in reasonably good agreement with the measurements over the range of values for R, especially in the downstream limit ($\Delta u_m/\Delta u_0<0.2$, say) away from the effects of the precise injection conditions (see below). The prediction of the variation in length z_c of the initial region, with R, is compared in Fig. 7.33c with data collected and deduced (by curve fitting of velocity decays) by Snel (82), and with the correlation of Kamotami and Greber (39) (Chapter 4).

In Fig. 7.33, only in the extreme case $R^{-1}=u_0/w=4$ is the velocity decay overpredicted by the present model. In this case, the neglected pressure distortion effects may be considerable (see later), but another possible explanation is as follows. Sucec and Bowley (89) report Kamotami and Greber's observation (39) that, for $R^{-1}<4$ (strong crossflows), the vortex structure in the cross-sections (Chapter 4) does not have time to become fully established, due to the extremely rapid rate of mixing-out of the injected material with the crossflow. This led Sucec and Bowley (89) to use a larger value for the drag coefficient C_D when $R^{-1}<4$: for $R^{-1}>4$, this coefficient was reduced (from 1.8 to 1.0) upon the assumption that the then dominant vortex structure behaved like suction through the rear surface of a cylinder (after Jordinson (75,81) - see Chapter 4), so reducing the total drag. The author's investigation of the present model showed that an increase in C_D (increasing deflection) acts to reduce the predicted rate of velocity decay (probably through the consequent relative increase in the value of the 'coflowing stream' component w of the crossflow velocity, which inhibits mixing through the propagation equation - Section 7.2.2), so that such a procedure would improve the prediction of the case $R^{-1}=4$ in Fig. 7.33a. It might be concluded from this investigation that cases for which $R^{-1}<4$ should be treated separately (89,81).

The velocity decay comparisons with data in Fig. 7.33 display some similarities with a number of the axisymmetric jet velocity decay results in Section 7.2. In general, the prediction of the downstream limit ($\Delta u_m/\Delta u_0 < 0.2$, say) is good (perhaps $R^{-1}=21.2$ is an exception). The presence in Patrick's experiments (70) of boundary layers on the inside of the nozzle cannot be ruled out, although no such details are given (70). If a nozzle boundary layer is introduced through the arbitrary setting $r_c(0)/r_0=0.9$ (see 7.2), a significant improvement in the solution for velocity decay is observed, as illustrated in Fig. 7.34. The reduced rate of velocity decay in the transition region of the different jets is also evident in Fig. 7.33: this effect becomes less pronounced as the ratio R, and hence jet spreading rate, increases (Fig. 7.33). Without further detailed information upon the initial conditions in the experiments, it is only possible to say that the decay of maximum velocity appears to be successfully reproduced by the model, over a wide range of the velocity ratio parameter R.

This section is concluded with an assessment of the prediction of maximum nozzle fluid concentration decay with penetration ξ. Modelling considerations (Chapter 5) dictate that these predictions are of a more approximate character than those pertaining to jet velocity.

Computed axial concentration decays, for several transverse injections into uniform crossflows, at different values of velocity ratio R, are shown in Fig. 7.35, and comparisons are made with the data of Patrick (70): the agreement appears to be satisfactory. The concentration prediction when $R^{-1}=40.32$ (Fig. 7.35) is almost identical to that of Fig. 7.4b for the free jet ($R=0$), and the negligible influence of R in this case is supported by experiment (Fig. 7.35). The concentration of injected material condition 7.16a was approximately satisfied, in the initial region, with the use of the diffusion ratio coefficients as evaluated in Section 7.2.1, for the location of the

'scalar' mixing boundaries.

A further investigation of the scalar mixing field predictions is undertaken in Section 7.3.8 (jets of variable composition).

7.3.5d Entrainment And Jet Spread

The settings for coefficients in the propagation equation must be further assessed by comparison with entrainment related observations other than velocity decay. The increase in mass flux and jet area with penetration, for transverse injection into uniform crossflows, has been measured and reported by several workers (39,74,82,110).

Estimates of cross-section area A at different axial stations in deflected jets are reproduced in Fig. 7.36. The area A is of course very difficult to determine experimentally and the values will be imprecise. Campbell and Schetz (94) estimated the width b_Y of the cross-section (Fig. 7.25) from photographs (109), and determined A by assuming a fixed elliptical shape for the section. These estimates, however, imply less rapid spread than in an axisymmetric jet (Fig. 7.36), which is contrary to the principle of enhanced mixing in a crossflow (Chapter 4). The theoretical model of Campbell and Schetz underpredicted their own measurements (94), calling into question the setting of empirical entrainment coefficients (Section 7.3.2). The predictions of jet spread by the present model in the relevant cases are also shown in Fig. 7.36. For the strongest crossflow, $R^{-1}=6$, the jet mixes out very rapidly, losing its excess velocity and becoming alligned with the crossflow within a relatively short distance (see earlier): the spreading rate decreases in the 'far region' (Chapter 4) and this jet does not spread, in total, as much as some less greatly deflected jets (Fig. 7.36).

Measurements of the increase in jet mass flux with ξ are reproduced in Fig. 7.37: the results of Rajaratnam and Gangadharaiah (110) and Kamotami and Greber (39), at similar

values for R, show little correlation (data for the free jet case is shown for comparison). The measurements were obtained (39,110) by integration of measured velocity distributions U_v over cross-sections, within the domain $U_v>0.1$, in order to offset the indeterminacy in the location of the jet edge ($U_v \to 0$). The jet mass flux $\dot{m}$ is defined as:-

$$\dot{m} = \int_A \rho u dA = h_v I_1 + w\cos\beta I_0 \qquad (7.22)$$

in the notation of Chapter 4.

Adler and Baron (63) found that their model gave slight underprediction of $\dot{m}$ according to the data of Kamotami and Greber (39). In the present work, jet spreading rates are greatly increased relative to Adler and Baron (63) (see Section 7.3.5b), and the present predictions are in better agreement with the results of Rajaratnam and Gangadharaiah (110), although the data is very scarce (Fig. 7.37). The model of Campbell and Schetz (79) consistently underpredicted the data of Kamotami and Greber (39).

Further experimental data is available in the case of oblique injection into uniform crossflows at constant density ($\beta<\pi/2$ at injection - (37,111). Shown in Fig. 7.38 are predicted axes ξ, for different injection angles, at two values of R: the results agree with the measured maximum velocity axes. Jet mass flux was also measured by Zandebergen and Joosen (111), and predictions are compared with this data in Fig. 7.39a for the three different injection angles. Again, the model of Adler and Baron (63) underpredicted $\dot{m}$ according to these results (Fig. 7.35b).

Calculated jet spread may also be assessed against observations of the jet envelope, by virtue of the prediction of jet shape distortion. This is done in Section 7.3.7.

7.3.6 Pressure Effects

7.3.6a The Pressure Force In The Centreline Direction

The contribution of the pressure term AdP/dz to the decay of jet maximum velocity (Chapter 4) was ommitted from the model in obtaining the results for the previous section. Distortion of cross-sections and velocity profiles was also ignored. In view of the omission of the pressure term, it might be supposed that too great a value for the crossflow related spreading rate coefficient, $G_1(z)$, must be assigned, in order to include this 'pressure' contribution to velocity decay in the 'entrainment' related decay (for the optimisation in Fig. 7.28). The implication would be that, upon inclusion of the pressure force, the magnitude of $G_1(z)$ may be correspondingly reduced. However, this has not been found to be the case in the present work.

Two predictions of velocity decay along the axis of jets in uniform crossflows are reproduced in Fig. 7.40 from Fig. 7.33. The effect on velocity decay, upon inclusion of the centreline pressure force in the equations (Chapter 4) is also illustrated. An increase in the rate of velocity decay is observed for $\Delta u_m/\Delta u_\theta < 0.5$ (approx.). At $R^{-1}=6$, the 'asymptotic' behaviour of the excess velocity function is lost in the new solution (Fig. 7.40a), while in the weaker crossflow example ($R^{-1}=15.7$ in Fig. 7.40b) the jet axial velocity is only slightly reduced. As a consequence of this difference in the character of the solutions, the author was unable to determine a single (reduced) value for $G_1(z)=G_{1M}$ (Section 7.3.5a) which gave velocity decay results, as accurate as those of Section 7.3.5c (Fig. 7.33), in both the $R^{-1}=6$ and $R^{-1}=15.7$ cases (a possible explanation is that the pressure effects - AdP/dz and cross-section shape and profile distortion - should be included or omitted together from the modelling). Thus, the pressure term has been neglected from subsequent computations, noting that its influence on velocity decay in moderate crossflows is slight (Fig. 7.40b), and that spreading rates do not appear to be seriously overpredicted as a result of its omission (Section 7.3.5d).

7.3.6b Cross-Section Distortion

The inclusion of a model for the representation of the continuous distortion of cross-section shapes, and property distributions, in deflected jets represents a significant advance in the sophistication of integral models (Adler and Baron (63), Packer (35) and Chapter 4). Adler and Baron (63), however, gave no account of the sensitivity of their momentum theory to the nonsimilar velocity profiles which were generated during the numerical solution (see Fig. 4.5). Packer (35) studied parametrically the effect of distortion of U_v on predicted jet velocity (h_v), area (A), and entrainment (E_m): the investigation indicated that the distorting profiles acted to inhibit axial velocity decay, compared with a solution assuming similarity of U_v with z (see Fig. 7.41). This effect will be explained later.

The cross-section distortion sub-model and its computer implementation was fully described by Packer (35). For a particular problem, the rate of 'rolling-up' (distortion) of the jet cross-section is determined, in the vortex-sheet model (35), by the viscous damping term (Chapter 6), and in particular the 'turbulent dynamic viscosity' ν_T. For the present work, ν_T is considered to be an empirical constant. Packer (35) showed, parametrically, the effect of ν_T on predicted jet shape at a fixed axial station in a given problem (Fig. 7.42). An increase in the value of ν_T arrests the rate of shape distortion.

For a model aimed at quantitative predictions, ν_T must be prescribed by comparison of observed and predicted jet shapes in a test case. Following Adler and Baron (63), the measurements of Kamotami and Greber (39) were used for this purpose. As shown in Fig. 7.43, a good representation of shape distortion is obtained in the present model when the damping parameter takes the value:-

$$\nu_T = 7 \times 10^{7} \; ; \quad \begin{array}{l}\text{dynamic viscosity of air } \nu_a \\ \text{1 bar and } 20^0\text{C} = 1.6 \times 10^{-5} \\ \nu_T/\nu_a = 0.044\end{array} \qquad (7.23)$$

The setting for ν_T appropriate to very dense jets is not

known at present (Chapter 8). The velocity profile, given empirically by the methods described in Chapter 6, is in broad agreement with the data (39) (Fig. 7.43).

With the distortion rate properly set, the distorted profiles U_v can be used in the numerical evaluation of the profile integrals I_n (Chapter 4), for the 'full' calculation of a deflected jet. The uniform crossflow case $R^{-1}=18$ (Section 7.3.5) was recomputed in this manner. For the 'similarity' predictions of Section 7.3.5, circular cross sections were assumed and U_v taken from axisymmetric jet work (no distortion): for the full calculation, U_v is generated by the finite-difference solution of Poisson's equation over each new jet shape (Chapter 6), incurring a penalty in computer time as follows for the Honeywell Multics machine:-

Problem $R^{-1}=18$	Average solution time per step
Full calculation with generation of distorted velocity profiles by the subroutine 'epdel' (Chapter 6)	25cpu seconds
U_v as in an axisymmetric jet (Section 7.3.5)	5cpu seconds

This overhead can only be justified if the predictions are greatly affected by the use of distorted profiles. However, in the case $R^{-1}=18$, no significant difference in the prediction of the principal flow properties (axial velocity, concentration, entrainment and trajectory) could be identified between the distorting U_v and 'similarity' schemes. The same conclusion was reached by comparison of predictions from the 'similarity' and 'full' calculation schemes for other cases in the range $R^{-1} \in [4,30]$.

Distortion of the profile U_v was followed by monitoring the average value of U_v over the cross-section A. At constant density:-

$$\bar{U}_v(z) = \frac{1}{A}\int_A U_v dA = \frac{I_1}{\rho_\infty A}$$

(see Chapter 4). At R^{-1}=18, predicted jet shape and velocity profile distortion follows the sequence shown in Fig. 7.44; the sweeping action of the crossflow results in a continuous displacement of the maximum velocity point toward the upstream jet boundary (Fig. 7.44a). The average value $\bar{U}_v(z)$ changes only very slightly, even though shape distortion is considerable, the trend being a slow decrease in its value with increasing penetration (Fig. 7.44). It is pointed out that, according to the empirical formulations in Chapter 6, scalar and velocity profiles are 'identical' at any station, although the scalar profiles are defined over a relatively larger area. The evaluation of the profile average may be affected by the error in the computation of the distorted shape in the sub-model, which was discussed in Chapter 6.

It was seen during the analysis of developing velocity profiles in the transition region (Chapter 3) that a change in U_v would affect velocity decay principally through the derivatives dI_n/dz:-

$$\frac{dI_n}{dz} = K_n\frac{dA}{dz} + A\frac{dK_n}{dz} \quad ; \quad K_n(z) = \frac{I_n}{A} \qquad (7.24)$$

In the transition region, $dK_n/dz<0$ (Chapter 3) as the velocity profile fullness decreases, and the rate of decay of velocity is inhibited. From above, $dK_n/dz<0$ also for the distorting U_v profile ($\bar{U}_v$ very slightly decreasing with z), so that the effect will again be a reduction in the velocity decay rate. This was the effect reported by Packer (35) (Fig. 7.41): decreasing the damping factor ν_T accelerates the rate of distortion, increasing $|dK_n/dz|$ and so the inhibiting effect upon velocity decay. For ν_T/ν_a=0.044 (the value used in the present work), the results of Packer suggest a very slight but observable effect on jet maximum velocity near the downstream limit (b and c, Fig. 7.41, z>15mm). However, Packer (35) used the spreading rate

coefficient G_{1M}=0.38 from Adler and Baron (63), while in the present work the value G_{1M}=1.7 has been ascribed, to give agreement with experimental velocity decay (Section 7.3.5a). This re-evaluation of G_{1M} implies that the spreading rate dA/dz is greatly increased relative to the Packer work, and in 7.24 this causes the decay-inhibiting term AdK_n/dz to be swamped by the term $K_n dA/dz$, so that no influence of profile distortion on velocity decay is observed.

From this discussion it is concluded that the similarity assumptions of Section 7.3.5 allow sufficiently accurate predictions of the principal flow properties to be made while keeping computer time requirements very low (compared with the full calculation scheme including profile distortion). The cross-section distortion sub-model contains two major subroutines (chapter 6):-

1/ subroutine vortex - displacement of seeded vortices to produce the cross-section shape (Fig. 7.44).

2/ subroutine epdel - solution of Poisson's equation over the jet shape for generation of U_v (Fig. 7.44b etc).

Thus, it is possible to divorce jet shape predictions (1/ above), which incur no serious time penalties, from the time-consuming profile generation (2/ above). In this way, predicted jet shapes may be appended to the similarity model of Section 7.3.5, to give a facility for the representation of jet spread (by the simple method for locating the maximum velocity point illustrated in Fig. 7.44i). Predictions of this type are reported in the next section. Recent applications of cross-section distortion techniques are also described by Ng (112).

7.3.7 Other Crossflow Types

In order to place some bounds upon the scope of the work, three types of crossflow were compared and contrasted:-

a) Shear flow,
b) Swirl (solid body rotation)
c) a variant of solid body rotation.

7.3.7a Shear Flow

Measurements of the trajectory of jets issuing at right angles to a shear flow have been made by Shirakashi and Tomita (90). In the experiments, the crossflow was given by:-

$$w = w_0(1 + 0.035y_z/D_0) \quad ; \quad w_0 = 0.1ms^{-1}$$

(w is always parallel to the axis x_z, as for a uniform crossflow), and several different injection velocities were considered. Comparisons between predictions and experiment are shown in Fig. 7.45; the correct deflection characteristics are observed. The injection velocity profile in the experiments was not uniform (90), and the predictions in Fig. 7.45 were obtained by matching nozzle momentum flux with the experimental boundary conditions. This type of crossflow has been considered mainly for comparison with swirl trajectory results, described below.

7.3.7b Swirl (Solid Body Rotation)

The results of a parametric study of the effect of swirl rate ω ($w=\omega r_z$) on the principal flow quantities in a constant density jet are shown in Fig. 7.46. The (uniform) injection velocity u_0 was again $100ms^{-1}$ and the nozzle diameter D_0 was set at 0.002m. Three non-zero swirl rates were considered, ω=250, 500 and 1000rad/sec, and the submerged jet case (ω=0 - Section 7.2.1) is included for comparison.

The estimated axes ξ for these deflected jets are shown in Fig. 7.46a. Maximum penetration is shown to decrease with

increasing swirl rate, as the jet mixes out and is deflected increasingly more quickly. The prediction of each jet is terminated when the excess axial velocity becomes zero (Chapter 6).

The dependence of the rate of decay of the excess jet axial velocity function $h_v(z)$ upon swirl rate ω is shown in Fig. 7.46b. In contrast to the effect of the parameter $\mathcal{R}$ on the initial region length z_c in uniform crossflow cases (Fig. 7.33a-c), there is no great influence of ω upon z_c when $\omega\epsilon[0,1000]$ (Fig. 7.46b). This of course is because the crossflow velocity $w=\omega r_z$ remains small over the length of the initial region; downstream from z_c, the velocity decay rate is greatly affected by ω, being extremely rapid at 1000rad/sec. The character of the decay of h_v is very different to that of Δu_m (given by 7.3) in Fig. 7.33; in particular, there is no asymptotic approach to $h_v=0$ (see later).

The decay of axial concentration c is less rapid than the decay of h_v when $\omega>0$ (Fig. 7.46c). In particular, at ω=1000rad/sec, a considerable injectant concentration at the axis remains ($c_m/c_0\simeq0.25$) when there is no longer any excess jet velocity. This may indicate imperfect mixing, or the 'overswirling' effect discussed by Packer (35), in which the jet does not come into contact with as much of the chamber fluid as some less greatly deflected jets (see also Section 7.3.5d). The effect of ω on the increase in jet mass flux is shown in Fig. 7.46d.

It is interseting to compare jet deflection in swirl with that in the other crossflows discussed above. The trajectory in swirl at ω=500rad/sec (Fig. 7.46a) is reproduced in Fig. 7.47a, and compared with the predicted axis of a jet in a uniform crossflow at $\mathcal{R}^{-1}=18$ (from Fig. 7.31). The latter case was chosen as the mean swirl velocity, over the distance to which the ω=250rad/sec jet penetrates, satisfies $w_{mean}/u_0\simeq18$. The effect of the increasing crossflow velocity of the crossflow with penetration for the swirled case is

clearly shown, and its effect is also apparent in a comparison of the predicted decay of h_v for the two cases (Fig. 7.47b).

A simple model for the prediction of jet trajectories in swirl has been devised at Bath University by Fraudeau (45). The model was based on that described by Wooler (86), and extended earlier analytical work at the University by Idoum (44). An initial simplifying assumption was made that the swirl velocity $w=\omega r_z(z)$ at any penetration z (where the radial penetration is $r_z=(x_z,y_z)$) could be replaced by the expression $w=\omega y_z$ (equivalent to assuming jet deflection to be very small). This crossflow is of course very similar to the shear flow described in Section 7.3.7a. In Fig. 7.48 predictions of trajectories in shear flow and swirl (at two different values of the parameter ω) are compared: as would be expected, the jet is deflected more rapidly (and will mix out more quickly) in the case of swirl, due to the relatively larger normal component of the crossflow velocity w. At the lower value for ω (Fig. 7.48a) the 'shear-flow' axis is displaced from the 'swirl' axis but is of the same general character, while with an increase in the value of ω (Fig. 7.48b) the difference in the nature of the deflection becomes more pronounced. Thus the simplifying assumption made by Fraudeau (45) would have a significant effect on the setting of empirical coefficients in a simple model.

Predictions of the envelopes of jets in swirl (at constant density) may be compared with photographic records of jet mixing, from experimental studies using the Bath University water rig (34,35,36). Although the injection conditions in the experiments are not known exactly (36,44), such studies are useful for assessing predicted jet spread. Three comparisons with experiment for water-water jets are shown in Fig. 7.49-51. Only by accounting for the cross-section shape distortion can the elongation in the trajectory plane be correctly represented (Fig. 7.49). The predictions were taken as far as that axial station where $h_v \to 0$ (Fig. 7.49), or to the point of impingement on the chamber wall

(Fig. 7.50-51), and compared with the observed jet development at approximately the same stage. The location of the mixing region in these examples appears to be suffisiently well predicted, although more detailed measurements and a more precise knowledge of experimental boundary conditions are required for further assessment of these predictions under swirl.

It is noted that side injection into swirl cannot be studied with the model in its present form (see Chapter 4 and Chapter 8).

7.3.7c Variant Of Solid Body Rotation

The flowfields generated in engine combustion chambers and specialised experimental apparatus cannot usually be represented as solid body rotation (Chapter 1), as shown by the measured velocity profiles in the work of Rife and Heywood (7) and Elkotb and Rafat (18,41). In order to assess the effect of nonuniformities in the external flow, the following hypothetical example was considered: solid body rotation (swirl velocity $\omega_0$rad/sec) is modified so that the swirl rate varies with radial penetration as illustrated in Fig. 7.52a, with the crossflow velocity becoming zero at the chamber wall, assumed to be stationary. This external flowfield may be described by:-

$$w=\omega_1 r_z \; ; \qquad \omega_1 \begin{cases} = \omega_0 & r_z < \frac{r}{3}m \\ = \frac{\omega}{2}0 & \frac{r}{3}m < r_z < \frac{2r}{3}m \\ \text{linear variation from } \frac{\omega}{2}0 \text{ to zero} & \frac{2r}{3}m < r_z < r_m \end{cases}$$

where r_m is the chamber radius. Nonuniform crossflows such as this are easily prescribed in the computer program as the crossflow velocity w is evaluated prior to each incremental solution step (Chapter 6).

The predicted axes ξ for two values of ω_0 are shown in Fig. 7.52b, and compared with the trajectory predicted for

the corresponding solid body rotation case, $w=\omega_0 r_z$. Deflection is markedly arrested by the decrease in swirl rate in the nonuniform examples: the difference in the trajectories is less significant in the higher ω_0 case (ω_0=500rad/sec), due to the greater deflection in the first ($\omega=\omega_0$) region.

7.3.8 The Effects Of Composition Variation

7.3.8a Comparison With Experiment For Air-Air Jets

Relatively little data is available concerning jet spread and property decay at variable density. The experiments of Ramsey (78) concern jets with velocity ratios $R^{-1}\simeq 2$, while the present work is directed toward cases where $R^{-1}>4$ (Chapter 4 - the validity of the model at higher relative crossflow velocities has not been investigated at present). The useful data here is that of Kamotami and Greber (39), for transverse injection into a uniform crossflow, and is considered below.

Shown in Fig. 7.53a are measurements of the decay of normalised, axial excess temperature with penetration when $R^{-1}=4.96$ and $\theta=T_0/T_\infty=1.62$ (T_∞=300K, P=1bar). The prediction of $h_T(z)$ (defined in 5.16a) by the program (using the similarity assumptions of Section 7.3.5 for integral evaluations) is also shown in Fig. 7.53a, and is in reasonable agreement with the data: uniform injection property profiles were prescribed. The prediction at smaller values of ξ/D_0 (<10, say) would be further improved by the inclusion of the slight nozzle boundary layer apparent in the experiment (Section 7.2.1). The prediction at $R^{-1}=4.96$ is compared with the submerged jet (R=0) prediction from Fig. 7.15 (Section 7.2.3b) at a similar value for θ, in order to show the effect of a crossflow on temperature decay. The pointwise jet C_p was calculated from 7.11. A further comparison with experiment, for a lower crossflow velocity ($R^{-1}=9.8$) is made in Fig. 7.3b: here, measurements of jet maximum temperature were only available in the downstream limit ($\xi/D_0\geq 10$). Again, the prediction appears to be reasonably good. The effect of velocity ratio R upon

predicted velocity and concentration decay was discussed in Section 7.3.5c, while examples of the effect of initial heating ($\theta>1$) on velocity decay are given below.

Shown in Fig. 7.54 are the predicted maximum velocity axes ξ associated with the heated air jet cases described above. The ξ axis is located approximately, from the centreline z, using the formula 7.17. The predicted axes compare well with the data of Kamotami and Greber (39) at the same injection conditions. The experimental results also show that the maximum temperature axis ξ_T (defined as the locus of maximum temperature points in successive cross-sections) falls below the velocity axis ξ (see Section 5.9). Although modelling simplifications prohibit this effect from being treated directly (U_T and U_v are assumed to be equal to one at the same point - Chapters 5 and 6), it is interesting to observe that the predicted momentum centreline z (the independent variable in the numerical solution) is a sufficiently good approximation to the temperature (or concentration (70)) axis, and that this may be useful for estimating purposes.

In order to show the influence of the initial degree of heating θ on the predictions, the uniform crossflow and injection velocities are fixed to give $\mathcal{R}^{-1}=6$, and three values for θ are considered: $\theta=0.5$ (cold air injection), $\theta=1.125$ and $\theta=2.0$ (hot air injection). Such problems may be characterised by means of the momentum ratio J^2. For air jets in air ($n=\theta$):-

$$J^2 = \frac{\rho_0 u_0^2}{\rho_\infty w^2} = \frac{T_\infty u_0^2}{T_0 w^2} = \frac{1}{\theta \mathcal{R}^2}$$

At $\mathcal{R}^{-1}=6$ (chosen arbitrarily for this study) the above values for θ were chosen to give:-

$J^2 = 18$ ($\theta=2$)
$J^2 = 32$ ($\theta=1.125$)
$J^2 = 72$ ($\theta=0.5$)

Experimentally determined maximum temperature trajectories, at these values for J^2, were reported by Jones and McGuirk (85). The significant effect of θ (so density ratio n) on jet deflection is shown in Fig. 7.55a in terms of the estimated maximum velocity axis ξ, while in Fig. 7.55b the predicted momentum centreline z again passes close to the measured temperature axis at the three values for θ. The hotter, less dense jets mix more rapidly than the cold (θ=0.5) jet, and this is illustrated in Fig. 7.55c by the decrease in the length of the initial region ($\Delta u_m/\Delta u_0$=1) with increasing θ, and the following more rapid decay of axial velocity. A similar effect on temperature is shown in Fig. 7.55d.

A comparison of the rates of decay of the axial velocity, temperature and concentration functions Δu_m, $\Delta T_m=h_T$ and c_m for the case θ=1.125 is given in Fig. 7.55e. The persistence of a significant temperature difference on the axis, even when the jet excess velocity is very small (ξ/D_0=20, say), was observed experimentally (39). The average C_p value in the heated air in air jet is always slightly greater than $C_{p\infty}$, the specific heat of air at the temperature of the external stream, and as a consequence, the relative rate of decay of excess temperature h_T is slightly less than that of injectant concentration c_m. When a uniform C_p distribution is prescribed across the jet ($C_{pl}=C_{p\infty}$ in 7.11), then the relative rates of decay of excess axial temperature and injectant concentration are the same. In the case of the cold (θ=0.5) jet, excess temperature decay is more rapid than that of concentration (see below).

7.3.8b Prediction Of Dense, Nonisothermal Jets In Swirl

For the first example, the case of a Freon-12 jet in air is recalled from Section 7.2.3b, with the complication of swirl at ω=500rad/sec. The remaining injection conditions are those in 7.12.

The predicted maximum velocity axis for this problem is shown in Fig. 7.56a, while in Fig. 7.56b the relative rates

of decay of the excess axial property functions h_v, h_c and h_T are given. No experimental data was available for assessment of the predicted rate of cross-section distortion for the dense jet, so that the validity of the setting for ν_T from 7.23 in this case cannot be confirmed. In Fig. 7.56b, the faster rate of decay of excess axial temperature compared with concentration is due to the C_p value for Freon-12 being less than that of the ambient air (see Section 7.2.3b).

The final predictions discussed here were obtained upon prescribing for the injectant the properties of the hydrocarbon n-tridecane ($C_{13}H_{28}$), with a molecular weight M_i=184. The other injection conditions were:-

injection velocity:	u_0=100ms^{-1}
chamber temperature:	T_∞=650K
chamber pressure:	P=60bar
injection temp.:	T_0=450K
density ratio $n=\rho_\infty/\rho_0$:	n=0.11
nozzle diamter:	D_0=0.2mm

and three swirl rates were considered for parametric variation: ω=100, 250 and 500rad/sec. The predicted jet trajectory at each swirl rate is shown in Fig. 7.57a, and the predicted axis for a constant density jet in a related case (ω=500rad/sec,n=1) is shown for comparison. The predicted excess velocity decay rates in the three cases are compared in Fig. 7.57b; velocity decay is extremely rapid beyond the end of the constant velocity core in the ω=250 and ω=500rad/sec case. The deflection of the jet in the initial region is negligibly small.

The relative axial property decay rates for the cold (θ<1) hydrocarbon jet at ω=500rad/sec are given in Fig. 7.57c. Pointwise specific heat for the hydrocarbon-air jet was calculated (at the nodes of a finite-difference grid - see Chapter 6) by a call to a gas property subroutine used by White (42) in a combustion model, itself derived from routines used in engine cycle simulation programs at Bath

University. This subroutine has also been used to compute air C_p values for the 'theory of mixtures' setting for pointwise jet C_p in other cases (Section 7.2.3b and Section 7.3.8a), by means of a single call with the ambient conditions $T=T_\infty$, $c=0$ (pure air). For the problem under discussion here, the injectant to air C_p ratio at injection was calculated as:-

$$\overline{C}_p = 2.41 \quad ; \quad \theta = 0.692$$

As a direct result of this difference in specific heat values, the temperature difference function $|h_T|$ decays much less rapidly than the axial concentration function c: when $\overline{C}_p \simeq 1$, these functions decay at approximately the same rate (Fig. 7.55e).

A jet with a nominal injection density ratio n=0.1 was considered by the author in a parametric study of an intermediate version of the present computer model (46), a direct implementation of the theory from Packer (35). From this study is shown, in Fig. 7.58, the effect of variation of the angle of injection β_0 on trajectory and mass entrainment rate for a dense jet in swirl. Entrainment (so mixing) is slightly enhanced by injecting 'into' the crossflow ($\beta_0 = 110^0$) - see also Fig. 7.39. This latter type of injection poses some modelling difficulties in that there exists in the first portion of the jet a 'counterflowing' 'counterflowing' component of the free stream velocity, instead of a coflowing stream component. According to Abramovich (32),an axisymmetric jet in a counterflowing stream spreads at the same rate as a jet in a quiescent medium, so that the predicted entrainment rates from the present model might be somewhat low in such cases (see Chapter 4). As entrainment is dominated by the 'vortex pair' growth term 4.18, this effect should be slight: however, no data was available for comparison with predictions.

7.3.9 Summary And Conclusions

The integral model has been assessed against the available experimental data for deflected jets, which concerns in the main constant (or near constant) density injections. Most significantly, the empirical coefficient controlling enhanced jet spread in a crossflow has been evaluated using reliable test data for axial velocity decay; consequent predictions of axial velocity, concentration and temperature, as well as jet trajectory, entrainment and spread compare favourably with measurements over a reasonable range of injection conditions; the quantitave prediction of these flow details appears to have recieved scant attention in the literature (except in the case of trajectory). The present work emphasises the relative importance of entrainment (compared with pressure deflection) in determining the jet path. A method for estimating the jet maximum velocity axis from the computed momentum centreline is included, in order to allow the proper matching of trajectories with experimental results.

A facility for the accurate representation of distorted jet shapes and property profiles has been included in the computer simulation. Good qualitative agreement is obtained for the deflected jet envelope according to experiments with the Bath University water rig. The large entrainment rates in the present model imply a negligible effect of distorting velocity profiles on predicted axial flow characteristics or jet trajectory (the effect already being slight in the initial implementation by Packer (35)). The use of circle similarity assumptions appears to be legitimate for all predictions with the exception, of course, of the location of the mixing region. Experimental data is insufficiently complete to match cross-section distortion rates in variable density jets.

Qualitatively correct predictions of the effect of swirl on dense (nominally fuel vapour) jets have been presented, illustrating an 'overswirling' effect where jet excess velocity becomes zero leaving significant concentrations

of fuel at the jet axis. The further influence of temperature and velocity nonuniformities in the external stream, which may be included in the modelling, would be of interest in such predictions: some representation of pressure gradients in the crossflow may be necessary for comprehensive quantitative predictions.

Some preliminary predictions of very dense two phase sprays, under engine like conditions, are described in the next chapter.

	A	B	
n	z_c/D_0 prediction	z_c/D_0 from 7.7	$\frac{A}{B}$x100
0.27	9.84	9.62	102.3%
1.00	4.92	5.00	98.4%
1.70	3.28	3.84	85.4%
1.85	3.06	3.68	83.2%
3.25	1.82	2.77	65.7%

TABLE 7.1 VARIATION WITH DENSITY RATIO n OF THE LENGTH OF THE INITIAL REGION IN A SUBMERGED JET AND COMPARISON WITH THE CORRELATION 7.7

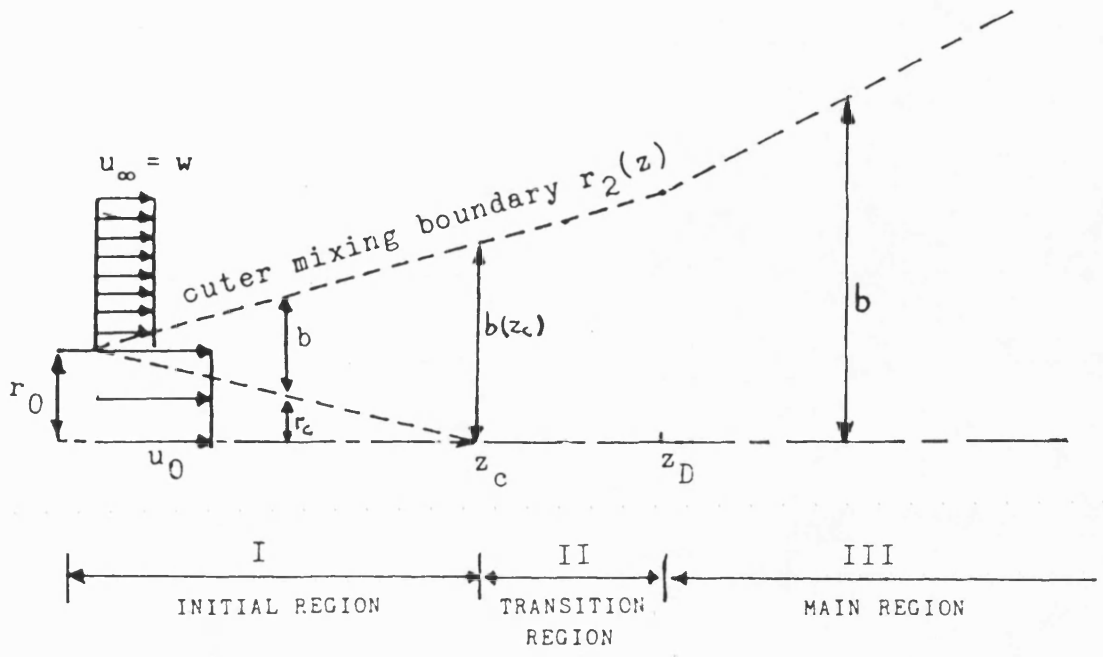

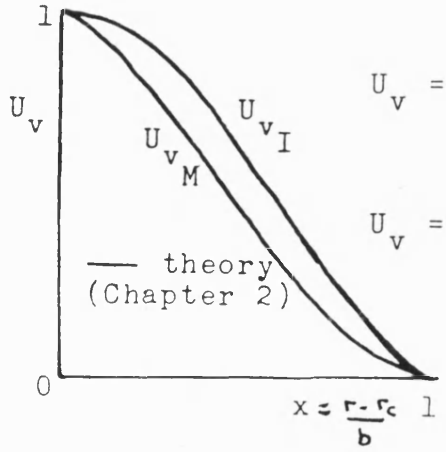

$$U_v = \begin{cases} U_{v_I}(x) & r \in [r_c, r_2] \quad z < z_c \\ 1 & r < r_c \end{cases}$$

$$U_v = U_{v_M}(x) \qquad z > z_D$$

At constant density :-

$$\frac{db}{dz} = \begin{cases} G_I = 0.22 \quad (z < z_c) \\ G(z) \text{ varying linearly between } G(z_c) \text{ (known) and } G(z_D) = G_M \\ G_M = 0.22 \quad (z > z_D) \end{cases}$$

(method extended directly to other cases by computation of $G(z_c)$ from $\frac{db}{dz}\Big|_{z_c}$

FIG. 7.1a FUNDAMENTAL GEOMETRIC RELATIONSHIPS FOR AN AXISYMMETRIC JET

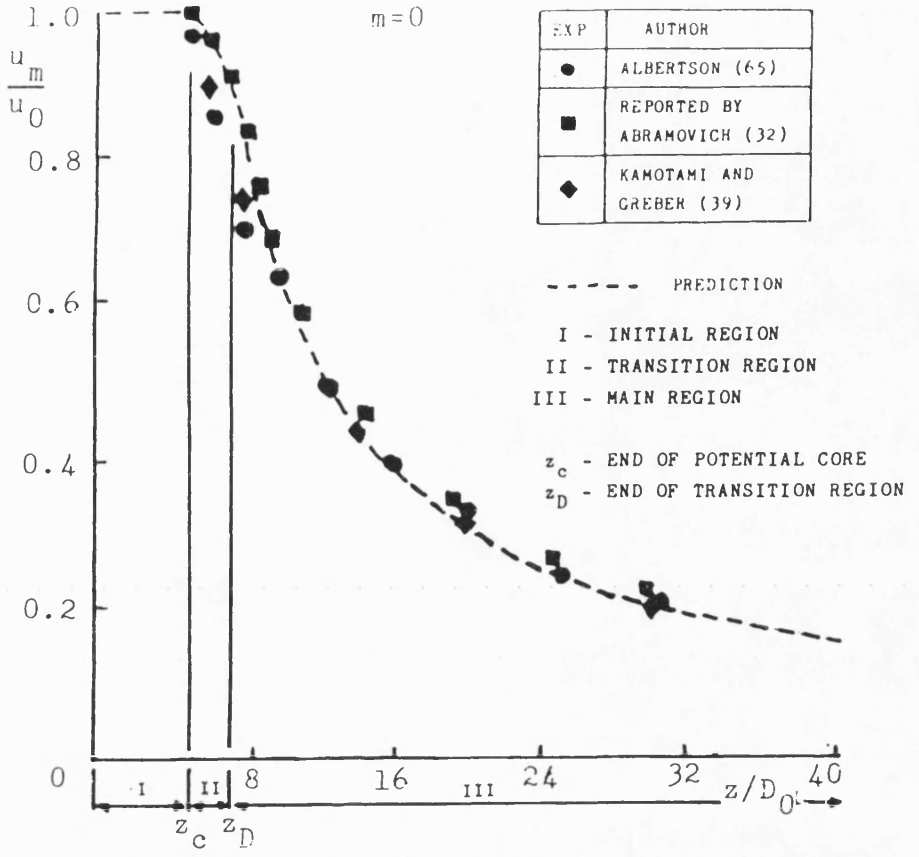

FIG. 7.1b AXIAL VELOCITY DECAY AT CONSTANT DENSITY

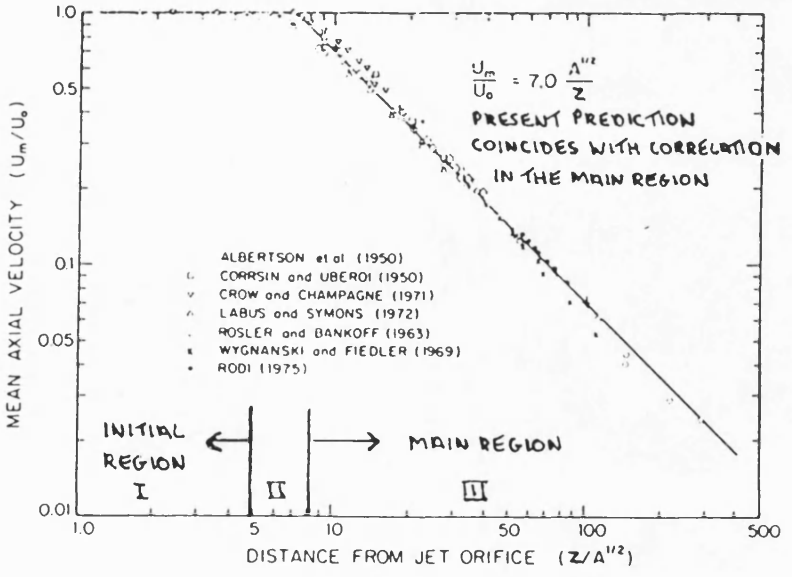

(DATA COLLECTED BY CHEN AND RODI (96))

FIG. 7.1c VELOCITY DECAY AT LARGE AXIAL DISTANCES

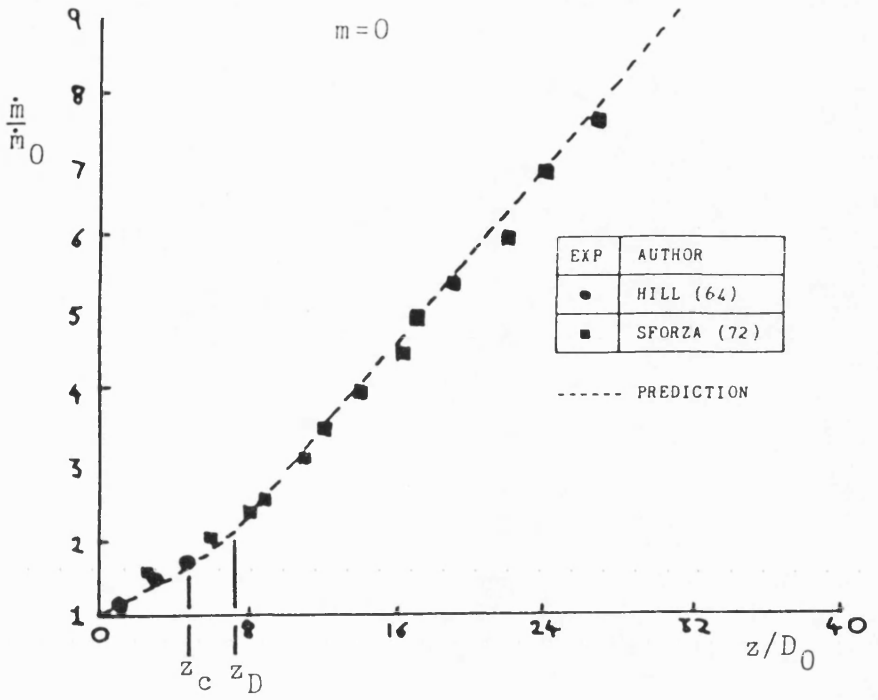

FIG. 7.2 INCREASE IN MASS FLUX AT CONSTANT DENSITY

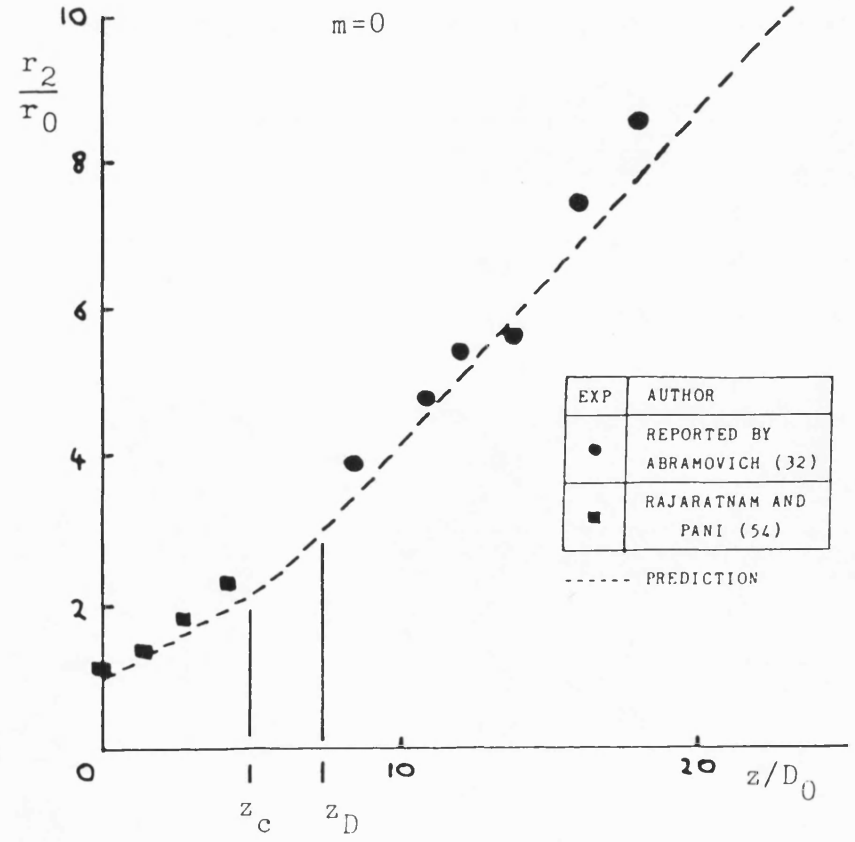

FIG. 7.3 SPREAD OF A JET AT CONSTANT DENSITY

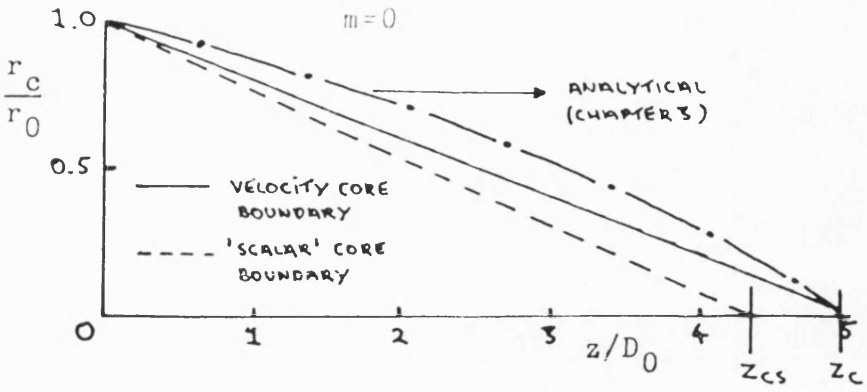

FIG. 7.4a PREDICTED CORE BOUNDARIES FOR VELOCITY AND CONCENTRATION AT CONSTANT DENSITY

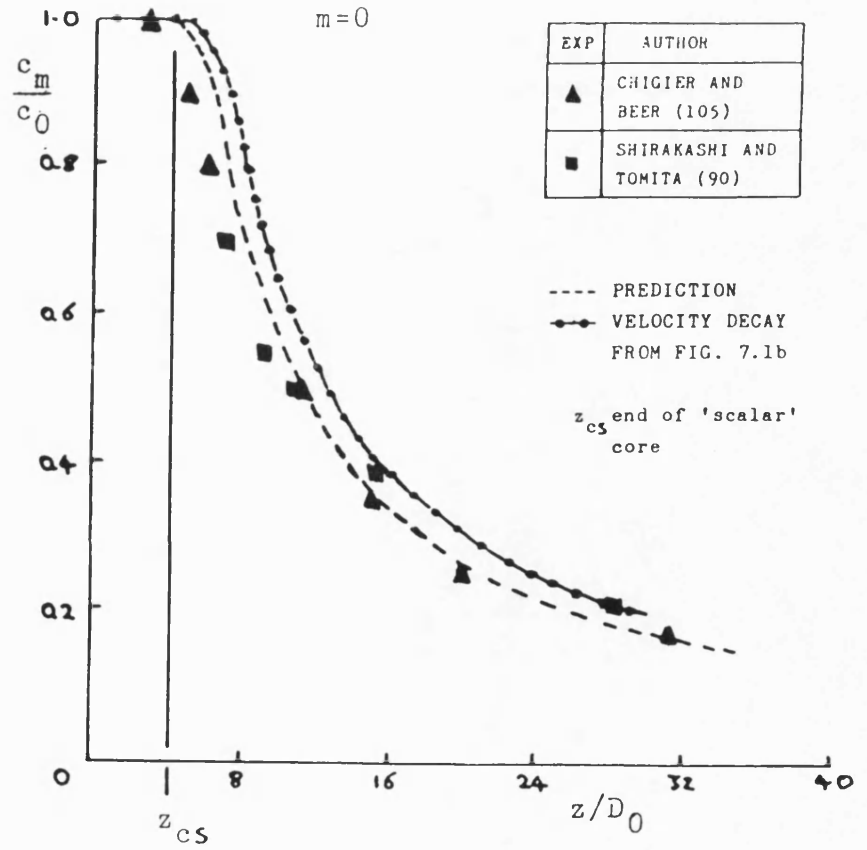

FIG. 7.4b AXIAL DECAY OF INJECTANT CONCENTRATION AT CONSTANT DENSITY

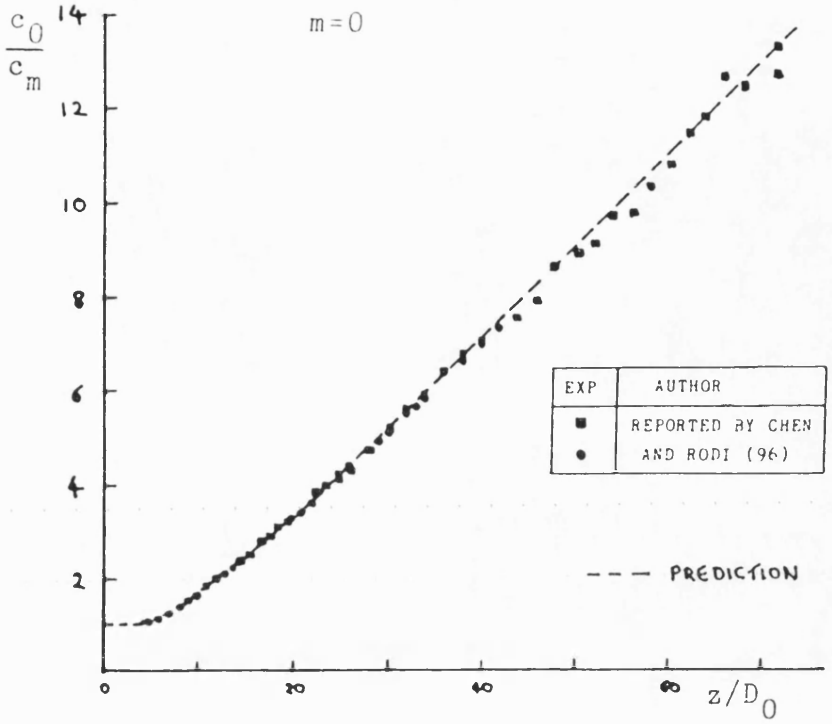

FIG. 7.4c CONCENTRATION DECAY AT LARGE AXIAL DISTANCES

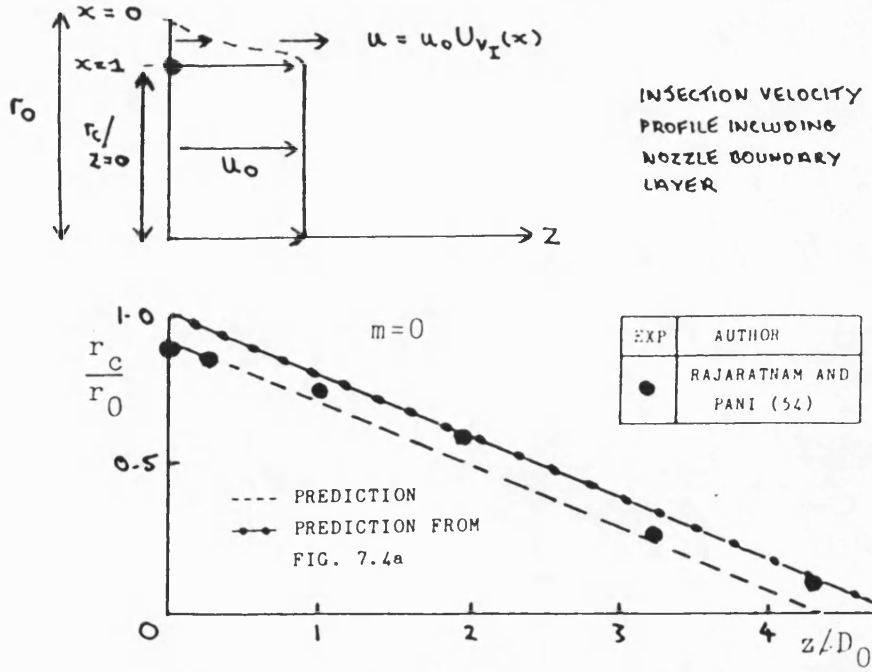

FIG. 7.5a EFFECT OF A NOZZLE BOUNDARY LAYER ON THE LENGTH OF THE INITIAL REGION

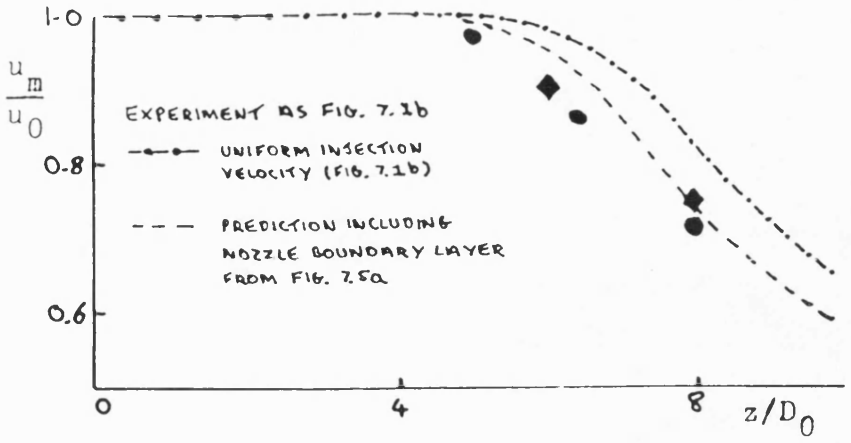

FIG. 7.5b PREDICTION OF VELOCITY DECAY NEAR THE NOZZLE ASSUMING A NOZZLE BOUNDARY LAYER

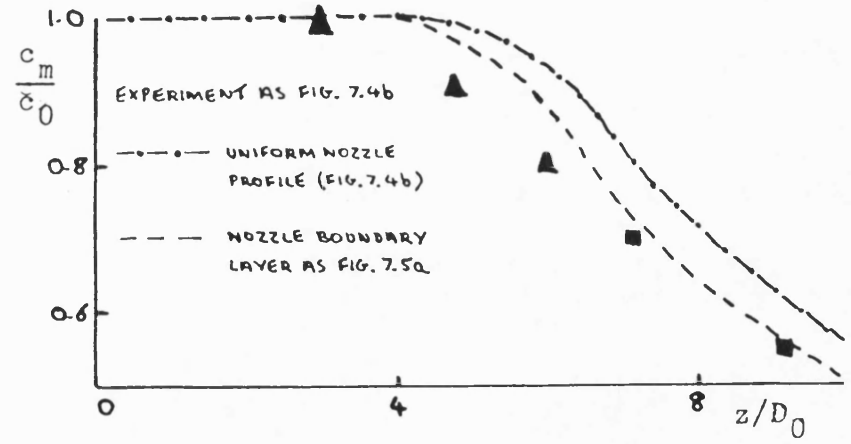

FIG. 7.5c EFFECT OF A NOZZLE BOUNDARY LAYER ON AXIAL CONCENTRATION DECAY

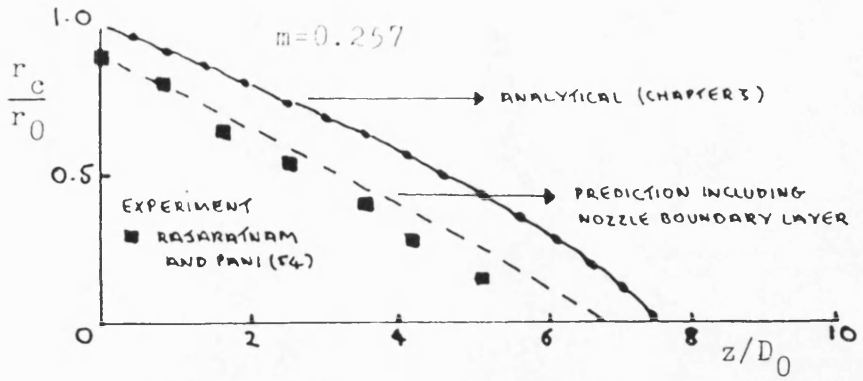

FIG. 7.6 PREDICTED CORE BOUNDARY FOR A CONSTANT DENSITY JET IN A COFLOWING STREAM

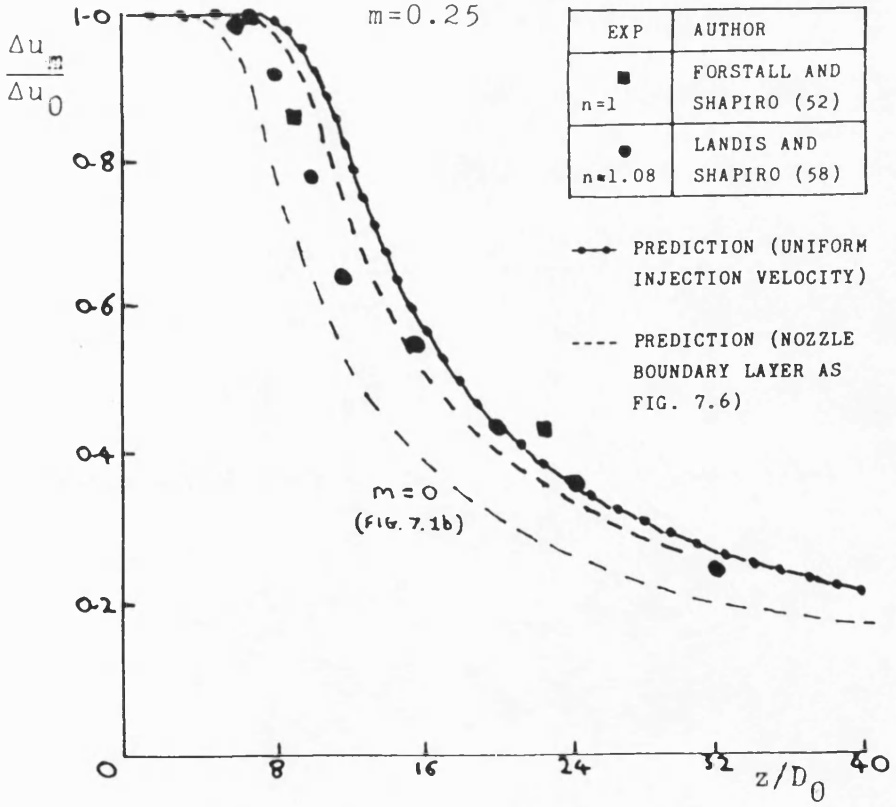

FIG. 7.7 EXCESS VELOCITY DECAY FOR A CONSTANT DENSITY JET IN A COFLOWING STREAM

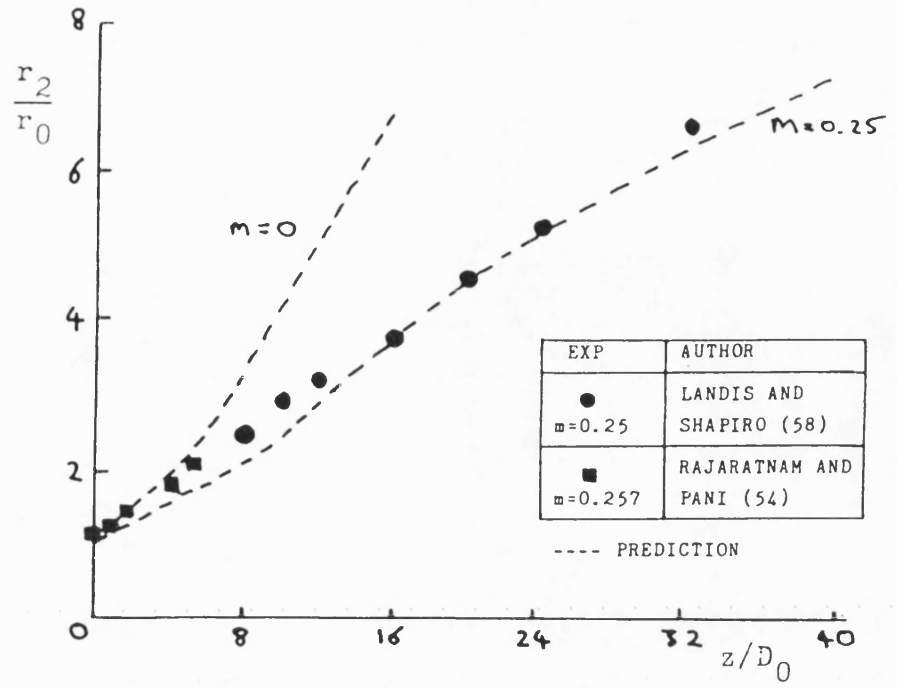

FIG. 7.8a THICKENING OF A CONSTANT DENSITY JET IN A COFLOWING STREAM

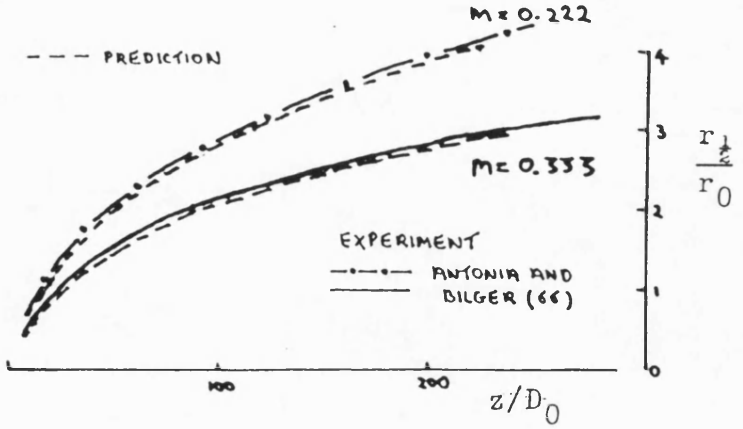

FIG. 7.8b INCREASE IN JET HALF-WIDTH WITH DISTANCE FOR JETS IN COFLOWING STREAMS

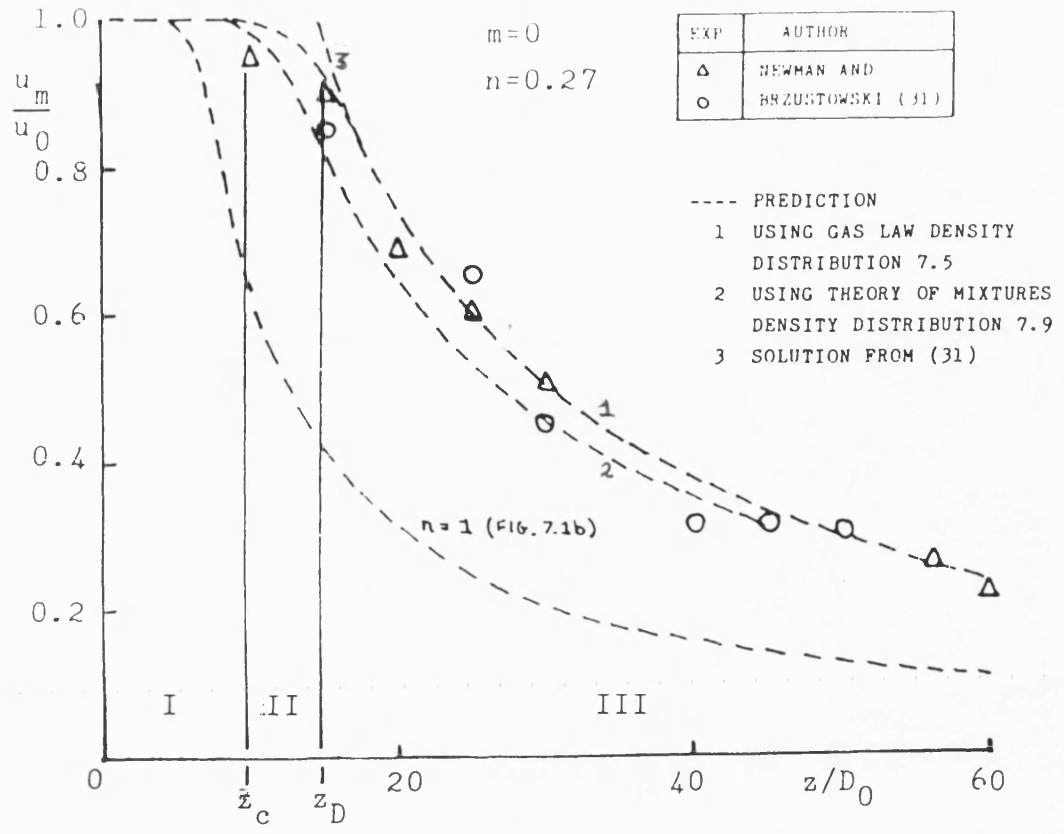

FIG. 7.9 VELOCITY DECAY IN A DENSE JET AND INFLUENCE OF THE ASSUMED DENSITY DISTRIBUTION

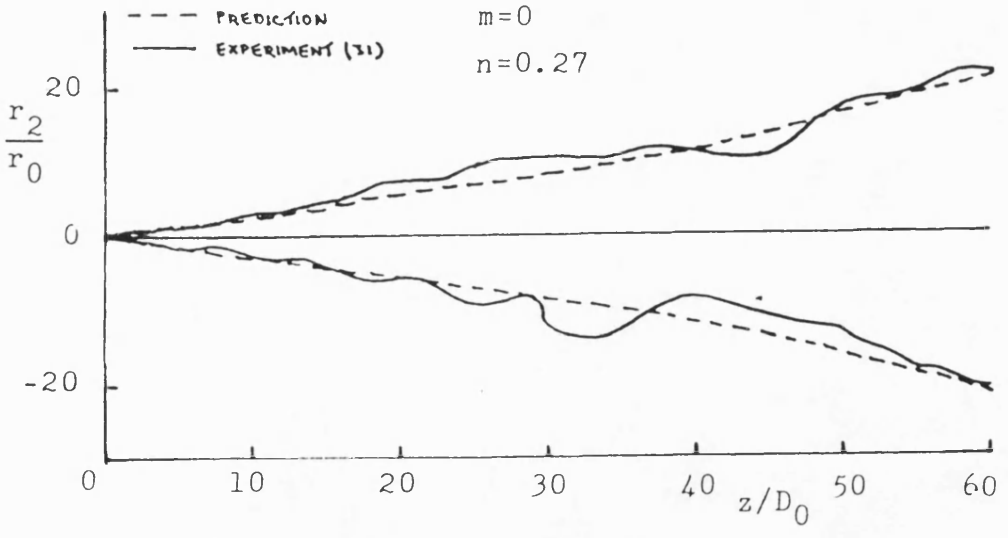

FIG. 7.10 PREDICTED SPREAD OF A DENSE JET AND COMPARISON WITH THE BOUNDARY TRACED FROM A PHOTOGRAPH (31)

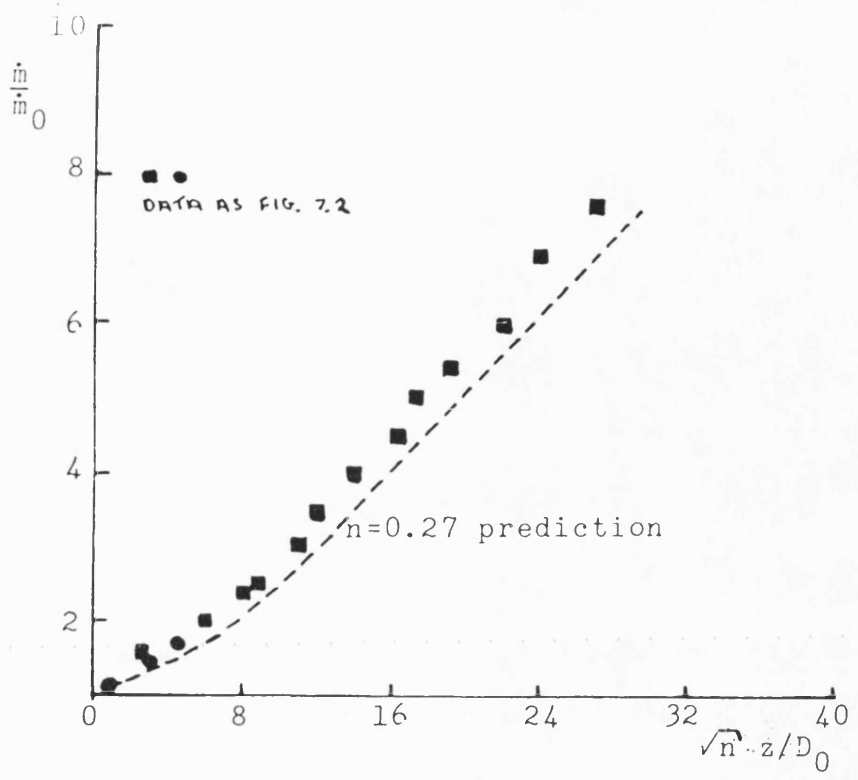

FIG. 7.11a INCREASE IN MASS FLUX WITH PENETRATION FOR A DENSE JET

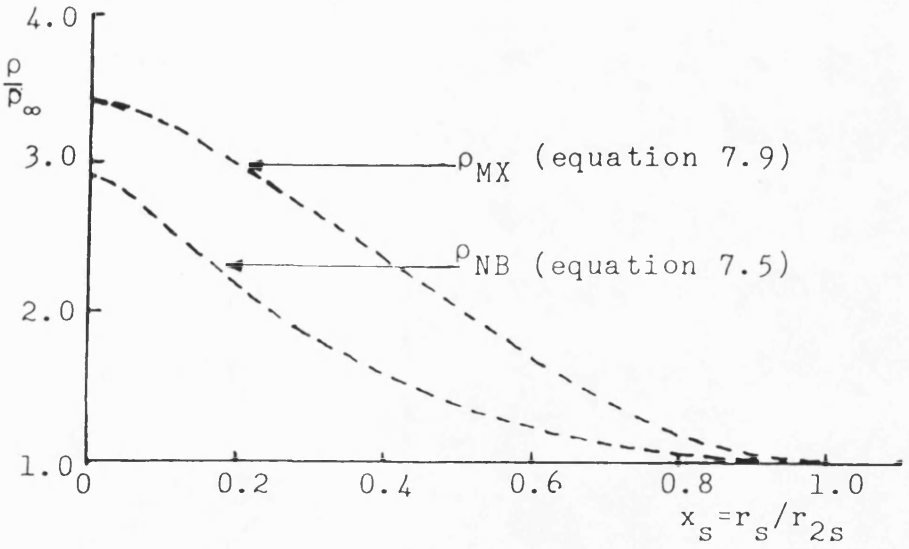

FIG. 7.11b COMPARISON BETWEEN DENSITY DISTRIBUTIONS

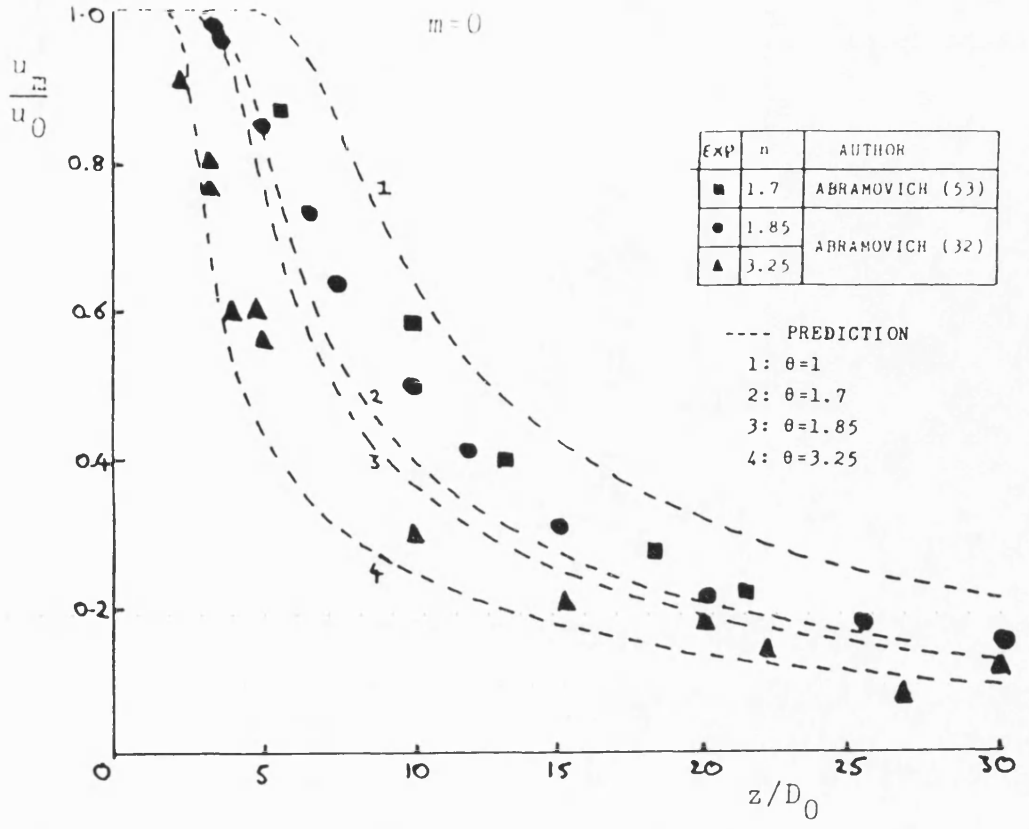

FIG. 7.13 AXIAL VELOCITY DECAY IN HEATED AIR-AIR JETS

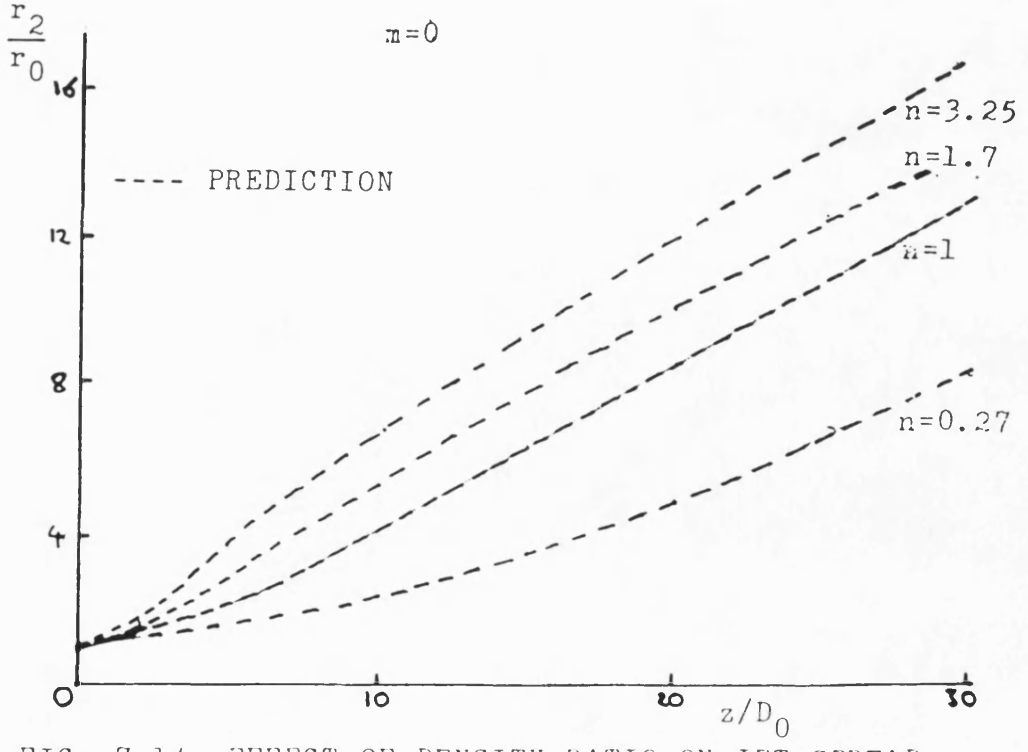

FIG. 7.14 EFFECT OF DENSITY RATIO ON JET SPREAD

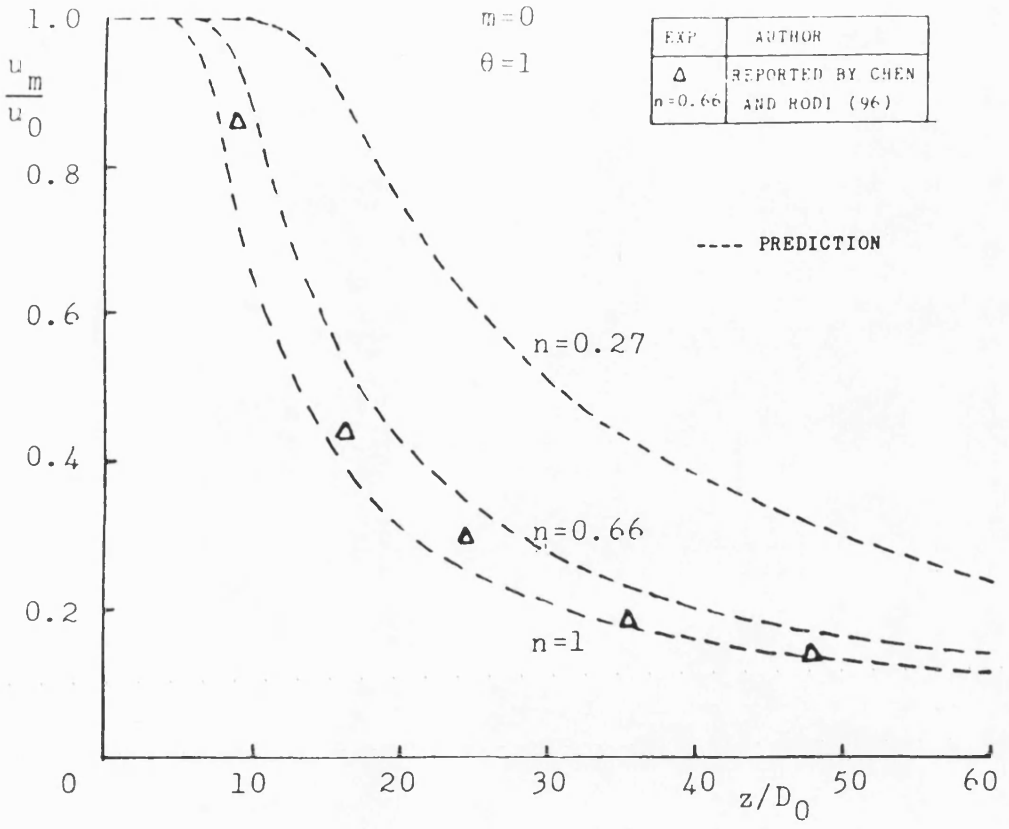

FIG. 7.12a EFFECT OF DENSITY RATIO ON AXIAL VELOCITY DECAY IN ISOTHERMAL AXISYMMETRIC JETS

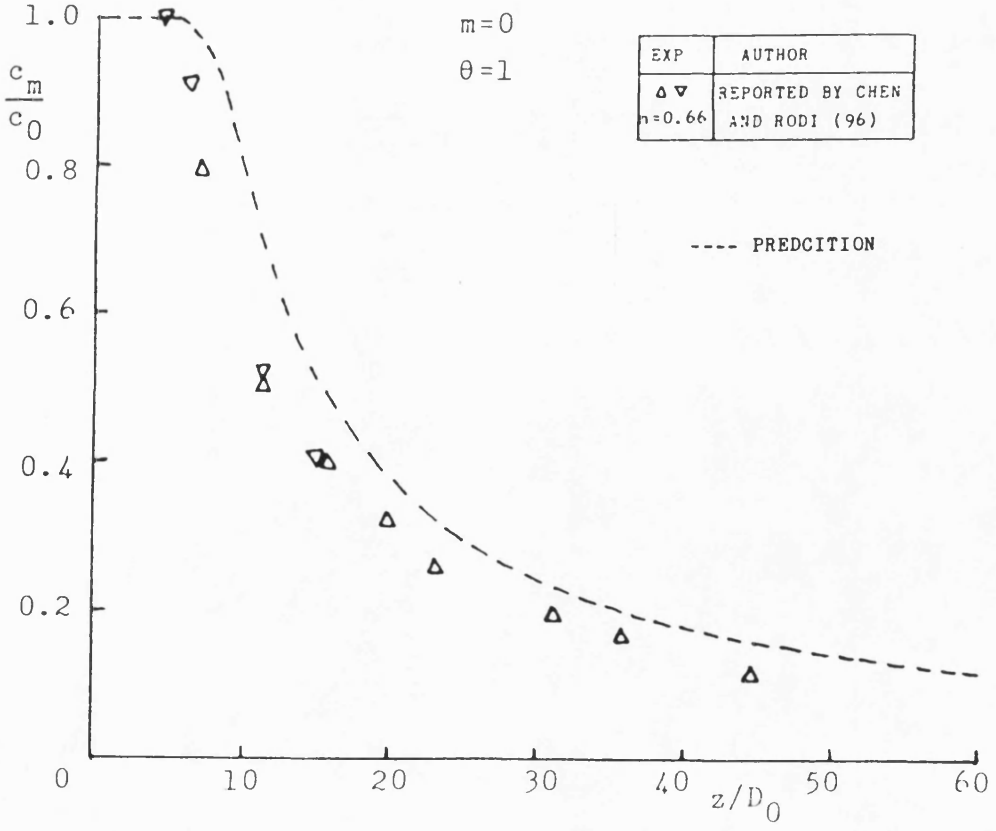

FIG. 7.12b AXIAL CONCENTRATION DECAY IN A DENSE JET

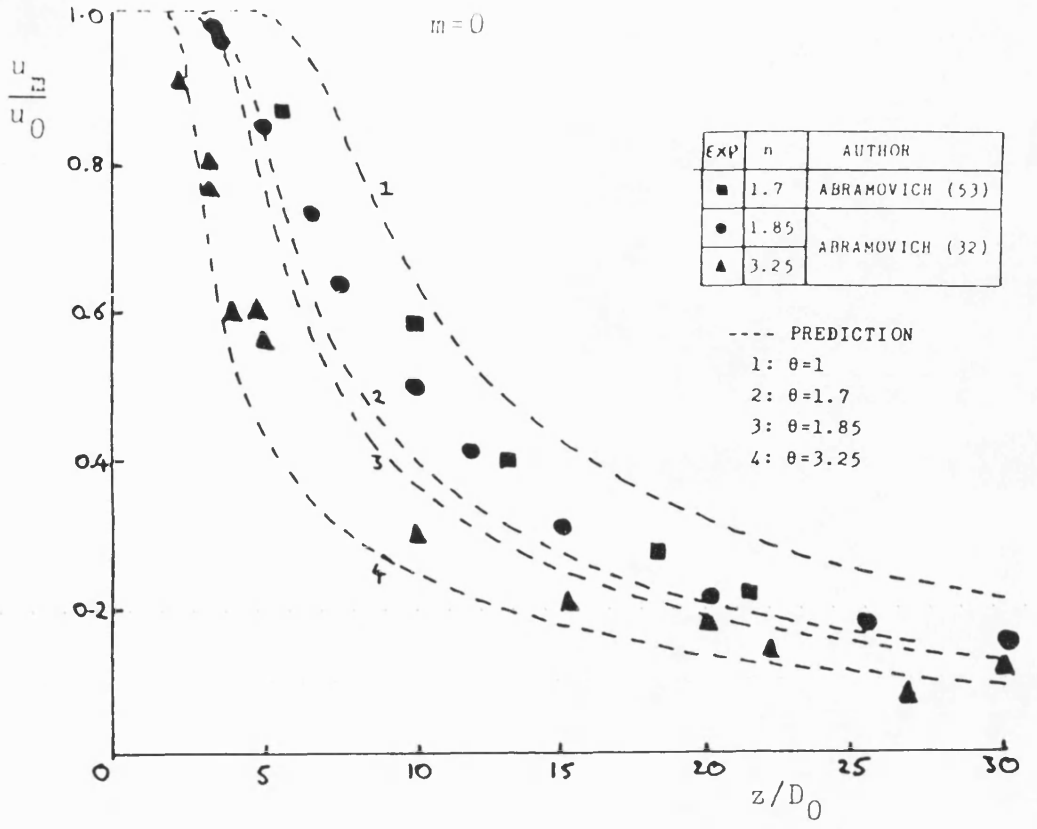

FIG. 7.13 AXIAL VELOCITY DECAY IN HEATED AIR-AIR JETS

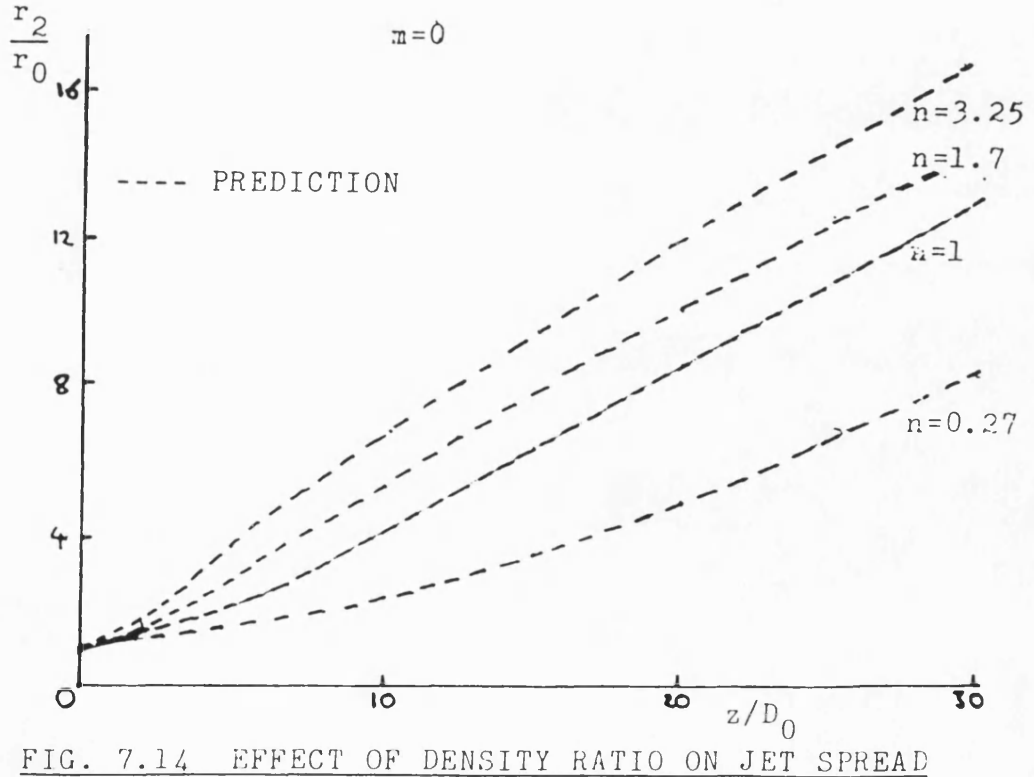

FIG. 7.14 EFFECT OF DENSITY RATIO ON JET SPREAD

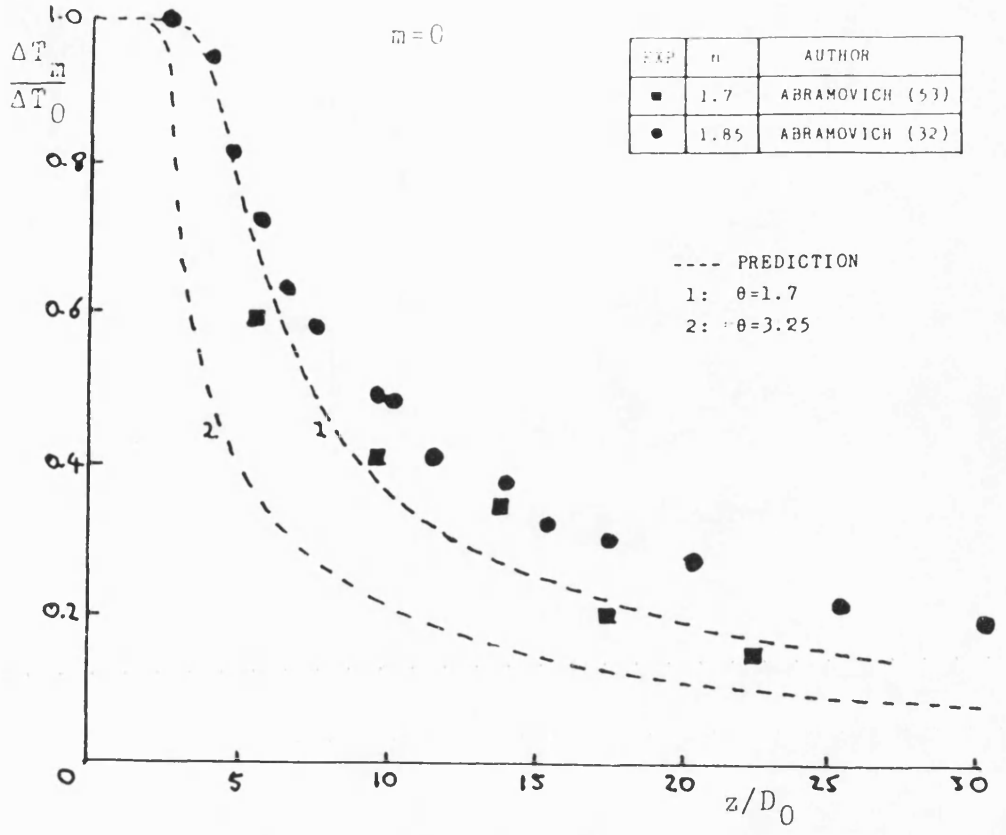

FIG. 7.15 AXIAL TEMPERATURE DECAY ASSOCIATED WITH THE VELOCITY DECAYS IN FIG. 7.13

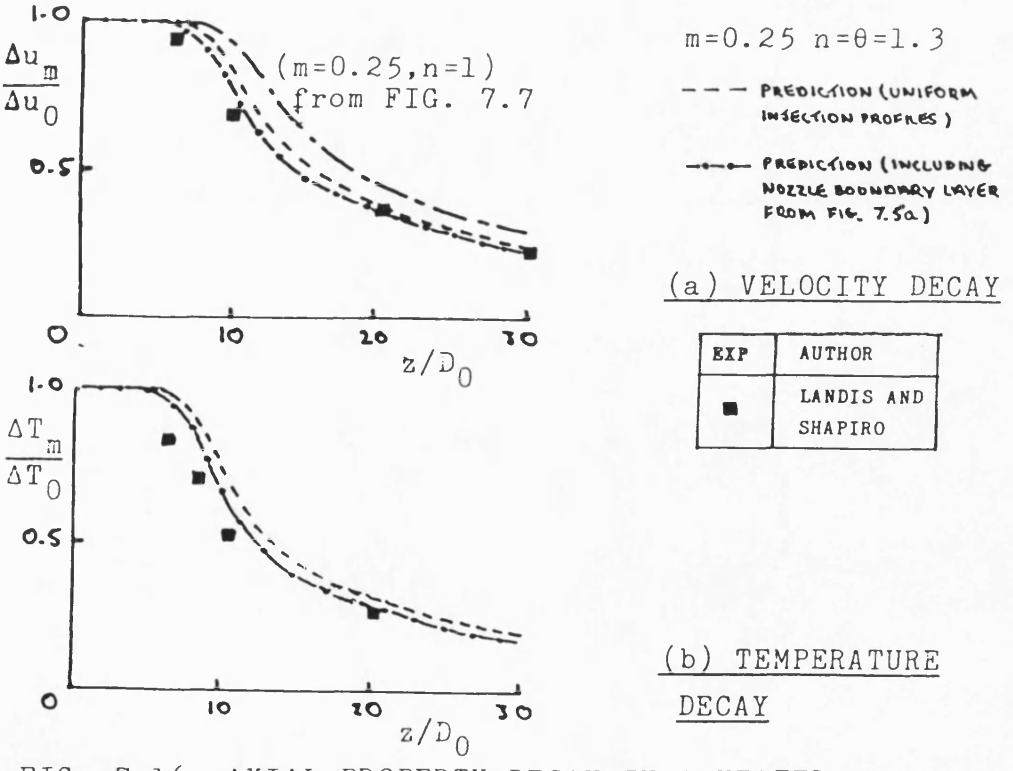

FIG. 7.16 AXIAL PROPERTY DECAY IN A HEATED AIR-AIR JET

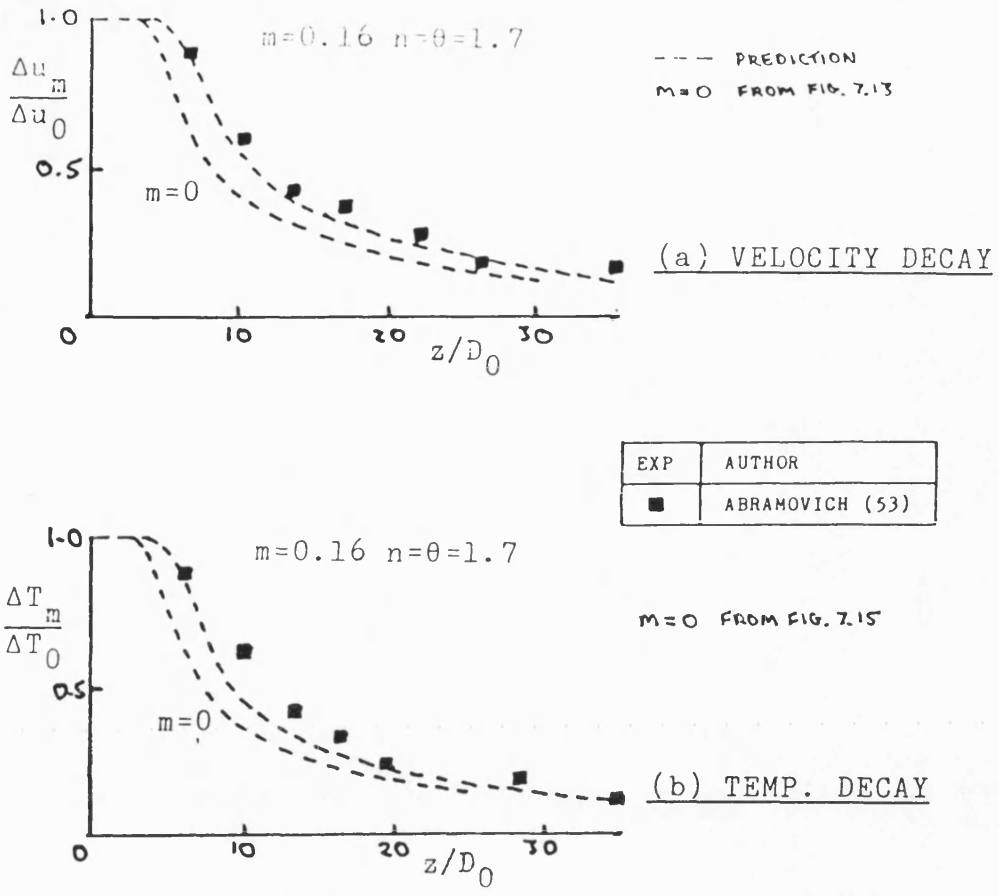

FIG. 7.17 AXIAL PROPERTY DECAY IN A HEATED AIR-AIR JET

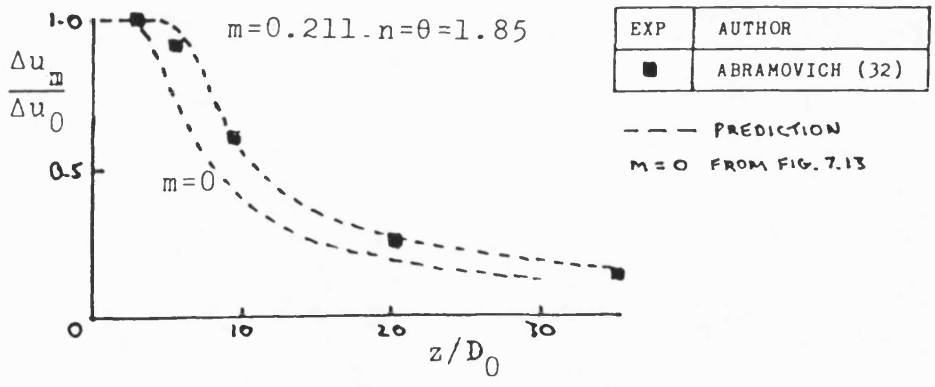

FIG. 7.18 VELOCITY DECAY IN A HEATED AIR-AIR JET

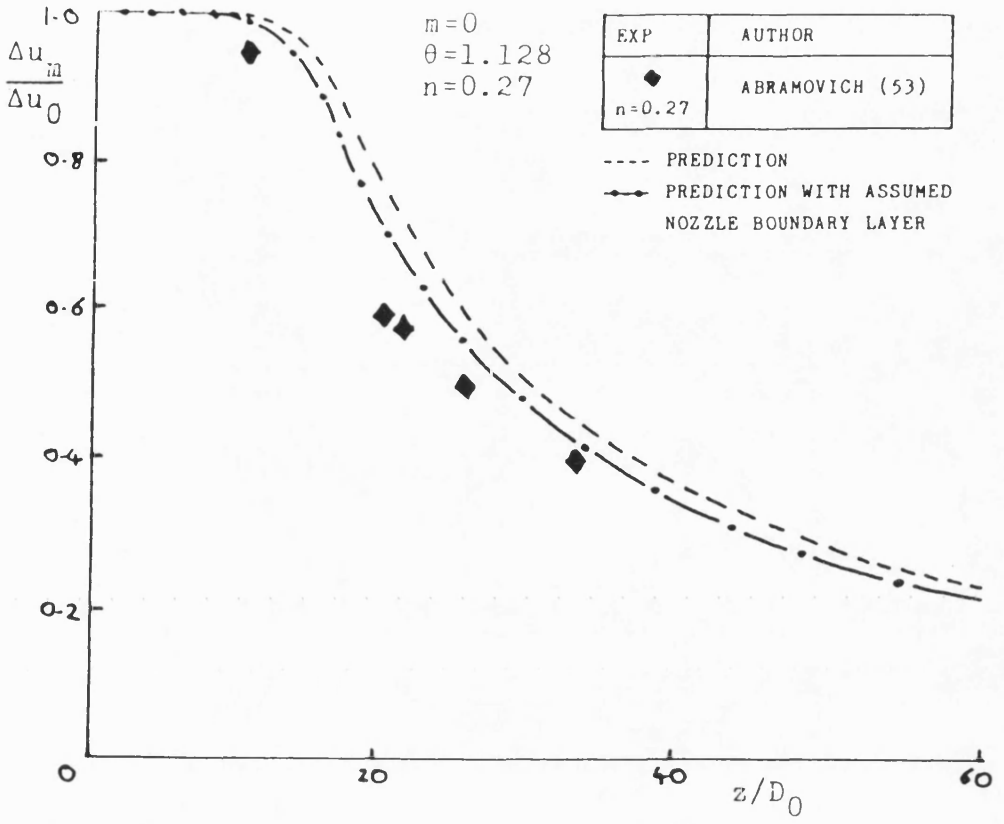

FIG. 7.19 VELOCITY DECAY ON THE AXIS OF A HEATED FREON-12 JET IN AIR

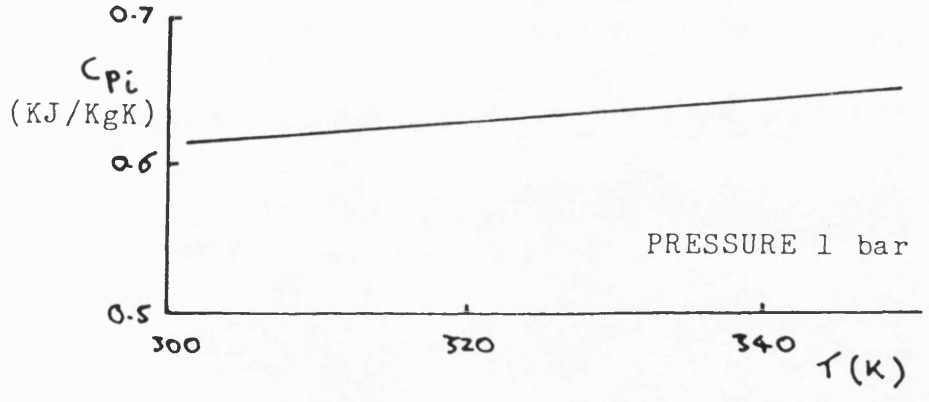

FIG. 7.20 VARIATION OF SPECIFIC HEAT WITH TEMPERATURE FROM THE TABULATED PROPERTIES OF FREON-12 (106)

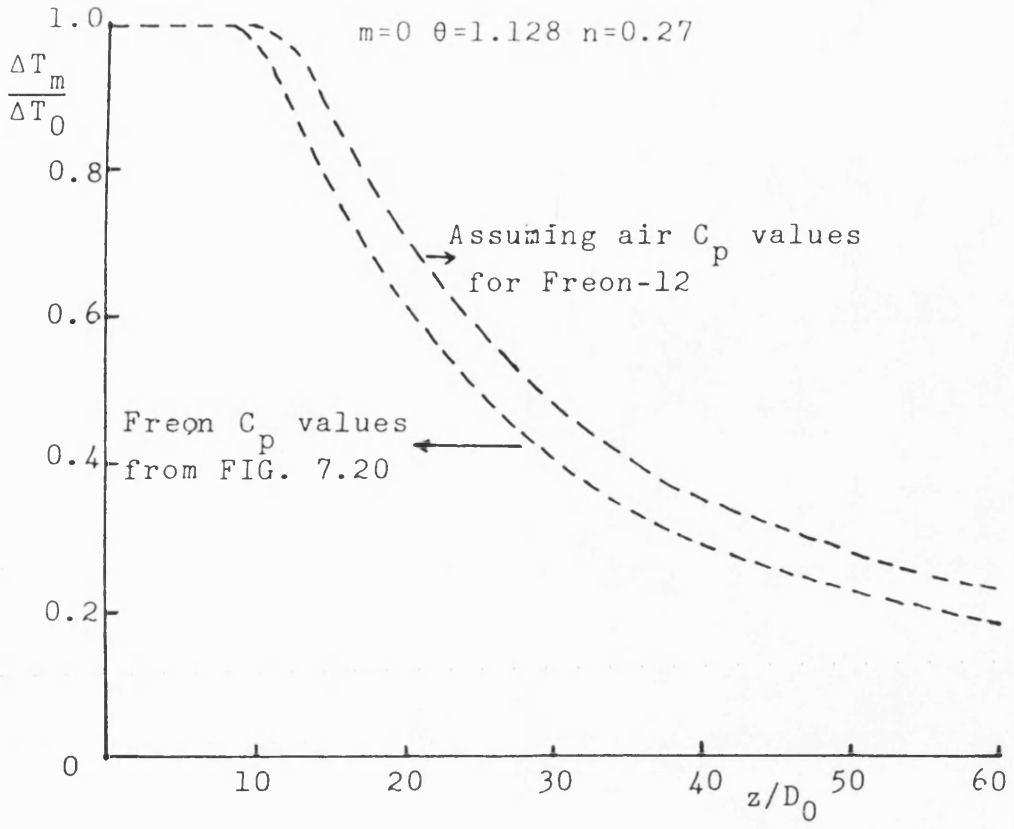

FIG. 7.21 EFFECT OF SPECIFIC HEAT FORMULATION ON AXIAL TEMPERATURE DECAY

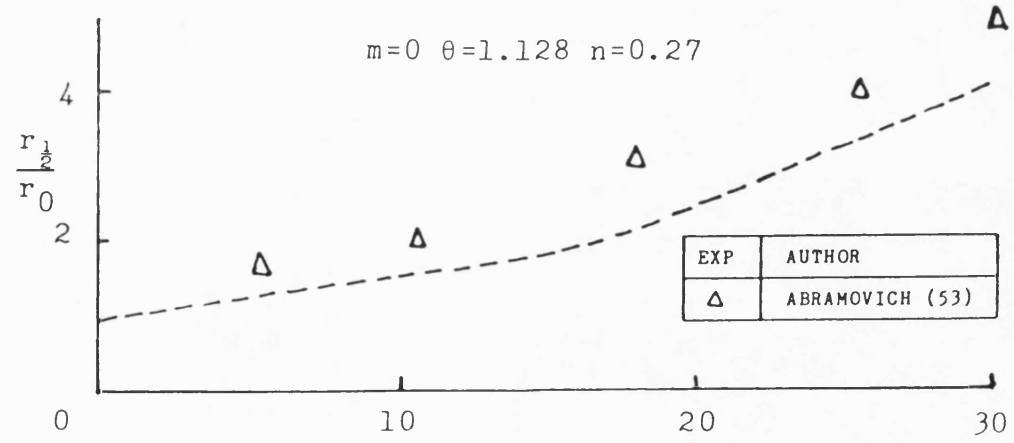

FIG. 7.22 GROWTH OF JET HALF-WIDTH FOR THE FREON-12 JET IN AIR

(a) AXIAL VELOCITY DECAY

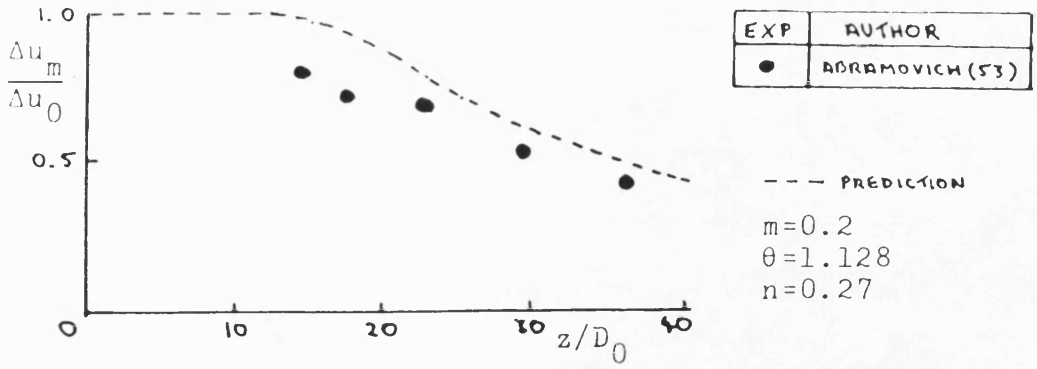

(b) AXIAL TEMPERATURE DECAY

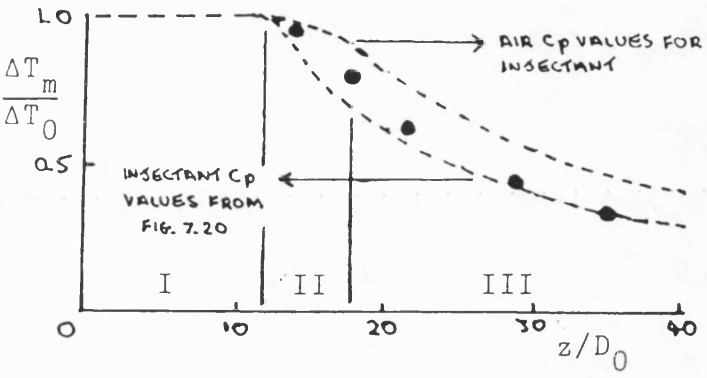

(c) HALF-WIDTH GROWTH

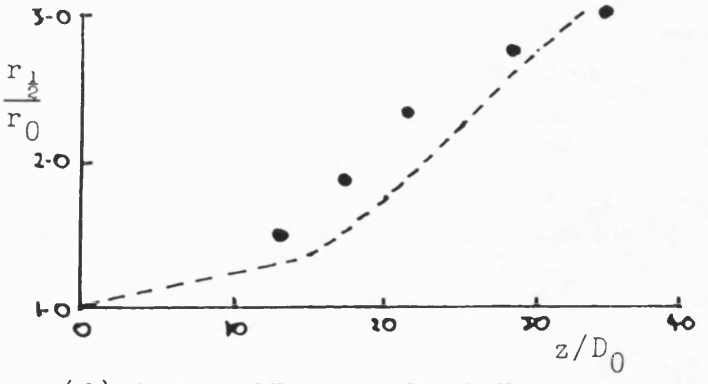

(d) INCREASE IN MASS FLUX

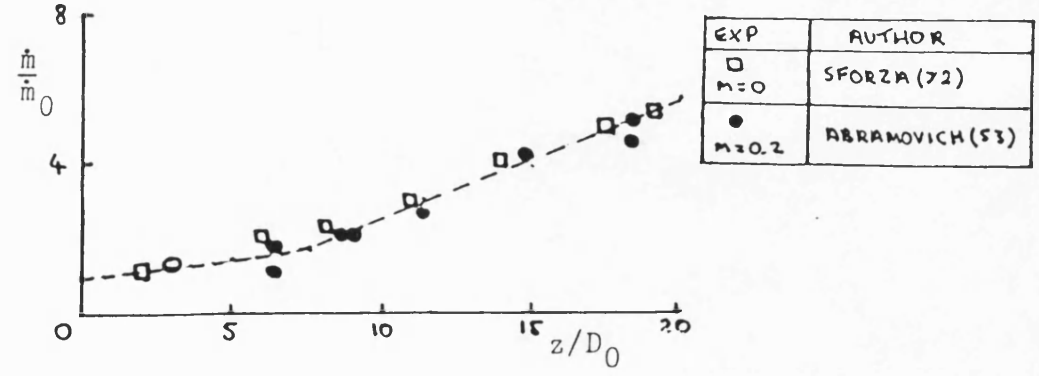

FIG. 7.23 PREDICTION OF A NONISOTHERMAL FREON-12-AIR JET IN A COFLOWING STREAM

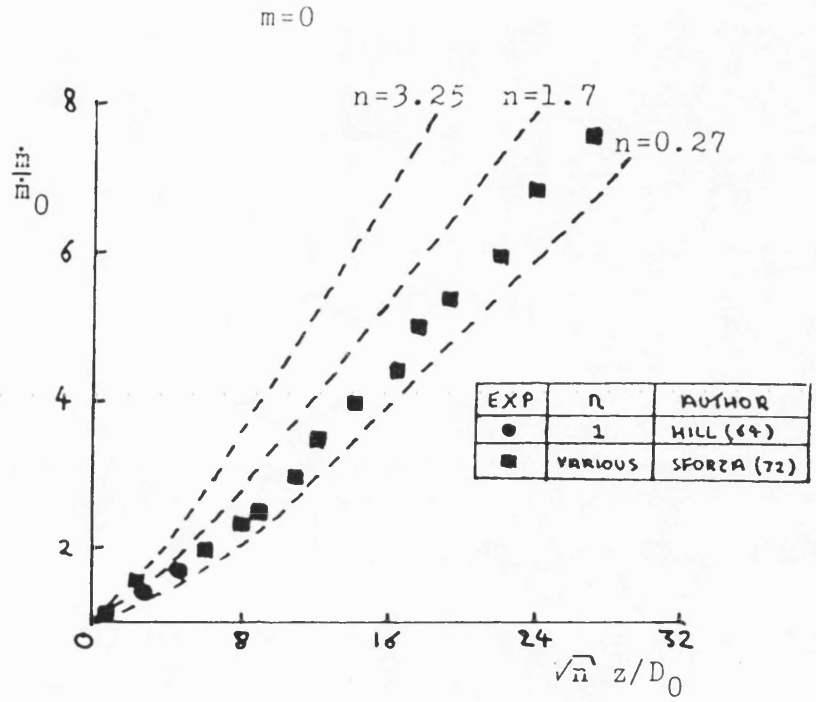

FIG. 7.24 PREDICTION OF INCREASE IN MASS FLUX FOR SUBMERGED AXISYMMETRIC JETS OF VARIABLE COMPOSITION AND COMPARISON WITH THE OBSERVED UNIVERSAL VARIATION

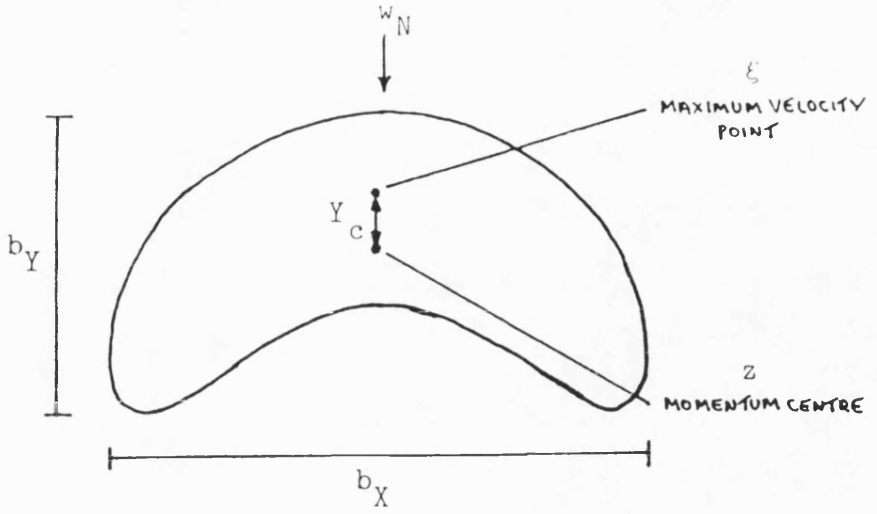

FIG. 7.25 DEFINITION SKETCH FOR A TYPICAL DISTORTED CROSS-SECTION

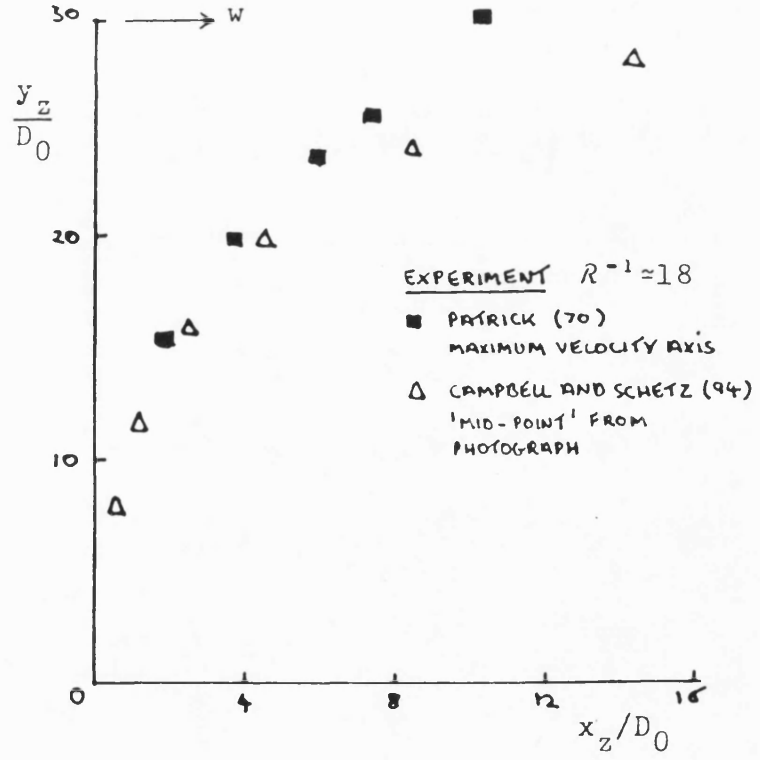

FIG. 7.26 DIFFERENT DEFINITIONS OF THE JET AXIS

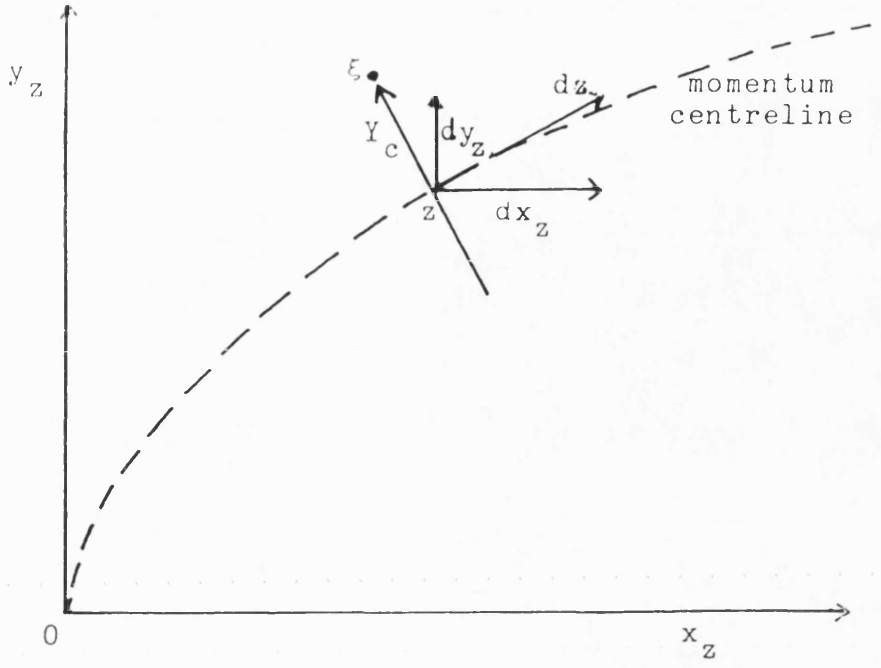

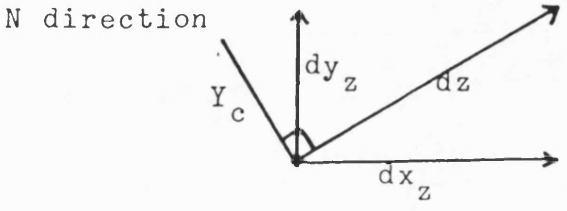

FIG. 7.27 LOCATION OF MAXIMUM VELOCITY POINT ξ FROM MOMENTUM CENTRE Z

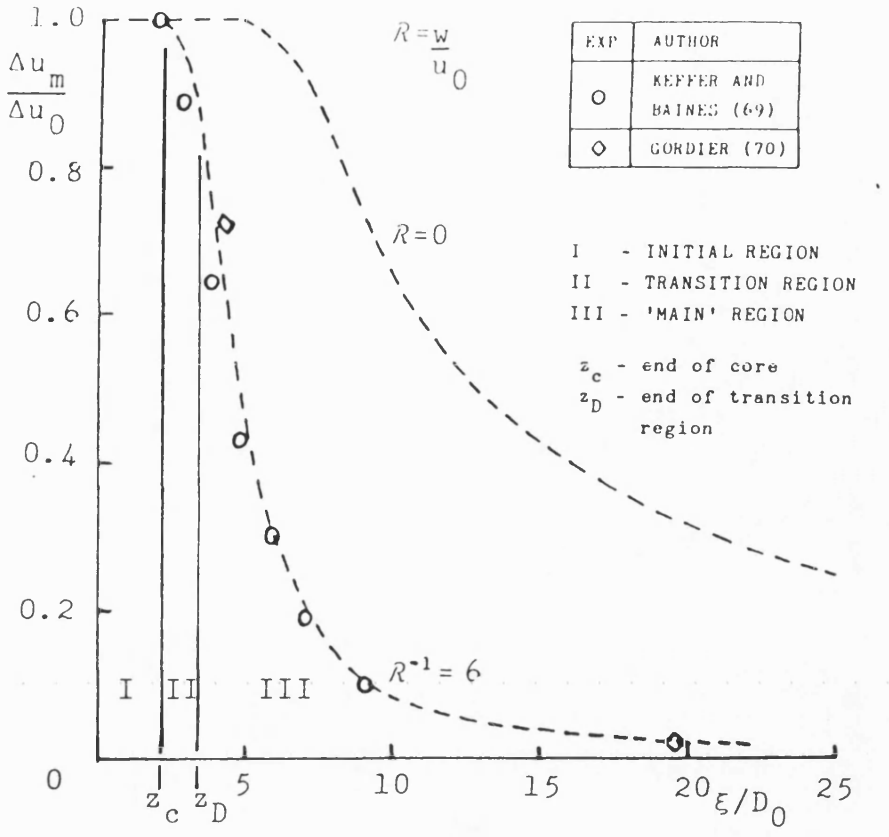

FIG. 7.28 AXIAL VELOCITY DECAY FOR TRANSVERSE INJECTION INTO A CONSTANT CROSSFLOW AT CONSTANT DENSITY

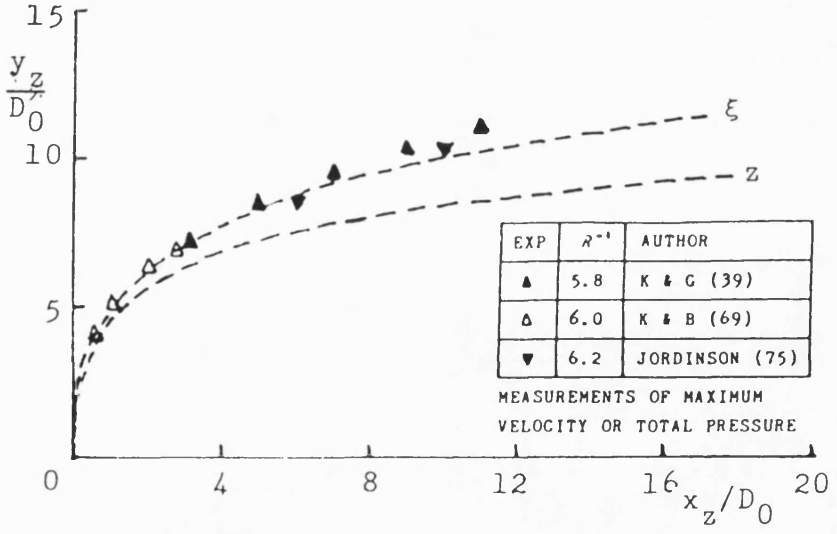

FIG. 7.29 PREDICTED MOMENTUM CENTRELINE AND ESTIMATED MAXIMUM VELOCITY AXIS AT $R^{-1}=6$

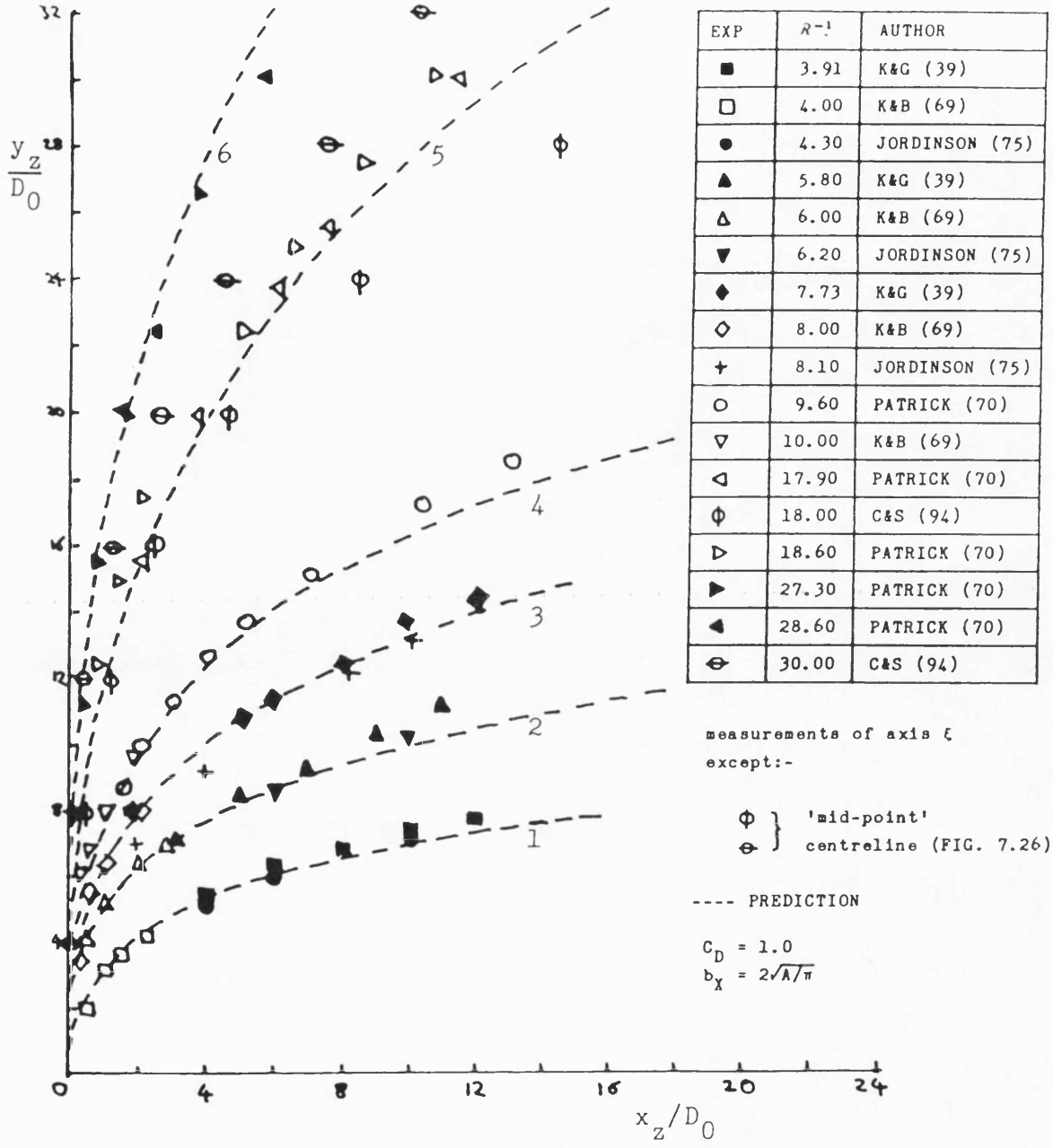

FIG. 7.30 PREDICTED AXES ξ FOR CONSTANT DENSITY JETS UNDER TRANSVERSE INJECTION INTO UNIFORM CROSSFLOWS

---	1	2	3	4	5	6
R^{-1}	4	6	8	10	18	30

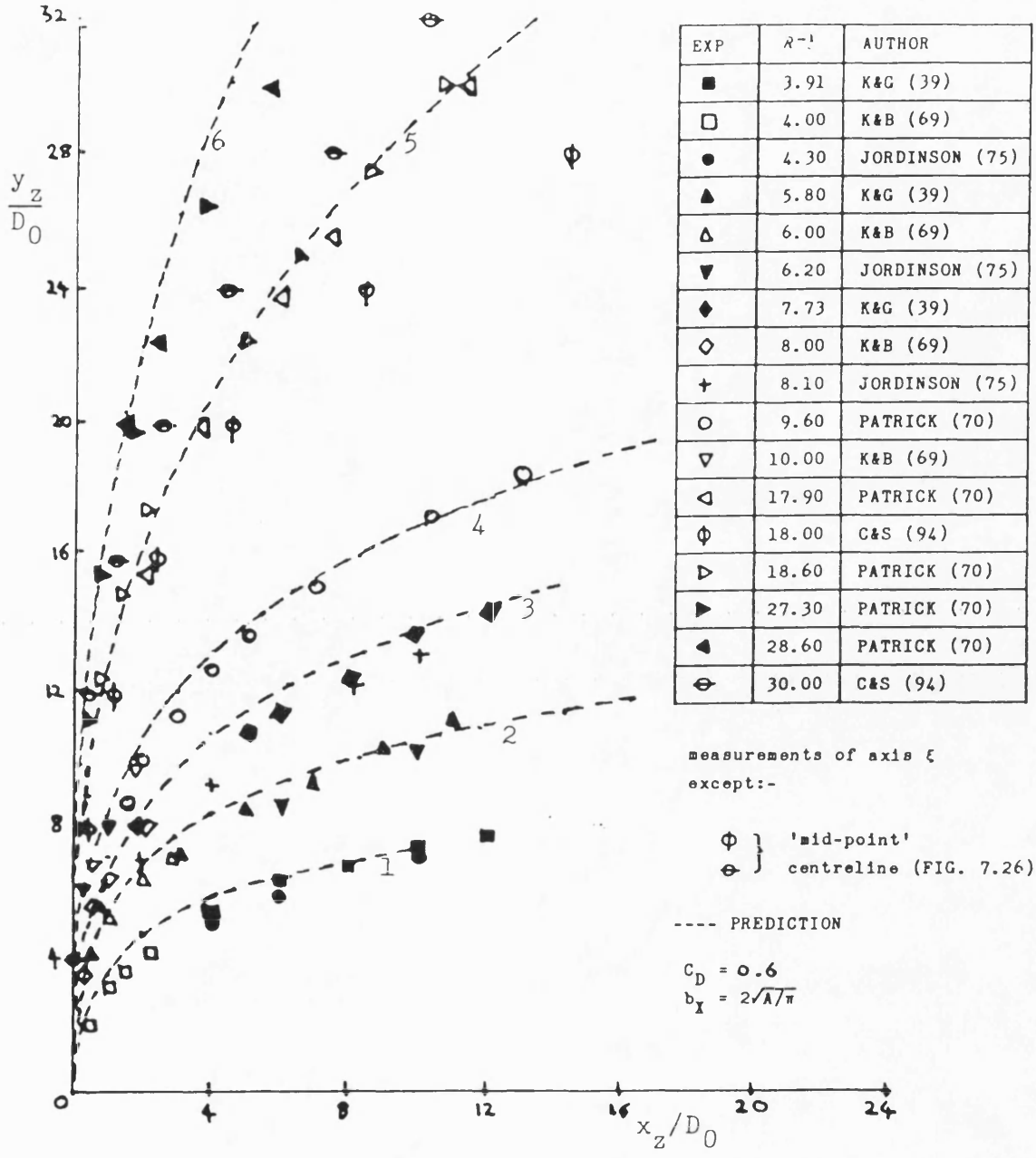

FIG. 7.31 OPTIMISED TRAJECTORY PREDICTIONS

---	1	2	3	4	5	6
R^{-1}	4	6	8	10	18	30

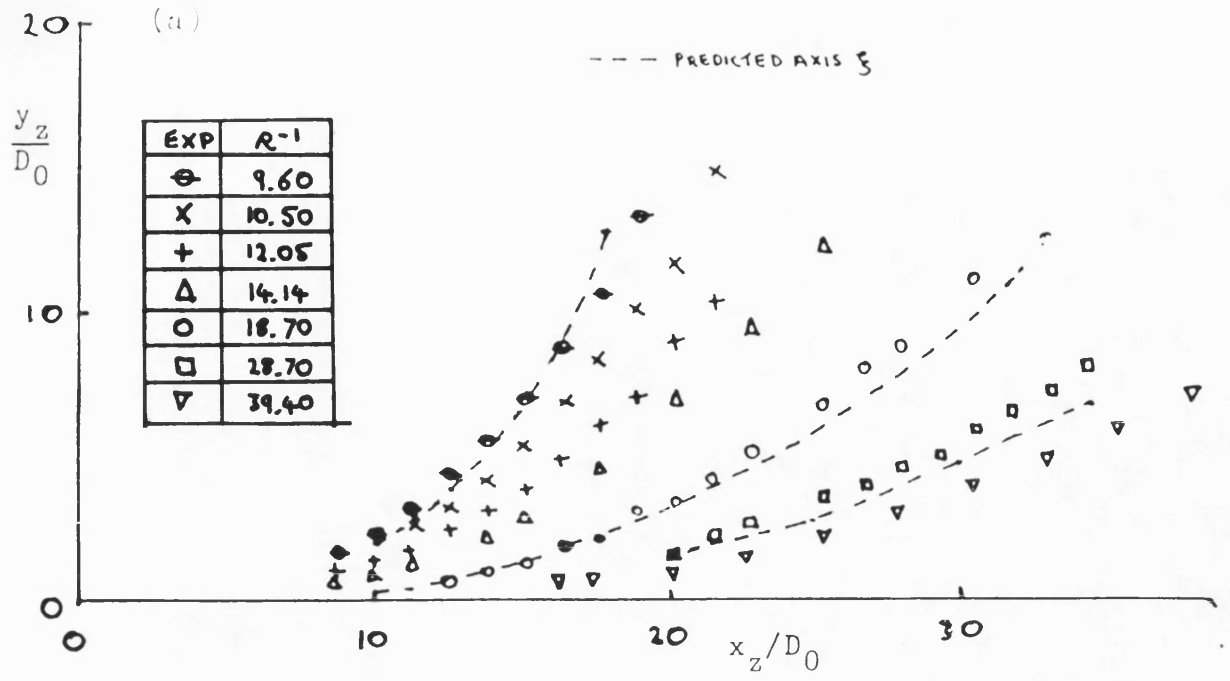

$C_D = 0.6$; $b_X = 2\sqrt{A/\pi}$

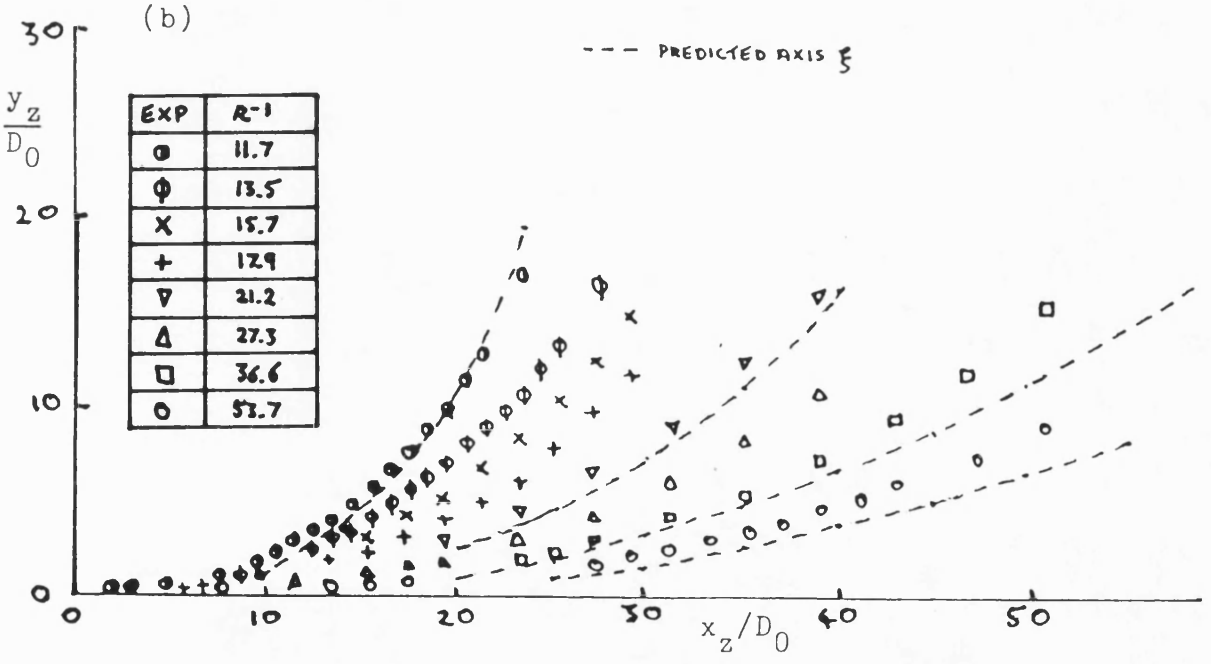

FIG. 7.32 TRAJECTORY PREDICTIONS COMPARED WITH THE EXPERIMENTS OF PATRICK (70)

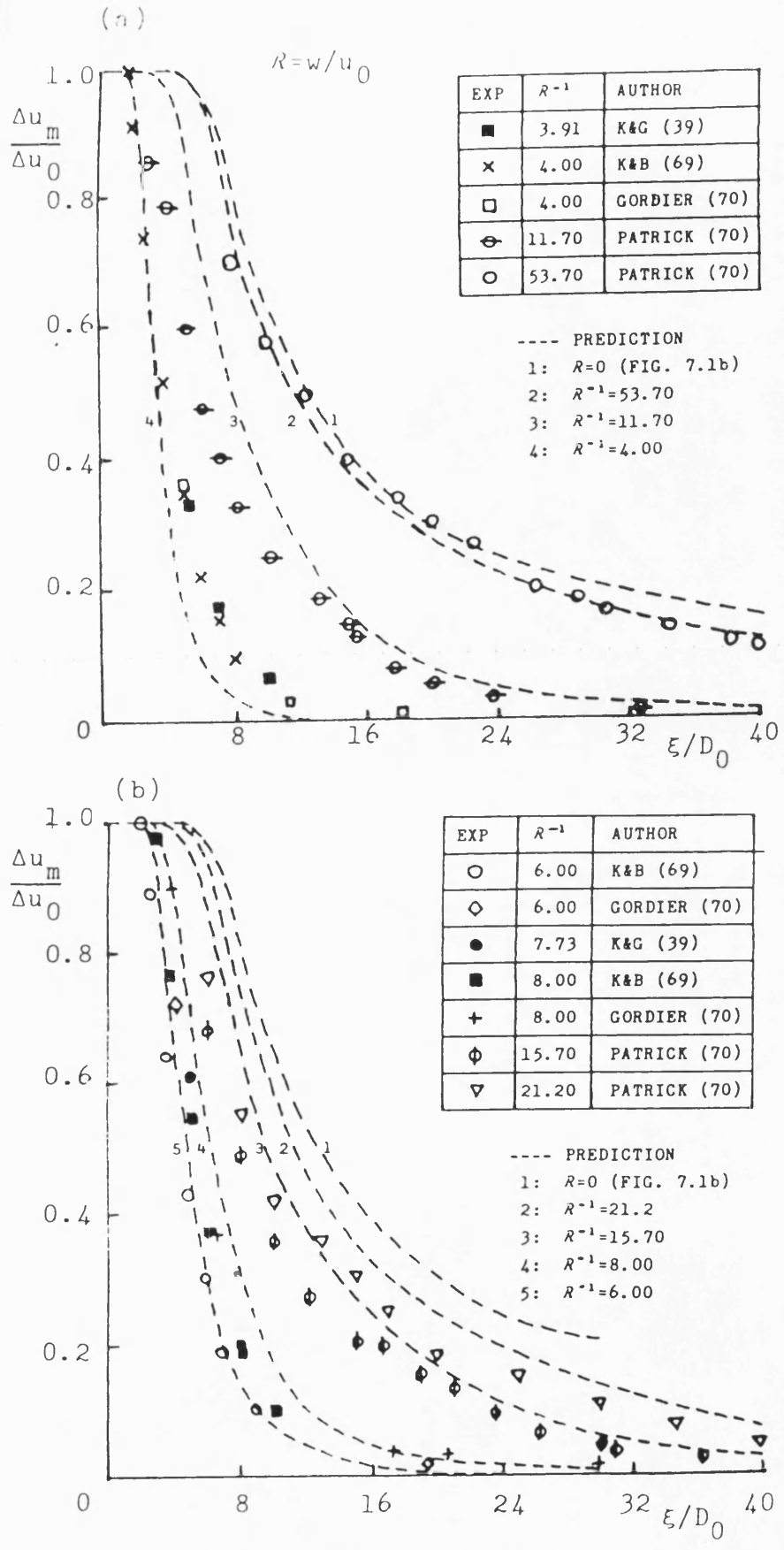

FIG. 7.33 PREDICTION OF VELOCITY DECAY FOR TRANSVERSE INJECTION INTO UNIFORM CROSSFLOW AT CONSTANT DENSITY

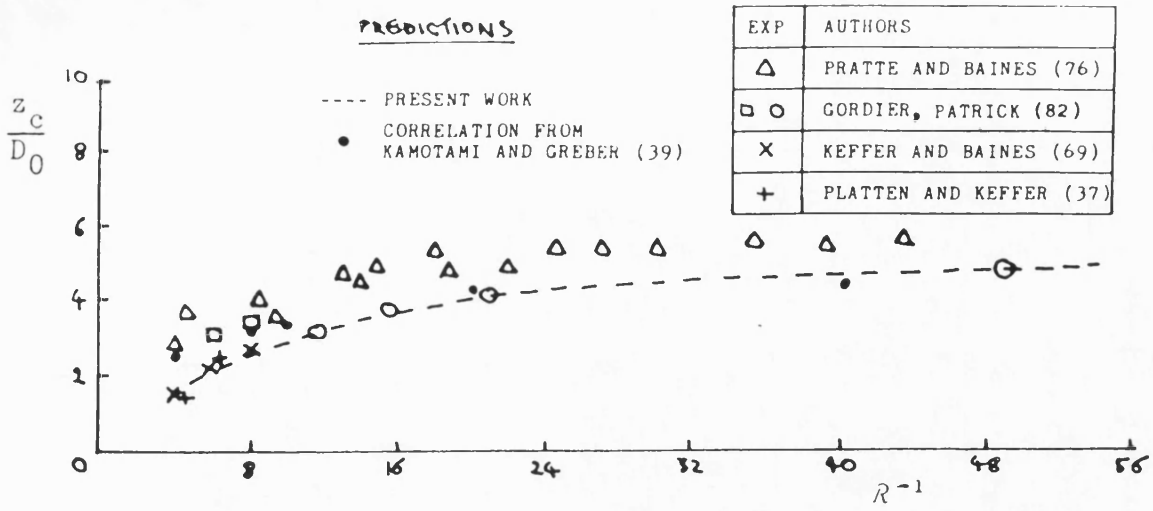

FIG. 7.33c EFFECT OF VELOCITY RATIO R ON THE LENGTH OF THE INITIAL REGION IN A CONSTANT DENSITY JET

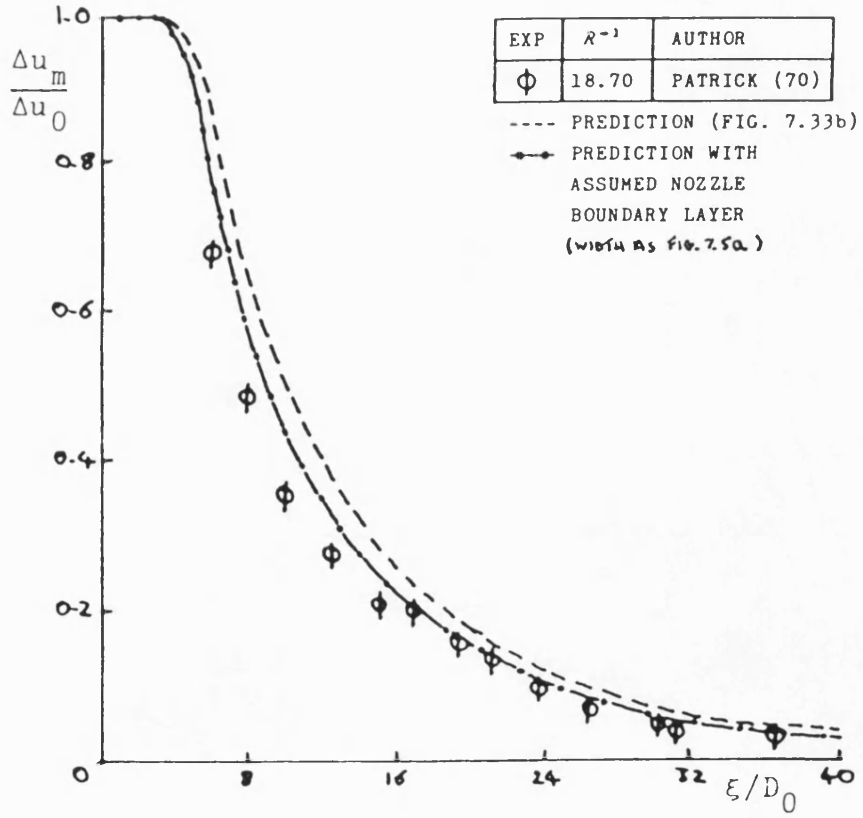

FIG. 7.34 EFFECT OF A NOZZLE BOUNDARY LAYER ON PREDICTED VELOCITY DECAY

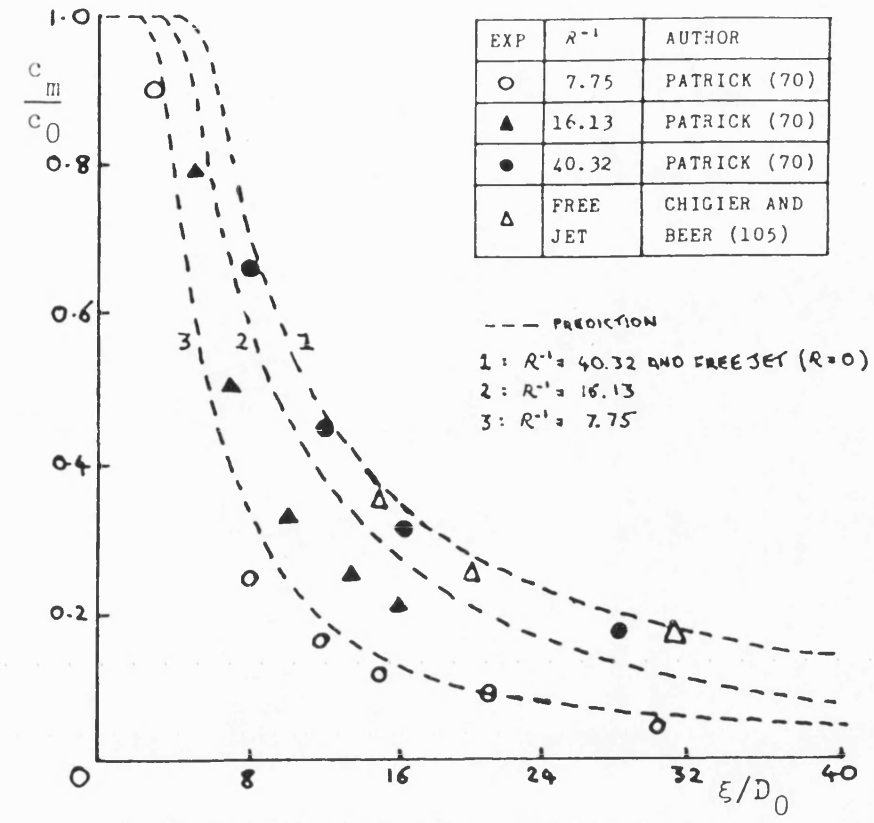

FIG. 7.35 EFFECT OF VELOCITY RATIO R ON AXIAL CONCENTRATION DECAY

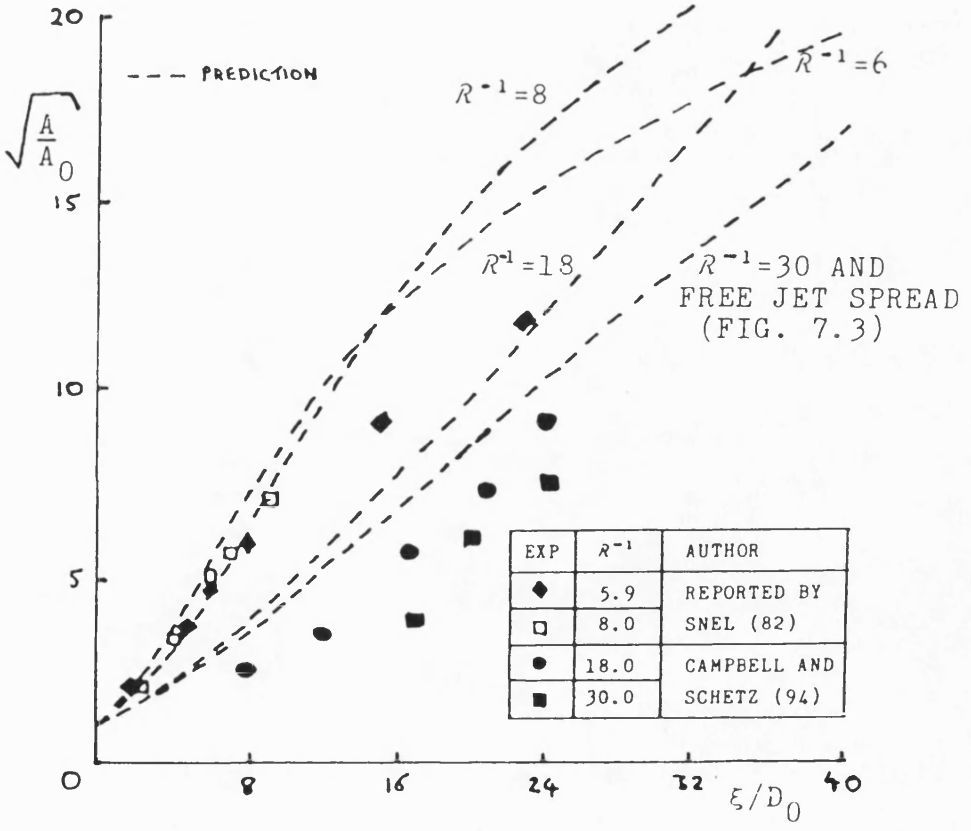

FIG. 7.36 EFFECT OF R ON JET SPREAD AT CONSTANT DENSITY

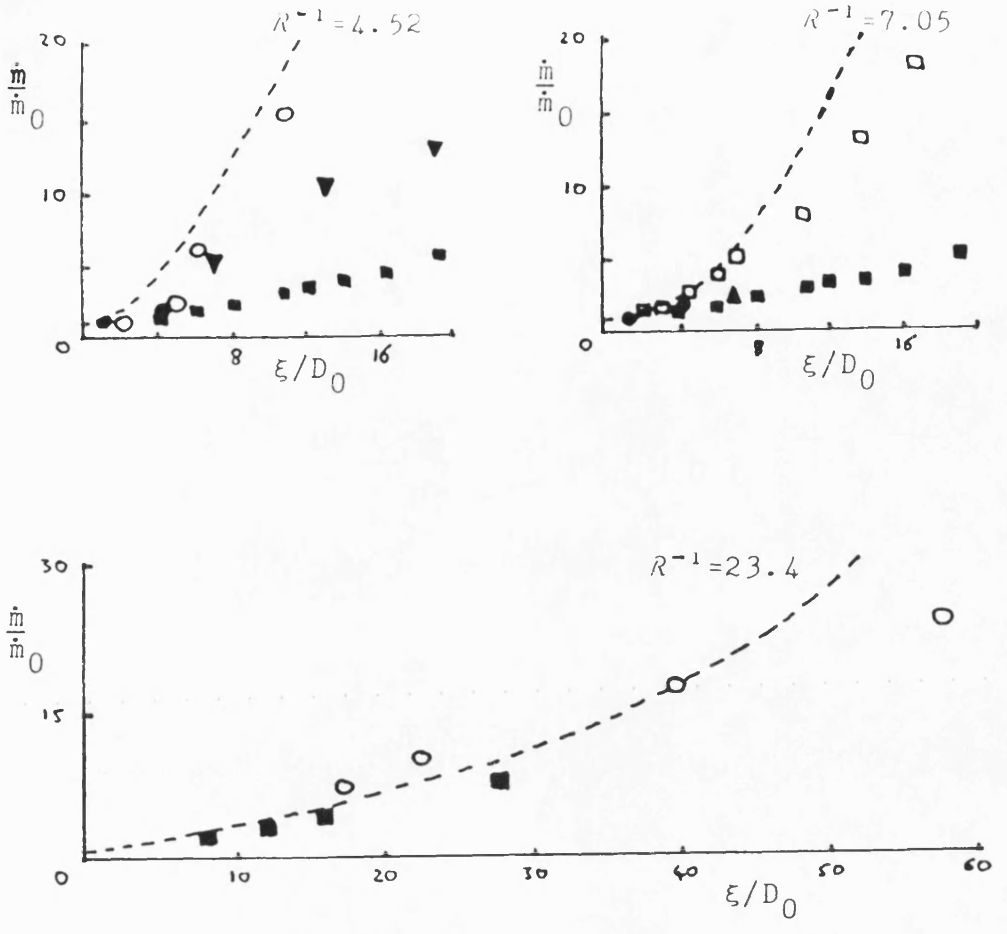

EXP	R^{-1}	AUTHOR
▼	3.91	K&G (39)
O	4.52	R&G (110)
□	7.05	R&G (110)
▲	7.73	K&G (39)
O	23.40	R&G (110)
■	FREE JET	SFORZA (72)

FIG. 7.37 PREDICTED INCREASE IN JET MASS FLUX WITH AXIAL PENETRATION INTO A UNIFORM CROSSFLOW AT CONSTANT DENSITY (TRANSVERSE INJECTION)

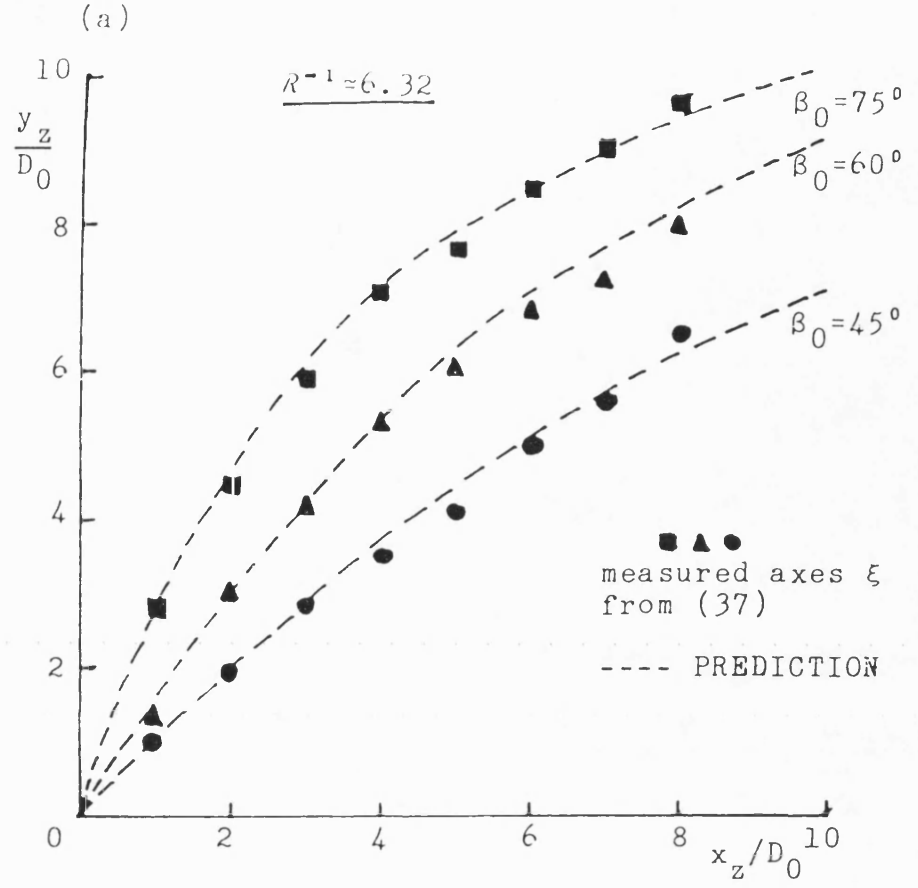

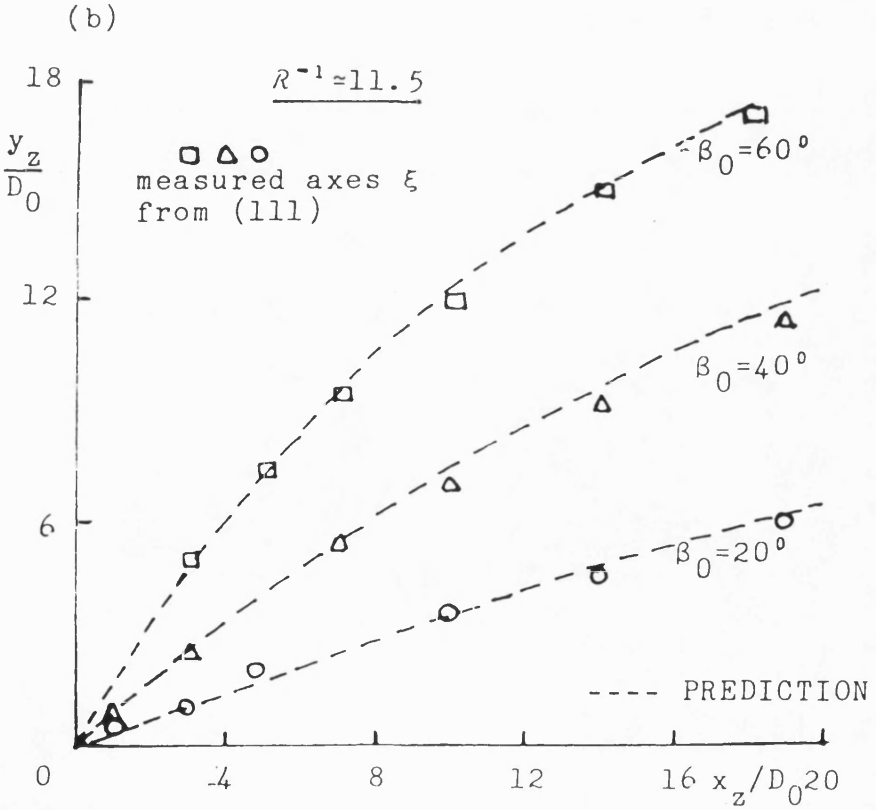

FIG. 7.38 OBLIQUE INJECTION INTO UNIFORM CROSSFLOW AT CONSTANT DENSITY

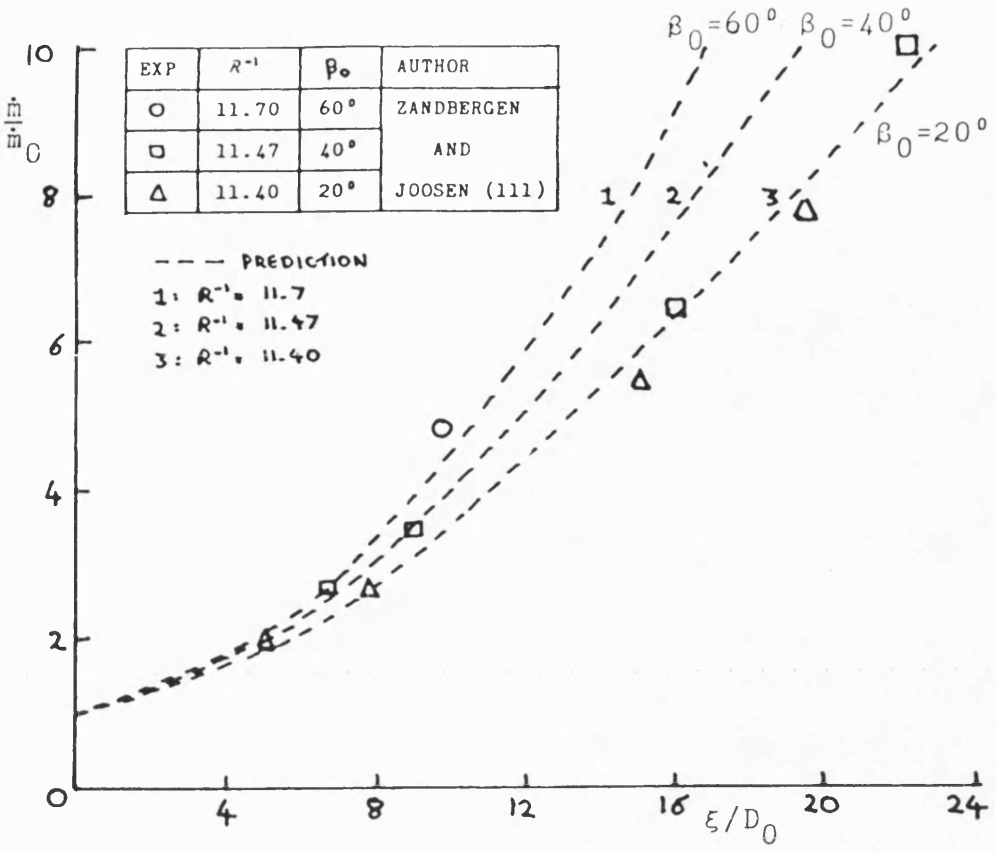

(a) PRESENT WORK

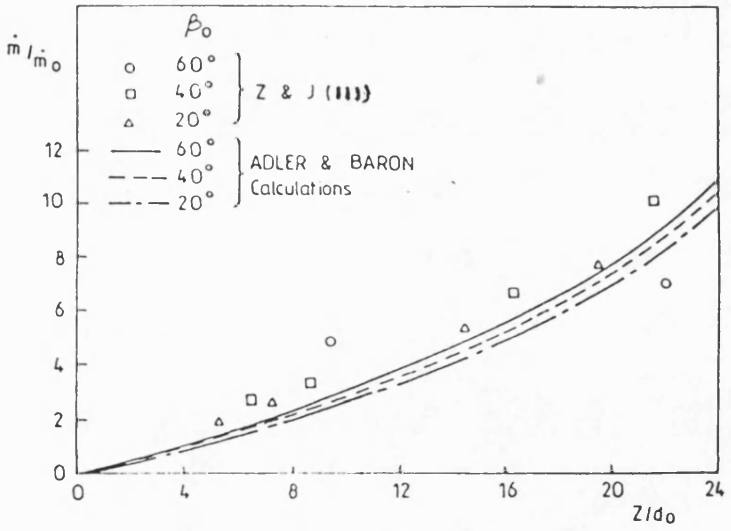

(b) FROM ADLER AND BARON (63)

FIG. 7.39 EFFECT OF INJECTION ANGLE ON INCREASE IN JET MASS FLUX WITH AXIAL PENETRATION

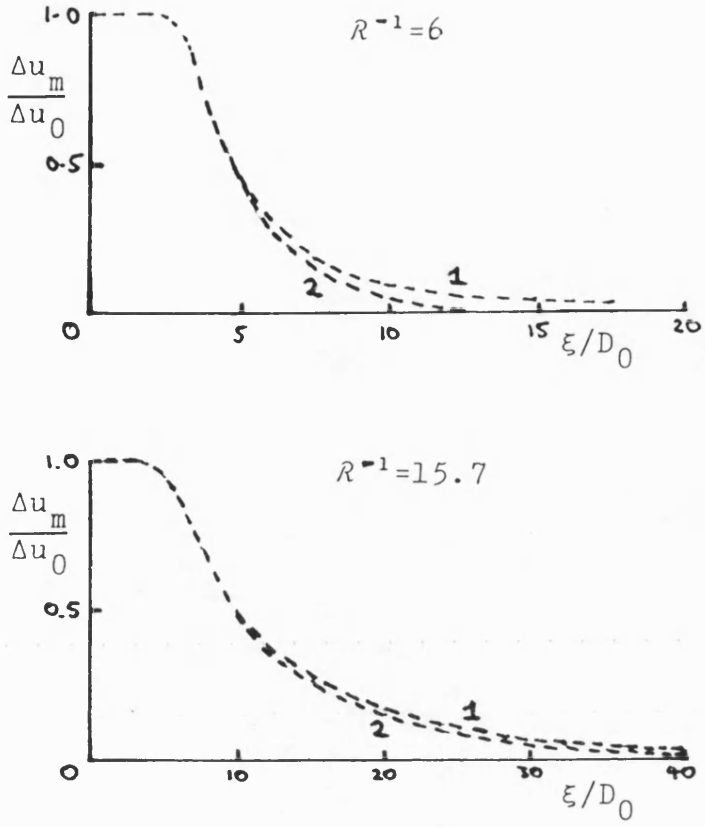

---- PREDICTION

1: FROM FIG. 7.33

2: INCLUDING PRESSURE FORCE IN CENTRELINE MOMENTUM EQUATION

FIG. 7.40 EFFECT OF CENTRELINE PRESSURE FORCE ON PREDICTED VELOCITY DECAY

FIG. 7.41 EFFECT OF CROSS-SECTION DISTORTION ON VELOCITY DECAY (PACKER (35))

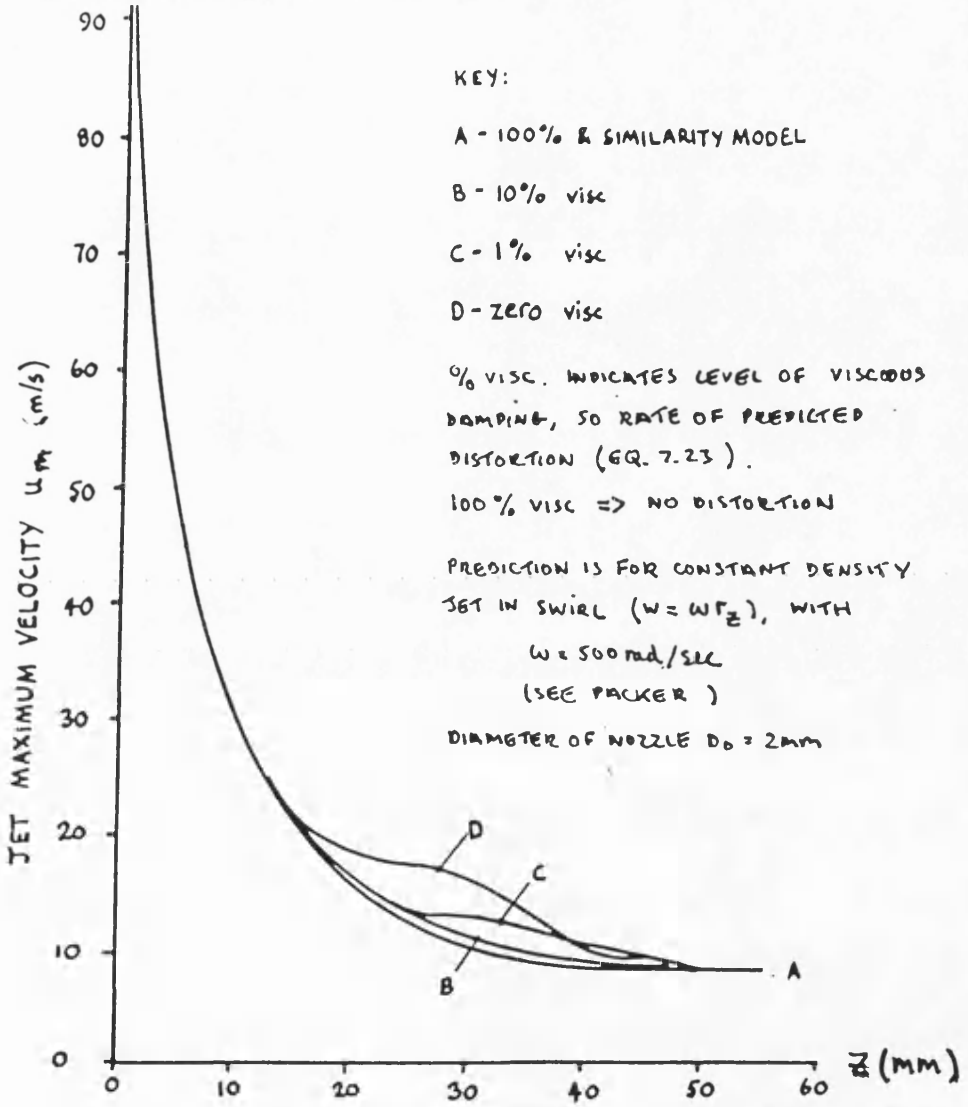

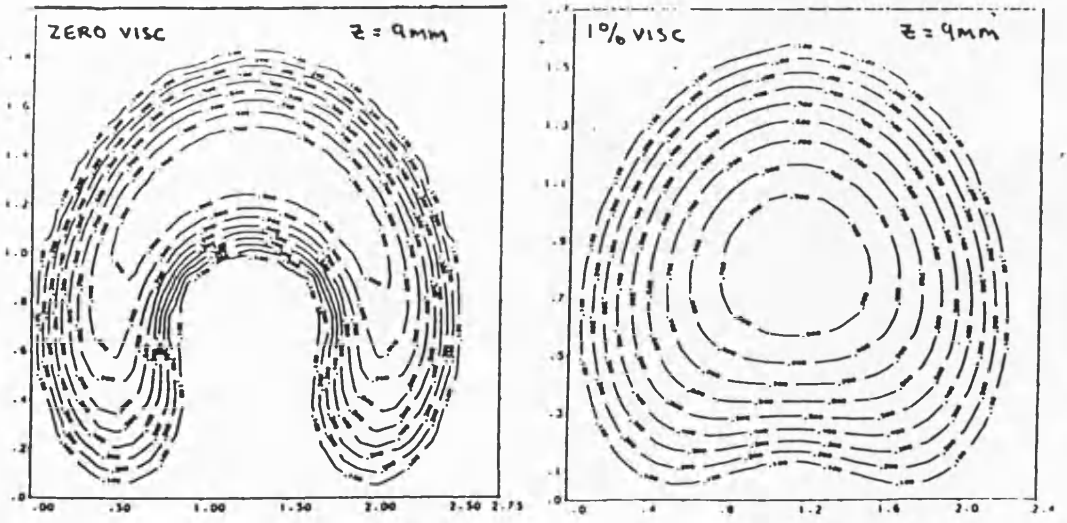

FIG. 7.42 EFFECT OF DAMPING FACTOR ON PREDICTED RATE OF CROSS-SECTION DISTORTION (PACKER (35))

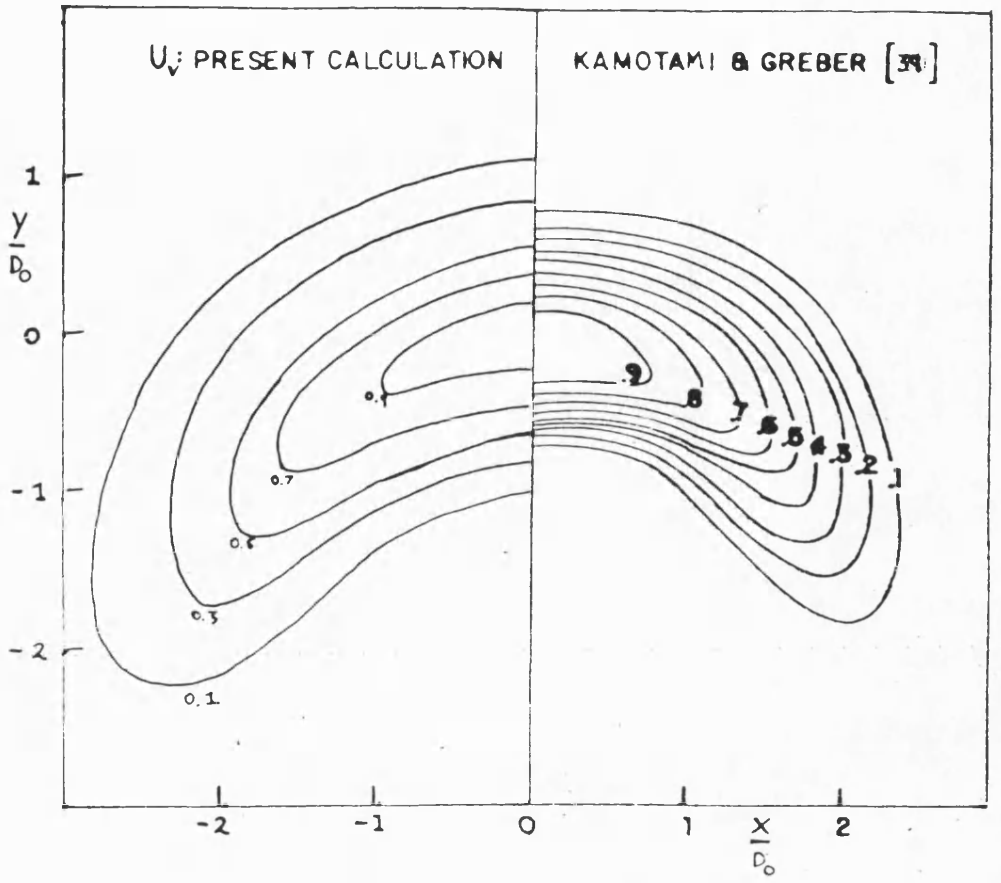

cross-section at $R^{-1}=3.91$, $\xi/D_0=7$

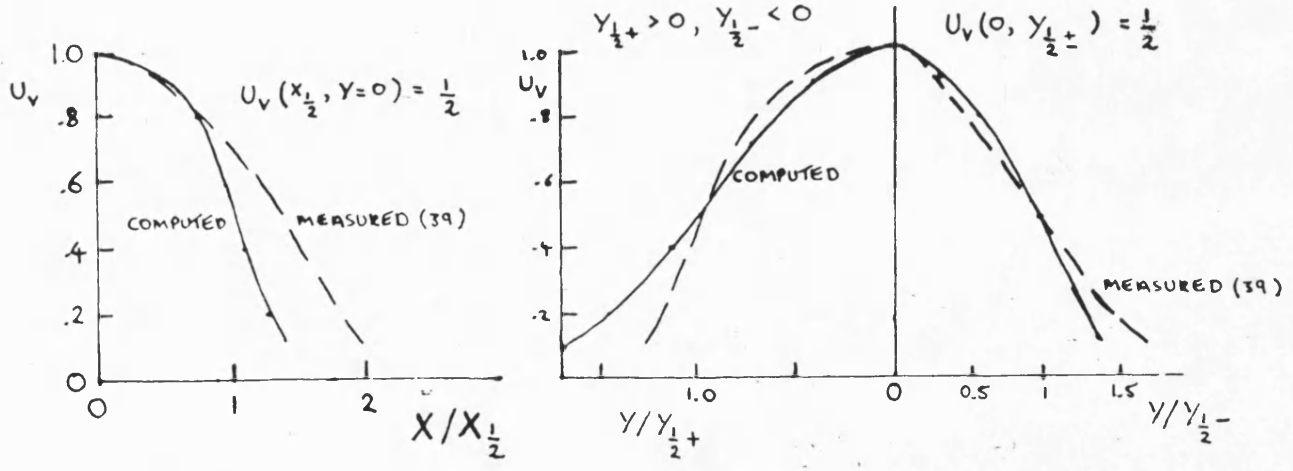

profile along Y=0 profile along X=0

FIG. 7.43 DISTORTED JET VELOCITY PROFILES IN COMPARISON WITH EXPERIMENT

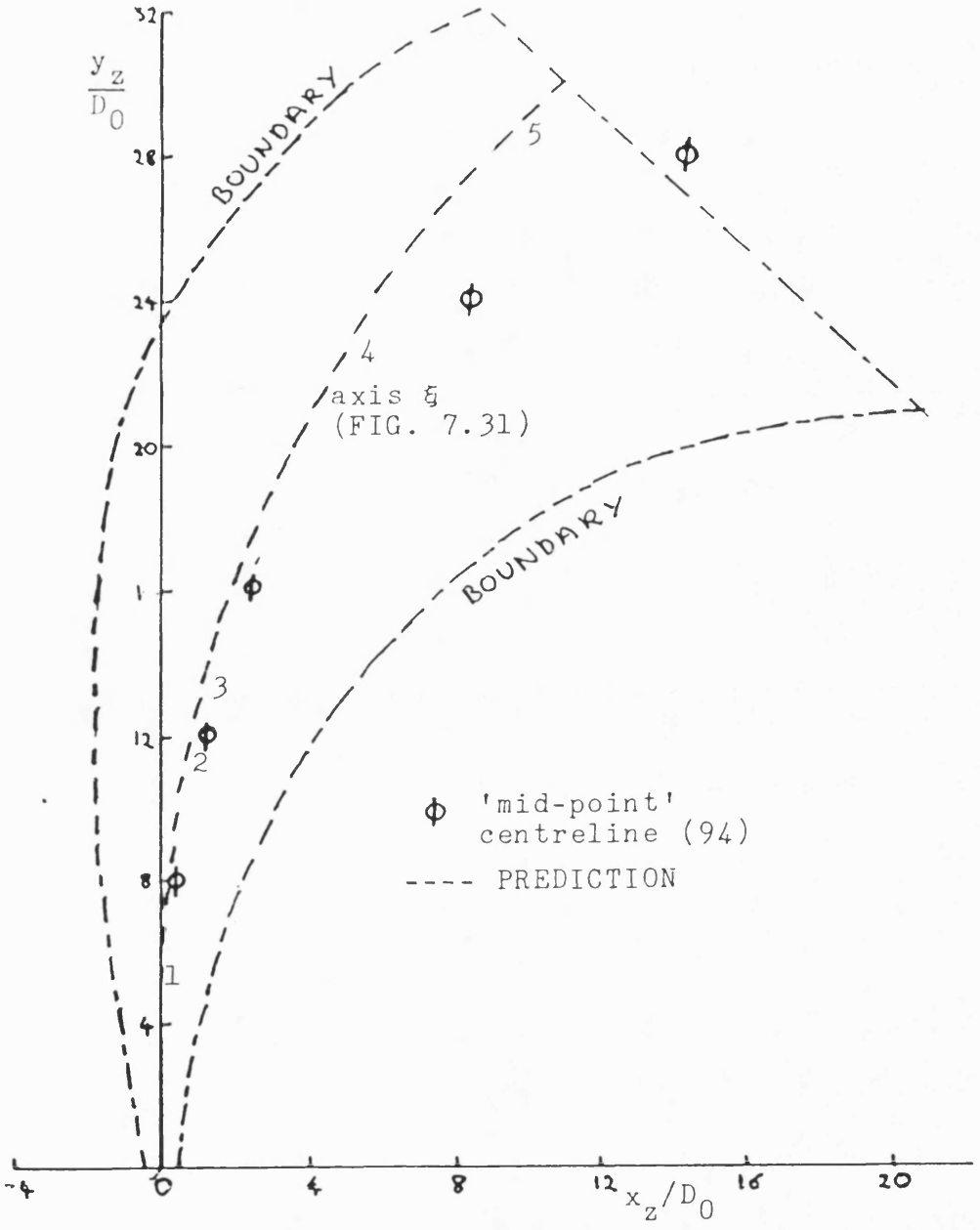

(cross-section structure at numbered points shown over page)

FIG. 7.44a PREDICTED JET BOUNDARY AT R^{-1}=18 WITH CROSS-SECTION DISTORTION

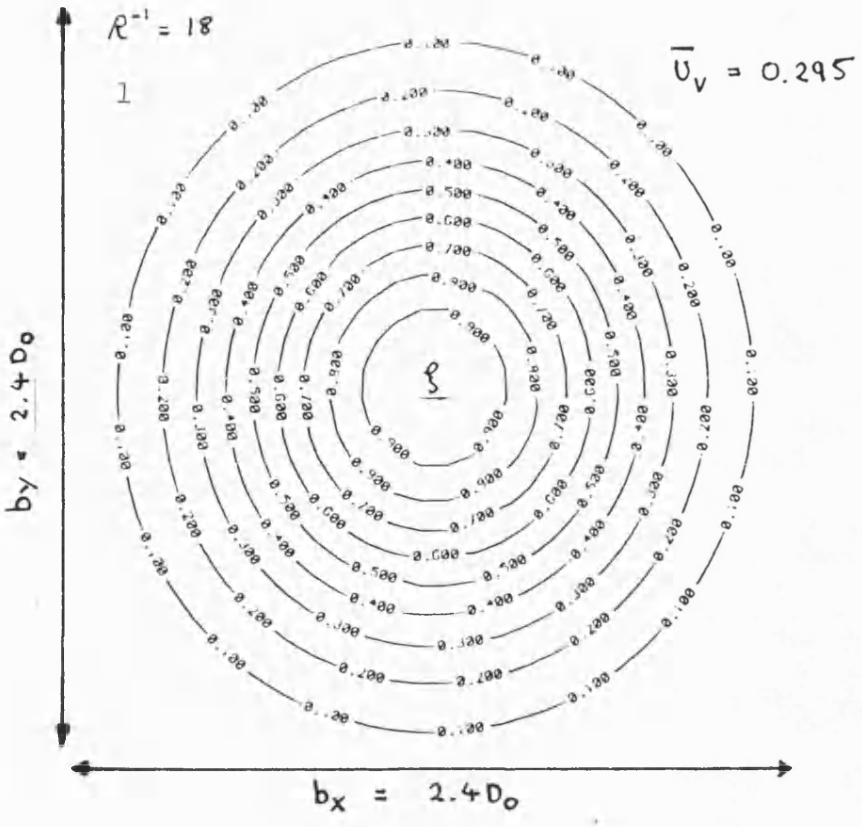

FIG. 7.44b VELOCITY PROFILE AT $\xi/D_o \simeq 5$

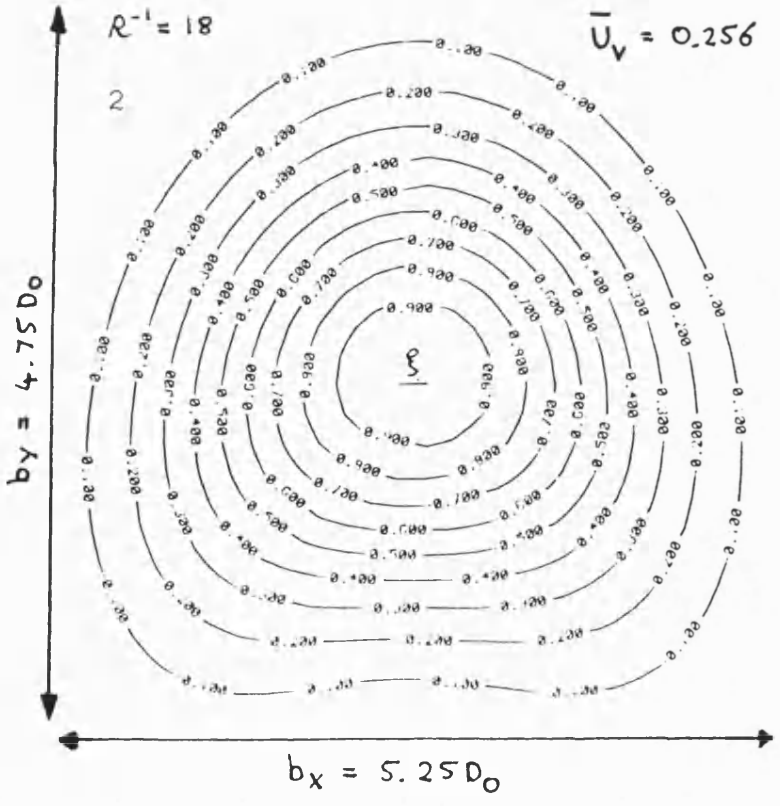

FIG. 7.44c VELOCITY PROFILE AT $\xi/D_o \simeq 11.5$

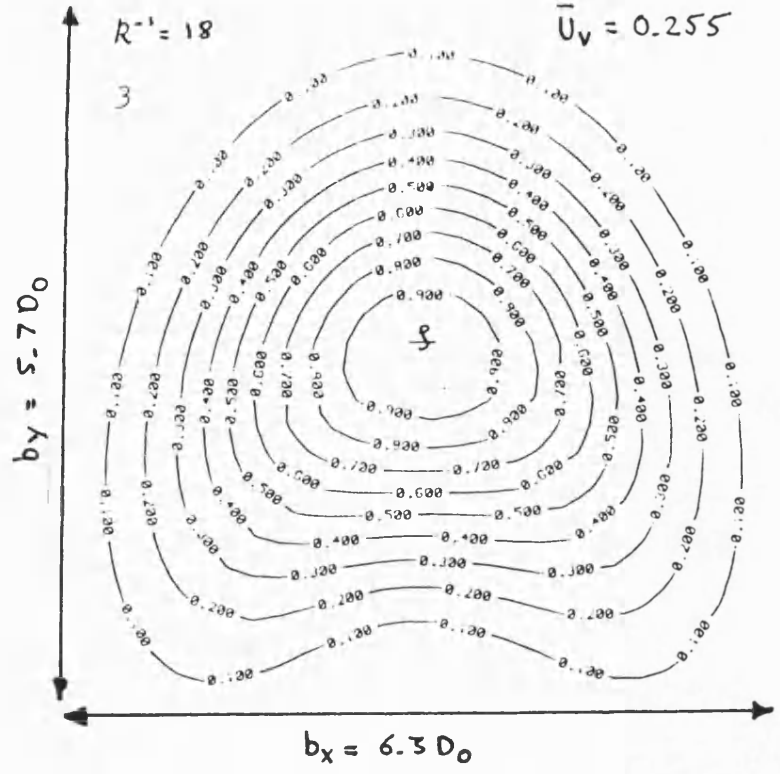

FIG. 7.44d VELOCITY PROFILE AT $\xi/D_o \simeq 13$

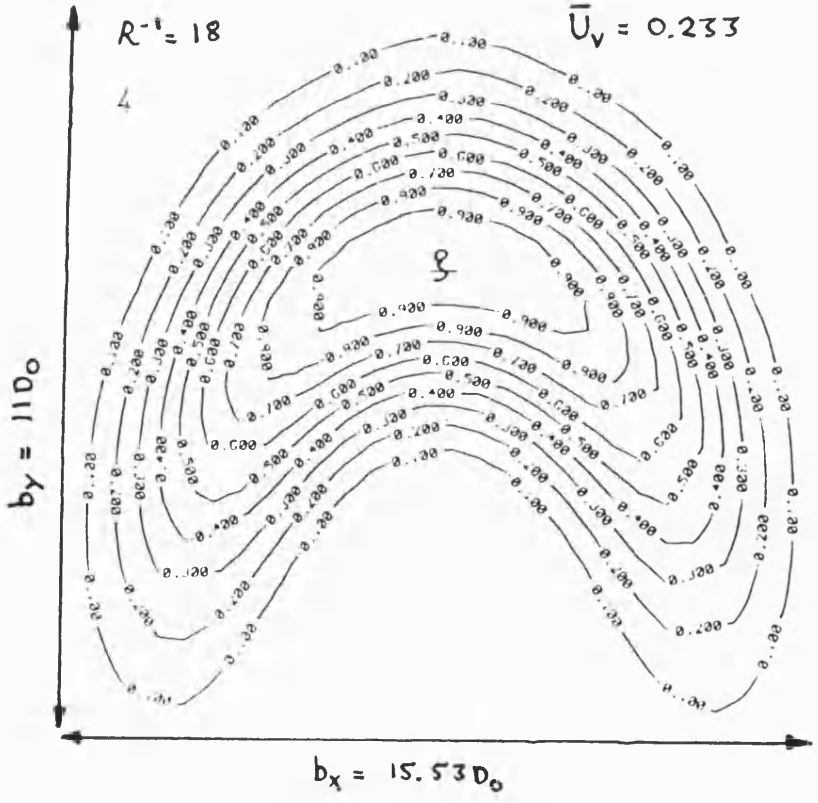

FIG. 7.44e VELOCITY PROFILE AT $\xi/D_o \simeq 24$

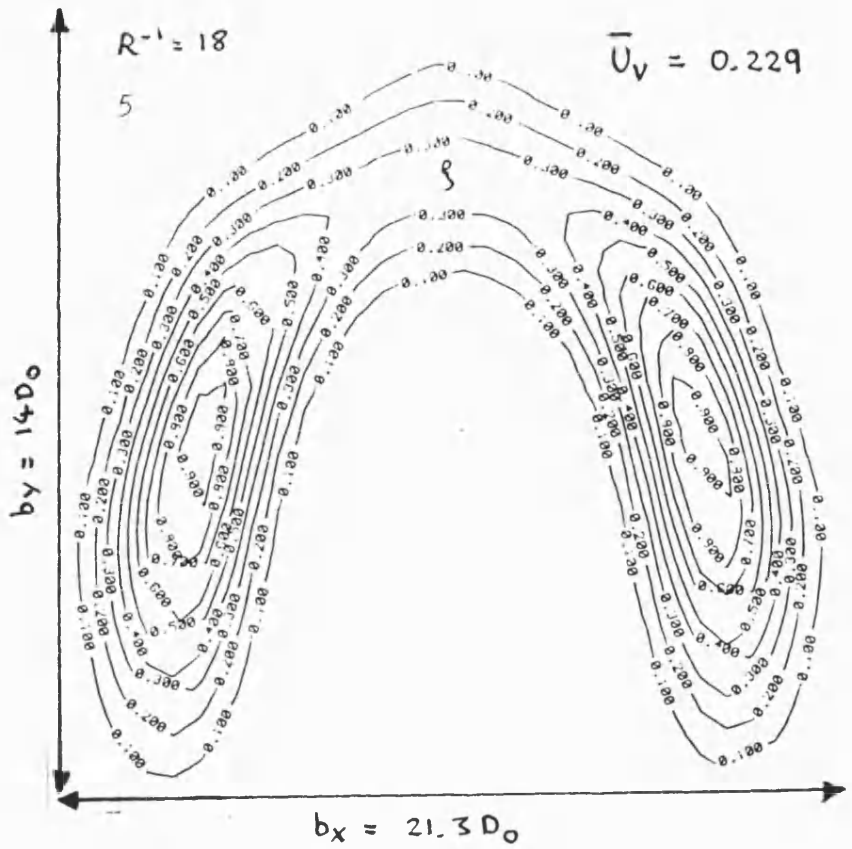

FIG. 7.44f VELOCITY PROFILE AT $\xi/D_0 \simeq 30$

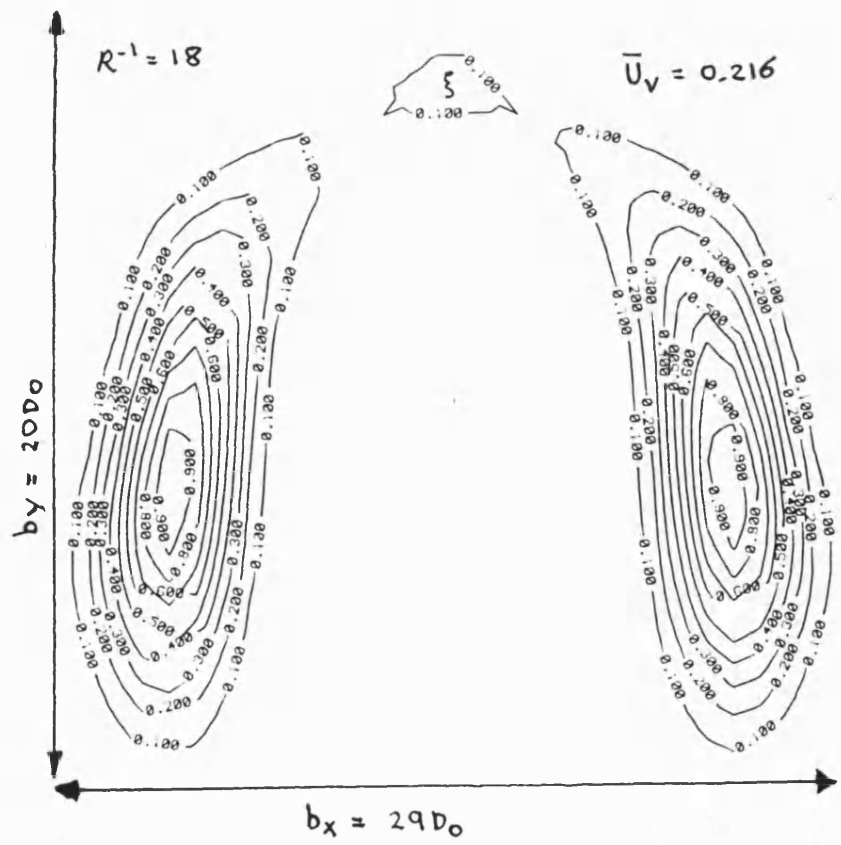

FIG. 7.44g VELOCITY PROFILE AT $\xi/D_0 \simeq 35$

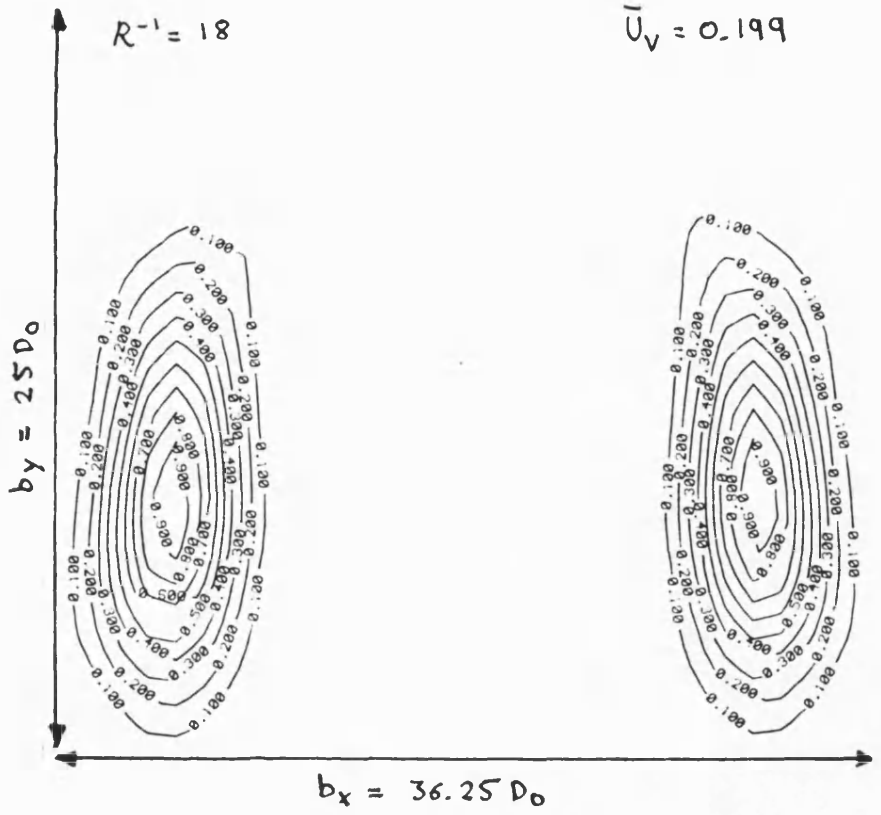

FIG. 7.44h VELOCITY PROFILE AT $\xi/D_o \simeq 40$

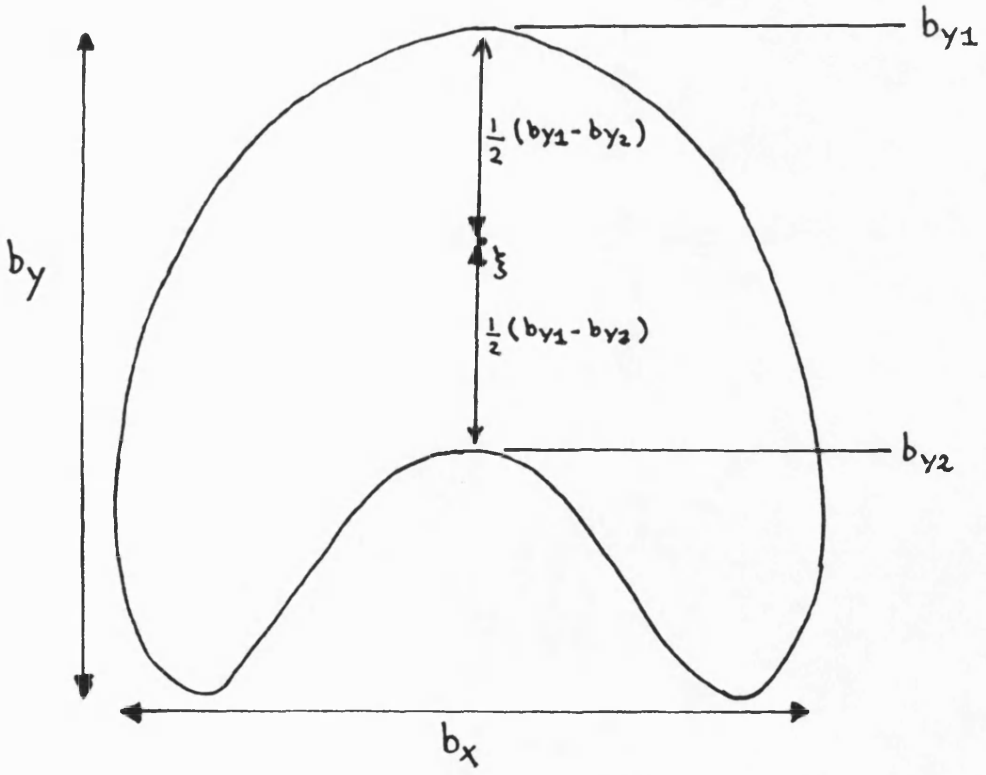

FIG. 7.44i APPROXIMATE POSITION OF THE MAXIMUM VELOCITY POINT IN A CROSS-SECTION

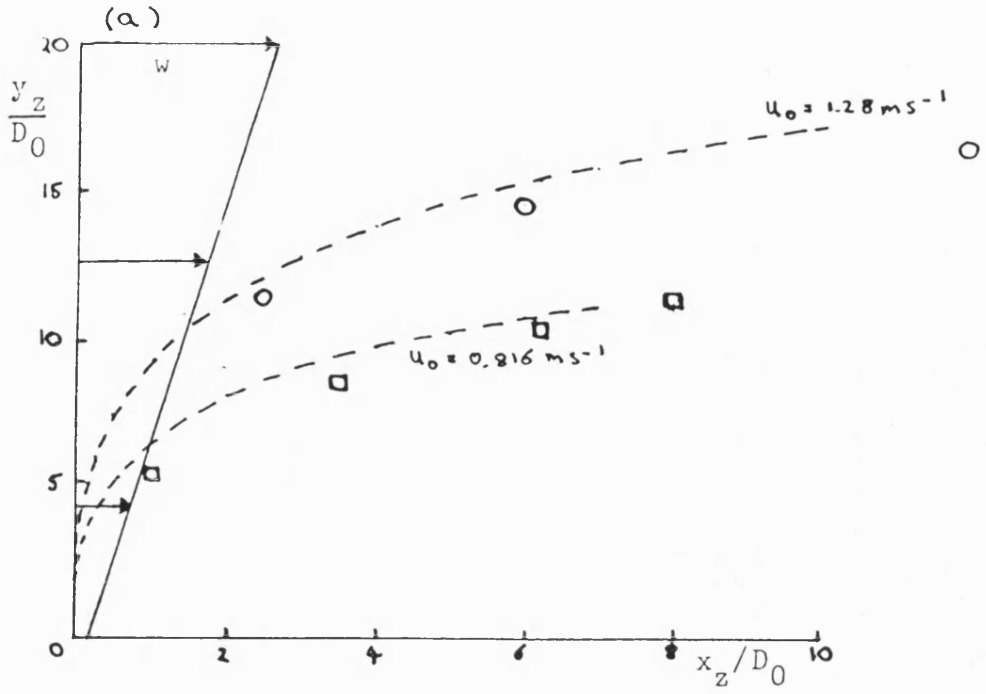

$w=0.1(1+0.035y_z/D_0)$

○ □ ■ ● experiments of Shirakashi and Tomita (90)

---- prediction

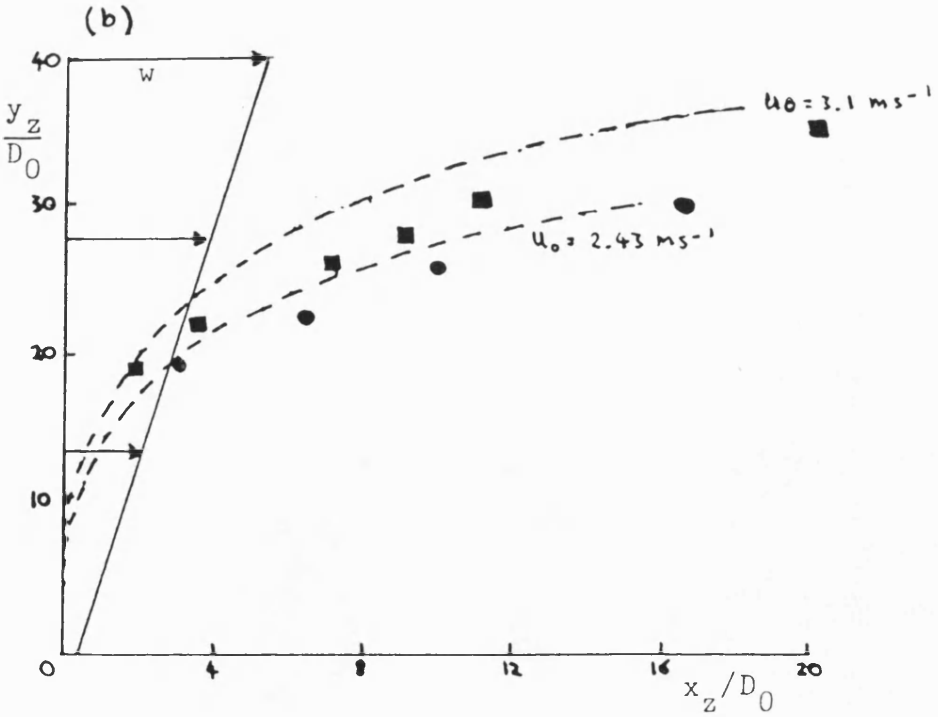

FIG. 7.45 PREDICTED AND MEASURED AXES ξ IN SHEAR FLOW

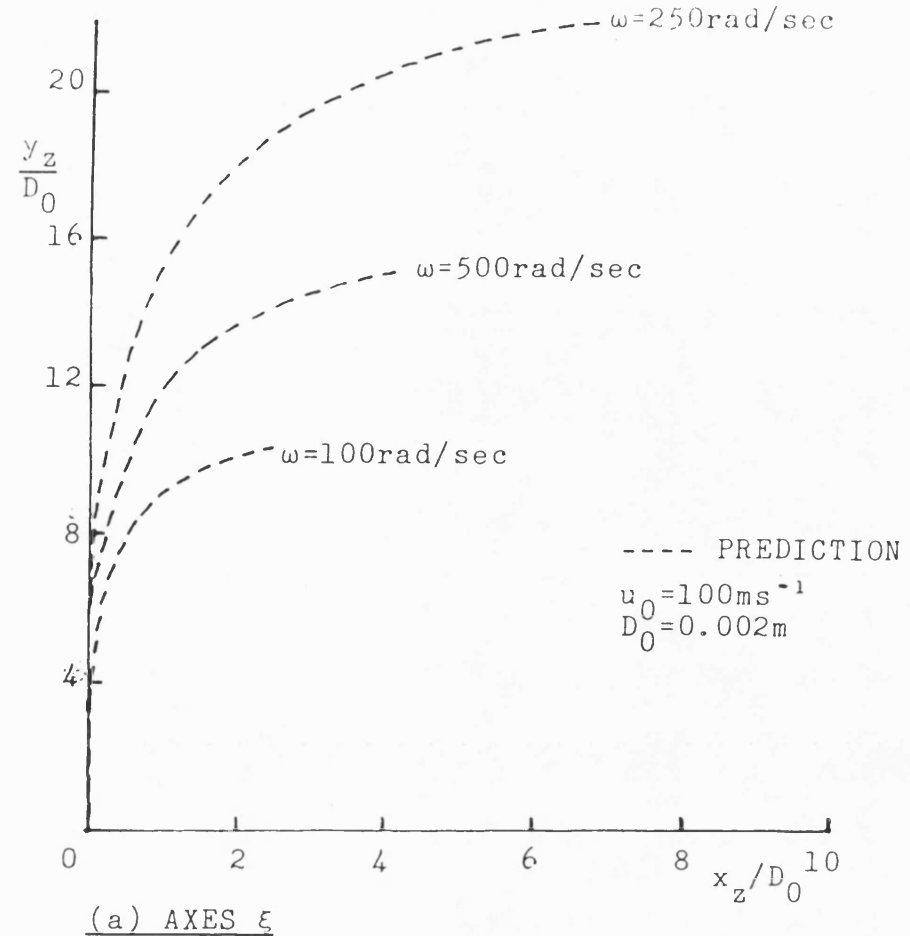

(a) AXES ξ

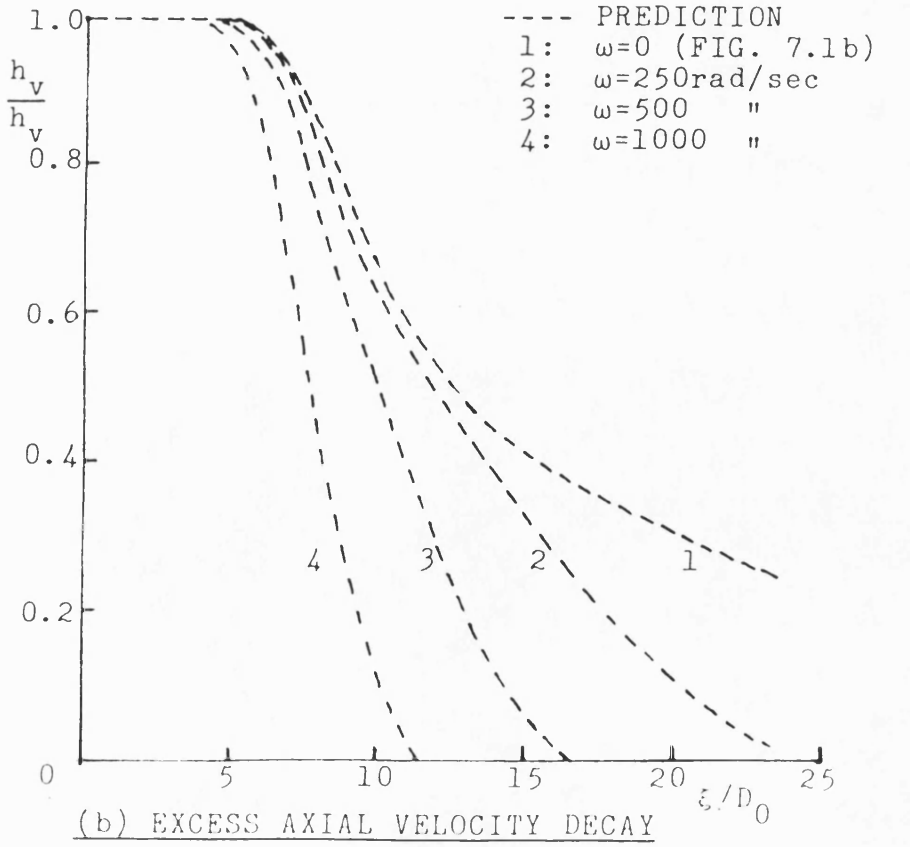

(b) EXCESS AXIAL VELOCITY DECAY

FIG. 7.46 PREDICTION OF CONSTANT DENSITY JETS IN SWIRL

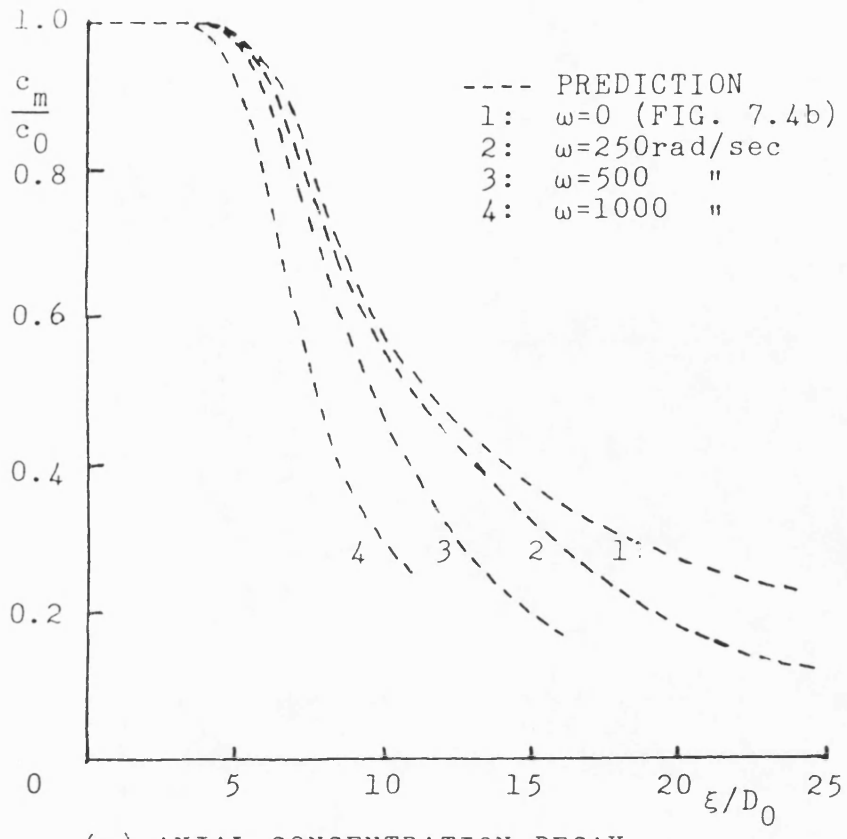

(c) AXIAL CONCENTRATION DECAY

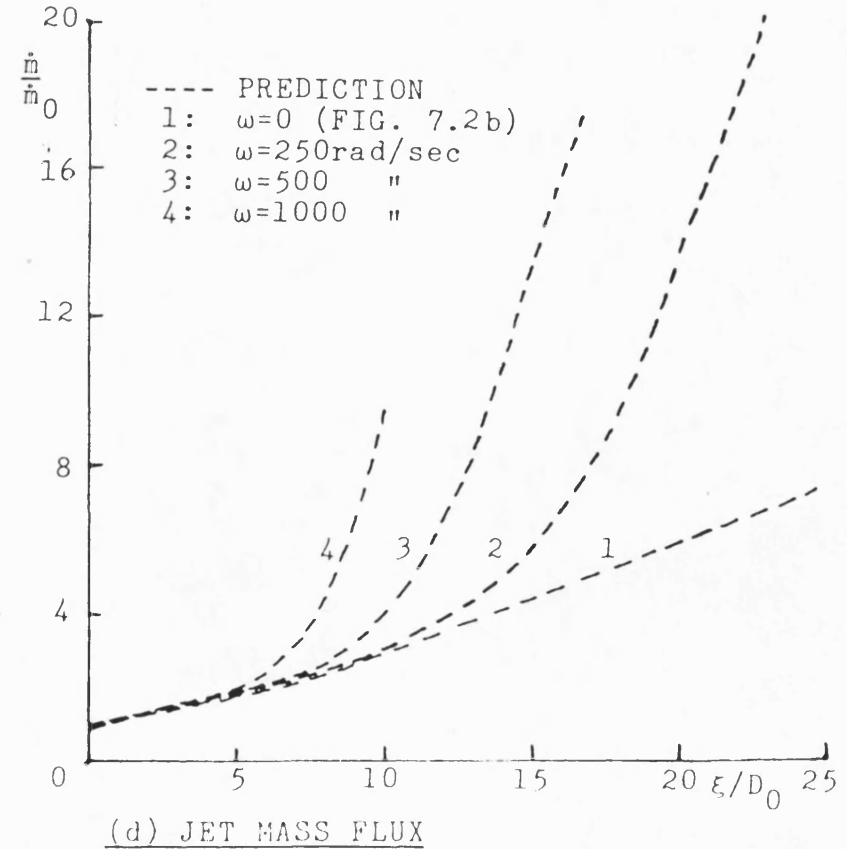

(d) JET MASS FLUX

FIG. 7.46 PREDICTION OF CONSTANT DENSITY JETS IN SWIRL

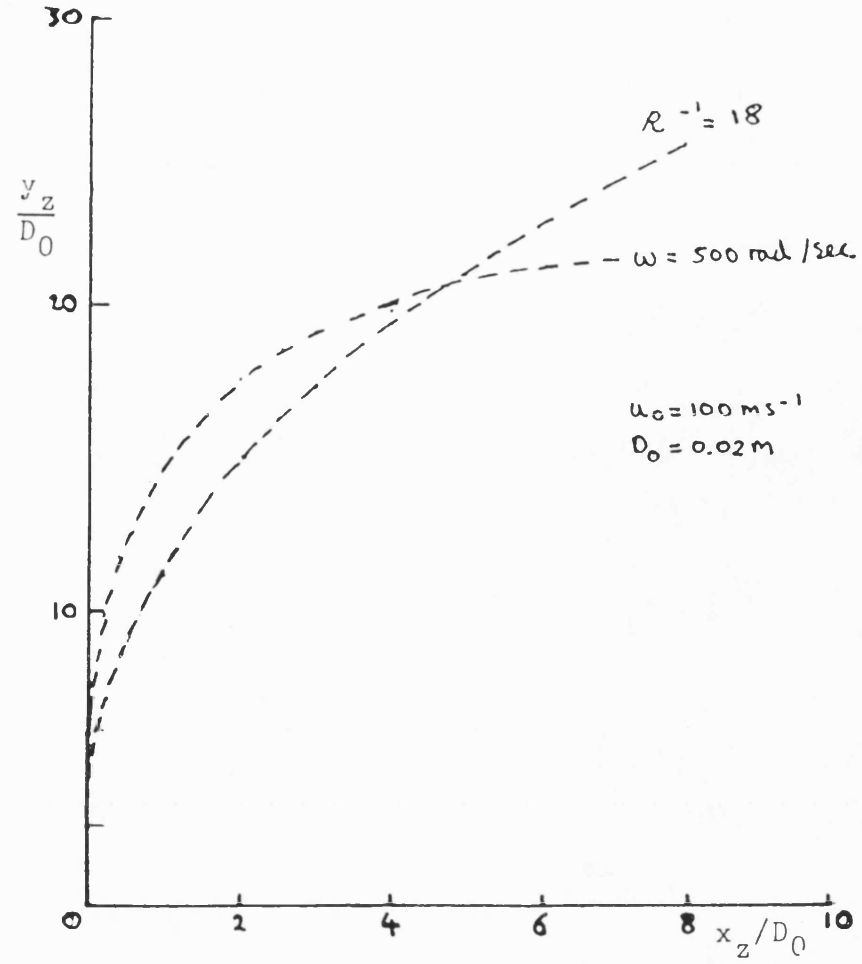

FIG. 7.47a PREDICTED AXES ξ IN UNIFORM AND SWIRLING CROSSFLOWS

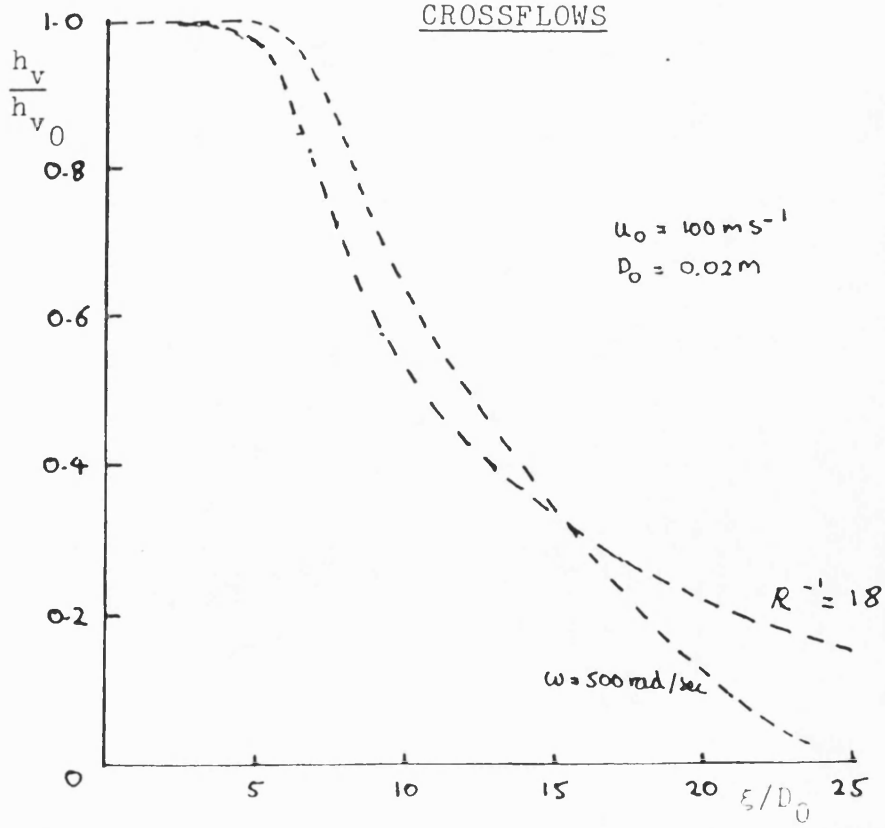

FIG. 7.47b PREDICTED EXCESS AXIAL VELOCITY DECAY IN UNIFORM AND SWIRLING CROSSFLOWS

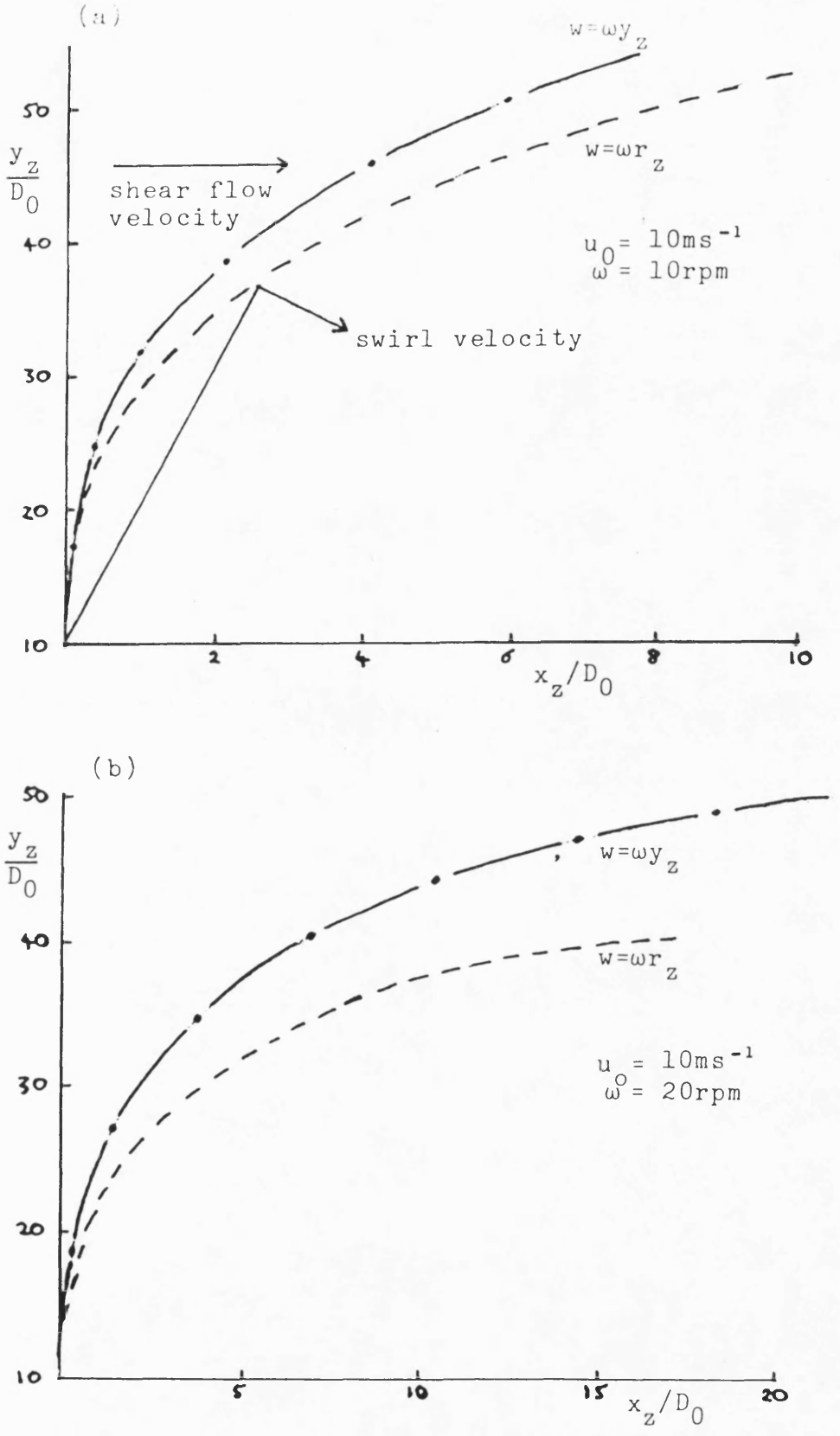

FIG. 7.48 PREDICTED AXES ξ IN SHEAR FLOW AND SWIRL

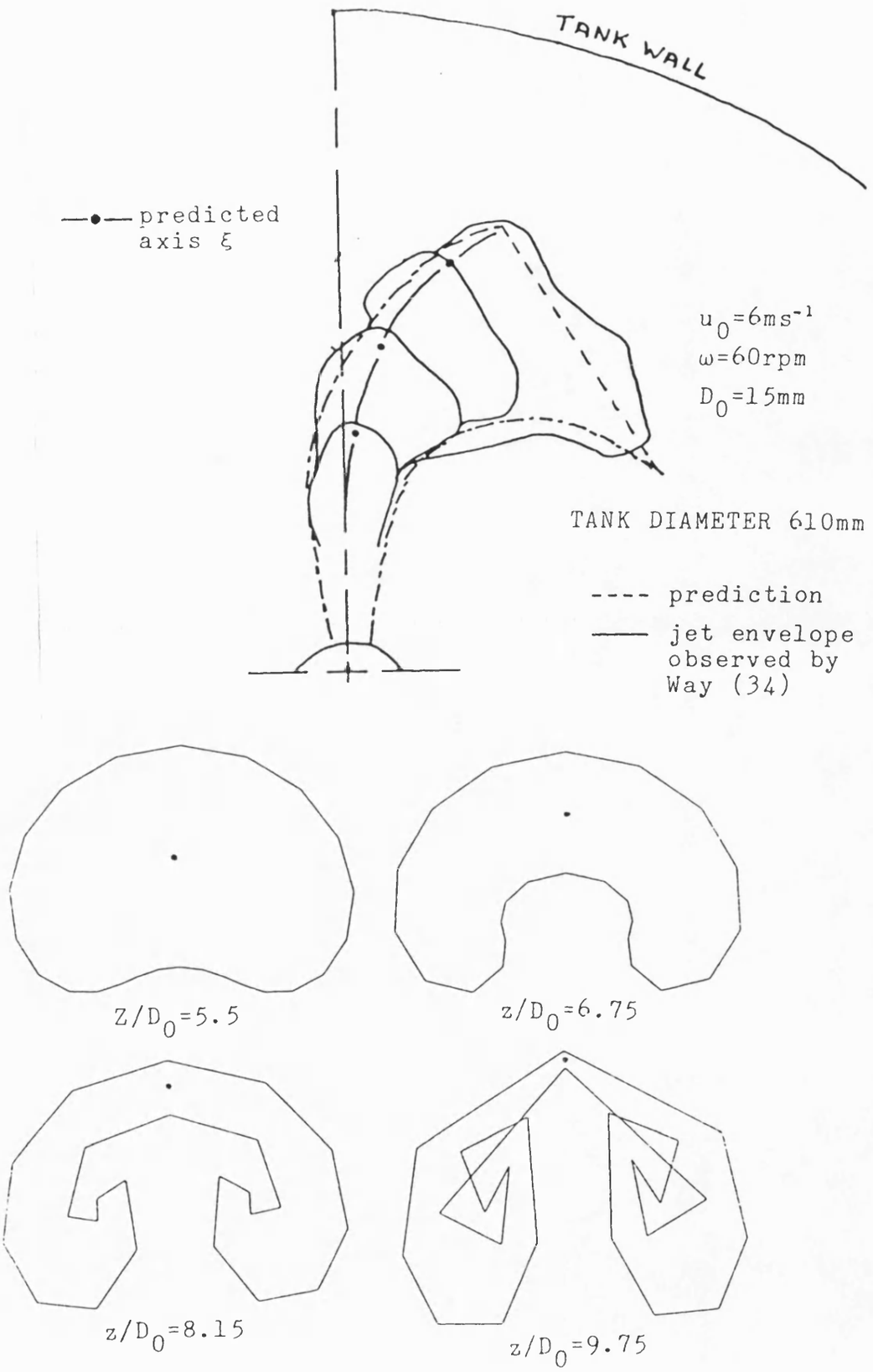

FIG. 7.49 COMPARISON OF WATER RIG AND JET MODEL RESULTS

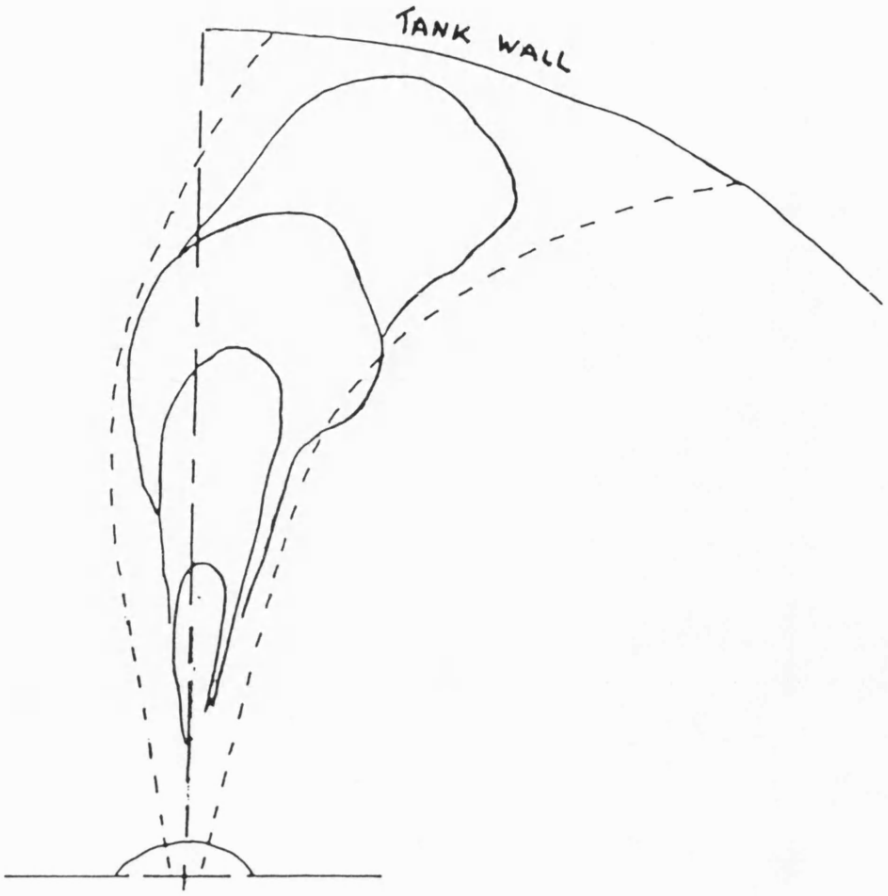

INJECTION CONDITIONS

u_0=17ms^{-1}

ω =70rpm

D_0=15mm

tank diameter 610mm

---- PREDICTION

—— OBSERVED BY MANIATACOS (36)

FIG. 7.50 COMPARISON OF WATER RIG AND JET MODEL RESULTS

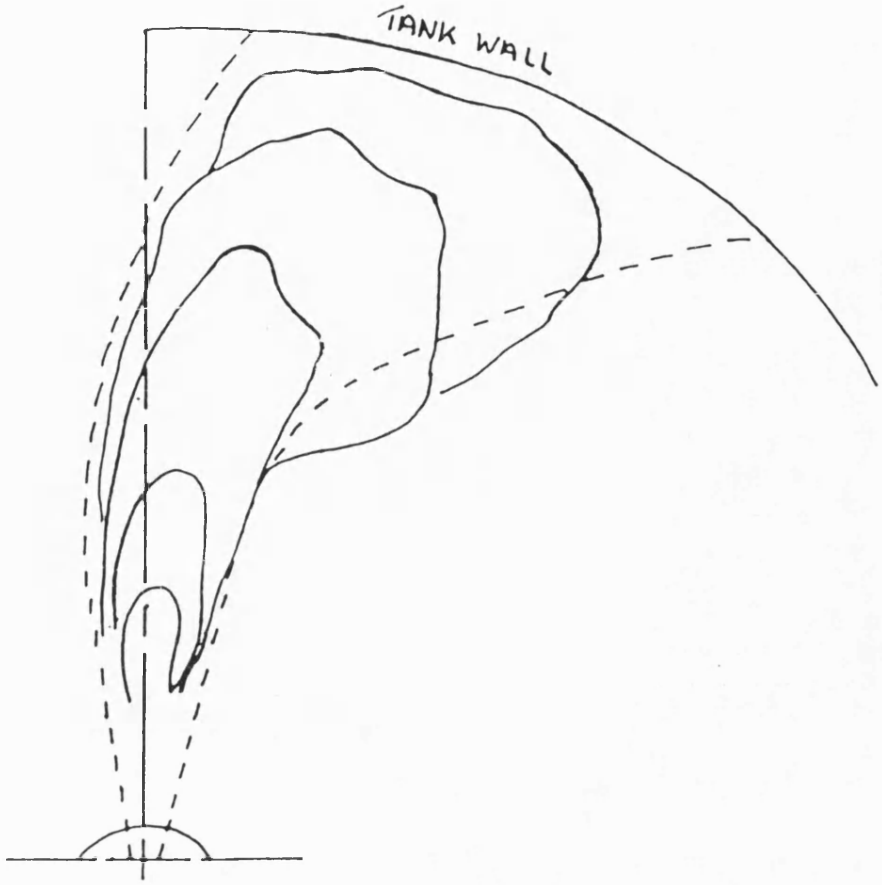

INJECTION CONDITIONS

u_0=20ms^{-1}
ω=74rpm
D_0=15mm
tank diameter 610mm

---- PREDICTION
—— OBSERVED BY MANIATACOS (36)

FIG. 7.51 COMPARISON OF WATER RIG AND JET MODEL RESULTS

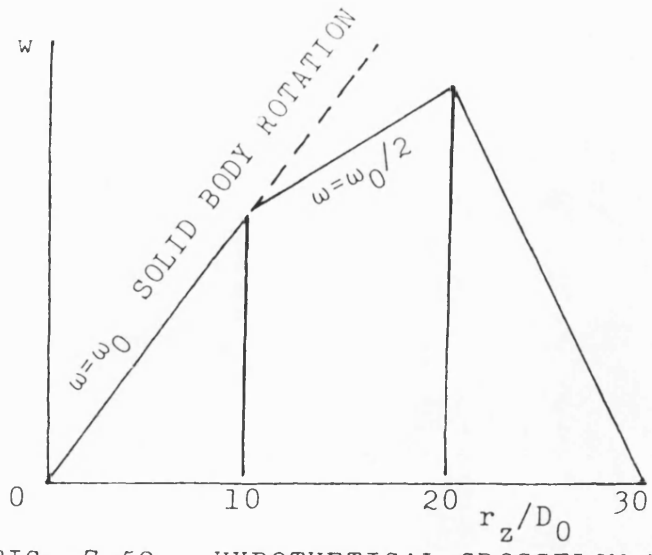

FIG. 7.52a HYPOTHETICAL CROSSFLOW WITH VARYING SWIRL RATE ω

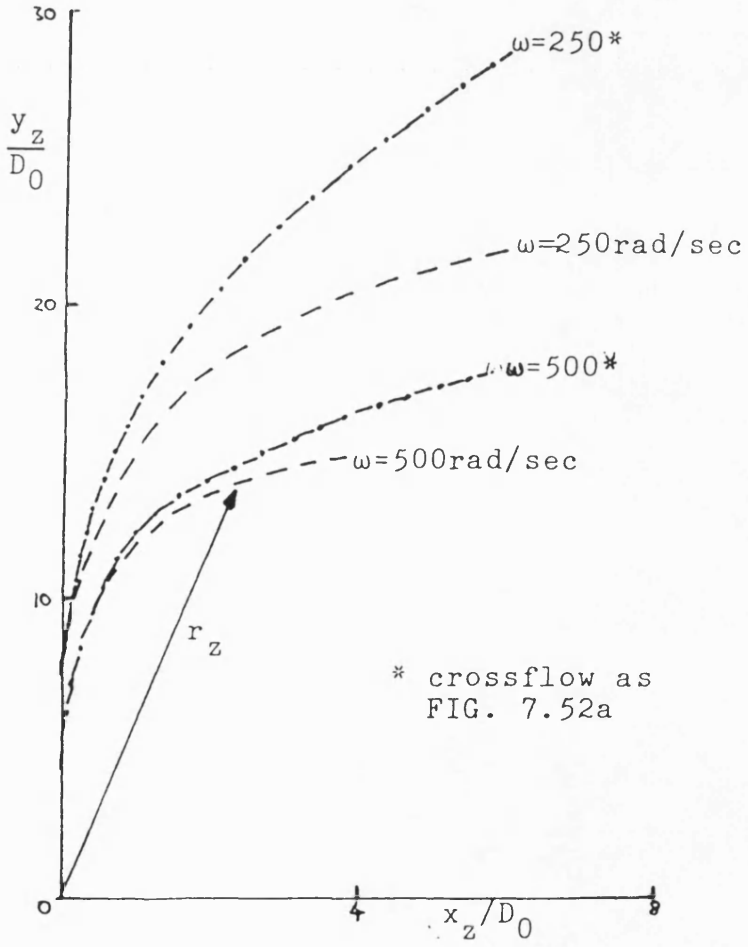

FIG. 7.52b EFFECT OF VARYING SWIRL RATE ON PREDICTED JET AXIS

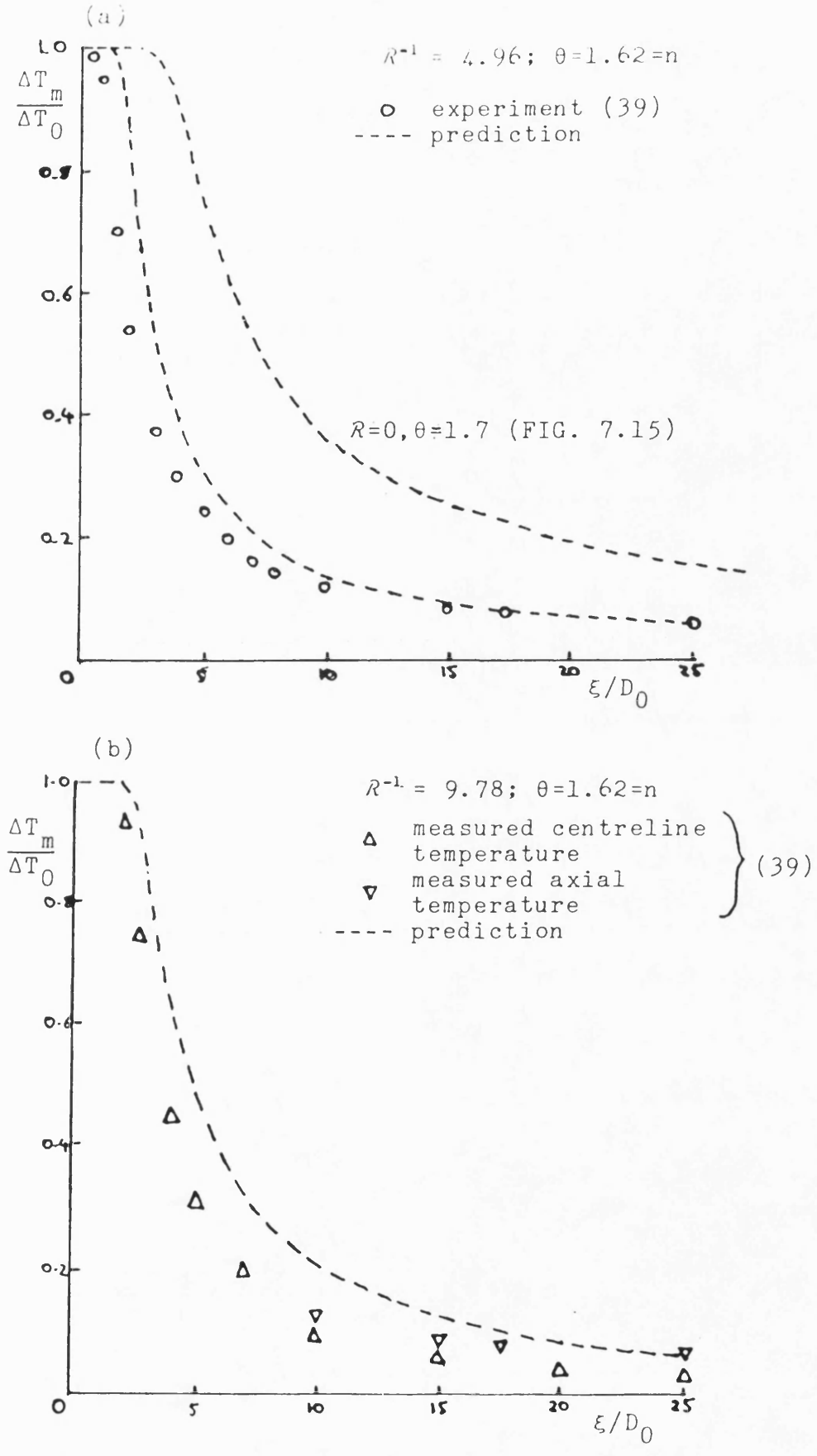

FIG. 7.53 EFFECT OF A UNIFORM CROSSFLOW ON AXIAL TEMPERATURE DECAY

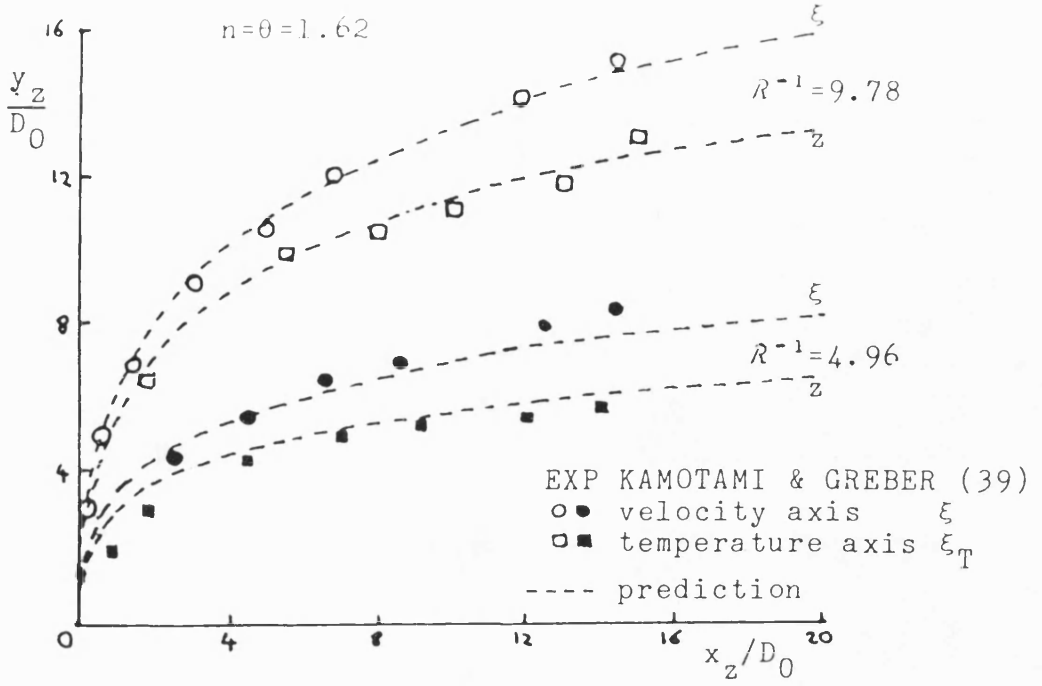

FIG. 7.54 VELOCITY AND TEMPERATURE AXES IN NONISOTHERMAL DEFLECTED JETS

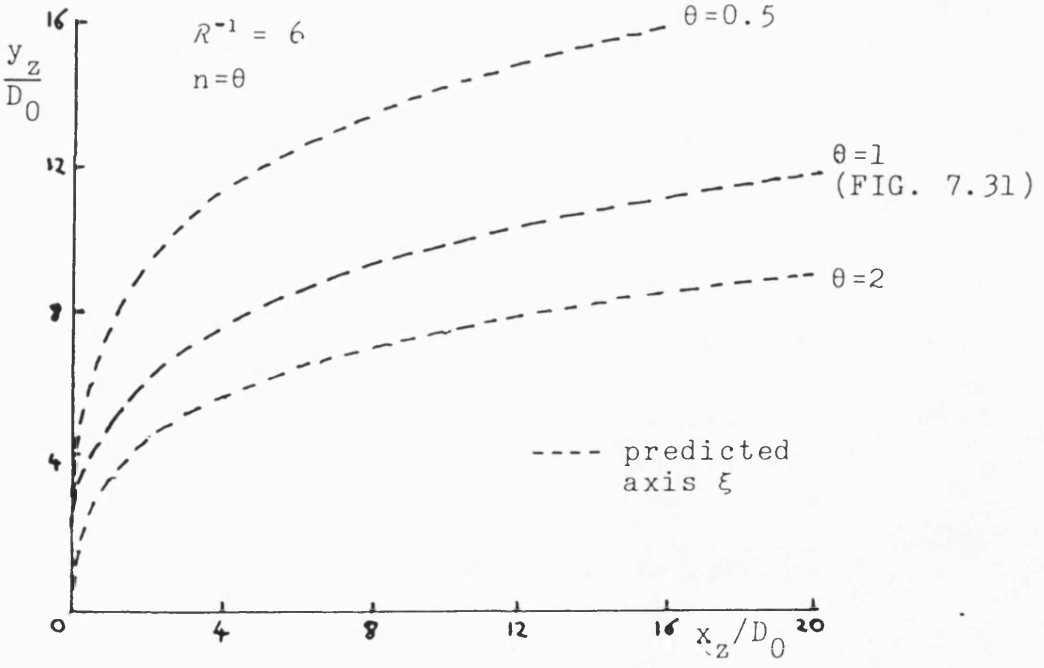

FIG. 7.55a EFFECT OF DENSITY RATIO ON PREDICTED JET TRAJECTORY IN A UNIFORM CROSSFLOW

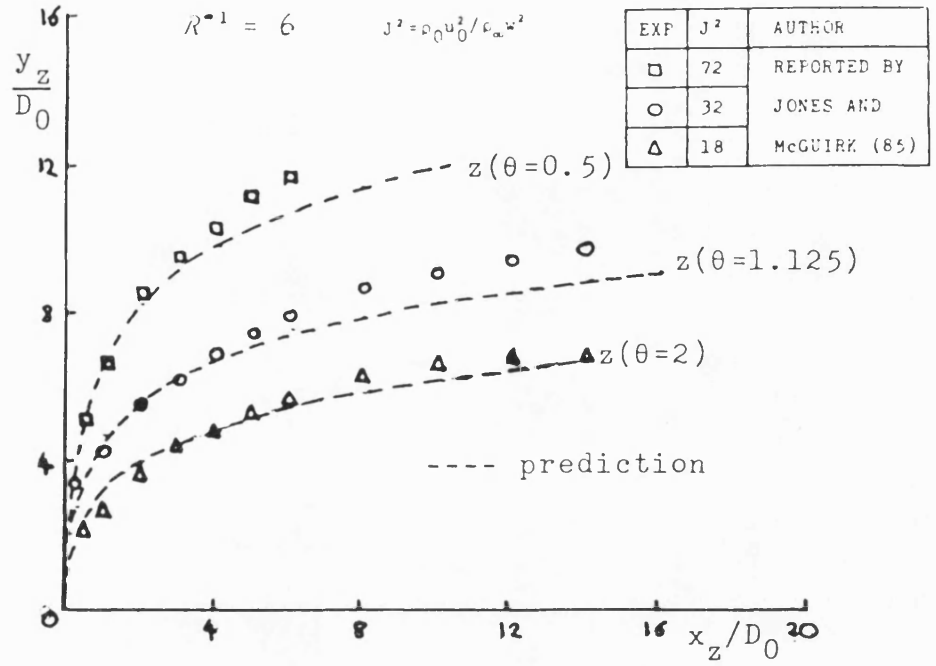

FIG. 7.55b MEASURED TEMPERATURE AXES AND PREDICTED MOMENTUM CENTRELINES

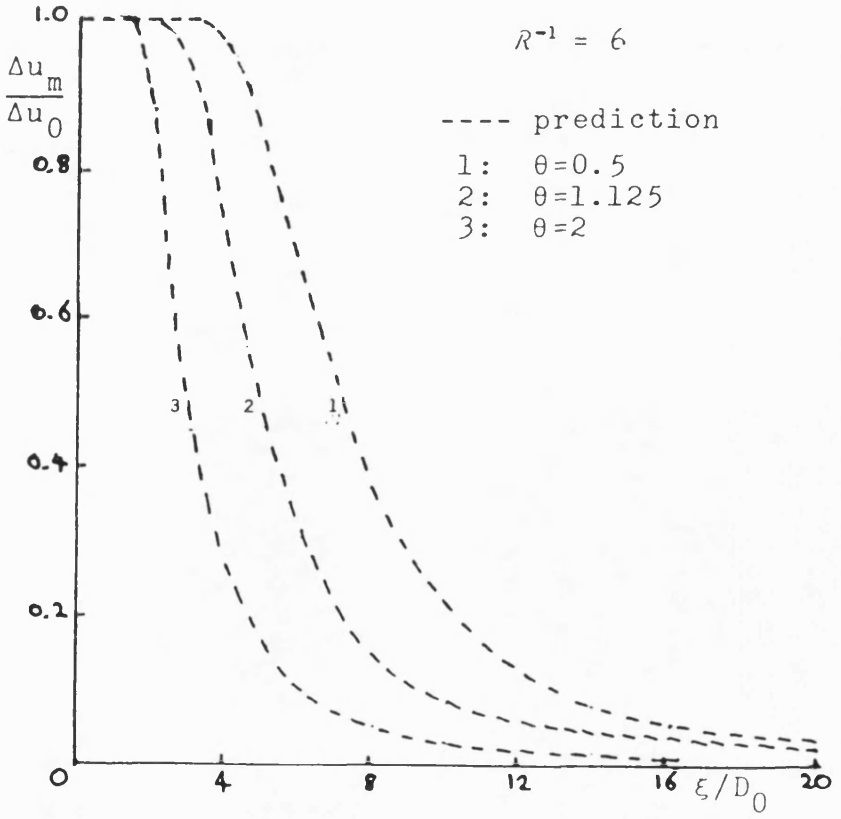

FIG. 7.55c EFFECT OF θ ON VELOCITY DECAY IN A DEFLECTED AIR JET

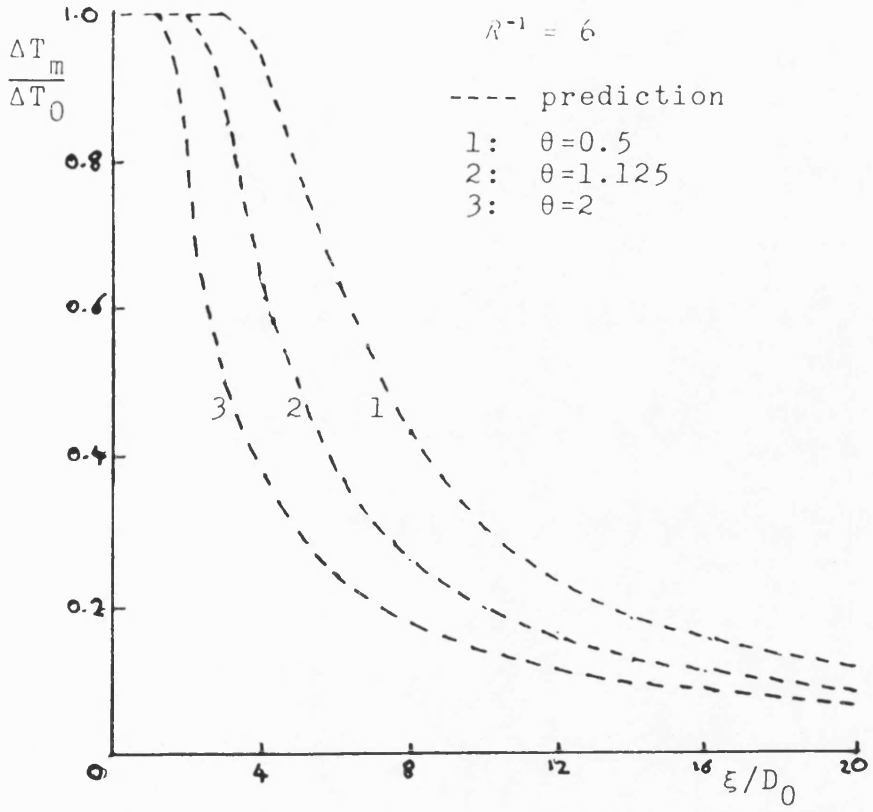

FIG. 7.55d EFFECT OF θ ON TEMPERATURE DECAY

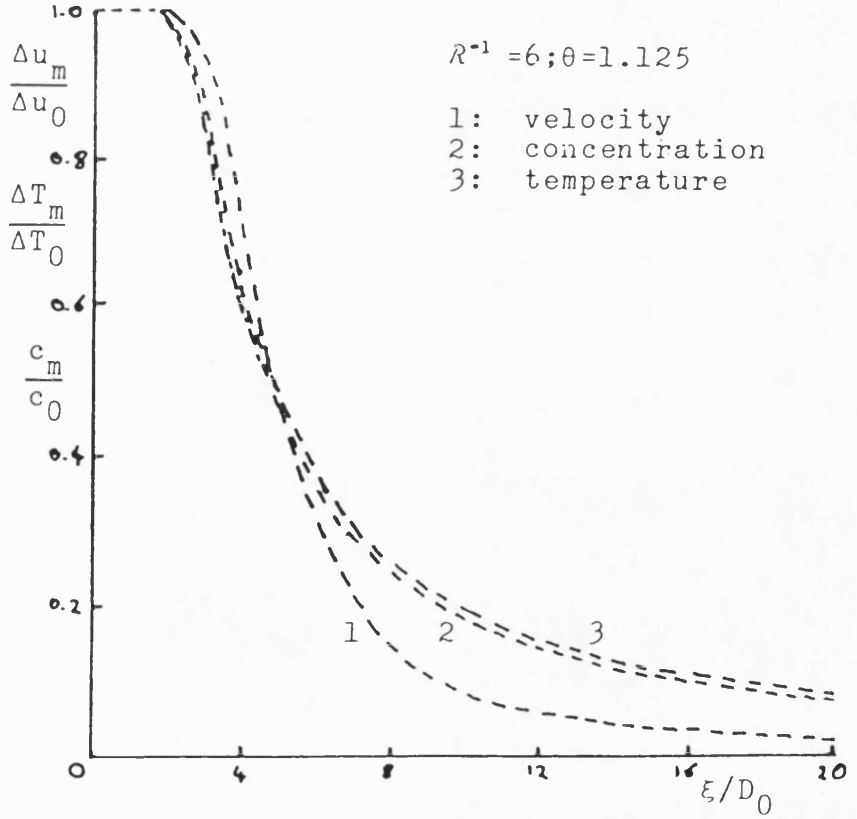

FIG. 7.55e RELATIVE RATES OF AXIAL PROPERTY DECAY

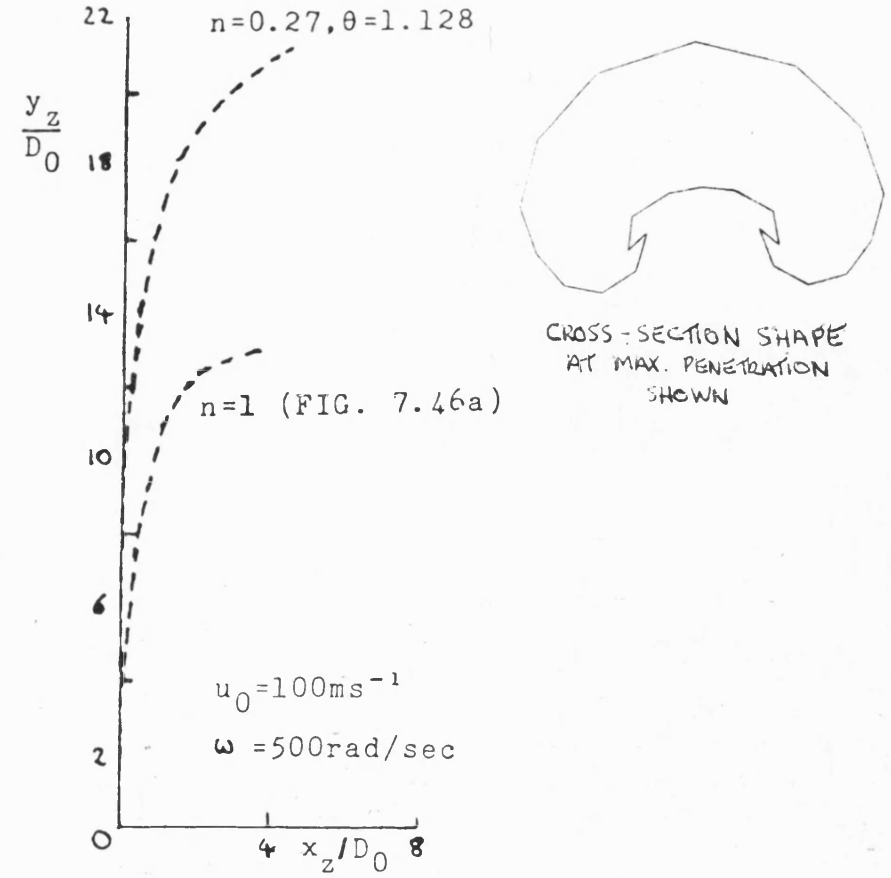

FIG. 7.56a PREDICTED AXIS FOR A FREON-AIR JET (n=0.27)

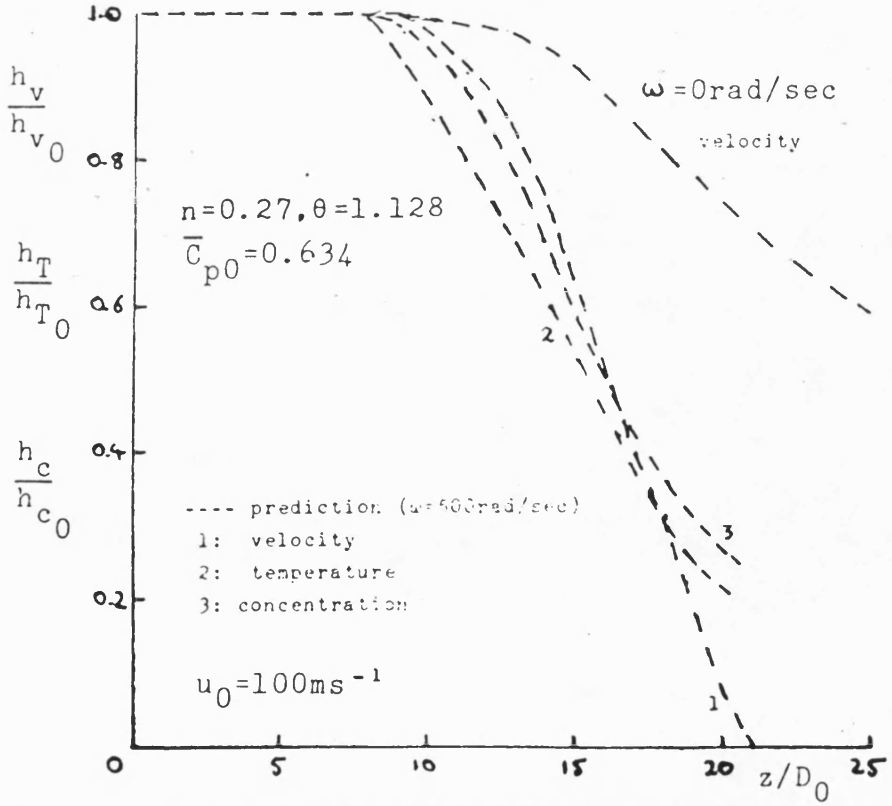

FIG. 7.56b RELATIVE RATES OF AXIAL PROPERTY DECAY IN A FREON-AIR JET

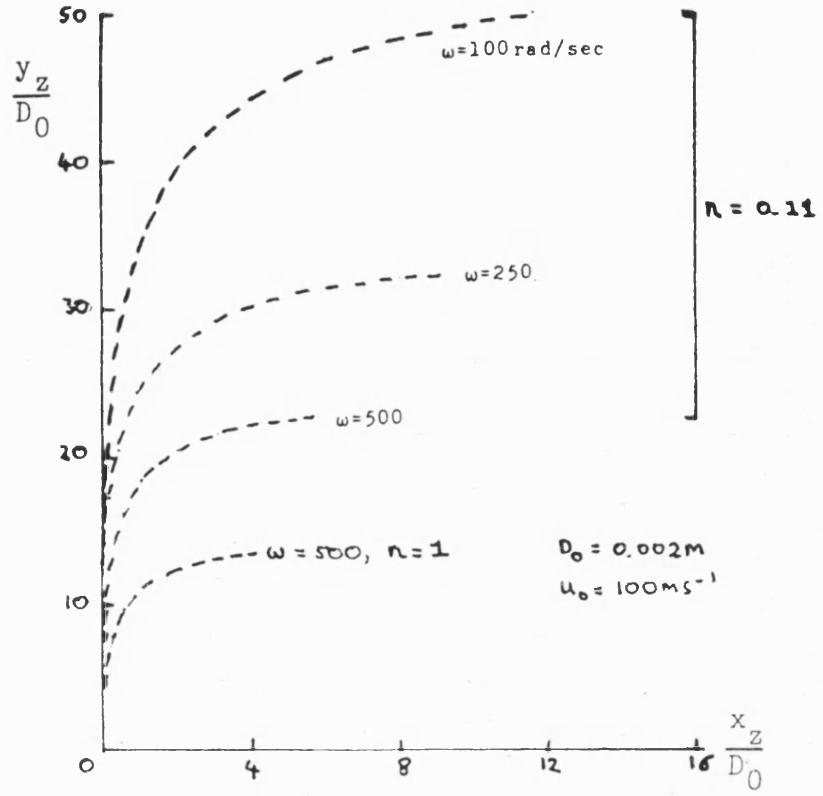

FIG. 7.57a TRAJECTORIES FOR DENSE JETS IN SWIRL

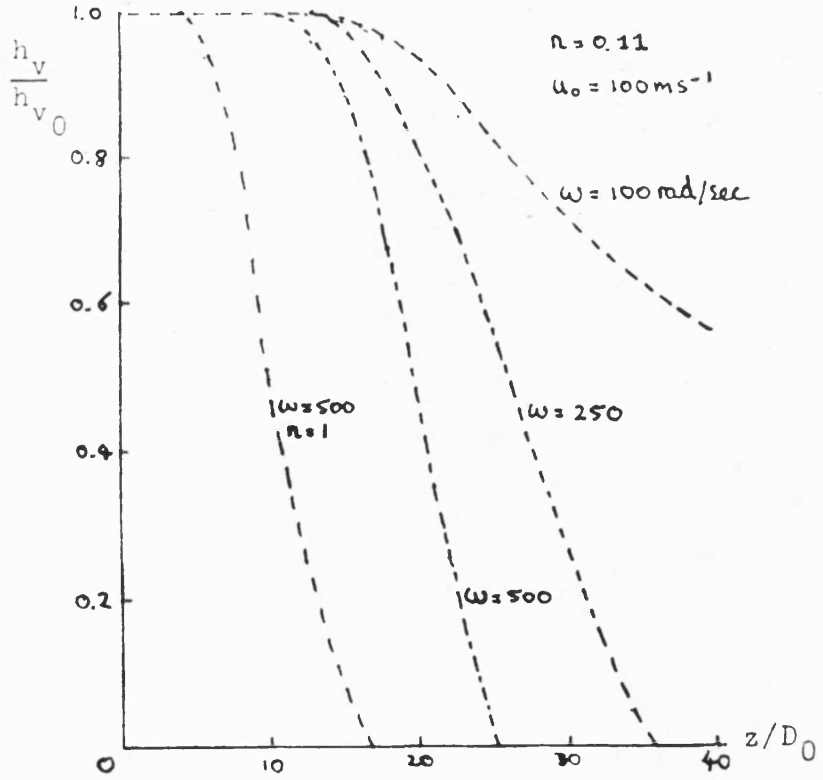

FIG. 7.57b EXCESS VELOCITY DECAY FOR DENSE JETS IN SWIRL

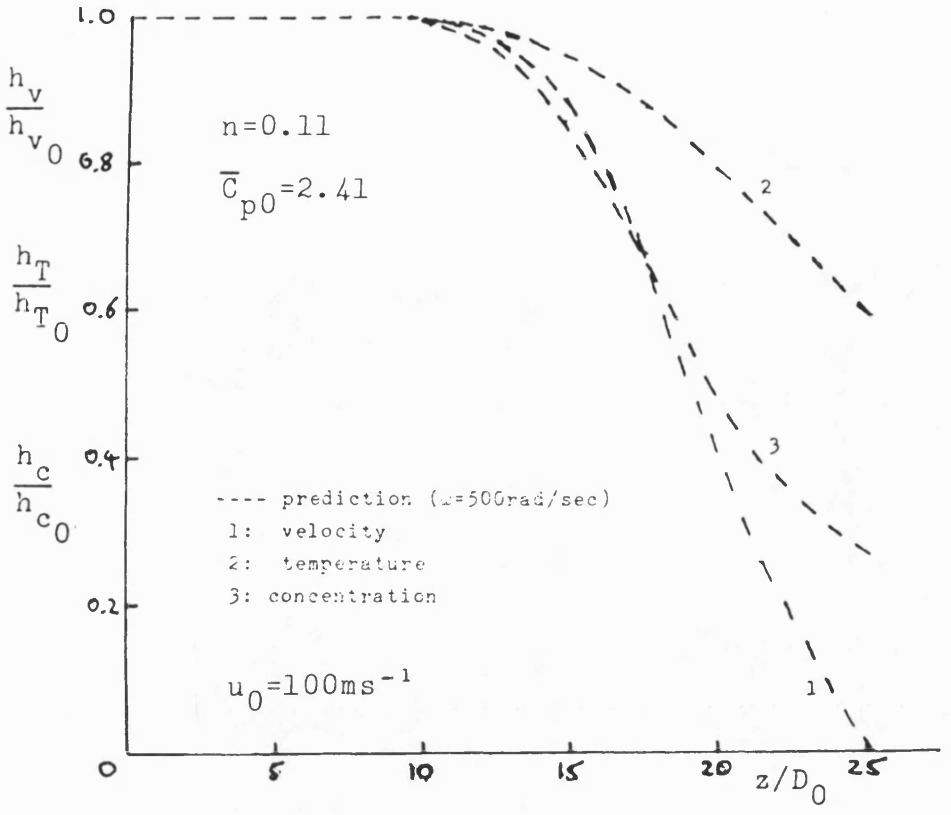

FIG. 7.57c RELATIVE RATES OF AXIAL PROPERTY DECAY IN A DENSE JET IN SWIRL

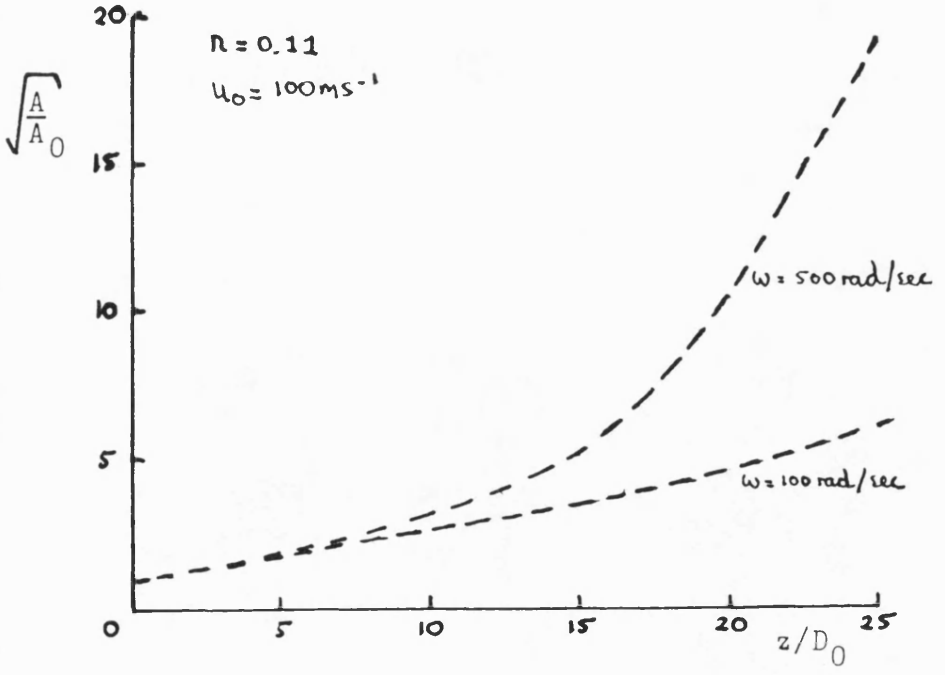

FIG. 7.57d EFFECT OF SWIRL RATE ON AREA GROWTH IN A DENSE JET

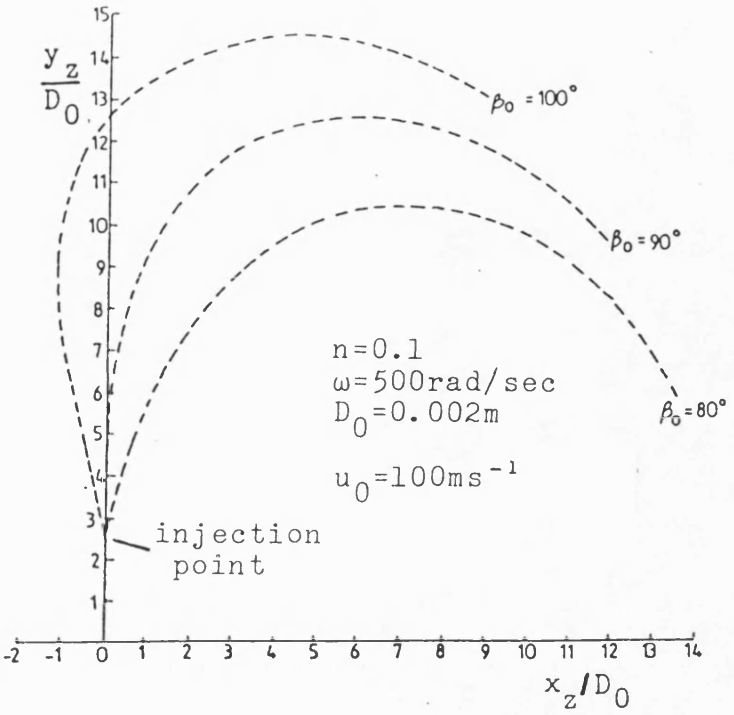

FIG. 7.58a EFFECT OF INJECTION ANGLE ON JET TRAJECTORY (FROM (46))

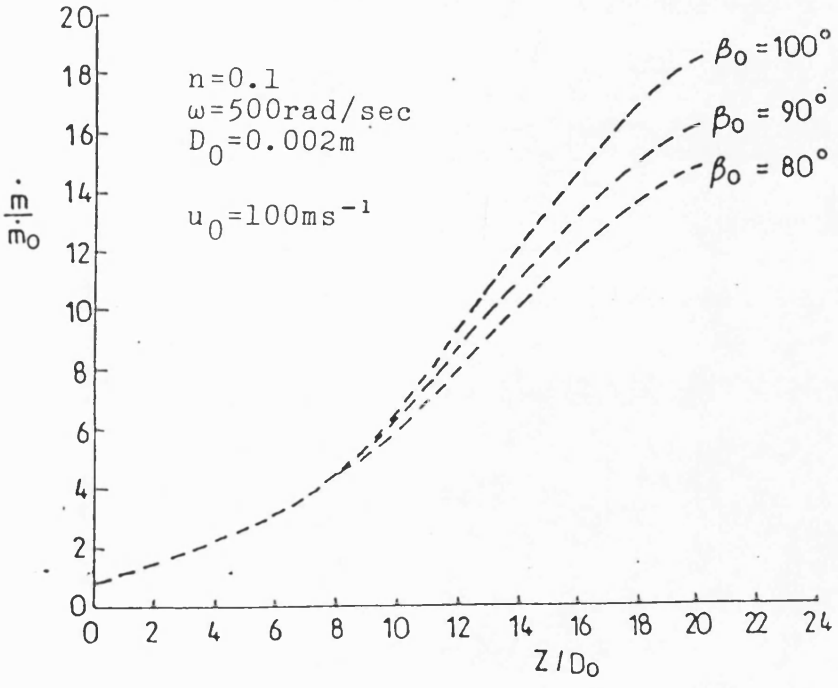

FIG. 7.58b EFFECT OF INJECTION ANGLE ON THE INCREASE IN JET MASS FLUX (FROM (46))

CHAPTER 8

APPLICATION TO DIESEL SPRAYS AND RECOMMENDATIONS FOR FUTURE WORK

Chapter 8 - Notation

A	-	jet area (m^2)
b	-	mixing zone width (m)
c	-	injectant concentration by mass
C_p	-	specific heat capacity (J/kgK)
D_0	-	nozzle diameter (m)
dz	-	solution step length (m)
G	-	width growth coefficient for the mixing zone
G_I	-	value for G in the initial region
h_v	-	maximum excess velocity function (ms^{-1})
k	-	evaporation function in 8.6a
m	-	$m_L+m_v+m_g$
m_g	-	mass of entrained gas (air)
m_L	-	mass of liquid
m_v	-	mass of vapour
M	-	molecular weight (kg/Kmol)
n	-	injection density ratio ($=\rho_\infty/\rho_0$)
P	-	pressure
R_0	-	universal gas constant
r_2	-	outer mixing boundary (m)
t	-	time (s)
T	-	temperature (K)
u	-	jet velocity (ms^{-1})
u_{mean}	-	average jet velocity over a cross-section
w	-	crossflow velocity (ms^{-1})
x_z, y_z	-	co-ordinates in trajectory plane
z	-	jet centreline co-ordinate
z_c	-	length of constant velocity core (m)
β	-	angle between centreline direction and crossflow
ν_T	-	turbulent dynamic viscosity
ξ	-	jet maximum velocity axis
ρ	-	density (kg/m^3)
ω	-	swirl rate

Subscripts

m	-	maximum in a cross-section
L	-	liquid

v	-	vapour
0	-	at the nozzle
1	-	on the jet axis
∞	-	in the external stream

Chapter 8
Application To Diesel Sprays And Recommendations For Future Work

8.1 Prediction Of Diesel Sprays

In view of the fundamental nature of the approach taken in developing the present jet mixing model, there is only scope here for an illustration of the validity and potential of its application to problems concerning two phase Diesel sprays. Work in this area is continuing.

The simplifying assumptions required for the analysis of a liquid-air spray as avery dense jet ($n<<1$) were given in Chapter 1 and concluded to be reasonably well founded. Integral modelling of Diesel sprays has been undertaken by Hakki (113)(1969), Melton (30)(1971), Vara Prasad and Subir Kar (16,17)(1977,1978), Mehta and Gupta (41)(1985) and others. The majority of these studies were linked to experimental observations on sprays in swirl.

The computer program assessed in Chapter 7 is extended to two phase problems by including liquid properties in the density and specific heat formulations. In the first instance, isothermal cases are considered and density computed from the relation derived by Adler and Lyn (19):-

$$\rho = \left[\frac{(1-c)R_0 T}{PM_\infty} + \frac{c}{\rho_L} \right]^{-1} \qquad (8.1)$$

(the extension to nonisothermal cases with phase change is given in Section 8.2.2). Changes in property formulations are easily made within the program (Chapter 6).

Data from the isothermal spray experiments of White (42) and Rife and Heywood (7) has been used for initial testing of the program. White (42) carried out experiments using the Bath University combustion rig, designed to reproduce the end of compression conditions occurring in a small to medium sized D.I. Diesel engine (35,42): swirl in the

combustion bomb is generated by a rotating drum within a constant volume chamber. The injection conditions for two isothermal tests were used as input to the computer program:-

air temperature:	$T=293K$
chamber pressure:	$210D_0$
chamber diameter:	$\omega_{drum}=10,000rpm$
drum speed:	$P_{inj}=200bar$
injection pressure:	light Diesel ($\rho_L=833Kg/m^3$)
fuel:	$D_0=0.46mm$
nozzle diameter:	$D_0=0.46mm$

According to White (42) the air swirl rate could be deduced from the drum swirl rate by $\omega\simeq 0.45\omega_{drum}$, giving $\omega\simeq 4,500rpm$ (solid body rotation is assumed). The uniform injection velocity u_0 was determined from (42):-

injection velocity: $$u_0=\left(\frac{2(P_{inj}-P)x10^5}{\rho_L}\right)^{\frac{1}{2}} x\ 0.6$$

giving:-

a) $P=35bar \Rightarrow u_0=123.4ms^{-1}$
b) $P=55bar \Rightarrow u_0=115.7ms^{-1}$

Shown in Fig. 8.1 is the predicted jet axis and spread under the two sets of conditions given above, in comparison with the corresponding, observed envelope prior to impingement on the chamber wall (42). The rate of cross section distortion is not known, but reasonable results (Fig. 8.1) are obtained upon assuming circle similarity for cross-sections: part of the discrepancies between prediction and experiment will be due to the relatively imprecise knowledge of the experimental boundary conditions (42).

The injection density ratio n for the two sprays in Fig. 8.1 lies in the range $n\simeq 0.05$-0.08. The validity of the semi-

empirical width growth law (Chapter 5) for values of n in this range was partially assessed by a further prediction, for an axisymmetric two phase spray, with the injection conditions chosen to match those in the experiment of Abramovich (97) for liquid nitrogen spreading in a medium of gaseous nitrogen at a supercritical thermodynamic pressure (n=0.05 - see Fig. 8.2). In Fig. 8.2, the predicted decay of total head ($\rho_l u_m^2$) shows some disagreement with the measured decay: part of the discrepancy may be attributed to the considerable overprediction of the length of the constant velocity core (Fig. 8.2). In the absence of any information concerning nozzle boundary layers in the experiment, it is noted that the core length prediction might be improved by including an initial region temperature profile closer to that observed in this case (97) than the assumed universal distribution ${}^{U}T_I$ from Chapter 5 (this point was discussed in Section 7.2.3b as well as in Chapter 5). The prediction of the 'downstream limit' in Fig. 8.2 ($z/D_0 \simeq 35$, say) is reasonably good.

The computer program is sensitive to the principal 'engine' parameters such as swirl level and injection pressure (through injection velocity u_0), nozzle diameter and chamber pressure. The latter has its effect through the resulting density ratio n, as illustrated in Fig. 8.3 in terms of jet spread (for the two Diesel sprays from Fig. 8.1). A parametric study for a single phase jet at n=0.1 was discussed in Section 7.3.8b.

Detailed experimental data for isothermal fuel sprays was given by Rife and Heywood (7). The chamber pressure P in the experiments was much lower than in the tests by White (42) (P≃10bar compared with P≃50bar): consequently, the injection density ratio is lower (n≃0.012). Shown in Fig. 8.4a are the measured values of axial velocity u_m for quiescent sprays at such a value for n (7) (predictions are discussed shortly): a length for the constant velocity core of $z_c \simeq 100 D_0$ is indicated.

For a jet in a quiescent medium, the width growth law used in Chapter 7 was (from Chapters 2 and 3):-

$$\frac{db}{dz} = G(z)\frac{(1+\bar{\rho})}{2} \quad ; \quad \bar{\rho}=\frac{\rho_\infty}{\rho_1} \quad ; \quad \rho_1 \text{ density on jet axis} \qquad (8.2a)$$

and this density dependence, extended to the deflected jet problem (Chapter 5), was used for the predictions discussed above. In the initial region, $\bar{\rho}\equiv n$ and $G(z)\equiv G_I$ (Chapter 3), and 8.2a is:-

$$\left.\frac{db}{dz}\right|_{\substack{\text{initial}\\ \text{region}}} = G_I\frac{(1+n)}{2} \qquad (8.2b)$$

For very dense sprays, n is very small (n=0.01-0.08 in this section) and, as $n\to 0$, 8.2b approaches the limiting form:-

$$\left.\frac{db}{dz}\right|_{\substack{\text{initial}\\ \text{region}}} \to \frac{G}{2}I \quad \text{as} \quad n\to 0 \qquad (8.2c)$$

so that the mixing zone in the initial region of a very dense spray in quiescent surroundings will be predicted to widen at about half the rate of that of a constant density jet (n=1). This, in turn, implies that there will be a limiting value for the predicted length z_c of the initial region in very dense jets (32): this limit was determined, in the present program, by using the limiting form 8.2c in the propagation equation, rather than 8.2b, in a computation at n=0.01:-

$$\left.\frac{z_c}{D_0}\right|_{\substack{n\to 0\\ w=0}} \simeq 15D_0 \qquad (8.3)$$

(that is, about three times the length of the initial region at constant density - Chapter 7). The result 8.3 is not in agreement with the measurements of Rife and Heywood (7), (Fig. 8.4a), Lakshminarayan and Dent (20) or

Chehroudi et al (114). According to the latter:-

$$\frac{z}{D_0 c} = \frac{c}{\sqrt{n}} \quad ; \quad c \simeq 7 \qquad (8.4a)$$

and this is in sufficiently good agreement with the correlation for single phase, submerged jets (w=0) discussed in Section 7.2.3a:-

$$\frac{z}{D_0 c} \simeq \frac{5}{\sqrt{n}} \qquad (8.4b)$$

The poor performance of the propagation equation in reproducing 8.4b for very dense jets (in view of 8.3) is due to the simplifications made during its derivation (Chapter 2).

Most integral models for Diesel sprays reported in the literature employ entrainment models rather than width growth laws, and the prescribed density dependence varies between the studies (7,41). For the present work, a sufficiently good prediction of the quiescent spray velocity decay in Fig. 8.4a was obtained using the following empirical width growth law:-

$$\frac{db}{dz} = \left(\frac{\rho_\infty}{\rho_1}\right)^{\frac{1}{2}} G(z) \qquad (8.5)$$

The prediction using 8.2a seriously overpredicts the velocity decay rate (Fig. 8.4a). In Fig. 8.4b, the predicted jet spread using 8.5 is compared with the observed mixing boundary (7). The computed axial velocity u_m may be integrated to locate the jet 'tip' in time, as shown in Fig. 8.4c in comparison with experiment. Part of the discrepancy may be atrributed to slight differences in the injectant properties in the experiment and computations (7), although the trend of the penetration is well represented.

Finally in this preliminary study, injection conditions were chosen to match (approximately) those in the deflected

spray experiments of Rife and Heywood (7). Central injection into swirl was assumed, although a velocity survey of the air motion in the experiment shows this to be an oversimplification (7). The assumed injection conditions and resulting jet axes are given in Fig. 8.5a in comparison with the experimental results (7). It is observed that the prediction at the higher swirl rate (ω=180rad/sec) is in better agreement with the appropriate data than than that at the lower swirl rate (ω=80rad/sec). Part of the error here will be due to the simplification concerning the external flow: it was shown in Fig. 7.52 that, if the 'swirl rate' ω is allowed to decrease with radial penetration (Section 7.3.7c), the predicted trajectory is more greatly influenced by the nonuniformity (in comparison with a prediction assuming solid body rotation) in the case of the lower 'initial' swirl rate.

The decay of the excess velocity function h_v with penetration, corresponding to these predicted trajectories, is shown in Fig. 8.5b. There is little effect of swirl rate ω on the length of the constant velocity core. Shown in Fig. 8.5c is the comparison between measured and computed tip position for the ω=180rad/sec case.

These results indicate that the model may be successfully applied to the prediction of two phase Diesel sprays. However, the uncertainty surrounding the 'correct' form for the propagation equation at very low values for density ratio n must be reconciled by further validation studies.

8.2 Recommendations For Future Work

8.2.1 Comparisons With Diesel Spray Data And Correlations

In the absence of further reliable experimental data for central injection into swirl, useful progress may be made by comparing axisymmetric and deflected spray predictions with the available correlations for tip position (27,115) and trajectory (27), for various values of density ratio n in the range [0.01,0.1]. The performance of the different formulations for density dependence in the propagation

equation:-

a) from 8.2a - giving reasonable trends at n=0.05 according to Fig. 8.2, or

b) from 8.5 - giving more realistic results at n=0.012 (Fig. 8.4)

may then be properly assessed over the range, and a more complete analytical prescription for jet spread prescribed.

The use of the cross-section distortion model for deflected Diesel sprays requires some reference data for the rate of shape change (for the setting of the damping factor ν_T in variable density cases. If the value from Chapter 7 - the constant density setting - is used for the cases in Fig. 8.1, the predicted boundary is not in agreement with the envelope observed by White (42)).

Recent integral models, developed specifically for the prediction of fuel spray deflection under engine-like conditions (40,41), have made use of data concerning side injection into swirl. In the present work, the derivation of the normal momentum equation (for the rate of change of the angle β - Chapter 4) is based upon that of Adler and Baron (63) and Packer (35), and is valid only for the central injection case. Principally, the $d\beta/dz$ equation does not remain valid when the angle β takes negative values, as would occur in the prediction of side injection into swirl (see Fig. 8.6): this is because the original force balance (Section 4.6.4) does not allow for changes in the curvature of the centreline (19). A more flexible formulation for the normal momentum equation, in which this deficiency is overcome, is given by Mehta and Gupta (41)): the equation is again worked into a differential equation for the orientation of the centreline with respect to the crossflow (the equivalent of the angle β), so that it is envisaged that this equation (41) will replace the present form in due course. Furthermore, the procedures of

Mehta and Gupta (41) may be followed in order to permit three-dimensional predictions for trajectories, allowing more complex and realistic crossflows to be prescribed.

8.2.2 Change Of Phase

For a preliminary study of the incorporation of this process, the evaporation function model of Adler and Lyn (19) (Chapter 1) was used in conjunction with the present program for the prediction of an evaporating Diesel spray in swirl. The model (19), its computer implementation, and performance under engine-like conditions, was described by Packer (35).

The Adler and Lyn model (19,35) produces, for a prescribed set of injection conditions, an evaporation history k(t) describing the mean state of vaporisation in the spray. At any point in a spray cross-section:-

$$k(t) = \frac{\text{mass of yet unevaporated liquid}}{\text{mass of liquid + mass of vapour}} \qquad (8.6a)$$

or, in obvious notation:-

$$k(t) = \frac{m_L}{m_L + m_v} \qquad (8.6b)$$

For simplicity k is assumed constant over a particular cross-section. The numerical results are in the form of a discrete set of values for k at n values for time $\{k(t_i);\ i=1,n;\ k(t_1)=k(0)=1;\ k(t_n)=0\}$. Evaporation may then be crudely represented in the computer program by finding the 'time' t at any axial station z, using here the jet mean velocity u_{mean} from Chapter 6 (to characterise the 'mean' droplet):-

$$t = \int_0^z \frac{dz}{u_{mean}} \qquad (8.6c)$$

(the integration is carried out incrementally at each solution step). The local value of k(z) may be deduced by

interpolation (where necessary) using the known variation of k(t).

The relevant formulations for pointwise jet density and specific heat in the program were prescribed following Adler and Lyn (19):-

$$\rho = \left\{ \frac{R_0 T}{P} \left[\frac{(1-c)}{M_\infty} + \frac{c(1-k)}{M_v} \right] + \frac{ck}{\rho_L} \right\}^{-1} \qquad (8.7a)$$

where M_v is the molecular weight of the fuel vapour and ρ_L the liquid density, and:-

$$C_p = \{kC_{pL} + (1-k)C_{pv} - C_{p\infty}\}c + C_{p\infty} \qquad (8.7b)$$

C_{pL} being the liquid specific heat and C_{pv} that of the vapour. For this study both were assumed constant (31).

Phase change was included in the formulation of the energy equation by consideration of the control volume shown in Fig. 8.7 (cf. Chapter 5):-

$$(H+KE)_2 + (PH) = (H+KE)_1 + (H+KE)_E \qquad (8.8)$$

(PH) is the energy required to evaporate the quantity of liquid injectant vaporised within the control volume. If Δm_L is the mass vaporised:-

$$\Delta m_L = \int_{A(z_2)} \frac{dm_L}{dm} dm - \int_{A(z_1)} \frac{dm_L}{dm} dm \qquad (8.9a)$$

where $dm = dm_L + dm_v + dm_g$ and m_g is the mass of entrained gas (air) at a point. From the definition of concentration c in Chapter 5:-

$$c = \frac{m_L + m_v}{m} \qquad (8.9b)$$

so that:-

$$\frac{m_L}{m_L+m_v} \cdot \frac{m_L+m_v}{m} = \frac{m_L}{m} = kc \qquad (8.9c)$$

Since $dm=\rho u dA$, taking the limit as $\delta z \to 0$ (Fig. 8.7):-

$$(PH) = \left\{ H_L \frac{d}{dz} \int_A kc\rho u dA \right\} dz \qquad (8.9d)$$

where H_L is the latent heat of vaporisation for the liquid. If k is constant over a cross-section, 8.9d becomes:-

$$(PH) = \left\{ H_L \frac{dk}{dz} \int_A c\rho u dA \right\} dz \qquad (8.9e)$$

because the integral term is constant, by conservation of injected material (Chapter 5). This term, 8.9e, may then be included in the formulation of an amended equation, from 8.8, for the rate of change of the temperature difference function $h_T(z)$ (by the methods of Chapter 5).

The injection conditions and resulting spray temperature prediction for an evaporating Diesel spray in swirl (at 3000rpm) are given in Fig. 8.8. For simplicity, a fully developed velocity profile (so scalar profiles) was prescribed. In this example no very great effect of the phase change complication upon axial temperature is observed, compared with a calculation without evaporation, and there appears to be two main reasons. First, the phase change terms in the energy equation are significantly smaller than the static enthalpy terms ($H_L=3\times10^5 J/Kg$ while $C_{pL}T_0 \simeq 2\times10^6 J/Kg$). Second, evaporation takes place at the fastest rate in a region where the relative injectant concentration has become small ($c_m(z)<0.2$ in Fig. 8.8), so that the considerable density changes associated with fuel evaporation are not very influential. This of course is due to the rapid mixing rate just downstream from the nozzle: the situation may be altered very considerably in the case of uniform injection property profiles and a significant core region, although this has not been

considered analytically at present. The effect of evaporation on jet velocity, trajectory etc. for the problem in Fig. 8.8 is very minor.

This study is a very crude, preliminary investigation of the phase change phenomena. The Adler and Lyn representation of evaporation (19,35) 'averages' the phase change process over a cross-section: for more realistic predictions it would be necessary to consider more detailed evaporation models (28).

8.2.3 Wall Jets

Mixing off the wall of a combustion chamber is an important process in the filmed combustion studies of Rife and Heywood (7) and White (42). Dent and Mehta (28) allowed for enhanced air entrainment rates following impingement in their (quiescent chamber) phenomenological combustion model. The integral analysis followed the methods described by Rajaratnam (43), and these have been investigated at Bath University by Idoum (44) and Fraudeau (45), also in relation to wall jet growth in the presence of a crossflow (116). Incorporation of the wall jet part of the process into the present mixing model, based upon this existing work, may be considered in due course.

8.2.4 Combustion Modelling

A phenomenological combustion model, after that of Chiu, Shahed and Lyn (27), has been developed at Bath University by White (42), and its performance assessed against test data. In the first instance, empirical spreading rate, penetration and trajectory correlations, which together with a prescribed functional variation for fuel concentration with penetration (42) define the envelope and structure of the (vapour) jet, could all be replaced by computed results from the present program. This would permit the extension of the range of applicability of the combustion model to more complicated crossflows than solid body rotation (to which the experimental correlations apply).

The combustion model of Dent and Mehta (28) gives a full account of spray development and burning in a quiescent chamber. This model should also be investigated in connection with the use of the very sophisticated spray mixing model developed here, as a base for theoretical engine combustion and performance studies.

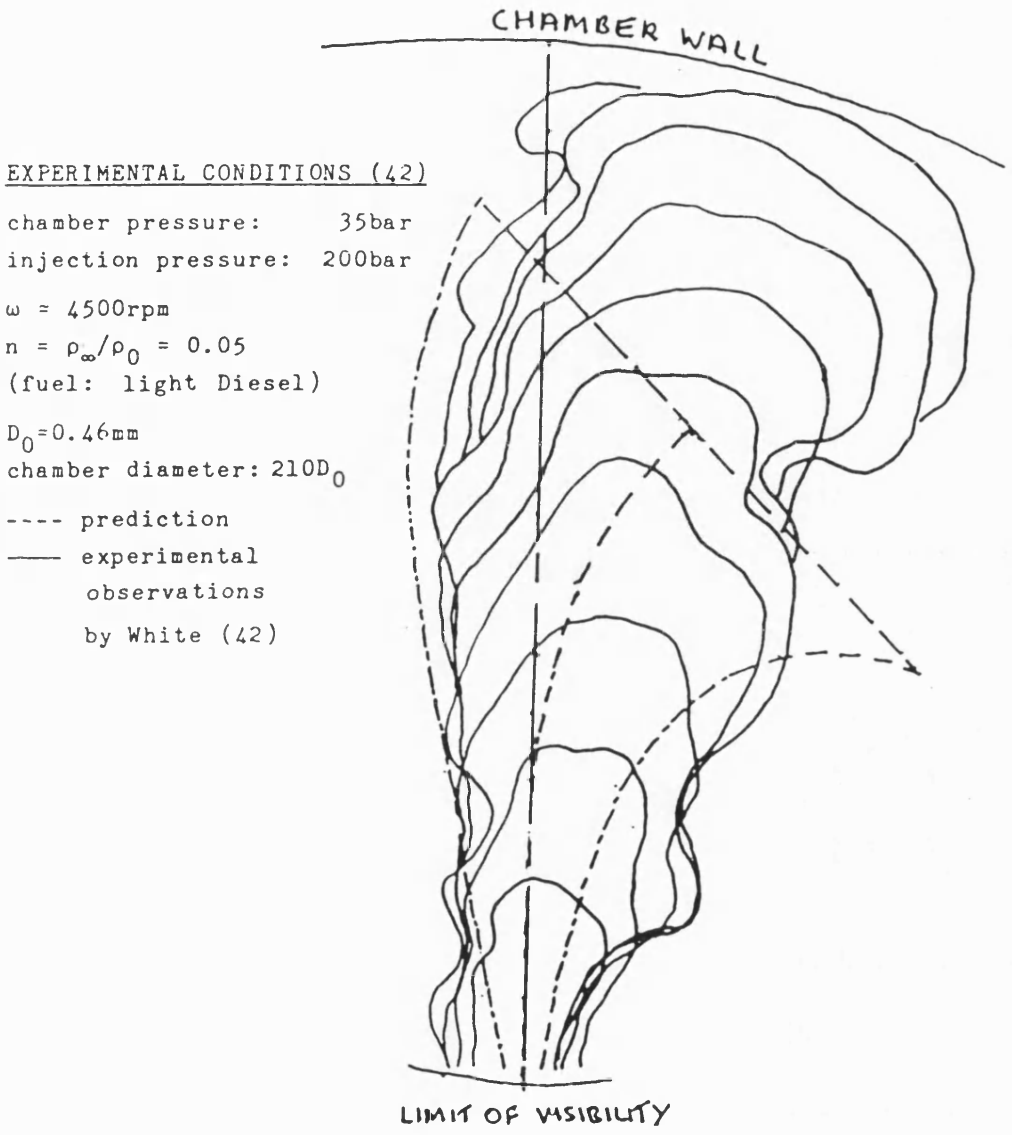

FIG. 8.1a COMPARISON OF SPRAY MODEL AND COMBUSTION RIG RESULTS FOR AN ISOTHERMAL DIESEL SPRAY IN SWIRL

EXPERIMENTAL CONDITIONS (42)

chamber pressure: 55bar
injection pressure: 200bar

ω = 4500rpm
$n = \rho_\infty/\rho_0 = 0.08$
(fuel: light Diesel)

D_0=0.46mm
chamber diameter: $210D_0$.

---- prediction
—— experimental observations by White (42)

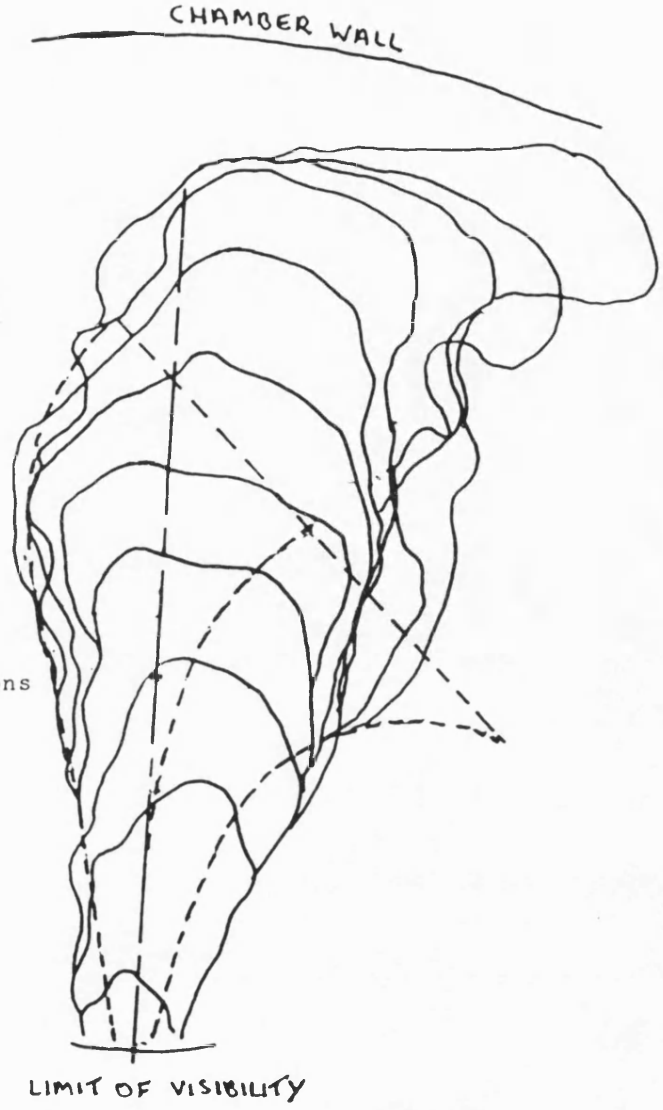

FIG. 8.1b COMPARISON OF SPRAY MODEL AND COMBUSTION RIG RESULTS FOR AN ISOTHERMAL DIESEL SPRAY IN SWIRL

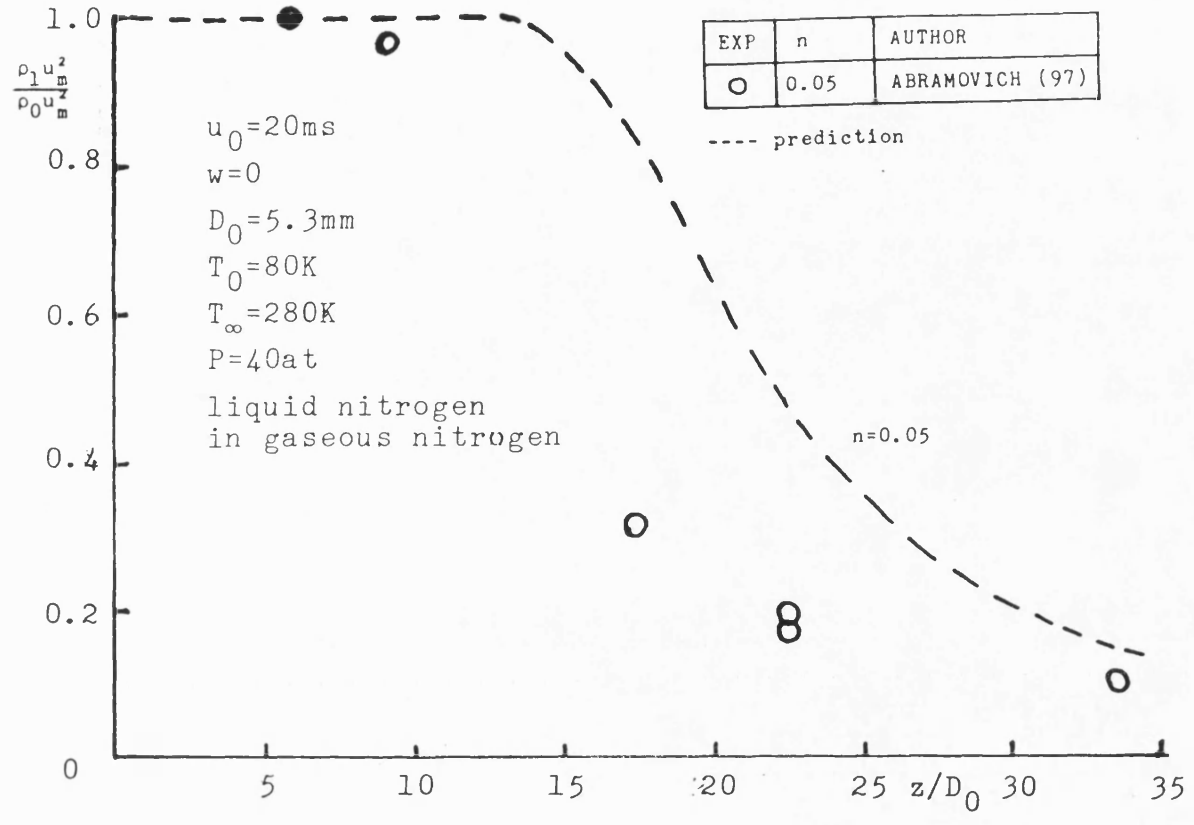

FIG. 8.2 DECAY OF RELATIVE TOTAL HEAD IN A DENSE, TWO PHASE AXISYMMETRIC JET

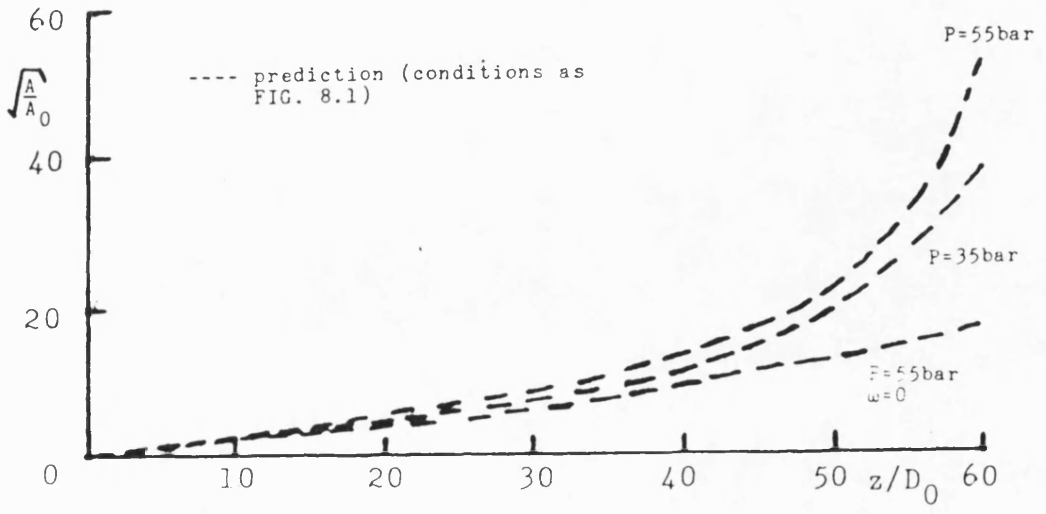

FIG. 8.3 EFFECT OF INJECTION PRESSURE ON SPREAD IN A DIESEL SPRAY

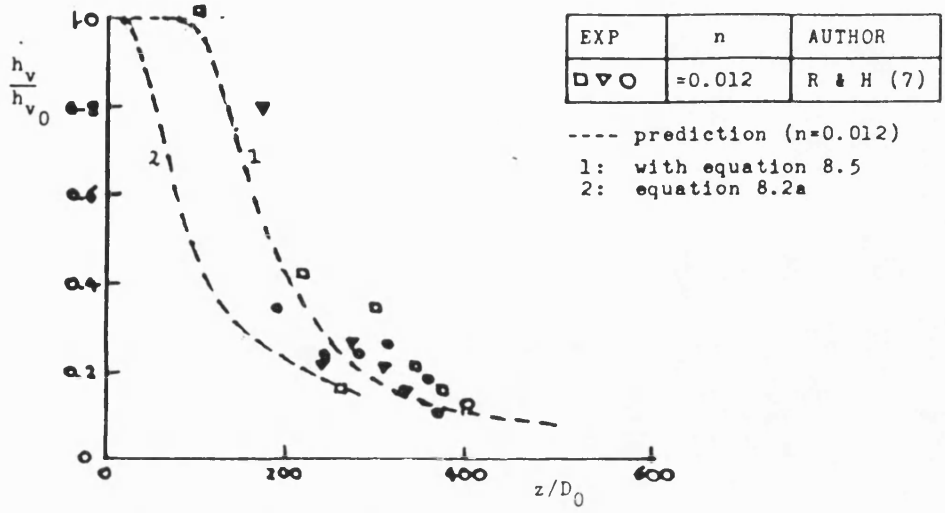

(a) VELOCITY DECAY

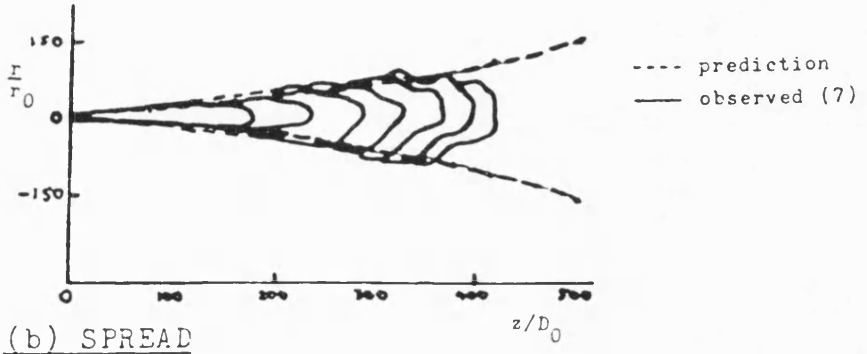

(b) SPREAD

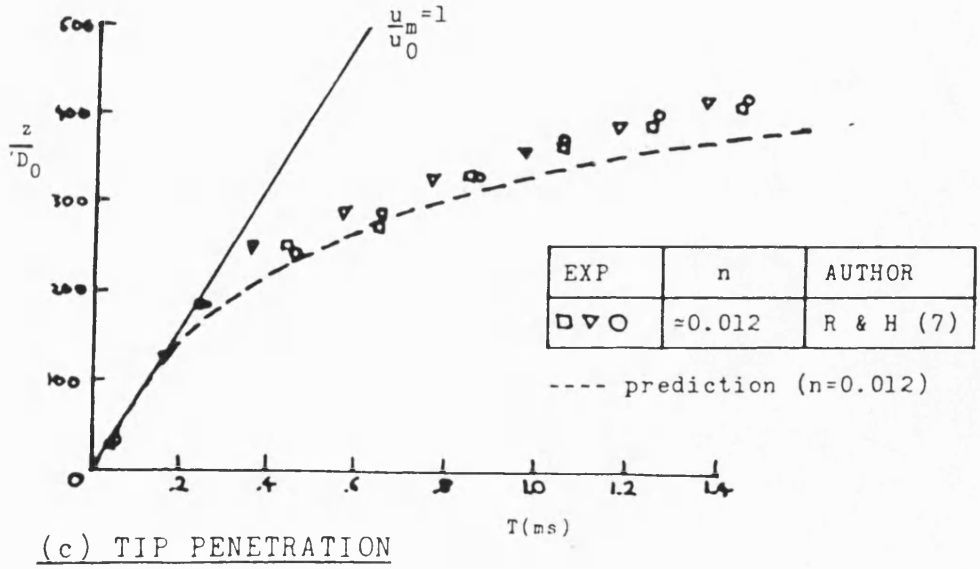

(c) TIP PENETRATION

FIG. 8.4 PREDICTION OF AN ISOTHERMAL FUEL SPRAY IN A QUIESCENT CHAMBER

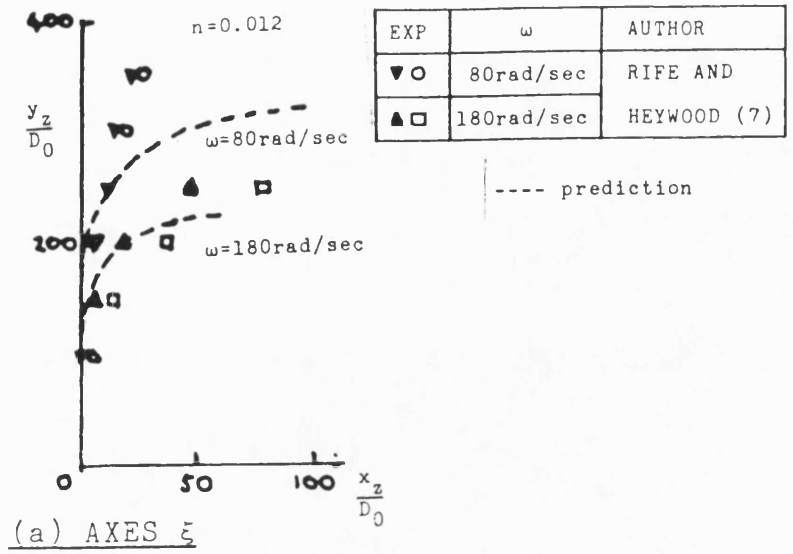

(a) AXES ξ

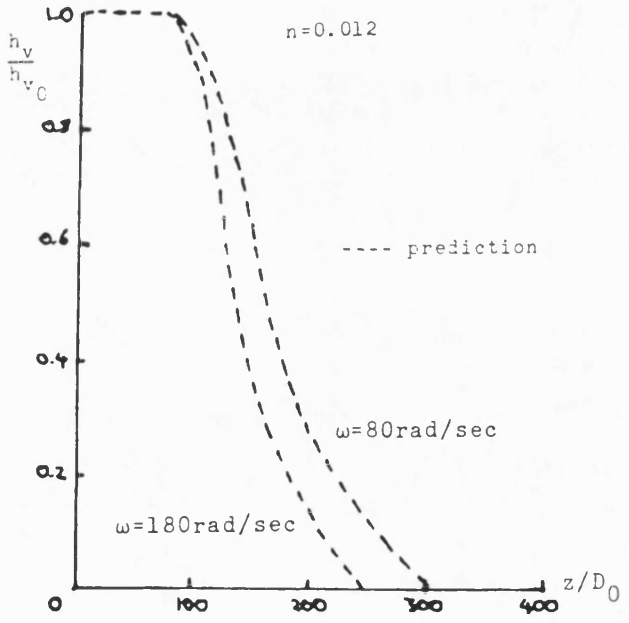

(b) EXCESS VELOCITY DECAY

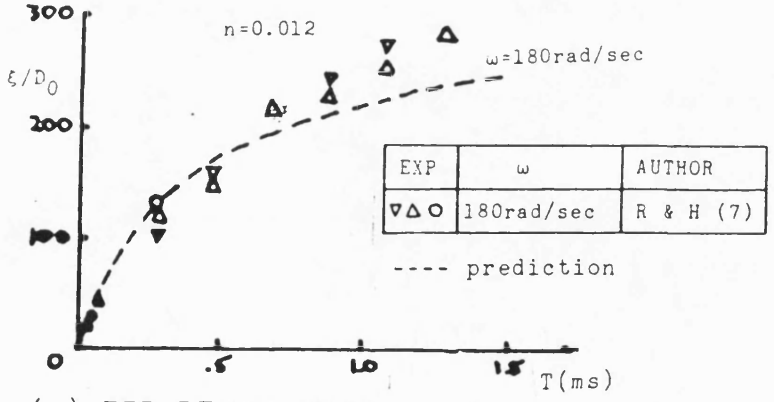

(c) TIP PENETRATION

FIG. 8.5 PREDICTION OF DIESEL SPRAYS IN SWIRL

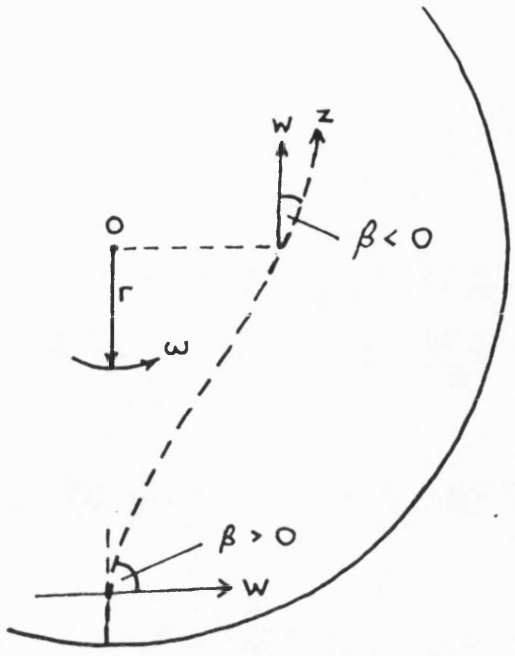

FIG. 8.6 MODELLING CONSIDERATIONS FOR SIDE INJECTION INTO SWIRL

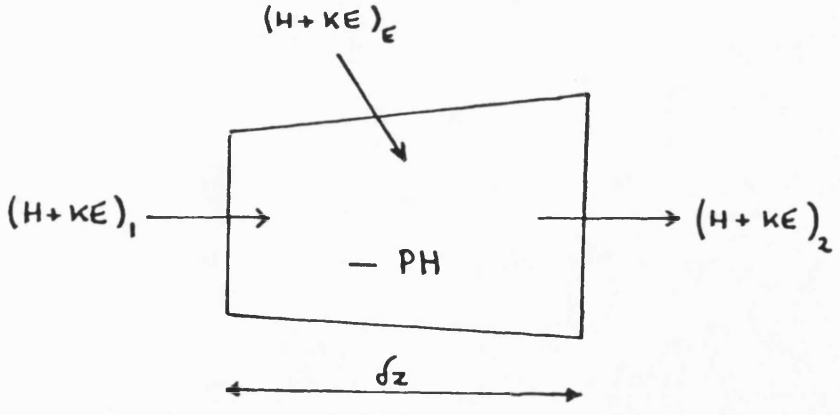

FIG. 8.7 CONTROL VOLUME FOR ENERGY BALANCE INCLUDING PHASE CHANGE

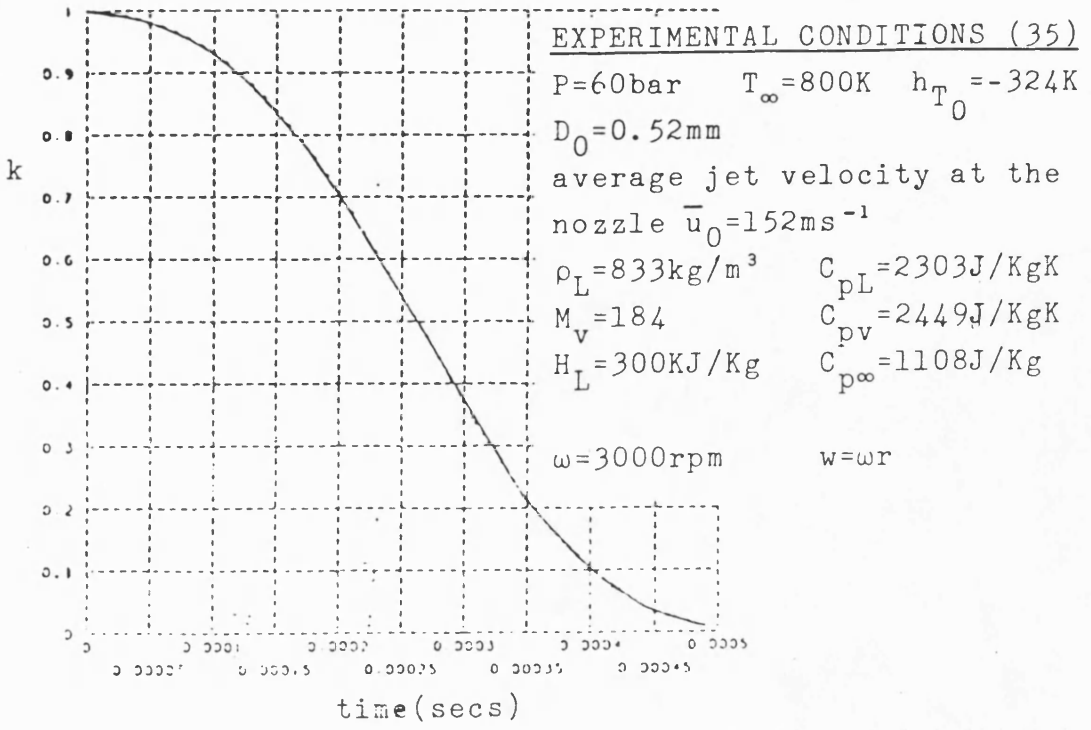

EVAPORATION FUNCTION vs TIME FROM ADLER/LYN MODEL (35)

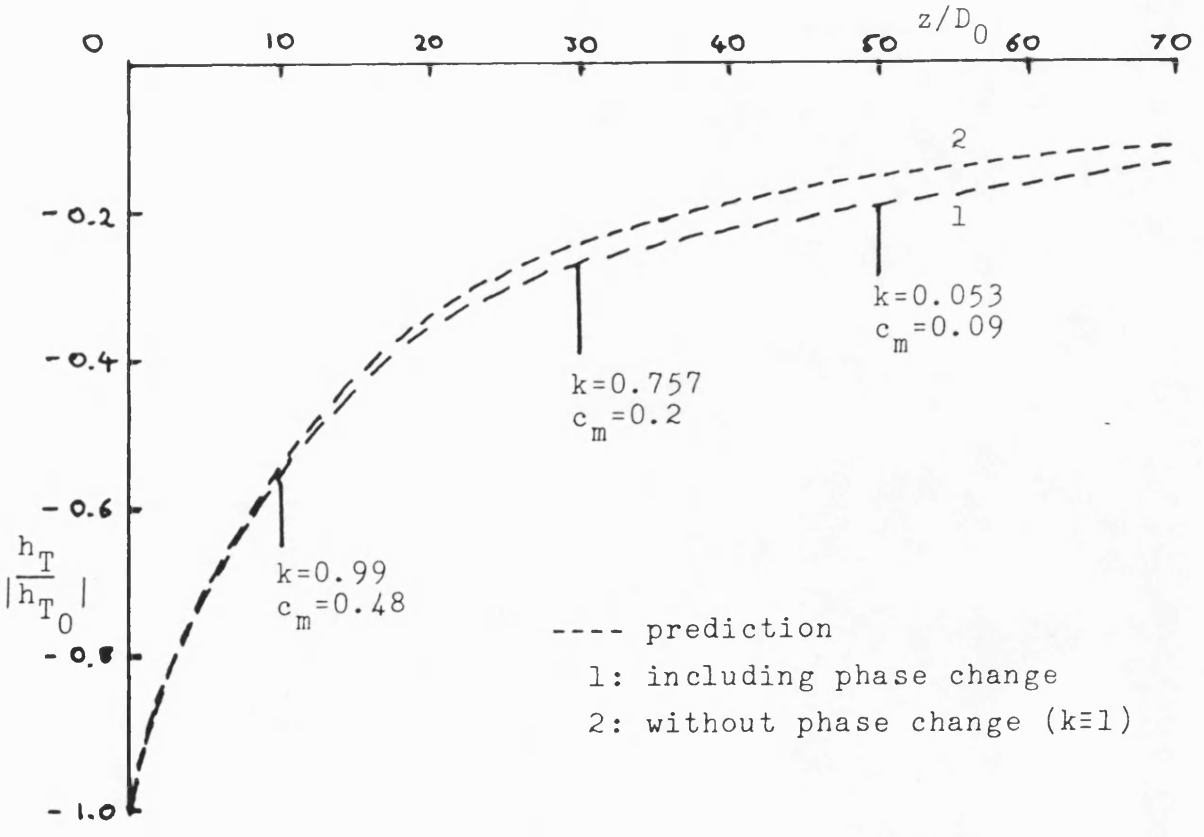

FIG. 8.8 EFFECT OF EVAPORATION ON PREDICTED AXIAL JET TEMPERATURE

REFERENCES

1. LYN, W.T. (1960) Study Of Burning Rate And Nature Of Combustion In Diesel Engines; 9th Symposium Of Combustion.

2. LYN, W.T. and VALDAMANIS, E. (1966-7) The Effects Of Physical Factors On Ignition Delay; Proc. I. Mech. E., vol 181.

3. PARKER, T.E. et al (1985) Induction Period For Fuel Sprays At High Temperatures And Pressures; SAE Paper 850087.

4. GRIGG, H.C. and SYED, M.H. (1970) The Problem Of Predicting Rate Of Heat Release In Diesel Engines; Paper 13 presented at the Symposium On Diesel Engine Combustion, Institution Of Mechanical Engineers.

5. MEGUERDICHIAN, M. and WATSON, N. (1978) Prediction Of Mixture Formation And Heat Release In Diesel Engines; SAE Paper 780225.

6. HENEIN, N.A. (1971) Combustion And Emission Formation In Fuel Sprays Injected In Swirling Air; SAE Paper 710220.

7. RIFE, J. and HEYWOOD, J.B. (1976) Photographic And Performance Studies Of Diesel Combustion With A Rapid Compression Machine; SAE Paper 740948.

8. WAKIL, M.M. EL, MYERS P.S. and VYEHARA, O.A. (1955) Fuel Vaporisation And Ignition Lag In Diesel Engines; SAE Golden Anniversary Diesel-Engine Meeting.

9. BORMAN, G.L. and JOHNSON, J.H. (1962) Unsteady Vaporisation Histories And Trajectories Of Fuel Droplets Injected Into Swirling Air; SAE Paper 598c.

10. OGASAWARA, M. and SAMI, M. (1967) A Study On The Behaviour Of A Fuel Droplet Injected Into The Combustion Chamber Of A Diesel Engine; SAE Paper 670468.

11. WAY, R.J.B. (1974) Heat Release And Thermal Loading In Pressure Chardged Automotive Type Diesel Engines; Ph.D. Thesis, University Of Bath.

12. VAN GERPEN, J.H., HUANG CHEN-WEN and BORMAN, G.L. (1985) The Effects Of Swirl And Injection Parameters On Diesel Combustion And Heat Transfer; SAE Paper 850265.

13. DENT, J.C. and DERHAM, J.A. (1974) Air Motion In A Four Stroke Direct Injection Diesel Engine; Proc. I. Mech. E., vol 188, pp 269-80.

14 WIGLEY, G. and RENSHAW, J. (1979) In-Cylinder Swirl Measurement By Laser Anemometry In A Production Diesel Engine; AERE Harwell, AERE-k9651.

15 MATSUOKA. et al (1985) LDA Measurement And A Theoretical Analysis Of The In-Cylinder Air Motion In A D.I. Diesel Engine; SAE Paper 850106.

16. VARA PRASAD, C.M. and SUBIR KAR (1977) An Investigation On The Diffusion Of Momentum And Mass Of Fuel In A Diesel Fuel Spray; ASME J. Eng. For Power, vol 99, pp 225-236.

17. VARA PRASAD, C.M. and SUBIR KAR (1978) An Investigation Of The Influence Of Back Pressure On The Diffusion Of Mass And Momentum Of Fuel In Diesel Sprays; ASME J. Eng. For Power, vol 100, pp 326.

18. ELKOTB, M.M. and RAFAT, N.M. (1978) Fuel Spray Trajectory In Diesel Engines; Trans. ASME, vol 100, pp 326-332.

19. ADLER, D. and LYN, W.T. (1971) The Steady Evaporation And Mixing Of A Spray In A Gaseous Swirl; Int. J. Of Heat And Mass Tran., vol 14, pp 793-812.

20. LAKSHMINARAYAN, P.A. and DENT, J.C. (1983) Interferometric Studies Of Vaporising And Combusting Sprays; SAE Paper 830244.

21. GOSMAN, A.D. and JOHNS, R.J.R. (1978) Development Of A Predictive Tool For In-Cylinder Gas Motion In Engines; SAE Paper 780315.

22. GOSMAN, A.D. and JOHNS, R.J.R. (1980) Computer Analysis Of Fuel-Air Mixing In Direct-Injection Diesel Engines; SAE Paper 800091.

23. GOSMAN, A.D. and HARVEY, P.S. (1982) Computer Analysis Of Fuel-Air Mixing And Combustion In An Axisymmetric D.I. Diesel Engine; SAE Paper 820036.

24. BRANDSTÄTTER, W., JOHNS, R.J.R. and WIGLEY, G. (1985) The Effect Of Inlet Port Geometry On In-Cylinder Flow Structure; SAE Paper 850499.

25. BASSOLI, C., BODRITTI, G. and CORNETTI, G.M. (1985) Optimum Air Momentum And Spray Formation For D.I. Diesel; SAE Paper 850501.

26. WHITEHOUSE, N.D. and ABUGHRES, S.M. (1975) Calculation Of Fuel-Air Mixing In A Diesel Engine For The Purpose Of Heat Release Prediction; I. Mech. E., Combustion In Engines.

27. CHIU, W.S., SHAHED, S.M. and LYN, W.T. (1976) A Transient Spray Mixing Model For Diesel Combustion; SAE Paper 760128.

28. DENT, J.C. and MEHTA, P.S. (1981) Phenomenological Combustion Model For A Quiescent Chamber Diesel Engine; SAE Paper 811235.

29. BOSE, A.K. and PEI, C.T. (1964) Evaporation Rates In Spray Drying; Can. J. Chem. Eng., vol 42, pp 252 262.

30. MELTON, R.B. (1971) Diesel Fuel Injection Viewed As A Jet Phenomenon; SAE Paper 710132.

31. NEWMAN, J.A. and BRZUSTOWSKI, T.A. (1971) Behaviour Of A Liquid Jet Near The Thermodynamic Critical Region; AIAA J., vol 9, pp 1595-1602.

32. ABRAMOVICH, G.N. (1963) The theory Of Turbulent Jets; MIT Press.

33. AGGARWAL, G.P. (1976) Penetration And Mixing Of A Fuel Jet Spray In A Swirling Flow - A Water Model Investigation; M.Sc. Thesis, University Of Bath.

34. WAY, R.J.B. (1977) Investigation Of Interaction Between Swirl And Jets In D.I. Diesel Engines Using A Water Model; SAE Paper 770412.

35. PACKER, J.P. (1983) Diesel Type Combustion Studies In High Swirl Chambers; Ph.D. Thesis, University Of Bath.

36. MANIATACOS, P. (1984) Analytical And Experimental Study Of Free Jets Injected Into A Quiescent Or Swirling Medium; M.Sc. Thesis, University Of Bath.

37. PLATTEN, J.L. and KEFFER, J.F. (1971) Entrainment In Deflected Axisymmetric Jets At Various Angles To The Stream; Tech. Rep. 6808, Dep't. Mech. Eng., University Of Toronto.

38. PLATTEN, J,L. and KEFFER, J.F. (1971) Deflected Turbulent Jet Flows; ASME J. Appl. Mech., pp 756-58

39. KAMOTAMI, Y. and GREBER, I. (1971) Experiments On A Turbulent Jet In A Crossflow; Case Western Reserve Univ., FTAS/TR-71-62.

40. SINNAMON, J.E., LANCASTER, D.R. and STEINER, J.C. (1980) An Experimental And Analytical Study Of Engine Fuel Spray Trajectories; SAE Paper 800135.

41. MEHTA, P.S. and GUPTA, A.K. (1985) Modelling Of Spray-Swirl Interaction In Direct Injection Diesel Engine Combustion Chambers; Proc. I. Mech. E., vol 199.

42. WHITE, C.L. (1986) Experimental And Analytical Studies Based On A High Swirl Combustion Chamber Representing The D.I. Diesel Engine Combustion System; Ph.D. Thesis, University Of Bath.

43. RAJARATNAM, N. (1976) Turbulent Jets; Developments In Water Science, Elsevier Publishing Company, Amsterdam.

44. IDOUM, A. (1984) Investigation Of The Effect Of Swirl And Impingement On Fuel-Air Mixing In Diesel Engines Using A Water Model; University Of Bath.

45. FRAUDEAU, C. (1985) Theoretical And Experimental Analysis Of A Jet In A Swirling Crossflow; University Of Bath.

46. PACKER, J.P., ADLER, D., WILSON, M. and WALLACE, F.J. (1984) An Integral Model Of Jet Mixing In An Arbitrary Crossflow Including The Effects Of Concentration, Temperature And Pressure Gradients; University Of Bath.

47. KUO, T.W. and BRACCO, F.V. (1982) On The Scaling Of Transient Laminar, Turbulent And Spray Jets; SAE Paper 820038.

48. SPALDING, D.B. (1980) Numerical Modelling Of Fluid Mechanics, Heat Transfer And Combustion Processes; A Lecture Course; Imperial College CFDU Report HTS/80/1.

49. SCHETZ, J.A. (1980) Injection And Mixing In Turbulent Flow; Progress In Astronautics And Aeronautics, vol 68.

50. KUETHE, A.M. (1935) Investigation Of The Turbulent Mixing Regions Formed By Jets; ASME J. Appl. Mech., pp 87-95.

51. CORRSIN, S. (1946) Investigation Of Flow In An Axially Symmetric Heated Jet Of Air; NACA Wartime Report W-94.

52. FORSTALL, W. and SHAPIRO, A.H. (1950) Momentum And Mass Transfer In Co-Axial Jets; ASME J. Appl. Mech., pp. 399-408.

53. ABRAMOVICH, G.N., YAKOVLEVSKY, O.V., SMIRNOVA, I.P., SECUNDOV, A,N, and KRASHENINNIKOV, S. YU. (1967) An Investigation Of The Turbulent Jets Of Different Gases In A General Stream; Astronautica Acta, vol 14, pp 229-240.

54. RAJARATNAM, N. and PANI, B,S. (1972) Turbulent Compund Annular Shear Layers; ASCE J. Hydraul. Div., vol 100, p 69.

55. SCHLICHTING, H. (1942) Boundary Layer Theory; McGraw-Hill, New York.

56. HINZE, J.O. and ZIJNEN, B.G. VAN DER HEGGE (1949) Transfer Of Heat And Matter In The Turbulent Mixing Zone Of An Axially Symmetric Jet; J. Appl. Sci. Res., A1, pp 435-461.

57. CORRSIN, S. and UBEROI, M.S. (1950) Further Experiments On The Flow And Heat Transfer In A Heated Turbulent Air Jet; Rep't. 998, NACA.

58. LANDIS, F. and SHAPIRO, A.H. (1951) The Turbulent Mixing Of Coaxial Jets; Heat Transfer And Fluid Mechanics Inst., Preprints And Papers, Stanford Univ. Press, Stanford, Calif.

59. CHRISS, D.E. (1968) Experimental Study Of Turbulent Mixing Of Subsonic Axisymmetric Gas Streams; Arnold Engineering Development Centre, AEDC-TR-68-133.

60. MORTON, B.R. et al (1956) Turbulent Gravitational Convection From Maintained And Instantaneous Sources; Pro. Roy. Soc., A234.

61. RICOU, F.P. and SPALDING, D.B. (1961) Measurements Of Entrainment By Axisymmetrical Turbulent Jets; J. Fluid Mech., vol 11, pp 21-32.

62. SILL, B. and SCHETZ, J.A. (1977) The Interrelationship Between Eddy Viscosity Mixing Length, Entrainment And Width Growth Models In Turbulent Flows; ASME Paper 77-FE-20.

63. ADLER, D. and BARON, A. (1978) Prediction Of A Three-Dimensional Circular Turbulent Jet In Crossflow; AIAA J., vol 17 no. 2, pp 168-174.

64. HILL, B.J. (1971) Measurement Of The Local Entrainment Rate In The Initial Region Of Axisymmetric Turbulent Air Jets; J. Fluid Mech., vol 51, pp 773-779.

65. ALBERTSON, M.L., DAI, Y.B., JENSEN, R.A. and ROUSE, H. (1950) Diffusion Of Submerged Jets; Trans. ASCE, vol 115, pp 639-697.

66. ANTONIA, R.A. and BILGER, R.W. (1973) An Experimental Investigation Of An Axisymmetric Jet In A Coflowing Air Stream; J. Fluid Mech., vol 61, pp 805-822.

67. SCHETZ, J.A. (1968) Turbulent Mixing Of A Jet In A Coflowing Stream; AIAA J., vol 6, pp 2008-2010.

68. GORDIER, R.L. (1959) Studies On Fluid Jets Discharging Normally Into A Moving Liquid; St. Anthoni Falls Hydraulics Lab., University Of Minnesota, Minneapolis, Tech. Pap. 28, Ser. B.

69. KEFFER, J.F. and BAINES, W.D. (1963) The Round Turbulent Jet In A Cross-Wind; J. Fluid. Mech., vol 15, pp 481-496.

70. PATRICK, M.A. (1967) Experimental Investigation Of The Mixing And Penetration Of A Round Turbulent Jet Injected Perpendicularly Into A Transverse Stream; Trans. Inst'n Chem. Eng'rs, vol 45, p T16.

71. BARON, A. (1978) Prediction Of A Three-Dimensional Circular Turbulent Jet In A Cross-Flow; M.Sc. Thesis, Technion, Haifa.

72. SFORZA, P. (1978) Mass Momentum And Energy Transport In Turbulent Free Jets; Int. J. Of Heat And Mass Tran., vol 21, pp 271-284.

73. SCHATZMANN, M. (1977) A Mathematical Model For The Prediction Of Plume Rise In Stratified Flows; Proc. Penn State Symp. "On Turbulent Shear Flows", Penn State Univ., USA.

74. RUGGERI, R., CALLAGHAN, E. and BOWDEN, D. (1950) Penetration Of Air Jets Issuing From Circular, Square And Elliptical Orifices Directed Perpendicularly To An Air Stream; NACA TN 2019.

75. JORDINSON, R. (1956) Flow In A Jet Directed Normal To The Wind; R&M no. 3074, British Aeronautical Council.

76. PRATTE, B.D. and BAINES, W.D. (1967) Profiles Of The Round Turbulent Jet In A Cross-Flow; Proc. ASCE, J. Hydraul. Div., pp 56-63.

77. MARGASON, R.J. (1968) The Path Of A Jet Directed At Large Angles To A Subsonic Free Stream; NASA TN-D4919.

78. RAMSEY, J.W. (1969) The Interaction Of A Heated Air Jet With A Deflecting Flow; Ph.D. Thesis, University Of Minnesota.

79. CAMPBELL, J.F. and SCHETZ, J.A. (1973) Analysis Of Injection Of A Heated Turbulent Jet Into A Cross-Flow; NASA TR R-413.

80. CRABB, D. (1979) Jets In Crossflow; Ph.D. Thesis, Imperial College, University Of London.

81. KEFFER, J.F. (1969) The Physical Nature Of The Subsonic Jet In A Cross-Stream; NASA SP-218.

82. SNEL, H. (1971) A Semi-Empirical Model For The Development Of A Round Turbulent Jet In A Crossflow; Nat. Aerospace Lab. Netherlands, Report NLR TR 71107U.

83. BRAUN, G.W. and McALLISTER, J.D. (1969) Cross-Wind Effects On Trajectory And Cross-Sections Of Turbulent Jets; NASA SP-218.

84. CHIEN, C.J. and SCHETZ, J.A. (1975) Numerical Solution Of The Three Dimensional Navier Stokes Equations With Application To Channel Flows And A Buoyant Jet In A Cross-Flow; J. Appl. Mech., vol 42, pp 575-579.

85. JONES, W.P. and McGUIRK, J.J. (1979) Computation Of A Round Turbulent Jet Discharging Into A Confined Free Stream; Turb. Shear Flows 2, pp 233-245.

86. WOOLER, P.T. (1969) Development Of An Analytical Model For The Flow Of A Jet Into A Subsonic Cross-Wind; NASA-SP-218.

87. HACKET, J.E. and MILLER, H.R. (1969) The Aerodynamics Of The Lifting Jet In A Cross Flowing Stream; NASA-SP-218.

88. MARGASON, R.J. (1969) Analytic Description Of Jet-Wake Cross-Sections For A Jet Normal To A Subsonic Free Stream; NASA-SP-218.

89. SUCEC, J. and BOWLEY, W.W. (1976) Trajectory And Spreading Of A Turbulent Jet In The Presence Of A Crossflow Of Arbitrary Velocity Distribution; ASME J. Fluid. Eng., vol 98.

90. SHIRAKASHI, M. and TOMITA, Y. (1978) Diffusion Of Jets In Crossflows; JSME, vol.21, no. 157, pp 1160-1167.

91. HOULT, D.P. and WEIL, J.C. (1972) Turbulent Plume In A Laminar Cross-Flow; Atmospheric Environment, vol 6, Pergamon Press.

92. TULIN, M.P. and SCHWARTZ, J. (1971) The Motion Of Turbulent Vortex Pairs In Homogeneous And Density Stratified Media; Hydronautics Inc.

93. SCHWARTZ, J. and TULIN, M.P. (1972) Chimney Plumes In Neutral And Stable Surroundings; Atmospheric Environment, Pergamon Press.

94. CAMPBELL, J.F. and SCHETZ, J.A. (1973) Flow Properties Of Submerged Heated Effluents In A Waterway; AIAA J., vol 11, no. 2, pp 223-230.

95. THRING, M.W. and NEWBY, M.P. (1953) Combustion Length Of Enclosed Turbulent Jet Flames; Fourth Symposium (International) On Combustion, The Combustion Institute, Pittsburgh, Pennsylvania, pp 789-796.

96. CHEN, C.J. and RODI, W. (1982) Turbulent Buoyant Jets And Plumes; The Science And Applications Of Heat And Mass Transfer, vol 6, Ed. D.B. Spalding, Pergamon Press, Oxford.

97. ABRAMOVICH, G.N., BAKULEV, V.I., GOLUBEV, V.A. and SMOLIN, G.G. (1966) An Investigation Into Turbulent Submerged Jets Over A Wide Temperature Range; Int. J. Of Heat And Mass Tran., vol 9, pp 1047-1060.

98. STEWARD, F.R. and GURUZ, A.G. (1977) Aerodynamics Of A Confined Jet With Variable Density; Combustion Science And Technology, vol 16, pp 20-45.

99. HABER, S. (1970) Numerical Evaluation Of Multiple Integrals; SIAM Review, vol 12, no. 4, pp 481-526.

100. NAGFLIB Program Library, Honeywell Multics Implementation Documents.

101. DAVIS, P.J. and RABINOWITZ, P.R. (1967) Numerical Integration; Blaiswell Publishing Company.

102. GERALD, C.F. (1980) Applied Numerical Analysis; Addison-Wesley Publishing Company.

103. TENDLER, J.M., BICKART, T.A. and PICEL, Z. (1978) Algorithm 534 (STINT); ACM Transactions On Mathematical Software, vol 4, no. 4, pp 399-403.

104. HALL, G. and WATT, J.M. (1976) Modern Numerical Methods For Ordinary Differential Equations; Clarendon Press.

105. CHIGIER, N.A. and BEÉR, J.M. (1964) The Flow Region Near The Nozzle In Double Concentric Jets; Trans. ASME J. Basic Eng., vol 4, pp 797-804.

106. Thermophysical Properties Of Refrigerant 12 (1975); National Engineering Laboratory, HMSO, Edinborough.

107. ZAKKAY, V., KRAUSE, E. and WOO, S.D.L. (1964) Turbulent Transport Properties Of Axisymmetric Heterogeneous Mixing; AIAA J., vol 2, pp 1939-47.

108. ALPINIERI, L. (1964) Turbulent Mixing Of Coaxial Jets; AIAA J., vol 2, pp 1560-67.

109. CAMPBELL, J.F. and SCHETZ, J.A. (1971) Penetration And Mixing Of Heated Jets In A Waterway With Application To The Thermal Power Problem; AIAA Paper 71-524, New York.

110. RAJARATNAM, N. and GANGADHARAIAH, T. (1982) Entrainment By Circular Jets In Cross-Flow; Journal Of Wind Eng. And Industrial Aerodynamics, vol 9, pp 251-255.

111. ZANDBERGEN, T. and JOOSEN, C.J.J. (1973) Experimental Investigation Of A Round Turbulent Jet In A Cross-Flow; NLR-TR-74013

112. NG, D.N. (1982) A Study Of The Mean Flow Structure Of Circular And Rectangular Exit Turbulent Jets Initially At A Small Incidence Angle To A Uniform Mainstream; Ph.D. Thesis, University Of Southampton.

113. HAKKI, Oz, I. (1969) Calculation Of Spray Penetration In Diesel Engines; SAE Trans., vol 78, Sec. 2.

114. CHEHROUDI, B., CHEN, SHIH-HSIUNG, BRACCO, F.V and ONUMA, Y. (1985) On The Intact Core Of Full Cone Sprays; SAE Paper 850126.

115. DENT, J.C. (1971) A Basis For The Comparison Of Various Experimental Methods For Studying Spray Penetration; SAE Paper 710571.

116. IDOUM, A., PACKER, J.P., WALLACE, F.J. and CHARLTON, S.J. (1985) An Experimental And Analytical Study Of Jet Impingement And Wall Jets In High Swirl D.I. Diesel Engines Using The Hydraulic Analogy; SAE Paper 850263.

APPENDIX A

TURBULENCE MODELLING

Appendix A - Notation

C_μ	-	constant in equation 10
$C_{\varepsilon 1}, C_{\varepsilon 2}$	-	constants in equation 15
k	-	turbulence kinetic energy
P	-	pressure
p	-	pressure fluctuation
P_k	-	production of k defined in equation 14
S_ψ	-	source term for property ψ
t	-	time
u_j'	-	j-component of fluctuating velocity
U_j	-	j-component of mean velocity
x_i	-	co-ordinate in i-direction
ℓ	-	mixing length

Superscripts

$\overline{\quad}$	-	average
$\sim$	-	instantaneous

Subscripts

ε	-	dissipation rate of turbulence energy
μ	-	laminar dynamic viscosity
ν	-	laminar viscosity
ν_T	-	eddy viscosity
ρ	-	density
Γ_ψ		diffusion coefficient for property ψ
$\sigma_k, \sigma_\varepsilon$ σ_ϕ	-	turbulent Prandtl numbers
Φ	-	mean scalar flow property
ϕ'	-	fluctuation of scalar property
ψ	-	general flow property

Appendix A Turbulence Modelling

Introduction

This review is based upon a specific part of the material presented during lecture courses at the two major centres of activity in the U.K. in computational fluid dynamics. The courses were:-

1/ Turbulence Models For Computational Fluid Dynamics
- Imperial College Of Science And Technology, London (30 April - 2 May 1984)

2/ Numerical Methods In Heat And Fluid Flow
- UMIST, Manchester
I - Introductory Course (26 - 28 June 1984)
II - Advanced Course (18 - 21 Sept 1984)

The complete lecture notes for each course are available[1,2,3] and the contents may be broadly categorised as follows:-

a) The mathematical representation of turbulent flows

b) The analysis of complicating features (strongly curved streamlines, density stratified flows, near wall flows, two-phase flows, etc)

c) Numerical solution schemes and comparisons between predictions and measurements

and it is useful to consider these topics individually. The following is a very brief account of the subject matter of a), the objectives being to indicate the necessity for the rational simplification of the exact governing equations and to establish the heirarchy of the most common methods by which this is achieved.

§1. The Characterisation Of Turbulent Flow

It is understood that a turbulent flow within a volume V can be adequately represented by the three-dimensional, time dependent Navier-Stokes equations representing the principles of conservation of mass (continuity), momentum (Newton's second law of motion) and scalar quantities - for example energy (first law of thermodynamics) or chemical species - once appropriate boundary conditions have been supplied over the boundary surface of V.

A general equation set is written below, in tensor notation, for the motion of a Newtonian fluid using terms defined in the notation. An account of their construction is given by Spalding[4]:-

Continuity

$$\frac{\partial}{\partial t}\{\tilde{\rho}\} + \frac{\partial}{\partial x_j}\{\tilde{\rho}\tilde{u}_j\} = 0 \qquad (1)$$

Conservation Of Momentum (i-component)

$$\frac{\partial}{\partial t}\{\tilde{\rho}\tilde{u}_i\} + \frac{\partial}{\partial x_j}\{\tilde{\rho}\tilde{u}_j\tilde{u}_i\} = -\frac{\partial \tilde{P}}{\partial x_i} + \frac{\partial}{\partial x_j}\left[\mu\left(\frac{\partial \tilde{u}_i}{\partial x_j} + \frac{\partial \tilde{u}_j}{\partial x_i}\right)\right] + S_{\tilde{u}_i} \qquad (2)$$

Conservation Of Scalar Quantity $\tilde{\phi}$

$$\frac{\partial}{\partial t}\{\tilde{\rho}\tilde{\phi}\} + \frac{\partial}{\partial x_j}\{\tilde{\rho}\tilde{u}_j\tilde{\phi}\} = S_{\tilde{\phi}} + \frac{\partial}{\partial x_j}\left[\Gamma_{\tilde{\phi}}\frac{\partial \tilde{\phi}}{\partial x_j}\right] \qquad (3)$$

The similarity of form is evident and motivates the expression of each of the above equations in the general form:-

$$\frac{\partial\{\tilde{\rho}\tilde{\psi}\}}{\partial t} + \frac{\partial}{\partial x_j}\{\tilde{\rho}\tilde{u}_j\tilde{\psi}\} = \frac{\partial}{\partial x_j}\left[\Gamma_{\tilde{\psi}}\frac{\partial\tilde{\psi}}{\partial x_j}\right] + S_{\tilde{\psi}} \qquad (4)$$

unsteady convection diffusion source

so that (1) is recovered via $\tilde{\psi}\equiv 1$ and (2) via $\tilde{\psi}\equiv\tilde{u}_i$, the latter demonstrating that the definition of $S_{\tilde{\psi}}$ is extended to include all the convection and diffusion terms additional to the groupings declared as well as all real sources and sinks. The unity of form can be instructive and is clearly an advantage for numerical solution schemes. It is noted that (4) can be considered to represent the mathematical formulation of a particular flow if the boundary conditions are assumed to be prescribed; since (4) contains first order time and second order spatial derivatives boundary conditions will comprise one constraint on t (the initial condition) and two such on each x_j.

With the flow represented in this way an attempt at the solution of the closed system may proceed. All turbulent flows suffer fluctuations in all three directions, even those which are, for example, two-dimensional in the mean. Thus each variable is a function of all four dependent variables, and analytic solutions will only be possible in limiting cases, particularly where fully developed flow prevails. Thus, numerical solutions must in general be sought. The most common strategy is to replace (4) by a set of finite-difference equations and solve at each node of a suitable mesh imposed over the flow domain the resulting set of algebraic equations. The discretisation error incurred (as a consequence of replacing the differential operators by difference operators) implies that even an exact solution of the new system is only an approximation, at each nodal point, to the true solution of (4) over the flow domain V. In the following discussion (4') is taken to represent the finite-difference system derived

from (4).

Direct Numerical Solution

The problem in attempting to solve exactly the system (4') on present computers is one of resolution of scale. For the complete solution to be achieved the numerical scheme must represent the largest scales of the flow motion, corresponding to the largest flow dimension, as well as the smallest, the scales of the eddies in which the dissipation of turbulence energy is considered to occur. The latter are characterised by the Kolmogorov microscales (Bradshaw[5]), and in general the velocity scale associated with dissipation will be smaller than 1mm and dependent upon Reynolds number. Even for moderate Reynolds number it is beyond the resources of current computing capacity to resolve such a range of scales and this restriction is unlikely to be lifted in the foreseeable future, if indeed at all.

Once this restriction is admitted it becomes necessary to identify a procedure which will reduce the magnitude of the numerical task which (4') represents. Again, even an exact solution of the system after further simplification will comprise only an approximate description of the real flow. The derivation from (4) of mean flow equations is the basis for the bulk of what follows, but a related approach is described for completeness.

Large Eddy Simulation

Work around this topic stems from the meteriological field and in particular from researchers at Stanford University. The philosophy is that the detail of microscale processes ideally delivered by the direct solution is largely irrelevant to mean flow properties, these being influenced predominantly

by the larger scale energy containing eddies: it is mainly on this scale that modelling proves difficult. Thus, with the use to the limit of the available computing capacity, the full equation system (4') is solved using a numerical grid which will characterise the larger eddies and allow adequate modelling of the motions on the 'sub-grid' scale using properly resolved quantities. The computing times are not prohibitive, but difficulties arise in representing the interaction between the exact and modelled solution components. The modelling is usually accomplished by transport approximations as described later. At the present time, because of the matching problem, there appears to be little benefit from this pragmatic approach.

Mean Flow Equations

The traditional route to the simplification of the system (4) is initiated by time averaging (or ensemble averaging over many repeats of an experiment[1,2]) to obtain the Reynolds equations for the mean flow:-

Continuity

$$\frac{\partial}{\partial x_j}\{\rho U_j\} = 0 \qquad (5)$$

Momentum (i-component)

$$\frac{\partial}{\partial x_j}\{\rho U_j U_i\} = -\frac{\partial \tilde{P}}{\partial x_i} + \frac{\partial}{\partial x_j}\{\mu \frac{\partial U_i}{\partial x_j}\} - \frac{\partial}{\partial x_j}\{\rho \overline{u'_j u'_i}\} + S_{U_i} \qquad (6)$$

Scalar

$$\frac{\partial}{\partial x_j}\{\rho U_j \Phi\} = \frac{\partial}{\partial x_j}\{\Gamma_\Phi \frac{\partial \Phi}{\partial x_j}\} - \frac{\partial}{\partial x_j}\{\rho \overline{u'_j \phi'}\} + S_\Phi \qquad (7)$$

where the instantaneous general property $\tilde{\Psi}$ in (4) and other terms in (4) have been decomposed into mean and fluctuating

parts:-

$$\rho = \rho + \rho' \; ; \quad \tilde{u}_j = U_j + u_j' \; ; \quad \tilde{\Psi} = \Psi + \psi'$$

and the time average (denoted by an overbar) of fluctuating components is zero:-

$$\overline{\rho}' = 0 \; ; \quad \overline{\psi}_j' = 0 \quad \text{and} \quad \overline{\rho' \psi'} = 0$$

(the last condition is known as the Van Dreist hypothesis).

It is noted that (5),(6) and (7) could again be expressed in a general form such as (4), but with the mean flow property ψ as the dependent variable. However, the convective term in (4) is nonlinear, and in general the mean product of $\tilde{u}_j$ and $\tilde{\Psi}$ is not the same as the product of the means: the difference is the turbulent transport of $\tilde{\Psi}$. Except in special cases, such as flow very near a wall, the turbulent fluxes are certainly not negligible, so that the unknown fluctuation correlations $\overline{\rho u_j' \psi'}$ must be accounted for, in order to render the system mathematically closed. The set of equations supplied for this purpose is deemed the turbulence model.

§2. The Representation Of The Turbulent Fluxes

2.1 Mixing Length Models

The turbulent fluxes of (6) and (7) are required as functions of known or determinable flow properties. If fluctuations in density are neglected for the purposes of this exposition: -

$$\overline{\rho u_j' \psi'} = \rho \overline{u_j' \psi'}$$

The correlations are then modelled by

$$\overline{u_i' u_j'} = F_1(x_1, x_2, x_3) \quad \text{and} \quad \overline{u_j' \phi'} = F_2(x_1, x_2, x_3)$$

with the general functions F_1, F_2 known either implicitly or explicitly. Usually the fluxes are expressed, with some physical insight, in terms of the values and gradients of the dependent variables of the Reynolds equations (this is certainly true of the models of this section); since these are all means, such models are often termed 'mean-flow' models. The empirical content of F_1 and F_2 demonstrates the approximate fashion by which the turbulent nature of a flow is represented and demonstrates that the turbulence model which the chosen functions comprise will depend upon the particular flow in question, precluding universality. This aspect is illustrated later.

The simplest models relate turbulent fluxes to the mean flow via a length scale ℓ specified by an algebraic function based upon the correlation of appropriate data. Such a model, attributed to Prandtl (1915), takes its analogy from the kinetic theory of gases. For a two-dimensional, thin shear flow:-

$$- \overline{u_1' u_2'} = \ell^2 \left|\frac{\partial U_1}{\partial x_2}\right| \frac{\partial U_1}{\partial x_2} \qquad (8)$$

The simplified flow regime is chosen for clarity and because it is in this type of problem that such models are most widely applied. For such a case the only important turbulent flux term is the one shown above; since the turbulent flux term in (6) in this case is a momentum transfer mechanism analogous to Newtonian shear in laminar flow, the grouping $(-\overline{u_1 u_2})$ has been termed the turbulent shear or Reynolds stress. The definition extends to the Reynolds stress tensor $\overline{u_i' u_j'}$.

The mixing length ℓ is usually related to the width $\ell(x_1)$ of the shear layer in a simple way. For a free jet:-

$$\ell \simeq C\ell(x_1) \quad \text{with } C \simeq 0.1$$

The characteristic time scale implied by (8) is $|\partial U_1/\partial x_2|^{-1}$. Various extensions to the model have been proposed in more complicated cases - for example in flows near walls where ℓ has been allowed to vary linearly with distance from the wall (Cebeci and Smith 1974)[1]. Models related to (8) include the eddy viscosity model:-

$$- \overline{u_1' u_2'} = \nu_T \frac{\partial U_1}{\partial x_2} \quad ; \quad \nu_T = \kappa \ell(x_1) |U_{1max} - U_{1min}| \qquad (9)$$

ν_T is an effective eddy viscosity in analogy with the laminar viscosity ν. κ maintained constant over a shear layer cross section implies that ν_T remains constant over the section. From (8) and (9) it is seen that:-

$$\nu_T = \ell^2 \left|\frac{\partial U_1}{\partial x_2}\right|$$

so that there is essentially no difference between the two forms. Mean flow models have been widely used because of their simplicity and good results have been recovered in many cases (including recirculating flows), although often by elaborate adjustments to prescribed ℓ-distributions over the flow domain.

More sophisticated models of this type reflect the experimental observation that the constants implied in (8) and (9) are related to the turbulence properties of the flow, none of which are accounted for explicitly in the models so far described. The Prandtl-Kolmogorov model (1942) was the first to include the influence of turbulence energy, as well as scale, on the Reynolds stress. The turbulent kinetic energy, k, is that due to the fluctuating components of velocity, viz:-

$$k^2 = \frac{1}{2}\overline{u_i' u_i'}$$

and is incorporated in the definition of the eddy viscosity to produce the new model:-

$$-\overline{u_1' u_2'} = \nu_T \frac{\partial U_1}{\partial x_2} \quad ; \quad \nu_T = C_\mu k^{1/2} \ell \qquad (10)$$

C_μ is a constant and must be experimentally determined. Most workers use $C_\mu = 0.09$. The mixing length ℓ must be prescribed and the variation for k over the flow domain must be available. It is supplied by the solution of a differential transport equation and for this reason models of this type have been deemed 'one-equation' models. The equation itself is derived from the exact describing set (4) by multiplying each component momentum equation by the corresponding component

velocity fluctuation, followed by averaging and summation. Again, the resulting transport equation is written for a steady, two-dimensional thin shear flow:-

$$U_j\frac{dk}{dx_j} = \nu_T\left(\frac{\partial U_1}{\partial x_2}\right)^2 + \frac{\partial}{\partial x_2}\left(\frac{\nu_T}{\sigma_k}\frac{\partial k}{\partial x_2}\right) - \sum_i \nu\left(\overline{\frac{\partial u_i'}{\partial x_j}}\right)^2 \qquad (11)$$

convection production diffusion viscous dissipation

The familiar groupings are again observed. The constant σ_k is the turbulent Prandtl number for diffusion of k and suggestions vary from about 1.0 (UMIST) to 1.5 (IC). The final term representing viscous dissipation is usually the subject of further modelling, and the process serves to indicate some of the idealisations of turbulence which are often invoked in modelling work.

The Energy Cascade

It is seen from (11) that production of turbulence energy is by mean shear, and is considered to be achieved by a process known as vortex stretching (Tennekes and Lumley[6]). As has been indicated, turbulent fluctuations cover a range of different wavelengths bounded by the flow dimensions and the dissipative eddies described by the Kolmogorov scales. In the cascade view of turbulence it is in the larger eddies that the greatest contribution to turbulence energy production occurs (the latter entering from the mean flow as described in (11)); the large eddies are then broken down by repeated interactions (vortex stretching) so that turbulence energy is continually transferred from the large to the small scales of motion. Eventually the eddies are so small and velocity gradients are sufficiently steep to allow destruction of kinetic energy by viscous dissipation - the finest scale

motions are thought adaptable to ensure that energy is destroyed as quickly as it is received.

Local Isotropy

Although energy may be transferred to large eddies which have a preferred direction, for example in a two-dimensional shear flow the largest motions may be only weakly three dimensional, the reduction of scale described above causes this bias to be progressively diminished as a consequence of the repeated interactions. Provided these are numerous enough, the eddies in which turbulence energy is converted to heat may have no preferred direction; the turbulence is then termed locally isotropic.

The High Reynolds Number Hypothesis

This takes the view that at high Reynolds number the fine scale viscosity-dependent eddies are not influential in governing the important turbulent processes, these being determined by high Reynolds number, large scale eddy interactions. The structure of the fine scale motions is considered isotropic as described above.

The ideas described assist in re-expressing the final term on the right-hand side of (11). The energy equation on derivation is usually written so that the formal dissipation rate appears as molecular diffusion;

$$\varepsilon = \sum_i \nu \overline{\frac{\partial u_i'}{\partial x_j}\left(\frac{\partial u_i'}{\partial x_j} + \frac{\partial u_j'}{\partial x_i}\right)} \rightarrow \sum_i \nu \overline{\left(\frac{\partial u_i'}{\partial x_j}\right)^2} \qquad (12)$$

as a consequence of the assumption of isotropic turbulence. A complete description is given by Launder[3] in the context

of second moment closure, discussed in a later section, when further remarks on the dissipative terms will be more appropriate. At high Reynolds number turbulence is generated in the large scale motions characterised by a length scale ℓ and the generation rate will govern the rate of dissipation (from the energy cascade). Dimensional analysis suggests:-

$$\varepsilon \equiv \nu \sum_i \overline{\left(\frac{\partial u_i'}{\partial x_j}\right)^2} = \frac{k^{3/2}}{\ell} \qquad (13)$$

this being the means by which the dissipation term of (11) is usually expressed. It is still necessary at this stage to prescribe the length scale distribution.

Local Equilibrium

One important facet of (11) is revealed by considering flow in a region of very strong shear, for example near a wall, where the k equation is dominated by its production and dissipation contributions. A flow in which the convection and diffusion of k is negligible is said to be in local equilibrium: the k equation, for a two dimensional thin shear, becomes:-

$$P_k \simeq \varepsilon \quad ; \quad P_k \simeq \nu_T \left(\frac{\partial U_1}{\partial x_2}\right)^2, \quad \varepsilon = \frac{k^{3/2}}{\ell} \qquad (14)$$

As will be indicated, use is often made of this special case in completing more sophisticated turbulence models than those so far discussed.

Summary

Mixing length and eddy viscosity models are the simplest closures for the Reynolds equations (5),(6),(7). The models have been widely applied and modified to suit differing flow regimes, and good agreement with experiment can be achieved. Their use is most justified in two dimensional boundary layer flows where the mixing length is relatively simple to specify. Turbulence characteristics may be introduced into this type of model through the effective turbulent viscosity ν_T, viz equation (10), which is then affected by, for example, diffusion of k towards the centreline of a jet[2], or diffusion of k in free-stream turbulence. This formulation involves the penalty that an extra differential equation, for k, must be included, thus increasing the expense of numerical solution.

There are two major disadvantages in the use of this type of model. First, the need to specify the ℓ distribution becomes a prohibitive handicap in complicated flows such as recirculation. Even in apparently related free flows, for example plane and axisymmetric jets, wakes and mixing layers, where $\ell \simeq C(x_1)$ as above, the value for C has been found by experiment to differ markedly between the flow types named. Also, the ℓ distribution in the region of *merging* shear layers is not easy to specify. It is this variation in characteristic length scale which implies that ℓ should be *determined* during the solution scheme rather than imposed upon it. Second, all the models described so far assume a gradient transport formulation for the turbulent fluxes:-

$$\overline{u_1' u_2'} \propto \frac{\partial U_1}{\partial x_2} \quad ; \quad \overline{u_2' \phi'} = \frac{\nu_T}{\sigma_\phi} \frac{\partial \phi}{\partial x_2}$$

σ_ϕ turbulent Prandtl number for scalar property ϕ (computer optimised)

etc.; in general this implies too direct a relationship between the mean flow and the turbulent stresses. It is in the derivation of the higher level closures discussed below that these two restrictions are successively relaxed.

2.2 Two Equation Models

Two equation models use an isotropic eddy viscosity concept to represent the Reynolds stresses, still via the gradient transport formulation:-

$$-\overline{u_i' u_j'} = \nu_T \left(\frac{\partial U_i}{\partial x_j} + \frac{\partial U_j}{\partial x_i} \right) - \frac{2}{3} k \delta_{ij}$$

This is a generalisation of (10) which is invariant under transformation of co-ordinate axes; there are many such generalisations, the above being the simplest. It is noted that the normal stresses (i=j) are poorly represented by the above, although these are often of only minor importance in determining the nature of the mean flow. The eddy viscosity is defined as in (10) so that k and ℓ need to be known throughout the flow. Scalar fluxes are represented through the turbulent Prandtl number as described.

The kinetic energy k is determined in the manner described above. In a similar fashion, a differential equation may be formulated not for ℓ itself but for a new quantity Z, where $Z = k^{\alpha} \ell^{\beta}$, from which the length scale may be inferred. Many such variables have been considered:

Variable	k/ℓ^2	$k^{3/2}/\ell$	$k^{1/2}/\ell$
	"vorticity squared" of stress bearing eddies	spectral transfer rate of energy (ε)	"frequency" of energy containing motion

The most popular and convenient choice is $Z=\varepsilon=k^{3/2}/\ell$ which is (with some difficulty) a measurable quantity. The transport equation for ε, the dissipation rate of turbulence energy (equation (12)), is formally obtained from manipulation of the Navier-Stokes equations (IC Lecture 5) The result, however, includes terms which represent very fine scale motions and is not useful for modelling, as ε is considered to be governed by the large scale motions; see Launder[3]. The full equation may be reduced through an order of magnitude analysis which represents each term by means of length and velocity scales defined for the large scale and fine scale motions (the latter being the Kolmogorov scales), Launder[3]. With the knowledge of the final equation achieved by this approach it is usual to form a similar equation by an intuitive argument which admits dimensional considerations and analogy with the equation for the transport of k, the argument running as follows: in analogy with the already known equation for k, (11), the transport equation for ε must contain at least terms representing a source and a sink for that quantity. A source term is needed to ensure that any increase in k results in a greater rate of dissipation; the usual form assumed is:-

$$P_\varepsilon \propto P_k \frac{\varepsilon}{k}$$

The generation rate for k is multiplied by the turbulent motion time-scale to ensure the correct dimensions for the generation of dissipation rate. A sink term is required so that k decaying to zero (as in the decay of homogeneous turbulence behind a grid) cannot result in k becoming negative. A term which ensures this property is:-

$$S_\varepsilon \propto \frac{\varepsilon^2}{k}$$

Finally, a diffusive like term is required, for example, to allow finite levels for ε on the axis of a turbulent jet. The assumed form is:-

$$D_\varepsilon \propto \nu_T \frac{\partial \varepsilon}{\partial x_2}$$

(for a two dimensional thin shear flow). Terms of this character are revealed when closure approximations are made to the exact dissipation rate transport equation simplified by dimensional analysis (closure approximations are required for triple velocity correlations which are unknown within the framework of this level of turbulence model, and are replaced using a gradient transport hypothesis similar to that used here to represent the second order correlation Reynolds stresses). The full k-ε two equation turbulence model for a two dimensional, steady, thin shear layer may be written as:-

$$\left.\begin{aligned} U_j \frac{dk}{dx_j} &= \frac{\partial}{\partial x_2}\left(\frac{\nu_T}{\sigma_k}\frac{\partial k}{\partial x_2}\right) + P_k - \varepsilon \\ U_j \frac{d\varepsilon}{dx_j} &= \frac{\partial}{\partial x_2}\left(\frac{\nu_T}{\sigma_\varepsilon}\frac{\partial \varepsilon}{\partial x_2}\right) + C_{\varepsilon 1}\frac{\varepsilon}{k}P_k - C_{\varepsilon 2}\frac{\varepsilon^2}{k} \end{aligned}\right\} \quad (15)$$

$$P_k = \nu_T\left(\frac{\partial U_1}{\partial x_2}\right)^2 \; ; \quad \nu_T = C_\mu \frac{k^2}{\varepsilon}$$

Here σ_k, σ_ε are turbulent Prandtl numbers for diffusion of the respective dependent variables. It is also necessary to assign a value to C_μ, and to the new constants of proportionality $C_{\varepsilon 1}$, $C_{\varepsilon 2}$. The task of determining values for constants is overcome by a combination of reference to experiments in which it may be hoped that the character of the turbulent

flow is understood, and by optimisation on a computer in the light of validated experimental data. Both these criteria imply that to use constants determined for particular flows in predicting more complex flows, using the same model, is formally unattested. In practice, changes are only made when the prediction of a particular flow is seen to be unacceptably poor.

The constant $C_{\varepsilon 2}$ is fixed with respect to the decay of isotropic turbulence downstream of a rectangular grid for which the k and ε transport equations reduce to:-

$$U_1 \frac{dk}{dx_1} = -\varepsilon \quad ; \quad \frac{d}{dx_1}\{u_1'\varepsilon\} = -C_{\varepsilon 2}\frac{\varepsilon^2}{k}$$

The variation for k for this problem has been determined as:-

$$k \propto x_1^{-n} \quad \Rightarrow \quad C_{\varepsilon 2} = \frac{n+1}{n}$$

The exponent n is determined experimentally:-

$$n \simeq 1.25 \Rightarrow C_{\varepsilon 2} \simeq 1.80 \quad \text{(IC)}$$
$$n \simeq 1.20 \Rightarrow C_{\varepsilon 2} \simeq 1.85 \quad \text{(UMIST)}$$

The constants σ_ε and $C_{\varepsilon 2}$ are evaluated from the consideration of near wall turbulence in local equilibrium (described above) where convective transport of ε is negligible and the k generation rate is known[2]:-

$$P_k \simeq \varepsilon \simeq \frac{(\tau_w/\rho)^{3/2}}{\kappa x_2}$$

τ_w: wall shear stress
κ: Von Karman constant

The equation for ε is used to give:-

$$\sigma_\varepsilon \simeq \sqrt{C_\mu}\,/\kappa^2(C_{\varepsilon 2}-C_{\varepsilon 1}) \quad ; \quad C_\mu = \left[\frac{\tau_w}{\rho k}\right]^2 \simeq 0.09$$

$C_{\varepsilon 1}$ is usually adjusted to give the best agreement with the measured rate of spread for free shear flows. The model is highly sensitive to variations in $C_{\varepsilon 1}$ or $C_{\varepsilon 2}$ alone and it is usual to overcome this by maintaining a constant difference between the two, that is, variation in values determined for $C_{\varepsilon 2}$ are compensated by imposing $C_{\varepsilon 1}=C_{\varepsilon 2}-0.47$.[2] An optimised, recommended set is agreed by most workers:-

C_μ	$C_{\varepsilon 1}$	$C_{\varepsilon 2}$	σ_k	σ_ε
0.09	1.44	1.92	1.0	1.3

With these constants, the spreading rate of a plane jet is well predicted; the spreading rate of a round jet is overpredicted by some 30%.[2] It is clear from its derivation that the dissipation rate equation is the weakest link in the turbulence model and indeed the majority of the error described has been attributed to the ε equation. It has been remedied by empirical modification of constants and by the introduction of extra terms enhancing the generation rate for ε in its transport equation. It has proved more difficult to remedy the poor prediction of length scale which is observed, with the standard model, near a wall as a boundary layer approaches separation. Lastly, C_μ must be re-optimised for flows far removed from the condition of local equilibrium, for example weak shear flows.

The k-ε model, as the most convenient representative of closure at the two-equation model level, may be applied to

to free flows and wall flows without modification. Because the need to specify length scale has been superseded two equation models are very more general in predictive ability than simpler models. The major weaknesses are the gradient transport hypothesis, formally justified only for thin shear flows and unlikely to give sufficiently good evaluation of the turbulent stresses in complex flows (where, for example, the poorly predicted normal stresses may matter), and the comparatively weak formulation of the dissipation rate equation. Since an equation of this type usually appears in yet more sophisticated models (see below), much effort is now concentrated in establishing it in a stronger form; see Launder[3].

It is at the final level of closure discussed here that the restrictive gradient transport hypothesis is avoided, by making the non-zero Reynolds stresses the subject of further transport equations.

2.3 Reynolds Stress Closure

In the same manner by which the transport equations for k and (in the general sense) the length-scale determining quantity Z were derived, manipulation of the Navier Stokes equations leads to a transport equation of similar form for the correlation $\overline{u_i' u_j'}$. Such an equation was established by Rotta (1951), although turbulence models incorporating it became practical only after the introduction of large digital computers. Using the exact equation set (4), the $\tilde{u}_i$ component momentum equation is multiplied the fluctuating velocity component u_j' and vice-versa. The equations are then summed and averaged and the resulting equation is written in the following reorganised form:-

$$U_k \frac{\partial}{\partial x_k}\{\overline{u'_i u'_j}\} = -\left(\overline{u'_i u'_k}\frac{\partial U_j}{\partial x_k} + \overline{u'_j u'_k}\frac{\partial U_i}{\partial x_k}\right) - 2\nu\overline{\frac{\partial U_i}{\partial x_k}\frac{\partial U_j}{\partial x_k}}$$

convection by mean flow — P_{ij} — ε_{ij}

$$+ \overline{\frac{p}{\rho}\left(\frac{\partial u'_i}{\partial x_j} + \frac{\partial u'_j}{\partial x_i}\right)} \qquad (16)$$

Φ_{ij}

$$- \frac{\partial}{\partial x_k}\left(\overline{u'_i u'_j u'_k} + \overline{\frac{p}{\rho}\left(u'_j \delta_{ik} + u'_i \delta_{jk}\right)}\right)$$

d_{ij}

The flow is assumed to be steady in the mean, and for simplicity gravitational effects and pressure fluctuations are neglected. The grouping defined in the equation is well established and serves to represent the following processes:-

P_{ij}: Production of $\overline{u'_i u'_j}$ by mean shear

ε_{ij}: Viscous dissipation of $\overline{u'_i u'_j}$

Φ_{ij}: Pressure-strain interactions

d_{ij}: diffusion of $\overline{u'_i u'_j}$, a) turbulent
b) pressure

Some modelling is still required for unknown terms before

closure is achieved and this is described below. It is worthwhile to point out that at present the most complete practical level of closure arrives with such equations for the Reynolds stresses; the next level of closure (which has been investigated in some detail) seeks to provide transport equations for the triple velocity correlations $\overline{u_i' u_j' u_k'}$ which appear in (16). However, the further increase in the number of differential equations requiring solution that this involves results in models which are computationally too expensive, and adequate data is unavailable to validate the further modelling assumptions which are necessary (for example, an exact transport equation for triple correlations will involve quadruple correlations, and so on). Once (16) is arrived at, it is usual to invoke the *principle of receding influence* to suggest that relatively crude closure approximations for the triple correlations are adequate within the framework of exact equations for the $\overline{u_i' u_j'}$. The Reynolds stress models, of which the foundation is (16), are the most sophisticated turbulence models which are of manageable complexity and retain a promise of formal generality, since the processes governing $\overline{u_i' u_j'}$ levels are treated more realistically than is possible with gradient transport formulations. It is clear that manipulations analogous to those which resulted in (16) could be employed to produce equations for the transport of scalar fluxes $\overline{u_j' \phi'}$ although the treatment of scalars will not be discussed in this report.

Some comments can be made about the nature of the terms in (16). If the latter is contracted by setting i=j an equation is obtained for the transport of turbulence energy, which is similar to (11) except that ν_T is superseded by more precise expressions involving fluctuating velocity correlations. It is

observed that no pressure strain term appears in the equation; this indicates that the action of Φ_{ij} in (16) is purely in redistributing energy among the normal stress components. Intercoupling among the stress components due to the production tensor P_{ij} is exemplified by the consideration of a steady, thin, locally isotropic horizontal shear flow at high Reynolds number, for which $\partial U_1/\partial x_2$ is the only significant strain rate. If T represents mean flow + turbulent transport of the stress component, (16) gives:-

$$T(\overline{u_1' u_2'}) = -\overline{u_2'^2}\frac{\partial U_1}{\partial x_2} + \overline{\frac{p}{\rho}\left(\frac{\partial u_1'}{\partial x_2} + \frac{\partial u_2'}{\partial x_1}\right)} - 0$$

$$T(\tfrac{1}{2}\overline{u_1'^2}) = -\overline{u_1' u_2'}\frac{\partial U_1}{\partial x_2} + \overline{\frac{p\partial u_1'}{\rho\partial x_1}} - \frac{\varepsilon}{3}$$

$$T(\tfrac{1}{2}\overline{u_2'^2}) = 0 + \overline{\frac{p\partial u_2'}{\rho\partial x_2}} - \frac{\varepsilon}{3}$$

$$T(\tfrac{1}{2}\overline{u_3'^2}) = 0 + \overline{\frac{p\partial u_3'}{\rho\partial x_3}} - \frac{\varepsilon}{3}$$

$$P_{ij} \qquad \Phi_{ij} \qquad \varepsilon_{ij}$$

The ε_{ij} terms have been modelled using the local isotropy hypothesis (see below). The shear stress generation rate P_{12} shows why $\overline{u_1' u_2'}$ has an opposite sign to the mean velocity gradient and why free shear flows spread more rapidly than boundary layers ($\overline{u_2'^2}$ is inhibited in wall flow). It is the turbulent velocity fluctuations in the direction of the mean velocity gradient (i.e. $\overline{u_2'}$) which promote shear stress growth through P_{12}. As a consequence, the streamwise fluctuations ($\overline{u_1'}$) are augmented through P_{11}. Although there is no direct production of the other normal stresses, energy is deflected

in these directions from the streamwise through the pressure fluctuations of Φ_{ij}. Thus the fluctuations in the direction of the mean velocity gradient are intensified and the cycle is repeated - hence the self-sustaining character of turbulence in a simple shear. Finally, it is through P_{ij} that the sensitivity to secondary strains is captured, for consider a shear flow with weak streamline curvature:-

$$\frac{\partial U_2}{\partial x_1} \simeq 10^{-2}\frac{\partial U_1}{\partial x_2} \quad ; \quad P_{12} = -\left(\overline{u'^2_2}\frac{\partial U_1}{\partial x_2} + \overline{u'^2_1}\frac{\partial U_2}{\partial x_1}\right)$$

In the presence of a wall, $\overline{u'^2_1}$ is several times larger than $\overline{u'^2_2}$ so that the importance of the smaller mean velocity gradient is amplified in the production term. Thus the small extra strain becomes a significant influence on determining the turbulent stresses.

In the terms of the right hand side of (16), closure approximations will be required for the following unknown quantities:-

1/ Viscous dissipation (ε_{ij})

2/ Pressure strain rate (Φ_{ij})

3/ triple velocity correlations and pressure diffusion terms (d_{ij})

P_{ij} is directly evaluated since only the Reynolds stress tensor (which is part of the solution scheme) and mean velocity gradients are involved.

The viscous dissipation term is modelled following the idea

of local isotropy at high Reynolds number. The correlation

$$\overline{\frac{\partial u_i'}{\partial x_k}\frac{\partial u_j'}{\partial x_k}}$$

is associated with fine-scale motion and should therefore be independent of the orientation of axes. If the direction of x_i is reversed the above correlation changes sign; therefore its value must be zero. In the full equation for transport of $\overline{u_i' u_j'}$ there also appears dissipative terms of the form

$$\overline{\frac{\partial u_i'}{\partial x_k}\frac{\partial u_k'}{\partial x_j}}$$

and again these are zero under the assumed conditions and were omitted from (16). Thus:-

$$\varepsilon_{ij} = \frac{2}{3}\delta_{ij}\varepsilon$$

It is usual to incorporate a dissipation rate equation similar to that described earlier, with again velocity correlations replacing the eddy viscosity in the diffusion term. In this respect, in fact, two equation models can be considered as simplified schemes derived from the Reynolds stress closure, as it has been indicated that the contraction of (16) produces a transport equation for k.

Pressure Strain Rate

Only a very brief overview is given of the most popular approach to the modelling of Φ_{ij}, shown to be vital in sustaining the turbulent motions. An exhaustive exposition is undertaken by Launder[3]

The pressure fluctuations of Φ_{ij} are expressed in terms of velocity correlations via the Navier-Stokes equations. Differentiating equation (2) with respect to x_i yields a Poisson equation for the pressure field. After subtraction of the mean part:-

$$\frac{1}{\rho}\frac{\partial^2 p}{\partial x_i^2} = -\underbrace{\frac{\partial^2}{\partial x_k \partial x_l}\left(u_l' u_k' - \overline{u_l' u_k'}\right)}_{A} - 2\frac{\partial U_k}{\partial x_l}\frac{\partial u_l'}{\partial x_k}$$

is the result for flows without sources (eg. gravity effects neglected). For turbulence remote from walls the theory of Poisson equations allows a general solution:-

$$\frac{\breve{p}}{\rho} = \frac{1}{4\pi}\int_{vol} \frac{A' \, dvol}{r}$$

A' is A evaluated at distance r from p

the integration being carried out over all values of r, the magnitude of the separation vector for each p. The pressure fluctuations are then replaced to give, finally, Φ_{ij} in the following form:-

$$\overline{\frac{\breve{p}}{\rho}\left(\frac{\partial u_i'}{\partial x_j} + \frac{\partial u_j'}{\partial x_i}\right)} = \underbrace{\frac{1}{4\pi}\int_{vol} \overline{\left(\frac{\partial u_l'}{\partial x_l} u_m'\right)' \left(\frac{\partial u_i'}{\partial x_j} + \frac{\partial u_j'}{\partial x_i}\right)} \frac{dvol}{r}}_{\Phi_{ij,1}}$$

$$+ \underbrace{\frac{1}{2\pi}\int_{vol} \frac{\partial U_l'}{\partial x_m} \overline{\frac{\partial u_m'}{\partial x_l}\left(\frac{\partial u_i'}{\partial x_j} + \frac{\partial u_j'}{\partial x_i}\right)} \frac{dvol}{r}}_{\Phi_{ij,2}} \qquad (17)$$

$$+ \text{surface integrals } \{\Phi_{ij,1w} + \Phi_{ij,2w}\}$$

in homogeneous flow.

Of the groupings in (17) $\Phi_{ij,1}$ contains only fluctuating quantities while $\Phi_{ij,2}$ is affected by mean strain rates. The unspecified surface integrals are significant near solid surfaces: hence the additional subscript w.

If an anisotropic, homogeneous turbulence field is allowed to decay it is $\Phi_{ij,1}$ which decides whether isotropy is recovered during the decay. The term has been modelled using the *return to isotropy* hypothesis of Rotta (1951):-

$$\Phi_{ij,1} = - C_1 \varepsilon a_{ij} \quad ; \quad a_{ij} = (\overline{u'_i u'_j} - \tfrac{2}{3}\delta_{ij} k)/k \qquad (18)$$

a_{ij} being the anisotropic part of the Reynolds stress tensor made dimensionless by k. The anisotropy of the stresses will increase according to (18) if $C_1<1$ and decrease if $C_1>1$. Proposed values range from 1.4 to 3 with the most favoured value being about 1.8. Alternatives to (18) have been proposed in order to represent the non-linearity of the real process with a model which is non-linear in the Reynolds stresses and good agreement with experiment has been achieved.

Many workers have omitted the contribution to the pressure strain rate of $\Phi_{ij,2}$. The usual manifestation of this is in an increased value for C_1, taking it outside the range quoted above. It is now generally agreed that a model for the processes desribed by $\Phi_{ij.2}$ is required and two major methods have been investigated.

The Isotropisation Of Production Model (IP)

This model was originally proposed by Naot, Shavit and Wolfshtein[2] (1970) as a replacement for $\Phi_{ij,1}$ although now used in conjunction with the model for it, and mirrors the

Rotta model of (18):-

$$\Phi_{ij,2} = - C_2(P_{ij} - \tfrac{1}{3}\delta_{ij}P_{kk}) \qquad (19)$$

The model is intuitively based and expresses the idea that pressure fluctuations will tend to diminish and isotropise the effective stress generation rate by mean shear. The constant has been evaluated with reference to rapidly distorted isotropic turbulence where $C_2 = 0.6$ gives the exact result; the choice $C_2 = 0.55$ appears to be more widely applicable.

The Quasi-Isotropic Model(QI)

This more complex approach attempts to evaluate $\Phi_{ij,2}$ directly from the form stated in (17), subject to some simplifications. In free shear flows the mean strain is considered uniform and taken outside the integral. The integral is written as a fourth order tensor and submitted to various kinematic constraints (Launder[3], IC L4). The final expression reveals a single constant which has been evaluated for a simple shear flow.

Although the QI model is derived analytically, the simplifying assumptions are restrictive and improvement over the performance of the IP model is not confirmed. QI reflects the different values for $\overline{u_2'^2}$ and $\overline{u_3'^2}$ observed in homogeneous shear flows whereas IP permits only equal values, but IP predicts a swirling jet much more accurately than QI. IP is also more readily extended to depend upon turbulence structure and extrapolates better than QI to more complex flows.

Diffusive Transport

Relatively simple models for the terms of d_{ij} are deemed to suffice as this process is not usually of great influence in flows of engineering interest. Some terms contributing to d_{ij} and representing diffusion by molecular action have been omitted from (16) as these are nearly always negligible; the difference between the retained and the neglected terms is that the former are composed of fluctuating velocity derivatives which are large in the fine scale motions while the latter contain fluctuations of velocities themselves which are small. Most workers have neglected the 'pressure diffusion' part of d_{ij} although a model has been proposed which relates it directly to triple velocity correlations. Thus a representation of correlations such as $\overline{u_i' u_j' u_k'}$ is necessary; higher closure levels solve transport equations for these quantities, but in Reynolds stress closure these exact equations are subjected to simplification: the most important procedure is that terms representing convective transport of $\overline{u_i' u_j' u_k'}$ are ignored and this has the effect of reducing the differential equation to an algebraic one which is much more economical to solve. One such equation has been derived in the following form:-

$$-\overline{u_i' u_j' u_k'} = C_s \frac{k}{\varepsilon}\left(\overline{u_i' u_l'}\frac{\partial \overline{u_j' u_k'}}{\partial x_l} + \overline{u_j' u_l'}\frac{\partial \overline{u_i' u_k'}}{\partial x_l} + \overline{u_k' u_l'}\frac{\partial \overline{u_i' u_j'}}{\partial x_l}\right)$$

C_s being a constant determined by computer optimisation. This in principle completes the closure at the level of the Reynolds stresses with respect to the unknown quantities of (16).

Algebraic Stress Models (ASM's)

Motivated by the simplification of the triple velocity correlation transport equation described above, it is noted

that if the convective and diffusive transport terms in the modelled form of (16) are themselves modelled in terms of quantities other than stress gradients, then the order of the Reynolds stress equation is reduced and an algebraic formula for $\overline{u_i' u_j'}$ results. One approach, due to Rodi, is to approximate the transport of stresses in terms of turbulence energy transport, by:-

$$T(\overline{u_i' u_j'}) = \frac{\overline{u_i' u_j'}}{k} . T(k) = \frac{\overline{u_i' u_j'}}{k} . (P_k - \varepsilon) \qquad \text{(see 11)}$$

which may be shown to be approximately true if $\overline{u_i' u_j'}/k$ varies slowly across the flow. Since the number of differential equations in the turbulence model is reduced by these approximations, ASM's are computationally less expensive than the full Reynolds stress models, and some applications indicate that the accuracy of ASM's can be competitive; the penalty is that the algebraic equations may be less stable than their differential counterparts.

§3 The Prediction Of Turbulent Jets

Turbulence closures at all the levels described above have been applied to the axisymmetric free jet problem. Many of the studies are compared and discussed by Schetz[7], and from this review are reproduced solutions (Fig. A1) from various workers using mixing length, eddy viscosity and one-equation (for turbulence kinetic energy) models: all the models appear to give reasonable predictions, although the numerical solutions are often started within the potential core region, downstream from the nozzle[7]. The one-equation models incur an added complication in that estimated boundary conditions must be given for the turbulent kinetic energy k, to which the solution may be sensitive. Two equation (k-ε) models, in which turbulence length scale is treated more directly, do not appear to give markedly improved predictions compared with those in Fig. A1, as illustrated in Fig. A2. It is

worthwhile to note that a set of constants for the k-ε model, 'tuned' to give good results for planar jets, gives significantly overpredicted spread for axisymmetric jets[7]. Errors of this sort have been attributed to deficiencies in the modelling of source terms in the dissipation rate (ε) equation. The use of very sophisticated Reynolds stress models, with the associated, very great increase in computational complexity, does not appear to resolve the problem, and in some instances predicted jet spreading rates are even poorer[7]. Thus, the generality of the higher order models, in predicting accurately both planar and axisymmetric jets, is not established.

The author has implemented at Bath University a general purpose fluid flow package employing a 'built-in' k-ε model of turbulence[8]. Two jet mixing demonstration cases have been studied in connection with the present work[9,10]. In the first[9], a straightforward application to planar and axisymmetric jets in a coflowing stream is made: numerical results are reasonably good (Fig. A3), although non-standard settings for some numerical solution controls were required in order to procure convergence for the round jet problem. The author was not able to obtain a convergent solution at the first station downstream from the nozzle when the external stream velocity was set to zero. In the second case[10], a more detailed application to the axisymmetric jet is undertaken, with the k-ε turbulence model being replaced by a k-W model (transport equations for turbulent kinetic energy and mean square vorticity fluctuations) modified to achieve agreements with experiment for round jets[10]. An equation for the mean square concentration fluctuations is also included in order to predict the (passive scalar) concentration field. A turbulent Prandtl number σ_c=0.7 was used, based upon experiment. The downstream marching solution procedure employs a finite-difference grid which expands with the jet width[10]: computer storage and time requirements are very modest. Numerical results for a round jet are summarised in Fig. A4, the modified turbulence model ensuring good results. From the predictions, the

author investigated the approach to similarity of the radial mixing zone velocity and concentration profiles in the early part of the jet, the results being illustrated in Fig. A5. In the initial region especially the precise location of the mixing zone boundaries is difficult to determine, and this indeterminacy may influence the representation of the profiles: however, continuous development and decreasing fullness of profiles through the transition region appears to be indicated. The model[10] may be extended to the case of variable density jets.

Jets deflected by a crossflow present a more difficult modelling task. In the first instance, a Cartesian co-ordinate grid which encloses the curved jet flow will contain regions of very little disturbance in the external stream, so that nonuniform grid spacings are required for detailed studies. Furthermore, the boundary conditions apllied to the edges of the flow domain will significantly affect the predictions unless the boundaries themselves are sufficiently remote. Two equation models appear to be the optimum choice for turbulence closure[1]: the details of the turbulence field are not as influential as in the axisymmetric jet as the flow structure is determined largely by pressure effects. Reynolds stress models, more formally correct for flows with strong streamline curvature, prove too expensive computationally when the fully three dimensional flow equations are to be solved, and extra computing capacity is more usefully taken up with refinement of the solution grid. Solution procedures using different turbulence closures depending upon the degree of streamline curvature have been investigated[2].

A detailed description of the prediction of nonisothermal deflected air jets has been given by Jones and McGuirk[11]. A turbulent Prandtl number $\sigma_T=0.9$ was used for the prediction of the temperature field. The predicted distortion of the jet shape is illustrated in Fig. A6: maximum temperature axes compare sufficiently well with experimental data, although jet spread appears to be overpredicted (Fig. A7).

The author has constructed a very crude jet into crossflow model using the package described earlier[8]. A demonstration case for mixing at a T-junction[12] was modified in order to represent injection from a square nozzle. Resulting passive scalar contours in the trajectory plane, generated as line-printer plots, are shown in Fig. A8 for different ratios of the uniform injection to free stream velocities. An extremely coarse computational grid (20x10x10) was used in these examples, so that lateral jet spread is likely to be greatly overpredicted, through the effect known as 'false' or 'numerical' diffusion which occurs when the flow is skewed relative to the grid.

Notation For Figures

C	-	injectant concentration
d	-	nozzle diameter
U	-	axially directed velocity
x	-	axial distance

Subscripts

0	-	at the nozzle
c	-	on the jet axis
∞	-	in the external stream

TKE - turbulence kinetic energy equation

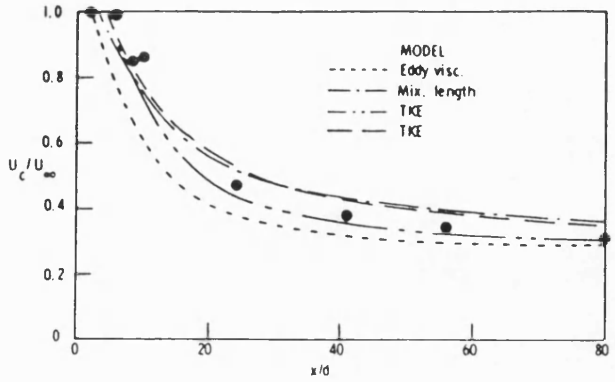

Axial Velocity Decay In An Air-Air Jet

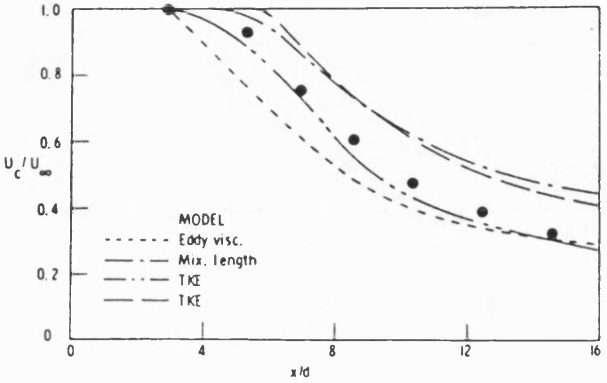

Axial Velocity Decay In An H_2-Air Jet

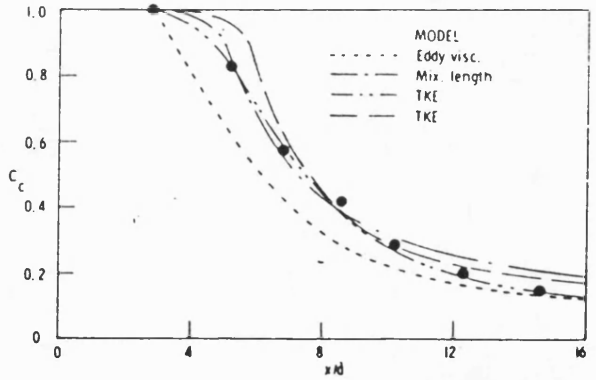

Axial Concentration Decay In An H_2-Air Jet

predictions and data collected by Schetz[7]

FIG. A1 PREDICTION OF AXISYMMETRIC JETS BY TURBULENCE MODEL METHODS

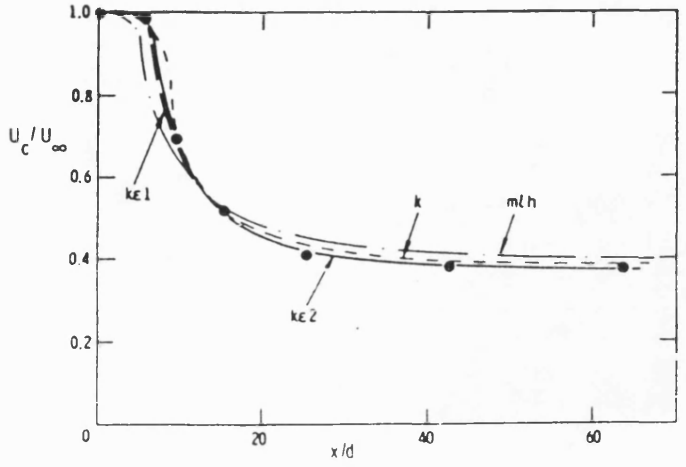

Axial Velocity Decay In An H_2-Air Jet

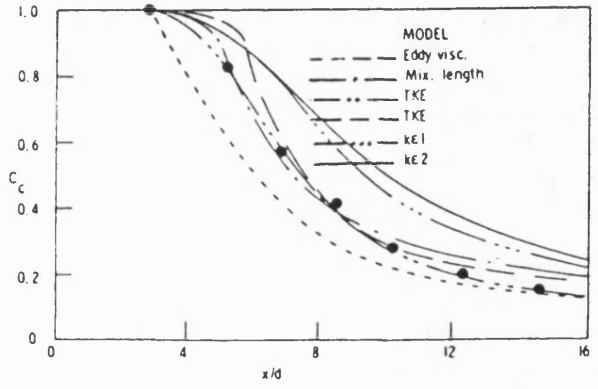

Axial Concentration Decay In An H_2-Air Jet

predictions and data collected by Schetz[7]

FIG. A2 PREDICTION OF AXISYMMETRIC JETS BY TWO-EQUATION TURBULENCE MODELS

$U_0 / U_\infty = 6.25$

The results of the plane-jet case are compared with the experimental values of Bradbury (1965) at 50 slot-heights downstream of the slot. As the diagram on the right shows, the predicted axial-velocity profile is in excellent agreement with the experimental values.

δ: HALF WIDTH $\left(\frac{U - U_\infty}{U_c} = 0.5 \right)$

r: RADIAL DISTANCE

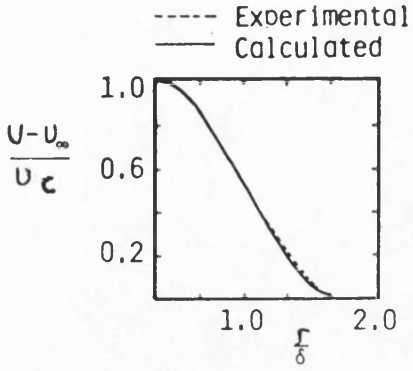

CHAM PDR/1		DOWNSTREAM VELOCITY PROFILE

The decay of the centre-line velocity and the spread of the jet with downstream distance are shown on the right.

h: NOZZLE SLOT HEIGHT

x: AXIAL DISTANCE

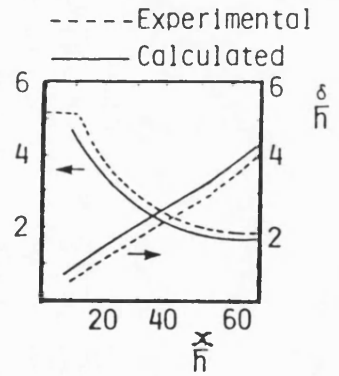

CHAM PDR/1		CENTRE-LINE VELOCITY DECAY, AND JET SPREAD

FIG. A3 PREDICTIONS FROM REF. 9

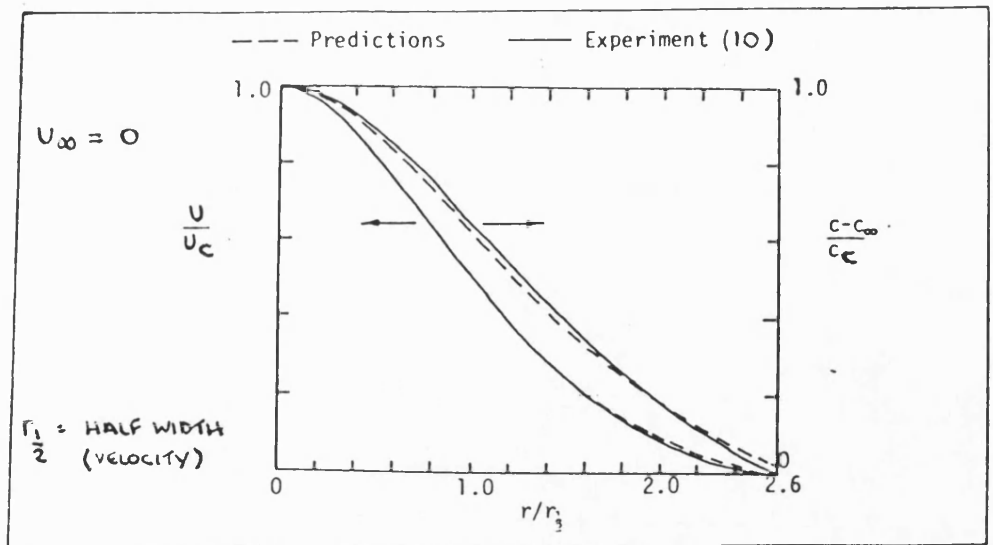

CHAM PDR/18		ROUND JET: COMPARISON OF PREDICTED AND EXPERIMENTAL MEAN-VELOCITY AND MEAN-CONCENTRATION SIMILARITY PROFILES

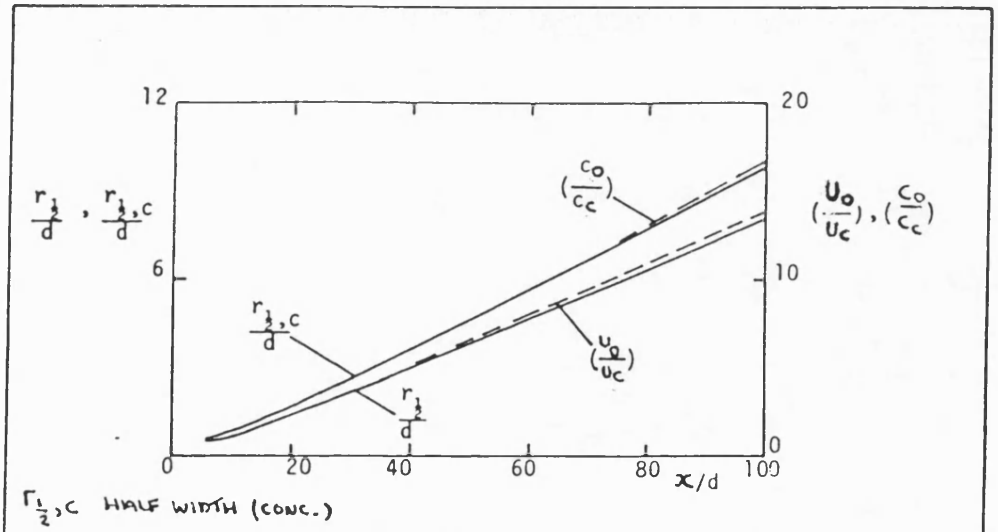

CHAM PDR/18		ROUND JET: PREDICTED AXIAL VARIATION OF MEAN-FLOW CHARACTERISTICS

FIG. A4 PREDICTIONS FROM REF. 10

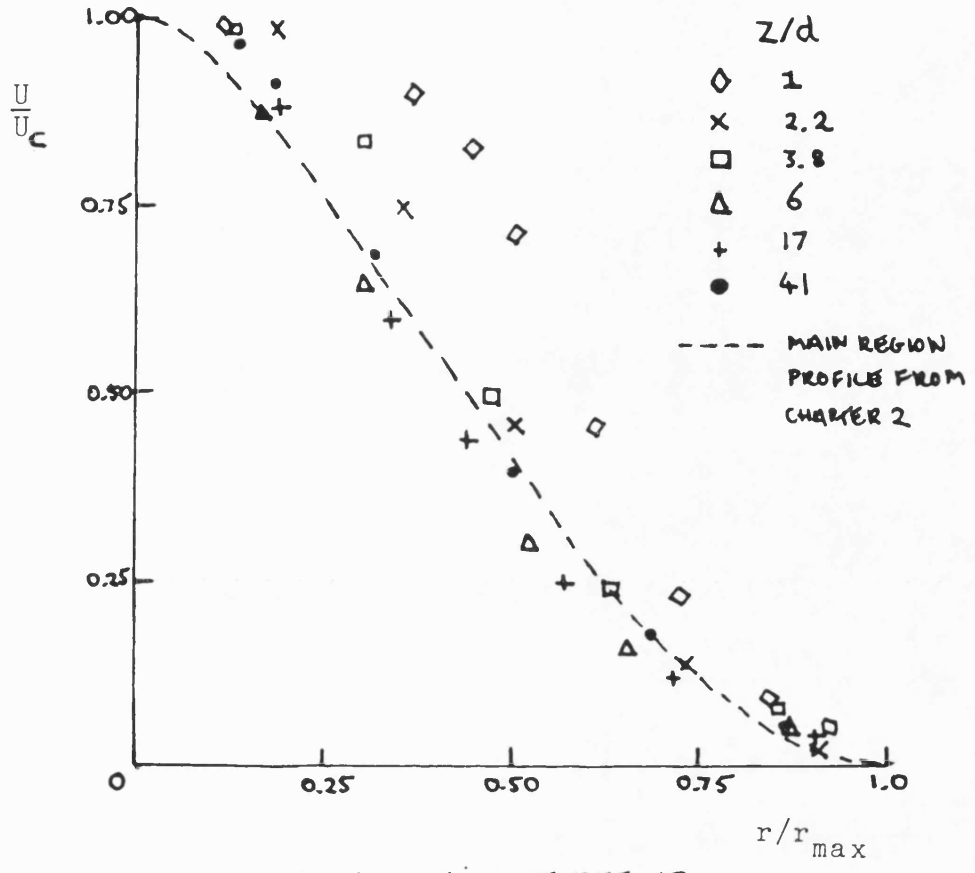

predicted axial velocity begins at
$z/d \approx 4$ (10)

FIG. A5 VELOCITY PROFILES IN AN AXISYMMETRIC JET

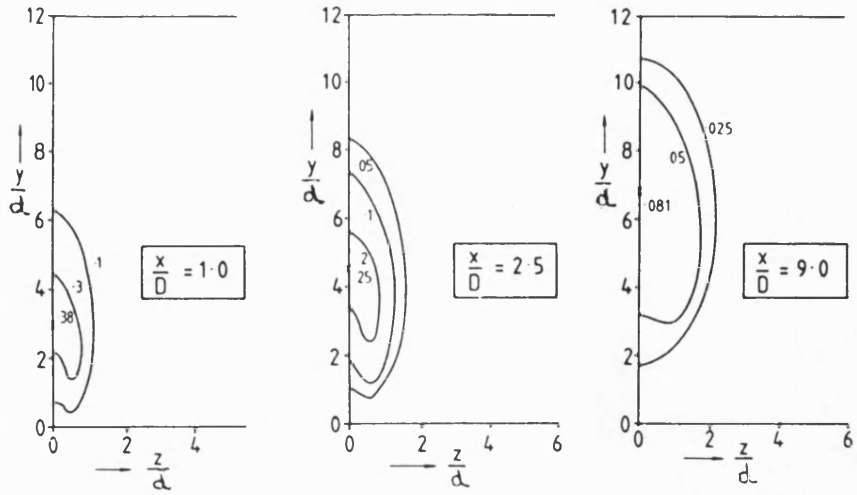

FIG. A6 TEMPERATURE CONTOURS IN CROSS-SECTIONS PREDICTED BY JONES AND McGUIRK (11)

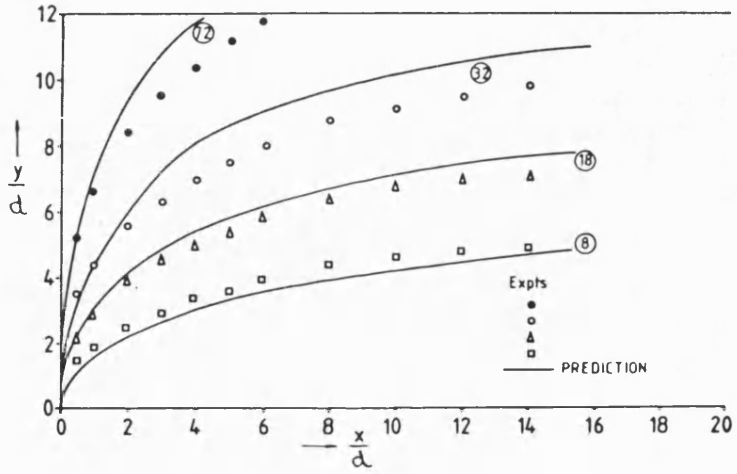

PREDICTED TEMPERATURE TRAJECTORIES

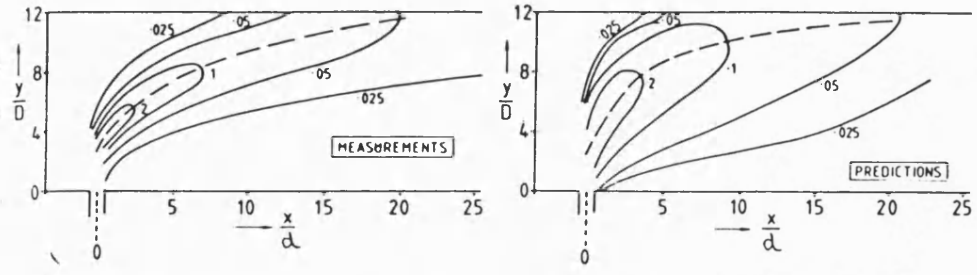

TEMPERATURE CONTOURS IN THE TRAJECTORY PLANE

FIG. A7 PREDICTIONS COMPARED WITH DATA FROM (11)

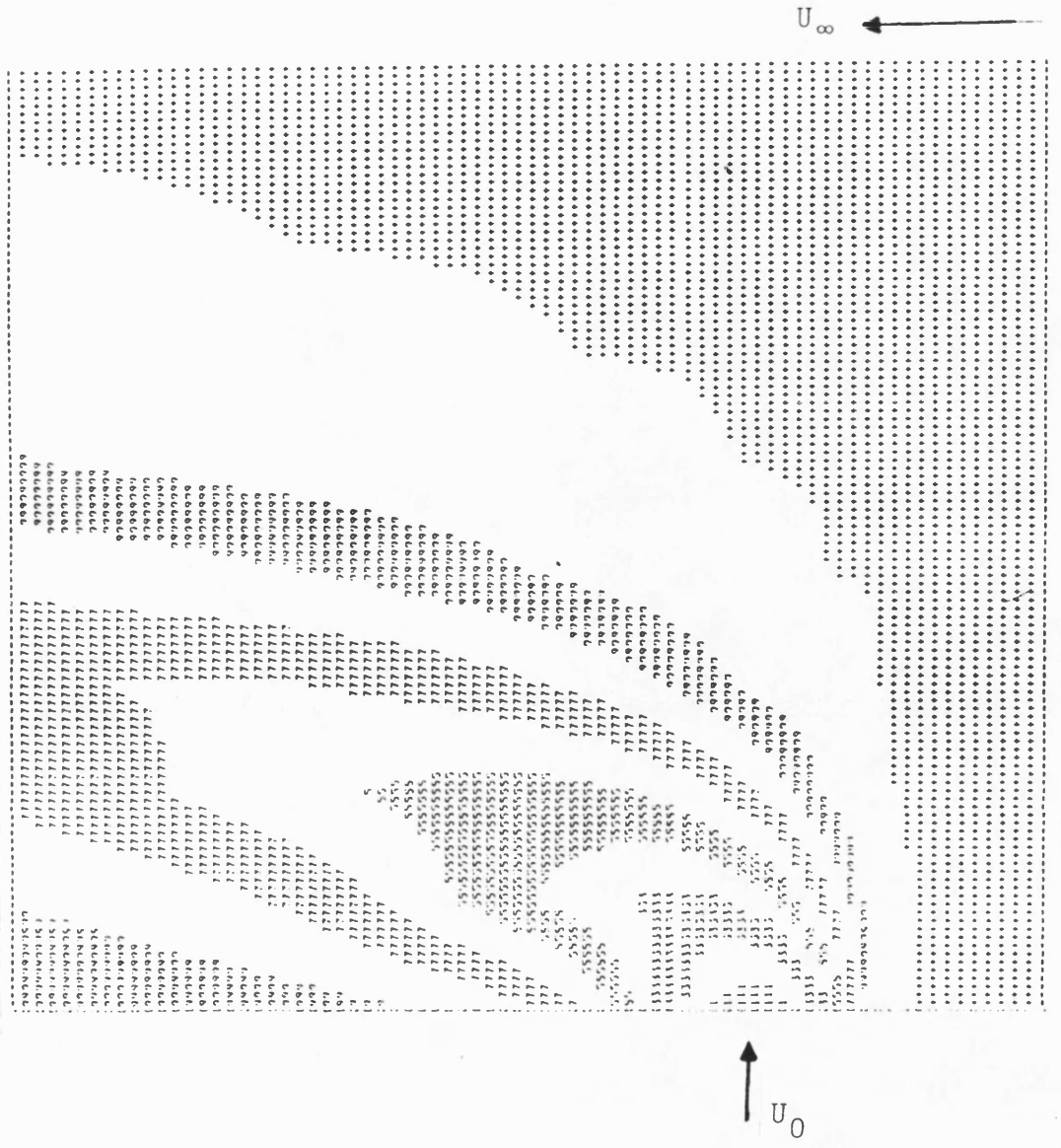

$$\frac{U_0}{U_\infty} = \frac{1}{2}$$

FIG. A8a PREDICTED SCALAR CONTOURS IN A DEFLECTED JET

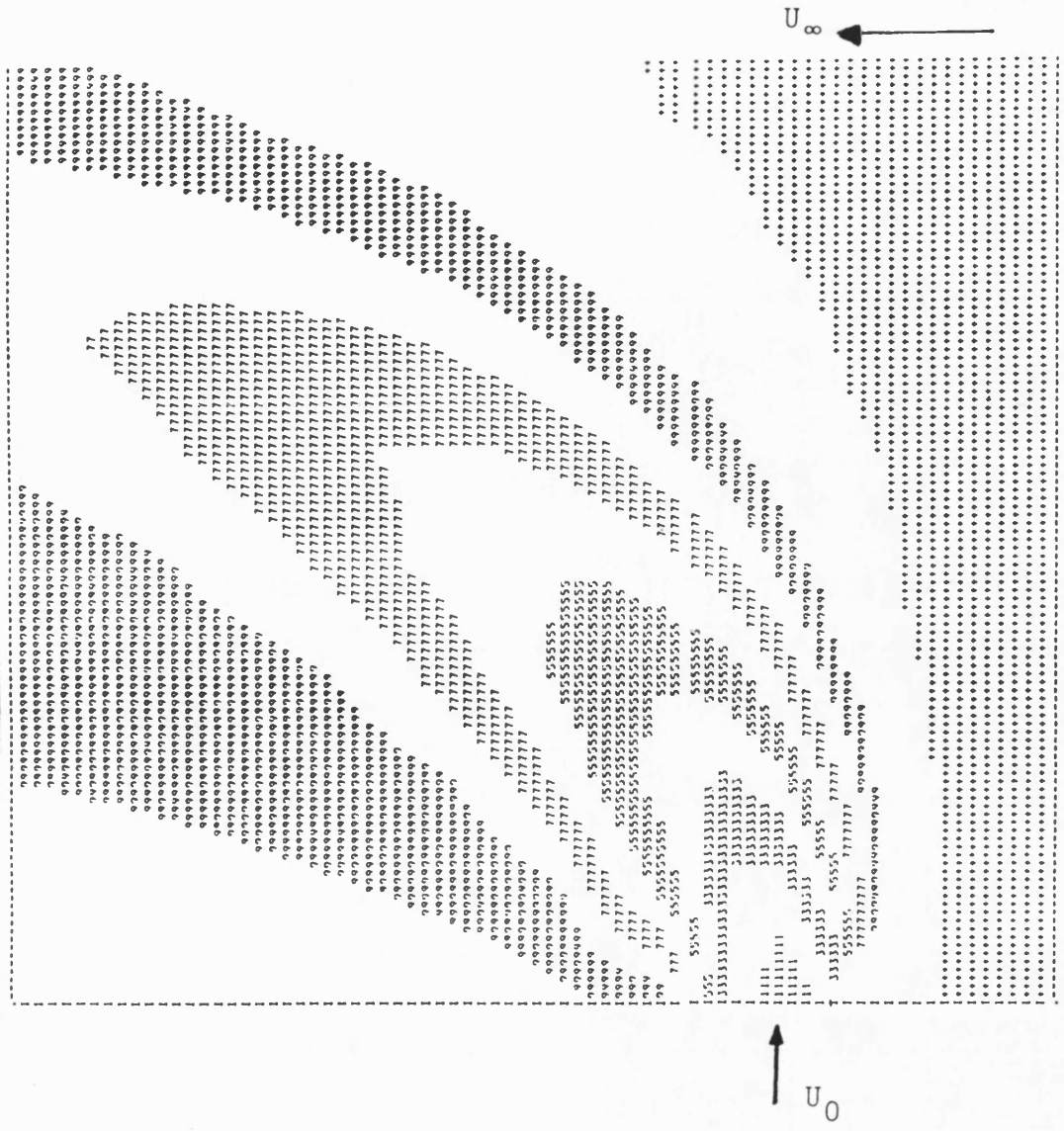

$$\frac{U_0}{U_\infty} = \frac{1}{4}$$

FIG. A8b PREDICTED SCALAR CONTOURS IN A DEFLECTED JET

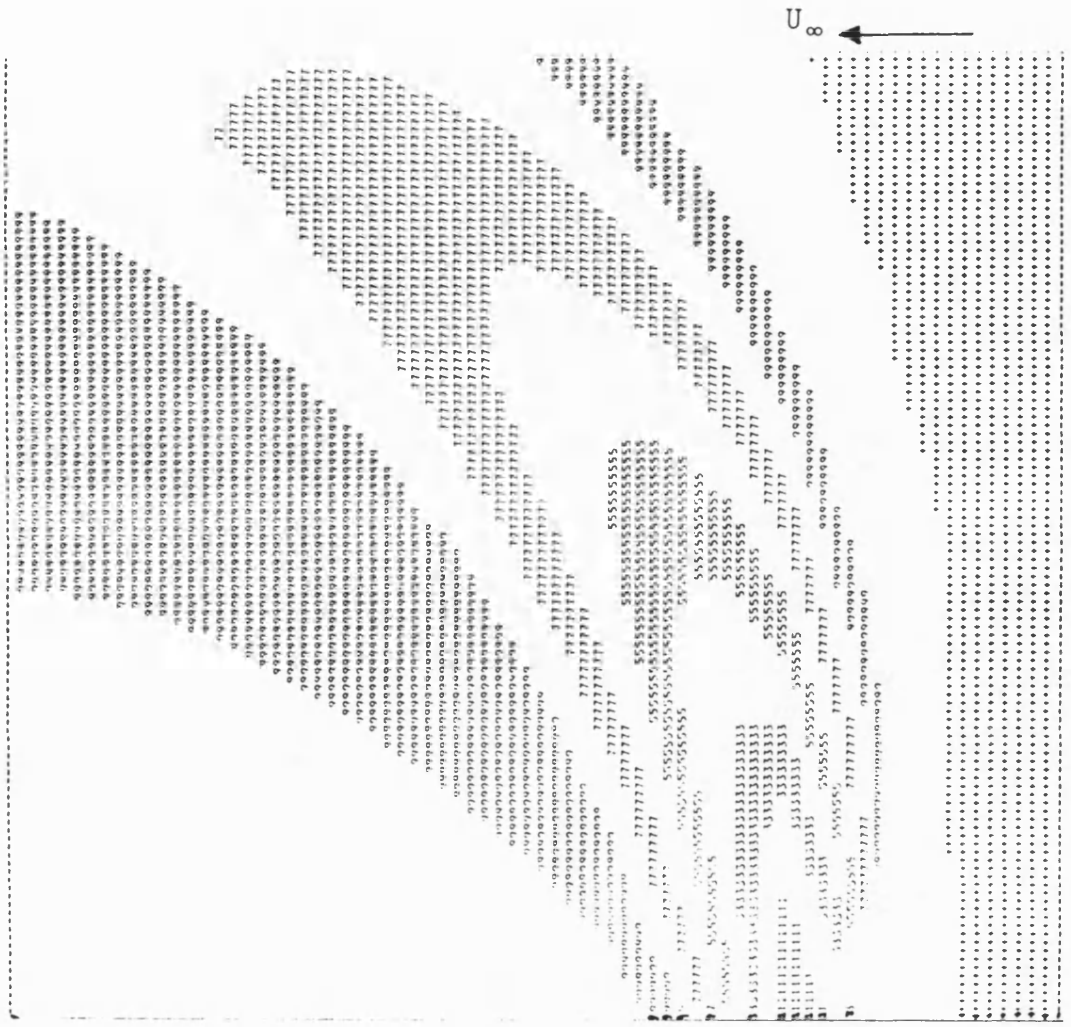

FIG. A8c PREDICTED SCALAR CONTOURS IN A DEFLECTED JET

REFERENCES FOR APPENDIX A

1. GIBSON, M.M., JONES, W.P., McGUIRK, J.J. and WHITELAW, J.H. (1984) Turbulence Models For Computational Fluid Dynamics; Outline Lecture Notes, Imperial College, London.

2. LAUNDER, B.E., LESCHZINER, M.A. and BETTS, P.L. (1984) Numerical Methods In Heat And Fluid Flow (I and II); UMIST, Manchester.

3. LAUNDER, B.E. (1983) Second-Moment Closure: Methodology And Practice; UMIST, Manchester.

4. SPALDING, D.B. (1980) Numerical Modelling Of Fluid Mechanics, Heat Transfer And Combustion Processes: A Lecture Course; Imperial College CFDU Report HTS/80/81.

5. BRADSHAW, P. (1977) Turbulence; Topics In Applied Physics, 12, Springer-Verlag, Berlin.

6. TENNEKES, H. and LUMLEY, J.L. (1972) A First Course In Turbulence; MIT Press.

7. SCHETZ, J.A. (1980) Injection And Mixing In Turbulent Flow; Progress In Astronautics And Aeronautics, vol 68.

8. PHOENICS User Manual (1981); CHAM, London.

9. MALIN, M.R. and ROSTEN, H.I. (1982) Turbulent Jet Issuing Into A Free Stream; PDR/CHAM UK/1

10. MALIN, M.R. (1983) Prediction Of The Hydrodynamic And Thermal Characteristics Of Self-Presrving Free Jets By Use Of A Revised k-W-g Model Of Turbulence; PDR/CHAM UK/18.

11. JONES, W.P. and McGUIRK, J.J. (1979) Computation Of A Round Turbulent Jet Discharging Into A Confined Free Stream; Turb. Shear Flows 2, pp 233-245.

12. ROSTEN, H.I. and TATCHELL, D.G. (1982) Mixing At A T-Junction; PDR/CHAM UK/2.